CHARACTERISATION OF DEFORMATION AND BREAKAGE OF AGGLOMERATES

by

Abdolreza Samimi

A thesis submitted for the degree of

Doctor of Philosophy

in the

University of Surrey

Guildford, Surrey, GU2 7XH

September 2003

To Farahnaz, Saeid and Sahar

ABSTRACT

Producing agglomerates with appropriate strength to withstand handling and storage and to break when desired is a challenging task in industries involving particulate solids. For design of appropriate machinery, it is necessary to characterise the breakage of these materials. In view of the above objective, this thesis addresses the deformation and breakage characteristics of three types of model agglomerates under different modes of loading, strain rates, number of impacts and impact angles.

The yield stress and strength of the agglomerates are determined by single particle and bulk compression analyses. For soft granules, the yield pressure obtained from the Heckel analysis of the bulk compression data is found to be lower than the yield stress obtained from the single granule tests. The difference is of great interest as previous workers have argued that the bulk analysis method gives directly a measure of the single particle yield stress. It is also shown that the initial part of the bed pressure-displacement data should not be considered as solely rearrangement of granules in bed as yielding of granules may also occur in this part. A correlation is proposed relating the yield stress and apparent strength of the granules.

The granules have also been tested under impact condition. The observations of the impact products reveal a macroscopic plastic deformation of the impact site and microscopic ductile failure of the binder (elongation and rupture of the binders) within the crack openings. It is shown that the irregular and porous structure of these granules provides sufficient stress concentration by which semi-brittle fragmentation of the granules occurs. Furthermore, the complement modulus (defined as the slope of the line of cumulative mass fraction undersize of debris and small fragments plotted on a log-log scale as a function of normalised size) of the fragments is independent of impact velocity and impact angle. However, the extent of breakage of these agglomerates increases with decreasing impact angle, as measured between the incident direction and target plane. The repeated impact of soft granules reveals that the average extent of breakage per impact increases to a maximum at a certain impact number. This maximum breakage per impact depends directly on the impact velocity and the granule feed size. An empirical correlation is proposed in which the cumulative extent of breakage is varied as a function of impact number and maximum average breakage per impact.

The work presented in this thesis is an extensive study of the deformation and the breakage of soft agglomerates and provides a better understanding of the failure behaviour of such complex structures.

ACKNOWLEDGEMENTS

I would like to express my sincere gratitude and appreciation to my supervisor Professor Mojtaba Ghadiri for giving me not only the opportunity of working in this project but also for his continuous support during my PhD duration. This work would not have been possible without his constant encouragement and support. His experience and timely attention motivated me greatly. I wholeheartedly thank for his supervision and friendship. I would like also to thank Dr Jamie Cleaver my second supervisor at the University of Surrey for his guidance.

Working in Professor Ghadiri's Research Group at the School of Engineering of the University of Surrey gave me this chance to develop friendship with a large number of people. It is not possible to name them all here. However, I would like to thank them for their support, friendship and hand-on help. In particular, I thank Mr. Ali Hassanpour for his friendship and collaboration by doing simulations using Distinct Element Method. Discussion with Dr. Roberto Moreno enhanced my understanding of the breakage of agglomerates for which I am grateful. Miss Chih Chi Kwan's help during the past years has been of significant value to me.

The personnel of School of Engineering of the University of Surrey need special thanks for their constant help and their efforts to support this project. In particular I am indebted to Mr Dave Arnall for his help with the instruments of the impact rigs, Mr Gerald Shurlock for his mechanical workshop help and Dr Andy Tate for his computer support. I would also like to thank Mr Bryan Underwood and Mrs Penny Briggs for their administrative helps, and Mrs Maureen Harvey and Mrs Carol Prouse from finance office for their help over these years.

Financial support of Ministry of Science Research and Technology of Iran for my studentship is gratefully acknowledged. I would also like to thank Unilever Research, Vlaardingen, for their financial support of the research programmes as well as preparation and sending of the test materials. In this context, I especially thank Drs Renee Boerefijn, Reinhard Kohlus and Andrew Groot.

Last but not least, this work could not have been done without continuous encouragement, patience and support of my family, my beloved wife Farahnaz and children Saeid and Sahar. It was a difficult duration especially for my children to lose their best time due to the education of their father. I hope completion of this work makes them feel that their patience was worthy.

CONTENTS

NOTATION

a_c	Constant in Equation 6.23	-
a	Constant of Kawakita Equation 2.30	-
a_f	Fracture surface area Equation 2.4	m^2
A_o	Total cross section area of bed	m^2
A_t	Total cross section area of active column of particles in bed	m^2
A_r	Real contact area between the particles	m^2
A	Constant parameter of Heckel model Equation 2.24	-
b	Kawakita *et al.* parameter in Equation 2.30	Pa^{-1}
c	Crack length	m
$C_1 - C_3$	Constants in Equations 6.12 – 6.14	-
d	Diameter of spherical particle	m
D	Relative density	-
D_c	Diameter of compression cell	m
e	Coefficient of restitution	-
E	Young's modulus	Pa
E^*	Effective Young's modulus of elasticity of an agglomerate	Pa
$E_{m,kin}$	Impact energy	$J\ kg^{-1}$
$E_{m,c}$	Critical energy	$J\ kg^{-1}$
f	Strain hardening exponent in Equation 2.47	-
f_{mat}	Material parameter in Equation 2.11	$kg\ J^{-1}m^{-1}$
F_b	Applied force on confined bed of particles	N
F	Mean value of inter-particle bond force	N
F_f	Failure force of single granule	N
G_c	Critical strain energy release rate	$J\ m^{-2}$
G_i	Fracture energy at crack initiation	$J\ m^{-2}$
G_R	Fracture energy	$J\ m^{-2}$
h_a	Length characteristic of surface asperities	m
h_o	Initial bed height at zero bed pressure	m
h_p	Bed height at the bed pressure of P	m
H	Hardness	Pa
j	Strain rate exponent in Equation 2.47	-

k_1	Weibul parameter in Equation 2.1	m s^{-1}
k_2	Proportionality constant in Equation 2.27	-
k_3	Proportionality constant in Equation 2.37	-
k_4	Proportionality constant in Equation 2.39	-
k_5	Proportionality constant in Equation 2.50	-
k_l	Parameter in Equation 6.19	
k_n	Average incremental breakage per impact Equation 6.7	-
k_v	Proportionality factor.	
k_{max}	Maximum average breakage per impact	-
K	Heckel parameter	Pa^{-1}
K_c	Fracture toughness	N $m^{-3/2}$
K^*_c	Effective fracture toughness of an agglomerate	N $m^{-3/2}$
L	Particle size	m
L_o	Initial particle size	m
L_c	Critical particle size	m
m	Weibul parameter in Equation 2.1	-
M	Mass of sphere in Equation 2.48	kg
M_L	Total mass of unbroken particles with size L	m
$M_{c(i)}$	Mass of particles collected after the i^{th} impact	kg
$M_{f(i)}$	Mass of particles fed to the i^{th} impact	kg
$M_{de(i)}$	Mass of debris after the i^{th} impact	kg
$M_{m(i)}$	Mass of mother particles after the i^{th} impact	kg
n	Number of impact	-
P	Bed pressure	Pa
P_a	Axial applied bed pressure	Pa
P_l	Lateral bed pressure	Pa
P_t	Axial transmitted bed pressure	Pa
P_y	Yield pressure	Pa
r_p	Size of process zone at the crack tip	m
R	Regression fitting of data	-
R_s	Radius spheres in Equation 2.48	m
s_l	Specific breakage rate of particle size of L in Equation 2.13	-
St_v	Stokes number in Equation 2.48	-

St^*_v	Critical stokes number in Equation 2.49	-
S_L	Specific breakage rate of particle size of L in Equation 2.12	-
t	Time	s
T_a	Tearing modulus	J m^{-4}
U_e	Elastic strain energy stored in the solid	J
U_s	Surface energy	J
U	Absorbed energy by specimen in impact	J
v_b	Bridge volume	m^3
v^*_b	Dimensionless bridge volume	-
V	Impact velocity	m s^{-1}
V_c	Critical impact velocity	m s^{-1}
V_f	Normal failure velocity	m s^{-1}
V_o	Collision velocity of spheres in Equation 2.48	m s^{-1}
V_p	Poisson ratio	-
w_e	Weber number	-
W	Rupture energy	J
W^*	Dimensionless rupture energy in Equation 2.50	-
$Y_L(n)$	Cumulative mass fraction (or percentage) of unbroken particles with initial size of L	-
$Y(L)$	Cumulative mass fraction (or percentage) undersize L	-
Z	Co-ordination number	-

Greek characters

α	Lateral pressure coefficient in Equation 2.35	-
α_1	Proportionality constant in Equation 2.3	-
α'	Adams *et al.* parameter in Equation 2.41	-
β	Proportionality constant in Equation 2.9	-
γ	Surface energy (surface tension)	J m^{-2}
δ_b	Binder thickness around the particle in Equation 2.49	m
Γ	Interface energy	J m^{-2}
Γ_{eq}	Interface energy measured at equilibrium	J m^{-2}
Γ_f	Interface energy measured at fracture	J m^{-2}

Δ	Damage ratio	-
Δ'	Number of broken contact per primary particle	-
Δ_c	Crack size increase in Equations 2.57 and 2.58	m
ε	Strain	-
ε_e	Engineering strain	-
ε_n	Natural strain	-
$\dot{\varepsilon}$	Strain rate	s^{-1}
ζ	Breakage probability	-
ϕ	Packing or solid fraction	-
η	Attrition propensity	-
φ_1	The angle of wedge shape target	o
φ	Dimensionless parameter in Equation 2.57	-
χ	Exponent of Equation 2.14	-
κ	Constant in Equation 2.14	-
κ_1	Constant in Equation 2.47	various
λ	Distribution modulus of complement	-
μ	Viscosity	P
μ_f	Wall friction coefficient	-
ν_o	Initial bed porosity	-
ν	Bed porosity	-
ξ	Extent of breakage	-
ξ_i^-	Incremental lower extent of breakage at i^{th} impact in Equation 6.1	-
ξ_i^+	Incremental upper extent of breakage at i^{th} impact in Equation 6.2	-
ξ_i^*	Incremental extent of breakage at i^{th} impact in Equation 6.3	-
$\xi^-_{c(n)}$	Cumulative lower extent of breakage at i^{th} impact in Equation 6.4	-
$\xi^+_{c(n)}$	Cumulative upper extent of breakage at i^{th} impact in Equation 6.5	-
$\xi^*_{c(n)}$	Cumulative extent of breakage at i^{th} impact in Equation 6.6	-
π	Pi equal to 3.1415926536	-

θ	Impact angle	^{o}
ρ	Density	kg m^{-3}
ρ_{bulk}	Bulk density	kg m^{-3}
ρ_{true}	true density	kg m^{-3}
τ	Shear failure stress	Pa
τ_o	Cohesive strength of single particle	Pa
τ_o'	Adams *et al.* parameter Equation 2.43	Pa
σ	Uni-axial pressure (stress)	Pa
σ_f	Tensile strength in Equations 2.51, 2.53, 2.59 and 2.61	Pa
σ_y	Yield stress	Pa
σ_{ayp}	Apparent yield pressure	Pa
σ_{os}	Single particle apparent strength	Pa
σ_{by}	Confined yield stress	Pa
ψ	Porosity or void fraction	-
ψ_s	Stress distribution factor	-

LIST OF FIGURES

1 INTRODUCTION

1.1 Background

Particle Technology deals with the transformation of solids system by predominantly mechanical operations in order to modify their mechanical properties (Rumpf 1990). In recent years, the development of particle processing technologies especially in food, hygienic and pharmaceutical industries has had an important impact on changing the quality of human life. For example, a major part of the products of Unilever and Nestle, two well-known and multi-national food-base companies are in granular or particulate form. The products of other industries like mineral processing, oil, petrochemical, paint, agrochemical are also mostly in particulate form. The operations applied to these solids involve size reduction, agglomeration or size enlargement, solid-solid separation, dispersion, suspension, solid mixing, coating, pneumatic transport, storage, tabletting and many others.

Granulation as an industrial generic terminology is defined as agglomeration by agitation (Ennis and Litster 1997), where agitative processes include fluid bed, pan (or disc), drum, and mixer granulators. The objectives of the formation of granules are to improve flowability, in-use performance, and appearance, or to form desired product structures and compositions by enabling precise quantities of an active ingredient to be reacted or blended with often-larger quantities of carriers. The achievement of these final aims is highly dependent on the mechanical properties, which in turn depend on a number of structural and microscopic characteristics of granules such as porosity, shape and size distribution of primary particles, and the distribution of particles and binders in the granules. The mechanical and structural characteristics of granular products can be affected by the process routes and their operative variables. Furthermore, material formulation such as bond type and its characteristics are also important, affecting the intrinsic mechanical and structural properties of granules.

The mechanical *strength* of granules plays an important role in balancing the necessary strength of granules to withstand stresses during transportation, handling, and storage, and to disintegrate to the required size when necessary. Mechanistic approaches to the determination of the strength of agglomerates basically rely on principles of fracture mechanics, which yields three important mechanical parameters of *hardness*, *Young's modulus* and *fracture toughness*. Hence, a fundamental understanding of granule failure behaviour requires a detailed structural study and mechanical property characterisation.

The failure behaviour of granules may also be affected by the mode of contact loading. The mode of loading includes load direction, rate of loading, and conformation of load application. Applied load direction with respect to the solid surface in contact areas may be normal or tangential, leading to different stress fields in the granules such as tensile or shear stresses. Loading rate may change from *quasi-static*, where distribution of stress field is considered in equilibrium state and the rate of loading is slow, to *dynamic,* where high strain rates and shock wave propagation determines the intensity of the developed stress fields in granules. Stress field may be *localised* as in compression of sharp corners and small contact area of agglomerates or *distributed* as in compression of large contact area between two flat platens and bulk compaction of granules bed. However various combinations of agglomerates mechanical and structural properties with *mode of loading* may lead the granules failing in three distinct *failure modes* known as *brittle, semi-brittle*, and *ductile*. The failure mode may cause different regimes of breakage and material removal such as *chipping* and *fragmentation*. The material removal from the surfaces of the particulate solids in the form of *debris* of thin platelets is referred to as chipping. On the other hand, fragmentation is defined as splitting of the original particle to a number of large pieces, which usually occurs at higher loading. Therefore, the characterisation of the mechanical and structural properties of the granules as well as their failure behaviour under different modes of loading facilitates the design of appropriate granulation processes in order to achieve the in-use objectives of the granules production, i.e. proper strength of these materials during handling. The above interrelations among the structural and mechanical

properties of granules, mode of loading, mode of failure, and granulation process parameters have been illustrated in Figure 1.1.

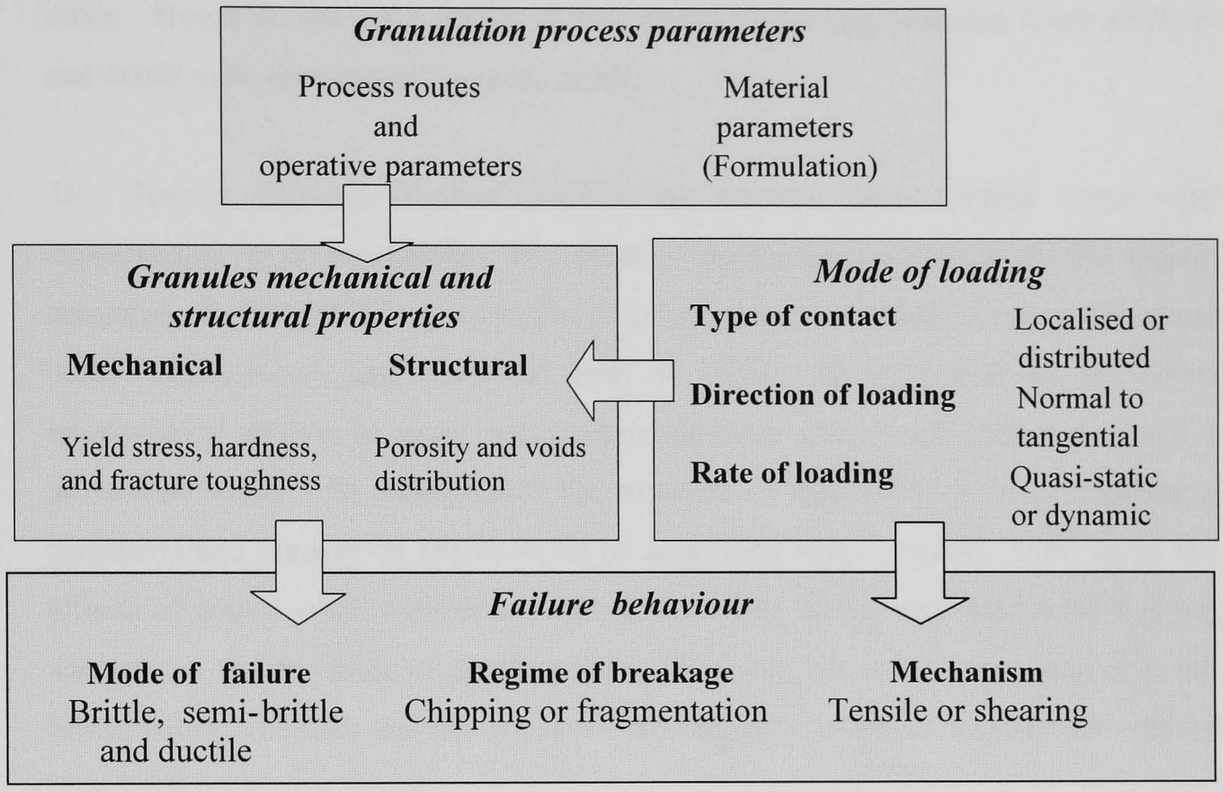

Figure 1.1: *Interrelations of the structural and mechanical properties, mode of loading and failure behaviour of granules.*

1.2 Project Introduction

The attrition behaviour of different particulate solids from crystalline to more complicated structures such as porous and agglomerated solids has been extensively investigated by Ghadiri and co-workers. Most of their investigations have focused on the impact breakage characterisation of brittle and semi-brittle materials. The breakage propensity of semi-brittle solids in the chipping regime has been modelled as a function of macroscopic mechanical properties such as hardness and fracture toughness (Ghadiri and Zhang 2002). Papadopoulos (1998) investigated the validation of this model for a wide variety of particulate solids using single particle

impact testing method. Evaluation of the experimental data of his work and the literature indicates that the Ghadiri and Zhang (2002) model is a powerful tool for predicting the chipping propensity of particulate solids failing by the semi-brittle mode. However, the applicability of this model to the agglomerates is not obvious and needs to be investigated in more detail.

The Distinct Element Method (DEM) has recently been applied along with experimental work to elucidate the effect of agglomerate structure on the impact breakage. Subero (2001) systematically investigated this effect using experimental model agglomerates and simulated them by DEM. He developed an innovative experimental method to make agglomerates of large glass beads (given size) and a polymeric binder. He manipulated the structure of agglomerates by introducing a predetermined number of macro-voids of controlled sizes. Subero could show the effects of macro-voids number as well as their size along with inter-particle bond strength on the breakage of agglomerates. However, his work was confined to the brittle failure of binder and has not addressed the other modes of bond failure such as liquid and paste type binders.

Increasing interest toward agglomerate materials and lack of information about their structural and mechanical properties as well as their breakage behaviour under different modes of loading necessitate the experimental work on industrial samples. Some detergent granules are of these types, for which there is limited breakage information. At a first glance detergent granules seem soft with low porosity and high ratio of binder to solid. These paste type granules, which show appreciable plastic flow under relatively small-applied stresses, are regarded as soft granules. As they dry up, their failure mode may switch from ductile to semi-brittle and may even become fully brittle. Furthermore, strain rate, temperature, and relative humidity may have significant effect on their strength and failure mode. In detergent processing, the produced granules often have a wide size distribution so that the fines must be returned to granulator and the oversize granules have to be milled. Selection of the optimum granulation process parameters as well as the appropriate post-processing milling facilities in order to produce granules with a narrow size

distribution and desired in-use characteristic have revealed the need for a mechanistic breakage characterisation of this type granules.

1.3 Objectives and structure of the thesis

The main objective of this thesis is to elucidate the breakage behaviour of three model agglomerates: one made of large calcium carbonate particles (known commercially as Durcal) with a polyethylene binder and the other two made of detergent base granules with the same formulation but produced through different manufacturing routes. The test materials have been selected with the aim to extend the breakage study of agglomerates to the material type with properties and structures that are different from those tested previously. In fact, the selection of tests materials combines their scientific merits with current industrial interest. In the investigations, characterising the sensitivity of granule strength to different modes of loading is the prime task. The influence of strain rate on granule strength for various types of granules with different properties and process history is addressed. A further objective of the study is to investigate the effect of number of impact and impact angle on the breakage propensity of granules. The study is designed with the aim to elucidate the breakage dependency of the granules on stress, strain rates, and breakage input energy in different environmental conditions so that the results can be used for the selection of milling method and granulation process. The approach is experimental and is supported by theoretical analyses when appropriate. A major part of the work is focussed on the impact testing of single granules. However, the other modes of loading especially quasi-static single and bulk compressions are also studied. This work is the first systematic experimental study of soft granule breakage, and provides a new insight on the failure behaviour of such complex structures.

A comprehensive and up to date review of the literature is presented first. The characteristics of test materials including information about physical properties, and preparation of samples for tests are addressed. Then, the results of the experimental investigation are presented in three chapters. In these chapters, the experimental

procedures and tests results are presented and discussed. The breakage behaviour of the granules are characterised on several scales by various techniques such as quasi-static single and multi-particle compression, and dynamic single particle impact tests. The breakage of samples in dynamic conditions is quantified using the modified single particle impact test device developed originally by Yüregir *et al.*, (1987). This enables the relationships among the extent of breakage, impact velocity and particle size to be established. The effects of temperature, moisture content, angle of impact and the number of impacts on the extent of breakage are also investigated. Optical microscopy and high-speed video recording along with image analysis are employed to observe the breakage and to analyse the mechanism under different operating conditions. A more detailed outline of the thesis and a description of chapters are given below.

Chapter 2 A literature review of theoretical and experimental work on particle breakage is presented in this chapter. An overview of particle attrition including theoretical models and failure mechanisms are described first. The literature regarding the agglomeration processes and agglomerate properties are then reviewed. In this section, existing models of strength, and mechanical and structural properties of agglomerates are discussed and their inadequacies especially for soft material are identified.

Chapter 3 In this chapter the characteristics of granules of interest are listed and the methods employed for the preparation of representative samples are described. Three types of test granules are selected based on their different processing methods and evolved structural characteristics. The preparation steps include sieving of materials in order to produce required sieve cuts, finding out the size distribution of representative samples, and analysing microscopic image of the original granules before experiments.

Chapter 4 This chapter provides the quasi-static compression results of single granules and a bed of granules. The main purpose is to quantify the strength of single granule and to investigate the effect of strain rate on the strength. Force-displacement data of bulk compression tests at different strain rates are used to

calculate the apparent strength of single granules based on exiting models. The single granule compression tests are also conducted to observe the load-strain and failure behaviour of single granules as well as to compare the strength of granules, obtained according to the single and bulk compression analyses.

Chapter 5 In this chapter the impact breakage patterns of granules are qualified by observation of the impact events and impact products using a high-speed digital video camera, scanning electron microscopy (SEM) and reflected light microscopy (RLM). The captured digital images obtained from high-speed video recordings during impacts as well as microscopic images of the impact products are analysed and discussed.

Chapter 6 The extensive impact tests carried out on the granules are presented here. Chipping and fragmentation regimes of breakage are determined for different samples and granule sizes at different conditions. The effect of impact angle, number of impacts, moisture content and temperature of granules on extent of breakage are quantified.

Chapter 7 The general conclusions of this work have been summarised here. Moreover, this chapter addresses the guidelines for further studies that would contribute to further developments in the field.

2 LITERATURE REVIEW

2.1 Introduction

Wet agglomerates and extruded pastes are generally regarded as soft agglomerates, as significant plastic deformation is expected when subjected to loading. Although characterisation of the deformation and breakage of soft agglomerates has recently attracted some attention (Briscoe *et al.* 1998, Pepin *et al.* 2001, Fu *et al.* 2002 and Samimi *et al.* 2003), nevertheless, the literature on the failure behaviour of these materials under different modes of loading and environmental conditions is scanty.

The focus of this chapter is on the deformation and breakage characteristics of agglomerates in general and soft granules in particular. However, at first a general overview of the literature regarding the attrition of particulate solids is presented. In this context, the impact breakage of particles in the brittle, semi-brittle, and ductile failure modes and factors affecting the transition between them are outlined. A special attention is paid to the semi-brittle and ductile failure mechanisms, as those are more relevant to this study. The literature survey on single and bulk compression of particles is then presented, in which the existing models are critically reviewed. An overview of agglomeration and agglomerate characteristics is presented next. This section is followed by reviewing the breakage behaviour of agglomerates. Inadequacies of the existing models describing the strength as a function of structural properties are also discussed for the soft agglomerates.

2.2 Overview of breakage of particulate solids

Attrition and comminution are commonly used in the literature to describe the breakage of particulate solids. Attrition is defined as unwanted breakage of particulate solids, while comminution is the intentionally induced breakage, in order to bring about size reduction of particles (Bemrose and bridgewater, 1987). Attrition traditionally has been used to define a slow breakage of material during handling and processing caused by local damage, whereas comminution term is applied to any types of mechanical processes that lead to size reduction of particulates, e.g. in milling processes.

Comminution of solids in process industries is highly energy consuming. According to published data, 1.3% of annual electrical energy in USA was used by comminution equipment (Davies, 1995). This huge amount of energy consumption is due to the inefficient force application in size reduction, in which a significant part of the energy is dissipated as heat, etc. In the analysis of the comminution process, the details of applied stresses to the material and the way that the material fails under loading need to be considered. The former depends on the mechanical and process design, whilst the latter depends on the mechanical and structural properties of the material. To design an efficient comminution process with a narrow size distribution of the product, the relationship between the dominant failure behaviour, the mode of loading, and the mechanical/structural properties of the particulate needs to be established.

Strain-rate and contact geometry are two main factors, which can cause a switch in the failure mode. The contact geometry is related to particle size and shape, whereas the strain-rate can be affected by rate of loading from quasi-static to dynamic case such as impact. It is generally accepted that if large particles break through the brittle mode, the smaller sizes of same material may switch to the semi-brittle and even ductile failure mode. Therefore, the critical conditions must be dominated by transition between modes of failure. These critical transition conditions will be discussed in section 2.2.3.

2.2.1 Impact deformation and breakage of particulate solids

Inter-particle or particle-target impacts cause transient stresses whose magnitude depends on the mechanical properties, impact velocity, particle size and loading configuration. Impact behaviour of particles can substantially be affected by the contact characteristics. The important contact parameters are contact pressure, contact radius, and contact time. The pressure essentially determines the elastic or plastic response of the particle. If the transient stress does not reached the plastic yield stress of the particle, then its deformation is considered as elastic. In this case, the maximum impact force is obtained by assuming that the functional relationship between the impact force and displacement is the same as the static elastic contact given by Hertz analysis (see Johnson, 1985). For elastic-perfectly plastic case, a mathematical approach has been suggested by Ning (1995), where Hertz analysis is employed to describe the pre-yield behaviour and a combination of elastic and plastic analysis is used for the post-yield behaviour of impact deformation. For perfectly plastic impact condition, however, the maximum contact force is characterised by first calculating the yield pressure (Ning, 1995). As the contact yield stress does not change for perfectly plastic material, the maximum force can then be estimated from the contact area, and this in turn, can be found according to the energy balance between the impact energy and work of the plastic deformation, from which the maximum contact area and consequently, maximum contact force is calculated.

Another aspect of the particle impact is to evaluate dissipated energy by introducing the coefficient of restitution, which is defined as the ratio of rebound velocity to impact velocity. Impact kinetic energy during loading can be stored as elastic energy, or partially/or fully dissipated. The dissipation can occur as plastic deformation, interface adhesion, and inter-particle failure. The unloading process may be followed by sticking of the particle to the target (fully dissipative) or by partially releasing the stored elastic energy through rebounding of the particle from the target. In this context, Thornton and Ning (1998) theoretically modelled the inter-particle and particle-wall impact behaviour of adhesive, elastic-perfectly-plastic spheres. They presented an analytical solution for the coefficient of restitution on the basis of theoretical contact mechanics including Hertzian relations and JKR theory

(Johnson *et al.*, 1971) combined with impact energy balance. The model quantifies the coefficient of restitution as a function of impact velocity, critical sticking velocity and yielding velocity assuming the energy dissipation is due to the plastic deformation and interface adhesion. The critical sticking velocity is defined here as a velocity below which the particle sticks to the target (zero coefficient of restitution), while the yielding velocity is a threshold velocity, above which the plastic deformation initiates. Thornton and Ning (1998) showed that if the impact velocity is greater than sticking velocity but less than yielding velocity the coefficient of restitution increases rapidly to a maximum with increasing the impact velocity. However, ultimately it follows a decreasing trend with further increasing impact velocity (Thornton and Ning, 1998). This theoretical model, however, neglects the energy dissipation due to fracture. Fu *et al.* (2002) measured experimentally the impact coefficient of restitution of the wet granules with different characteristics. In this context, their measurements showed that more than 97% of the initial kinetic energy of the granule was dissipated at the conditions of impact. The method developed by them clearly revealed the effects of impact velocity, binder content, primary particle size, granulation age and surface binder on the restitution coefficient.

Linear Elastic Fracture Mechanics (LEFM) has been employed to characterise the breakage of brittle particulate solids (Mullier, *et al.* 1987, Kendall 1988; Lawn 1993). In LEFM analysis, the crack growth is described by Griffith (1920) theory, in which the criterion for crack propagation is based on the release rate of elastic strain energy. The stored elastic stain energy is the source of energy to drive the crack at the required energy release rate to produce new surfaces. Considering an impact process where the deformation is elastic but it is accompanied by brittle fracture, the processes using the stored elastic strain energy are crack propagation, the plastic deformation on the crack tip and the rebound of the particle. Although, for brittle materials the plastic zone ahead of crack tip is not so large to affect the crack propagation, nevertheless, this extra energy dissipation must also be taken into account through modification of the LEFM model (Abdel-Ghani *et al.*, 1991; Seville, 1994). For ductile materials, however, more energy is dissipated in plastic deformation of the crack tip. Therefore, cracks cannot develop unstably and strain

energy must be supplied continuously to furnish the work required for plastic deformation and crack propagation. In some cases, the plastic zone area may become comparable to the particle size, for which most of the supplied energy is dissipated as plastic deformation and no crack propagates.

2.2.2 Modes of particle breakage

The description of failure modes was originally made based on quasi-static indentation of a rigid indenter on a flat surface of semi-infinite solid surface (e.g. Lawn *et al.*, 1975; Lawn and Marshal, 1979). Subsequently, the application of the indentation fracture mechanics was extended to the breakage of particulate solids. However, for the particulate solids, the crack length can be comparable with the particle size. This may lead to material removal and hence different pattern of breakage as compared to semi-finite solids.

Three breakage modes of brittle, semi-brittle and ductile are categorised depending on the mechanical properties of particle and target, the value of load, as well as the contact geometry. These mechanisms of material removal from the particles are discussed in the following.

2.2.2.1 Brittle failure mode

Brittle mode of failure occurs when the material fractures without noticeable plastic deformation. In this case, the damage zone underneath the contact area is theoretically in fully elastic stress state. This mode of failure occurs due to the presence of pre-existing internal or surface flaws. The spherical shape orange-segmented fragments, which originate from surface flaws, usually occur when the elastic compliance of contact is high (see, e.g., Shipway and Hutchings, 1993 and 1993a). Internal flaws are responsible for diametrical cracks, when the elastic compliance of contact is low. This type of crack propagation often splits the particle into two or more large fragments. In this context, Shipway and Hutching (1993a)

presented the theoretical and experimental studies of fragmentation of lead-glass and saphire spheres under uni-axial compression and impact, using analytical solutions of the elastic stress field given by Dean *et al.* (1952) and Hiramatsu and Oka (1966). Their theoretical analysis shows that the stress distributions in the elastic spheres are broadly similar under both quasi-static and impact conditions, therefore, causing similar pattern of breakage. This conclusion is also supported by the experimental work of Arbiter *et al.* (1969), in which they showed the insensitivity of pattern of breakage of particles to the strain rate in the range of employed impact velocity.

Hertzian cone cracks propagate when the contact loading is more localised. The ring and conical cracks were observed by Arbiter *et al.* (1969) for sand-cement and soda-lime glass spheres and by Salman *et al.* (1995) for aluminium oxide spheres. The ring and cone cracks would develop round the contact circle because of the high longitudinal tensile stress as prevailing there. If this cone angle is tilted (e.g. in the presence of frictional traction, acting tangential to the surface in oblique impacts) small chips can be separated from particle. The conical cracks and subsequent chipping have been observed for glass (Rumpf and Schönert, 1972), for soda-lime glass spheres (Salman and Gorham, 1997) and for molecular sieve and porous silica (Papadopoulos, 1998).

In analysing the brittle mode of breakage, the knowledge of the size and the position of the flaws are essential. However, due to general lack of this information the empirical determination of the crushing strength of particle seems to be the only way to characterise the breakdown patterns. In this context, the similarity of breakage patterns observed by Arbiter *et al.* (1969), Salman *et al.* (1995), Salman and Gorham (1997) represents the same mechanisms of stress field development and breakage pattern for such a brittle particulate solids. With reference to the observed similarities, however, the normal impact of particles in brittle mode can produce different breakage patterns, which is outlined as follows:

- At low impact velocities, a large tensile hoop stress is set up under the contact zone, causing a conical fractured region pushing down into the material. The formed cone usually remains free from internal cracks. Consequently, on the

tip of the cone, the meridian fracture planes may initiate, leading to one of the following four patterns: (i) a meridian fracture plane with splitting the specimen into two symmetrical fractured hemispheres, or (ii) three meridian planes (multiple meridian) causing one hemisphere and two quadrants, or (iii) three equal meridian segments, or (iv) four meridian planes with four fractured quadrants. In this case, similar patterns are observed under quasi-static compression, showing independency of the brittle failure to the strain rate.

- At high impact velocities, when the probability of breakage is high, a different failure pattern may be dominated. In this case, a cone of crushed and compacted material along with a number of oblique cracks is observed (Salman and Gorham, 1997; and Arbiter *et al.*, 1969).

Numerical simulations of brittle particles, impacted on a rigid target, indicated a more complicated fracture patterns, as compared to experimental results. For example, the impact breakage patterns observed by Potapov and Cambell (1994) show development of a fan-like cracks originating radially outwards from the contact point (mechanism I). This pattern of breakage occurred mainly during the loading time of impact. Further crack developments were observed during rebound of the particles from target, in which the cracks propagated perpendicular to the fan-like cracks (mechanism II). In fact, these cracks developed because of imbalance of the tensile and compressive stresses in the fragments. The patterns of breakage observed by Potapov and Cambell (1994, 1997) show evidence of the meridian and oblique breakage. However, a large number of the secondary breakages were also produced because of the extensive breakage, which in turn depended on the strength of the particle and impact energy.

Oblique impact of brittle particles: The fracture patterns in oblique impact of the brittle particles can be different as the mode of loading might be different, compared to the normal impact. In an oblique impact, particles are subjected to normal and tangential loading, which their amounts depend on the impact angle and impact

velocity. The impact angle is defined as the angle between the target and impact direction, measured clockwise. The tangential component of the oblique loading can greatly enhance tension at one end of the contact area, leading to a greater possibility of crack initiation at this point (Hamilton and Goodman, 1966; Rumpf and Schönert, 1973, Salman *et al.* 1995). Furthermore, the frictional traction reduces the angle between the conical cracks and the free surface of the particle thus enhancing the possibility of a conical crack leading to material removal as chips (Evans, 1979; Lawn, 1991). Limited experimental works and numerical simulations have been reported regarding to the effect of impact angle on the pattern and extent of breakage of particulate solids. Vervoorn (1986) investigated the effect of impact angle on the breakage of cylindrical alumina extrudates at different impact velocities. He described that in the chipping regime and low velocities the contribution of the tangential component of velocity to breakage was negligible, compared to that of the normal component. In contrast, the tangential component was responsible for the breakage at moderate and high impact velocities and low impact angles, where abrasion (rolling and sliding contact) might be dominating. He showed that the importance of the tangential component increases significantly in the range of velocities greater than the normal component. This was shown clearly by impacting the particles onto a moving target by which more controllable combination of the normal and tangential components of impact velocities were achieved, e.g. low normal and high tangential components of velocity. Vervoorn (1986) observed that in repeated impacts and under the shallow impact angles with relatively high tangential and low normal components of velocity, more attrition occurred, compared to the larger impact angles.

Salman *et al.* (1995), Salman *et al.* (2002, 2002a) and Maxim *et al.* (2002) reported on the breakage probability of spherical alumina extrudates and fertiliser granules for single particle impacts in the range of 10^{o}-90^{o} and impact velocities up to 35 m s^{-1}. They quantified the probability of breakage based on counting the number of unbroken particles after impact. Salman and his co-workers observed that the probability of breakage for both types of particulate solids was not affected in the range of 50^{o}-90^{o}, but decreased rapidly below the 50^{o}, for a given impact velocity. They showed that the percentage of broken particles was negligible at the impact

angles less than 20° for alumina extrudates and 10° for fertiliser granules. Besides, they found that for each particle size or impact angle, there was a threshold impact velocity, below which no fragmentation occurred. They developed an experimental model, in which the number of unbroken particles (N_u) could be described as a function of impact velocity (V) by a two-parameter cumulative Weibull distribution, given as:

$$N_u = 100 \exp\left(-\left(\frac{V}{k_1}\right)^m\right) \tag{2.1}$$

where k_1 and m are the Weibull parameters. The parameter of k_1 is related to the velocity at which the probability of damage is 36.8% or 100/e. Therefore, k_1 is considered as a parameter that represents the average strength of a given particle size under the specific loading condition. The parameter m is termed as Weibull modulus and is linked to the slope of the curve, so it represents a distribution of strengths for the population of particles. Salman *et al.* (1995) for the alumina extrudates and Maxim *et al.* (2002) for fertilisers granules showed that the parameter k_1 varied by impact angle as well as particles size, while the parameter m is almost constant and independent of impact angle and particles size. In this context, Maxim *et al.* (2002) developed a relationship, which simply describes the effect of impact angle (θ) on the parameter k_1 as follows:

$$k_1 = \frac{V_f}{\sin\theta} \tag{2.2}$$

where, V_f is defined as the normal failure velocity. The particles employed by Salman and co-workers displayed a brittle failure mode in which fracture usually occurred along the meridian planes, depending on the impact velocity. Salman *et al.* (1995) showed that this breakage pattern, however, was dominated at higher impact angles near to the normal. Another form of damage appeared to occur under lower angles of impact, which its frequency was maximum at the impact angle about 40°. In this case, the microscopic observation of the impact product showed detachment

of a small single fragment from the impact zone, leaving an uneven fracture surface. Salman *et al.* (1995) described that the occurrence of this type of damage was because of the tangential loading, by which a greatly enhanced tension was developed at the one end of contact area.

Papadopoulos (1998) investigated the effect of impact angle on the mass fraction of debris produced during impact tests of porous silica (PS) particles. He reported that the extent of breakage of PS particles decreased when the impact angle was reduced at a given impact velocity. He showed that at low impact velocities normal component of the impact velocity was responsible for the chipping process, where the fractional mass loss was found to be just function of the normal component independent of tangential component. However, at the higher velocities when fragmentation dominated, the tangential component played an important role as the breakage increased with increasing the tangential component at constant normal components.

2.2.2.2 Semi-brittle failure mode

The semi-brittle failure is recognised by a limited plastic deformation underneath the contact area, precedes crack development and failure. In this case, the particle contact area is often smaller than the critical elastic-plastic transition size; therefore, the localised stresses reach the threshold of yielding as defined by Puttick (1980). This type of contact is usually made in the impact or quasi-static loading of the corners or edges of angular particulate solids. The material removal mechanism as the semi-brittle failure have been investigated in detail by Chaudri *et al.* (1981) and Yüregir *et al.* (1987) for solution- and melt-grown sodium chloride crystals, by Cleaver *et al.* (1993) for rhombic sodium carbonate monohydrate crystals, Zhang (1994) for sodium chloride (solution- and melt-grown crystals), potassium chloride and magnesium oxide melt-grown crystals, and Papadopoulos (1998) for corner and edge impact of PMMA extrudates and ammonium nitrate prills.

The observations of the breakage patterns by above workers elucidate that the impact loading of corners and its plastic deformation causes development of the compressive radial stresses, and tensile hoop stresses underneath of the plastic zone. This may lead to the initiation of radial and median cracks, which ultimately causes the material removal as chipping and/or fragmentation.

Another type of semi-brittle crack propagation is the lateral crack, which may occur during unloading of compressive load when the residual tensile stresses, formed by elastic unloading, generate sub-surface lateral cracks. This type of crack is commonly propagated laterally in the vicinity of the elastic and plastic boundary. In this case, hardness plays a key role in characterising the extent of breakage, which is related to the yield stress, and Young's modulus. Generally, it is believed that hard materials undergo less plastic deformation than soft materials, but can store greater residual stresses. Therefore, the tendency of hard materials for generation of lateral cracks may be greater than soft materials. Due to separation of small chips from mother particle, the regime of breakage in this type of crack propagation is usually nominated as chipping. The mechanism of semi-brittle particle chipping due to the sub-surface lateral cracks has been modelled by Ghadiri and Zhang (2002), Equation 2.3, in which fractional loss per impact, ξ, (the ratio of the volume of debris removed from a particle to the volume of the original mother particle) is a function of the indentation mechanical properties. According to the model, the mass fractional loss per impact is given by

$$\xi = \alpha_1 \eta = \alpha_1 \frac{\rho V^2 d H}{K_c^2} \tag{2.3}$$

where η is the attrition propensity, ρ is the particle density, V is the impact velocity, d is linear dimension of particle, H is the hardness, K_c is fracture toughness, and α_1 is proportionality factor, which depends on particle shape and impact geometry and is determined experimentally.

2.2.2.3 Ductile failure mode

Ductile mode of failure is a type of damage that commonly occurs for metals and soft materials such as polymers. The breakdown of particulate solids by this mode of failure has not been widely investigated and therefore the numbers of literature explaining the evolved mechanisms is low. In fact, the literature has mostly focused on the failure behaviour of ductile surfaces as a result of erosion effect of the particles impact, rather than exploring the damages occurring in the particles.

In ductile failure, cracking does not readily occur; instead, the plastic rupture may operate. The process is dominated by extensive plastic deformation, producing a plastic zone underneath the contact area. Consequently, extensive shear deformation may occur leading to the rupture of the places constrained by physical boundaries. To explain the process of ductile material removal, two distinct mechanisms of ploughing and cutting have so far been identified (Hutching, 1992). The distinction between these two mechanisms, however, lies in the direction of surface material flow with respect to the direction of particle (indenter) impact and/or slide. In ploughing, the material flows to the sides and front of the impact site in the direction of particle impact, whereas in cutting the material flows up and makes a lip or a separated chip in front of the impression site. The ploughing and cutting effects essentially depend on the contact geometry, normal load and mechanical properties of the particle and surface such as Young modulus to hardness ratio of the surface. In this context, contact geometry is regarded as angle of attack for sharp indenters (e.g. cones) or ratio of contact width to indenter radii for spherical indenters. On the other hand, friction made between the particle and surface plays a major role when the hard particle slides or rolls over a ductile surface.

Particle failure under the ductile mode is commonly encountered under quasi-static compression and in some cases under dynamic impact of a very soft and/or small particle. The ductile failure is also observed in the impact of the weak agglomerates. In the later case, the numerical and experimental data obtained from the single impact of weak lactose agglomerates (low surface energy keeping the primary particles together) both show a mechanism similar to the ductile failure (Ning *et al.*,

1997). The ductile failure is considered here, as a macroscopic deformation between the contact area of agglomerate and target during impact. In this case, significant plastic deformation in the contact zone consequently leads to disintegration of the original agglomerate to the large clusters.

Samimi *et al.* (2002, 2003) recently conducted a number of quasi-static single and confined bulk compression, and impact tests on the soft detergent based agglomerates. In this case, the microscopic observations of cracks developed in the crushed agglomerates reveal that the opening up of cracks proceeds through ductile elongation and rupture of the inter-particle binder ligaments. In some cases, in spite of the extensive crack propagation, still, the fragments were kept in aggregate with the mother agglomerate by some not ruptured but elongated binders in the cracks. Therefore, the ductile mechanism of failure can be considered for these materials because of extensive macroscopic plastic deformation in the contact zone as well as microscopic inter-granular elongation and rupture of binders. At the moment, no model is available to describe the breakage behaviour of this type of agglomerates.

2.2.3 Fracture mechanics considerations and effect of particle size on transition of the breakage mode

One practical approach for the breakage analysis of material relies on the fracture mechanics considerations and energy balance manipulations. Theoretically, in the brittle mode of breakage, a crack initiates and then propagates in an unstable manner when the applied stress on the sample increases to a maximum at which the critical strain energy release rate is equal to the fracture energy. The analysis method proposed for brittle mode of fracture can be found in numerous references of linear elastic fracture mechanics (e.g. Atkins and Mai, 1985; Broek, 1989). When the size of plastic zone at the crack tip becomes considerable, the fracture has a semi-brittle character. In this case a correction to the length accounts for plastic zone (e.g. Irwin, 1958). In terms of complete ductile behaviour of particulates when the crack propagation is fully stable, Vu-Khanh (1988) has proposed a method to determine the impact failure parameters of ductile polymers, using non-linear fracture mechanics.

He has shown that the inconsistency of the linear elastic fracture mechanics in analysing crack propagation is due to the variation of fracture energy with crack propagation. This method is based on a constant rate of increase in crack growth resistance with stable crack extension. The method proposes two parameters of fracture energy at crack initiation and equivalent tearing modulus. This procedure reduces abnormally high value of fracture energy and eliminates the inconsistent negative intercept of absorbed energy versus fracture surface area for ductile polymers, when interpreting by using linear elastic fracture mechanics. Vu-Khanh (1988) showed the compatibility of experimental measurements (obtained from impact Charpy and Izod testing and three point bend testing method) with his proposed model by plotting the specimen-absorbed energy (U) as a function of fracture surface area (a_f) of fully ductile polymers, which surprisingly followed a polynomial relationship. The developed correlation is as follows:

$$U = G_i a_f + \frac{1}{2} T_a a_f^{\,2} \tag{2.4}$$

or

$$\frac{dU}{d a_f} = G_i + T_a a_f \tag{2.5}$$

or

$$G_R = G_i + T_a a_f \tag{2.6}$$

where G_R is fracture energy, G_i is the fracture energy at crack initiation, and T_a is equivalent tearing modulus. However, in this model G_i and T_a can be characterised as the material parameters. T_a is considered as the rate of fracture increase. Although the tearing modulus is only defined for small magnitudes of crack extension, the idea was extended to the case of stable impact fracture as well, (Vu-Khanh, 1988).

Irwin (1958), based on the energy requirements for crack nucleation and propagation proposed a parameter, which was used later to assign the ductility effect of a process zone at the crack tip on the failure of the particulate solids. Depending on the brittle to ductile behaviour of particles, process zone is defined as a region that energy can be dissipated there through micro-cracking or yielding. The radius of this zone is given by

$$r_p = \frac{1}{2\pi}\left(\frac{K_c}{\sigma_y}\right)^2 \tag{2.7}$$

Where, r_p is process zone size, K_c is fracture toughness and σ_y is yield stress. In this area elastic stress reaches the yield stress of material and a plastic deformation occurs. The nature of this zone plays a key role in defining the mechanism of failure. It has been postulated that there exists a minimum particle size below which the particle can only be deformed plastically and cannot be fractured, irrespective of the level of stress. This implies that the particles smaller than this limiting size cannot be fractured in either brittle or semi-brittle mode. However, those can still be reduced in size by the mechanisms of ductile failure mode and cracks can be induced by plastic deformation processes such as shearing.

There are several models for this limiting size. Kendall 1978, illustrated this by defining the grinding limit of brittle materials or critical particle size (L_c) as

$$L_c = \frac{32}{3}\frac{EG_c}{\sigma_y^2} \approx 60 r_p \tag{2.8}$$

where G_c is the critical strain energy release rate due to Griffith (1920) and E is modulus of elasticity.

Puttick (1980) proposed a general theory of fracture transition in which transition from elastic-plastic to fully plastic conditions occurred when the specimen size reaches a critical length scale of (L_c), shown below.

$$L_c = \beta r_p \tag{2.9}$$

where β is a constant depending on the loading conditions. In the case of indentation, $\beta \sim 10^3$ whereas for notch bar test $\beta \sim 1$.

Hagan (1981) proposed another model, which appears to provide a closer agreement with the experimental data. This relation is as follow:

$$L_c \cong 30\left(\frac{K_c}{H}\right)^2 \tag{2.10}$$

It is now well understood that in addition to fracture properties and flaw distribution, particle size and mode of loading also play important roles in attrition by governing fracture transitions. In fact, loading the particulate solids with large critical sizes will lead to an extensive plastic deformation (Mullier, *et al.*1987), which may change the dominant mechanism of failure of particulate from tensile crack opening to shearing. On the other hand loading the particles with small critical size will result in gross fracture or breakage. Therefore, collision of a particle with a size smaller than the critical size (L_c) with a rigid target may cause a significant dissipation of impact energy within the plastic zone of particle. In this case, there will be insufficient stored elastic strain energy to initiate gross fracture and the kinetic energy of particle is largely dissipated as plastic deformation.

For ductile materials, development of a damage model also requires consideration of the strain rate sensitivity of material's mechanical properties. During impact, the particles may be affected by high strain rate of deformation in the order of 10^3 to 10^6 s^{-1}, whereas the mechanical properties are commonly measured at low strain rates (quasi-static, 10^{-4} to 10^{-1} s^{-1}). Therefore, if a material is strain rate sensitive, mechanical properties measured quasi-statically may be significantly different from those at high strain rates. Roberts and Rowe (1985) proposed a term as strain rate sensitivity (SRS) to quantify this change, defined as the percentage increase in the yield stress as the punch velocity increases from 0.033 mm s^{-1} to 300 mm s^{-1}.

According to Equation 2.7, process zone size depends on the fracture toughness and yield stress. As these parameters can be affected by strain rate, hence, process zone size can ultimately vary as a function of strain rate. For most materials that are sensitive to the strain rate, the increase of yield stress with the strain rate is well understood. However, the increase of their fracture toughness with strain rate is not thoroughly quantified. For some materials such as PMMA increasing the strain rate from quasi-static to 10^3-10^4 s^{-1} can cause a significant increase in the crack propagation speed (e.g. impact velocity of 3 m s^{-1} produces about 220 m s^{-1} crack speed) and consequently a substantial temperature rise at crack tip (about 530 ^{o}C), (Swallowe *et al.*, 1984). This temperature rise will be accompanied by melting and softening of the crack tip and consequent crack blunting (Hodgkinson and Williams, 1982), which ultimately leads to increasing the fracture toughness. Nevertheless, for PMMA, with increasing the strain rate, the literature data show that despite the increase of fracture toughness the plastic zone size reduces (Papadopoulus, 1998; Gorham and Salman, 1998). Considering Equation 2.7, this implies that the yield stress should increase at a faster rate than the fracture toughness.

2.3 Review of experimental methods for study of particle breakage

The need for a systematic investigation of attrition has led to development of various test devices. Generally, the experimental techniques can be classified into two major categories of multi-particle and single-particle testing methods. Multi-particle tests simulate a more practical situation of breakage whereas single-particle tests investigate the effects of individual and isolated parameters on the particle damage. The latter enhances the fundamental understanding of breakage mechanisms. Bemrose and Bridgwater (1987) have presented a general review of attrition test methods. However, in the following a brief but more up-to-date review of related literature is presented.

2.3.1 Multi-particle testing methods

The typical experimental methods of this category focus on various types of grinding systems, bulk compressions, shear cells and fluidised beds.

The grinding mill tests consist of small-scale mills aiming to obtain direct results for scaling-up of comminution process.

Bulk compression tests evaluate the strength of particles in an assembly under the compressive loading (Ouwerkerk, 1991; Couroyer *et al.,* 2000). A number of research workers have developed bulk compression models, which link the pressure–displacement or pressure-strain behaviour of bed to the single particle breakage strength and yield stresses (Heckel, 1961, Kawakita and Lüdde 1970; Adams *et al.*, 1994; Adams and Mckeown, 1996).

Shear cell testing of bulk solids has mainly employed to investigate the effect of shear stress and strain on the attrition of particles. This method of testing is particularly useful when the particles undergo considerable shear strains, e.g. in silos and moving beds. In a shear cell, a compressed bed of particles is subjected to sliding under a normal load (Paramanathan and Bridgwater, 1983, 1983a; Ouwerkerk, 1991; Neil and Bridgwater, 1994; Ghadiri *et al.* 1997; Ghadiri *et al.* 2000). Typical parameters that are varied in the shear tests are the applied normal load, the shear strain and the shear rate.

Fluidised bed test is used commonly for the attrition study of fine powders; the results are directly applicable to fluidisation processes. The orifice velocity, superficial velocity, jet angle and retention time of material are the major parameters in this method of testing (Forsythe and Hertwig, 1949; Gwyn, 1969; Veesler *et al.*, 1993; Ghadiri *et al.*, 1994; Boerifijn *et al.*, 1997; Boerifijn *et al.*, 2000).

The main problem of multi-particle tests is the difficulty in analysing the results, because the effects of particles interaction in real processes are not well understood. Nevertheless, recent progress in computer simulations has elucidated some

phenomena occurring in multi-particle tests (Ouwerkerk, 1991; Ning and Ghadiri, 1996).

2.3.2 Single-particle testing methods

Single-particle tests can essentially be sorted as three methods of indentation, compression between two platens and impact on a target.

Quasi-static indentation of particles has been employed to characterise mechanical properties such as Young's modulus, yield stress, hardness and fracture toughness (Puttick, 1987; Gahn and Mersman 1995). These properties are broadly used as a tool for modelling the attrition and comminution processes (Ghadir and Zhang, 2002). Recent improvement of the indentation testing method has led to development of nano-indentation technique (Pollock *et al.*, 1986; Oliver and Pharr, 1992; Pollock 1992), which has extended the capability of mechanical properties characterisation of particles down to the size of approximately 5 μm (Arteaga *et al.*, 1993).

Compression of a particle between two rigid platens, which is also known as side crushing strength test (SCS) has been used to determine the particle strength (Arbiter *et al.*, 1969; Kendall, 1978a; Puttick and Badrick, 1987; Bermose and Bridgwater, 1987; Quwerkek, 1991; Shipway and Hutchings, 1993, 1993a, 1993c). In this method load-displacement behaviour of single particles can be analysed under the uni-axial compression until particle failure.

In single-particle impact testing, the extent of breakage is readily quantified at high strain rates through striking the single particles on a rigid target (e.g. Arbiter 1969; Papadopoulos and Ghadiri, 1996; Samimi *et al.* 2003). The mechanism (brittle, semi-brittle, ductile) and regime (chipping or fragmentation) of damage can be analysed along with microscopic analysis of impact products. In addition to the impact velocity, the effects of impact angle, particle size, environmental conditions, target material and its thickness can also be investigated.

Researchers have used different designs of impact apparatus, from free-fall to particle accelerating systems using compressed air and vacuum. Recently, a vibration cell design has also been used for repeated impact of particles (Pitchumani *et al.,* 2001, 2002). Arbiter *et al.* (1969) employed the free-fall impacts of particles to study the breakage patterns and the size distribution of resulting fragments of sand-cement and glass spheres. Using air guns and accelerating systems of particles such as compressed air and vacuum have enhanced the range of impact velocities to higher than 100 m s^{-1}. Modern test methods are equipped with computerised optical accessories such as high-speed video recording for capturing the impact and rebound images of particles. The impact and rebound velocities, and contact time could easily be determined. The deformation and breakage behaviour of particles during impact could be observed. Using strain gauges mounted on the target has also extended the ability of these devices to measure the impact force profile (Okudu and Choi, 1979; Salman *et al.,* 1995; Salman and Gorham, 1997, Papadopoulos and Ghadiri, 1996; Couroyer *et al.*, 2000, Boerefijn *et al.*, 2000, Subero 2001).

At present the use of the single particle tests data to predict the particle breakage in the actual processes is difficult because of lack of adequate hydrodynamic models of the process. However, the strong advantage of the single particle tests is the well-defined and controlled conditions of loading, which enables the study of the effects of various factors to be easily done.

2.4 Breakage indices and breakage functions

In single particle tests, two approaches of the breakage indices and the breakage functions can be adopted to characterise the breakage behaviour of the impact products. The breakage index describes the fraction of unbroken or broken particles produced in the experiment, while the breakage function correlates the size distribution of fragments.

2.4.1 Breakage indices

In the literature, the breakage index is considered as either mass fraction of the particles below a certain size (Vervoorn and Austin, 1990; Ghadiri and Zhang, 2002; Papadopoulos and Ghadiri, 1996, Vogel and Peukert, 2003) or ratio of the number of broken particles to the total number of the particles impacted (Rumpf and Schönert, 1973; Salman *et al.*, 1995). When gravimetric analysis is carried out, the mass fraction undersize of a certain size is traditionally specified by a cut-off size, corresponding to the aperture's size of a standard sieve. In this context, Vogel and Peukert (2003) considered mass fraction of material smaller than original sieve size of particles before impact and termed it the breakage probability. They developed a model according to the dimensional analysis approach proposed by Rumpf (1973). The model characterises the breakage probability (ζ) as a function of a group based on Weibull relationship given as follows:

$$\zeta = 1 - \exp\left\{-f_{mat}\, L_o\, n\left(E_{m,kin} - E_{m,c}\right)\right\} \tag{2.11}$$

where, f_{mat} (kg J^{-1} m^{-1}) is a fitted parameter, L_o is the initial size of particles and n is the number of impacts. Furthermore, two mass-specific kinetic energies of $E_{m,kin}$ and $E_{m,c}$ (J kg^{-1}) are denoted as impact energy and critical impact energy, respectively. Critical impact energy is defined as the threshold of the impact energy below which no crack propagation and fragmentation occurs and any mass loss of particles during impact is as the result of chipping regime of breakage. In fact, ($E_{m,kin}$ - $E_{m,c}$), represents the net mass-specific impact energy required for breakage of particles. f_{mat} is a fitted parameter which is determined experimentally by data fitting based on the Weibull relationship (Equation 2.11) and is suggested to reflect the material properties. Vogel and Peukert (2003) showed that the breakage probability of different materials (PMMA polymers, limestone and glass) of various sizes (95 μm to 8 mm) could be described by a single master-curve. They characterised quantitatively the two material parameters of f_{mat} and $E_{m,c}$ for the above test materials to differentiate their impact breakage behaviour.

The breakage indices may also be adopted using the criterion of mass fraction of material less than a given sieve size, which is taken here as two standard sieve sizes below the original size of the particles before impact. The previous studies of single particle impact tests have shown that this criterion can be adequately used in the chipping regime of breakage in which debris of the impact product are much finer than the mother particles (Cleaver *et al.* 1993; Papadopoulos and Ghadiri, 1996; Boerefijn *et al.* 2000). In the fragmentation, also, depending on the impact velocity, the impact product might be partitioned into two categories: the large fragments, which contain partially damaged mother particles and small fragments, and the debris. As it will be discussed in the next section, the distinct cut-off size is usually matched with a sieve size, which is two standard sizes less than original size of the particles (Papadopoulos and Ghadiri, 1996, Samimi *et al.* 2003).

The breakage indices can then be expressed as a function of either time or number of individual impacts. Vervoorn and Austin (1990) formulated a model based on the concept of a first order rate process, which was originally developed by Kelsall *et al.* (1967/68) for continuous grinding. The model of Kesall *et al.* is as follows

$$-\frac{dM_L}{dt} = S_L\, M_L \tag{2.12}$$

where M_L is the total mass of particles of size L which remain unbroken after time t and S_L is the specific breakage rate. The parameter S_L depends on both process conditions and material properties and is assumed constant. The model of Vervoorn and Austin (1990) is obtained by simply substituting the independent variable of time by impact number. Equation 2.12 can be normalised with respect to the original feed mass M_f. The mass fraction of unbroken particles with particle size of L after n impacts, $Y_{L(n)}$, is given by:

$$-\frac{dY_{L(n)}}{dn} = s_l\, Y_{L(n)} \tag{2.13}$$

where s_1 is termed as specific breakage constant. Vervoorn and Austin (1990) examined their model for impacts of 3 mm alumina cylinders and concluded that s_1 was independent of impact number. However, they reported that specific breakage rate was a function of impact velocity with the power index of 4.33. The specific breakage constant defined by Vervoorn and Austin is equivalent to the specific breakage rate defined by Kelsall *et al.*, as shown in Equation 2.12.

For simulating the impact breakage of agglomerates with a mono-dispersed-structure Kafui and Thornton (1993) defined an alternative breakage index as the ratio of the number of the broken bonds between primary particles to the initial number of bonds prior to the impact of the agglomerate termed 'damage ratio'. They simulated the impact damage of spherical agglomerates on collision with a wall by Distinct Element Method and showed that the damage ratio, Δ, was a function of Weber number, w_e, as follows:

$$\Delta = \kappa\left(\sqrt{w_e}\right)^{\chi} \tag{2.14}$$

where κ and χ are constants determined by data fitting. Weber number is given by:

$$w_e = \frac{\rho V^2 d}{\Gamma} \tag{2.15}$$

where d is diameter of agglomerate, Γ is the fracture surface energy (i.e. the interparticle bond strength), V is impact velocity and ρ is the density of agglomerate. On the other hand, Thornton *et al.* (1995) reported that the mass fraction of fines, made of singlets and doublets was linearly proportional to the Weber number. They modified their simulation by employing the mechanisms of energy dissipation. Their simulation results are in agreement with the model of Ghadiri and Zhang (2002), Equation (2.3), which has been experimentally shown to be valid for the chipping of particulate solids, (Papadopoulos, 1998) in the semi-brittle mode. Therefore, it can be concluded that in the semi-brittle chipping of particles, the breakage index defined as the breakage propensity (Equation 2.3) is linearly proportion to Weber number.

Thornton *et al.* (1996) consequently modified the Weber number by introducing a threshold velocity, V_o, at which significant breakage started (Equation 2.16).

$$w_e^{'} = \left[\frac{\rho (V - V_o)^2 d}{\Gamma} \right]^{1/2} \tag{2.16}$$

A certain degree of unification was observed in the plots of damage ratio as a function of modified Weber number ($W_e^{'}$) as shown by Thornton *et al.* (1996), and Subero *et al.* (1999).

Moreno (2003) proposed a new dimensionless number (Equation 2.17) based on the hypothesis that the work of breakage of contacts is proportional to initial kinetic energy before impact. The new dimensionless group is made of product of the original Weber number (Equation 2.15) and elastic adhesion index, I_e, which the latter is defined as the ratio of elastic force to bonding force (Kafui and Thornton, 2000) as given in Equation 2.18.

$$w_e^{''} = w_e \, I_e^{2/3} \tag{2.17}$$

$$I_e = \frac{E \, d}{\Gamma} \tag{2.18}$$

where, E is Young's modulus of agglomerates. Moreno (2003) evaluated the model for the glomerates made of 200 and 3000 single elastic primary particles whose elastic modulus was 31 GPa, density 2000 kg m^{-3} and Poisson's ratio 0.3. The agglomerates were tested for the values of interface energy 0.35 J m^{-2}, 3.5 J m^{-2} and 35 J m^{-2}. A good unification of plots of damage ratio as a function of $V^2/\Gamma^{5/3}$ was obtained for different interface energies, suggesting the validity of the proposed model.

2.4.2 Breakage functions

Breakage functions, as a means to characterise the size distribution of broken particles are important in the assessment of the size reduction performance. A number of different models have been proposed to describe the size distribution of the breakage product. The formulating basis of some of the breakage functions is empirical (Rosin and Ramler, 1933; Schumann, 1940). However, in other cases, the breakage functions are characterised according to the statistical criteria (Klimpel and Austin, 1965; Barnard and Bull, 1985).

The Gates-Gaudin-Shumann (1940) model (GGS model) is one of the two parametric size distribution models, which has been extensively used in the literature (Arbiter *et al.,* 1969; Potapov and Cambell, 1994 and 1997; Thornton *et al.,* 1995; Papadopoulos, 1998). This model was initially developed based on the log-log plot of cumulative mass fraction undersize as a function of size of fragments (L). However, in the most of recent literature, the GGS distributions are commonly normalised with respect to the original particle size (L_o). In fact, this size normalisation is useful when comparing the breakage behaviour of material with different initial sizes.

The size distribution analysis of a number of particulate materials according to GGS model shows a common feature depending on the impact velocity and initial particle size. In this context, the size distribution plot of the material after impact may be classified into two distinguishable linear lines, with different slopes (e.g. Arbiter. *et al.,* 1969; Kafui and Thornton 1995, Papadopoulos, 1998). The lines are usually identified by a natural cut, which divides the distribution plot into two parts of residue (coarse fragments and unbroken particles) and complement (fines formed on impact). In this case, the slopes of complement and residue lines are defined as complement and residue distribution moduli. As the impact velocity increases, the natural cut may gradually disappear and the two distinct straight lines become a single one. This could be a manifestation of the gradual transition from chipping to fragmentation as shown by Papadopoulos (1998).

The functional dependence of the size distribution on the impact velocity has been investigated by a number of workers. Arbiter *et al.* (1969) developed an equation, which showed a reasonable unification of the results for free fall impacts of the sand-cement complements. The original correlation was presented based on the free fall height. However, as the free fall height and impact velocity are related, therefore equation of Arbiter *et al.* (1969) can be modified into the follow form.

$$Y(L) = C_1 L^{\lambda}(V^2 - V_c^2) \tag{2.19}$$

where, *Y(L)* is the mass fraction of fragments under the size L in the complement region, C_1 is a constant, λ is the distribution modulus of complement, V and V_c are impact velocity and critical velocity, respectively. Critical velocity is defined as the velocity below which no fragmentation occurs. As it is clear from Equation 2.19, this empirical model seems to be independent of the original particle size (L_o).

Kafui and Thornton (1995) used GGS distribution model to describe the unification of the breakage results of agglomerates with a face-centred cubic packing structure on impact with a wall. They presented their simulation results according to the following equation:

$$Y(L) = C_2 \left[kV^2 \left(\frac{L}{L_o} \right)^{\lambda} \right] \tag{2.20}$$

where, C_2 is a constant. The validity of this approach was assessed by Papadopoulos (1998), using experimental data of single particle impacts, performed on a variety of test materials. He showed that the combined effect of impact velocity and particle size on the size distribution of complement of porous silica (PS) granules may be represented by Equation 2.21, which provides a good unification of the results for various feed particle sizes and impact velocities.

$$Y(L) = -0.289\left[(V^2 L_o)\left(\frac{L}{L_o}\right)\right]^{1.62} \tag{2.21}$$

In this equation, $Y(L)$ is independent of original size of granules (L_o). Papadopoulos (1998) presented the correlation in the above form deliberately to keep the term V^2L_o similar to the chipping model of Ghadiri and Zhang (1992 and 2002).

2.5 Bulk compression of particles

Bulk compression of particles is generally conducted to increase the bulk density. This objective is the basis of the densification, as used in the production of tablets. However, the bulk compression of particles has also been considered as a useful method to characterise some properties of individual particulate solids being compressed in the bed.

A large number of correlations have been developed mainly based on the experimental fittings of data to relate the applied pressure on the bed to some state of consolidation measures of powders in the bed such as bed volume, strain and relative density. A literature survey shows that over 200 papers per year are published in relation to the bulk compression (Denny, 2002). In spite of the extent of publications, the level of understanding of the compression mechanism and its relation to the physical and mechanical parameters is poor. It is generally believed that three mechanisms are responsible for the bulk compression of particles in a packed bed. At first, during the initial stage of compression, i.e. at low pressures, the particles are subjected to some sliding and rearrangement without any plastic deformation and breakage. This part of compression process generally shows some non-linearity in the stress-strain plot. Denny (2002) asserts that, in some cases, even at the first stage of compression, deformation and failure of the particles might occur. This is the part that most of the models ignore and assume it is simply sliding and rearrangement of the particles. The Denny's arguments will be discussed in the next section. The first stage is then followed by extensive plastic deformation and

fragmentation of the particles at higher pressures, in which the progressive filling of the interstitial voids occurs along with decreasing the bed porosity. This is the stage that commonly makes the linear part of the logarithm plot. Most of models have in fact concentrated on this part. At last, the bed may eventually show an elastic behaviour at very high pressures, when bed porosity is reduced to a minimum value, sometimes zero for plastic materials. This part of the plot is usually non-linear. It is highly unlikely that a single compression equation fits all these mechanisms. Therefore, in interpreting the compression curves, it is essential to identify the operating mechanism over the different stages of compression.

In the following, three compression models of Heckel (1961), Kawakita and Lüdde (1970), and Adams *et al.* (1994) are critically reviewed. The reason for selection of these models is that they have been widely used in the recent literature. In this context, the key parameters of the equations that in some way are related to the physical and mechanical properties of the material are clarified and some aspects of the theoretical basis of the models are addressed.

2.5.1 Heckel's equation

This equation was in fact initially proposed by Shapiro (1944), 17 years before Heckel (1961), who modified the model for uni-axial compression of metal particles and characterised the constant factor of the equation. The model is initially derived using a first order differential equation as follows:

$$-\frac{d\nu}{dP} = K\nu \tag{2.22}$$

where, ν is the bed porosity, P is the applied pressure and K is termed as Heckel parameter. Integrating the equation and putting ν_o as the initial porosity of the bed at zero pressure gives:

$$\ln\frac{1}{\nu}=\ln\frac{1}{\nu_o}+K\,P \tag{2.23}$$

A simple form of Equation 2.23 can be derived by replacing the term of ν in the equation with (1-D), and considering the $\ln(1/\nu_o)$ as a constant parameter of A, as shown in Equation 2.24. The parameter D in Equation 2.24 is defined as relative bed density and is related to the bed bulk density, ρ_{bulk}, and true density of the particles, ρ_{true}, based on Equation 2.25.

$$\ln\frac{1}{1-D}=A+K\,P \tag{2.24}$$

$$D=\frac{\rho_{bulk}}{\rho_{true}} \tag{2.25}$$

In fact, Equation 2.24 is the main form of the Heckel equation, which has widely been used in the literature. In this case, the slope and intercept of the linear relationship of $\ln[1/(1-D)]$ versus the applied bed pressure, P, determine the Heckel parameters of K and A, respectively. As it was mentioned above, most of the actual experimental data show some curvature at low and high-pressure regions and just in the middle pressure range, a linear relationship may be observed. For metal powders, however, different cases may be seen (Denny, 2002). For example, for iron and nickel powders, the linear part of the relationship usually extends to the higher pressures in such a way that the third non-linear part may not be seen. On the other hand, zinc powder does not even show the straight region after the initial curvature. The uni-axial compression of relatively softer metals particles, lead and tin, may lead to a complete straight line without any non-linearity at the early and last stages of compression.

Heckel (1961) showed that an empirical relationship may explain K as a function of the yield strength (σ_y) of individual metal particle, given as:

$$K = \frac{1}{3\sigma_y} = \frac{1}{p_y} \tag{2.26}$$

The term $3\sigma_y$ (=1/K) is often called the yield pressure, p_y, of single particle (Roberts and Rowe, 1987). In fact, K is inversely related to the ability of the material to deform plastically. Therefore, the Heckel model can mainly be employed for the materials that compressed by plastic deformation. In order to characterise the Heckel parameter, Roberts and Rowe (1987) investigated the relation between the yield pressures ($1/K = p_y$) obtained based on the bulk compression tests, and the values of hardness and Young's modulus measured by indentation testing method. They found that the $1/K$ of wide range of materials (metals, inorganic halides and polymers) was in agreement with the yield pressure obtained according to the indentation tests. However, Hassanpour and Ghadiri (2003) have recently analysed the Heckel model by DEM simulation of the bulk compression of particles with different yield stresses and Young's moduli. They have reported that for elastic spherical particles (low values of the ratio of Young's modulus over yield stress, typically lower than 30), $1/K$ reflects the Young's modulus, rather than the yield stress.

The uncertainty regarding the applicability of Heckel's model to some materials as well as the identity of the parameter that is essentially characterised by the model has been questioned in some literature. Nicklasson and Alderborn (2000) reported that the Heckel parameter was not sensitive to the porosity change of the agglomerates, made of microcrystalline cellulose (MCC) primary particles and water and ethanol binders. Adams and McKeown (1996) employed Heckel model for agglomerates, made of inorganic primary particles and different types of soft binders. They found a large deviation from linearity using Equation 2.27. Denny (2002) have recently modified of the Heckel equation. He has emphasised that the non-linearity in the Heckel's plot would be due to considering of the yield stress of particles in the bed independent of the pressure. Hence, he proposed a pressure dependent term for characterising the confined yield stress in the bed, σ_{yb}, as follows:

$$\sigma_{yb} = \sigma_y + k_2 P \tag{2.27}$$

where, the term k_2P is equivalent to the confined lateral pressure, P_l ($=k_2 P$). In Equation 2.27, it is supposed that the lateral pressure is proportional to the axial bed pressure, P, with the proportionality constant, k_2. Considering $K=1/3\sigma_{yb}$ and substituting the Equation 2.27 in K and the resultant term in Equation 2.22 leads to Equation 2.28.

$$-\frac{dv}{dP}=\frac{1}{3(\sigma_y+k_2 P)}v \tag{2.28}$$

Integrating the above equation gives Equation 2.29, which is the modified version of Heckel's equation.

$$\ln\frac{1}{v}=\ln\frac{1}{v_o}+\frac{1}{3k_2}\ln\left(1+\frac{k_2 P}{\sigma_y}\right) \tag{2.29}$$

Equation 2.29 can be the same as the normal Heckel equation (Equation 2.23), when k_2P/σ_y is less than 0.1 (low pressures, where $k_2P<<\sigma_y$). Therefore, the yield stress can be characterised based on linear fittings of data at low bed pressures. In fact, in most plots, this part is located in the early stages of compression process, the region that is commonly assumed as rearrangement and sliding of the particles.

2.5.2 Kawakita's equation

This equation is another empirical model, which has been proposed by Kawakita and Ludde (1970) as follows:

$$\frac{P}{\varepsilon_e}=\frac{1}{ab}+\frac{P}{a} \tag{2.30}$$

A linear relationship between P/ε_e and P/a allows that the equation constants, a and b, to be evaluated. In the equation, ε_e is defined as degree of volume reduction,

which is equivalent to engineering strain. Constant a is related to the initial bed voidage and constant b is related to the resistance force. The term $(1/b)$ is termed as Kawakita parameter, which represents the failure stress. The engineering strain of the bed is related to the bed height at applied pressures of zero (h_o) and at pressure P (h_p) as follows:

$$\varepsilon_e = \frac{h_o - h_p}{h_o} \tag{2.31}$$

Some test data based on Kawakita plots give good linear relationship throughout the whole range of applied pressures. However, some other data show curvatures especially at the low-pressure range. Kawakita and Ludde (1970) stated that this equation holds best fit for soft and fluffy pharmaceutical powders. However, they have also emphasised that particular attention must be paid to the measurement of the initial bed height, h_o, as deviations from the linearity sometimes might be due to the fluctuations in the measured value of the initial height.

By a simple modification of Equation 2.30, Denny, 2002 developed a new form of Kawakita equation and showed that it is the same as the modified form of Heckel's equation. In this context, the engineering strain, ε_e, can be shown to have a relationship with the bed's porosity according to Equation 2.32.

$$\varepsilon_e = \frac{h_o - h_p}{h_o} = \frac{\nu_o - \nu}{1 - \nu} \tag{2.32}$$

Then, the modified form of Kawakita's equation is achieved by substituting the right hand side of Equation 2.32 and the initial bed porosity, ν_o, in Equation 2.30, respectively, instead of the engineering strain and the parameter a. Rearranging and taking the logarithm from the resultant equation will lead to a relationship (Equation 2.33), which is similar to the modified Heckel model (Equation 2.29). This Equation is given as follows:

$$\ln\frac{1}{\nu}=\ln\frac{1}{\nu_o}+\ln\left[1+b(1-\nu_o)P\right] \tag{2.33}$$

In a special case, when the term, $b(1-\nu_o)P$, is lower than 0.1, then, another form of Kawakita equation is given as follows:

$$\ln\frac{1}{\nu}=\ln\frac{1}{\nu_o}+b(1-\nu_o)P \tag{2.34}$$

In fact, Equation 2.34 is the same as the original form of Heckel's model, which applies at low bed pressures. Comparing Equation 2.29 (the modified Heckel equation) and Equation 2.33 (the modified Kawakita equation) reveals that the two equations are identical, if the constant of Heckel equation, k_1, equals 1/3 and the initial bed porosity in Kawakita equation equals 0.66. Therefore, Kawakita and Ludde (1970) model, similar to Heckel's model, follows a first order lumped-parameter approach.

2.5.3 Adams equation

Adams *et al.* (1994) propose another relationship, by which the strength of an individual particle can be characterised according to the bulk compression pressure-strain data. In this model, the compression of particles in the bed is theoretically modelled based on a series of parallel load-bearing columns, where the system is regarded entirely dissipative, i.e. the compressive energy applied to the bed is totally dissipated as plastic deformation, inter-particle and particle-wall friction, and fracture of the particles, and no elastic recovery is considered. However, similar to the models of Heckel (1961) and Kawakita and Ludde (1970), an approximate first order lumped-parameter approach is used to explain the bed's pressure-strain behaviour.

In this model, a set of active parallel columns of particles is considered, for which the failure of a single particle within the column would be due to the uni-axial compression stress (P_a), constrained by the radial stress (P_l) that acts laterally by the granules of the neighbouring columns (Figure 2.1).

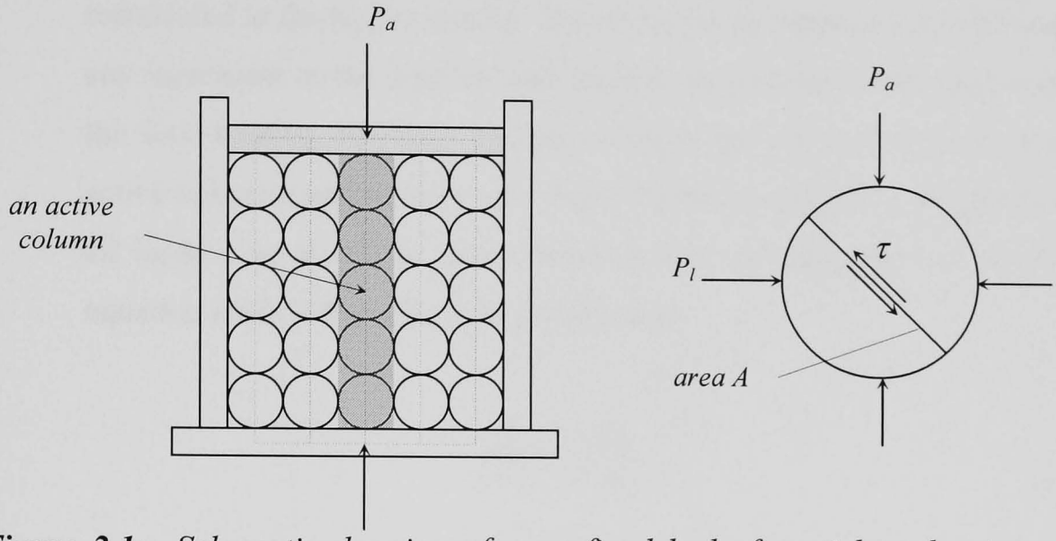

Figure 2.1: *Schematic drawing of a confined bed of particles, showing parallel compression model and axial and radial pressures acting on a single particle in the column.*

Adams *et al.* (1994) employed the Mohr-Coulomb's criterion to explain the macroscopic failure stress, in which the shear failure stress, τ, of granules in the bed is characterised as follows:

$$\tau = \tau_o + \alpha P_l \tag{2.35}$$

where τ_o is the cohesive shear strength of single granules, α is the lateral pressure coefficient, and P_l is the lateral pressure. In fact, in Equation 2.35, τ_o is considered as the apparent crushing strength of single particles under unconfined stress condition and the parameter α is related to the inter-particle friction along the bed's compression direction. The model has basically been established on the basis of two main simplifying assumptions:

a. The failure load of each column is the same and the total load is summed over all parallel active columns. The failure load represents the maximum force that the column resists and corresponds to the failure force of the weakest particle in the column. In practice, as the compression proceeds and particles fail, the columns in which the particles fail may become inactive and only be reactivated at the higher strains. However, in this approach it is assumed that any increment in the applied load implies an increase in the total number of the load-bearing columns and accordingly the total cross section area of active columns under the punch. Applying this assumption, the summation of all loads over all of the active columns and differentiation of the resultant equation leads to the following relationship:

$$dP_a = \tau \frac{dA_t}{A_o} \tag{2.36}$$

where dP_a is the increment in nominal axial pressure, A_t and A_o are the total cross-sectional areas of the active columns and the bed, respectively.

b. The total active area is directly proportional to the strain. It means that any increase in bed strain is reflected as an increase in total cross section area of the active columns. Hence:

$$\frac{dA_t}{A_o} = -k_3 \frac{dh}{h} \tag{2.37}$$

In Equation 2.37, k_3 is a proportional constant.

Combining Equations 2.36 and 2.37 gives:

$$dP_a = -k_3 \tau \frac{dh}{h} \tag{2.38}$$

Equation 2.38 is a first order differential equation that relates the axial pressure of the bed to the bed strain. However, substituting Equation 2.35 in Equation 2.38 and assuming that the lateral pressure, P_l, in the bed is proportional to the axial pressure, P_a, (based on Equation 2.39) leads to Equation 2.40:

$$P_l = k_4 P_a \tag{2.39}$$

$$dP_a = -k_3 (\tau_o + \alpha k_4 P_a) \frac{dh}{h} \tag{2.40}$$

In Equation 2.39, k_4 is a constant relating the lateral and axial pressures, and is thought to be independent of the applied stress during compression. Integrating Equation 2.40 and simply substituting P instead of P_a, ultimately, leads to Equation 2.41.

$$\ln P = \ln\left(\frac{\tau_o'}{\alpha'}\right) + \alpha' \varepsilon_n + \ln\left(1 - e^{(-\alpha' \varepsilon_n)}\right) \tag{2.41}$$

where ε_n is the bed natural strain, defined by:

$$\varepsilon_n = \ln\left(\frac{h_o}{h_p}\right) \tag{2.42}$$

In Equation 2.42, h_o and h_p are bed heights at applied pressure zero and pressure P, respectively. At high natural strains, the last term of Equation 2.41 becomes negligible and can be eliminated, leaving a linear function. The intercept and slope of the linear part of the relationship is used to calculate τ'_o and α'.

The parameters of τ_o' and α', are related to their analogous parameters τ_o and α, as follows:

$$\tau_o' = k_3 \tau_o \tag{2.43}$$

$$\alpha' = k_3 k_4 \alpha \tag{2.44}$$

The coefficient, k_3, in Equation 2.43 is similar to that of Adams and McKeown (1996) presented in their theoretical approach. However, for the term k_3k_4 in Equation 2.44, they lumped it into one coefficient, k. Although, the characteristics of the coefficients (k_3 and k_4) are essentially different, nevertheless, consideration of only one coefficient (k) does not affect the outcome of the model (Equation 2.41). In general, according to Equation 2.37, the constant factor, k_3, represents the rate of increase of the failure area because of the bed strain. The increase can be due to either the plastic deformation or the breakage of particles in bed. On the other hand, the parameter k_4 is considered as the pressure factor, relating confining inter-particles axial and lateral pressures.

Adams and McKeown (1996) employed the Adams *et al.* (1994) model to a number of experimental agglomerates made of fine inorganic particulates and a range of soft binders. They found linear trends at a certain part of plot compatible with the theory. They also investigated the effect of aspect ratio on the apparent strength and defined the parameter of the agglomerate strength at zero aspect ratio, which was obtained by linear extrapolation. They showed a close relationship of this parameter with the crushing strength, obtained from single granule compression tests. However, they emphasised that no theoretical justification for this extrapolation procedure might be offered. Furthermore, they did not probe the role of the agglomerates size and its relation with aspect ratio.

Adams and McKeown (1996) extended their model further and proposed an equation similar to Kawakita equation (Equation 2.30). The equation that they derived is as follows:

$$\frac{P}{\varepsilon_e} = \frac{2\pi c^*}{s^2}\sigma_y + \frac{2\pi c^*}{s^2}\alpha k_4 P \tag{2.45}$$

where, c^* is the yielding constraint factor, s is the particle spacing parameter, σ_y is uni-axial failure or yield strength at zero lateral pressure. It should be noted that in the lumped parameter model developed by Adams *et al.* (1994) the dominant mechanism of particle failure in the bed is considered as shearing. However, the work of Adams and McKeown (1996) shows that the agglomerates fail by crack opening. Therefore, in Equation 2.45, the yield strength, σ_y, has been substituted instead of the shear failure stress, τ_o.

Comparing the equations of Adams *et al.* and Kawakita shows the following relationship between Kawakita parameter ($1/b$) and yield strength:

$$\frac{1}{b}=\frac{\sigma_y}{\alpha k_4} \tag{2.46}$$

Adams and McKeown (1996) reported that for their test materials αk_4 is of order of unity.

Although, Adams *et al.* (1994) model is the only model, which was originally developed, based on the theoretical basis, nevertheless, it has some simplifying assumptions that may limit its application. The model has been successfully tested for some types of agglomerates with soft binders to characterise the strength of granules. However, its capability has not investigated for wider type of particulate solids.

2.5.4 Effect of strain rate on bulk compression behaviour of particles

The response of a confined bed of particles when loaded quasi-statically is often different from when loaded dynamically. In general, materials such as polymers exhibit some degree of sensitivity to the rate of loading and strain rate. In this context, most researchers have concentrated on the study of the effect of strain rate on the quality of the finished product (i.e. tablet product) and little effort has been paid to the behaviour of particles in the bed during compression. However, some

workers (Robert and Rowe, 1985 and 1987; Sarumi and Al-Hassani, 1991; Es-Saheb, 1992 and 1993) have tried to characterise the compression behaviour of some pharmaceutical materials during compression. The experimental analysis of the pressure curves of these materials shows different sensitivity to the strain rate. The researchers have mainly employed the Heckel model, although the model of Kawakita has also been used to characterise the yield pressure of the particles under the low, medium and high strain rates. Roberts and Row (1987) employed the Heckel relationship and proposed a factor to describe the strain rate sensitivity (SRS) as defined by the percentage increase in the yield stress when punch velocity is increased from 0.033 mm s^{-1} to 300 mm s^{-1}. However, in all the above investigations, only the effect of strain rate on the yield pressure has been analysed and other parameters, such as the strength of the particles, have not been considered extensively. Furthermore, the governing underlying mechanisms of particle compression at different strain rates have not been clarified.

From the analysis of the large amount of experimental data resulting from the above piece of works, it may be readily deduced that the general tendency is that the axial compression pressure exhibits an increase with the strain rate. In fact, at high strain rates the particles in the bed demonstrate a stiffening behaviour along with a lower lateral confining pressure. Sarumi and Al-Hassani (1991), and Es-Saheb (1992) showed that when a constant axial pressure is applied the radial pressure (measured as average pressure at the die wall) increases as the strain rate decreases. For example, they have reported that the uni-axial compression of sodium chloride particles at 100 MPa axial pressure displayed the lateral pressures of about 10 MPa and 45 MPa corresponding to the strain rates of 300 s^{-1} and 0.14 s^{-1}, respectively. At low strain rates or low range of applied pressure, the experimental results showed a linear relationship between lateral and axial pressures, as it was already shown in Equation 2.39. In contrast, at high strain rates and wider range of applied pressure, the trends became non-linear. However, in the linear part of plots the constant of Equation 2.39 decreases with increasing the strain rate.

The higher sensitivity of soft and ductile materials to the strain rate might be explained by the creeping and relaxation effects of the bed. In this context, Es-Saheb

(1992) compared the compression behaviour of different materials under constant loading as well as constant volume. He found that for more ductile materials such as Dipac sugar and sodium chloride powders, the rate of axial pressure relaxation (pressure reduction) with time is higher as compared harder materials. Furthermore, he showed that the rate of radial relaxation of powders in the bed is much lower than the axial relaxation. The conclusion drawn from relaxation tests is that the time dependent mechanism of relaxation at high strain rates may not be important, i.e. at lower strain rates the effect of bed relaxation on pressure strain curves may be significant. In other words, alongside the increase in pressure due to the resistance of the powder to the imposed reduction of volume, there is also a tendency for pressure reduction with time. It means that less pressure is required at the lower rates for compression of the bed. However, at the higher strain rates, the time needed for relaxation is probably too short to affect the pressure increase in the bed.

In summary, it can be expected that as much as the material is more sensitive to relaxation (more plastic), the effect of strain rate on the pressure-strain curves becomes more recognisable. As the plasticity of particles is time-dependent, the amount of plastic flow increases with time, under a given set of stress conditions. It is therefore expected that at a high strain rate, there is less plastic deformation at the contacts between the particles in the bed.

To explain the effect of strain rate and work hardening on the bulk compression behaviour of pharmaceutical particles, Es-Saheb (1993) employed a power law relationship, Equation 2.47, which has been widely used and accepted for describing the creep behaviour of the metalic particulate solids (e.g. Soliman, 1987).

$$\sigma = \kappa_1 \varepsilon^f \dot{\varepsilon}^j \tag{2.47}$$

where, σ is axial pressure (stress) for an induced strain, ε, κ_1 is a constant, $\dot{\varepsilon}$ is the strain rate, f and j are strain hardening and strain rate exponents. In order to characterise the power law parameters f and j, it is necessary to separate the effects of strain, ε, and strain hardening from the strain rate, $\dot{\varepsilon}$. Hence, in a series of

compression tests, for each strain rate the variation of axial bed pressure (σ) is plotted on logarithmic scale as a function of strain. The slope of the linear trend of the plotted data characterises the strain hardening parameter, *f*, for that strain rate. By performing experiments under different strain rates, the effect of strain rate on the parameter *f* can be evaluated. The power law relationship can be implemented to find the strain rate exponent *j*. In this case, at first, the compression test is performed with the aim of determining the flow pressure (yield stress) of particles at different strain rates. Es-Saheb (1993) employed the Heckel model to determine the yield stress of particles based on the procedure described earlier in section 2.5.1. Then, by plotting the yield stress versus strain rate on log-log scale and finding the slope of the obtained linear trend, the parameter *j* is characterised. In some cases, even on log-log scale, a linear trend might not be obtained. In this case, the resulting curve is divided into linear parts and the parameter *j* is found for a narrow range of strain rates, for which a linear trend is fitted.

Es-Saheb (1993) implemented the above method to investigate the effect of strain rate on the parameters, *f* and *j* for pharmaceutical powders such as Dipac sugar, Paracetamol, Avicel (microcrystalline cellulose) and lactose (α-monohydrate). He generally noticed that with increasing the strain rate, the strain hardening parameter, *f*, increases. He also observed that for brittle material behaviour, the value of strain hardening is higher than that for the more plastic materials. He found that lower values of yield stress (obtained according to the Heckel model) coincide with lower values of *f*. Hence, the yield stress of these materials is increased with strain rate. Es-Saheb (1993) has also reported that for all materials, the non-linearity is observed in the Heckel plots over the whole range of compression pressures and strain rates. His results show that as the strain rate increases the non-linearity of the plots also increases. This non-linearity behaviour in all the Heckel plots makes it difficult to determine the exact value of mean the yield stress. However, to overcome this problem, Es-Saheb (1993) considered the middle part of the plots for each case, for which more linearity was observed. The same effect is obtained for the strain rate exponent, *j*, as it was increased with increasing the compression rate.

In summary, the work of Es-Saheb (1993) shows that the effects of deformation mechanisms, morphology, and chemical structure of the particles as well as the strain rate are combined and they could be described by the parameters of f and j, obtained based on the power law relationship.

2.6 Literature review of agglomeration and agglomerate characteristics

Size enlargement by agglomeration or granulation is used as a general term for a variety of unit-operation processes, whereby particles are stuck together in such a way that relatively larger particles are obtained, although the primary particles can still be distinguished. The terms "agglomeration" and "granulation" may vary in meaning between different industries. However, these are commonly used synonymously. Pietsch (1991) has defined granulation as "a general term for the production of solids in granular form either by size enlargement or size reduction" and agglomeration as "the action or process of gathering of particulate matter in conglomerates".

The agglomeration processes can be divided into two main methods of agitative (such as fluidised bed, pan, drum, and mixer granulators) and compressive (such as briquetting and tableting). In agitative methods, driving force for agglomeration is provided by mixing of solid particles with a binder, whereas in compressive processes, agglomeration is promoted by pressure (Ennis and Litster, 1997).
Agglomeration may occur spontaneously as in caking in silos or intentionally as employed in a wide range of industries such as pharmaceuticals, foods, mineral processing, and construction. However, for both cases the common phenomena are due to cohesive nature of particulate solids, the presence of adhesive moisture or binder among the particles, sintering or partial melting of particles, dissolution and re-crystallisation in solid contacts. There are numerous industrial advantages in granulation and a comprehensive list has been provided by Capes (1980), Pietsch (1991), and Ennis and Litster (1997). Improvement of structural characteristics and

bulk density of materials, elimination of dust handling hazards or losses and control of solubility of granules are some of the common benefits.

2.6.1 Granulation

The mechanisms of the granulation processes have been studied by a number of investigators, including Cape (1980), Ennis *et al.* (1991), Iveson *et al* (1996), Ennis and Litster (1997), Keningley *et al.* (1997), Litster *et al.* (1998), Iveson and Litster (1998, 1998a), Mills *et al.* (2000), Knight *et al.* (2000), and Simons and Fairbrother (2000).

The current view of wet granulation mechanisms includes three sets of key rate processes of i) wetting and nucleation, ii) consolidation and growth, and iii) breakage and attrition (Iveson *et al.*, 2001).

In the wetting and nucleation, liquid binder is brought into contact with dry powders and is well distributed through the bed to form first nuclei granules. The initial wetting of particles by binder fluid is strongly affected by binder and particles properties as well as operational characteristics such as fluid distribution. In order to quantify the mechanisms of wetting and nucleation, the nucleation zone (also called wetting zone) must be defined first. This zone is where the liquid binder and powder surface first come into contact and form initial nuclei (Iveson *et al.*, 2001). Two processes of nuclei formation and binder dispersion in fact occur in the nucleation zone. The former process is a function of wetting thermodynamics and kinetics, whereas the latter is a function of process variables. The literature investigating the wetting thermodynamics have essentially focused on two aspects: effect of the contact angle between the solid surface and binder, and the spreading coefficient of liquid phase over solid phase. In terms of contact angle, the experimental results have revealed that the lower in the contact angle between the powder and liquid, the better is the wettability of the powder mixture and the larger is the mean granule size. Spreading coefficient is a measure of the tendency of liquid to spread over the surfaces of the solid. It is related to the work of adhesion (Iveson *et al.*, 2001). In

fact, the spreading coefficient determines whether spreading occurs thermodynamically or not. A positive spreading coefficient indicates spontaneous spreading of the liquid binder on the powder. Zajic and Buckton (1990) have been measured the spreading coefficient of different materials according to the concepts of fractional polarity and surface free energy of the system. The kinetics of nucleation has only recently drawn the attention of the researchers (Knight *et al.*, 1998; Tardos *et al.,* 1997). The relative sizes of the binder droplet to primary particles will influence the nucleation mechanism and consequently the kinetics. In this context, Schaefer and Mathiesen (1996) proposed two different mechanisms of nucleation depending on the relative size of the droplet and particle. If the drop is large as compared to the particles, the nucleation will occur by immersion of the smaller particles into the larger drops. In contrast, nucleation with relatively smaller droplets will proceed by distribution of drops on the surface of the particles. At the moment, there is no model describing the immersion mechanism. However, a theory does exist for the penetration of a single drop into a porous surface (Denesuk *et al.*, 1993), which characterise the penetration time according to the wetting thermodynamics (liquid surface tension and contact angle) and wetting kinetics terms (strongly affected by liquid viscosity and effective pore size of particle bed). In this model the penetration time is determined based on the concept that the flow is driven by capillary pressure and resisted by viscous dissipation.

The collision of granules, granules and feed powders, and granules and granulator leads to consolidation and growth, and forming the new bigger granules. Whether or not a collision between two granules leads to coalescence depends on a wide range of factors including the mechanical properties of the granules. As granules grow, they become more consolidated by compaction forces due to agitation of granules. The consolidation stage is responsible for the final granule porosity and strength, which can strongly be affected by granule material properties and intensity of mixing. There are a number of coalescence models predicting quantitatively the maximum granule size attainable and the effect of process and material variables (Iveson *et al.* 2001). These models are based on one of the following hypothesis: i) the models, which assume free movement of the granules with elastic characteristics (e.g. Ennis *et al.,* 1991), and ii) the models, which have been developed based on the plastic

nature of collisions (e.g. Simons *et al.,* 1994). However, none of these models are currently in use due to the lack of knowledge of the various parameters in the models. The most important parameters in this regard are the dynamic mechanical properties such as dynamic yield stress and elastic modulus, which must be measured at high strain rate.

Further agitation of granules in the granulator will lead to their attrition and breakage. The granules may break by wear, erosion in the granulator. At this stage a balance between the binding and destructive forces are established, which govern the final characteristics of the resultant granules, Simons (1996). The formulation properties and operating variables that control breakage are reasonably well known and models are available to predict granule breakage behaviour.

2.6.1.1 Material (formulation) and process variables

The dominant mechanism, governing the granulation, depends on two factors of operating parameters and material properties. The operating parameters are defined by the chosen granulation techniques (e.g. low or high shear mixing rates and peripheral processes such as spraying or premixing of binder fluid with primary particles). These are classified as process design features, whereas material properties such as binder viscosity, surface tension and particle size distribution are defined as product formulation (Ennis and Litster, 1997). The end-use characteristics of granulation product (such as porosity, strength and some other mechanical properties) are directly controlled by processing method as well as the granule formulation. Therefore, overcoming the end-use problems or modifying granules characteristics can often be sorted out by changing the processing conditions or product formulation.

A great deal of research on granulation in the last decade has been concentrated on the formulation of the material and determination of operative variables, such as the size distribution, surface tension and viscosity of binder, and agitation intensity etc. However, the mechanisms of granulation in relation to these variables are not well

understood and the choice of suitable equipment and subsequent manipulation of process conditions to optimise granulation is still largely empirical. Ennis *et al.* (1991) in their attempt to elucidate the fundamental mechanisms of wet granulation in fluidised bed developed an expression for the minimum velocity required for the particle rebound. The model is based on a force balance between two wet spherical particles in collisions, by considering both capillary and viscous dissipation energies. In this model, a Stokes number is considered as a criterion for the rebound of two identical spheres (radius, R_s) after collision. Stokes number (St_v) is defined as:

$$St_v = \frac{2MV_o}{3\pi\mu R^2} = \frac{8\rho V_o R_s}{9\mu} \tag{2.48}$$

where M is the mass of the spheres, μ is the viscosity and V_o is the normal collision velocity. The critical Stokes number above which rebound occurs is defined as:

$$St_v^* = \left[1+\frac{1}{e}\right]\ln\left[\frac{\delta_b}{h_a}\right] \tag{2.49}$$

where h_a is a length characteristics of surface asperities, e is the coefficient of restitution and δ represents the binder thickness around the particle. Based on the model, if the operating Stokes number (St_v) exceeds the critical value (St_v^*), then rebound of colliding particles will occur. In a granulator, particles with different sizes collide at different velocities. On the other hand, the particles may be covered by a liquid layer with a non-uniform thickness. As a result, different mechanism and rate of granule growth may govern the granulation process, depending on whether the operating Stokes number (St_v) falls above or below St_v^*. Three granulation regimes are defined:

- If $St_v << St_v^*$ non-inertial regime (no rebound occurs and all collisions lead to successful adhesion).
- If $St_v = St_v^*$ inertial regime (some collisions successful).
- If $St_v >> St_v^*$ coating regime (no collisions successful).

However, it should be noted that this model is derived based on some assumptions such as non-porous characteristic of particles and elastic collisions, where the consolidation of granules may occur at much slower rate than growth. Therefore, this model is applicable to low agitation intensities. In reality, particles may deform plastically or break on impact, as it is more probable in high agitation intensities. Nevertheless, a significant step has been taken by Ennis *et al.* (1991) to elucidate the relationship of some governing operative and material properties in wet granulation.

Simons *et al.* (1994) investigated the granulation phenomenon in a different way to that of Ennis *et al.* (1991). They developed a model to provide an approximate value for the rupture energy of pendular liquid bridges. Focusing on bridge formation, they considered the reverse situation of bridge rupture. They suggested that if the kinetic energy of the colliding particles were below the required energy to break the liquid bond, then the particles would adhere together. A simple correlation, which estimated the rupture energy of a pendular liquid bridge, was derived as follows:

$$W^* = k_5 \, v_b^{*0.5} \tag{2.50}$$

where W^* is the dimensionless rupture energy ($=W/\gamma R^2$), v_b^* is the dimensionless bridge volume ($=v_b/R^3$) and k_5 is a constant. Thus an approximation of the rupture energy, W, of a liquid bridge can be made according to parameters of bridge volume, v_b, particle size, R, and binder surface tension, γ. However, this model has some limitations such as equi-sized sphere wetted with a binder giving a zero contact angle in static situation. Furthermore, the model considers only the capillary force, which is not applicable to the higher states of saturation and highly viscous binder type.

Litster *et al.* (1998) proposed that granule growth behaviour is a function of the system's liquid binder pore saturation and rate of consolidation. They stated that at very low amounts of binder to solid ratio or liquid saturation, particles will remain either as separate entities or form nuclei due to van der Waals interactions, but will not grow any further. At high amounts of liquid binder to solid ratio granules grow very fast, but further increasing the liquid content to a very high amount will lead to

the formation of slurry. However, for medium levels of binder contents, highly deformable granules will grow steadily, whilst low deformable granules with slow consolidation characteristics will need an induction period to initiate the steady growth.

The consolidation or deformability characteristic of granules is very important in dissipation of break up energies and has a large effect on growing the granule, especially at high mixing rates. It depends on a number of the material properties such as primary particle size, binder's viscosity, surface tension, and amounts of binder to solid ratio. Some researchers have investigated the role of these parameters on consolidation and growth of granules. Knight and Seville (1998) suggested that mixing causes particles to pack more closely together and the interior air of granules to be expelled until liquid completely fill the granules pores. At this stage, further close packing of the particles will lead to extrusion of binder to the surface of granules, therefore, the growing rate of granules will increase significantly. Both Simon *et al.* (1994) and Ennis *et al.* (1991) proposed that consolidation of granules might be retarded by viscous forces due to increasing the viscosity or intensity of agitation. Iveson and co-workers (Iveson *et al*, 1996; Iveson and Litster, 1998, 1998a) in their attempts to characterise the effects of material properties on granule consolidation elucidated that the consolidation in tumbling granulation is controlled by the balance between interparticle friction and viscous dissipations, which may cause resistance against deformation. They found that the rate of consolidation decreases with decreasing the particle size due to increasing the frictional losses. As the liquid content increases, interparticle friction effects are decreased, but on other hand viscous dissipation becomes more significant. They have also studied the effect of surface tension on consolidation rate, which in some cases may become important. Therefore, it can generally be concluded that with increasing binder viscosity and surface tension and decreasing particle size the consolidation rate decreases, and this is due to increasing influence of friction and viscous dissipation forces. Iveson and Litster in another study (Iveson and Litster, 1998b) based on a special experimental procedure could characterise the effect of strain rate on the consolidation rate. They found that with increasing viscosity, surface tension and strain rate, the dynamic yield stress increases but the consolidation rate decreases. For binders with a

viscosity lower than 1 Pa s, Keningley *et al.*(1997) showed that the surface tension forces dominated and consolidation reduced. However, for viscosities higher than 1 Pa s, the data were consistent with domination of viscosity effect on consolidation retardation.

The breakage and attrition of granules is the last stage of granulation process, where growth continues until disruptive and growth forces are balanced in the process. This last equilibrium stage of growth represents a balance between dissipation and collision kinetic energy. The analysis of the breakage of granules and the related mechanisms is presented in more detail in the next section.

2.6.2 Strength, mechanical properties and structural characteristics of agglomerates

The understanding of the breakage behaviour of solid particles does not easily extend to agglomerates. The main reason for this is the discrete nature of agglomerated materials. Subero (2001) has discussed the complexity of agglomerate behaviour in detail, addressing the general issues of load propagation, failure mechanism and the effect of structural characteristics.

Generally, load exerted on an agglomerate propagates through the interparticle contacts. However, not all the contacts are load bearing (Thornton, 2000). The load distribution strongly depends on solid fraction, co-ordination number and the contact orientation.

It is still questionable whether the failure mode of agglomerate is similar to solid particle. Ning *et al* (1997) and Boerefijn *et al.* (1998) in their analysis of the failure of weak lactose agglomerates reported that the macroscopic failure of these agglomerates resembled ductile failure, although the interparticle failure was brittle. Samimi *et al.* (2001) in their attempt to elucidate the effect of humidity on the mechanism of breakage of detergent granules observed plastic deformation at both microscopic (binder elongation) and macroscopic levels (contact plastic deformation

at loading zone). They showed that cracks were propagated through ductile elongation and then rupture of the bonds.

A number of researchers have spent a considerable effort to elucidate the role of the structural parameters and to characterise the strength and some other mechanical properties of the agglomerates. In the following, a review of important literature information is presented.

2.6.2.1 Strength and mechanical properties of agglomerates

Rumpf (1962) has been the pioneer in developing a theory for the strength of agglomerates. Although Rumpf's theory is now proved to be too simplistic, it however, elucidates the main factors affecting the strength of a granule, i.e. porosity and the size of primary particles. Based on Rumpf's model, the granules interparticle contacts fail in a tensile rather than shear or compression manner. The tensile strength calculated here is the force necessary for failure divided by the cross section area of granules. Rumpf (1962) developed his model based on the following assumptions:

- The failure of all bonds occurs simultaneously in the fracture plane, which is made of sufficiently large number of bonds.
- The primary particles are all the same size. In the case of polydisperse granules, the smaller particles cover the bigger ones.
- The primary particles are homogeneously distributed in the granule.
- The strength is the average value of all bonds and it is distributed closely around mean value.

Using these assumptions, and taking into account structural and geometrical considerations, Rumpf (1962) derived the following correlation for the tensile strength of agglomerates, σ_f.

$$\sigma_f = \frac{1.1(1-\psi)Z}{\pi d^2} F = \frac{1.1\phi Z}{\pi d^2} F \tag{2.51}$$

where ψ is the void fraction, Z is the co-ordination number, d is the diameter of the primary particles (mono-disperse size), F is the average value of strength for the individual bonds, and ϕ is the solid fraction.

There are a number of empirical correlations, which relate the co-ordination number as a function of porosity or solid fraction. Rumpf (1962) employed the following relation, given by Smith *et al.* (1930)

$$Z \cong \frac{\pi}{\psi} = \frac{\pi}{1-\phi} \tag{2.52}$$

Using Equation 2.52 in 2.51 leads to the following equation.

$$\sigma_f = \frac{1.1(1-\psi)}{\psi d^2} F = \frac{1.1\phi}{(1-\phi) d^2} F \tag{2.53}$$

Equation 2.53 is the general relationship of granule strength as a function of individual contact force and porosity, according to Rumpf's theory.

Rumpf (1962) also tried to develop the correlation of granule's strength by investigating different bond types corresponding to interparticle force (F). He considered binding mechanisms such as auto-adhesive, solid bridge, non-moveable or moveable liquid bonds with different filling space conditions from discrete lens-shaped (pendular state) to coalesced network of a liquid layer covering the particles (funicular state), or complete filling of the voids with liquid (capillary state). For each one he determined F and consequently, σ_f.

A more fundamental model of agglomerates mechanical properties has been developed by Kendal *et al.* (1986), based on the energy balance proposed by Griffith (1920) for crack propagation (see Lawn, 1993). Griffith considers variation of two

energies during fracture: a surface energy, which is required for the creation of new surfaces and the mechanical energy, which is a deriving force to develop the crack. The mechanical energy is itself made of the elastic strain energy stored within the solid and the potential energy due to the displacement of loading point as a result of external load. Griffith theory implies that a crack would only propagate if the variation of the total energy of the system with the crack length is negative.

Kendal *et al.* (1986) applied the Griffith theory to agglomerates made of smooth, mono-disperse spherical particles, addressing first the case of two spheres in contact with interface energy Γ. They calculated the energy required for creation of new surfaces during detachment of spheres, U_s, based on the model of Johnson *et al.* (1971) as shown in the following.

$$U_s = \pi a^2 \Gamma = \left[\frac{81}{256} \frac{\pi^5 \Gamma^5 d^4}{E^2} (1 - \nu_p{}^2)^2 \right]^{1/3} \tag{2.54}$$

Consequently, they calculated the elastic energy stored in the solid, U_e, for separation of the two particles:

$$U_e = \left[0.02025 \frac{\pi^5 \Gamma^5 d^4}{E^2} (1 - \nu_p{}^2)^2 \right]^{1/3} \tag{2.55}$$

Thornton and Ning (1998) calculated the work done in the separation of two adhesive particles, and obtained a slightly different constant. However, the total energy to separate two elastic particles held together by adhesive bond is obtained as the difference between Equations 2.54 and 2.55.

Kendal *et al.* (1986) and Kendal (1988) applied this theory to a number of ordered packings of spheres. By considering the cleavage planes of these packings, they developed a relationship for the fracture energy of the assembly, G^*, as a function of solid fraction, ϕ, fracture interface energy, Γ_{fr}, and properties of solid material:

$$G^* = 56\,\phi^4 \left(\frac{\Gamma_{fr}^5}{E^2 d^2} \right)^{1/3} \tag{2.56}$$

Kendal *et al.* (1986) applied similar approach to obtain the elastic modulus of assemblies, E^*. They employed these models to the random packed agglomerates assuming the same trends as the ordered ones on order to calculate the effective fracture surface energy and elastic modulus of the assemblies.

According to LEFM, the strength of brittle solids is controlled by the presence of defects such as flaws, micro-cracks, voids, dislocations, etc. These defects behave as stress concentrators, which in their vicinity can generate local stresses above the theoretical strength of material. Therefore, from the fracture point of view, the strength of continuum solids is expected to depend on intrinsic mechanical properties of material and flaw distribution. In particular, these are fracture toughness (K_c), which characterises material strength against crack propagation, and crack length (c). Irwin (1958) showed that for brittle material, K_c, is derived by general form of

$$K_c = \varphi\, \sigma_f \sqrt{\pi c} = \sqrt{G_c E} \tag{2.57}$$

where σ_f is the applied fracture stress, G_c is the critical strain energy release rate, c is flaw size, φ is a dimensionless parameter, which is a function of the specimen dimensions and flaw size, and E is Young's modulus. Irwin (1958) further proposed that in Equation 2.57 an amount of Δc should be added to the flaw or crack size, c to account for the effect of the plastic zone. Δc was previously defined as process zone or plastic zone size, r_p, (Equation 2.7). This zone is a spherical volume on the tip of defect, which micro-cracks or plastic deformation occurs there. For brittle granules, process zone is small enough that is neglected; hence, Equation 2.57 can directly be applied. However, for ductile granules, Irwin (1958) showed that due to the yielding at the tip of the crack, plastic zone size should be added to the crack length. Therefore, fracture toughness was then modified by the following equation.

$$K_c = \varphi\, \sigma_f \sqrt{\pi (c + \Delta c)} \tag{2.58}$$

Rearranging Equation 2.58, the fracture stress of a material is given by

$$\sigma_f = \frac{K_c}{\varphi \sqrt{\pi (c + \Delta c)}} = \frac{\sqrt{G_R\, E}}{\varphi \sqrt{\pi (c + \Delta c)}} \tag{2.59}$$

Kendal *et al.* (1987, 1987a), and Kendal *et al.* (1988) applied LEFM theory (Equation 2.56) to relate Young's modulus and fracture energy of particle assemblies (E^* and G^*) to the fracture toughness, K^*_c, and fracture strength of agglomerates, σ_f, given by

$$K_c^* = \frac{31(1-\psi)^4\, \Gamma_f^{5/6}\, \Gamma_{eq}^{\ 1/6}}{\sqrt{d}} \tag{2.60}$$

$$\sigma_f = \frac{15.6(1-\psi)^4\, \Gamma_f^{5/6}\, \Gamma_{eq}^{\ 1/6}}{\sqrt{d\, c}} \tag{2.61}$$

where Γ_f and Γ_{eq} are the interfacial energy of a bond at the fracture and equilibrium conditions.

As it is seen, the model of Kendall for agglomerate strength (Equation 2.61) is significantly different from the model of Rumpf (Equation 2.53). Kendall (1988) argues that the assumptions suggested by Rumpf for the calculation of the granule tensile strength overestimate the strength. Compared to the Rumpf's model, Kendall found a weaker dependency on primary particle size and a stronger (fourth power) dependency on solid volume fraction (ϕ). However, Subero (2001) recently showed that the terms of porosity/solid fraction in Rumpf and Kendall equations are correlated linearly for the values of solid fraction between 0.36 and 0.76.

The work of Kendall and co-workers can be considered as the most comprehensive theoretical model so far, which relates the macroscopic mechanical properties of

granules to its structural parameters and bond characteristics. Although, Kendall's model has shown to give the correct dependence of strength on particle size and granule viodage, further work by Mullier *et al.* (1987) and Abdel-Ghani *et al.* (1991) indicated that Equation 2.60 underestimates K_c^* by several orders of magnitude. The main reason for this discrepancy is that Kendall's model neglects the dissipative processes at the crack tip arising from extensive micro-cracking or plastic deformation and considers only the crack propagation along the main fracture plain. Mullier *et al.* (1987) in their experimental investigations employed three-point-bend tests of beam specimens to measure the fracture energy and fracture toughness using agglomerates made of glass beads adhered together with a polymeric binder. According to their experimental results, complications are mainly due to flaw distribution within the polymeric bridge, whereas Kendall's theory considers the fracture toughness only due to flaw distribution within the agglomerate. On the other hand, Kendall's model is established based on Equation 2.57, in which strain energy release rate or fracture energy (G_c) is constant. However, for some of the polymeric binders with ductile characteristics, fracture energy may increase during unstable crack propagation.

For characterising the strength, fracture toughness and fracture energy of agglomerates most of researchers have applied the three-point and four point bending tests on a bar which has been pre-notched or cracked (Plati and Williams, 1975; Adams 1985; Mullier, *et al.*1987; Kendall, 1988; Adams, *et al.* 1989; Ennis and Sunshion, 1993). Applying the three-point bend testing method to a series of such bars with different notch depths using Equations 2.58 and 2.59 in an iterative manner will yield K_c and Δc. Adams (1985), employed a similar approach to brittle and ductile agglomerates and found that for dried agglomerate made of sand particles and PVP binder, a linear relation of $(\sigma_f \varphi)^2$ as a function of $1/c$ is valid, i.e. LEFM applies, but ductile material such humidified samples of sand and PVP displayed a significant deviation from linearity. He showed that for inelastic materials the LEFM theory could also be applied, if nominal crack length was corrected by adding the plastic zone size. Adams *et al.* (1989) then determined the plastic zone size of typical agglomerates, which were in order of a few millimetres. Mullier *et al.* (1987)

in the same manner found relatively high value of plastic zone to about five particles diameter.

2.7 Conclusions

Given inherent heterogeneity of agglomerates with a wide variety of structural characteristics, it is not obvious that the existing highly idealised micro-mechanical models can describe the mechanical properties of such a complex material. As mentioned above the two models of Rumpf and Kendall and co-workers address the agglomerates strength as a function of porosity according to the some simplistic assumptions. Even, these models predict the strength of the granules with different dependency on porosity (or solid fraction). In Rumpf's model the strength scales with $\phi/(1-\phi)$, whereas in Kendal's model the dependence follows the form of ϕ^4. However, Subero (2001) showed that the terms of porosity/solid fraction in Rumpf and Kendall equations are correlated linearly for the values of solid fraction between 0.36 and 0.76. For wider range of porosities, the two terms no longer show linear dependency. On the other hand both models have been established based on the overall porosity rather than local structural characteristics of a specific region (i.e. contact loading zone). This may in turn affect the overall agglomerate damage behaviour. This highly discontinuous and heterogeneous characteristic makes it difficult to predict the load and stress transmitted within the agglomerates. The structural heterogeneity of agglomerates such as porosity distribution and the characteristics of the inter-particle bonds make it difficult to develop of a universal model covering all conditions. For this reason, the agglomerates' mechanical properties are still characterised based on the empirical correlations and experimental methods. Clearly further work is needed in this area to get more insight on the effect of porosity distribution and inter-particle bond characteristics on the mechanical properties of agglomerates.

In terms of mode of failure, again, the local structure may affect the failure pattern of the agglomerates. It is unclear whether the classic definitions of failure mode as brittle, semi-brittle and ductile are applicable to agglomerates. At least, for ductile

failure, workers have reported different breakage behaviours. Ning *et al.* (1997) and Boerifijn *et al.* (1998) reported macroscopic ductile and microscopic brittle inter-particle failures for weak lactose agglomerates. In contrast, Samimi *et al.* (2003) observed an extensive plastic deformation and consequently ductile failure for both macroscopic and microscopic scales of soft agglomerates.

The use of the breakage functions, as a means to characterise the size distribution of broken particles is important in the assessment of the size reduction performance. The functional dependency of size distribution of the impact product on impact velocity was investigated by some workers for different particulate solids, in which the governing relationships were commonly correlated with velocity power index of 2. However, for agglomerates this functionality is not obvious and needs to be investigated in more detail. Subero (2001) in his attempt to quantify the impact breakage of agglomerates made of glass beads and brittle polymeric binder showed that the extent of breakage followed a power law trend with impact velocity. He reported the velocity index in the range of 1.00-1.80, i.e. below the value of 2. This is presumably because of the effect of the agglomerate structure on the breakage behaviour.

The modulus of the complement part of the particle size distribution has been considered by a number of investigators as a key parameter in characterising the size distribution of impact product. In this context, the physical significance of the modulus and factors affecting it (e.g. structure of agglomerates) are of practical interest. For a large number of particulate solids the modulus was found to be independent of the impact velocity. However, for agglomerates other effects such as size and angle of impact have not been investigated in detail.

In terms of bulk compression of particulate solids, three models of Heckel (1961), Kawakita and Ludde (1970), and Adams *et al.* (1994) were critically reviewed and the meanings of the parameters characterised experimentally were discussed. However, the applicability of the models to different types of agglomerate and the strain rate effects are features, which require further work.

3 PHYSICAL PROPERTIES OF TEST MATERIALS AND PREPARATION OF SAMPLES

3.1 Introduction

The selection of test materials in this work is based on the current industrial interest to improve the material and process design. Nevertheless, there is significant scientific interest regarding the physical and structural properties as well as the breakage behaviour of these materials.

In this chapter, the test materials and their physical properties and size distribution of the samples are described. Furthermore, the preparation methods of representative samples for experimental work are described.

3.2 Test materials

Three types of agglomerate are investigated here. The granular materials, all, have been produced and despatched to the University of Surrey by Unilever Research Vlaardingen (URV). It should be noted that there is a limitation in reporting the details of the processing methods of these materials for confidentiality. Nevertheless, the properties of agglomerates are described in sufficient detail for use in the analysis of their breakage behaviour. In this context, the samples throughout the thesis are simply identified as Samples 1, 2 and 3.

Sample 1 is a model agglomerate, which has been made of calcium carbonate powders (known commercially as Durcal) as the primary particles and Polyethylene glycol (PEG) as the binder. Samples 2 and 3 are detergent based granules. These samples have different evolved structures arisen from their different manufacturing methods. Samples 1 and 2 have been produced by fluidised bed granulation but

Sample 3 has been made using high shear mixing granulation. Samples 2 and 3 have the same formulation.

3.3 Preparation of representative samples

Each sample type was despatched to the University of Surrey in 50 kg barrels. In order to obtain smaller batches of representative samples, the process of riffling was carried out on all samples by using a splitter device (Porta Splitter, model SP-2, Gilson INC). The splitter device consisted of two adjacent chutes and two collecting bins at the bottom of the chutes. In the splitter, there is an equal chance of a particle going into either of the two adjacent chutes. When the shutter of the chutes is opened, the particles will flow down the two adjacent chutes and the bulk is split into equal amount in the two containers underneath. Sample splitting was continued until approximately 6 kg samples were made.

The Samples were then sieved manually by the complete series of BS410 sieves according to ASTM C136 standards by tapping the sieves with wooden stick and rotating them so that the granules have the opportunity to pass with different orientations over the mesh (Allen, 1981). The particle size distribution of samples was obtained by sieving about 1 kg of feed particles. Five minutes tapping of each sieve was found adequate to produce an effective separation. To produce sufficient amount of each sieve cut each sample was first subjected to mechanical sieving with the complete series of standard sieves (large capacity) and then each mechanical sieve cut was sieved again manually with the similar sieve size, but with smaller capacity. The products of sieving were collected in the bottles and kept for the planned experiments.

For visual examination of feed material of various samples a light microscope was used. For particle size and shape analysis an image analysis system comprising a Sony DXC 930 3CCD video camera, mounted on a MEJI stereomicroscope was used. The reflected light microscope (RLM) images were acquired digitally and subsequently processed using Optimas 6.1 image analysis software on a Pentium PC.

via an IC-PCI frame grabber board. For higher magnifications and better observation of structure of granules, scanning electron microscopy (SEM) was employed. The system consists of a Hitachi S-3200N variable pressure SEM with back-scattered electron detection, quantitative X-ray analysis, X-ray mapping and image analysis.

3.4 Size distribution of samples

3.4.1 Size distribution of Sample 1

The frequency and cumulative particle size distributions of Sample 1 are shown in Figures 3.1 and 3.2. The figures illustrate a granule size distribution in range of 8000 μm to 63 μm. However, the mode of size distribution is between 500 and 600 μm, in which about 50 wt% of original granules are over the size of 600 μm. Moreover, the cumulative size distribution of granules shows that about 90% of granules are larger than 355 μm and less than 10 % of granules are larger than 850 μm. The almost uni-modal size distribution of the granules might be as a result of the physically uniform binder distribution and uniform wetting of the primary particles during granulation along with proper mixing the granules in the granulator. In this case, best binder distribution and consequently narrow size distribution is achieved by increasing the gas flow-rate in a small dispersion area of fluidised bed system (Iveson *et al.*; 2001).

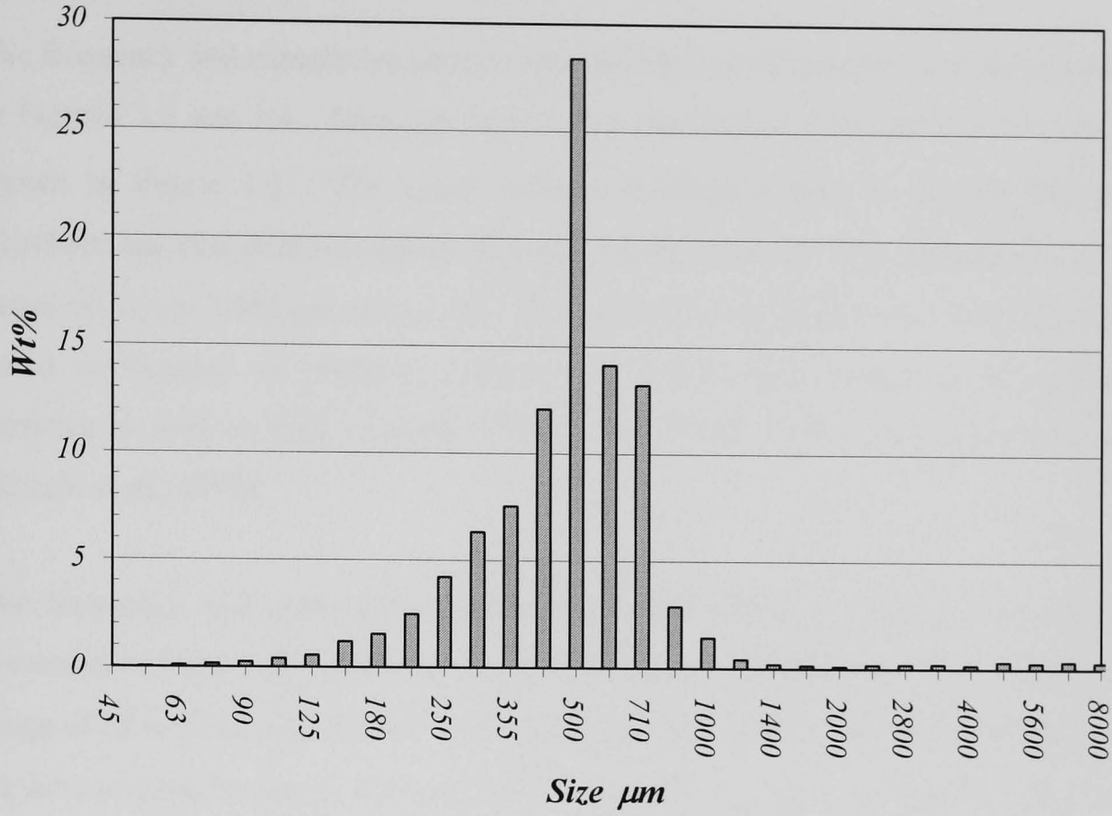

Figure 3.1: *Size distribution of Sample 1 granules.*

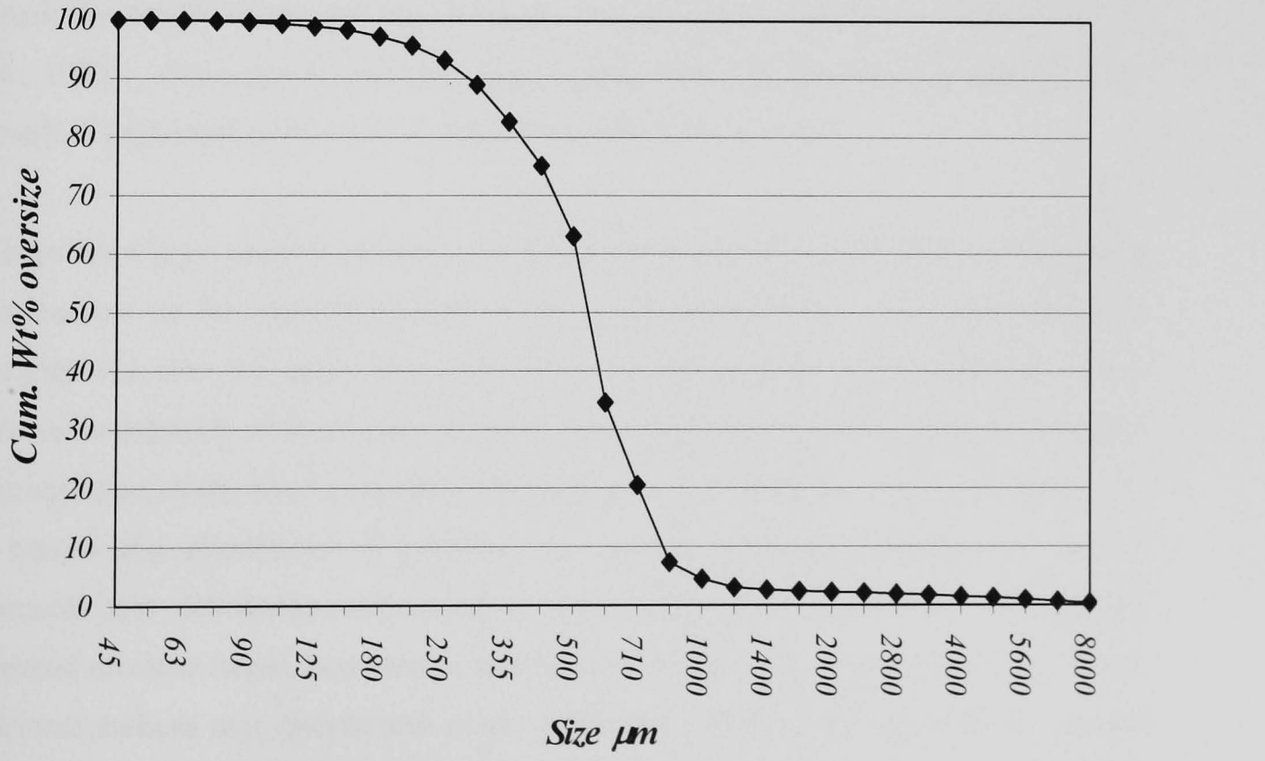

Figure 3.2: *Cumulative particle size distribution of Sample 1.*

3.4.2 Size distribution of Samples 2 and 3

The frequency and cumulative particle size distribution of Sample 2 can be observed in Figures 3.3 and 3.4. Granules have a size distribution from 2800 to 63 μm, as shown in Figure 3.3. The mode of size distribution here is around 420 μm. However, the distributions appear bimodal, where about 80 wt% of particles are in range of 212 to 1000 μm sieve size. The bimodal size distribution of the granules could be because of relatively non-uniform binder distribution on the primary particles as well as high viscosity effect of the binder during granulation process (Knight *et al.*, 1998).

The frequency and cumulative particle size distributions of Sample 3 have been presented in Figures 3.5 and 3.6. The particle size of Sample 3 is distributed in the range of 38 to 3350 μm, for which mean granule size is about 425 μm. Furthermore, 80 wt% of particles are in the range of 150 to 1000 μm. As it is seen in Figure 3.5, for Sample 3, also, the frequency distribution of the original granule appears to be bimodal. In high shear mixing granulation, basically, the product size distribution are independent of the uniformity of binder distribution, as the intensive shear forces crush the initial flocks and agglomerates formed during nucleation stage (Holm *et al.*; 1983). However, in this case, the bimodal size distribution may obtain as the result of high binder viscosity (Schaufer and Mathiesen; 1996).

There are a large number of articles in the literature reporting the effect of processing parameters on the size distribution of the produced granules. The binder delivery method can alter the nuclei size distribution and subsequent granule growth. There are three methods of the binder delivery including pouring, atomising and melting. Atomisation of the binder together with high rate of mixing can lead to production of a narrow size distribution of granules. In contrast, pouring the binder may lead to bimodal size distribution depending on the mixing rate. In this case, the granules formed are also larger, less porous and have faster growth rate (Iveson *et al.*, 2001). Several authors (e.g. Schaafsma *et al.*, 1998) have studied the effect of the droplet size of binder on the size distribution of the granules. They have found strong relationship between the binder droplet and granule sizes. However, it was found

that for high shear mixing granulation, the amount of binder has negligible effect on the granules size as intensive shearing breaks the granules during granulation.

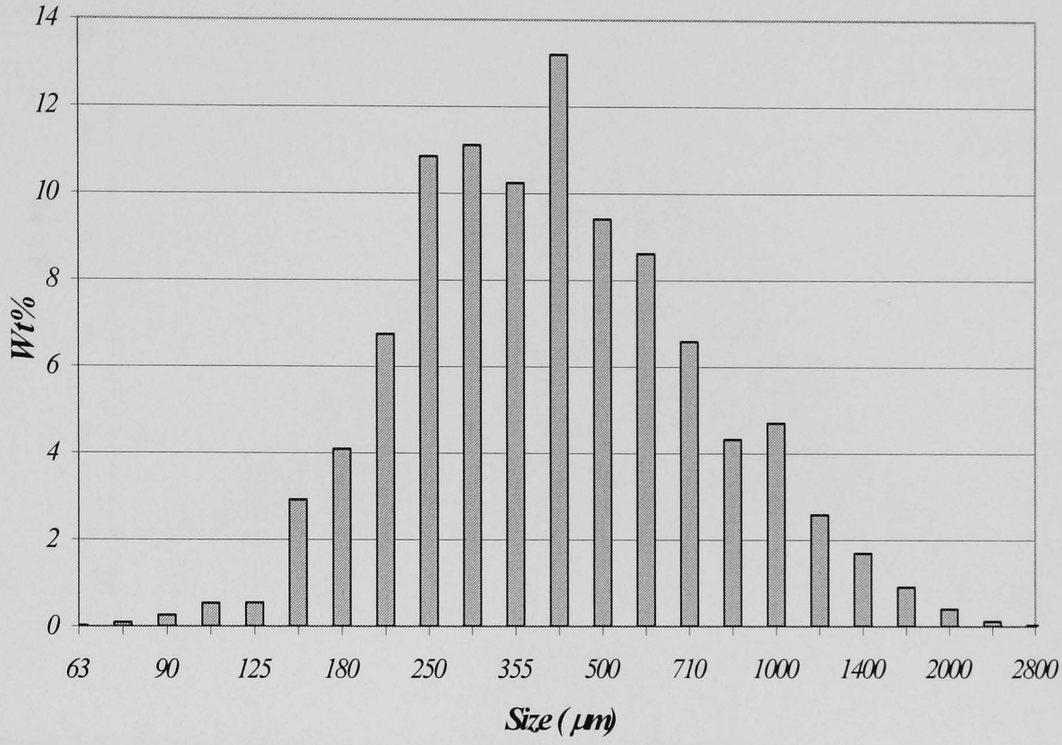

Figure 3.3: *Frequency particle size distribution of Sample 2.*

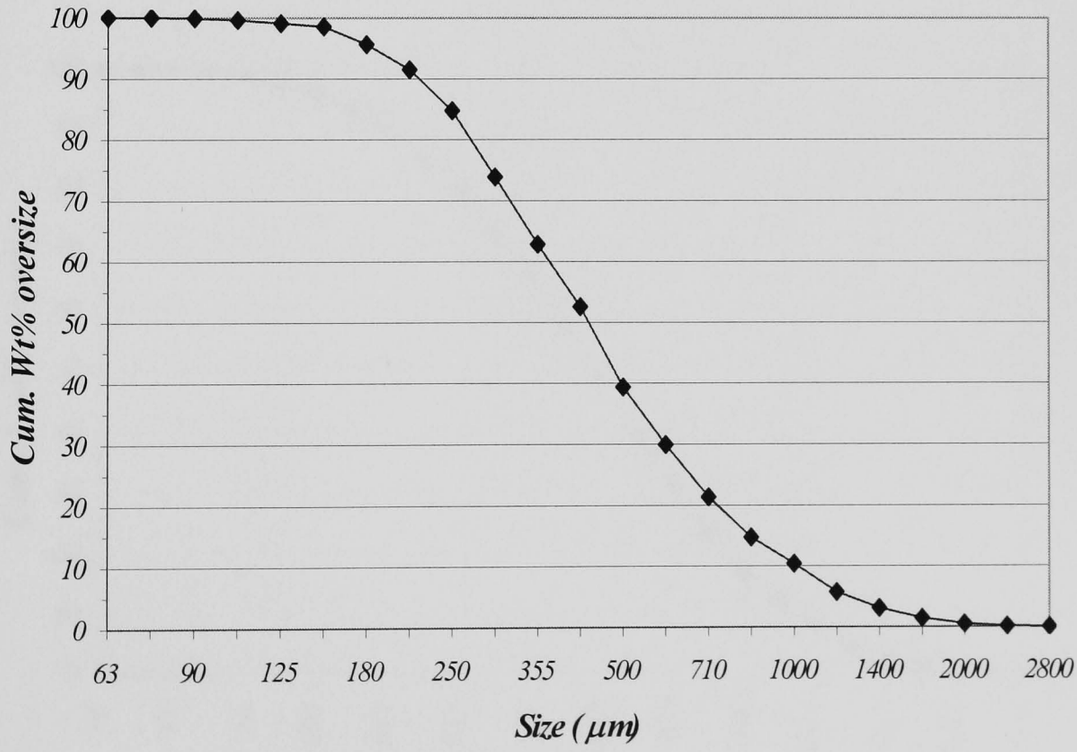

Figure 3.4: *Cumulative particle size distribution of Sample 2.*

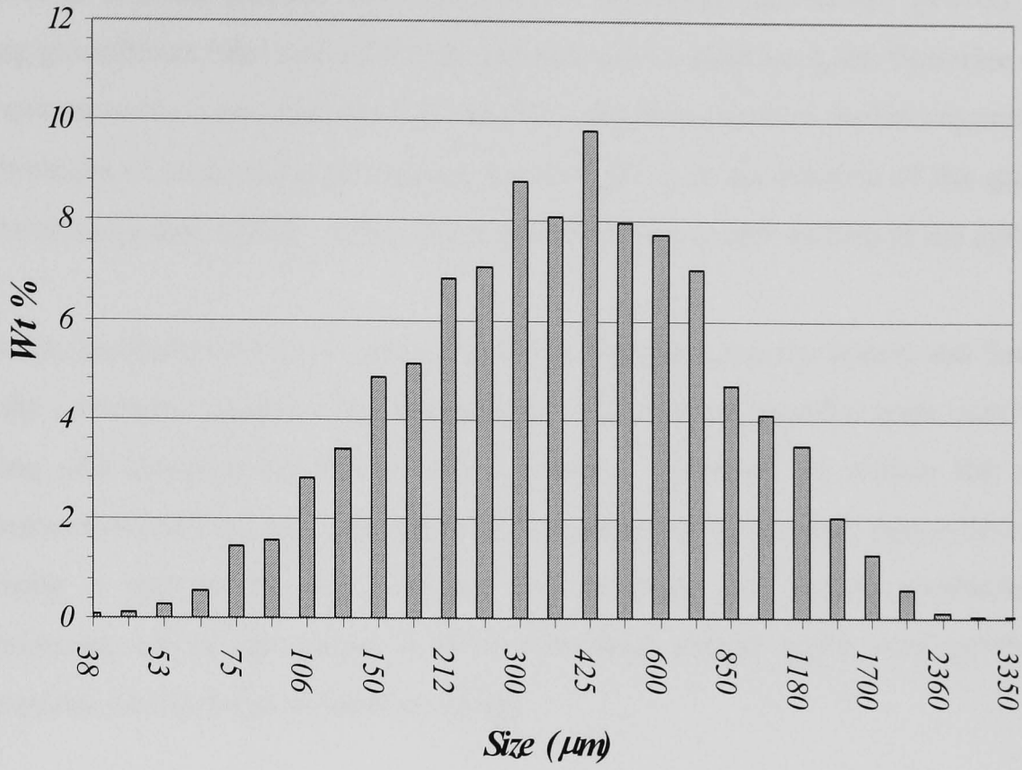

Figure 3.5: *Frequency particle size distribution of Sample 3.*

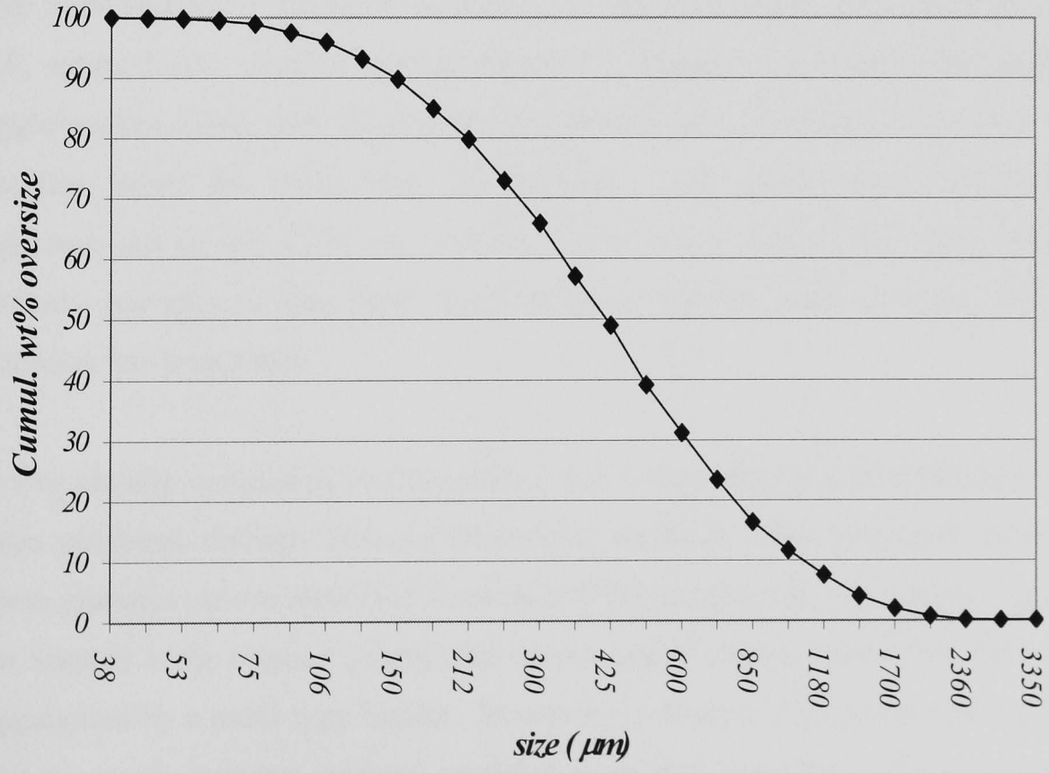

Figure 3.6: *Cumulative particle size distribution of Sample 3.*

The binder distribution can become worse as the binder viscosity increases leading to wide even bimodal granule size distribution. The flow rate of the sprayed binder during granulation may also affect the granule size as increasing the flow-rate causes an increase in the mean granule size. In short, the experimental results suggest that a combination of processing parameters controls the size distribution of the granules, the parameters that initially affect the binder distribution and mixing of the system.

As it can be observed from Figures 3.1 to 3.6, Sample 3 has the widest and Sample 1 has the narrowest particle size distribution. All of these samples were sensitive to sieving and cleaning the sieves with a brush. Therefore, to reduce the risk of agglomerates breakage or deformation before performing any test, precautions (such as using a soft brush) were taken. Nevertheless, just before conducting the experiments, all of the prepared sieve cuts were sieved again very gently with appropriate sieve size to separate the fines.

3.5 Microscopic observations of agglomerates

The SEM and RLM images of Samples 1, 2 and 3 are shown in Figures 3.7, 3.8 and 3.9, respectively. As it is seen in Figure 3.7, Sample 1 is made of irregular shape agglomerates along with large primary particles, low coordination number, and big cavities inside the main body of granules. The microscopic observations of agglomerates reveal PEG has covered almost major part of the outer surfaces of primary particles so that thick solid bridge at contact areas between the primary particles has been made.

It was already mentioned that Samples 2 and 3 have the same formulation, but have been produced through different processing methods. The structural difference of these granules can be identified from their SEM images. As it is seen in Figure 3.8a, for Sample 2, the original granule has been made of a large number of small clusters, aggregated by a paste type binder. However, in Sample 3 no small clusters are seen and the voids between primary particles seem that have been filled by the binder (Figure 3.9a).

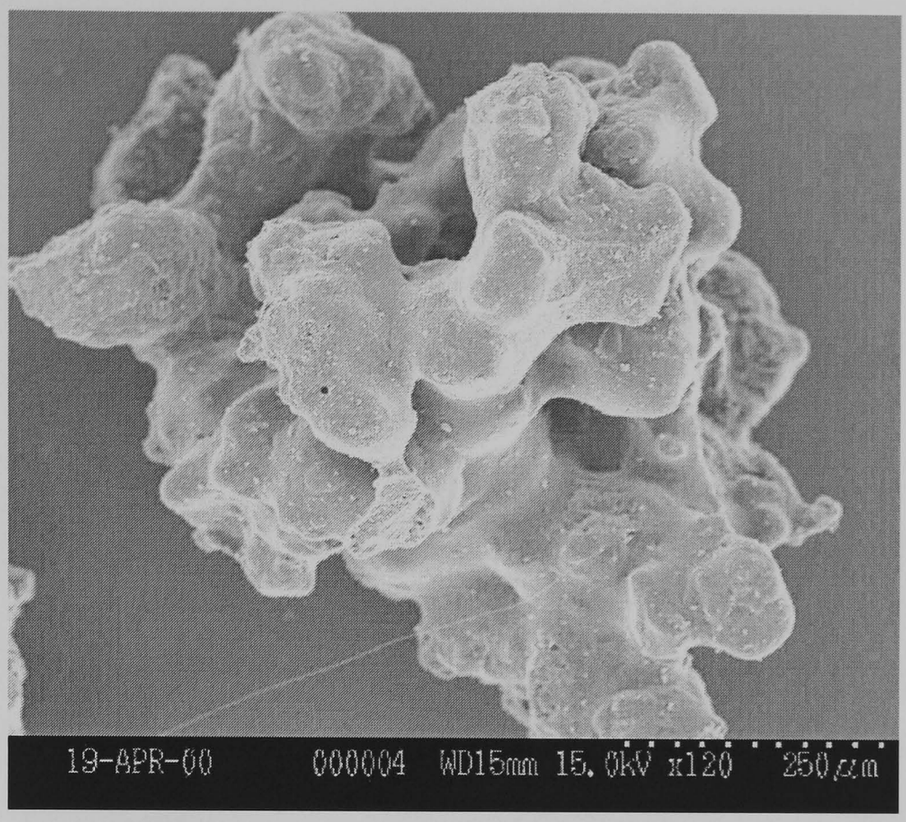

(a)

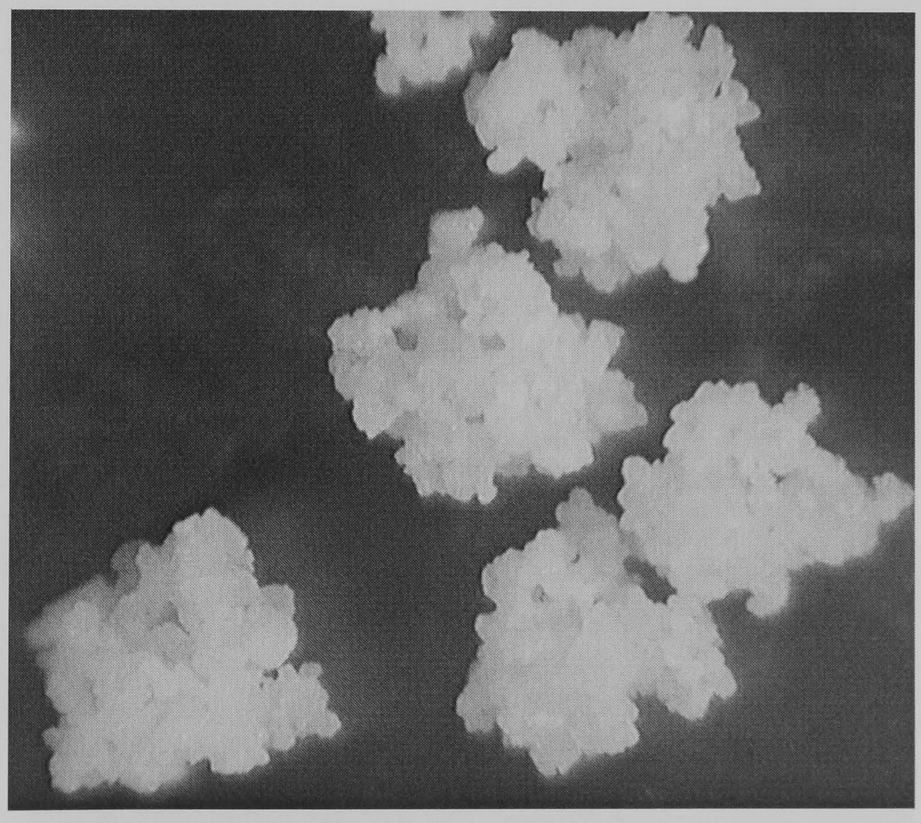

(b)

Figure 3.7: *Microscopic images of Sample 1 granules (a) SEM (b) RLM.*

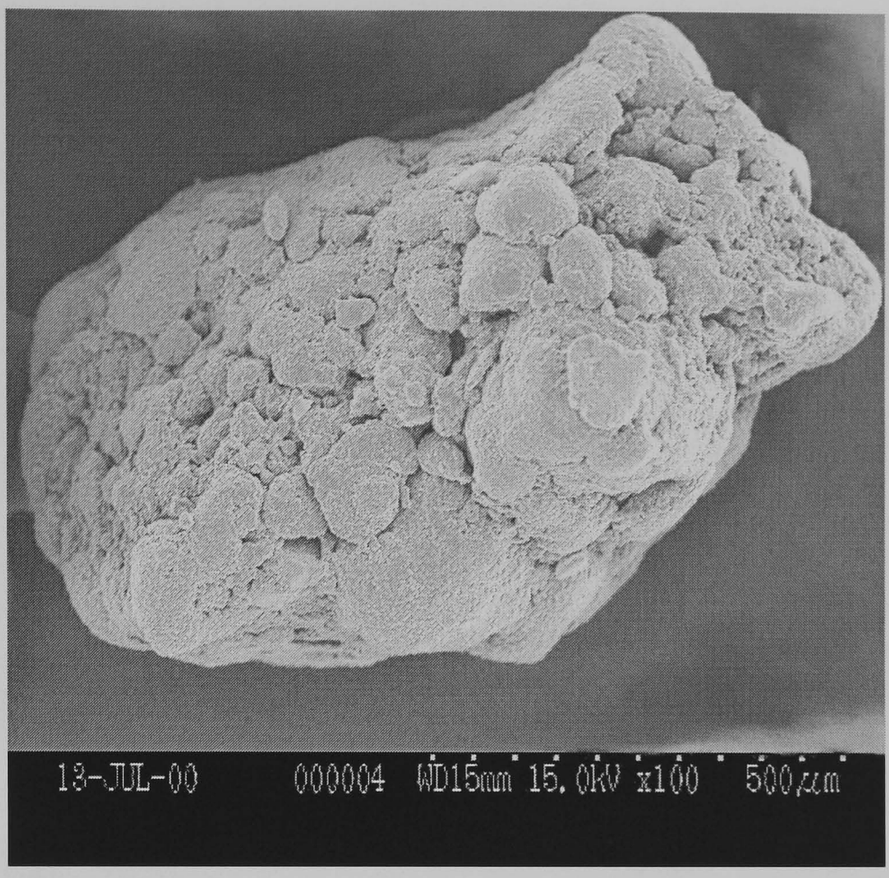

(a)

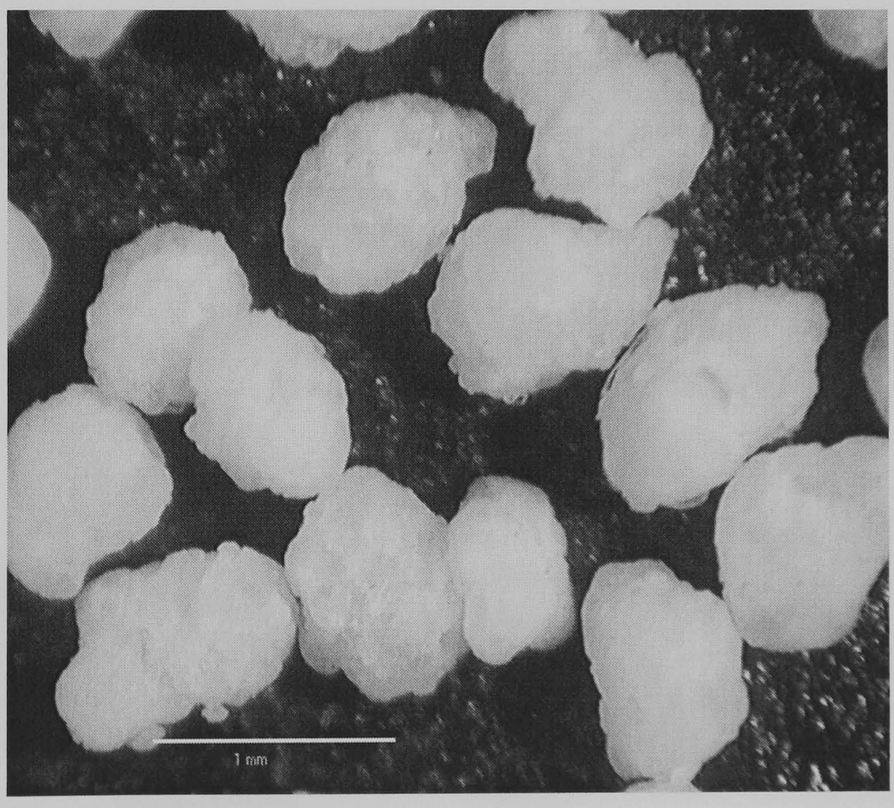

(b)

Figure 3.8: *Microscopic images of Sample 2 granules (a) SEM (b) RLM.*

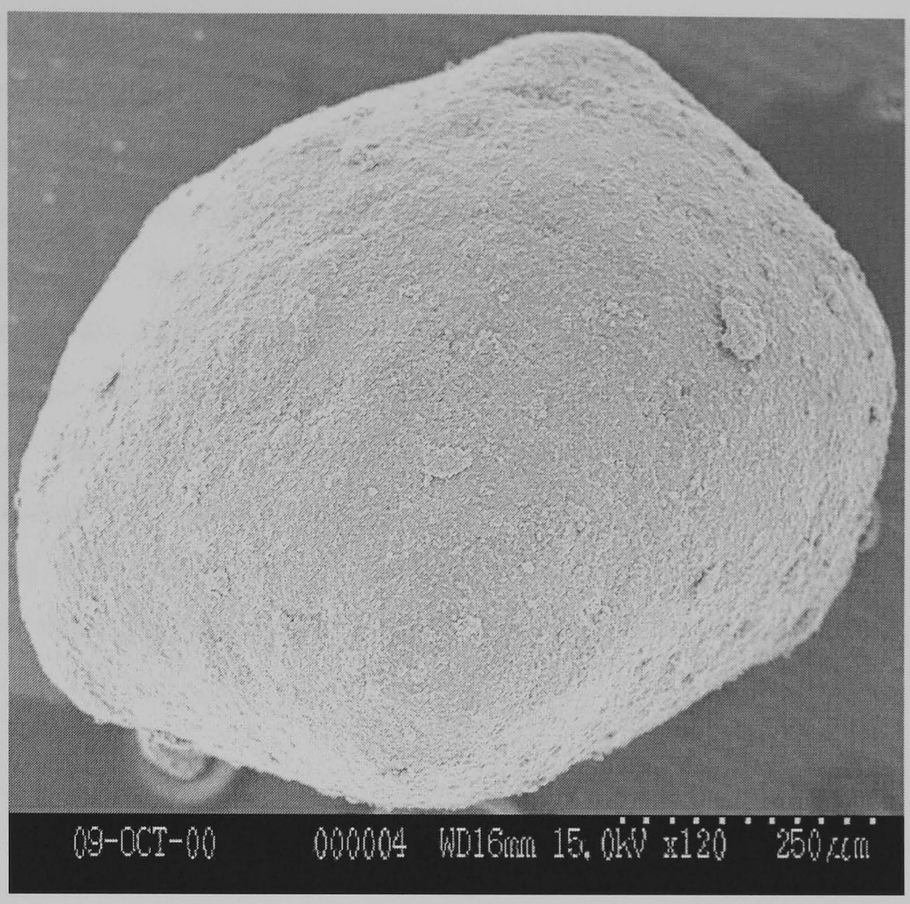

(a)

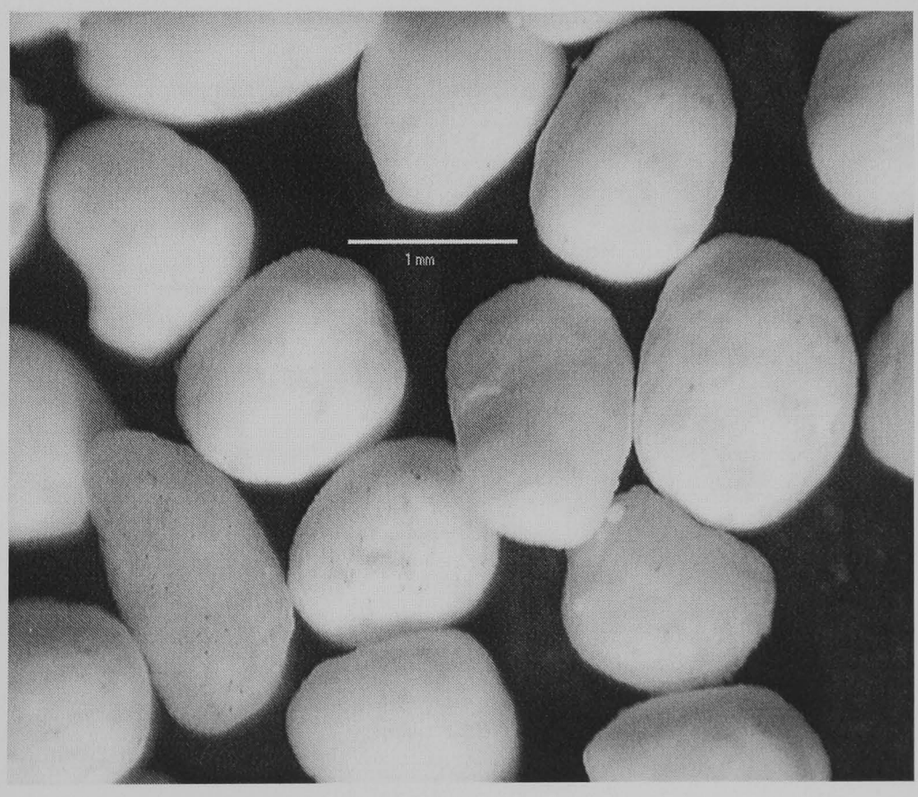

(b)

Figure 3.9: *Microscopic images of Sample 3 granules (a) SEM (b) RLM.*

In fact, for Sample 2, the granule growth has progressed by the coalescence of granular clusters, where the impact of granules during agitation leads to aggregation. In contrast, Sample 3 granules seem that have been made according to the mechanism of layering, for which fine particles stick on to the surface of large pre-existing granules. Both coalescence and layering are traditionally referred in the literatures as two main mechanisms of granule growth. However, during growth, granules might be consolidated, for which the liquid pore saturation increases, and porosity of the granules decreases. As consolidation is often accompanied by gradual alteration of mechanical properties of the granule, it must be considered in conjunction with the growth mechanism. More information regarding to the structure of these granules and their breakage pattern can be found in Chapter 5.

3.6 Physical properties of granules

Some physical properties of the test materials are shown in Table 3.1, provided by URV.

Table 3.1: *Physical properties of the test materials.*

Material		Sample 1	Sample 2	Sample 3
Bulk density (kg m^{-3})		640	780	900
Primary particle mean size(μm)		90	1.2	1.2
Liquid to solid ratio (v/v)		0.69	1.22	1.12
Porosity (v/v)	600-710* (μm)	_	0.16	0.095
	1180-1400* (μm)	_	0.20	0.075
	1700-2000* (μm)	_	0.24	0.060
Yield stress of binder at 20 °C (kPa)		_	38.6	51.0

* *Sieve size*

It is apparent that some of the physical properties of the samples are quite different. Those are noticeable even for Samples 2 and 3, which have the same formulation. In this context, the bulk density of Sample 3 appears to be higher than Sample 2, as its granulation method is different. In literature, the maximum bulk density has been reported for compact detergents, which is 850 kg m^{-3} (Knight, 2001). However, this bulk density is lower than that of Sample 3, but higher than that of Sample 2. High bulk density detergents are directly produced by high shear mixing granulation. In principle, it is possible to make granules having a bulk density larger than 910 kg m^{-3} by preparing non-cohesive, spherical granules having a very wide size distribution. For such granules, the minimum bed porosity and the theoretical bulk density have been reported as 0.4, 990 kg m^{-3}, respectively. However, the granules with this range of bulk density would have poor dispersion and dissolution in application (Knight, 2001).

The skeleton density of the detergent based granules (Samples 2 and 3) was measured as 1676 kg m^{-3} using Helium pycnometry. This value is in the range of density of typical detergent granules, reported in the literature, i.e. 1500 to 1800 kg m^{-3} (Knight, 2001).

The mean primary particle size of Samples 1 reported by manufacturer is about 90 μm. Nevertheless, the size distribution analysis of calcium carbonate particles (Durcal) carried out at Surrey shows a wide size distribution of the primary particles, for which 80% of particles have the size in range of 63 μm to 250 μm. In contrast, Samples 2 and 3 have been made of very fine primary particles having the mean primary particle size of 1.2 μm.

The interesting structural characteristic of Samples 2 and 3 is their porosity, which appears to vary with granule size. The porosity of the granules has been obtained by manufacturer using X-ray tomography. The method relies on characterising the spatial arrangement of components in the agglomerates and consequently analysing the data by simulation tools (Kohlus, 2002). However, the structural analysis of the granules reveals that the porosity increases for Sample 2 with increasing the size, whilst for Sample 3 it decreases. Furthermore, the porosity of Sample 2 granules

appears to be much higher than that of Sample 3. In fact, different trends of the porosity variations of Samples 2 and 3 with size show the size dependency of the porosity of these granules. As the strength of agglomerate depends inversely on the porosity, it would be expected that the strength of Samples 2 and 3 vary with size in somehow different ways. For Sample 2, the increase of the porosity with size shows that larger granules have been subjected to less consolidation during their growth. However, for Sample 3, the larger granules have been consolidated more, compared to the smaller ones, presumably due to the layering mechanism of the granules during granulation process.

4 SINGLE GRANULE AND BULK COMPRESSION TESTS

4.1 Introduction

The *strength* of a granule is sometimes measured using uni-axial compression of the granule between two platens. This method is known as side crushing test. A large number of granules must be tested in this method to obtain a reliable mean and standard deviation, particularly in cases where the distribution of strength is wide. To overcome this problem and to provide a test method, which better represents the bulk behaviour and of course is fast, a number of researchers have tried to relate the strength of single particles to the bulk properties using bulk compression testing method (Heckel, 1961; Kawakita and Lüdde, 1970; and Adams *et al.*, 1994). This technique is usually conducted quasi-statically. However, there are a few cases reported in the literature, where the bulk compression behaviour at high strain rates has also been investigated (Robert and Rowe, 1985; Sarumi and Al-Hassini, 1991; Es-Saheb, 1992&1993). The bulk compression test results, therefore, may provide valuable information for the relationship between single granule properties and bulk parameters of the granules of interest on the.

This chapter addresses the deformation and breakage behaviour of two types of detergent base granule, Samples 2 and 3. Sample 1 is not considered in this regard to focus on Samples 2 and 3 in more detail. Single granule and bulk uni-axial compression tests have been performed at small strain rates. The main objective of the chapter is to analyse the yield and failure strengths of single granules based on the quasi-static bulk uniaxial loading experiments. However, the compression plots are also analysed for characterising some of the physical properties of granules and bulk features such as bulk voidage. In this context, force-displacement data on the bulk compression of the granules are analysed to calculate the compression parameters of the models of Heckel (1961), Kawakita and Lüdde (1970), and Adams *et al.* (1994). The models have already been presented and discussed in Chapter 2. The compression parameters are compared with each other, as well as with single

granule compression results. In the following sections, details of testing methods, the results, discussion and conclusions are presented.

4.2 Materials and experimental methods

In these experiments, two types of detergent base granules, Sample 2 and Sample 3, have been used. The details of the physical properties and size distribution of these samples have been presented in Chapter 3. The samples have different evolved structures arising from differences in their manufacturing methods. In Figure 4.1, scanning electron micrographs (SEM) of the samples are shown. As discussed in chapter 3, Sample 2 has a cauliflower-type structure and seems to be more porous. In contrast Sample 3 seems more spherical and denser than Sample 2.

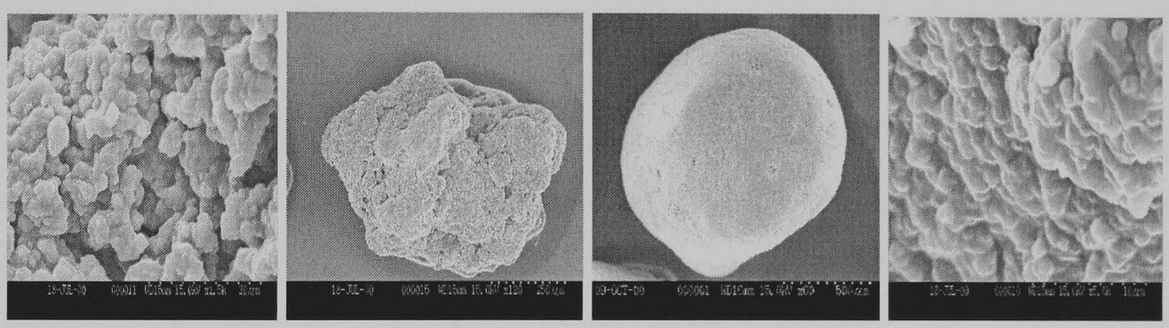

(a) (b)

Figure 4.1: *SEM views of the samples before impact at two different magnifications a) Sample 2, X2.5 k and X120; b) Sample 3, X5 k and X60.*

In single granule compression, about 100 granules were compressed individually between two rigid platens (Figure 4.2). The granules of Sample 3 were only tested, because their shape was more spherical, compared to Sample 2 granules. Moreover, only two sieve-cuts of 1.00-1.18 mm and 1.70-2.00 mm were tested because the resolutions of the testing machine did not permit using smaller granule sizes. Punch crosshead speeds (CHS) of 0.1-0.5 mm min^{-1} (corresponding to strain rates of typically below 5. 10^{-3} s^{-1}) were applied between the platens, using an Instron 4500 mechanical testing machine with a 10 N load cell. A maximum compression load of 1 N was set and on-line load-displacement data were recorded by the system's

computer. The acquired data were used for drawing the load displacement curves. Each individual curve was then investigated for the first sharp decrease in loading, which was usually positioned in the plastic flow region of the curve. The peak compression force before the decrease was considered as the major failure force of the granule, F_f, and was used to calculate the apparent single granule strength, σ_{os}, as follows:

$$\sigma_{os} = \frac{4F_f}{\pi d^2} \tag{4.1}$$

In Equation 4.1, d is the granule size, measured for each individual granule as diametrical distance between two platens when first contact was made between the moving platen and top face of the particle. The calculated strengths were then averaged for all the granules and the average was considered as the single granule apparent strength of the sample. In some experiments, repeated loading and unloading of a single granule was also performed. In this case, loading was carried out up to a maximum level that was lower than the expected peak failure load to investigate the elastic behaviour of granules. Furthermore, some of the granules were taken out of testing machine after unloading with the lower platen in order to observe the top-view of the failure area under a light microscope.

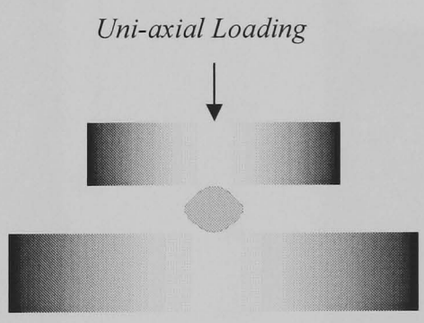

Figure 4.2: *Typical single granule compression system.*

In the confined bulk compression tests, a pre-weighted amount of granules was introduced into the cylindrical die and then tapped to improve packing and produce the required initial aspect ratio (the ratio of bed height to bed diameter). The

diameter and height of the cylinder were designed as 20 mm and 22 mm, respectively. A close-fitting stainless steel piston with a small peripheral clearance (0.2 mm) in the die (to release the trapped air in the die during loading) was used to apply the load. The base of the die was also made of stainless steel but the internal wall was lined with Teflon to reduce friction. Figure 4.3 shows a schematic drawing of the bulk compression system. In most of the experiments, the amount of sample and the initial bed height were chosen in such a way that a constant aspect ratio of 0.9 be achieved. However, for some other tests, the initial aspect ratios of 0.7 and 0.5 were also set up to study the effect of wall friction on the bed compression. Special care was taken in uniform die filling and tapping (the same manner of filling and number of tapping for each test) to get the same measured aspect ratio for all tests. Some preliminary tests were performed in this regard to determine the required weight of granules and tapping number for each sample size. The actual initial bed height was recorded by the system when first contact was made between the punch head and top of the bed. The actual aspect ratio was then calculated based on the actual height. Different bed compression rates were applied in the range of 1 mm min^{-1} to 600 mm min^{-1} (corresponding to the bed strain rates of 0.001 s^{-1} to 0.55 s^{-1}), using the Instron model 4500 mechanical testing machine with a 100 N load cell.

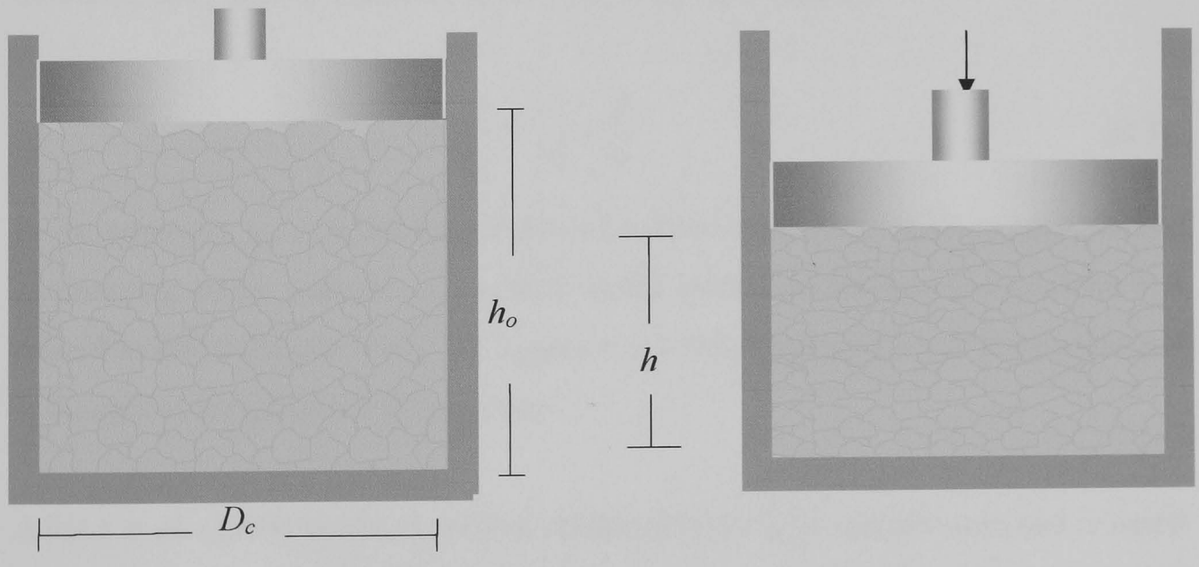

Figure 4.3: *Punch-die arrangement used for the bulk compression tests of granules.*

In this work four sieve cuts (1700-2000 μm, 1000-1180 μm, 600-710 μm and 212-250 μm) of Samples 2 and 3 were used under different constant loading rates. Each test, however, was repeated at least three times and the results were averaged. The loading and unloading experiments were performed up to the maximum load of 100 N, and the bed load-displacement data were recorded on line by the system. The data were then used to calculate the parameters of the models of Heckel (1961), Kawakita and Lüdde (1970), and Adams *et al.* (1994). In the following, a summary of the models is given. The details of these models can be found in Chapter 2.

In the Heckel's relationship, the relative bed density, D, and the applied pressure, P, are related according to Equation 4.2:

$$\ln\frac{1}{1-D} = KP + A \tag{4.2}$$

where K and A are constants suggested to describe particle deformability and initial porosity of bed, respectively (see Equation 2.20).

Another empirical model is due to Kawakita and Lüdde (1970), and is given specially in the following form so that a linear relationship between P/ε_e and P/a is obtained, allowing the constants a and b to be easily evaluated.

$$\frac{P}{\varepsilon_e} = \frac{1}{ab} + \frac{P}{a} \tag{4.3}$$

In the equation, ε_e is defined as degree of volume reduction, which is equivalent to engineering strain, constant a is related to the initial bed voidage and constant b is related to the resistance force. In Equation 4.3 $1/b$ is termed Kawakita constant and is thought to represent the failure stress.

Adams *et al.* (1994) model is another relationship for bulk compression and is based on the assumption that the bed acts as a series of parallel load-bearing columns and that the compressive energy applied to the bed is dissipated as plastic deformation, inter-particle friction, and fracture. The correlation is given by:

$$\ln P = \ln\left(\frac{\tau_o'}{\alpha'}\right) + \alpha'\varepsilon_n + \ln\left(1 - e^{(-\alpha'\varepsilon_n)}\right) \tag{4.4}$$

where τ'_o is the apparent single particle shear strength, α' is a parameter, which is related to the inter-particle friction and ε_n is the bed natural strain. At high values of the natural strain, the last term of the equation 4.4 becomes negligible and can be eliminated, leaving a linear function. The intercept and slope of this linear part of the relationship is used to calculate τ'_o.

4.3 Single granule compression test results

Figures 4.4a and 4.4b show four typical load-displacement plots each, out of hundred uni-axial single granule compression tests of Sample 3 granules, with the sizes of 1.00-1.18 mm and 1.70-2.00 mm respectively. As it can be seen, there are a wide variety of responses for apparently similar granules, which indicates a relatively wide distribution of mechanical properties such as the strength and yield stress. In general, it is clear from Figure 4.4 that most of the granules do not fail abruptly, while significant plastic flow occurs. This behaviour is basically due to the

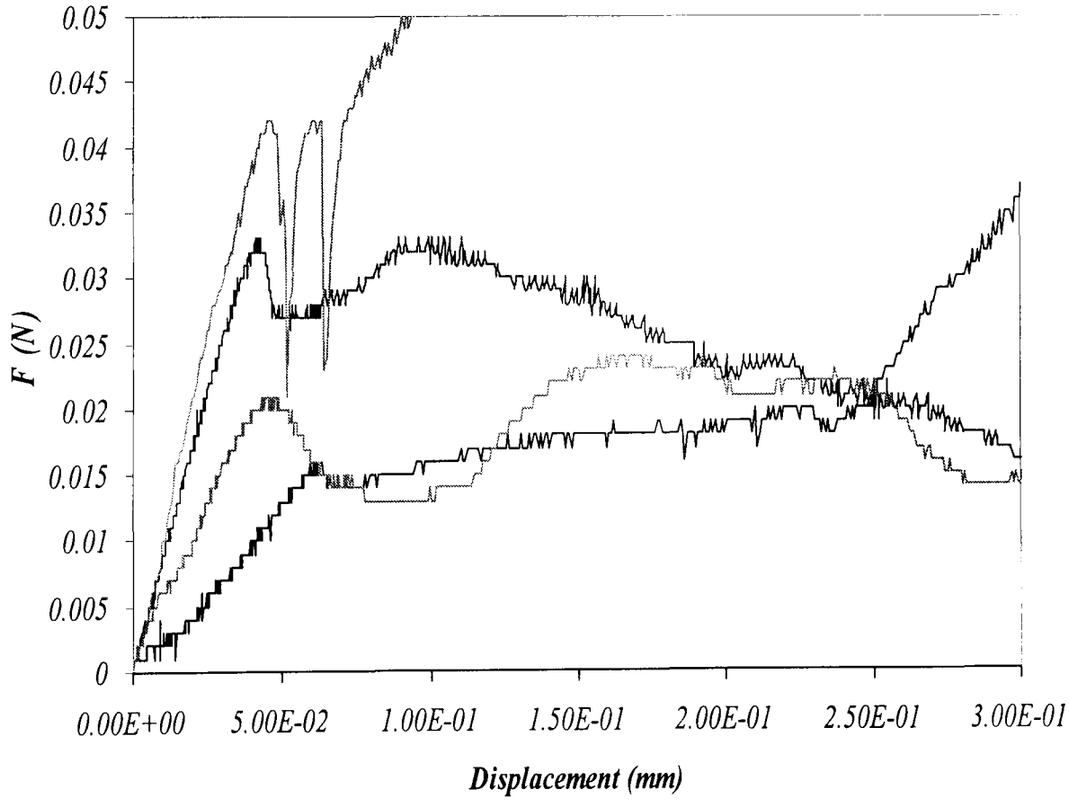

(a)

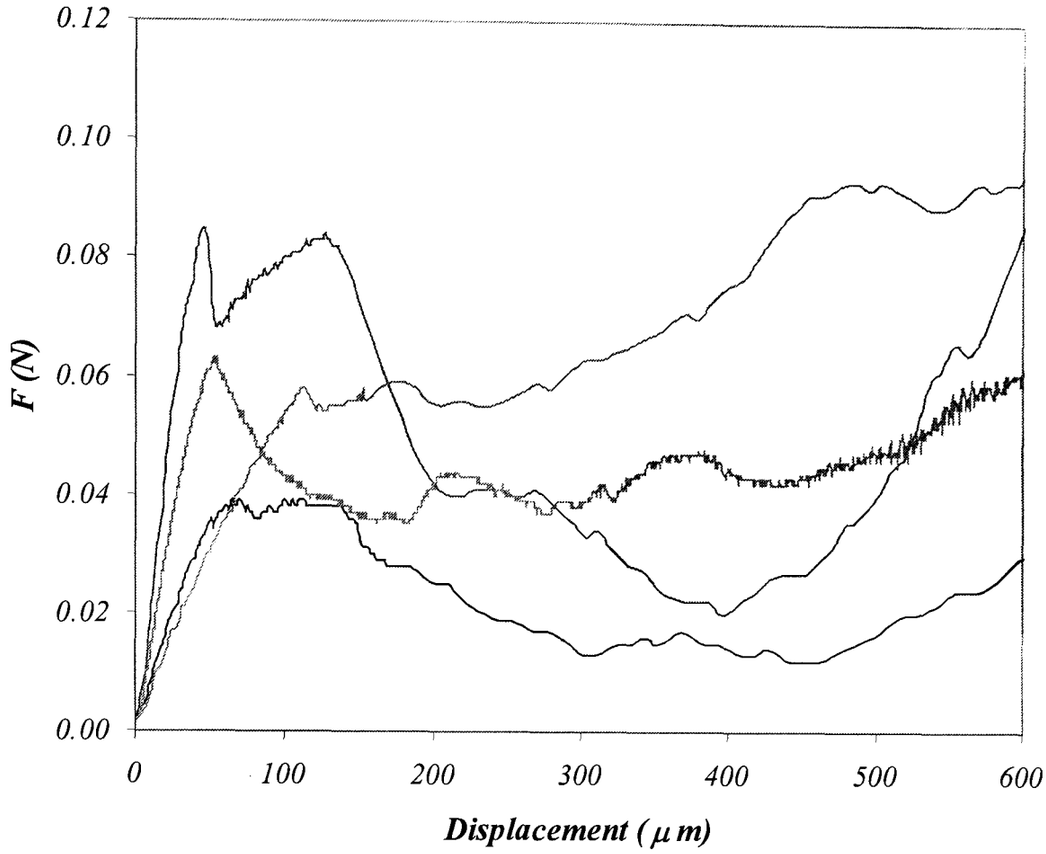

(b)

Figure 4.4: *Force displacement curves of a) 1.00-1.18 mm, b) 1.70-2.00 mm, Sample 3, single granule uni-axial compression.*

Figure 4.5 shows top-view images of failed granules due to uni-axial compression. The images show clearly that the failure occurs according to the crack-opening (failure mode I), as well as in-plane deformation and shearing (failure mode II). The crack-opening usually starts from circumpherence as a result of tensile hoop stresses developed around the loading contact area. Shearing occurs inside the granule and under the contact area through in-plane deformation with almost closed-crack development. Therefore, both tensile and shear stresses are involved in granule failure during single granule uni-axial compression. The common characteristic of both types of failure is similar for which cracks propagate stably during applying the load up to the complete damage of the granule.

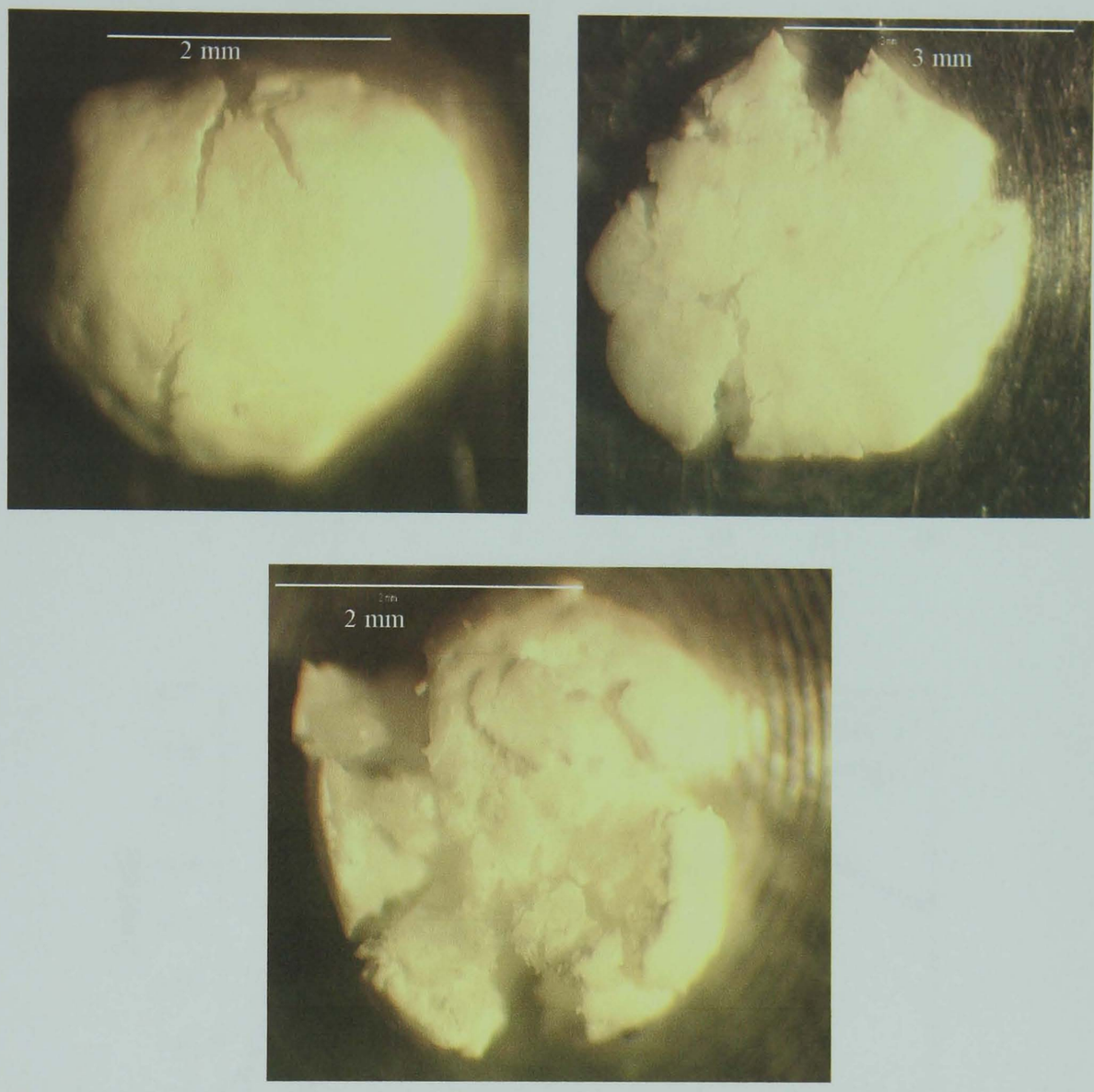

Figure 4.5: *Top-view images of failed granules (1.70-2.00 mm) of Sample 3 after uni-axial compression.*

Figure 4.6a shows two cycles of loading/unloading versus displacement of a single granule in which a same maximum load of 0.01 N has been used. The difference between two curves shows a different extent of inelastic deformation in each case. The hysteresis between loading and unloading of the second cycle indicates the effect of creep. Figure 4.6b shows a further loading/unloading on the same granule but at a higher load of 0.05 N and also the last loading curve during which the granule was crushed. The first two cycles of loading/unloading clearly indicate the inelastic behaviour of the granules, even at early stages of loading.

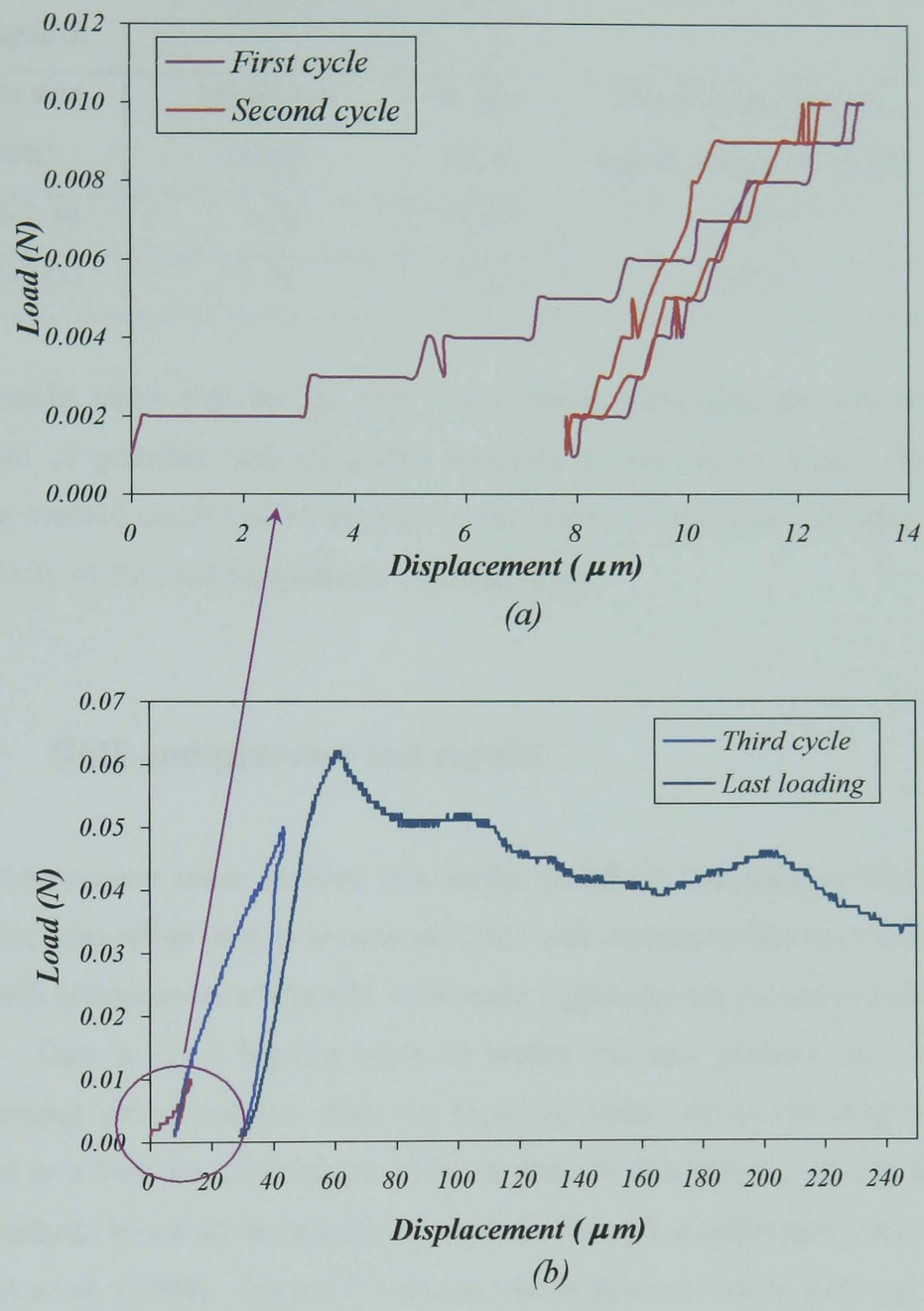

Figure 4.6: *Repeated compression curves of Sample 3, 1.70-2.00 mm granules. a) first and second loading/unloading curves b) third cycle and loading curves.*

Table 4.1 shows the single granule compression test results. The mean apparent strength and standard deviation of the granules have been characterised through investigating the 100 curves for peak compression force, F_f, and then calculating apparent single granule strength based on the procedure described in section 4.2, using equation 4.1.

Table 4.1: *Apparent strength, calculated based on single granule compression tests of Sample 3.*

Sieve size (mm)	Mean size (mm)	St. dev. (mm)	Mean single granule app. Strength σ_{os} (kPa)	St. dev. (kPa)
1.00-1.18	1.08	0.014	47.95	15.68
1.70-2.00	1.79	0.12	28.37	10.05

The results show that for the size range tested, increasing the size decreases the strength of granules and calculated standard deviations are high. However, the testing method could not be applied to the granules less than 1.00 mm because the sensitivity of the loading machine was inadequate.

4.4 Bulk compression test results

The compression curve analysis is a useful method to characterise the properties of granular material as well as to measure their bulk characteristics such as bed voidage. The bulk compression test results of Sample 3 granules are presented in two different plots: One is on a log-log scale in which the bed pressure is related to the engineering strain and the other on semi-log scale, where the relative density is plotted as a function of pressure. This is done in this way in order to facilitate the data analysis based on the models of Heckel (1961), Kawakita and Ludde (1970) and Adams *et al.* (1994). Figure 4.7 shows two typical curves of these plots for 1.70-2.00 mm granules of Sample 3. In Figure 4.7b, the semi-log compression curve comprises of two distinct regions, which are separated by a zone with gradual change in the slope. This transition zone is the onset of plastic flow and the pressure point identified by the intersection of tangents from the segments in the adjacent regions is taken as apparent yield pressure of the granules (σ_{ayp}). The semi-log relation between relative density and pressure and related analysis is known as onset analysis method developed by Knudsen (1959). The strain corresponding to the apparent yield pressure of granules can be obtained from Figure 4.7a. Both figures show a transition condition, which is thought to be due to a change in bed compression behaviour from rearrangement to plastic flow and macroscopic failures. Therefore,

in this way, the bed pressure and strain in which plastic flow of the granules occurs is characterised.

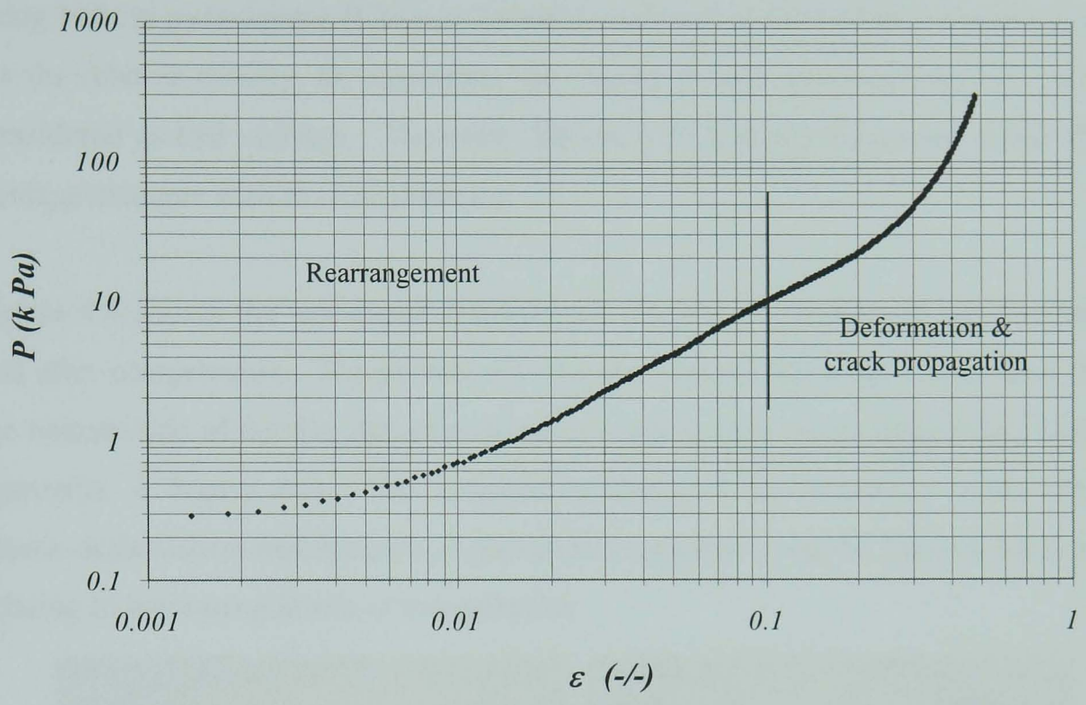

(a)

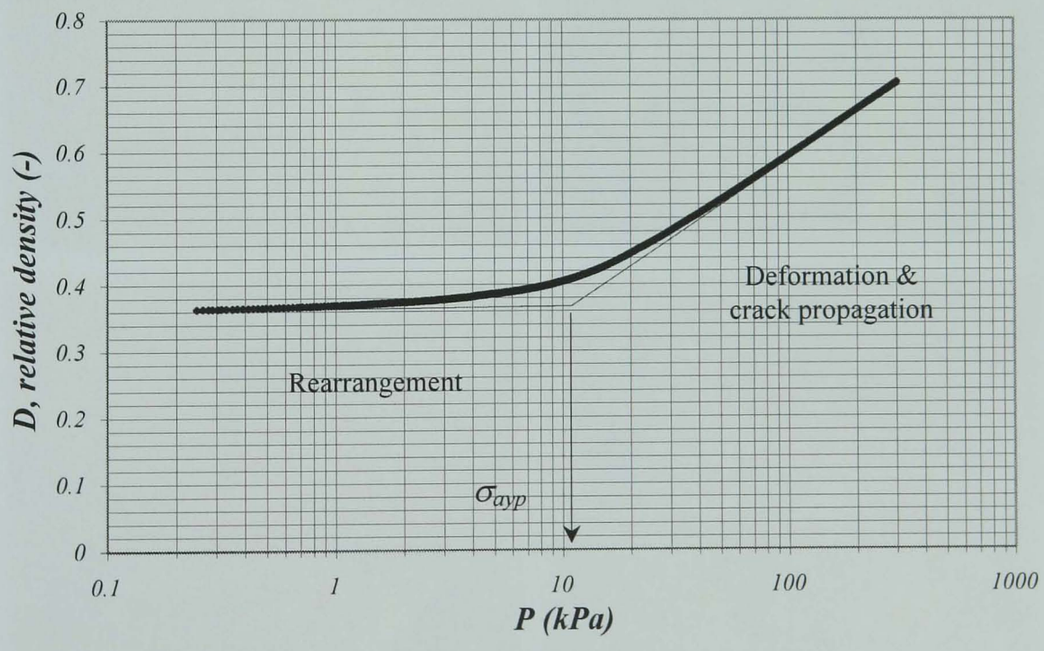

(b)

Figure 4.7: *Compression curves for 1.70-2.00 mm granules of Sample 3, under 1 mm min^{-1} CHS and 0.9 aspect ratio, a) bed pressure versus engineering strain, b) relative density versus bed pressure.*

In Figure 4.7b, the relative densities were calculated using Equation 2.22 in which the bulk densities, ρ_{bulk}, were determined through online acquisition of the bed height during compression. The true density (ρ_{true}) of Sample 3 granules was measured using helium pycnometry (Chapter 3) and was found to be 1.6775 ± 0.1321 g cm^{-3}. As the relative density, D, represents the degree of bed compression, $1\text{-}D$, may be considered as bed voidage. Therefore, Figure 4.7b also represents the trend of bed voidage changes with the bed pressure.

Figure 4.8 shows the associated microscopic images of granules in the bed before and after compression. The photos showing the pressed faces have been taken from the bottom side of the die, detached from its support base (more images are found in Appendix A Figure A1). The progressive filling of the interstitial voids through plastic deformation and fracture of granules is apparent from the Figures 4.8 b, c&d, relating to increasing levels of compression.

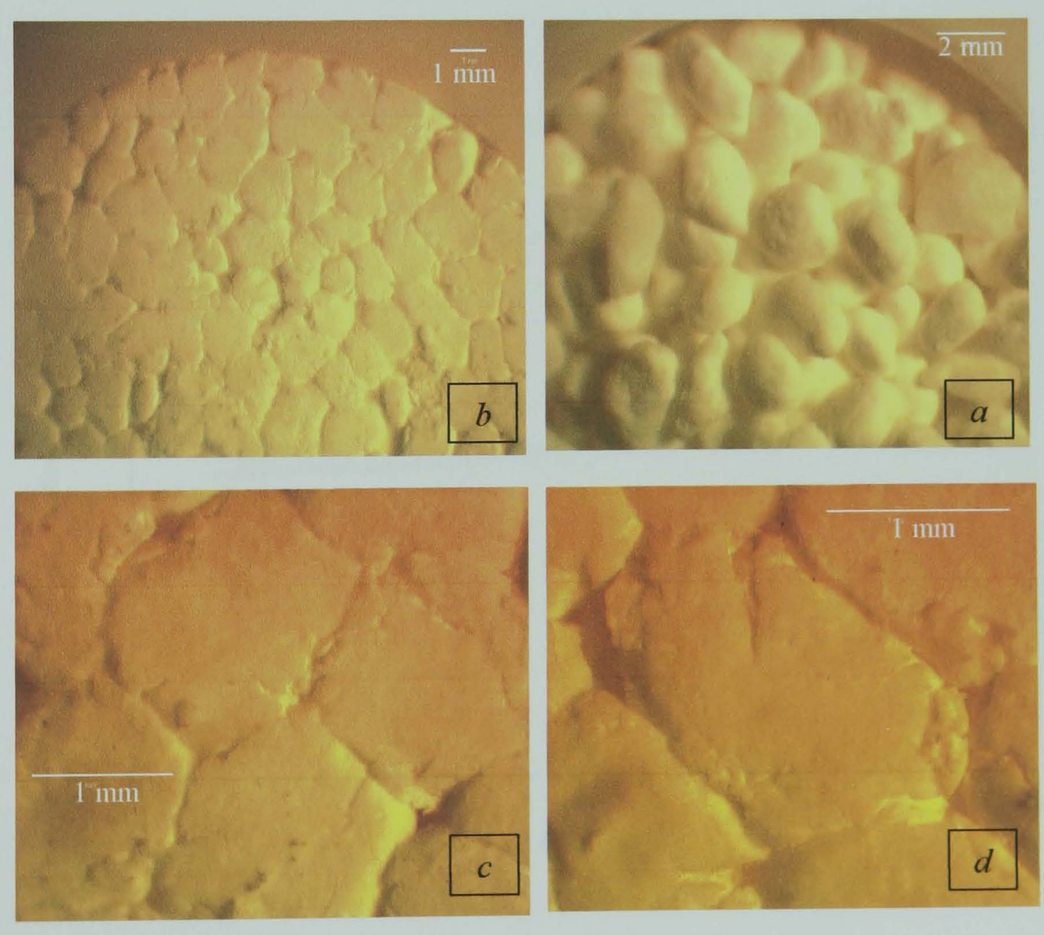

Figure 4.8: *Bulk compression of 1.70-2.00 mm granules of Sample 3. a) top-view of granules bed before compression, b,) c) and d) show bottom face of the bed after compression.*

In Figure 4.9, the effect of punch cross head speed (CHS) on the yield pressure, obtained from the onset analysis method, has been illustrated for 1.70-2.00 mm granules of the Sample 3. The similar plots and analysis for other granule sizes have been presented in Appendix A, Figure A2. Two points can be extracted from the Figure 4.9. First, the apparent yield stress of granules increases with increasing the compression rate. Second, almost similar initial relative density is obtained for the same granule size, independent of the applied compression rate. The latter can be used to characterise the initial bed voidage for each granule size. The initial relative density depends on the granule size as is shown in Figure 4.10a; it decreases as the particle size increases. The figure also indicates that with increasing the size the apparent yield stress decreases. Figure 4.10b illustrates similar experimental results, presented as the log-log plots of pressure vs. engineering strain. Figure 4.10b also shows the effect of granule size on the bed pressure, e.g. at 0.1 bed strain, the pressure decrease with increasing the granule size.

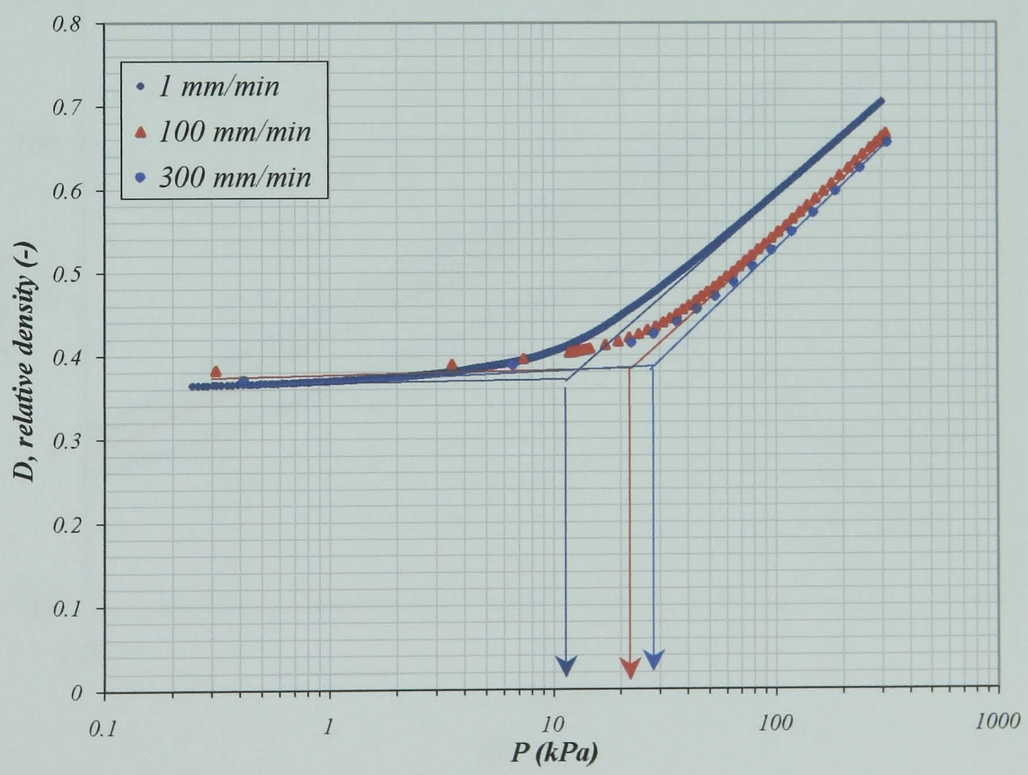

Figure 4.9: *Effect of compression rate on the apparent yield stress of 1.70-2.00 mm granules of Sample 3.*

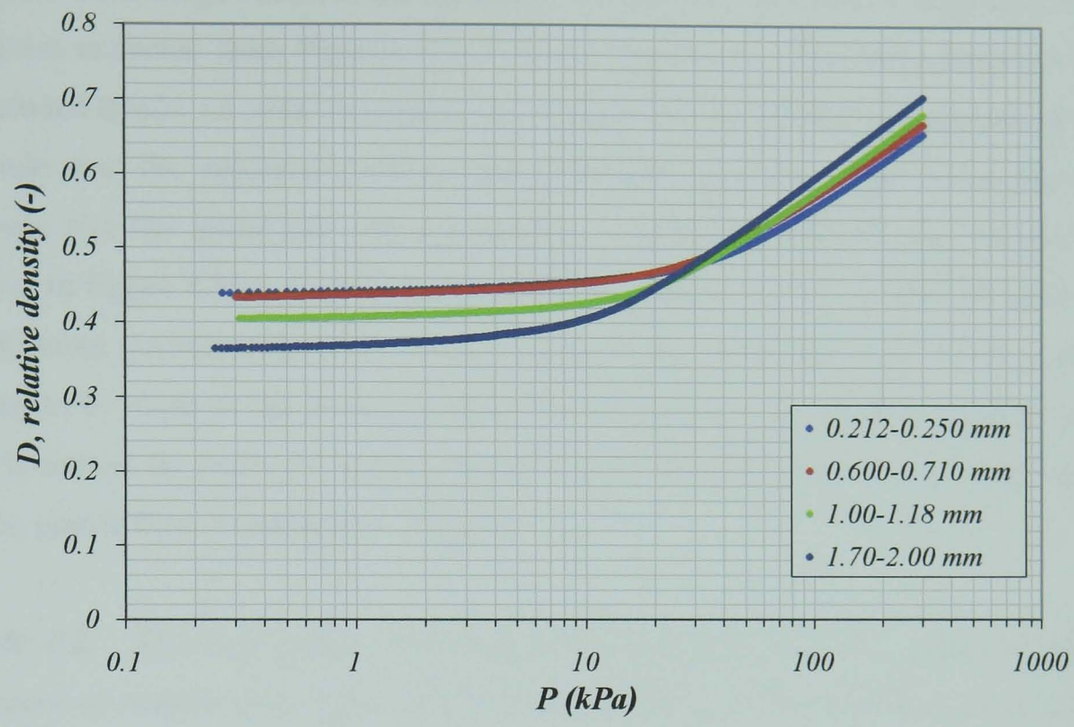

(a)

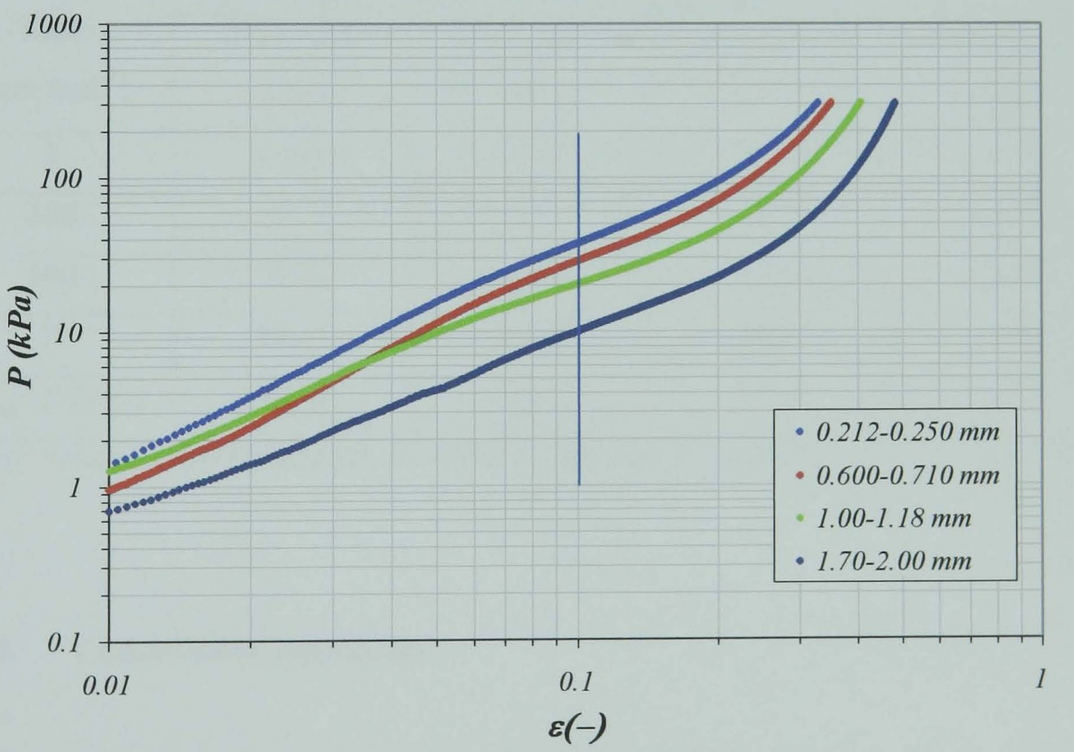

(b)

Figure 4.10: *Bulk compression curves of Sample 3, at 1 mm min^{-1} compression speed and 0.9 aspect ratio, showing the effect of granule size on the bed pressure and bed relative density, a) bed relative density as a function of bed pressure b) bed pressure as a function of bed engineering strain.*

In Table 4.2 average values of the apparent yield pressure and bed voidage are given, both are extracted from Figures 4.9, 4.10 and Figure A2. The table confirms the concluded trends, i.e. with increasing the compression rate (CHS) and decreasing the granule size the apparent yield pressure increases and also with increasing the granule size the initial bed voidage increase. Another result that was previously shown in Figure 4.10b, is also been presented in Table 4.2: this is the bed pressure of different granule sizes at 0.1 Engineering strain and 1 mm min^{-1} CHS, which seems to be close to the average apparent yield pressures at the same compression rate (compare the rows of 1 and 4). Hence, bed strain of 0.1 coincides with the onset of the plastic flow of granules in the bed.

Table 4.2: *Effect of compression rate and granule size on the apparent yield pressure of Sample 3 at 0.9 aspect ratio and during uni-axial bulk compression, using the onset analysis method.*

Compression Rate (mm min^{-1})	σ_{ayp} (kPa)			
	1.70-2.00 (mm)	1.00-1.18 (mm)	0.600-0.710 (mm)	0.212-0.250 (mm)
1	11.49	19.50	28.53	35.10
100	24.17	30.15	38.19	42.49
300	27.93	34.82	42.46	44.95
1^a	10.14	20.24	28.90	37.88
$\nu_{void}=1-D$ (-)	0.64	0.60	0.57	0.56

a) Obtained from Figure 4.10b at 1 mm min^{-1} CHS and 0.1 bed strain.

4.4.1 Compression parameters

As discussed briefly in section 4.2 and in detail in Chapter 2, there are three models of Heckel (1961), Kawakita and Ludde (1970), and Adams *et al.* (1994) from which the average single particle properties are deduced according to the macroscopic bed pressure-strain data. In Figure 4.11, three different plots of the same compression test have been shown. The bed pressure and strain data have been presented in this

way so that the parameters due to the models of Heckel (1961), Kawakita and Ludde (1970) and Adams *et al.* (1994) can be calculated from Figures 4.11a, 4.11b and 4.11c respectively. These parameters are: the reciprocal of K (P_y) and A from Heckel (1961) model, $1/b$ and a from Kawakita and Ludde (1970) model and τ_o' and α' from Adams *et al.* (1994) model obtained from Equations 4.2, 4.3 and 4.4, respectively.

As it is clear from Figure 4.11a, for the granules studied in this work, Heckel relationship ($ln\ [1/(1-D)]$ as a function of P shows a non-linear dependence, although a straight line can be fitted to the initial section. In contrast, the Kawakita and Ludde (1970) and Adams *et al.* (1994) relationships (Figures 4.11b and 4.11c) show a good linearity for most part of the plots except the initial part. In this context, the linear fitting of data after the bed pressure over about 20 kPa is shown in Figure 4.11b and the same for the bed strain over 0.1 in Figure 4.11c. As discussed in Chapter 2, according to the modified correlation of Heckel (Equation 2.29), the yield strength of the granules is characterised based on the linear fitting of the data from the initial low bed pressure section of the curve. Figure 4.7 suggests that the bed pressure of around 10 kPa causes plastic deformation of the granules, which occurs at the bed strain of 0.1. In practice, this point is located in the initial part of the Heckel curve. As it is seen in Figure 4.11c, the strain of 0.1 (corresponding to the bed pressure of 10 kpa) is also the onset of linear trend of the model of Adams *et al.* (1994). Therefore, the initial part of the Heckel curve should not be considered simply as the rearrangement of the granules in bed as yield strength of granules might be positioned in this section, in contrast to previous work, which generally discards this part on the ground of particle rearrangement. In this context, Figure 4.12a shows the initial part of Heckel curves (up to 20 kPa) for four granule sizes of Sample 3. Figure 4.12b shows the best linear regression of the data of Figure 4.12a, whilst the initial none-linear part is removed. The slope and intercept of the linear trends characterise the parameters of Heckel (K and A). Furthermore, the effect of granule size is apparent on the slope and intercepts changes of linear relationships. The similar trends are observed for compression curves of Sample 2 granules as shown in Figure A3 in Appendix A.

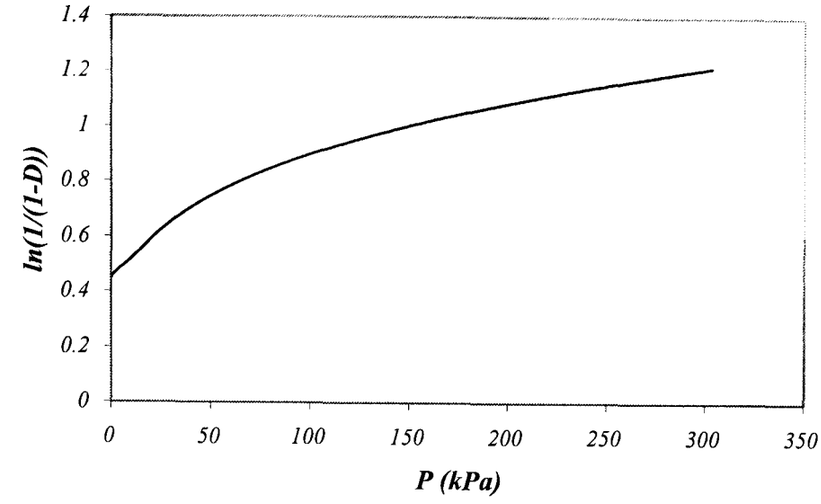

(a)

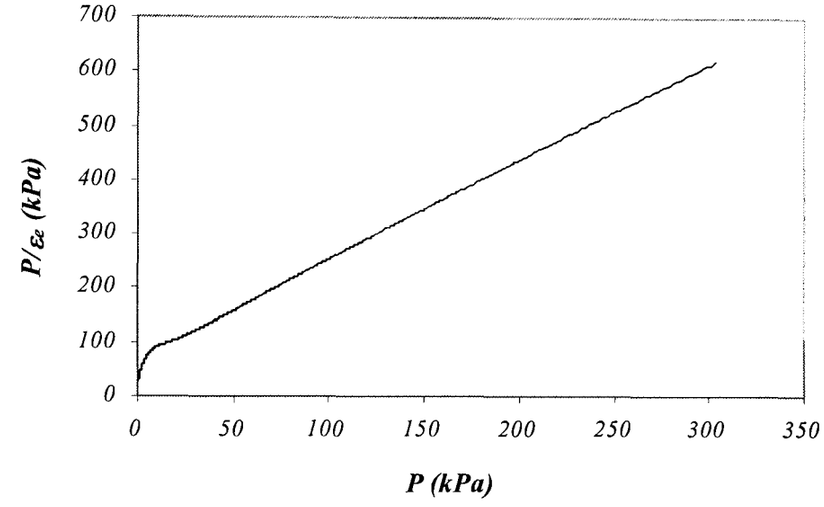

(b)

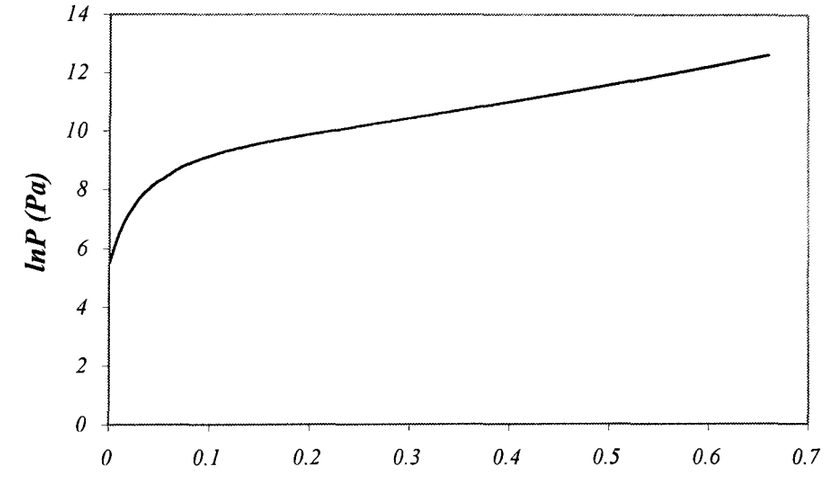

(c)

Figure 4.11: *Compression curves of 1.70-2.00 mm granule size, for Sample 3 at 0.9 aspect ratio a) Heckel relationship, b) Kawakita and Ludde (1970) relationship and c) Adams et al. (1994) relationship.*

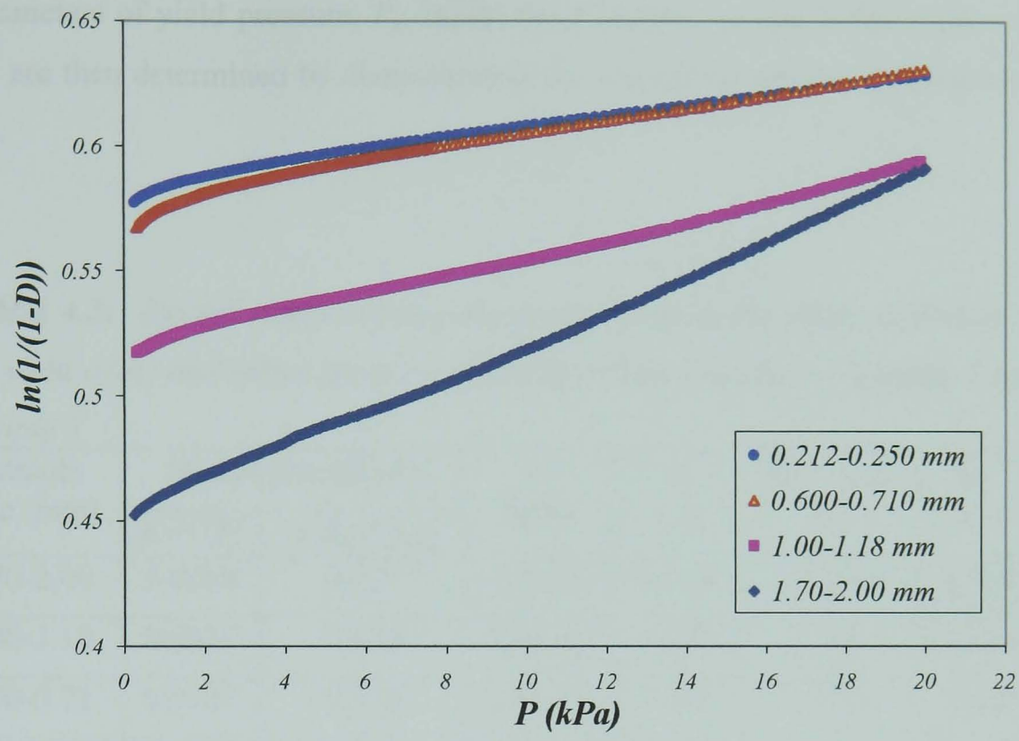

(a)

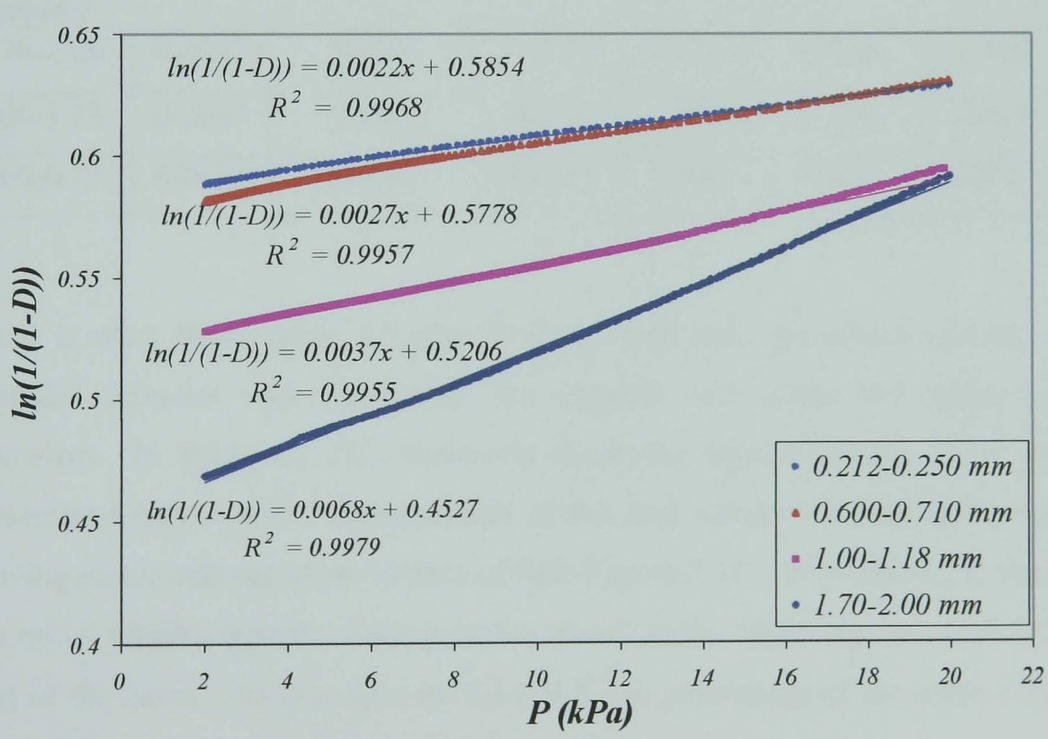

(b)

Figure 4.12: *Initial part of Heckel compression curves of Sample 3 granules at 0.9 aspect ratio for four granules sizes a) full data b) best linear regression.*

The parameters of Heckel obtained from Figure 4.12b are shown In Table 4.3. The parameters of yield pressure, P_y, initial bed porosity, ν_o, and initial relative density, D_o, are then determined by characterising the Heckel parameters, as shown in Table 4.3.

Tables 4.3: *Heckel compression parameters showing the effect of granule size on the yield stress and initial porosity and initial relative density of Samples 2 and 3.*

Sample 3

Granule Size (mm)	Heckel parameters		P_y (kPa)	ν_o (-)	$D_o = 1-\nu_o$ (-)	D_o^* (-)	δ_o (%)
	$K=1/P_y$	$A=\ln(1/\nu_o)$					
1.70-2.00	0.0068	0.453	147.06	0.636	0.364	0.384	0.08
1.00-1.18	0.0037	0.524	270.27	0.594	0.406	0.404	0.48
0.60-0.71	0.0027	0.578	370.37	0.561	0.439	0.433	1.33
0.212-0.25	0.0022	0.585	454.540	0.556	0.443	0.439	1.02

Sample 2

1.70-2.00	0.0075	0.423	133.33	0.655	0.345	0.348	0.08
1.00-1.18	0.0035	0.533	285.70	0.586	0.413	0.407	1.45
0.60-0.71	0.0025	0.604	400.00	0.546	0.453	0.447	1.37

As it is clear from Table 4.3, the yield pressure and the relative density of the granules increase with decreasing the granule size while the initial porosity decreases. In Table 4.3, D_o^*, represents the initial relative density of the granules determined based on the measurement of the first contact established between the moving piston and the upper surface of bed (Figure 4.13). In contrast, D_o, represents the initial relative density of the granules based on the linear regression of the linear part of the curve. As it is seen in Table 4.3, the percentage of deviation (δ_o) of D_o from D_o^* is larger for finer granules. This might be due to the more initial rearrangement of fine granules in the bed as compared to coarse one.

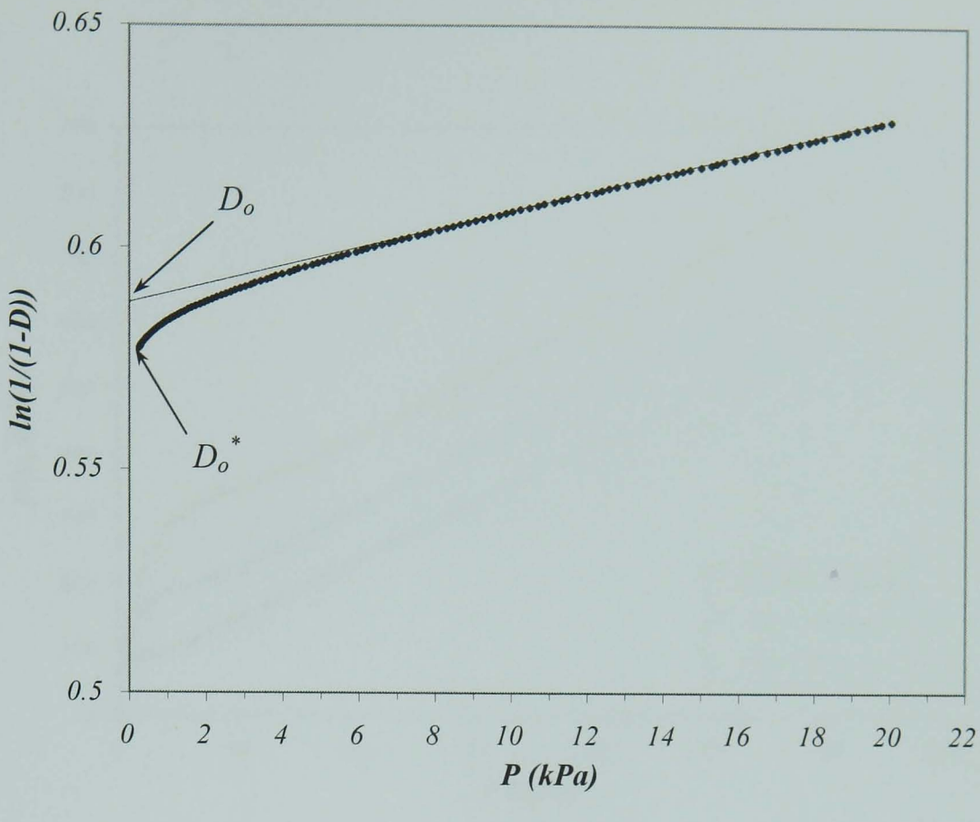

Figure 4.13: *Initial relative densities of the granules obtained according to linear regression and real initial contact of the bed and piston.*

Figures 4.14 and 4.15 show the bed pressure-strain plots of Samples 2 and 3, presented according to the Kawakita and Adams relationships, respectively. Both figures indicate the effect of granule size on the bed compression-strain plots. The curves are shifted down as the granule size increases. Figure 4.16 shows the best linear regression of the plots after elimination of the non-linear parts of the curves. The parameters of Kawakita and Ludde (1970) and Adams *et al.* (1994) are calculated by determining the intercept and slope of the regression equations, as shown in Figure 4.16.

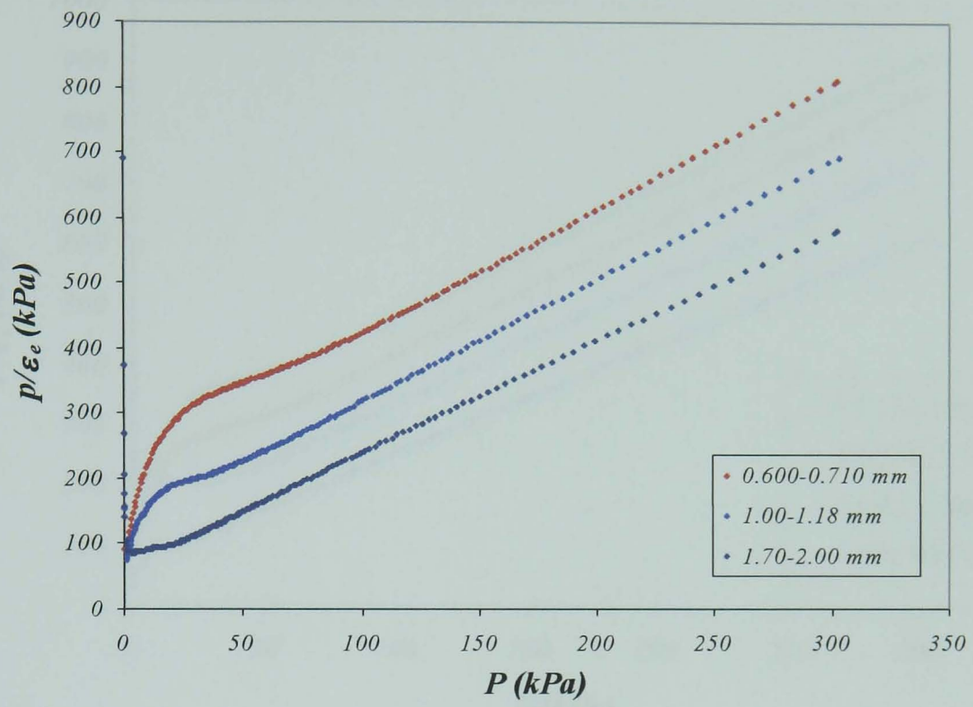

(a)

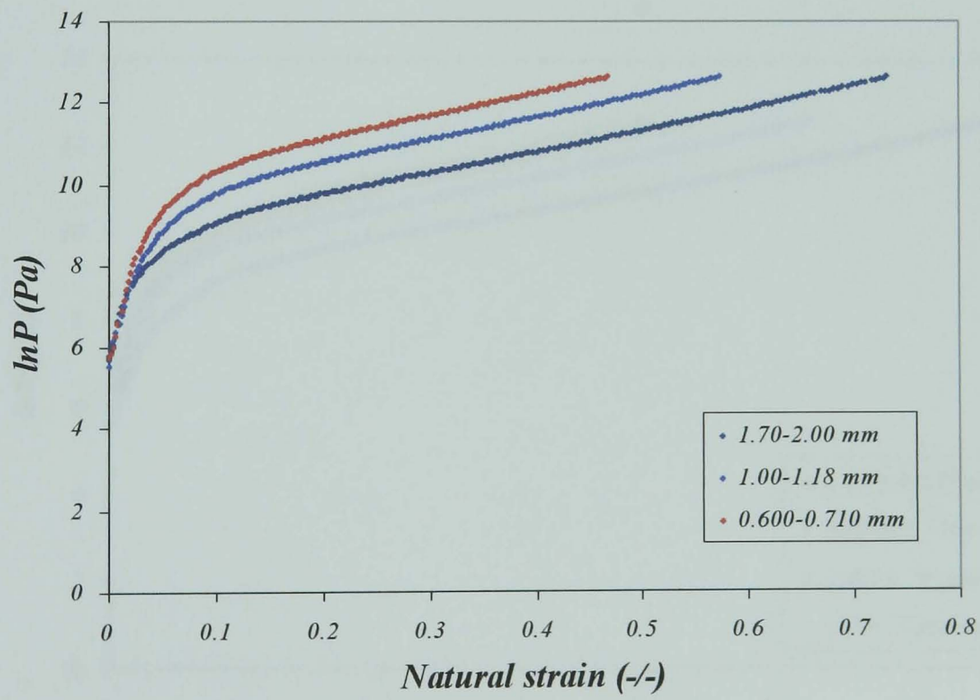

(b)

Figure 4.14: *Pressure-strain curves of Sample 2, performed on different granule sizes based on: a) Kawakita and Ludde (1970) relationship b) Adams et al. (1994) relationship, for 1 mm min^{-1} compression rate and 0.9 aspect ratio.*

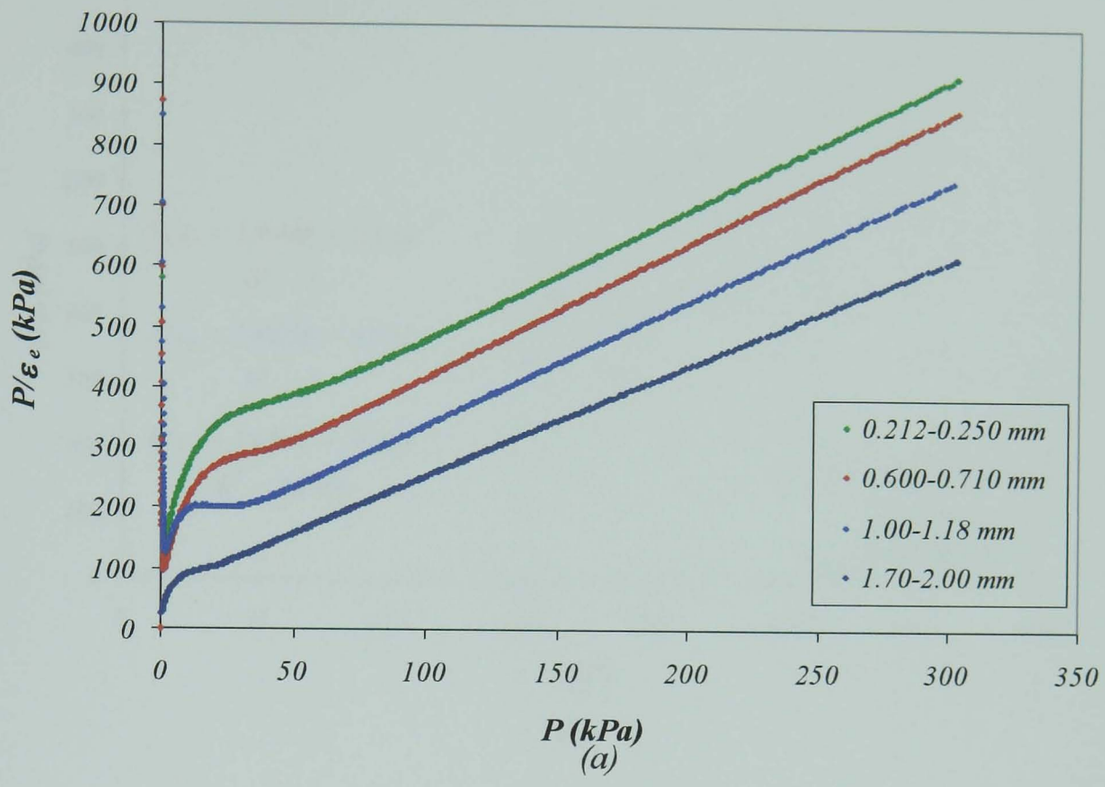

(a)

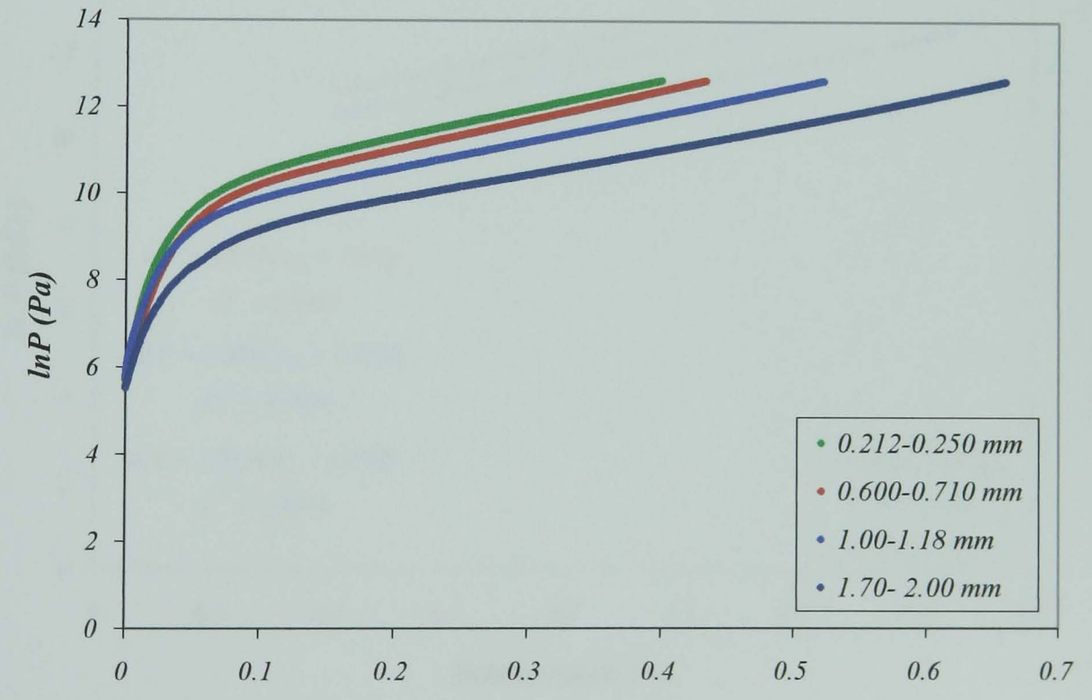

(b)

Figure 4.15: *Pressure-strain curves of Sample 3, performed on different granule sizes based on: a) Kawakita and Ludde (1970) relationship b) Adams et al. (1994) relationship, for 1 mm.min^{-1} compression rate and 0.9 aspect ratio.*

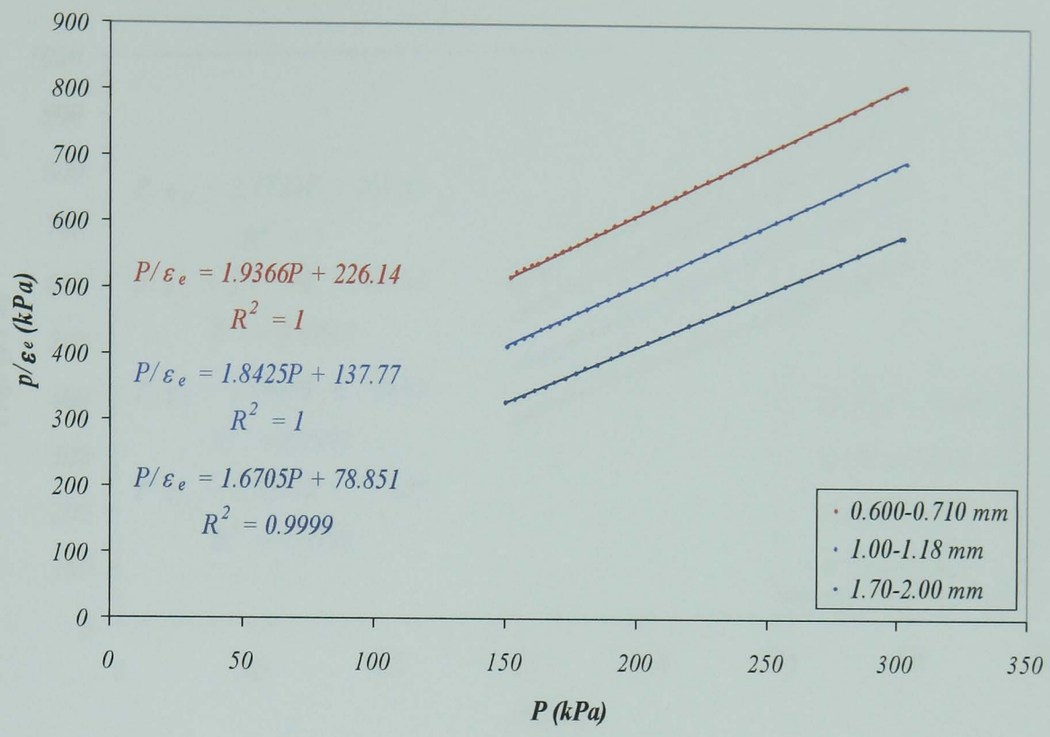
900
800
700
600
500
400
300
200
100
0
0
50
100
150
200
250
300
350
p/εe (kPa)
P (kPa)
P/εe = 1.9366P + 226.14
R2 = 1
P/εe = 1.8425P + 137.77
R2 = 1
P/εe = 1.6705P + 78.851
R2 = 0.9999
0.600-0.710 mm
1.00-1.18 mm
1.70-2.00 mm

(a)

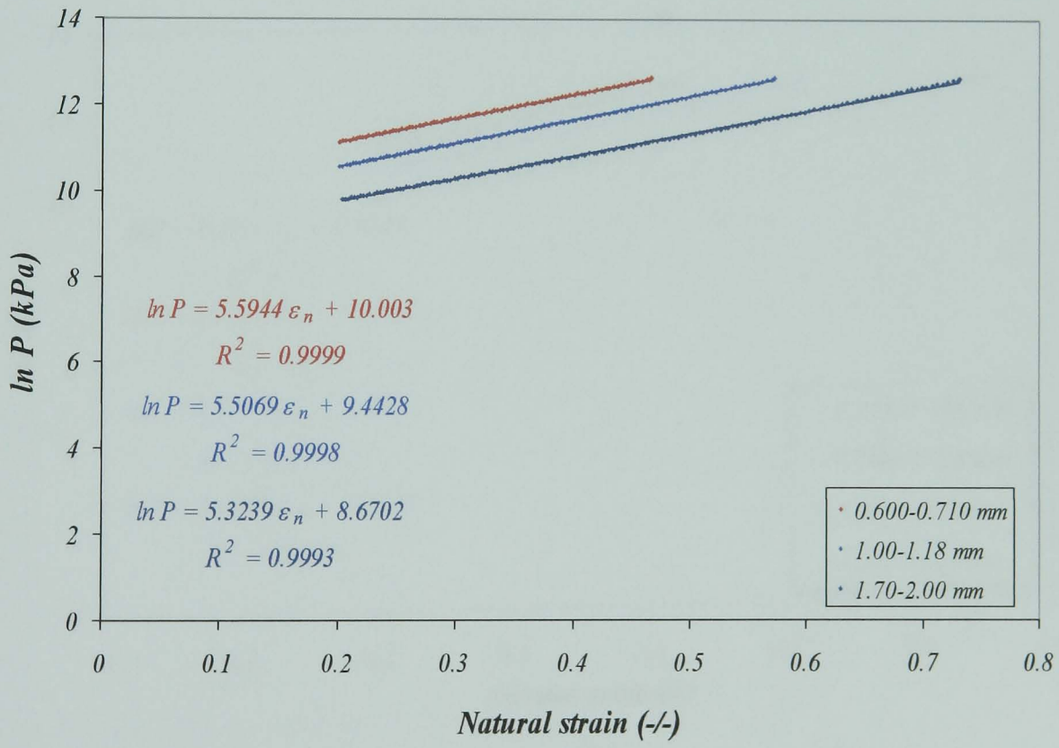
14
12
10
8
6
4
2
0
0
0.1
0.2
0.3
0.4
0.5
0.6
0.7
0.8
ln P (kPa)
Natural strain (-/-)
ln P = 5.5944 εn + 10.003
R2 = 0.9999
ln P = 5.5069 εn + 9.4428
R2 = 0.9998
ln P = 5.3239 εn + 8.6702
R2 = 0.9993
0.600-0.710 mm
1.00-1.18 mm
1.70-2.00 mm

(b)

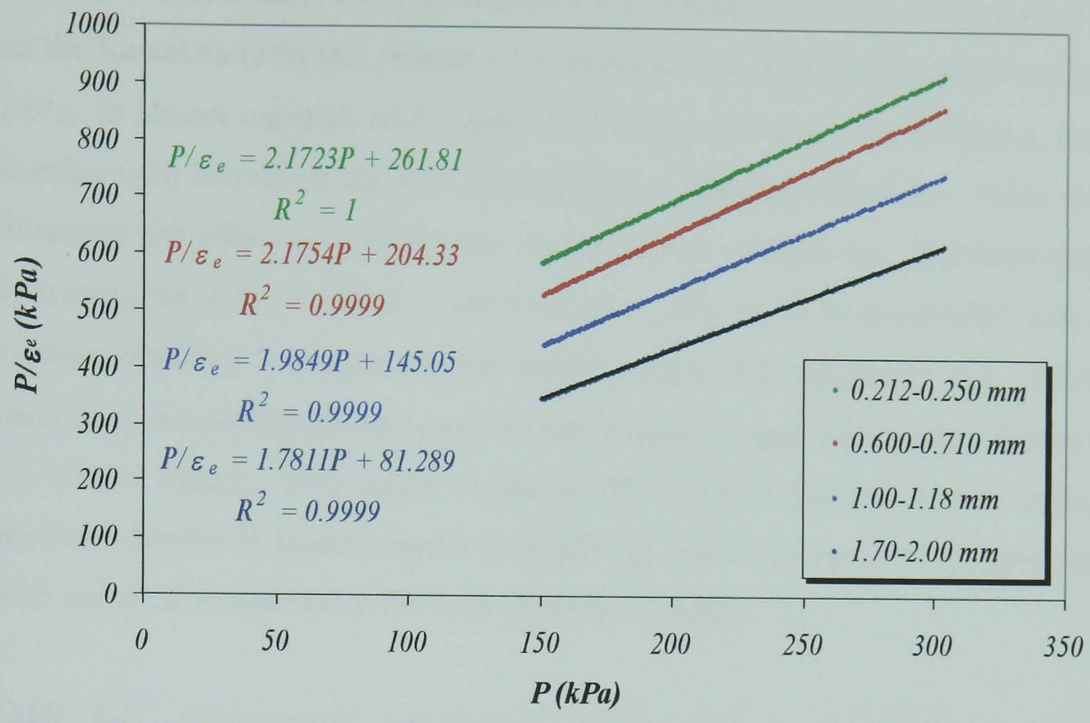

(c)

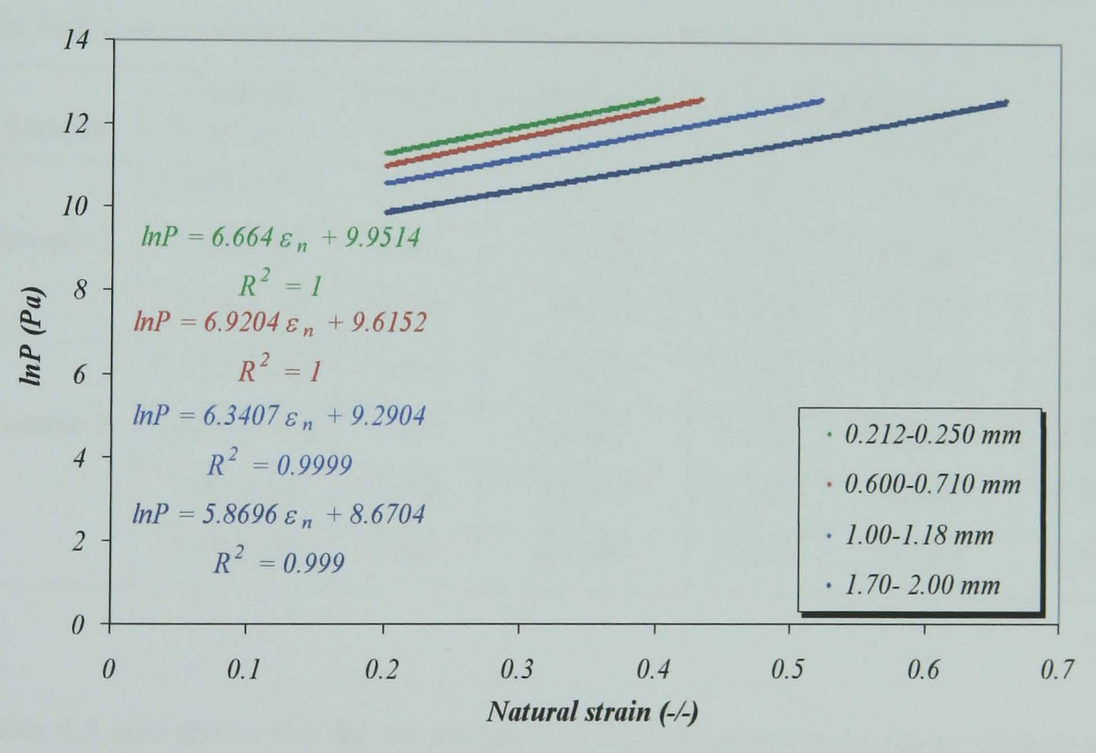

(d)

Figure 4.16: *Best linear regression of the pressure-strain plots by elimination of the non-linear parts of the curves. a) Sample 2, Kawakita equations b) Sample 2 Adams equations c) Sample 3 Kawakita equations d) Sample 3 Adams equation.*

In Table 4.4, the compression parameters obtained from Figure 4.16 have been outlined. As it is seen, the magnitudes of the apparent strength, characterised based on the Kawakita ($1/b$) and Adams (τ_o') equations, are quite close so that the ratio of $1/b/\tau_o'$ is almost constant and independent of granule size. Furthermore, for both samples with increasing the size, the strength of granules, decreases. Table 4.4 also illustrates the effect of granule size on initial bed voidage (a). For both samples, increasing the size produces larger viodages. This trend is compatible with intial voidage obtained based on Heckel model (Table 4.3, parameter ν_o). However, comparing the parameters of ν_o and a from Tables 4.3 and 4.4 reveals a higher value for Heckel model. This might be due to the using of the true density instead of envelope density in Heckel model in which the internal porosity of the granules has been included in addition to the inter-granular voidages.

Table 4.4: *Compression parameters obtained based on Kawakita and Adams equations, showing the effect of sample type and granule size on the parameters. All the bulk compression experiments performed at 1 mm min^{-1} compression rate.*

Sample	Granule Size (mm)	Kawakita parameters		Adams Parameters		
		a (-)	*1/b (kPa)*	α'	τ_o' *(kPa)*	$(1/b)/\tau_o'$
Sample 2	0.600-0.710	0.516	116.772	5.594	123.595	0.945
	1.00-1.18	0.542	74.773	5.507	69.480	1.076
	1.70-2.00	0.599	47.202	5.324	31.021	1.522
Sample 3	0.212-0.250	0.460	120.522	6.964	139.82	0.862
	0.600-0.710	0.459	93.927	6.920	103.743	0.905
	1.00-1.18	0.504	73.077	6.341	68.692	1.064
	1.70-2.00	0.561	45.640	5.870	34.207	1.334

Table 4.4 also shows that the parameter of α' for both samples decreases slightly with increasing the size and its value for Sample 3 is greater than Sample 2. As this parameter is in direct relation with inter-particle friction (refer to Chapter 2), hence, it can be concluded that with increasing the granules size the inter-particle friction also decreases. The detail discussion in this regard is postponed to the discussion section.

4.4.2 Effect of compression rate and granule size on models parameters

In order to study the effect of strain rate on the parameters of models of Kawakita and Adams some experiments were performed at higher crosshead speeds of punch, but all in the range of quasi-static compression rates. Each test was repeated three times to examine the reproducibility of the results especially at higher compression rates and also to calculate the average value and standard deviation. The repeated pressure-strain results for 1 mm min^{-1} cross head speed overlapped nicely each other, showing excellent reproducibility of the results with low standard deviations. However, at higher strain-rates some deviations were observed.

Figures 4.17 and 4.18 present the pressure-strain plots of Samples 2 and 3 respectively, showing effect of the compression rate on the bed pressure. The figures illustrate the results of experiments performed on the 1.70-2.00 mm granule size. The figures of the other sizes have been presented in the Figure A4. Again, the best linear regressions of the plots were found by elimination of the non-linear parts of the curves and the parameters of Kawakita and Adams were characterised, by finding the intercept and slope of the regression equations. Figure 4.19 shows the parameters of Adams and Kawakita (τ_o' and *1/b*) of Sample 3 versus the crosshead speed of punch. As it is seen the parameters of Kawakita and Adams have close values as given in even higher compression rates. Similar results were also observed for other sizes (Figure A5). In Figure 4.20, the apparent strength, τ_o', of Samples 2 and 3 have been compared for three granule sizes and two compression rates. A similar comparison has been made in Figure 4.21 using Kawakita parameter, *1/b*. The effect of granule size on the initial bed voidage, characterised based on the Kawakita parameter of *a*, is also shown in the figure. Figure 4.22 illustrates clearly the linear relation between the parameters of Kawakita and Adams for all the experiments. The average value of ratio (1/b)/τ_o' is 1.0398 and its standard deviation is $\pm$ 0.164.

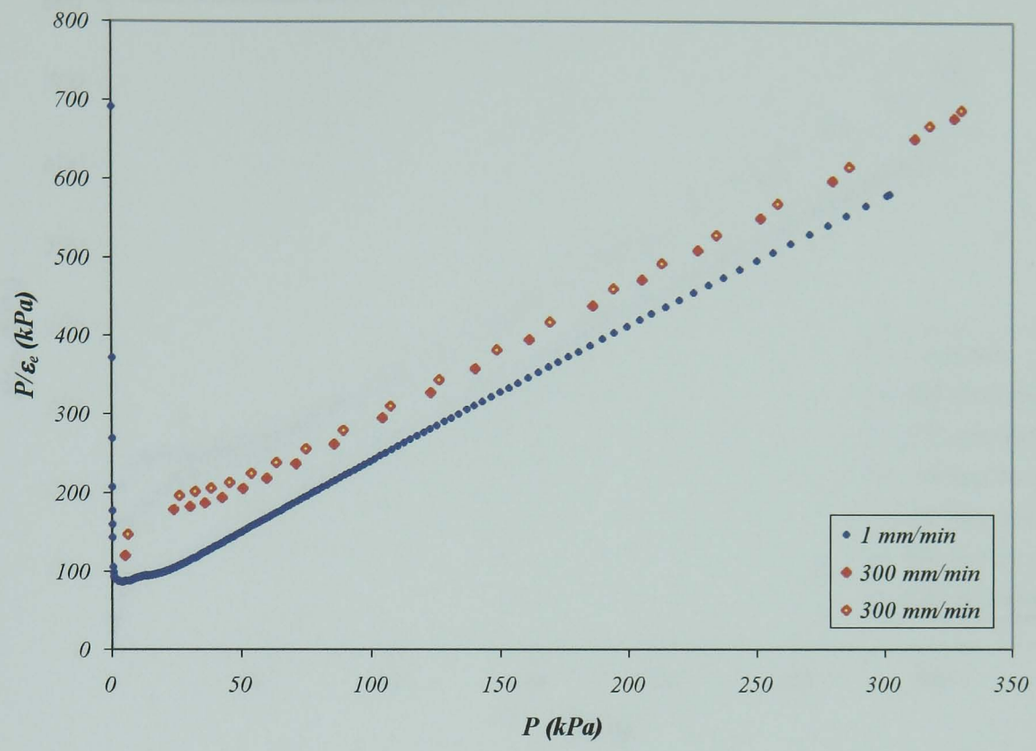

(a)

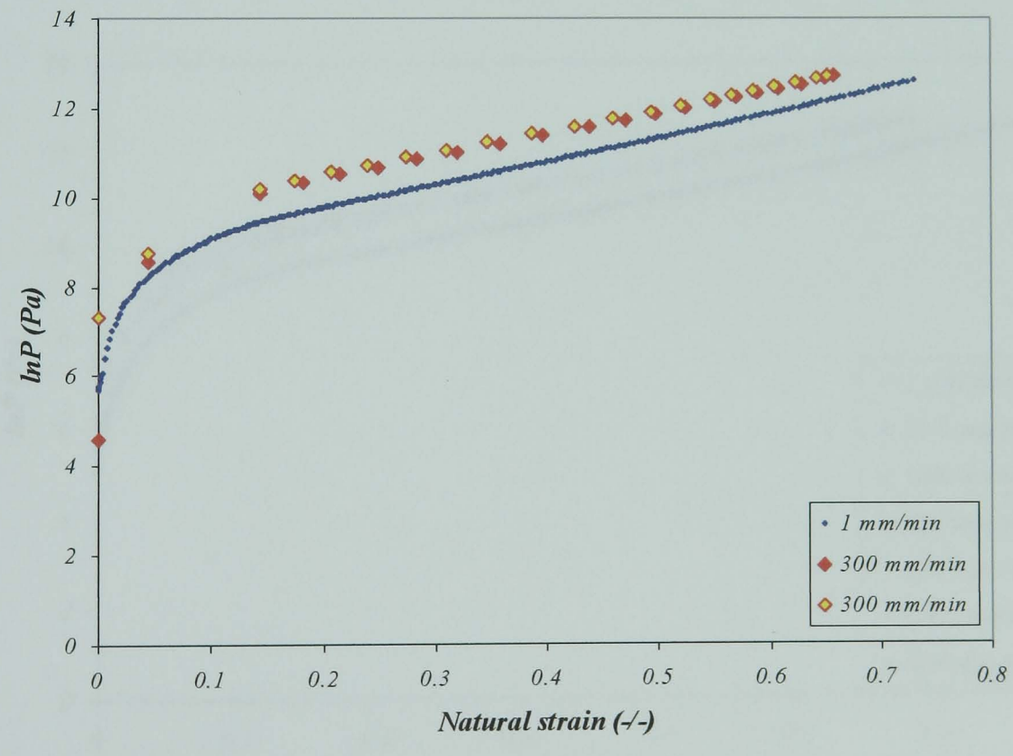

(b)

Figure 4.17: *Pressure-strain curves of Sample 2 at two compression rates, based on: a) Kawakita relationship b) Adams relationship for 1.70-2.00 mm granule size under the aspect ratio of 0.9.*

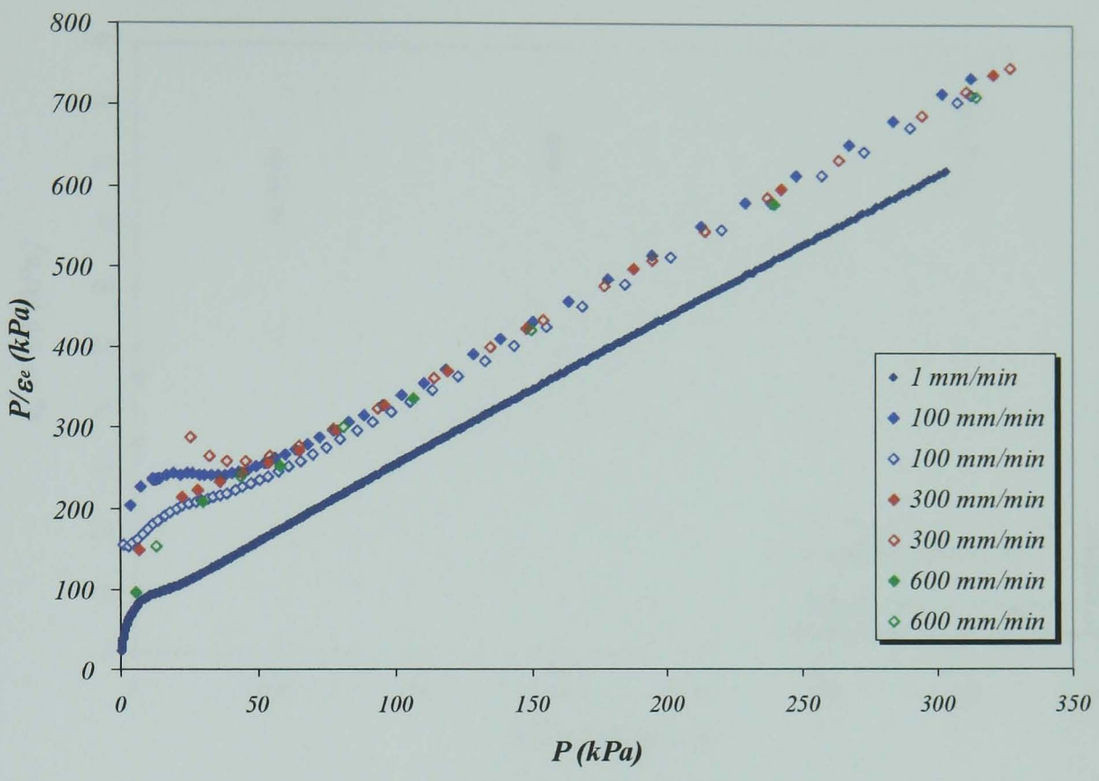

(a)

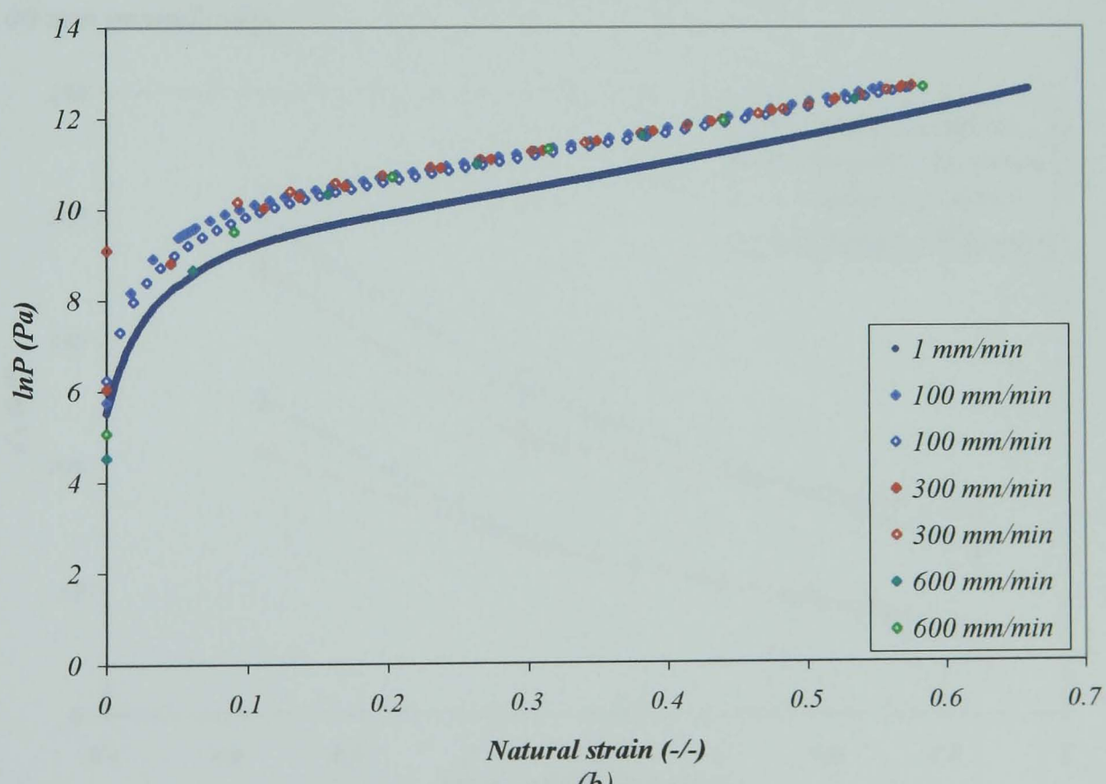

(b)

Figure 4.18: *Pressure-strain curves of Sample 3 at four compression rates, based on: a) Kawakita relationship b) Adams relationship for 1.70-2.00 mm granule size under the aspect ratio of 0.9.*

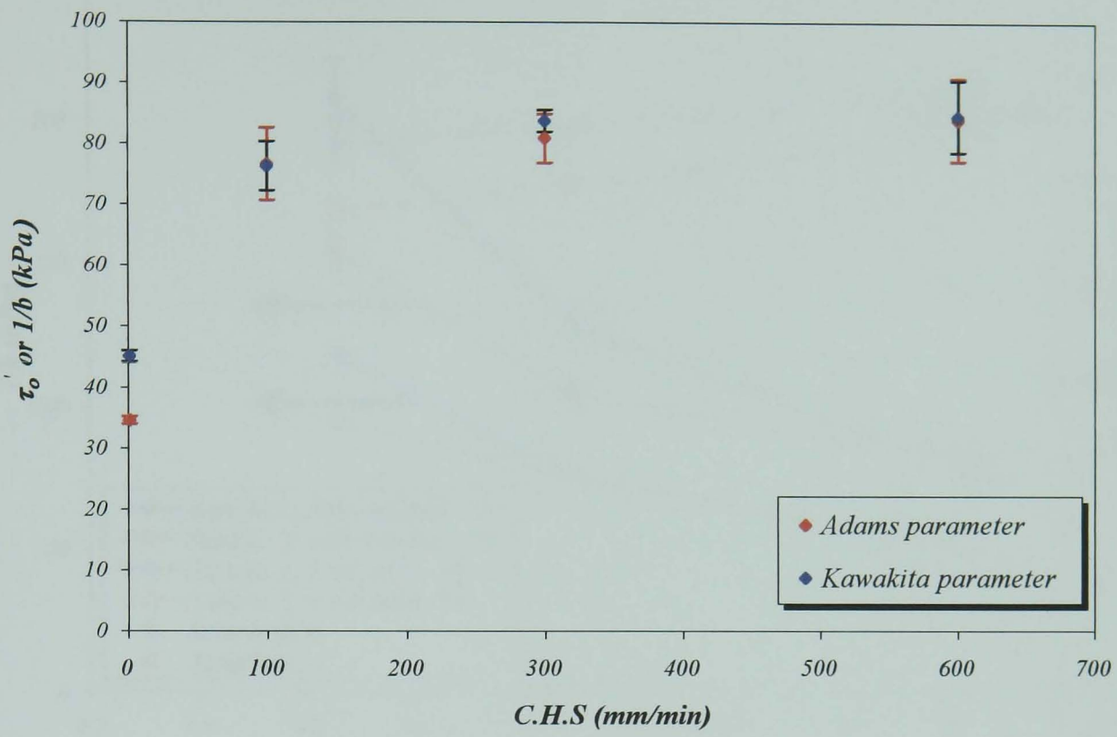

Figure 4.19: *Apparent strength of Sample 3 granules characterised on the basis of Kawakita and Adams models, as a function of crosshead speed of punch for the 1.70-2.00 mm granule size.*

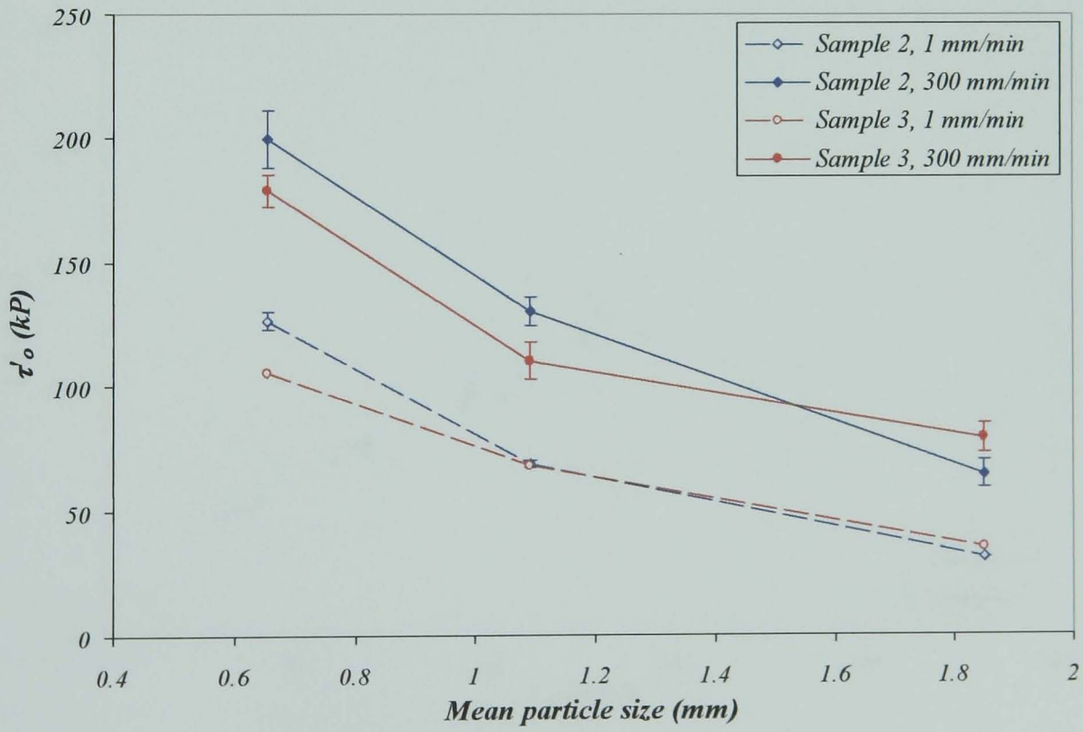

Figure 4.20: *Apparent strengths of Samples 2 and 3 granules, using Adams model.*

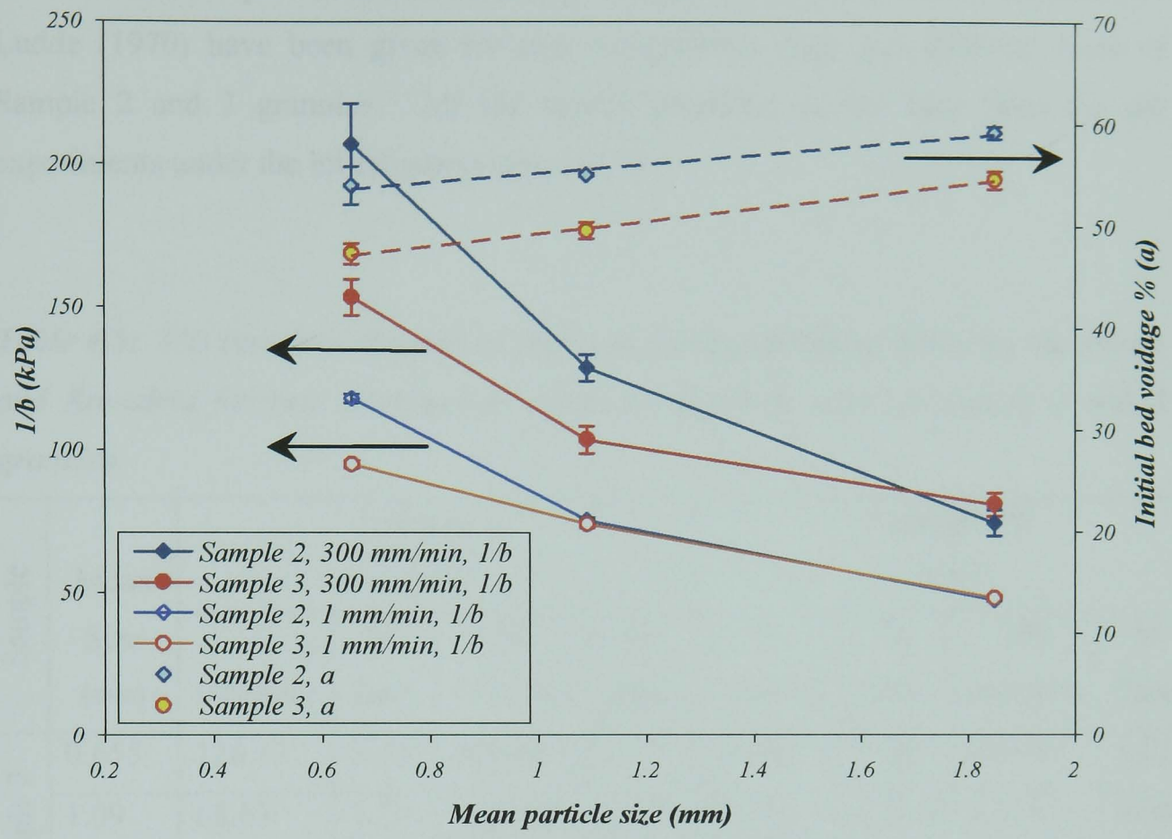

Figure 4.21: *Kawakita parameters for Samples 2 and 3, effect of granule size and strain rate on the parameters.*

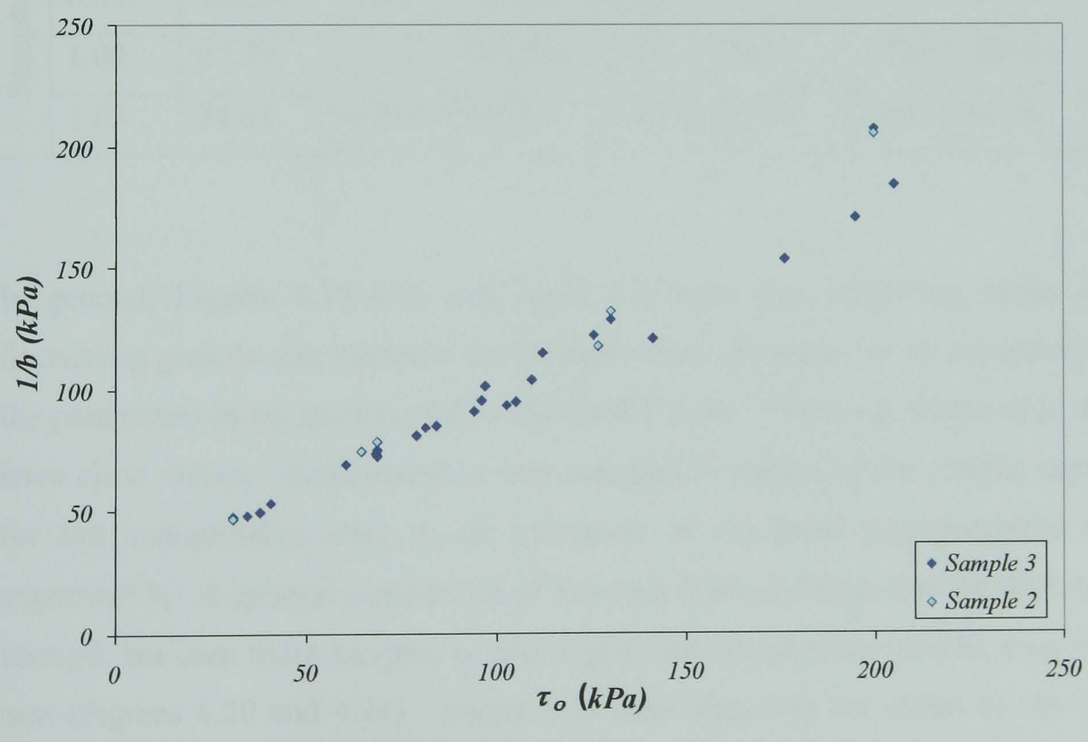

Figure 4.22: *Relationship between Kawakita and Adams parameters.*

In Table 4.5 the parameters of models of Adams *et al.* (1994) and Kawakita and Ludde (1970) have been given for two compression rates and different sizes of Sample 2 and 3 granules. All the results presented so far have been for the experiments under the initial aspect ratio of 0.9.

Table 4.5: *The apparent strength of single granules, calculated based on the Adams and Kawakita for two compression rates and different sizes of Sample 2 and 3 granules.*

Sample	Mean Size (mm)	Average τ_o' (kPa)				Average $1/b$ (kPa)			
		1 (mm/min)	St. Dev.	300 (mm/min)	St. Dev.	1 (mm/min)	St. Dev.	300 (mm/min)	St. Dev.
Sample 2	0.655	126.13	3.59	199.48	11.8	117.81	1.47	207.00	14.1
	1.09	68.63	1.20	129.90	5.98	75.39	0.87	128.90	4.66
	1.85	30.89	0.19	64.23	5.41	47.39	0.27	74.56	4.45
Sample 3	0.231	140.94	1.59	194.67	3.30	120.55	1.07	170.18	3.55
	0.655	105.04	1.84	178.78	6.62	94.87	1.32	153.31	6.42
	1.09	67.89	1.13	109.98	7.56	73.98	1.29	103.63	4.80
	1.85	34.61	0.57	78.60	5.91	48.20	0.90	81.10	4.03

In general, Figures 4.19-4.22 and Table 4.5 show that increasing strain rate or decreasing granule size increases the strength of the granules. In all the experiments, the parameters of the models of Kawakita and Ludde (1970) and Adams *et al.* (1994) have close values. Furthermore, a low standard deviation of the results, especially for low compression rates, is an indication of the good reproducibility of the experiments. A general comparison of Samples 2 and 3 shows that the difference in strength between these samples is only significant for particles smaller than about 1 mm (Figures 4.20 and 4.21). Figure 4.21 also illustrates the effect of size on the initial bed voidage. Sample 2 shows a higher initial voidage compared to Sample 3 for all particle sizes and the voidage increases with increasing the size.

4.4.3 Effect of initial aspect ratio on the parameters

In order to investigate the effect of aspect ratio on the apparent strength of granules, some more bulk compression tests were performed at the initial aspect ratios of 0.7 and 0.5. Figure 4.23 shows the variations of the apparent strength versus aspect ratio for three sizes of Samples 2 and 3 including the results of the aspect ratio 0.9 presented previously. In Figure 4.24, similar plots are shown for 1.00-1.18 mm granule size of Sample 3 at two compression rates of 1 and 100 mm min^{-1}. Table 4.6, summarise the parameters of Adams *et al.* model for Samples 2 and 3

As it is seen in Figures 4.23 and 4.24 as well as in Table 4.6 reducing the initial aspect ratio decrease the parameters of τ_o' and α'. Particularly, as the particle size is reduced the figures and the table show clearly the effect of size: increasing the granule size reduces τ_o' and α' for the same aspect ratios. Furthermore, for the range of aspect ratios examined, the apparent strength appears to decrease linearly with the aspect ratio. These results indicate that wall friction would have some effect on the bed compressibility of the samples. The slope of the lines of τ_o' as a function of A.R. seems to increase when the granule size decreases, showing an effect of granule size on wall friction. The trends suggest that for the larger granules the wall friction is lower. For 1.70-2.00 mm granules the apparent strength calculated for 0.9 bed initial aspect ratio is almost the same as the extrapolated value to the zero one. The effect of aspect ratio on the strength for Sample 2 seems to be more than for Sample 3, as the former has higher slopes.

Table 4.6 also show the values of the apparent strength, extrapolated to zero aspect ratio for which it is expected that the wall friction might be neglected. Figure 4.24 presents the same trend of τ_o' versus A.R for 100 mm.min^{-1} compression rate as compared to 1 mm min^{-1}, except that the standard deviations are higher.

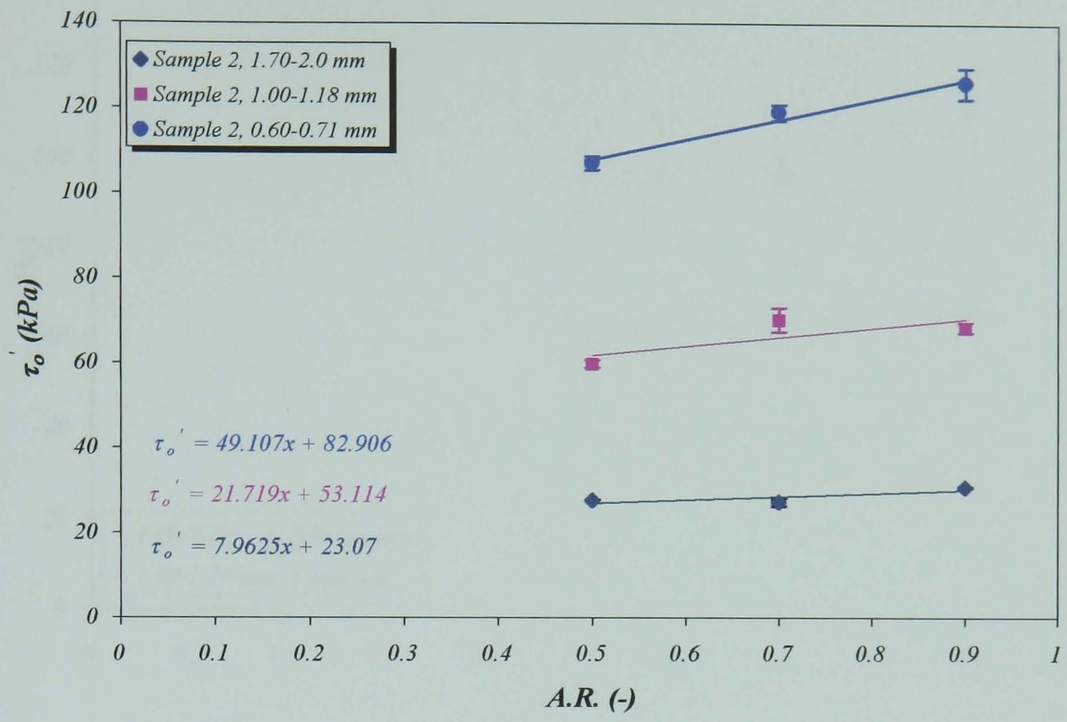

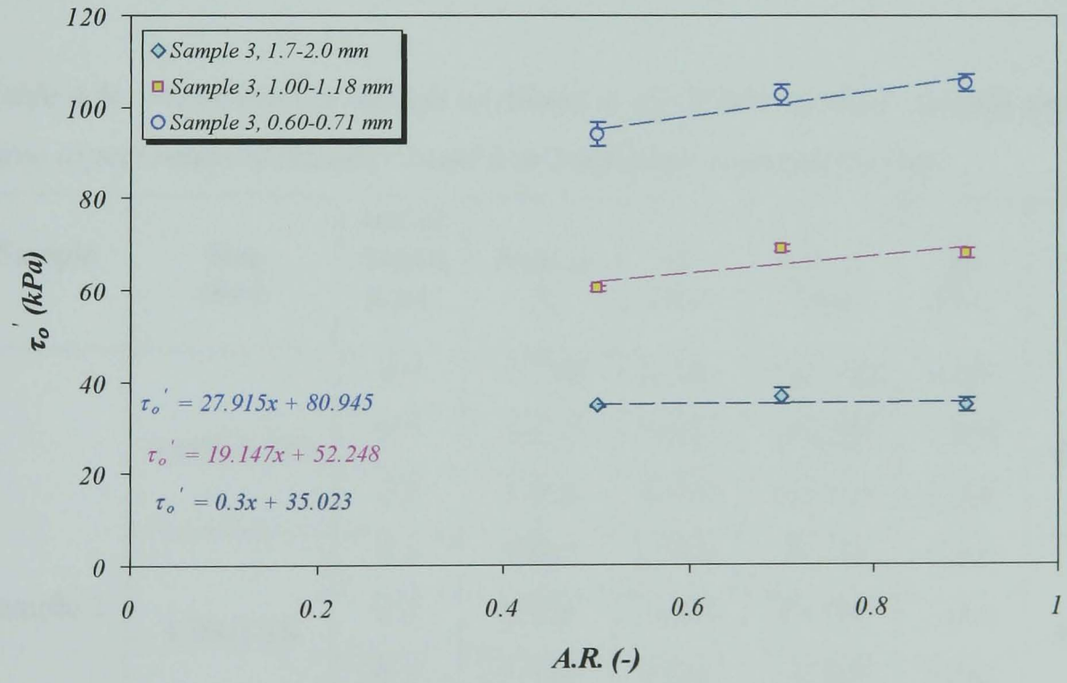

Figure 4.23: *Effect of initial aspect ratio on the apparent strength of Samples 2 and 3, investigating based on Adams relationship at 1 mm.min^{-1} compression rate.*

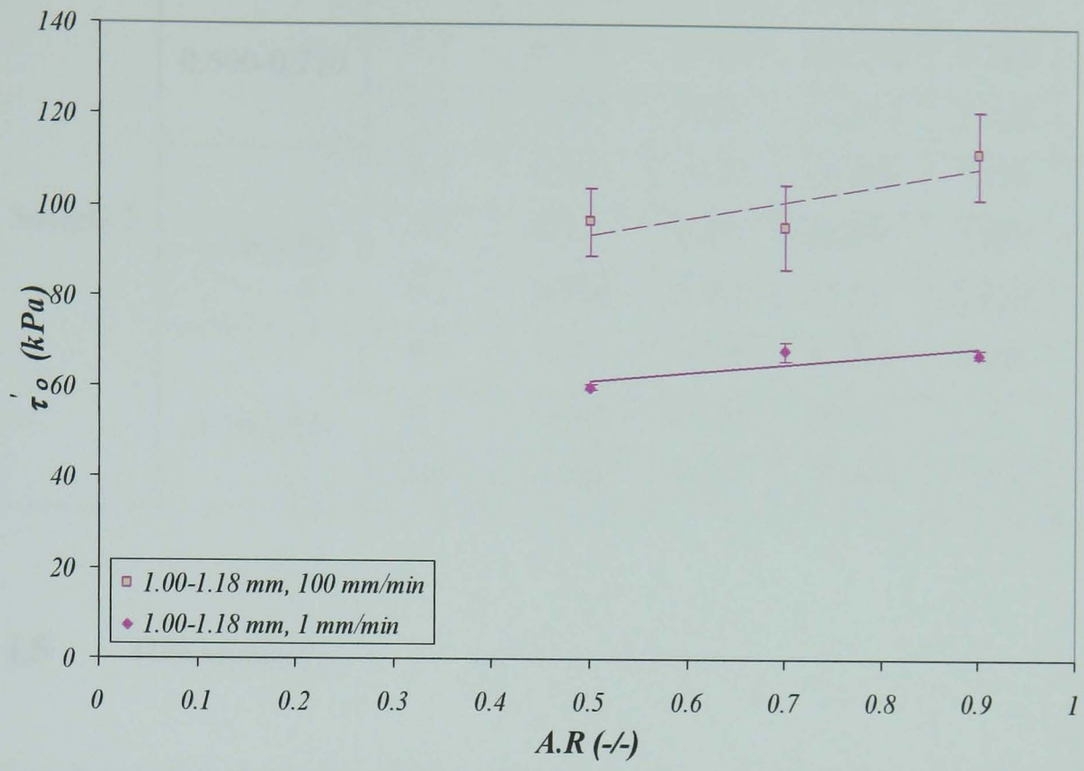

Figure 4.24: *Effect of initial aspect ratio on the apparent strength for 1.00-1.18 mm granule sizes of Sample 3 at two compression rates of 1 and 100 mm min^{-1}.*

Table 4.6: *Parameters of models of Adams et al. (1994) for three granule sizes and three aspect ratios of Samples 2 and 3 at 1 mm min^{-1} compression rate.*

Sample	Size (mm)	Initial Aspect Ratio (-)	Ave. α' (-)	St. Dev.	Ave. τ_o' (kPa)	St. Dev.	τ_o' at zero A.R. (kPa)
Sample 2	0.600-0.710	0.9	5.738	0.056	126.130	3.590	82.906
		0.7	5.617	0.041	119.226	1.850	
		0.5	5.475	0.002	107.622	1.636	
	1.00-1.18	0.9	5.607	0.032	68.630	1.200	53.114
		0.7	5.555	0.002	70.378	2.865	
		0.5	5.419	0.066	59.942	0.942	
	1.70-2.00	0.9	5.324	0.084	29.599	0.190	23.070
		0.7	5.270	0.062	27.335	0.886	
		0.5	5.213	0.020	27.709	0.060	

Sample 3	0.600-0.710	0.9	6.920	0.089	105.040	1.840	80.945
		0.7	6.716	0.060	102.542	4.185	
		0.5	6.497	0.026	93.874	2.748	
	1.00-1.18	0.9	6.341	0.082	67.890	1.130	52.248
		0.7	6.321	0.071	68.833	0.707	
		0.5	6.090	0.017	61.231	0.530	
	1.70-2.00	0.9	5.727	0.079	35.754	0.570	35.023
		0.7	5.672	0.058	36.600	1.731	
		0.5	5.560	0.117	34.490	0.258	

4.5 Discussion

Two types of detergent based granules were assessed quasi-statically using uni-axial single and bulk compression methods. The main aim of the experiments was to find out a reliable experimental method to characterise the strength of these soft granules. However, in this way, some aspects of single and bulk compression were also studied. In the following, the reliability of the experimental methods is first discussed. Then, a comparison is made between the single granule and bulk compression methods. The strength and weakness of the bulk compression models form the main discussion. Finally the dependency of the compression parameters (obtained from the models of Kawakita and Ludde; 1970, and Adams et al.; 1994) on granule size, compression rate and bed aspect ratio is discussed.

4.5.1 Assessment of reliability of experimental results

Two factors are addressed here regarding the reliability of the experimental results. First, the systematic error in determination of the primary parameters as well as the propagated errors in the correlations. Second, the reproducibility of the tests is examined through repeating the experiments and determination the standard deviation. In both cases, however, a comparison is also made between two methods of single and bulk compression tests.

The systematic error is related to the accuracy of the measuring instruments and skill of the operator (Taylor, 1980). The primary parameters, which have been used in the correlations of this chapter, are:

- diameter of cylinder (D_c), which was measured by Vernier Calipers with probable error, δD_c, of $\pm$ 0.02 mm. Therefore, the measured cylinder diameter, D_c, is 20.50 $\pm$ 0.02 mm.

- applied force on the single granule, F_f, and granule size, d, and the analogous ones in bulk compression, applied force on the bed, F_b, and bed displacement, h. According to the specifications manual of the Instron 4500 mechanical testing machine, the instrumental error of these parameters are δF_f or $\delta F_b = \pm 10^{-3}$ N and δd or $\delta h = \pm$ 50 μm.

The probable errors propagated in a function with the general form of

$$q = f(x,....,z) \tag{4.7}$$

is calculated from the following equation:

$$\delta q = \left[\left(\frac{\partial f}{\partial x} \delta x \right)^2 + ... \left(\frac{\partial f}{\partial z} \delta z \right)^2 \right]^{0.5} \tag{4.8}$$

where δx,..., δz are independent probable primary errors and δq is the propagated error of the function q.

The propagated errors can be determined by applying Equation 4.8 to some of the relationships used in this chapter, as given in the following.

$$\delta \sigma_{os} = \frac{4}{\pi} \sqrt{\left(\frac{\delta F_f}{d^2} \right)^2 + 4 \left(\frac{\delta d . F_f}{d^3} \right)^2} \tag{4.9}$$

$$\frac{\delta\sigma_{os}}{\sigma_{os}} = \sqrt{\left(\frac{\delta F_f}{F_f}\right)^2 + 4\left(\frac{\delta d}{d}\right)^2} \tag{4.10}$$

Equations 4.9 and 4.10 characterise the propagated error of apparent single granule strength based on Equation 4.1.

$$\delta P = \frac{4}{\pi}\sqrt{\left(\frac{\delta F_b}{D_c^2}\right)^2 + 4\left(\frac{\delta D_c . F_b}{D_c^3}\right)^2} \tag{4.11}$$

$$\delta\varepsilon_e = \sqrt{\left(\frac{\delta h}{h_o}\right)^2 + \left(\frac{\delta h^2}{h_o^2}\right)^2} \tag{4.12}$$

where δP and $\delta\varepsilon_e$ are the propagated errors of the bed pressure and engineering strain, respectively.

$$\delta(1/b) = \sqrt{\left[\left(\frac{a}{\varepsilon_e} - 1\right)\delta P\right]^2 + \left(\frac{P.a.\delta\varepsilon_e}{\varepsilon_e^2}\right)^2} \tag{4.13}$$

where $\delta(1/b)$ is the propagated error in the parameter of model Kawakita.

The systematic errors of the parameters using the above relationships are given below.

The systematic error of the apparent single granule strength, $\delta\sigma_{os}$, for 1.00-1.18 mm and 1.70-2.00 mm granule sizes of Sample 3 were calculated as $\pm$ 1.105 kPa ($\pm$ 2.30%) and $\pm$ 0.396 kPa ($\pm$ 1.40%), respectively. The errors were determined by applying the primary errors and the parameters outlined in the Table 4.1 to the Equations 4.9 and 4.10. The second term in Equations 4.9 and 4.10 can be neglected due to the low measurement error of the Instron machine for length ($\pm 50 .10^{-6}$ m). Furthermore, according to Equations 4.9 and 4.10, decreasing the granule size as well as failure force increases the systematic error of the apparent strength. For this

reason, the propagated error of the strength under the uni-axial loading of 1.70-2.00 mm granules at very low applied forces can increase to 10% (see Figure 4.6a),.

Pressure measurement error in the bulk compression tests, δP, is affected by the cylinder diameter, applied force on the bed, and their measurement errors (Equation 4.11). As the primary errors of the force and diameter are constant, only increasing the bed force can increase the bed pressure error. However, for most of the experiments the maximum systematic error of the bed pressure at the maximum obtained bed pressure of 300 kPa was as low as $\pm$ 0.600 kPa, which is quite acceptable. The systematic error of the engineering strain, calculated based on the Equation 4.12, is estimated as $\delta\varepsilon_e = 10^{-3}$, which is not considerable.

Equation 4.13 can be used to estimate the propagated error of the apparent strength, $\delta(1/b)$. Employing the a = 0.561 (-), δP = 0.600 (kPa) and maximum bed pressure of 300 kPa corresponding to the maximum engineering strain of ε_e = 0.5 (-) in Equation 4.13 gives an error of $\delta(1/b) = \pm$ 0.72 (kPa) or $\pm$ 1.45%. In this case, the range of systematic error is much lower than expected, showing high accuracy of experiments. It should be noted that as the pressure and strain decrease the error of Kawakita parameter increases (i.e. at bed pressure of 10 kPa corresponding to engineering strain of about 0.1, $\delta(1/b)$ equals $\pm$ 3.00 kPa, $\pm$ 6.22%).

In summary, the systematic error analysis of the single granule and bulk compression shows that firstly the single granule compression test is limited by the minimum granule size that can be used. As the size decreases the propagated error in the apparent strength increases accordingly and it may ultimately exceed the system resolutions. This turns out to be the case for granule sizes less than the 1.00 mm, for which the system could not acquire the results accurately. A more sensitive test machine would be needed for small granules. Secondly the propagated error of the apparent strength obtained from the bulk compression tests, using the equation of Kawakita is approximately the same as single granules as shown in Table 4.7, where a typical comparison of the methods for 1.70-2.00 mm granules of Sample 3 is given. Here, the bulk compression error has been obtained at maximum bed pressure of 300 kPa, initial aspect ratio of 0.9 and under the compression rate of 1 mm min^{-1}.

A similar error analysis for the equation of Adams *et al.* (1994) produces approximately the same result and is not reported here. However, as the propagated error of the single and bulk compression parameters never exceeds more than 1.5% in the all experiments, therefore, the accuracy of the results is not affected by the machine's systematic errors.

Table 4.7: *Comparison of apparent strength error between two methods of single granule and bulk compression performed on granule size of 1.70-2.00 mm of Sample 3.*

Test method	σ_{os} or $1/b$ (kPa)	$\lvert\delta\sigma_{os}\rvert$ or $\lvert\delta(1/b)\rvert$	
		(kPa)	%
Single granule compression	28.4	0.40	1.40
Bulk compression	48.20	0.70	1.45

Another reliability aspect of the experiments is examined by repeating the tests and characterising the average and standard deviation of the parameters. In the single granule compression method, experiments were repeated 100 times for each tested granule size. The standard deviation of the apparent strength, presented in the Table 4.1, is more than 30% for both granule sizes of 1.00-1.18 mm and 1.70-2.00 mm of Sample 3. In the bulk compression tests most of the experiments were repeated three times. However, the standard deviation was much lower as compared to that of the single granule compression tests. Table 4.8 shows a comparison between the two methods showing the average apparent strengths and standard deviations. In the table, the apparent strengths and standard deviations are presented for Sample 3 at 0.9 aspect ratio. As it is seen, the standard deviations of the parameters of the models of Kawakita and Ludde (1970) and Adams *et al.* (1994) are less than 2% in most of the cases at 1 mm min^{-1} compression rate, showing a good reproducibility of the results and high precision of the method as shown in Table 4.8 and also Tables 4.5 and 4.6.

Table 4.8: *Average apparent strength and standard deviation obtained from the single granule and bulk compression tests.*

Sample 3			Single granule compression			Bulk compression		
			Average	St. Dev.		Average	St. Dev.	
				±	%		±	%
1.00-1.18 mm	σ_{os} (kPa)		47.95	15.68	32.70			
	1/b (kPa)	1 mm.min^{-1}				73.98	1.29	1.74
		300 mm.min^{-1}				103.63	4.80	4.62
	τ_o' (kPa)	1 mm.min^{-1}				67.89	1.13	1.66
		300 mm.min^{-1}				109.98	7.56	6.87
1.70-2.00 mm	σ_{os} (kPa)		28.37	10.05	35.42			
	1/b (kPa)	1 mm.min^{-1}				48.20	0.90	1.87
		300 mm.min^{-1}				81.10	4.03	4.97
	τ_o' (kPa)	1 mm.min^{-1}				34.61	0.57	1.65
		300 mm.min^{-1}				78.60	5.91	7.52

At higher compression rates (e.g. 300 mm.min^{-1}), the standard deviations increases, and therefore increasing the number of tests may reduce the probable errors. However, even in this case, the standard deviations are much lower than single granule tests.

4.5.2 Characterising the properties of granules using single granule compression data

Discussion of some aspects of the single granule compression results may provide a deeper insight into the failure behaviour of soft agglomerates. Only few workers have tried to explain the relation between the deformation behaviour and mechanical properties of soft agglomerates. Pepin *et al.* (2001) applied the side crushing test method to typical soft agglomerates with significant plastic deformation on the contact area. They studied the role of liquid binder surface tension, viscosity, and inter-particle friction on the plastic behaviour of wet agglomerates. They developed

a theoretical model of agglomerate hardness based on the characteristics of the primary particles and liquid binder. Furthermore, they found that granular friction forces might explain the hardness of the wet agglomerates at low speeds of deformation. However, the main assumption in their model is that agglomerates undergo full plastic deformation with no change in porosity and co-ordination number, an assumption, which is not fully justified. They showed that the measured hardness of spherical agglomerates matched in some cases with the model prediction. Briscoe *et al.* (1998) observed the deformation and fracture of wet ceramic agglomerates by using an inverted optical microscope and a video camera, added to the uni-axial compression system. They found that some microscopic failures of weaker points occurred before the gross failure of the agglomerate. The micro failures were indicated by a number of fluctuations on the load-displacement curve. It is thought that the progression of these sequential ruptures makes the major cracks, which eventually leads to the complete failure of the agglomerate.

The observations of this work are in agreement with those of Briscoe *et al.* (1998), although the ranges of applied load and strength are not comparable. Figures 4.4-4.6 illustrate the same failure behaviour as observed by Briscoe *et al.* (1998). Sequential microscopic failure of the bonds and significant plastic flow are the dominant mechanisms of the granule disintegration. Figure 4.4 shows how the macroscopic trend of load displacement plots is associated with a large number of microscopic failures even before the plastic flow and large damages.

Experimental observations of some other workers (e.g. Pepin *et al.*, 2001 and Ennis *et al.*, 1991) also show negligible elastic component of compression energy for wet agglomerates. Pepin *et al.*, 2001 explained that the perfectly plastic deformation of the granule under unconfined uni-axial loading occurs sufficiently slow to let the primary particles in the agglomerate rearrange and particles have enough room to reposition. They suggest that during plastic deformation particles slide on each other while binder between them elongates and eventually ruptures. Briscoe *et al.* (1998) showed that micro-ruptures of the binders might be associated with some micro-relaxations underneath the flat platen, which could be reflected as force fluctuations in the force displacement records, the case that was also observed in this study.

It has been shown previously (Figure 4.6) that no elastic behaviour is experienced by these granules in the range of employed loads. However, an attempt was made to estimate the yield stress and modulus of elasticity of the granules by fitting the theoretical model of elastic-perfectly plastic contact deformation of Thornton and Ning (1998) as given by Equations 4.14 and 4.15 to the early part (maximum load of 0.01 N) of the force-displacement data (F and δ) reported in section 4.3.

$$F = \frac{\pi \sigma_y d}{4} \delta + \left(F_y - \frac{\pi \sigma_y d \delta_y}{4} \right) \tag{4.14}$$

$$E^* = \sqrt{\frac{\pi^3 \sigma_y{}^3 d^2}{24 F_y}} \tag{4.15}$$

In this equation F_y and δ_y are the yield load and yield displacement, respectively. Equation 4.14 is fitted to the linear part of the experimental data, where the slope of the line characterises the yield stress, σ_y, of the granule. Consequently, the elastic modulus of these granules is obtained using Equation 4.15. Figure 4.25a shows a typical force-displacement curve obtained for the compression of a 1.70- 2.00 mm granule of Sample 3. Due to the limitation of resolution of the machine the lines are stepwise. Therefore, data points are averaged for each step and then linear fitting is applied. In the figure, the linear plastic part of the curve is identified by a dark blue line. Figure 4.25b shows the best linear regression of the load-displacement lines for a number of single granule compression tests.

Employing the method to a large number of single granule compression tests of 1.00-1.18 and 1.70-2.00 mm granules of Sample 3 and then determining the yield stress and elastic modulus gives an average values as shown in Table 4.9. In the table the average fracture strength obtained based on single granule compression tests (see Table 4.8) and Heckel parameter, $1/K$, (see Table 4.3) are also shown for comparison. As it is seen the standard deviations are large showing the spread of strength of the granules. Nevertheless, these results provide a yardstick for comparison with the bulk data.

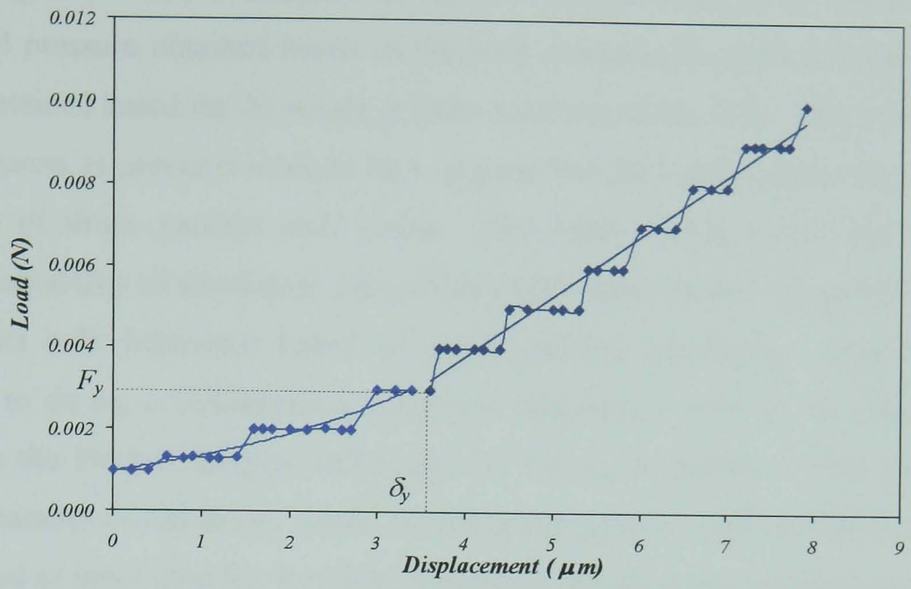

(a)

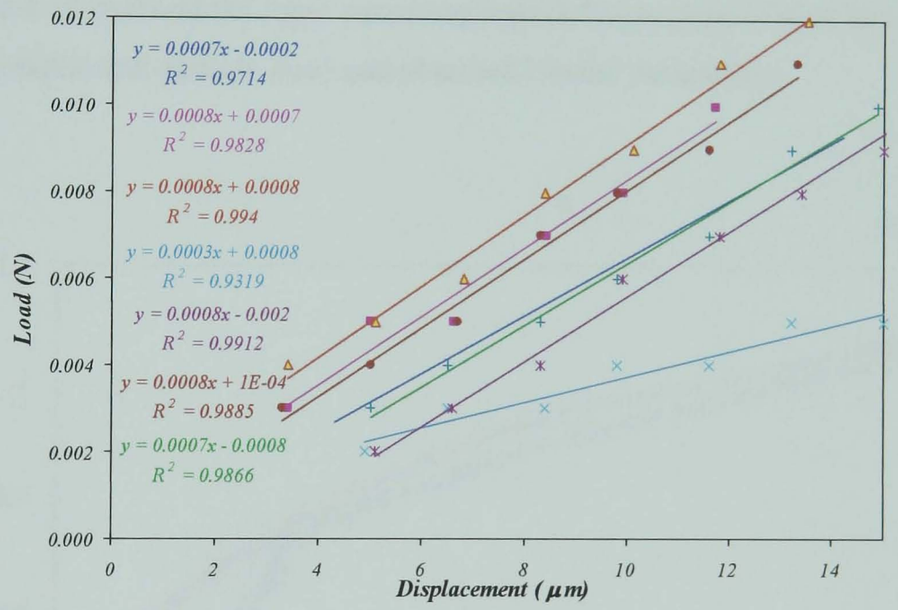

(b)

Figure 4.25: *Single granule force-displacement relationship for Sample 3 granules (a) typical compression data (b) best linear regression of data for a number of tests.*

Table 4.9: *Yield stress, modulus of elasticity and apparent fracture strength of Sample 3 granules obtained based on analysis of single granule compression data.*

Size (mm)	σ_y (kPa)	E^* (kPa)	σ_{os} (kPa)	$P_y=1/K$ (kPa)
1.70-2.00	297 $\pm$108	7470 $\pm$3026	28 $\pm$10	147
1.00-1.18	405 $\pm$151	10089 $\pm$5024	48 $\pm$16	270

According to the Heckel analysis, for the 1.70-2.00 mm and 1.00-1.18 mm granules the yield pressure obtained based on the bulk compression data is lower than yield stress obtained based on the single granule tests (see Table 4.3). The difference is of great interest as previous workers have argued that the bulk analysis method gives a measure of single particle yield stress. This turns out not to be case. With the current capability of simulation using Distinct Element Method, it should be possible to predict bulk behaviour based on single particle properties. Therefore, in an attempt to do so, a collaborative work was undertaken with Mr. A. Hassanpour to simulate the Heckel analysis and to predict the yield pressure. The properties of single granules (yield stress, elastic modulus and particle size) obtained in this work were used as input data for the DEM simulation of bulk compression from which the parameters of Heckel model was determined. Figure 4.26 shows the simulation plots and Table 4.10 outlined the input data (single particles properties such as yield stress, elastic modulus and particle size) and obtained Heckel parameters.

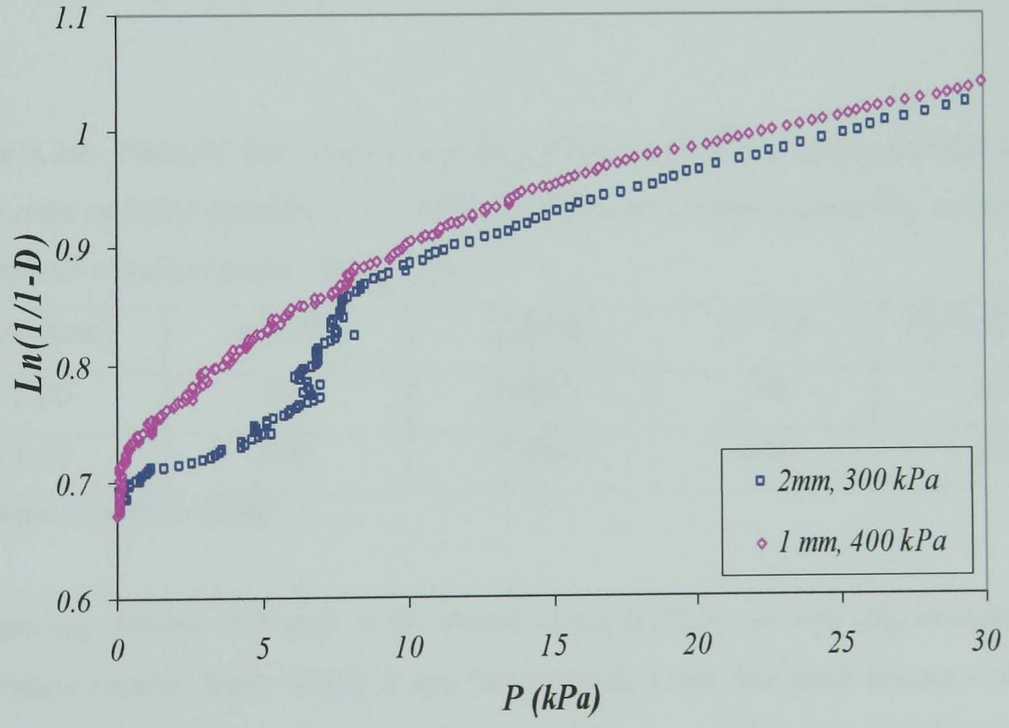

(a)

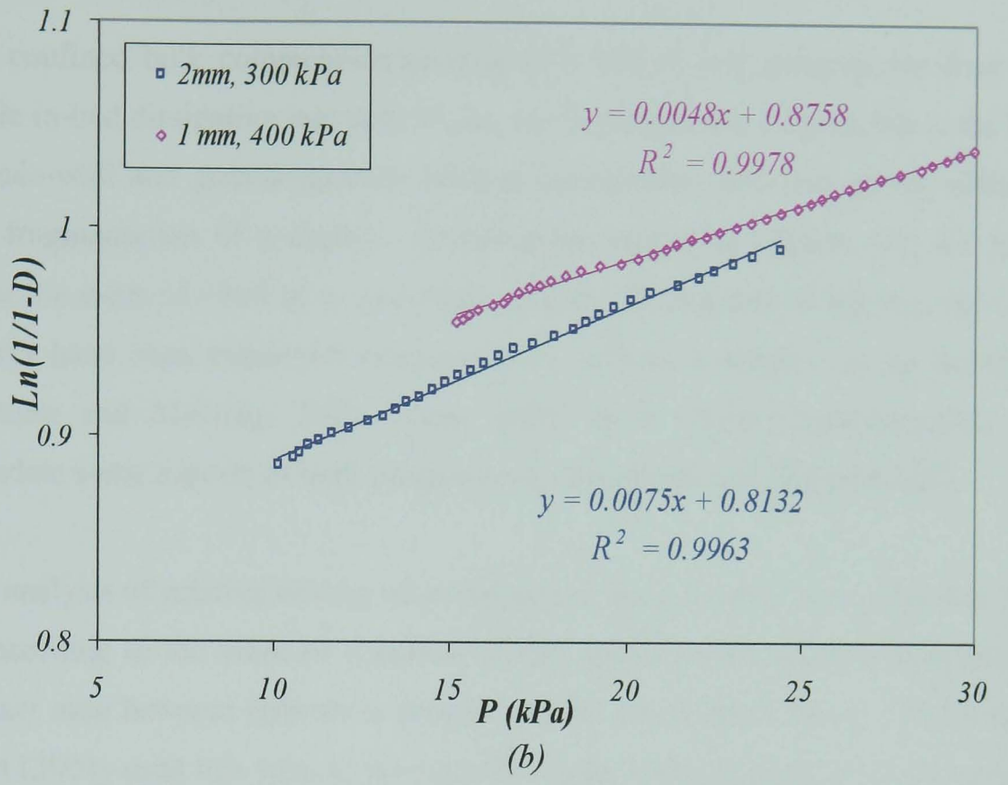

(b)

Figure 4.26: *DEM simulation curves presented based on Heckel model, a) full data, b) best linear regressions after elimination of initial non-linear data.*

Table 4.10: *Particle size, yield stress and elastic modulus of single particle used as input data in DEM simulations of Heckel model and yield pressure (P_y) as the result of analysis obtained from Figure 4.26.*

Size (mm)	σ_y (kPa)	E (kPa)	N^1 (-)	$P_y=1/K$ (kPa)
2.00	300	10000	700	131
1.00	400	15000	4000	208

1) Number of particles in bed

Comparing Tables 4.9 and 4.10 shows compatibility of the experimental and simulation results, from which it can be concluded that the yield pressure obtained based on the Heckel analysis is less than the yield stress and is almost half of σ_y.

4.5.3 Granules failure in confined uni-axial bulk compression

The confined bulk compression process of a bed of soft granules involves several subtle in-bed dissipative interactions, i.e. (i) rearrangement of granules in the bed, (ii) granule-wall and granule-granule friction interactions, and (iii) plastic deformation and fragmentation of granules. Compression curves in Figures 4.7, 4.9 and 4.10 show the steps of i and iii in two types of plot. Both types of log-log and semi-log figures have been employed extensively by various workers (e.g. Es-Saheb, 1993; Carneim and Messing, 2001, Mort, 2001) as a useful characterisation tool to elucidate some aspects of bulk compression of particles and agglomerates.

The analysis of relative density as a function of bed pressure using semi-log diagram is according to the work of Knudsen (1959) who showed that the logarithm of the contact area between spheres is proportional to the relative density of the compact. Mort (2001) used this type of plot and the onset analysis method for the spray-dried alumina granules and model agglomerates made of different binders system. He observed two transition points separating three regions of plot by the slope changes. He believed that the first transition point is the onset of extensive plastic deformation/failure of agglomerates (apparent yield pressure) along with the bed voidage decrease. He explained that at the second transition point, where transition occurs by reduction in slope, the bed voidage is almost zero and the relative density increase is due to the porosity decrease of the agglomerates. In our experiments, however, the second transition point was not observed (Figures 4.7b, 4.9 and 4.10a). This is due to the low range of applied load on bed. A higher bed pressure and relative density than the maximum pressure and density achieved in this work is needed to obtain the second transition point. In this work, however, apparent yield pressure of the granules were easily characterised by finding the first transition point, using onset analysis method.

The compression curves provided some useful information as summarised in the Table 4.2. For example, increasing the compression rate (CHS) or decreasing the granule size increases the apparent yield strength. Using larger granule size in the bed increases the initial bed voidage. Carneim and Messing (2001) employed the

semi-log plots of relative density as a function of bed pressure to investigate the effect of size of spray-dried alumina granules on the compression curve. Although, their sample was much harder than the samples in this work, nevertheless, the same trend was observed as here. Generally, for the larger granules, the ratio of surface area to volume is lower than the smaller ones, reducing the influence of die wall-friction on the bulk compaction. Therefore, the applied pressure to compress the larger granules is lower than the smaller granules for the same bed strain (or bed relative density). This is seen clearly in Figures 4.10a and 4.10b. Comparing the results presented in Table 4.2 indicates that the bed pressure of the different granule sizes at engineering strain of 0.1 (see row 4) are close to the average apparent yield pressure of the same granules (see row 1). This shows that the bed strain of 0.1 is the onset of the plastic flow of the granules in the bed under the compression rate of 1 $mm.min^{-1}$.

Most of the bulk compression studies have been done with the aim of characterising the tablet-forming ability of agglomerates. Few attempts have been made to the breakage behaviour of single agglomerates in the bed. In this context, the work of Adams *et al.* (1996) is one of them. They found that for granules made of soft binders, the breakage of the granules in the bed was associated with more in-plane shear fracture compared to crack opening or tensile fracture. In contrast, their observation from the examinations of a large number of agglomerates compressed individually showed the domination of the tensile fracture. The uni-axial single and bulk compression results for the samples in this work are also compatible with Adams results (Figures 4.5 and 4.8). However, the granules tested here were more plastic, for which considerable shear failure occurred even during single granule compression. In order to characterise the failure mechanism of granules in the bulk, Mort (2001) examined the SEM images of bulk-fractured surfaces after diametrical breakage of compressed tablets. He reported a gradual shift in breakage mode from partial side-line crack to the trans-granular fracture by increasing the maximum load. The threshold of the change was found to be around the second transition point in the semi-log diagrams. In the bulk compression of the samples in this work, most of the damage was in the peripheries and the trans-granular fractures were scanty. This was

as a result of the low-scale loading and more dissipation of energy as plastic deformation, in which most of the stable cracks could not propagate trans-granular.

4.5.4 Comparison of bulk compression models

Three models of Heckel (1961), Kawakita and Ludde (1970) and Adams *et al.* (1994) are considered here. As it was mentioned earlier Heckel's model describes the pressure-volume relationship of bulk compression in terms of two macroscopic parameters of relative density and bed pressure. This model in its linear form (Equation 4.2) has been widely used by many workers (e.g. Robert and Rowe, 1985 and 1987; Sarumi and Al-Hassani, 1991; Es-Saheb, 1992 and 1993). In this context, the reciprocal of the pressure factor, K, obtained from linear fitting of data, is thought to represent the mean yield stress of the single particles. However, for most of the experimental data, the linear fitting of data is not usually obtained for all parts of the plot. In all works above, the first and low bed pressure region was commonly assumed as rearrangement of the particles and therefore it was not considered for determining the yield pressure of particles. Instead, in most of the cases the middle range and sometimes the higher range of the bed pressure were looked for linear fitting. Adams and McKeown (1996) employed this relationship for bulk compression of granules made of inorganic primary particles and different types of soft binders. They reported a large deviation from linearity (Equation 4.2). However, their consideration was based on the whole curve and no attempt was made for linear fitting of data for a specific part of their data. Recently, Denny (2002) modified the model of Heckel and showed that depending on the properties of particles their yield stress might best be characterised based on the linear fitting of Heckle relationship (Equation 4.2) at low bed pressure range (see section 2.5.1). Nicklasson and Alderborn (2001) characterised the yield strength of microcrystalline cellulose (MCC) granules, agglomerated with water and ethanol binder, using the Heckel, (1961), Kawakita and Ludde (1969), and Adams *et. al.* (1994) relationships. However, for these granules the applicability of the model of Heckel to calculate the yield strength was also questioned. They found that the Heckel parameter, was not sensitive to the agglomerate's porosity change, while Kawakita ($1/b$) and Adams

parameters (τ_o') both varied with porosity and composition. The conclusion of Nicklasson and Alderborn (2001) is wrong, because it is based on the middle part. The use of the middle part of the curve and considering the initial part as simply rearrangement has in fact been a pitfall for the workers who have concluded that the yield stress of granules is characterised based on the latter part.

Heckel model was also examined for the agglomerates studied in this work. Figure 4.11a illustrates clearly deviation of Heckel relationship from linearity in the main part of the plot, except initial part. Figures 4.12 and A3 (the latter in Appendix A) show this linearity for different granule sizes of Samples 2 and 3 at early stages of compression (maximum 20 kPa). In contrast, the Kawakita and Adams plots (Figure 4.11b and 4.11c) show good linear trends over a wide range of bed strain, except the initial section. The relationship of Adams *et al.* (1994) is linear for the strains above 0.1, corresponding to the pressures above 10 kpa (Figure 4.11c). However, the linear part of the Heckel plot also falls within the strain range of 0.1-0.3 (Figure 4.11a). Therefore both models should in principles fit the experimental data equally.

The nonlinearity in Kawakita plots is commonly seen for the pressure range less than 25 kpa corresponding to the strains less than 0.25 (Figure 4.11b). Kawakita and Ludde (1970) suggested that this non-linearity is essentially originated from the measured value of the initial bed height as well as the method of sample preparation for the experiments. This corroborates the observation in this work. Figure 4.18a shows clearly two different trends of initial nonlinearity for the same strain rate (300 mm min^{-1} compression speed), while the linear parts nicely overlap. This confirms the justification of Kawakita and Ludde (1970) that for the characterisation of the apparent strength using their model, only the linear part of the plots should be considered.

In this work, the average ratio of the parameters (*1/b* over τ_o') was obtained as 1.04 with standard deviation of $\pm$ 0.164. This ratio for the agglomerates tested by Adams *et. al.* (1994) and Nicklasson and Alderborn (2001) was recorded as 1.42 and 0.84 respectively. In fact, as it is shown by Adams *et. al.* (1994), there is a similarity between the Kawakita and Adams equations, for which the same dependency of

pressure on strain is provided for both equations. In this context, rearranging both relationships, then driving the pressure term as a function of bed strain and equalising the corresponding relations leads to an equation as follows:

$$\frac{C_1}{b}\left(\frac{v_o - v}{v - v_{\min}}\right) \cong \frac{\tau_o'}{\alpha'}\left(\frac{v_o}{v}\right)^{\alpha'} \tag{4.16}$$

where C_1 is the proportionality constant and v_o, v *and* v_{min} are the initial bed volume, online volume during compression, and minimum bed volume, respectively. v_{min} is the bed volume at zero bed voidage and granule porosity. Minimum volume can be easily found using the true density of the granules and mass of material compressed in the die. Figure 4.27 shows a typical plot of $\ln(v_o\text{-}v)/(v\text{-}v_{min})$ *vs.* $\ln(v_o/v)$, which seems linear over a certain part of the bed strain. Similar plots are obtained for the other granule sizes and are not shown here.

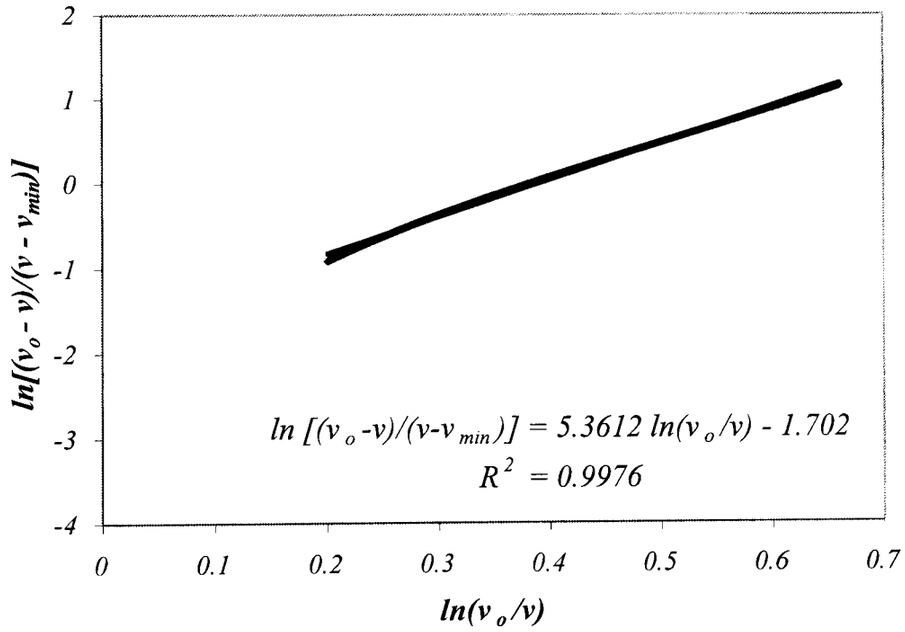

Figure 4.27: *Relation of* $\ln(v_o\text{-}v)/(v\text{-}v_{min})$ *vs.* $\ln(v_o/v)$ *for 1.70-2.00 mm granules of Sample 3, compressed at 1 mm.min*$^{-1}$ *cross head speed and 0.9 initial aspect ratio.*

α' and C_1 are determined from the slope and intercept of the regression line, and are 5.36 and 1.023, respectively. The constant C_1 in fact indicates the proportionality

constant of Adams and Kawakita parameters, so that for the sample tested above the relationship is given as:

$$\frac{1}{b} = 0.98\tau_o' \tag{4.17}$$

The constant of 0.98, which has been found from Figure 4.27 is in close agreement with the average constant of 1.039, obtained individually from the calculation of *1/b* and τ_o' for all the experiments.

Figure 4.28 shows the relationship for the parameters of Adams *et al.* (1994), Heckel (1961) and Kawakita and Ludde (1970). The data are for different granule sizes of Sample 3. As it was shown in Chapter 2 (compare Equations 2.20 and 2.31) two parameters of Kawakita and Heckel can be related according to Equation 4.18. This relation has been examined in Table 4.11 for Sample 3 granules.

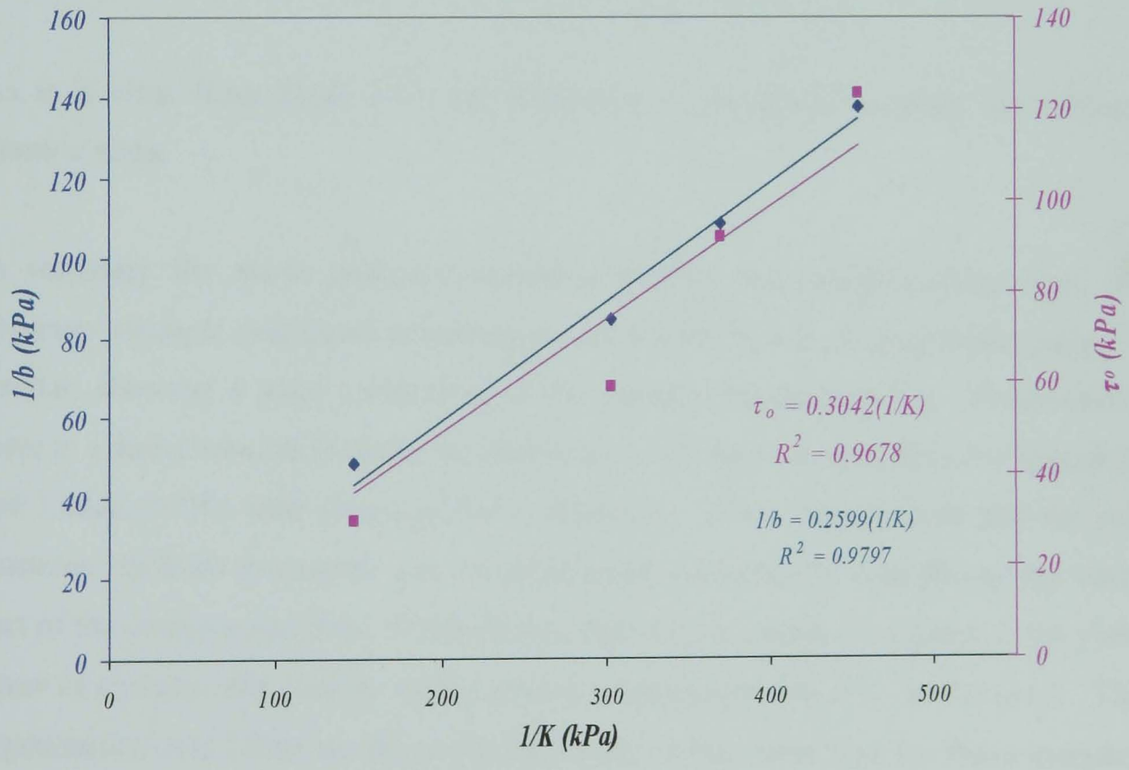

Figure 4.28: *Relationship between parameters of Adams et al. (1994) and Heckel (1961), and parameters of Kawakita and Ludde (1970) and Heckel (1961) for different granule sizes of Sample 3.*

$$\frac{1}{b}=C_2\frac{(1-\nu_o)}{K} \quad or \quad \frac{1}{b}=C_2\frac{D_o}{K} \tag{4.18}$$

where C_2 is a constant, and ν_o and D_o are initial bed voidage and initial relative density.

Table 4.11: *Relationship between Heckel and Kawakita parameters of Sample 3 granules.*

Granule Size (mm)	*1/K* (kPa)	ν_o (-)	$D_o = 1-\nu_o$ (-)	*1/b* (kPa)	$C_2=(1/b)/(D_o/K)$ (-)
1.70-2.00	147.06	0.636	0.364	48.20	0.79
1.00-1.18	270.27	0.594	0.406	73.98	0.64
0.60-0.71	370.37	0.561	0.439	94.87	0.64
0.212-0.25	454.54	0.556	0.443	120.55	0.63

As it is clear from Table 4.11, the parameter C_2 is almost constant for different granule sizes.

In summary the above analysis elucidates that for the samples tested here, the apparent strength calculated according to the Kawakita and Adams relationships is similar, showing a good correlation of the models (Equation 4.17). Furthermore, there is a direct relation between the parameters of Adams *et al.* (1994) and Kawakita and Ludde (1970) with Heckel (1961) parameter. These results show that for soft granules Heckel's parameter can be determined consistently considering the early part of the compression data. Furthermore, Heckel's parameter is related to the yield stress of granules obtained by single granule compression but it is not the same. The experimental and DEM results presented in this work show that for these granules the yield stress (σ_y) is about two times of the Heckel parameter ($1/K$).

4.5.5 Dependency of compression parameters on granule size

Figures 4.14 and 4.15 show the size dependency of the pressure/strain of Samples 2 and 3. It indicates that for larger granules, lower bed pressure is needed to compress the granules to a constant amount of the bed strain. In fact the larger granule size, the lower total contact number as well as total contact surface area between granules and granule-wall for a constant bed volume, hence, lower inter-granule and granule-wall friction during compression. Table 4.4 shows the effect of granule size on the bed friction parameter, α', obtained from Adams relationship, in which α' decreases with increasing the size for both samples. The same trend is observed for other initial aspect ratios in the Table 4.6. Therefore, for the samples and size range tested in this work, it can be obviously deduced that increasing the granule size diminishes the friction effect in the bed. They will be discussed further in the section 4.5.7.

The apparent strength data characterised according to the Adams and Kawakita relationships (τ_o' and *1/b*) have been plotted as a function of mean granule size in Figures 4.20 and 4.21, showing the effect of size on the apparent strength of both samples. The figures illustrate size sensitivity of granules, in which the granules strengthen with decreasing the size. The figures also indicate the strength superiority of Sample 2 over Sample 3, which reduces with increasing the size and even reverses. This effect is especially seen at higher compression rates. The dependency of the size on strength was also investigated by Adams and McKeown (1996), for which they found no systematic trends of strength with agglomerate size. The granules tested were in the range of 0.425-2.00 mm, harder than the samples used here but with some plastic deformation behaviour.

The initial bed voidage data, obtained indirectly based on the Kawakita parameter, *a*, have also been presented in the Figure 4.21. It was already shown in the Chapter 2 that *a*, is equal to the value of the initial porosity. In practice, this derived value does not agree well with the measured value (ν_o) as shown in Table 4.3. This difference has also been reported by Denny (2002). However, both Figure 4.21 and Table 4.3 show clearly the effect of the size on the bed voidage for Samples 2 and 3, in which increasing the size increases the initial voidage of the bed. This result is compatible

with experimental work of Arteaga and Tuzun (1990), who measured directly the packing fraction of binary mixtures of two different sizes of spherical particles. They found that as the fraction of fine particles increases, the packing fraction of the mixture approaches a maximum and beyond this point at extremes (100% fine or coarse particles), the bed voidage of the coarse particles are higher than the fines.

4.5.6 Dependency of compression parameters on bed strain rate

The response of a bed of particles when loaded quasi-statically is often different from when loaded dynamically. In this context, some researchers (Robert and Rowe, 1984 and 1987; Sarumi and Al-Hassani, 1991; Es-Saheb, 1992 and 1993) have employed the Heckel's model to study the effect of strain rate on the yield pressure of the particles. Roberts and Row (1987) proposed a factor to describe the strain rate sensitivity (SRS) as defined by the percentage increase in the yield stress when punch velocity is increased from 0.033 mm s^{-1} to 300 mm s^{-1}. However, in all the above investigations the effect of strain rate on the yield pressure has only been analysed and the effect of strain rate on the strength of individual particles have not been considered. Furthermore, almost all of the above studies are confined to materials with a relatively high stiffness and hardness rather than the soft granules of interest here.

For the samples studied in this work, the applied compression rates were in the quasi-static range of 1 to 600 mm min^{-1}, corresponding to the bed strain rates of 0.001 to 0.55 s^{-1} (based on initial bed height). However, even in this range, the compression parameters, characterised according to the Kawakita and Adams relationships, showed sensitivity to the compression rate. The Figures 4.19 and A5 (in Appendix A) as well as Table 4.5 show the apparent strength of granules, obtained based on the models of Kawakita and Ludde (1970), and Adams et al. (1994), as a function of compression rate, in which increasing the compression rate stiffens the granules.

The experiment data resulting from the above work shows readily that the general effect of strain rate is appeared as an increase in axial compression pressure of the

bed. The higher sensitivity of soft and ductile material to strain rate might be explained by their creeping and relaxation behaviour of granules in the bed. In this context, Es-Saheb (1992) and Sarumi and Al-Hassani (1991) compared the compression behaviour of different materials under the constant load and volume. They found that for the materials such as Dipac sugar and sodium chloride powders, the rate of axial pressure relaxation (pressure reduction) with time is higher, compared to the harder material. Furthermore, he showed that the rate of radial relaxation of powders in the bed is much lower than the axial relaxation. Sarumi and Al-Hassani (1991) also showed that the radial pressure (measured as average pressure on the die wall) is larger at lower strain rates when a same axial pressure is applied for both cases.

The conclusion drawn from above discussion is that the time dependent mechanism of relaxation at higher strain rates may not be important. In contrast, at lower strain rates the effect of bed relaxation on pressure-strain curves may be significant. In other words, alongside the increase in pressure due to the resistance of the granules to the imposed reduction of volume, there is also a tendency for pressure reduction with time. It means that less pressure is required at the lower rates for compression of the bed. However, at the higher strain rates, the time needed for relaxation is probably too short to affect the pressure increase in the bed.

For the soft granules employed in this work the forces holding the solids together are due to the adhesion of paste type binder to the surfaces of primary particles and flow stress (viscosity effect) of the binder. In this case, the effect of relaxation at lower strain rates might be even higher due the low yield strength of the binder (about 50 kpa at 20 °C, refer to Chapter 3). In fact, increasing the strain rate may cause the dynamic yield stress of the binder and probably hardness of granules to be increased, and the rate of consolidation of granule decreases (Iveson *et al.*, 1996; Iveson and litster, 1998). Therefore, with increasing the strain rate the mechanical properties of the granules may change in such a way that strength of granules may be affected. The enhancement of the strength even in the quasi-static range of the applied load is presumably due to the effect of the strain rate on viscous adhesion force of the binder, for which the binder adhesion force might increase with the strain rate.

4.5.7 Dependency of compression parameters on aspect ratio

In this section, the effect of initial aspect ratio on the compression parameters is only considered for the Adams parameters (τ_o' and α'), as the theory behind it applies to the discussions in this regard.

As discussed in Chapter 2, the parallel friction-element model of Adams *et al.* (1994), Equation 2.41, has been developed according to an approximate first order lumped-parameter approach, in which the system is regarded as entirely dissipative. The model considers a set of active parallel columns of granules, for which the failure stress is explained based on the Mohr-coulomb criterion. In Equation 2.41, however, the parameters of τ_o' and α' are determined experimentally and are related to their analogous parameters τ_o (cohesive strength of single granule) and α (lateral pressure coefficient) as follows:

$$\tau_o' = k_3 \tau_o \tag{4.19}$$

$$\alpha' = k_3 k_4 \alpha \tag{4.20}$$

The coefficient k_3 in the Equation 4.19 is similar to that Adams presented in his theoretical approach (Adams and McKeown, 1996). However, for the term k_3k_4 in Equation 4.20, they lumped it into one coefficient, k. Although, these parameters (k_3 and k_4) are essentially different, nevertheless, consideration of only one coefficient (k) does not affect the outcome the model (Equation 2.41). As discussed in Chapter 2, k_3 represents the rate of failure area increase because of bed strain (Equation 2.37), whilst k_4 is a constant relating the axial and lateral pressures in the bed. In the following, it is shown that the role of these parameters is more than that to be ignored.

To open the discussions, at first the results that was already deduced from Figures 4.23 and 4.24 and Table 4.6 are summarised as follows:

(i) For the same granule size, reducing the initial aspect ratio decreases the apparent strength, τ_o'. A linear relationship is obtained between τ_o' and initial aspect ratio for all the sizes tested in this work. However, for 1.70-2.00 mm granules of Samples 2 and 3, τ_o' is found almost constant and independent of the initial aspect ratio.

(ii) For the same initial aspect ratio, increasing the granule size reduces τ_o' and α'.

(iii) The slope of the line of τ_o' as a function of initial aspect ratio seems to decrease when the size of the granules increases.

Referring to the Mohr-coulomb criteria, Equation 2.35, as the single granule cohesive strength, τ_o, for a specific granule size should be constant; it could be considered that its magnitude would be close to the extrapolated strength at the zero aspect ratio, where the friction effect is negligible. Actually, for two granule sizes of 1.00-1.18 mm and 1.70-2.00 mm of Sample 3, the experimental results of this work show that they are in close agreement. This is clearly seen by comparing the single granule strength of the above-mentioned sizes (obtained from Table 4.1) with analogous values at zero aspect ratio (obtained from Table 4.6). Furthermore, it was found experimentally that for smaller granules τ_o' is directly proportional to the initial aspect ratio. As, τ_o is constant and τ_o' is directly proportional to the k_3 (Equation 4.19), therefore, it would be expected that k_3 is directly related to the initial aspect ratio. On the other hand, the experimental results show that for the smaller granules α' also changes directly with the initial aspect ratio. Hence, it would be expected that α' also has a direct relationship with k_3. Actually, the latter relation has been derived theoretically in the Equation 4.20.

The above discussions are also deduced from Table 4.12, where the parameters k_3 and $k_4\alpha$ have been presented as the granule size and aspect ratio for Samples of 2 and 3. In this context, k_3 values have been calculated based on Equation 4.19, in which τ_o has been substituted by the apparent strength at zero aspect ratio. The

values of $k_4\alpha$ have subsequently been calculated using Equation 4.20 and the values of α' and k_3.

Table 4.12: *Parameters of k_3 and k_4 for different granule sizes and initial aspect ratios for Samples 2 and 3.*

Sample 2

Size (mm)	Initial Aspect Ratio (-)	Ave. α' (-)	Ave. τ_o' (kPa)	τ_o' at zero aspect ratio (kPa)	k_3 (-)	$k_4\alpha$ (-)
0.60-0.71	0.9	5.738	126.130	82.906	1.521	3.772
0.60-0.71	0.7	5.617	119.226		1.438	3.906
0.60-0.71	0.5	5.475	107.622		1.298	4.218
1.00-1.18	0.9	5.607	68.630	53.411	1.285	4.363
1.00-1.18	0.7	5.555	70.378		1.318	4.216
1.00-1.18	0.5	5.419	60.942		1.141	4.749
1.70-2.00	0.9	5.324	29.599	23.070	1.283	4.150
1.70-2.00	0.7	5.270	27.335		1.184	4.448
1.70-2.00	0.5	5.213	27.709		1.201	4.340

Sample 3

Size (mm)	Initial Aspect Ratio (-)	Ave. α' (-)	Ave. τ_o' (kPa)	τ_o' at zero aspect ratio (kPa)	k_3 (-)	$k_4\alpha$ (-)
0.60-0.71	0.9	6.920	105.04	80.945	1.298	5.333
0.60-0.71	0.7	6.716	102.524		1.267	5.301
0.60-0.71	0.5	6.497	93.874		1.160	5.602
1.00-1.18	0.9	6.341	67.590	52.248	1.294	4.902
1.00-1.18	0.7	6.321	68.833		1.317	4.798
1.00-1.18	0.5	6.090	61.231		1.172	5.197
1.70-2.00	0.9	5.727	35.754	35.023	1.021	5.610
1.70-2.00	0.7	5.672	36.600		1.045	5.428
1.70-2.00	0.5	5.560	34.490		0.985	5.646

Figures 4.29, 4.30 and 4.31 show the variation of parameters of α', k_3 and $k_4\alpha$ with initial aspect ratio, respectively. As parameter, α', depends directly on the friction coefficient, its increase with the initial aspect ratio for 0.600-0.710 mm granule size (Figure 4.29) might be as the result of change of the friction coefficient with the initial aspect ratio. On the other hand, for the larger granules, 1.70-2.00 mm, Figure 4.29 indicates the insensitivity of the α' to the aspect ratio. Figure 4.29 also shows the higher magnitudes of α' for Sample 2, as compared to Sample 3 and for the smaller granules as compared to the larger ones. In fact, the sensitivity of α' to aspect ratio as well as larger amounts of α' for the smaller granules would be due to their higher friction parameter, α, which is arisen from the higher total contact area of the granules in the bed. In Figure 4.30, the effect of the initial aspect ratio on the parameter of k_3 has been shown. As it is seen, for all the plots, k_3 converge approximately to unity at zero aspect ratio, at which τ_o' equals the single granule strength, τ_o (Equation 4.19). Figure 4.30 also shows the higher values of k_3 for Sample 2 as compared to Sample 3. In general, according to Equation 2.37, it can be concluded that the higher magnitude of the parameter k_3 means the higher is the extent of new failure area of the granules developed in the bed as a result of the bed strain. Figure 4.30 shows the higher values of $k_4\alpha$ for Sample 2 as compared to Sample 3 but almost constant value, independent of the initial aspect ratio.

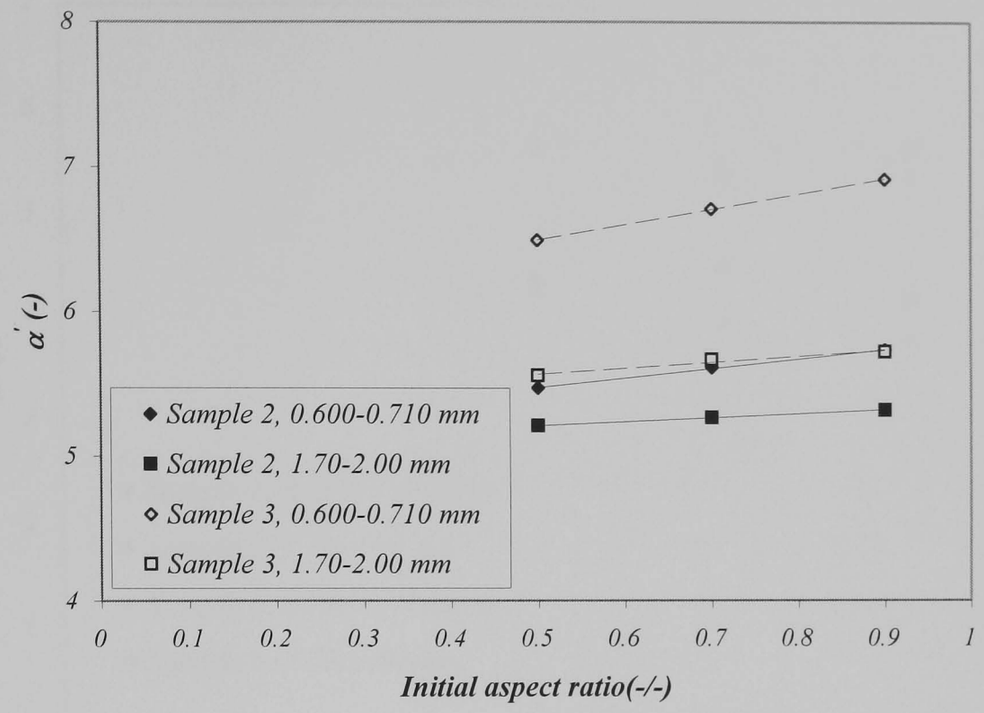

Figure 4.29: *Effect of the initial aspect ratio on the parameter α', for two sizes of Samples 2 and 3.*

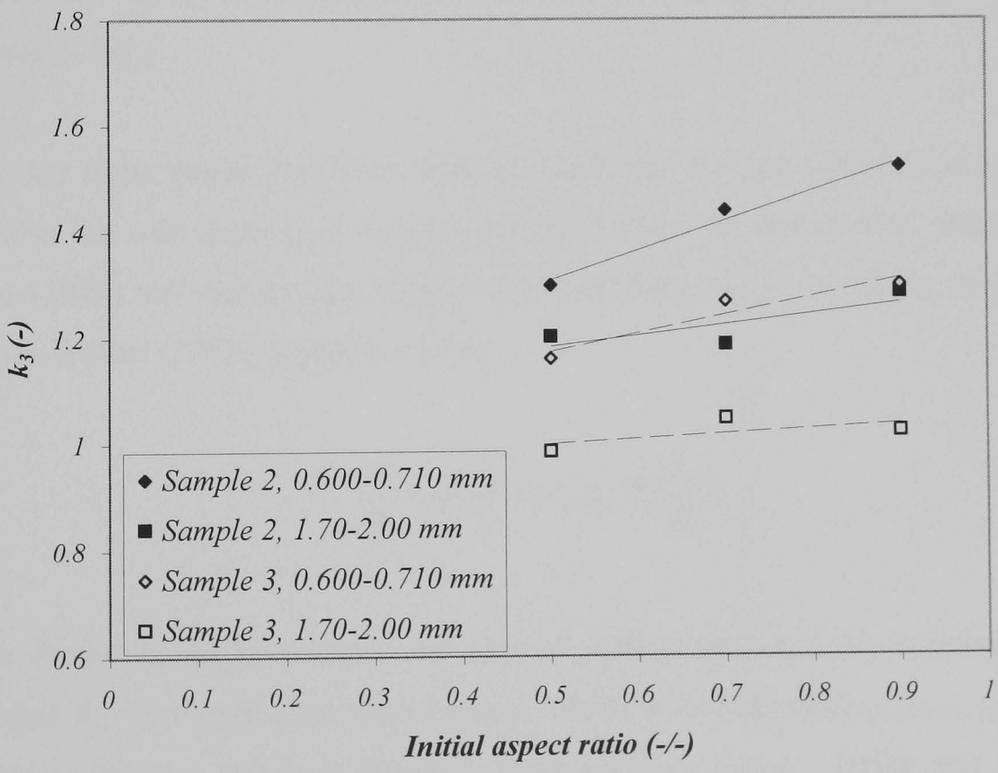

Figure 4.30: *Effect of the initial aspect ratio on the parameter k_3, for two sizes of Samples 2 and 3.*

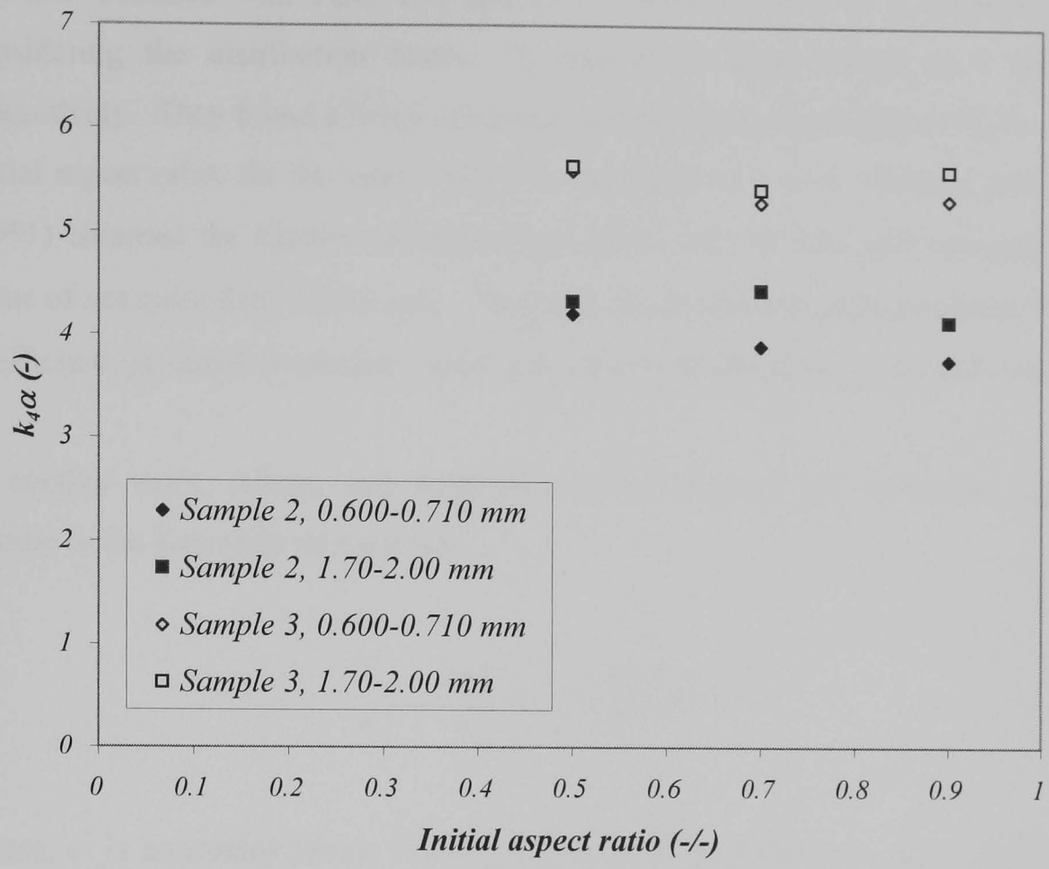

Figure 4.31: *Effect of the initial aspect ratio on the parameter $k_4\alpha$, for two sizes of Samples 2 and 3.*

There are some works that have tried to clarify the essence of the term $k_4\alpha$ with regard to the wall friction of the granules in the bed. In this context, Briscoe and Evans (1991) and Adams and McKeown (1996) have made use of the analysis of Janssen-Walker (1895), Equation (4.19).

$$\frac{P_t}{P_a} = \exp(-4\psi_s \mu_f \; k_4 \frac{h_o}{D_c}) \tag{4.21}$$

where P_t and P_a are transmitted and applied axial pressures, h_o/D_c is initial aspect ratio and Ψ_s, is a stress distribution factor, which is defined as $\sigma_{(yy)w}/\sigma_{(yy)}$, μ_f is wall friction coefficient and k_4 is lateral to axial pressure factor. Jenike and Johnson (1969) suggest that for most granules k_4 is estimated to be about 0.4. Briscoe and Evans (1991) employed Equation 4.21 to the bulk compression of granules (Alumina

granules bounded with PEG 400 and PVA 14000 binders) in a cylindrical die, considering the distribution factor, Ψ_s, and k_4 to have values as 1 and 0.4, respectively. They found a linear relationship between the logarithm of P_a/P_t and the initial aspect ratio, for the aspect ratios in the range of 1 to 5. Briscoe and Evans (1991) obtained the friction coefficient (μ_f) about 0.15 to 0.22 and consequently a value of not more than 0.1 for $\mu_f k_4$. They also showed that at high pressures, friction coefficient, μ_f, equals to pressure ratio, α (as it will be discussed in the following).

In another work, Adams and McKeown (1996) derived the following equation similar to the Kawakita relationship:

$$\frac{P}{\varepsilon_e} = \frac{2\pi c^*}{s^2}\sigma_y + \frac{2\pi c^*}{s^2}\alpha k_4 P \tag{4.22}$$

where, c^* is constraint factor, s is the particle spacing parameter, σ_y is yield stress. They explained that for granules made of quartz and PVP binder, αk_4 is about unity, which is less than our estimated value (Table 4.12). If it is supposed that in the Adams and McKeown (1996) experiments, k_4 is in order of 0.4, hence, the pressure coefficient, α, should be about 2.5. Comparing Equation 4.22 with the model of Kawakita and Ludde (1970), Equation 4.3, shows the following relationship between the Kawakita parameter, $1/b$, and the yield stress of single granule:

$$\frac{1}{b} = \frac{\sigma_y}{\alpha k_4} \tag{4.23}$$

It was previously shown in Equation 4.19 that for granules tested here, the Kawakita parameter ($1/b$) scales with the Adams parameter (τ_o') in a same order of magnitude. Furthermore, both parameters at zero aspect ratio are approximately equal to the apparent strength of granules obtained based on the single granule compression tests. On the other hand, as it is seen in Figure 4.28, Equation 4.18 and Table 4.11, the Heckel parameter ($1/K$) is at least three times of the Adams and Kawakita parameters. It was also shown that the yield stress of the granules (refer to section

4.5.2) obtained based on the single granule tests as well as DEM simulation is about two times of the Heckel parameter. For 1.70-2.00 mm granules of Sample 3, the above discussions are outlined in Equations 4.24 and 4.25.

$$\tau_o' \cong \frac{1}{b} = C_2 \frac{D_o}{K} \qquad C_2=0.79 \text{ and } D_o=0.36 \text{ (from Table 4.11)} \tag{4.24}$$

$$\frac{1}{K} = C_3 \sigma_y \qquad C_3=0.50 \tag{4.25}$$

Combining Equations 4.24 and 4.25 leads to the following equation:

$$\tau_o' \cong \frac{1}{b} = C_2 \, C_3 \, D_o \, \sigma_y = \frac{1}{7.03} \sigma_y \tag{4.26}$$

Substituting the value αk_4 of 1.70-2.00 mm granules of Sample 3 from Table 4.12 (the value of 5.60) in Equation 4.23 gives a coefficient approximately close to Equation 4.26. However, there is a small difference, which is thought to be due to the large standard deviation of the yield stress obtained based on the single granule compression test. Similar conclusion can be obtained for 1.00-1.18 mm granules that is not presented here.

In summary, the analysis presented in this work show that there is a rational relation between the apparent strength and yield stress of single granules as shown in Equation 4.27.

$$\tau_o' \cong \frac{1}{b_o} \cong \sigma_{os} \cong \frac{\sigma_y}{\alpha k_4} \tag{4.27}$$

where τ_o' and $1/b_o$ are the Adams and Kawakita parameters at zero aspect ratio and σ_{os} is the apparent strength obtained based on the single granule compression tests. The parameter αk_4 for different materials seems to vary from the values as less as 0.1 (Briscoe and Evans, 1991) to unity (Adams and McKeown 1996) and the values in

range of 4-5 in this work. To justify this large magnitude of αk_4, the friction mechanism of soft granules needs to be rationalised first. Briscoe (1991) reviews a fundamental basis for interpreting the friction of organic polymers and offers an approach based on a two-term non-interacting model. The model suggests two mechanisms of the adhesion at the interface and deformation at subsurface zones, in which the processes occurring in one mechanism are considered not to influence those occurring in the other. The deformation or ploughing effect essentially depends on the contact geometry, normal load and mechanical characteristics of ductile surfaces such as Young modulus to hardness ratio. This type of friction usually occurs when a hard indenter slides or rolls over a ductile surface. In this context, contact geometry is regarded as angle of attack for sharp indenters (e.g. cone indenters) or ratio of contact width to indenter radii for spherical indenters. However, the ploughing component might be ignored for the granules studied here, as in the bed the contacts are between the soft granules surfaces or between the granules and almost smooth die wall. Therefore, it is reasonable to assume that the adhesion mechanism accounts for all the frictional work, which arises from the shearing of the junctions formed at the discrete contact points.

The popular model for adhesion components of friction supposes a dissipative frictional force, which may be explained by:

$$F = \tau A_r \tag{4.28}$$

where A_r is the real contact area and τ is a parameter termed as the interface shear stress. This model is named as the adhesion model of friction, in which it is supposed that the friction work is transmitted to the surface layer by the action of adhesion forces operating at the areas of real contact. Employing the adhesion model of friction is accompanied by two major difficulties; the computation of real contact area and the acquisition of the value of τ. Furthermore, both these parameters are sensitive to the contact conditions particularly contact pressure and some other parameters such as contact temperature, sliding velocity, characteristic contact length

and also dissipation zone thickness (Briscoe, 1991). The contact pressure dependency of τ is empirically given as:

$$\tau = \tau_o + \alpha P_l \tag{4.29}$$

where τ_o is intrinsic shear strength and α is the pressure coefficient. Substituting τ by its equivalent term μP_l in Equation 4.29, gives the friction coefficient of granule array in the bed as:

$$\mu = \frac{\tau_o}{P_l} + \alpha \tag{4.30}$$

According to Equation 4.30, it is shown (Briscoe and Evans, 1991; Briscoe, 1991) that for single point contact between a smooth elastic sphere and a hard smooth plane the friction coefficient (μ) approaches to the pressure coefficient (α) with increasing the contact pressure. However, due to lack of direct measurement of τ as pressure for our granules it can logically be deduced that α and consequently μ might be higher than one for two reasons. First, the range of applied pressure (P_l) in our experiments is lower than the intrinsic shear strength of such adhesive granules. Therefore, in Equation 4.28, τ_o/P_l might be higher than unity. Second, it has been shown that the value of α, measured experimentally for polymers is higher for more ductile polymers (Briscoe, 1991) and even could be more than unity.

4.6 Conclusions

The deformation and breakage behaviour of two detergent base granules were investigated, using uni-axial single granule and bulk compression testing methods. Furthermore, the reliability of their tests results were assessed and compared. The validity of three models of Heckel, Kawakita and Adams were assessed for such soft granules in the bulk compression experiments and the dependency of their

compression parameters on granule size, strain rate and initial aspect ratio were investigated.

In general, the error analysis of the experimental results show better reliability of the bulk compression tests results as compared to the single granule compression. This was shown apparently in Table 4.8 by comparison of the obtained average values and standard deviations.

Microscopic examinations of the single granule compression test materials shows occurrence of two stable failure mechanisms of crack-opening or tensile (failure mode I) and in-plane deformation or shearing (failure mode II). Micro-ruptures of the binders were associated with some micro-relaxations between the flat platens, which were reflected in the force displacement figures as micro force fluctuations.

The yield stress and elastic modulus of the single granule was estimated by fitting the theoretical model of elastic-perfectly plastic of Thornton and Ning (1998) to the early parts of the single granule force-displacement data (maximum load of 0.01 N). For 1.70-2.00 mm and 1.00-1.18 granules of Sample 3 the average value of yield stress was found about two times of the yield pressure obtained based on the Heckel analysis. DEM simulation of Heckel parameter also confirms this conclusion by employing the same properties of particles as the experimental granules used in this work.

The apparent strength of the granules was determined for two granule sizes of 1.00-1.18 mm and 1.70-2.00 mm of sample 3 based on the single granule compression testing method. In practice, the force measurement sensitivity of the test machine limited acquiring the load displacement data of the granules less than 1.00 mm size. However, even for larger granules, although, the experiments were repeated 100 times, the average failure strengths were obtained with more than 30% errors.

In analysis of the bulk compression results, the plots presented based on Heckel relationship deviate from linearity in most part of the plots except the initial and low pressure range. In contrast, good linearity was observed in the large part of

Kawakita and Adams relationships except the initial part. However, comparing these plots reveals that the pressure-strain data corresponding to the initial linear part of Heckel plots are also fitted in the linear part of Adams plots. For the granules tested in this work, the parameters of Heckel, Kawakita and Adams were determined using the best linear regression of the linear part of plots. Close agreement was observed between the apparent strengths calculated based on the Adams and Kawakita relationships. However, the yield pressure obtained based on the model of Heckel was found more than three times of the apparent strength calculated based on the Kawakita and Adams models.

It was shown that reducing the initial aspect ratio in the bulk compression experiments decreased the apparent strength. In fact, for two granule sizes of 1.00-1.18 mm and 1.70-2.00 mm of the Sample 3, the apparent strengths obtained from the single granule compression tests were in close agreement with the extrapolated strength to the zero aspect ratio, where the friction effect of the bed is expected to be negligible. Therefore, the apparent strength of granules at zero aspect ratio might be considered as average single granule strength. It was also shown that with increasing the granule size the effect of initial aspect ratio on the strength became small.

The yield stress and apparent strength of the granules showed size sensitivity, in which these parameters were increased with decreasing granule size. Furthermore, increasing the strain rate even in the quasi-static range enhanced the strength and yield pressure of the granules. It was shown that the strength and the yield stress of these granules were correlated based on Equation 4.27.

The friction mechanism of the soft and adhesive granules was rationalised and used to justify the friction behaviour of the granules in the bed. It was shown that the term of αk_4 as product of two parameters of inter-particle friction coefficient and pressure factor plays a major role to make link between the yield stress and the strength of single granules.

5 SINGLE GRANULE IMPACT OBSERVATIONS

5.1 Introduction

There are two ways of carrying out the impact: impacting the particles at a target (e.g. Samimi *et al.*, 2003; Salman *et al.*2002) or impacting a projectile at a stationary particle (e.g. Tavares and King, 2002). A large number of particles can be tested quickly using the first method, whilst the second method is time consuming. The advantage of the single particle tests as compared to the bulk test, however, is the well-defined and controlled conditions of loading, which enables study of various factors to be facilitated.

The main objective of this chapter is to identify the breakage patterns of three types of agglomerate by the observation of the impact events using single particle impact apparatus along with the high-speed digital video camera. Moreover, the impact products are examined after impact using scanning electron microscopy (SEM) and reflected light microscopy (RLM). In this context, single impact experiments have been carried out to investigate the effects of impact velocity, granule size and impact angle on the mode and pattern of the failure.

The single particle impact test rig was originally developed by Yüregir *et al.* (1987) but the version used here has been modified to facilitate the operation of the device. Details of the impact rig and high-speed digital video camera and their accessories are given in the section 5.2. Observations of granules failure events under impact using high-speed digital imaging are presented in the section 5.3. The SEM results of impact products are presented afterward in the section 5.4. The discussion and conclusions are given in the sections of 5.4 and 5.5, respectively.

5.2 Description of impact test apparatus

A schematic drawing and photographs of the impact test apparatus, including its accessories, are shown in Figures 5.1 and 5.2, respectively. There are two designs of the impact rig, one with a long tube suitable for particles larger than 850 μm, and the other with a short tube for finer particles. Both of them work in the same manner. As it is seen, the system is equipped with an air eductor and a vacuum line connected to the bottom of the rig. Particles are fed from the top, using a spiral-vibrating feeder or through manual feeding and are entrained into the eductor. The particles are accelerated to the desired velocity by adjusting the flow-rate through the unit. This is done by manipulating the compressed air flow-rate and/or vacuum inside the chamber. Two highly porous sintered plates are mounted at the top and bottom of the rig. The top plate is used to straighten the airflow in the tube and the bottom one is used to support the filter in the collection chamber. The eductor is designed to produce a slight vacuum at the inlet of the accelerating tube, in to which the particles are entrained as a result of the Venturi effect.

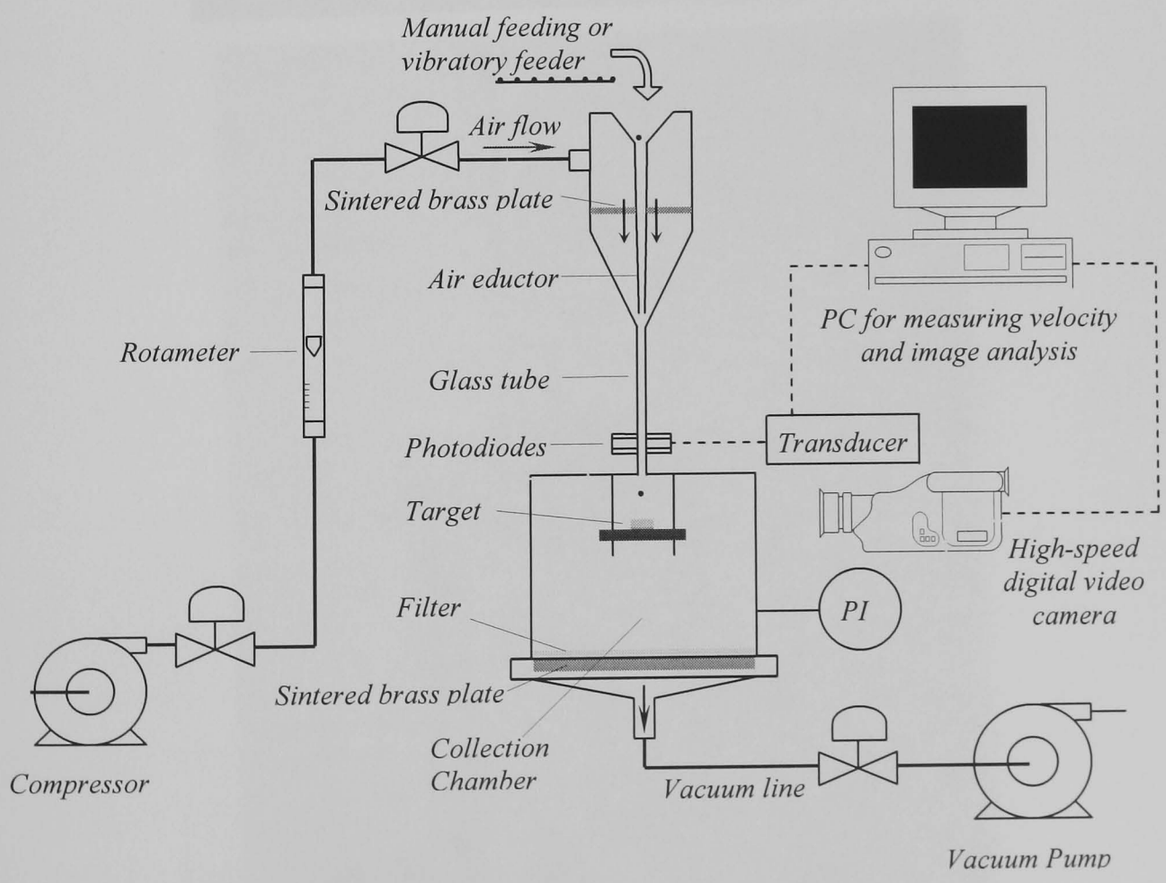

Figure 5.1: *Schematic illustration of the impact test rig.*

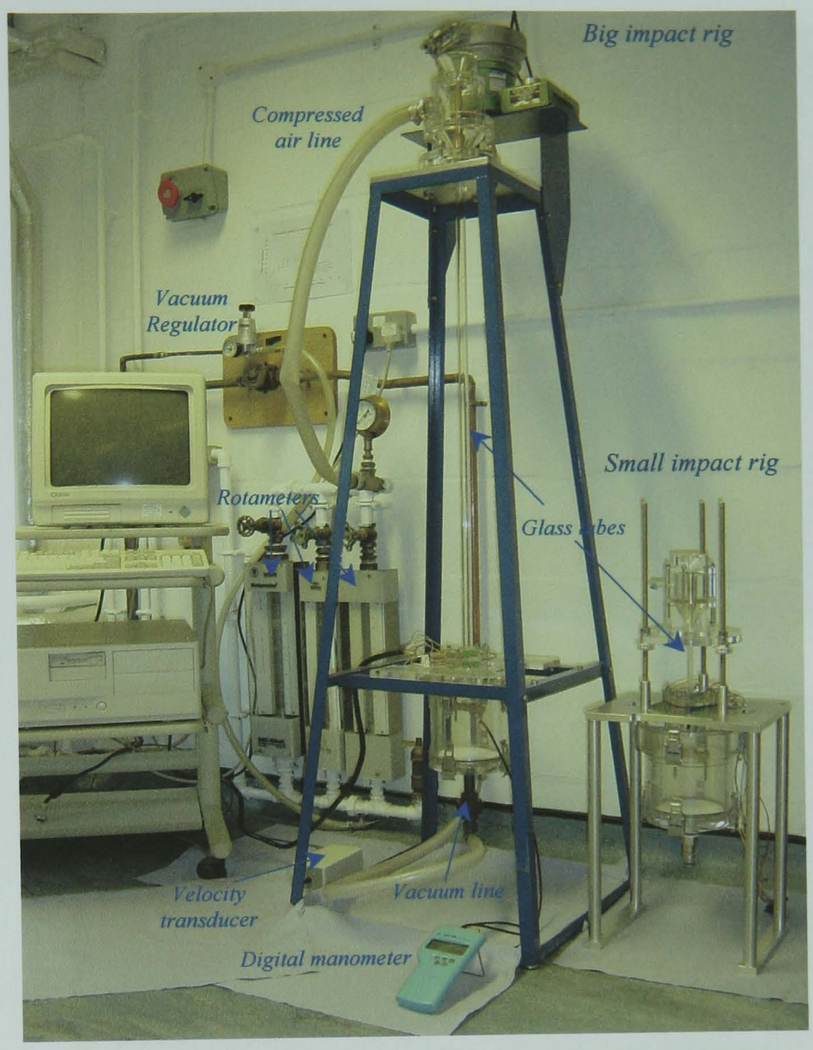
Big impact rig
Compressed air line
Vacuum Regulator
Small impact rig
Rotameters
Glass tubes
Velocity transducer
Vacuum line
Digital manometer

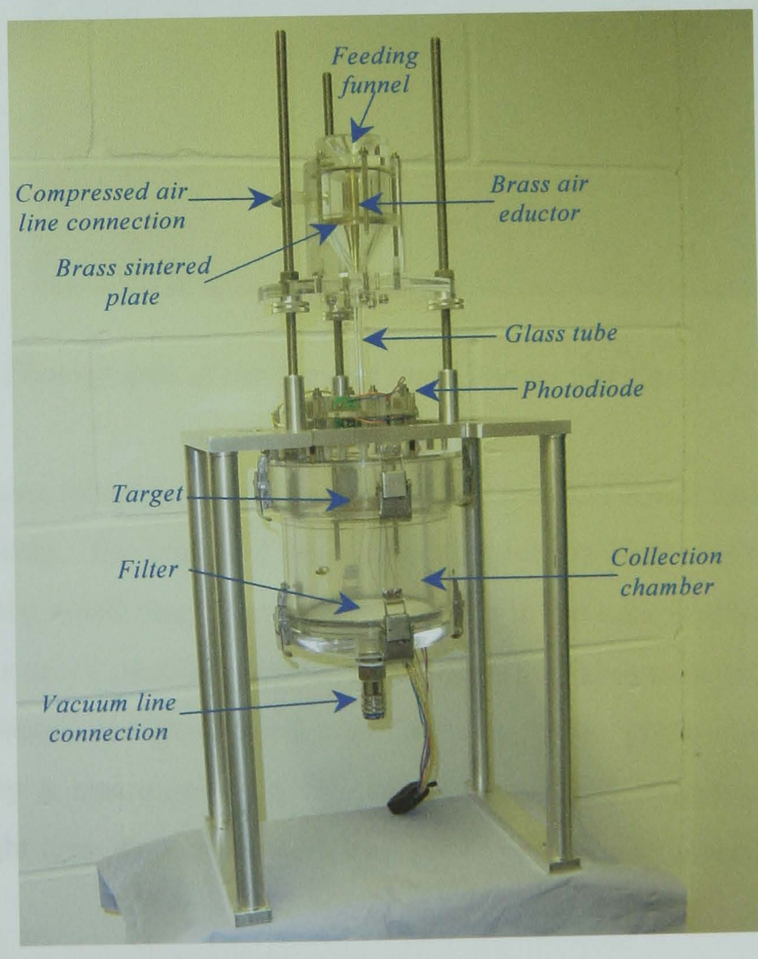
Feeding funnel
Compressed air line connection
Brass air eductor
Brass sintered plate
Glass tube
Photodiode
Target
Filter
Collection chamber
Vacuum line connection

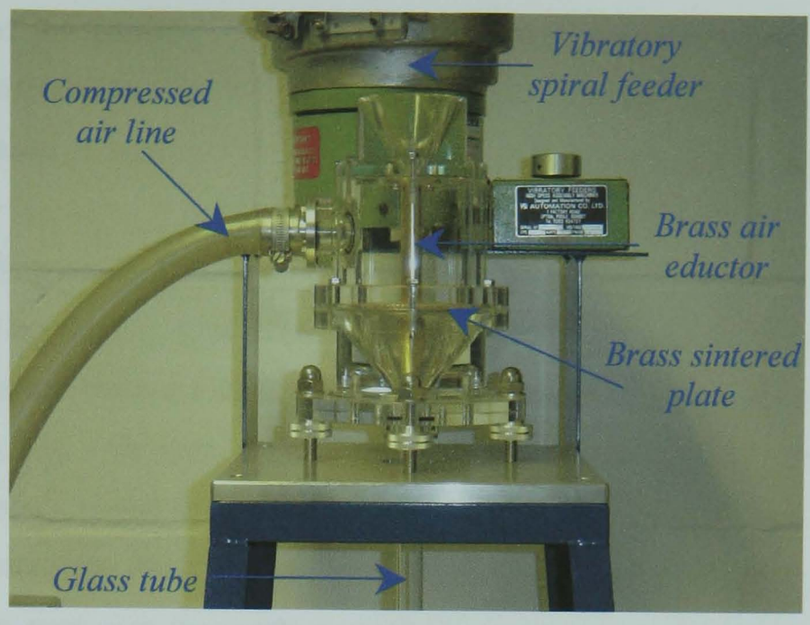

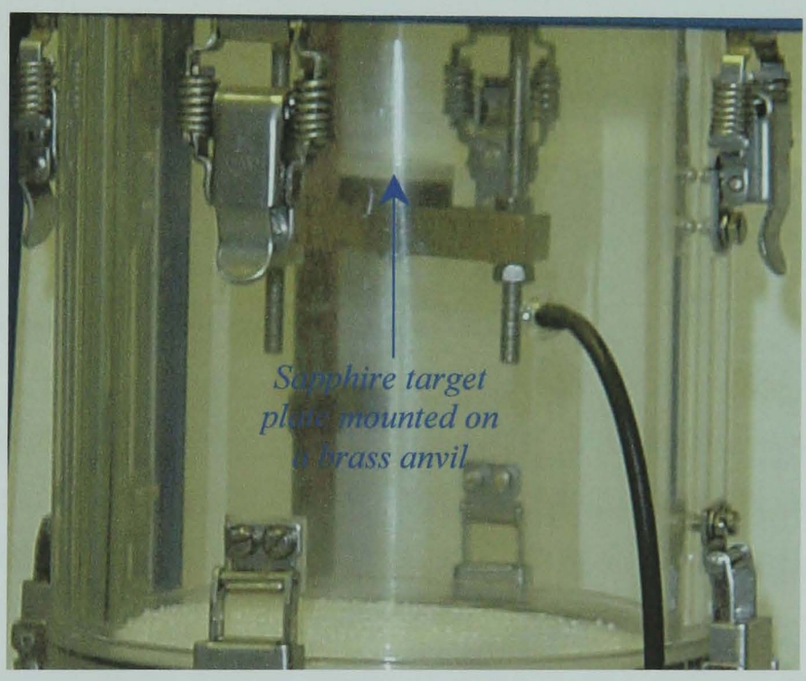

Figure 5.2: *Photographs of the big and small impact test rigs and accessories.*

The accelerating tubes' internal diameters are 20 mm and 5 mm for the big and small rigs, respectively. The length of the accelerating tube is 1000 mm for the big rig and 150 mm for the small one. The particle passage in the tube is sensed before impact by means of a set of parallel photo-diodes located just above the target. The vertical distance between the photo-diodes is 20 mm. The photo-diodes' signals are transmitted by a transducer to a PC, where a software programme measures the particle's flight time elapsed between two photo diodes, and consequently calculates

the velocity of the particle. The calculated velocities as well as the number of particles are displayed online by a monitor and are recorded. The recorded impact velocities can then be analysed to obtain the average velocity and standard deviation.

A round sapphire plate, 25 mm in diameter and 6 mm thick, is used as the target material in the normal impacts. However, in order to investigate the effect of impact angle, wedge shape stainless steel targets with different angles are substituted. The target is housed in a Perspex collection chamber approximately 30 mm under the accelerating tube's outlet and the chamber is connected to a vacuum line. The vacuum withdraws the incoming airflow through a cellulose filter paper (Whatman, Grade 2, 8 μm pore size for small rig and Grade 4, 25 μm for big rig), which is supported by a porous sintered brass plate. The level of the vacuum in the collection chamber is monitored by means of a Digitron Instrumentation digital micro-manometer.

5.2.1 High-speed digital video recording instrument

High-speed digital video recording is used as a facility to record the dynamic images of impact events. Its application in analysing the impact breakage of particulate solids has recently been investigated by various workers (e.g. Papadopoulos, 1998; Couroyer *et al.* 2000; Subero and Ghadiri, 2001; Samimi *et al.* 2003). Qualitative information about breakage regimes can be provided by this technique and linked to the material properties and impact conditions. Moreover, in some cases, contact time or rebound velocity can also be measured in this method.

In this study, a Kodak Ektapro high-speed digital video camera (Kodak Electronic Vision System, Hemel Hempstead) has been used to record the impact of the granules on the target. The system includes a Kodak Ektapro HS camera (Motion Analyser model 4540) with a lens Leica Mono-zoom 7, monitor, digital processor and a keypad. The displayed video images on the monitor can be selected and then be recorded by a video recorder. The digital images can also be sent to a PC-based

system, where the digitised images are processed by Optimas 6.1 image analysis software (Data Cell Ltd, Maidenhead), via an IC-PCI frame grabber board.

The Kodak image processor is equipped with a dynamic memory, in which 3,072 full frames of 256×256 pixels can be stored. The recording rate of imager can vary from 30 to 40,500 fps, for which the number of frames stored in the dynamic memory increases with the recording rate. However, enhancing the recording rate is at the expense of smaller frame area. In this study, different recording speeds have been used depending on the granule size and impact velocity. For low velocities (e.g. around free fall speed) usually 13,500 fps were found adequate to capture the impact event. However, at higher impact velocities 18,000 fps were employed to improve the recording quality.

The start and stop of recording are done manually. Between these two signals, the recorder stores the images in its on-board memory at a set-up recording rate. If the recording interval passes over the total memory capacity, the dynamic memory is filled with images and recording continues with overwriting the previous ones. For better capturing the impact events the impact rig's collection chamber is removed and video camera is zoomed on the target. The illumination of the impact event is carried out using two 50 mm halogens lamps, 500 W each, which provide a continuous light. Furthermore, the recorded frame of a spherical particle (such as glass bead with predetermined size) positioned on the target is employed as a scale in the analysing the impact event of granules with the same frame.

5.3 High-speed digital video recording of impacts

The impact events of Samples 1, 2 and 3, as described in chapter 3, were recorded using high-speed digital video recording system and the results are presented below.

Sample 1 Figure 5.3 illustrates the impact images for two granule sizes and two impact velocities. Observations of a large number of images reveals that these granules have a weak structure and disintegrate easily even at minimum impact velocity applied in this work (about 4 m s^{-1}).

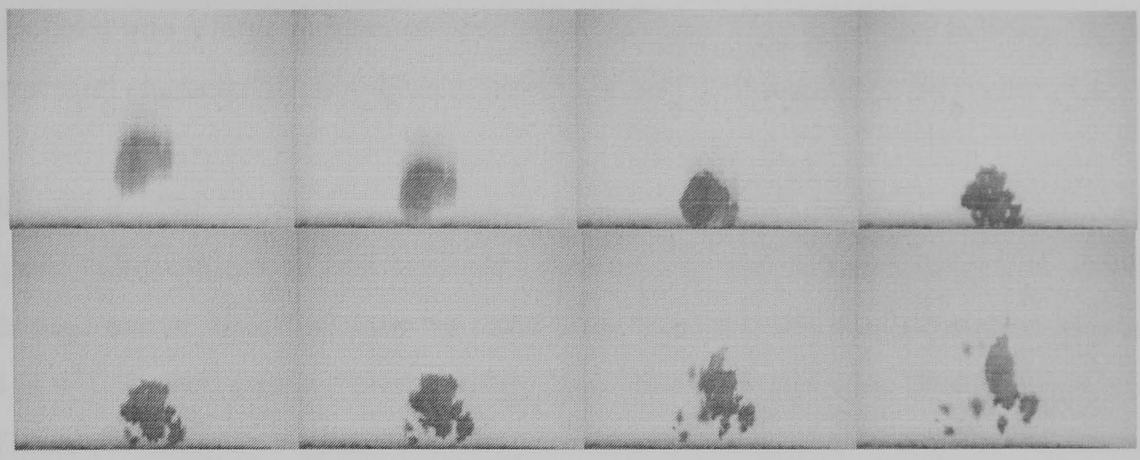

1.70-2.00 mm granules, 4 m s^{-1}

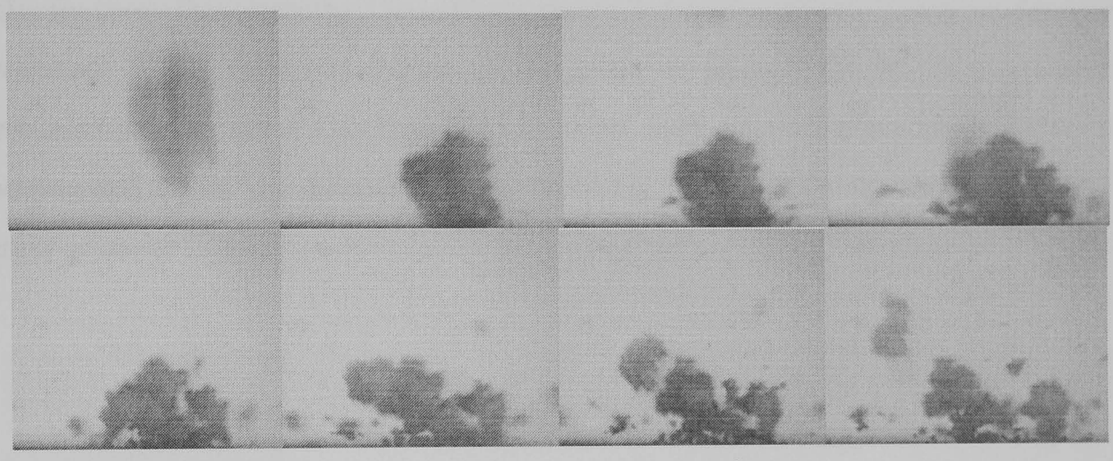

2.00-2.36 mm granules, 4 m s^{-1}

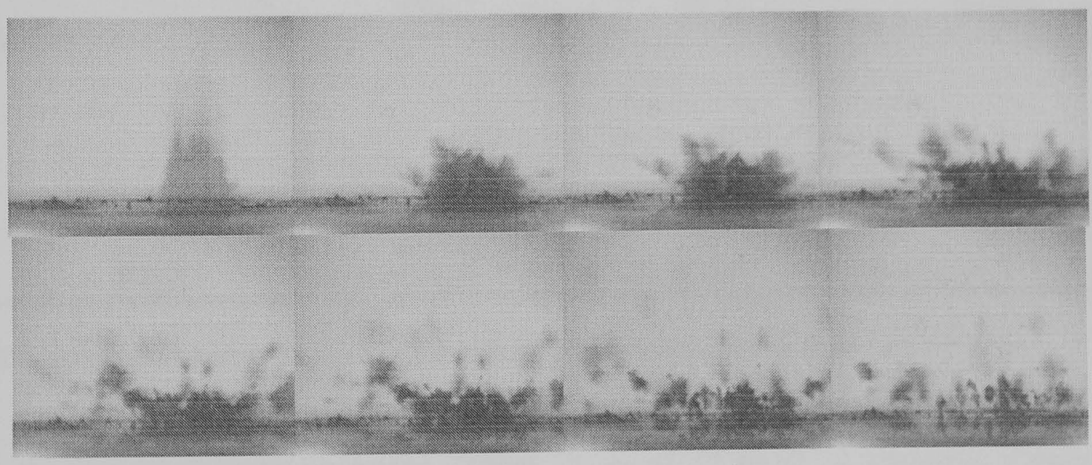

2.00-2.36 mm granules, 15 m s^{-1}

Figure 5.3: *High-speed video records of the impact event of Sample 1 granules.*

The sequence of the frames is from left to right and top to bottom. At both the free fall (4 m s^{-1}) and 15 m s^{-1} a complete disintegration of granule into small clusters with different sizes occurs. However, at the higher impact velocity the granule is

shattered into a large number of very small clusters. This behaviour is related to the structural characteristics of these granules and will be discussed in the section 5.4.

Sample 2 The lowest size, for which a clear image can be obtained by the high-speed video camera, is 1.00-1.18 mm. For this size and smaller granules, no visible damage can be identified from the video observations at the free fall impacts (around 4 m s^{-1}). In fact, onset of clear damage observation is found to be above 15 m.s^{-1}. In Figure 5.4 chipping regime of breakage is seen for the granule size of 1.70-2.00 mm at 16 m s^{-1} impact velocity. Observations of a large number of impact events at this velocity show that chipping consistently occurs but with different extent of the debris produced. The different extent of chipping is thought to be due to surface protuberances at the contact point. In most impacts, the granules usually start rotating and move to a direction during rebound, whilst debris are left behind on the target or move to another direction.

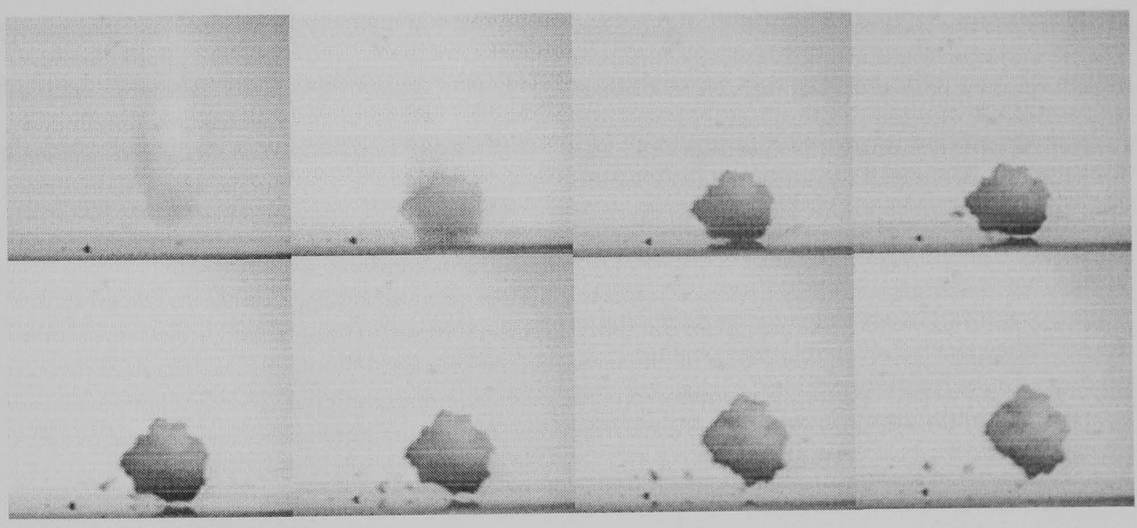

Figure 5.4: *Chipping of 1.70-2.00 mm granule size of the Sample 2 at 16 m s^{-1}.*

As the impact velocity increases further, at about 20 m s^{-1}, a transition occurs, in which one or two small fragments are separated together with the chips as shown in Figure 5.5. In this case, the amount of chips increases significantly. However, the fragmentation process does not occur consistently over all the observed impact events. The consistency of the fragmentation and the number of fragment produced increases with increasing the impact velocity.

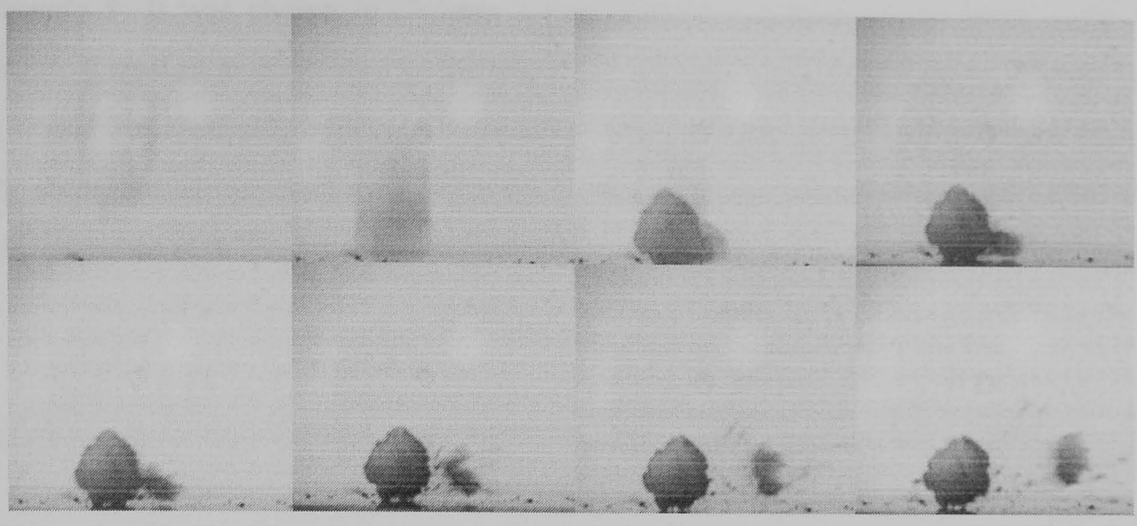

Figure 5.5: *High-speed video record of an impact event depicting the transition from chipping to fragmentation for a 1.70-2.00 mm granule of Sample 2 at 20 m* s^{-1} *impact velocity.*

At higher impact velocities, the granule disintegrates into a large number of small clusters. However, even under this condition, the chipping continues by the separation of debris from the impact area and also from the broken surfaces of the clusters. Figure 5.6 shows extensive fragmentation of the granule at 33 m s^{-1} impact velocity, which is consistently observed. The damage at this impact velocity leads to a product with a wide size distribution.

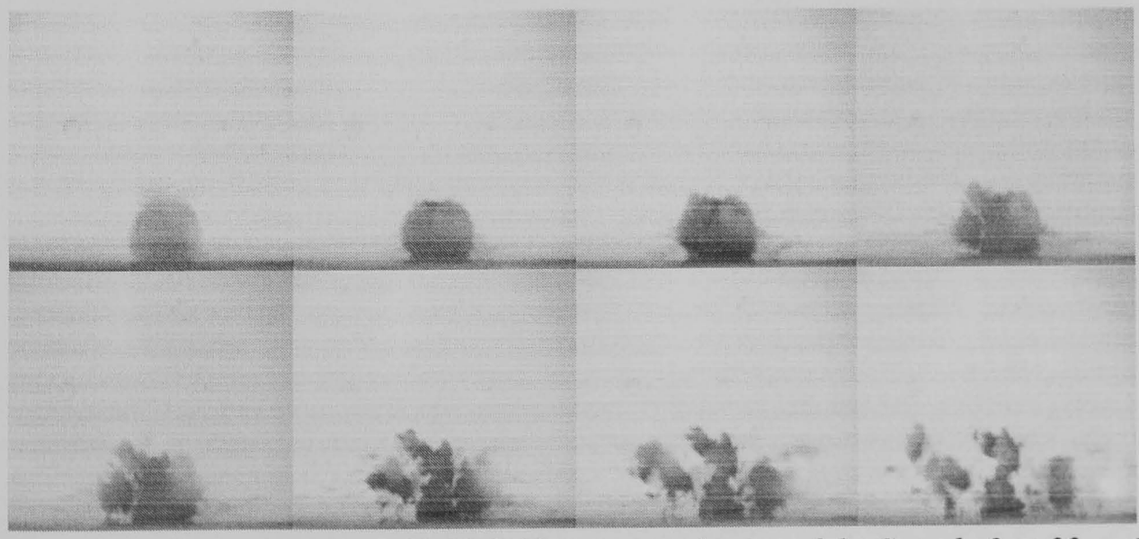

Figure 5.6: *Fragmentation of 1.70-2.00 mm granule size of the Sample 2 at 33 m* s^{-1} *impact velocity.*

Sample 3 It was shown in Chapter 3 that Sample 3 granules have been made of denser granules, as compared to Sample 2 but with the same formulation. Therefore, it would be intuitively expected to observe some differences in their breakage under the same operating condition. Figure 5.7 illustrates five impact events of 1.70-2.00 mm granules at different impact velocities.

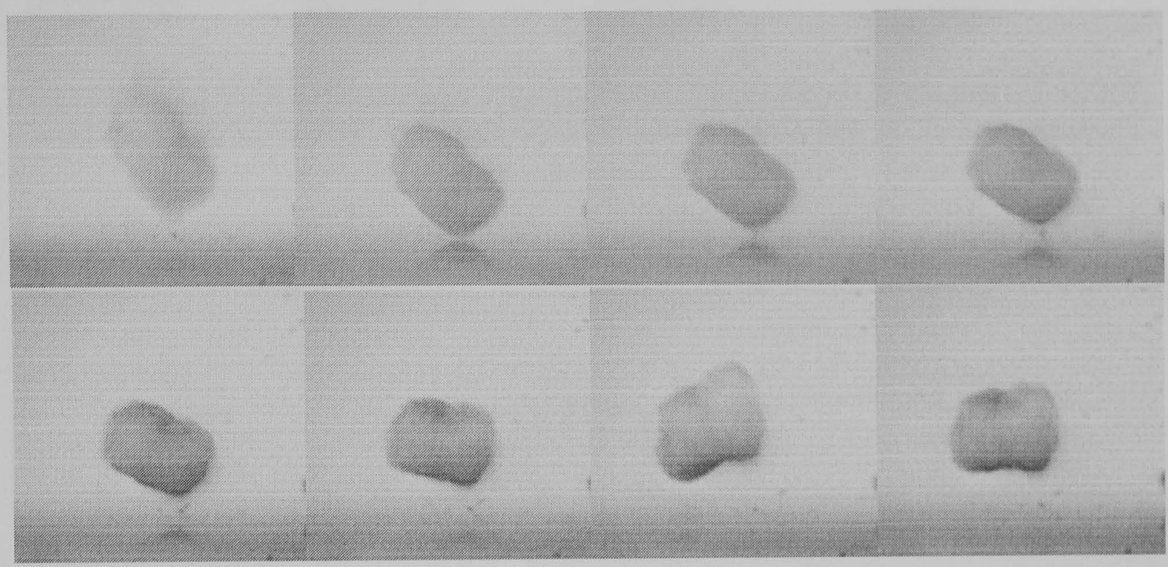

a) 1.70-2.00 mm granule size, 4 m s^{-1}.

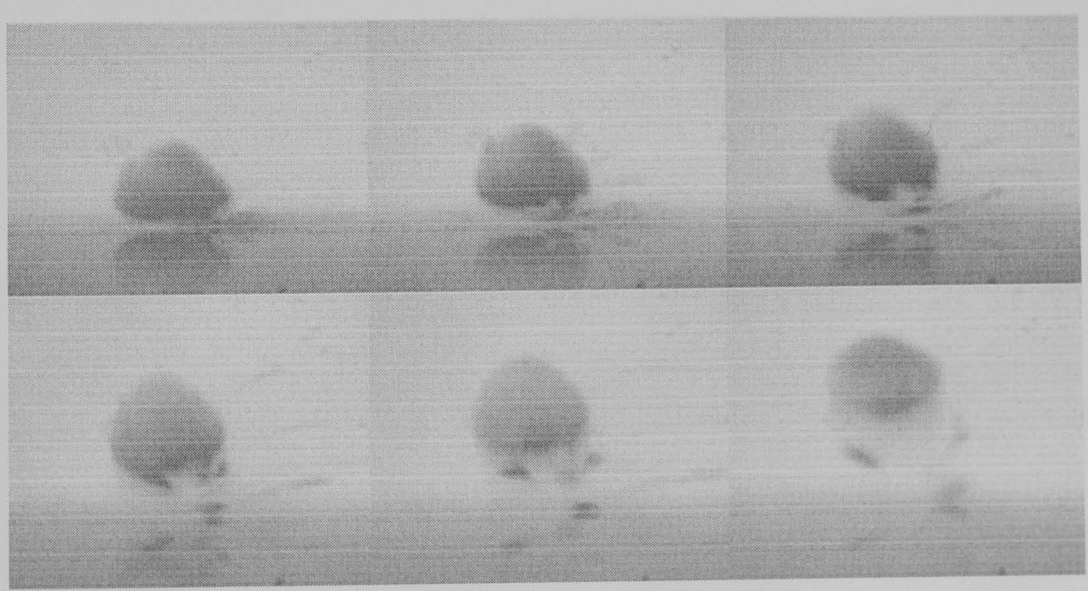

b) 1.70-2.00 mm granule size, 18 m s^{-1}.

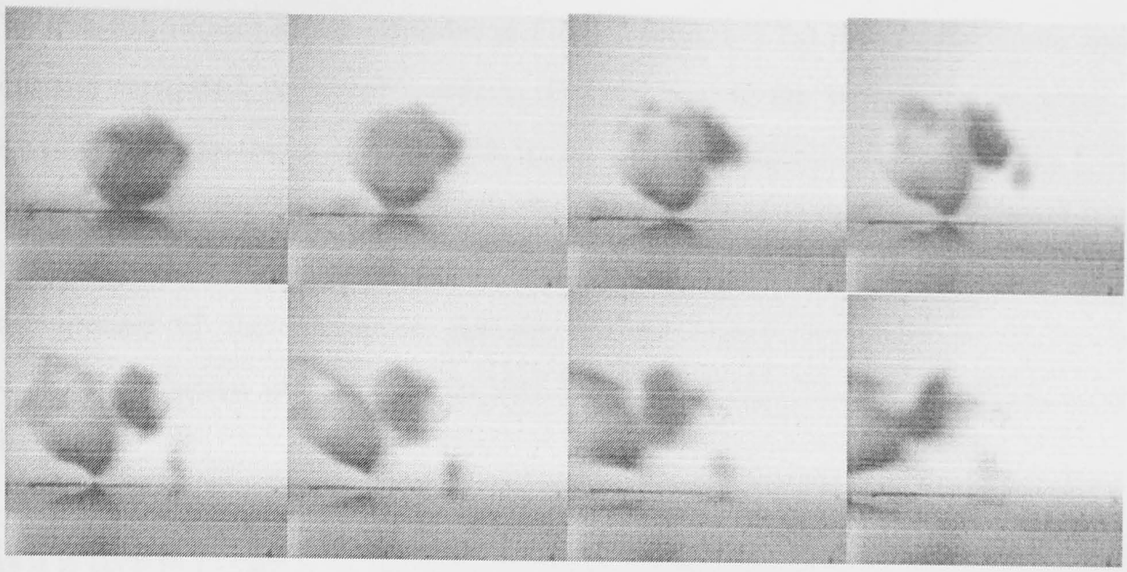

c) 1.70-2.00 mm granules 22 m s^{-1}.

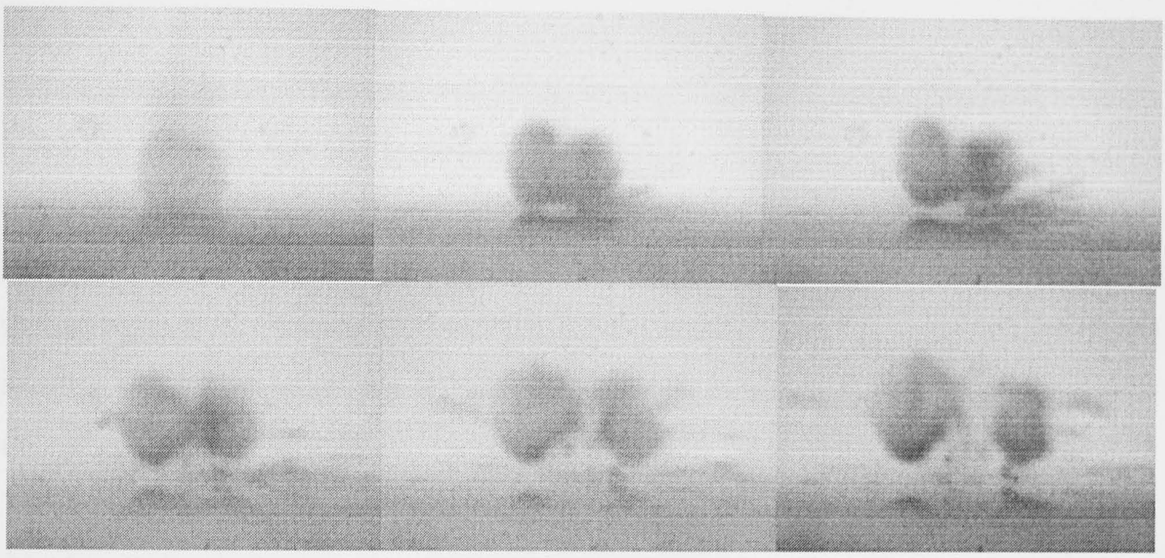

d) 1.70-2.00 mm granules, 26 m s^{-1}.

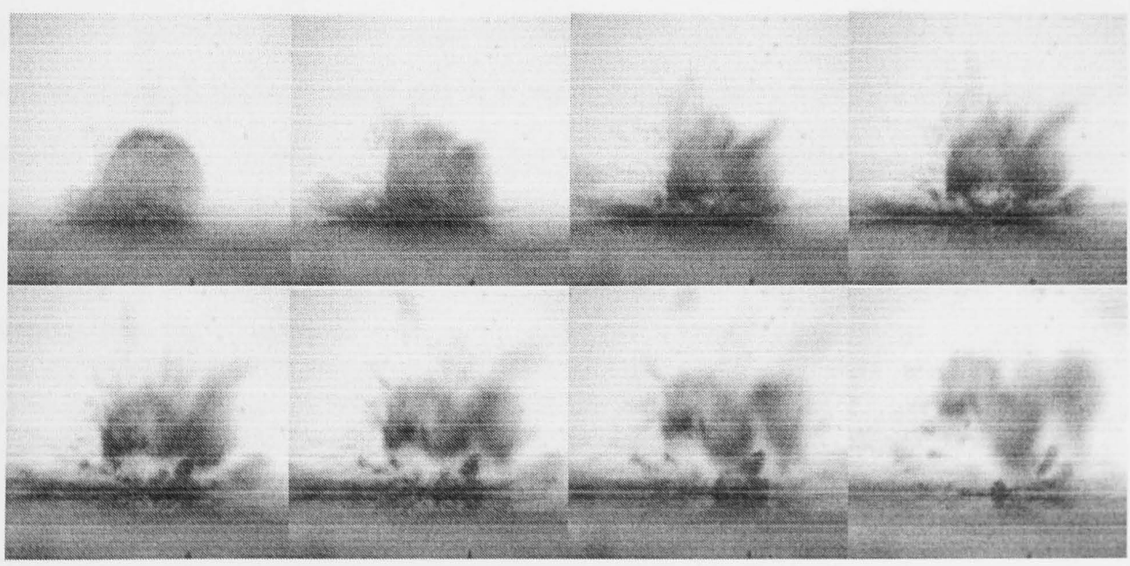

e) 1.70-2.00 mm granules, 34 m s^{-1}.

***Figure 5.7**: High-speed video records of Sample 3 impact events.*

The free fall impact of the granules at 4 m s^{-1} (Figure 5.7a) reveals that some small debris is separated, presumably due to adhered fines to the surfaces. The extent of chipping becomes more consistent at about 18 m s^{-1} impact velocity (Figure 5.7b). In this case, as the granule rebounds the damage leads to breakage of more chips from the impact site. However, a closer following of the sequences indicates a combination of fast departure the fine debris during loading and larger chip detachment during unloading. At this impact velocity, no fragmentation is still observed.

As it is seen in Figure 5.7c, the onset of fragmentation seems to be around 21-22 m s^{-1}. Increasing the impact velocity to about 26 m s^{-1} (Figure 5.7d) leads to the extensive formation of debris and consistent fragmentation of the granules into two large pieces. At higher impact velocities, where the fragmentation dominates (Figure 5.7e), the granules fracture to three or four clusters. In this case, the fragments break along with the scattering of a large amount of debris of different sizes. The debris is from the impact site as well as from the fractured surfaces during loading and unloading cycles. It seems that the fast detachment of the small debris occurs during loading but larger chips are detached from impact zone or neighbourhood during unloading.

At this stage, however, a qualitative comparison of the impact observations of Samples 2 and 3 reveals two clear differences. First, it seems that the chipping of Sample 3 granules produces more extensive fine debris, as compared to Sample 2. Second, at high impact velocities, Sample 2 granules fragment into a large number of smaller clusters, whereas Sample 3 granules are broken into a smaller number of larger fragments. In this respect, the sieve analysis of the samples after impact can quantitatively show a clear trend about the size distribution of the granules, and it is presented in the Chapter 6.

5.4 Microscopic observation of impact damage

The impact products were observed by scanning electron microscopy (SEM) and/or reflected light microscopy (RLM). In most cases, the identification of the impact site on the granules was impossible due to the rough and porous structure of the granules. Furthermore, jugged damaged surfaces with numerous cavities caused difficulties in characterising the crack patterns with reference to the standard crack morphologies. However, in some cases, where crack propagation did not lead to complete disintegration, the pattern of the damage has been identified.

Sample 1 SEM views of Sample 1 granules after impact are shown in Figure 5.8. As it is seen, impact of 1.18-1.40 mm granules at about 18 m s^{-1} has led to extensive breakage, revealing rough fractured surfaces, with a large number of internal flaws. In Figure 5.8, the fractured surfaces are indicated by white ovals and arrows pointing at the internal flaws.

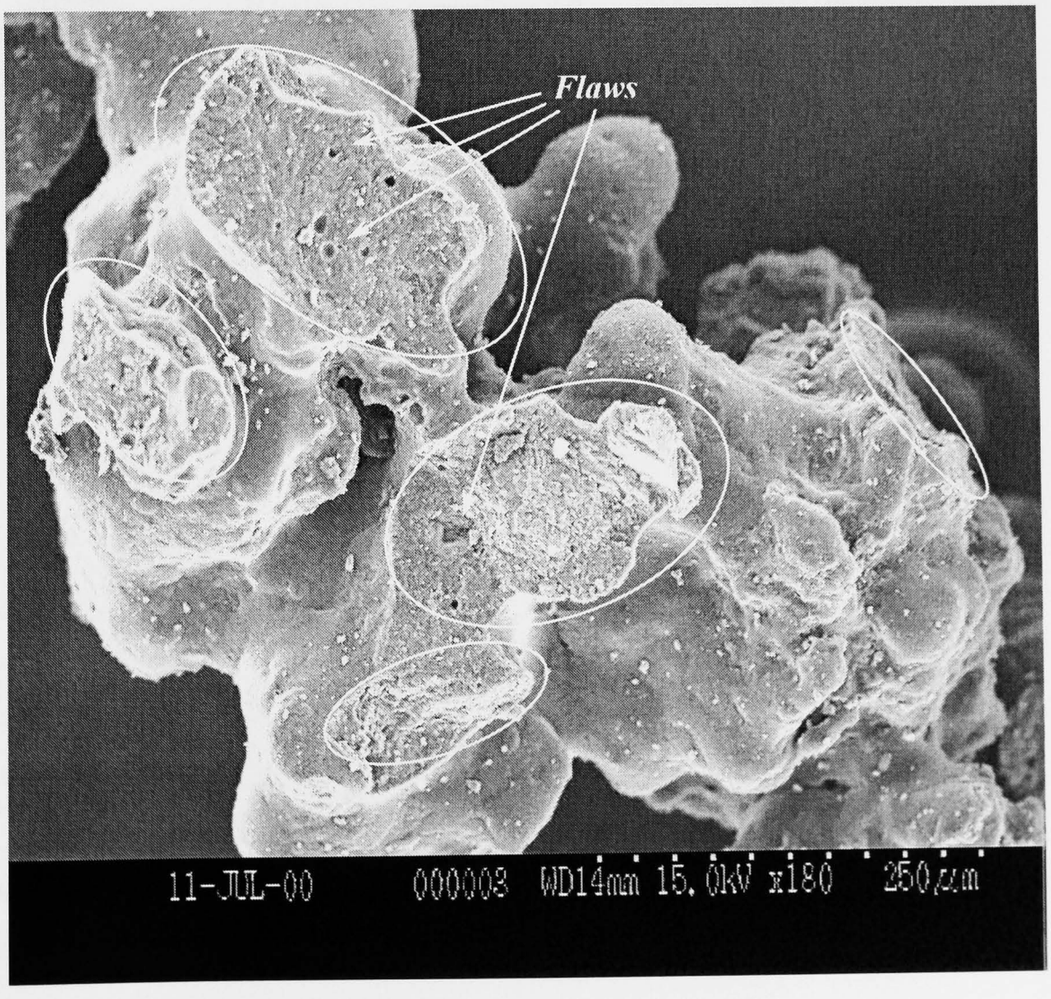

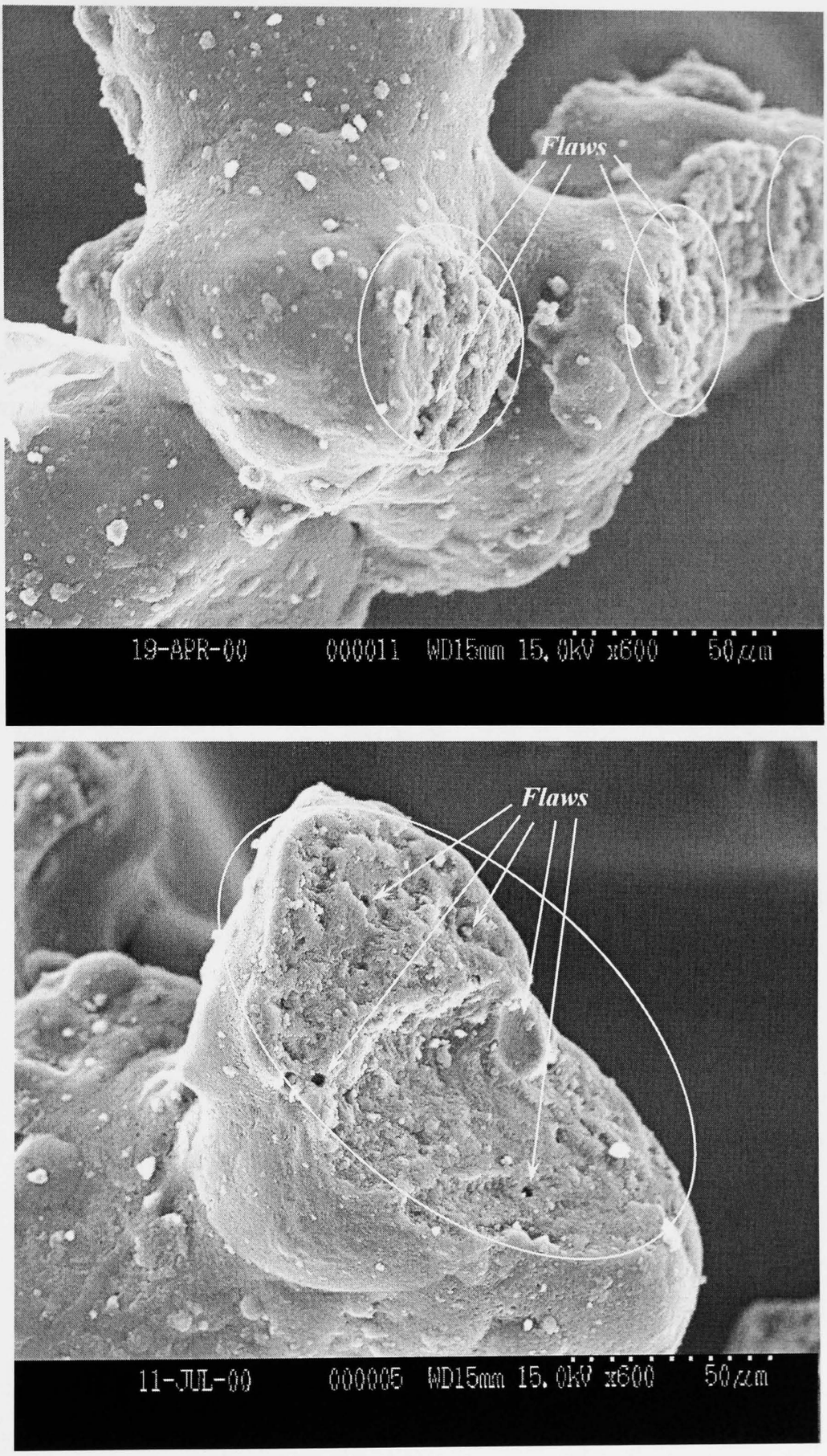

Figure 5.8: *SEM views of fractured surfaces of 1.18-1.40 mm granules of Sample 1, impacted at 18 m* s^{-1}.

As previously mentioned in Chapter 3, Sample 1 granules have been made by fluidised bed granulation process, using molten PEG binder and large primary particles (100 μm) of calcium carbonate. The produced granules have an irregular shape and highly porous structure with a low co-ordination number of the primary particles (Figure 5.9a). The microscopic observations of the granules show that the PEG binder has covered almost the major part of the outer surfaces of primary particles so that relatively thick solid bridges have been formed (Figure 5.9b). The presence of the pre-existing internal flaws in the PEG solid bridge as well as extensive macro-voids in the granules increase the probability of a brittle mode of breakage.

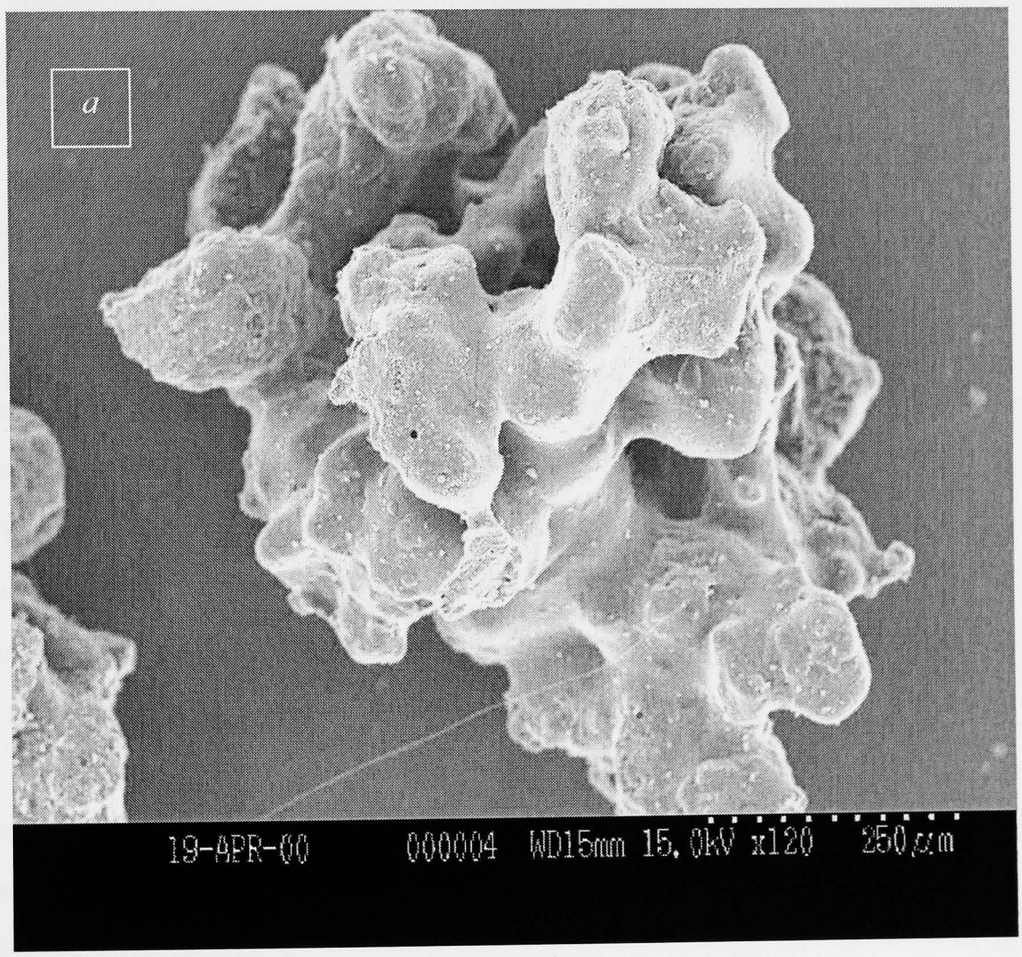

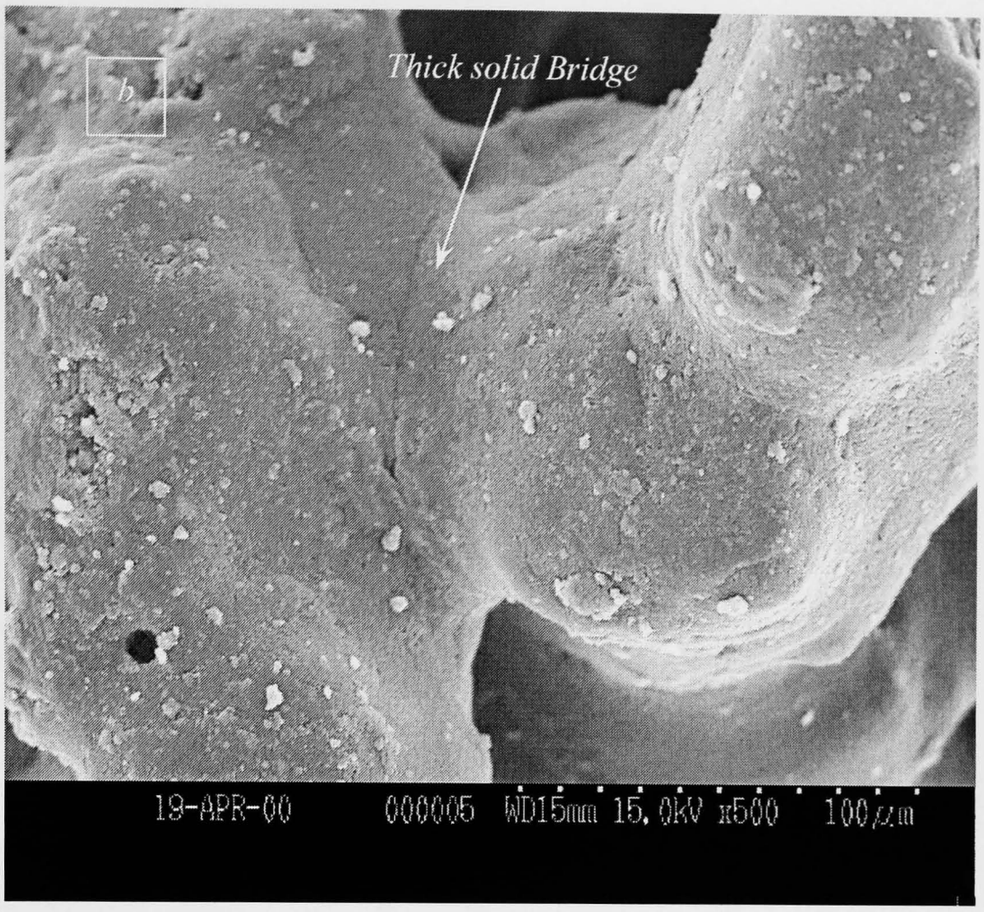

Figure 5.9: *SEM views of Sample 1 granule, showing the irregular shape, thick solid bridges and a highly porous structure.*

Sample 2 The detergent-based granules of Sample 2 have also been produced by fluidised bed granulation but with different formulation than the Sample 1. As it is seen in the Figures 5.10 and 5.11, the original granule has been made of a large number of smaller clusters, aggregated by a paste type binder as a cauliflower-type structure. Furthermore, the primary particles (about 1 μm size) in the clusters have embedded as filler in the same binder.

Figure 5.10 shows SEM views of two 1.70-2.00 mm granules after single impact at about 20 m s^{-1}. A close examination of the granules (Figures 5.10a and b) indicates that the regions marked by white arrows might be the impact zones, although, the exact impact sites are difficult to pinpoint. The SEM views of the granule residues show some empty spaces, which have been left as a result of the detachment of fragments from the neighbourhood of the impact site.

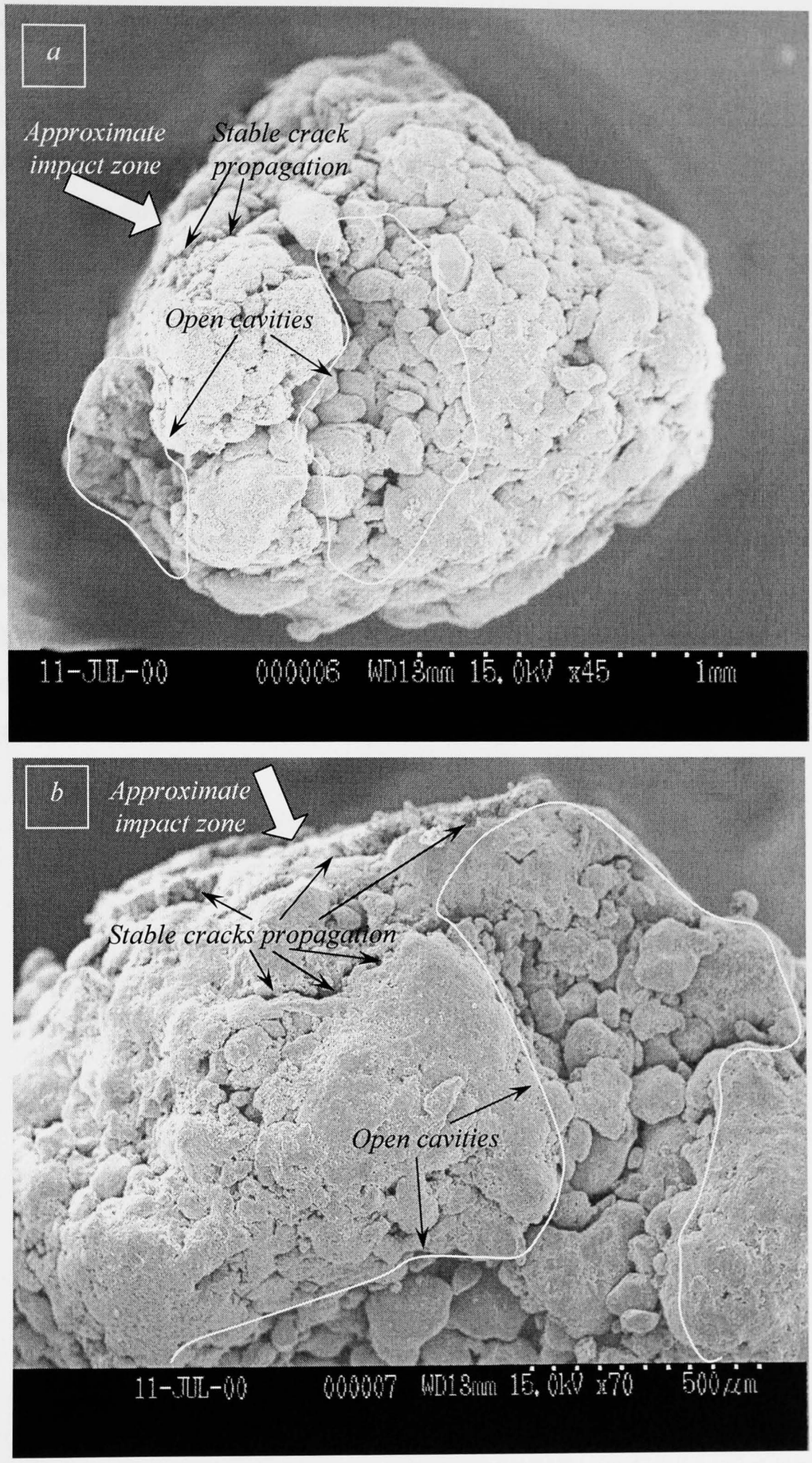

Figure 5.10: *SEM views of impact products of two 1.70-2.00 mm granules of Sample 2 at about 20 m s^{-1} velocity.*

Furthermore, some stable and irregular cracks are seen, which have propagated around the impact zones as shown in Figure 5.10a. A close inspection of the cracks shows that the binder ligaments keep the smaller fragments in the original granule. As the granule impacts on the target, the developed stresses lead to the propagation of stable cracks through elongation and rupture of the binder's ligaments as shown in Figure 5.11. This is the case especially for granules, which have been kept in humidified conditions. The effect of humidity on the extent of the breakage will be discussed in Chapter 6.

In summary, the observations of the impact events and SEM inspection of images of granules of Sample 2 indicate that these granules chipping occur as a result of the breakage of small clusters rather than primary particles. In contrast, fragmentation proceeds through opening up of ductile and stable large cracks, which lead to the detachment of larger fragments. Therefore, as the result of the cauliflower structure it would be expected that the chipping of Sample 2 granules be accompanied by the separation of the larger debris.

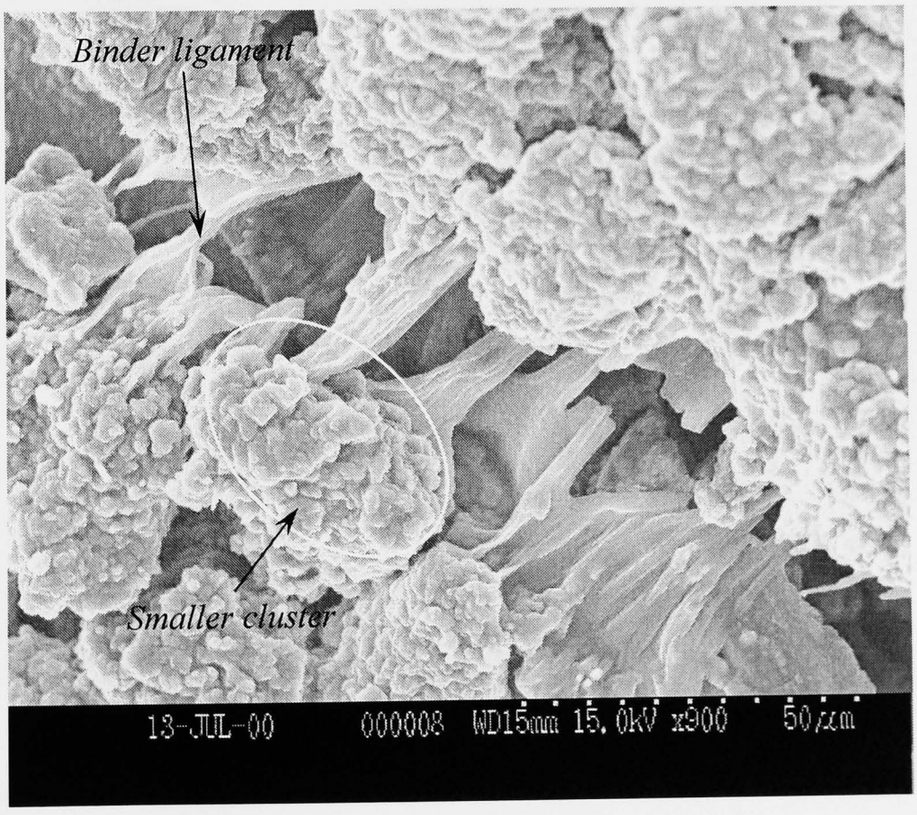

Figure 5.11: *Elongation and rupture of binder in the crack area of granules of Sample 2.*

Sample 3 The granules of Sample 3 have been made by high shear mixing granulation but with the same formulation as Sample 2. Denser structure, a more spherical shape and smoother surfaces are the structural features of Sample 3. However, for Sample 3 also there are some in-homogeneity inside the granule such as big cavities and segregation of the binder as it is shown in the Figure 5.12.

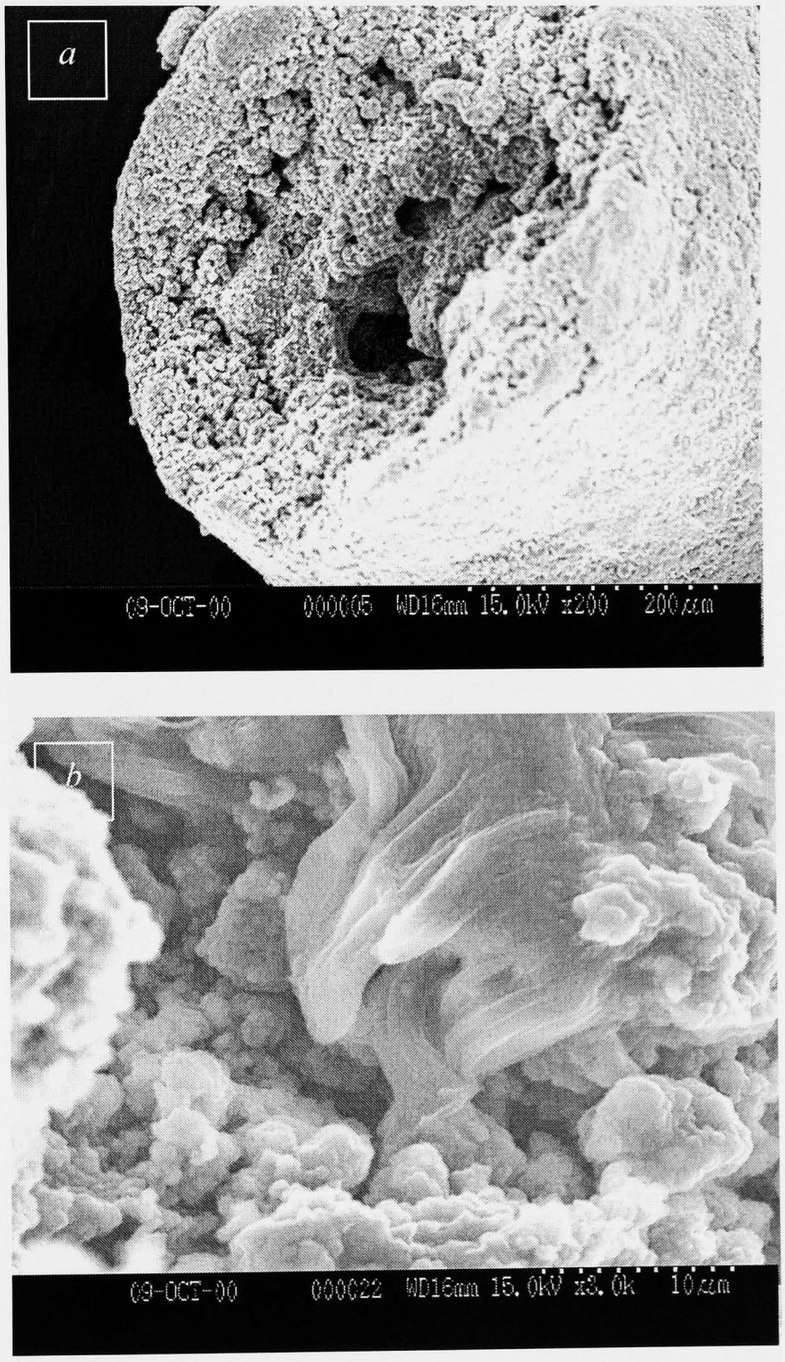

Figure 5.12: *SEM views of Sample 3 granules (a) big cavities inside the granules; (b) lump of binder.*

Observations of Sample 3 granules reveal a similar crack propagation mechanism to that of Sample 2, i.e. elongation and rupture of the binder. For Sample 3 granules, however, cracks propagate through rupture of tiny bonds, instead of the thicker inter-cluster ligaments as observed in Sample 2. Figure 5.13 illustrates two images, one of a crack route on the surface of a granule (*a*) and another a magnified crack, illustrating the ruptured binders (*b*).

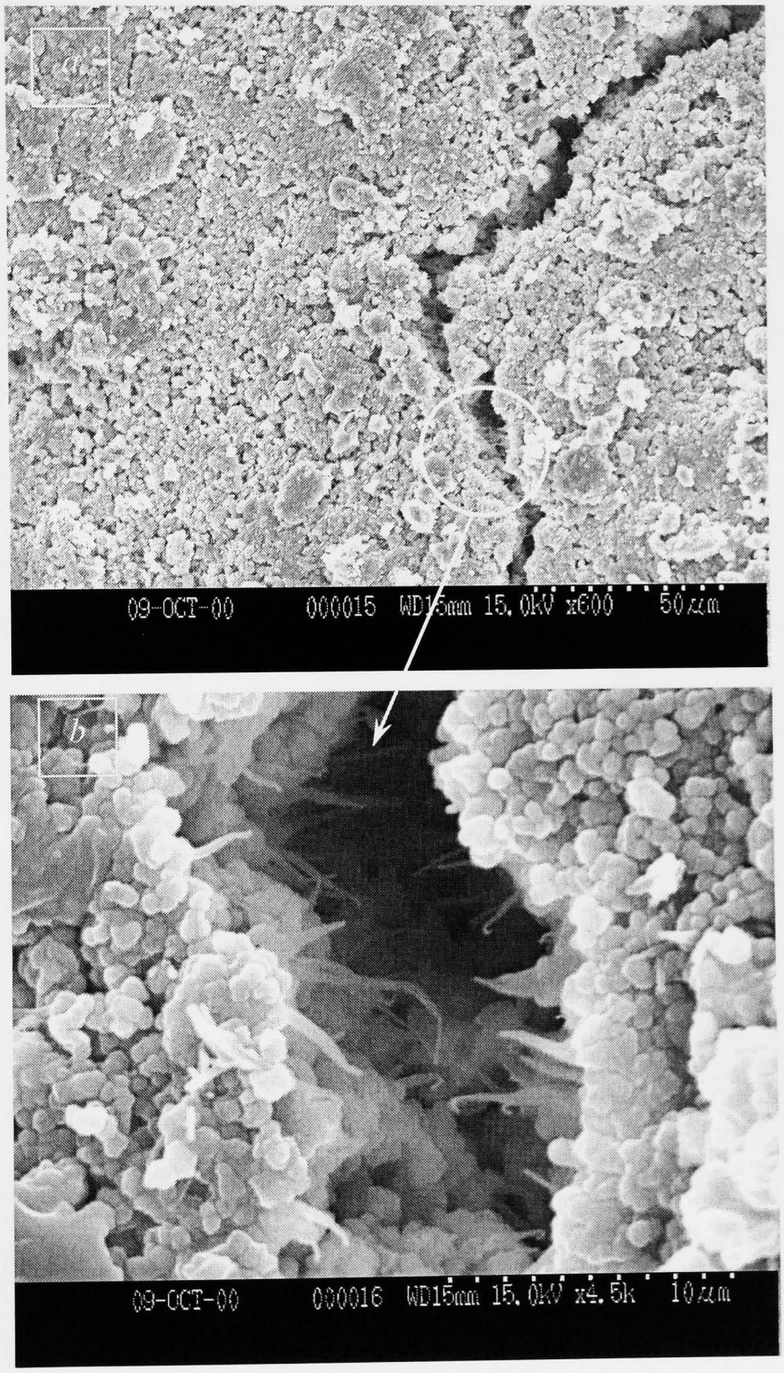

Figure 5.13: *SEM views of a crack propagated on the surface of a granule of Sample 3, (a) crack route, (b) magnified view of the crack zone.*

The stability of an elongated binder bridge within a crack and an image of a crack tip are shown in the Figure 5.14. The figure indicates embedding of very fine primary particles (about 1 μm) in the visco-elastic binder. As it is seen in Figure 5.14a, some primary particles have moved during the binder elongation. However, Figures 5.14a and b reveal that the binder neck and crack tip are free from the particles.

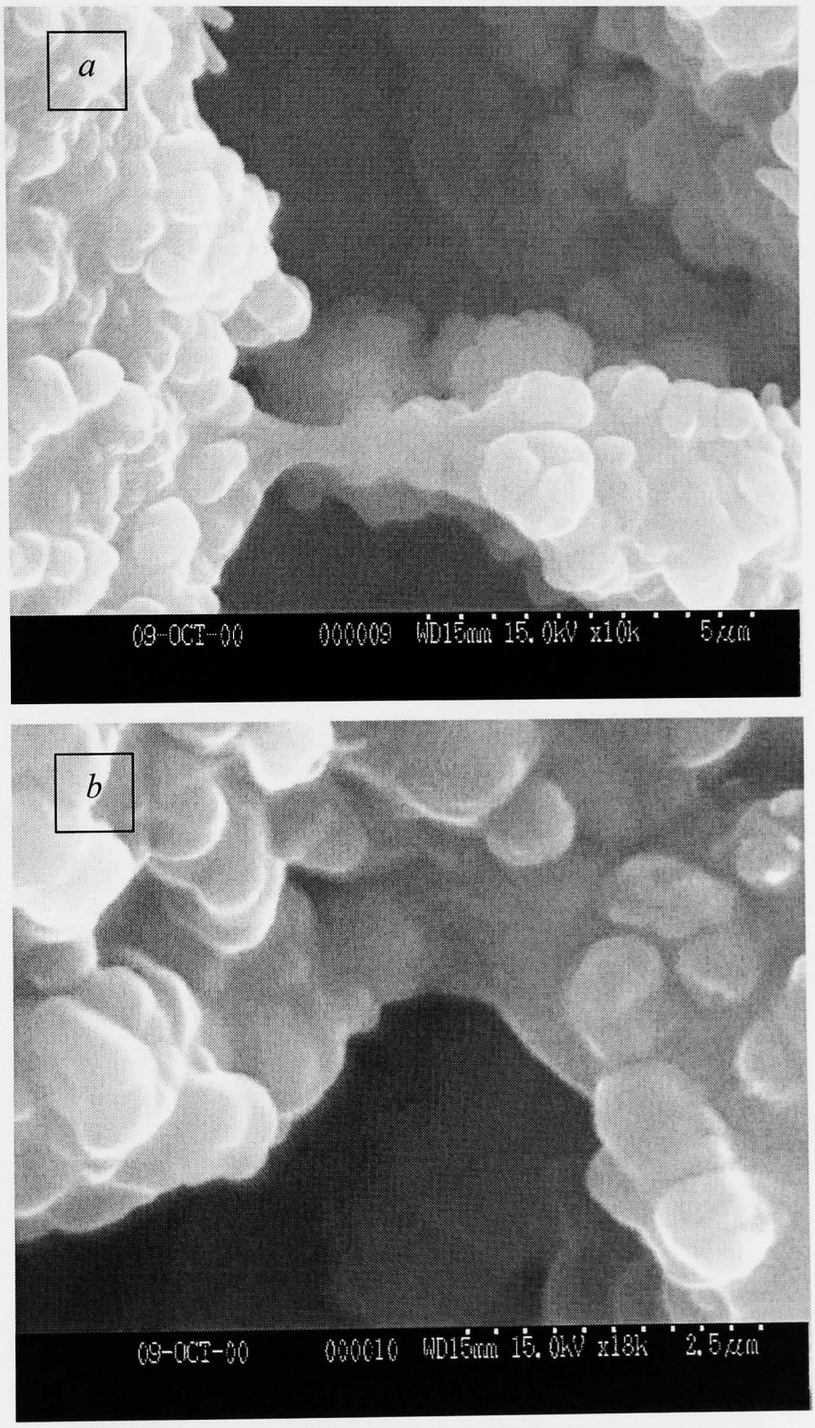

Figure 5.14: *SEM views of a crack of a granule of Sample 3, (a) stable bridge of binder in the crack (b) the crack tip.*

All SEM images presented so far have been taken from granules kept at ambient temperature and ambient humidity. A number of tests were carried out in which the granule temperature and ambient humidity were changed. In Figure 5.15 the breakage patterns of two granules of Sample 3 are shown. Figure 5.15a refers to the impact of granules, which was kept at -20 °C before impact at 17 m s^{-1}. Figure 5.15b refers to another impact for which the granule was kept in an airtight container under humidified atmosphere for couple of days before impact at 24 m s^{-1}. The humidified atmosphere was made in the container using a saturated sodium carbonate solution at the ambient temperature.

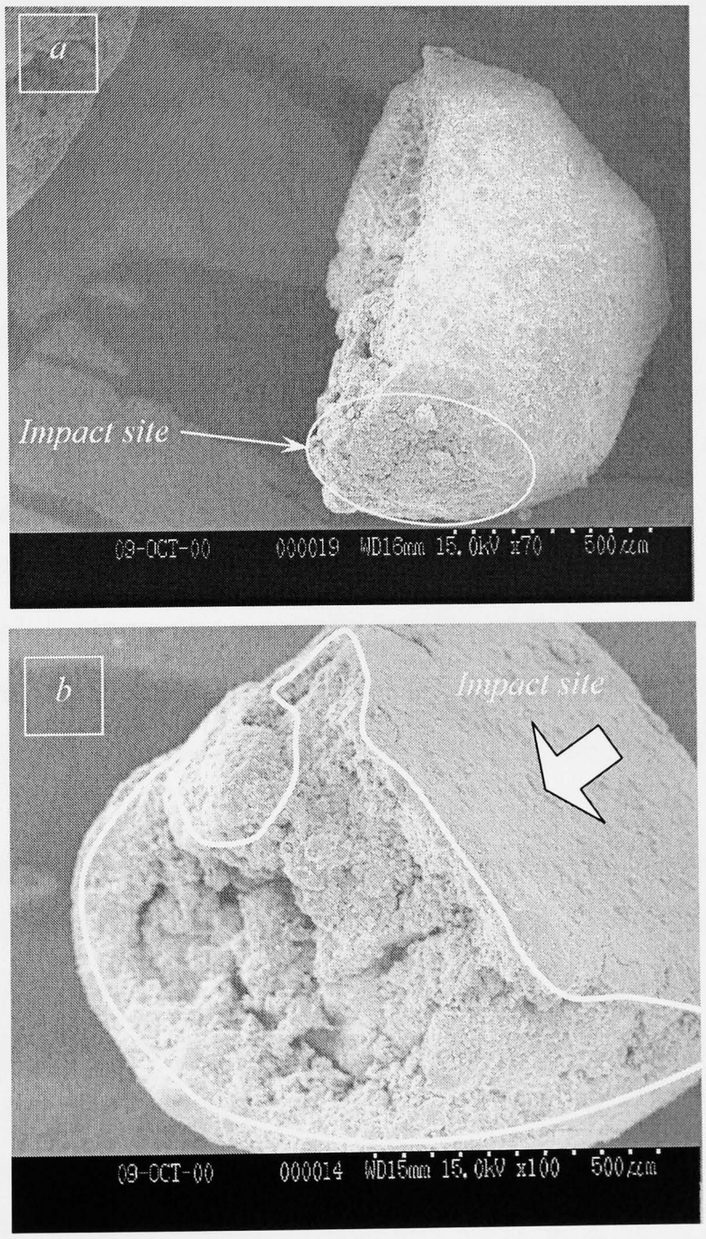

Figure 5.15: *Fragmentation of 1.00-1.18 mm granules of Sample 3 (a) a granule kept at –20 °C impacted at 17 m s^{-1}; (b) a humidified granule impacted at 24 m s^{-1}.*

The granule kept at -20 °C temperature (Figure 5.15a) has split diametrically along with local damage on the impact site. In contrast, the humidified granule has undergoes extensive deformation on the impact site and fragmentation (Figure 5.15b). These images show how the environmental changes can affect the breakage pattern of the same granules.

5.5 Discussion

Employing high-speed digital video recording enabled a large sequence of images to be stored in the buffer from which the best ones were downloaded into the computer for further processing via the digital image transfer interface. This together with SEM observation facilitated qualitative characterisation of the breakage patterns.

The breakage of agglomerates is more complicated than of solid particles. Agglomerates are made of distinct particles, which may be bonded together by distinct binders. Furthermore, the binding agent may remain entirely in liquid form or may solidify completely to a solid inter-particle bridge. The inter-connections between the primary particles play an important role in the breakage of the agglomerate, as the impact stress is distributed through a network of the inter-particle contacts. These contacts may be the weakest points in the agglomerate. However, in an assembly including the primary particles, binder and porosity, some contacts may not be loaded, depending on the distributed loading path routes in the agglomerate.

The numerical and experimental results of agglomerate impact suggest that the main parameters affecting the breakage behaviour of the agglomerates are bond strength, impact velocity, porosity or solid fraction, and co-ordination number of the agglomerate along with contact geometry between agglomerate and target. In this context, Mishra and Thornton (2001) investigated the effect of the above factors on the impact breakage patterns of spherical agglomerates with polydisperse primary particles using numerical DEM simulations. Their results show that a distinct fracture pattern occurs for dense agglomerates above a critical impact velocity, where two or more large fragments are produced with a clear fracture plane together

with some fines separated locally from the impact site. In contrast, for loose agglomerates with low solid fraction, the disintegration into a large number of small clusters occurs under identical testing conditions. Subero and Ghadiri (2001) investigated the effects of the structural parameters and impact velocity on the breakage pattern of model agglomerates made of glass beads glued together by a hard and brittle polymeric binder. These agglomerates were made in such a way that they contained macro-voids. They observed a shift from localised failure on the impact side towards the distributed fragmentation pattern by increasing the impact velocity or the size/number of the macro-voids. Furthermore, their experimental results reveal that fragmentation dominates mainly at the high impact velocity and only for agglomerates containing large number of macro-voids.

The high-speed video records of the impact events of Sample 1 indicate the complete disintegration (Figure 5.3) of the granules, even under the free fall impact. However, with increasing the impact velocity, the granule is shattered into larger number of smaller clusters. The occurrence of the disintegration suggests a combined effect of low bond strength, high porosity and low co-ordination number on the breakage of granules.

For Sample 1, fluidised bed granulation of large non-porous primary particles with molten PEG binder has led to the production of granules containing thick solid bridges with a large number of internal flaws and low co-ordination number. In this regard, close SEM observations of the granules after impact, Figure 5.8, show the location of the internal flaws mainly on the broken planes of the bridges. Figure 5.16 shows a photograph obtained by the reflected light microscopy of 1.18-1.40 mm granules of Sample 1, showing an irregular shape with sharp corners and highly porous structure. As shown in Figure 5.3, the granules usually impact on the target with their sharp corners and edges, generating high local stresses on the impact site. Furthermore, it is thought that the internal flaws in the solid bridges along with macro-void structure of the granule, which operate as stress concentrators, promote the unstable breakage. Therefore, the extensive breakage of Sample 1 granules might be facilitated due to a brittle breakage of pattern.

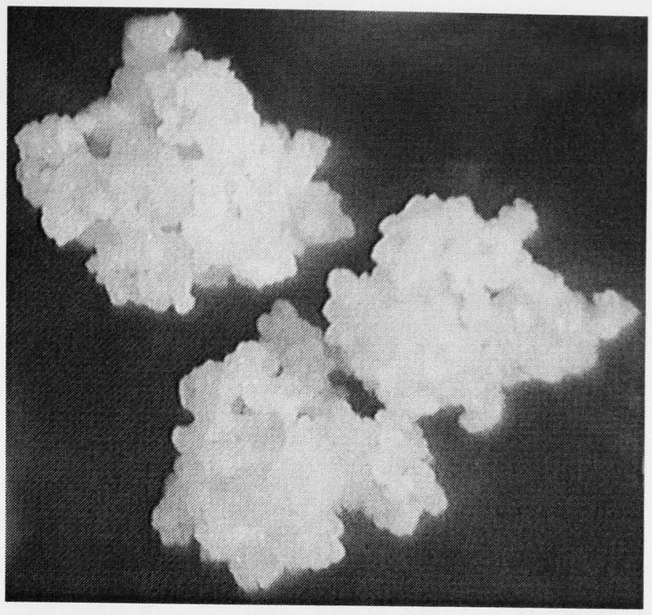

Figure 5.16: *Image obtained by reflected light microscopy of 1.18-1.40 mm granules of Sample 1, showing irregular shape and highly porous structure.*

Generally, brittle mode of failure occurs when the material fractures without noticeable plastic deformation. The presence of the pre-existing internal or surface flaws play an important role in propagation of the unstable cracks and hence the occurrence of the brittle breakage. For the agglomerates the pre-existing flaws are usually considered as the agglomerate's porosity and the bridge's micro-defeats are neglected. In this respect, Kendall (1986) developed a model in which the macroscopic strength of the granule is related to the macro-porosity and some bond characteristics rather than the micro flaws within the bridge.

For Sample 1 granules due to the complete disintegration of granule during impact and irregular and rough surfaces of the granule, there is no clear evidence showing the failure pattern of the impact site. Nevertheless, due to the polymeric nature of the PEG binder and as it has covered a major part of the primary particle surfaces, some local plastic deformation of the PEG surface layer is expected to occur on the impact sites especially on the sharp corners. Figure 5.17 shows the plastic deformation of a sharp corner, which is thought to be located on the impact site. This contradicts with earlier discussion about the brittle failure, in which no plastic deformation was supposed for these granules. However, although these local plastic deformations may not affect extensive and unstable disintegration of the granules during impact,

nevertheless the semi-brittle mechanism of breakage seems to be the main mechanism of breakage for these granules.

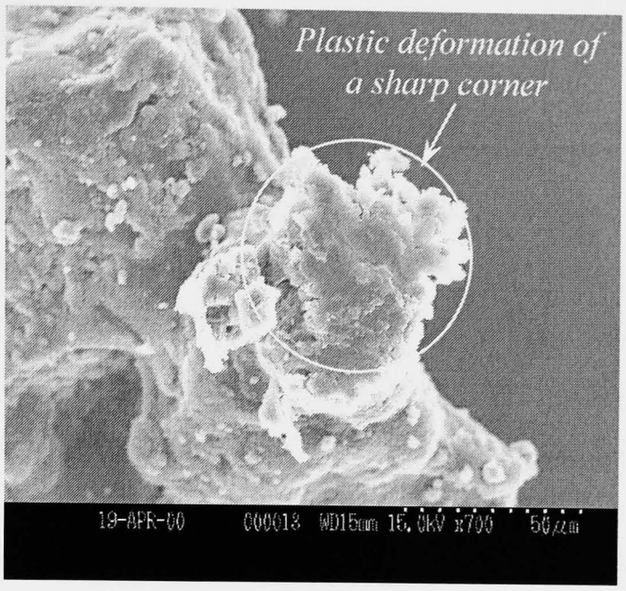

Figure 5.17: *Plastic deformation of a sharp corner of a Sample 1 granule.*

The high-speed recordings of Samples 2 impacts show clearly the occurrence of chipping, fragmentation and even complete disintegration of the granules for the size range and impact velocities tested in this work. The chipping is mainly observed as the breakage of the protuberances and small clusters mostly from the impact zone surface (Figure 5.4). Figures 5.5 and 5.10 and other observations reveal that the transition from chipping to fragmentation starts at a certain impact velocity by the breakage of one or two side fragments, from the impact site perimeter. Furthermore, the figures show that the fragmentation is accompanied by extensive local deformation and chipping of the impact site. Subero and Ghadiri (2001) have reported the detachment of fragments during the loading cycle along with extensive local (impact zone) chipping for the spherical glass beads agglomerates. They attribute the side fragment breakage to the oblique shear deformation around the impact site. Oblique cracks have also been reported by Arbiter *et al.* (1969) for sand-cemented agglomerates and by Salman and Gorham (1997) for glass particles. However, all these results have been obtained for the hard and brittle agglomerates. In our case, the side fragmentations are non-uniform and relatively one-sided due to the cauliflower and irregular structure of the granules and relatively soft and non-uniform distributed binder. Furthermore, post-event examinations of the impact

product (Figure 5.10) indicate the propagation of some stable and large cracks around the impact site. In this regard, close SEM observations of the crack openings illustrate the ductile mechanism of failure through elongation and rupture of the soft binder ligaments (Figure 5.11).

As it is seen in Figure 5.6, impacts of Sample 2 granules at higher velocities can ultimately lead to the complete disintegration. In this case, the high impact energy causes failure of the binder ligaments and consequently disintegration of the granule into a large number of clusters. Although, the structure and failure mode of Sample 2 granules are essentially different than the harder agglomerates, nevertheless, some similarities are seen in their breakage patterns. In this context, the similar transition of fragmentation to complete disintegration of agglomerates was observed by Mishra and Thornton (2001) through increasing the impact velocity in the impact simulation of lose poly-disperse spherical agglomerates with large primary particles and low contact number.

In general, the high-speed digital camera recordings and microscopic observations of Sample 2 granules show chipping, fragmentation and disintegration. Chipping occurs through the breakage of small clusters from the surface protuberances rather than primary particles. Hence, larger detached chips would be expected for Sample 2 as compared to Sample 3. In Figure 5.18, the images of the original granules before impact (Figures 5.18 a and b) and the fragments and debris after impacts at 18 $m.s^{-1}$ (Figures 5.19 c and d) are shown for Samples 2 and 3. For comparison the fragments and debris of impact product at about 25 $m.s^{-1}$ have also been presented in Figures 5.18 e and f. The debris after impact for both samples have been separated using standard sieve size of 1.18 mm. Comparing the debris of both samples at 18 and 25 $m\ s^{-1}$ indicates that the fragments of Sample 2 are larger than those of Sample 3. Furthermore, crack propagation in the weakened clusters in Sample 2 can lead to extensive disintegration of the granules at high impact velocities. Although, a large proportion of the impact energy is expected to be dissipated by the impact site densification and stable crack propagations, nevertheless there is sufficient stress concentration for the fragmentation or disintegration of the granule to occur at high impact velocities due to irregular and porous structure of the granule. Therefore, in

spite of the macroscopic plastic behaviour of these granules in the impact site and microscopic ductile failure within the crack openings, however, their breakage pattern is more similar to brittle and semi-brittle failure than ductile failure. A similar mechanism to that described for Sample 2 can also be concluded for Sample 3 with an exception that for Sample 3 cracks propagate through the rupture of tiny bonds, instead of the thicker inter-cluster ligaments. This is essentially due to the embedding of the fine primary particles in the visco-elastic binder.

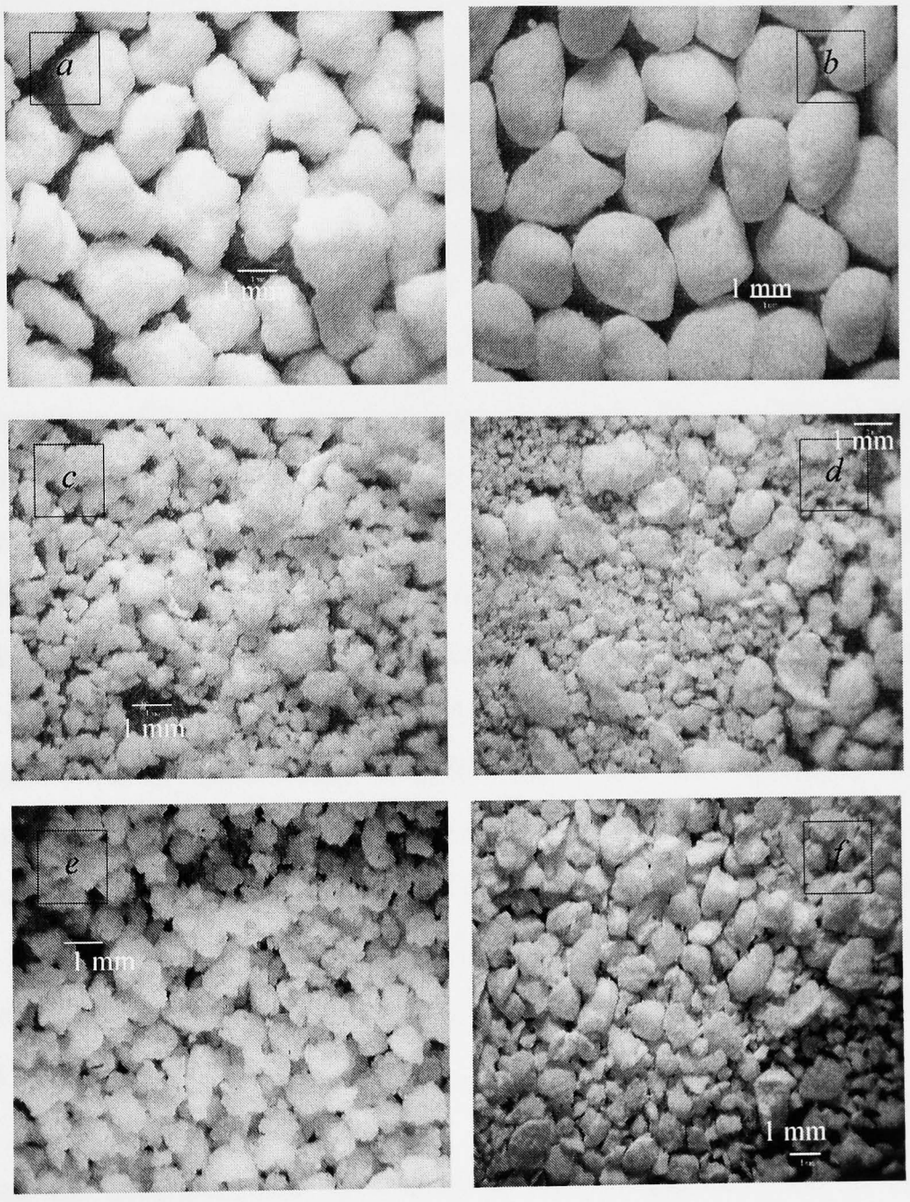

Figure 5.18: The RLM images of Samples 2 and 3 granules (1.70-2.00 mm) before and after impact at same magnification. a) Sample 2 granules before impact. b) Sample 3 granules before impact. c) Sample 2 debris after impact at 18 m s^{-1} d) Sample 3 debris after impact at 18 m s^{-1} e) Sample 2 debris after impact at 25 m s^{-1} f) Sample 3 debris after impact at 25 m s^{-1}.

For Sample 3 granules chipping or fragmentation can occur depending on the impact velocity. In this regard, the high-speed video recordings illustrate clearly the detachment of small debris at free fall impacts (Figure 5.7a). As it may be seen by careful examination of particles in the Figure 5.18b, the RLM image of the 1.70-2.00 mm granules before impact shows the presence of fines on the surfaces of Sample 3 granules. Therefore, at free fall impact of Sample 3 granules, the detached small chips might be due to these surface fines.

Extensive chipping was observed at the impact velocity about 18 m s^{-1} (Figure 5.7b). The chipping of the granule during unloading cycle is thought to be due to residual tensile stresses resulting from the elastic recovery of the material outside the plastic deformation zone as it was suggested by the Marshal *et al.*, 1982; Hagan and Swain 1978.

The fragmentation of Sample 3 granules occurs at higher impact velocities than those corresponding to Sample 2 producing a few numbers of large fragments (two to four fragments). However, the disintegration of the granules into the large number of small clusters was not observed for this sample even at the highest impact velocity. It is thought that the denser structure and smoother surfaces of Sample 3 granules are the main reasons preventing the complete disintegration of the granules. The experimental work of Subero and Ghadiri (2001) and the simulation results of Mishra and Thornton (2001) support the observations as discussed above. Figure 5.18 shows a more uniform size distribution of the broken debris for Sample 2 as compared to Sample 3. In this context, sieve analysis of the impact products can quantitatively draw a better view of the size distribution of the granules and breakage extent as it is presented in the Chapter 6.

Variation of the environmental conditions such as temperature and humidity can affect the breakage pattern significantly. Figure 5.16 shows clearly the effect of temperature (the sample kept at -20 °C) and humidity (the sample kept under humidified atmosphere) on the breakage pattern of Sample 3. In this context, the meridian and brittle breakage along with local degradation of the impact site are seen as the result of the subzero temperature effect. This breakage pattern has been

observed by many workers e.g. Arbiter *et al.* (1969), Thornton *et al* (1996) and Salman and Gorham (2000). In our case, large pre-existing internal flaws along with alteration of material properties presumably due to keeping the sample below the glass transition temperature seem to be responsible for brittle meridian fracture of the granules. Cooling the sample to -20 ^{o}C reduces the consolidation behaviour of the granules during impact due to a glasslike characteristic of the material properties especially the binder. Coupling this to the presence of large internal cavities, which acts as the stress concentrator leads to the observed brittle breakage pattern. In contrast, humidifying the sample increases the ductility of the granules mostly through altering the binder characteristics, presumably due to the viscosity change. In this regard, extensive plastic deformation in the impact site causes the ductile crack propagations, leading to the fragmentation. This breakage pattern is similar to the general fragmentation of Sample 3 granules, as discussed above, but with more extensive deformation of the impact site and detachment of larger fragments.

5.6 Conclusions

High-speed digital video imaging and visual observation of the granules by SEM and RLM have been employed to investigate the breakage patterns of three different types of the granules with different structures.

For Sample 1, fluidised bed granulation of large non-porous primary particles with molten PEG binder has led to the production of granules containing thick solid bridges with a large number of internal flaws and low co-ordination number. In this context, close SEM observations of the granules after impact showed the location of the internal flaws mainly on the broken planes of the bridges.

The high-speed video recordings of the impact events of Sample 1 granules indicated the complete disintegration of the granules, even under the free fall impact. However, with increasing the impact velocity, the granule was shattered into a larger number of small clusters. The high extent of disintegration is thought to be as the result of synergistic effect of low bond strength, high porosity and low co-ordination

number of the granules. The presence of pre-existing internal flaws within the PEG solid bridge as well as extensive macro-voids in the granules suggests that the predominant mode of breakage is likely to be brittle. However, precise examination of the impact sites revealed occurrence of some plastic deformation of the PEG surface layer especially on the sharp corners. The latter observations show that the semi-brittle mode of breakage should be the prevailed mode of breakage.

Samples 2 and 3 have been made through different processing methods of fluidised bed granulation and high shear mixing granulation, but with the same formulation. The SEM observations of Sample 2 granules revealed that these granules have been made of a large number of small clusters, aggregated by a paste type binder, where the primary particles (about 1 μm size) act as filler of the same binder. In contrast, in Sample 3 no small clusters were seen and the primary particles were embedded in the binder. A denser structure with a more spherical shape and smoother surfaces prevailed in Sample 3, as compared to the Sample 2.

The chipping of Sample 2 granules occurred through the breakage of small clusters from the surface protuberances, whereas for Sample 3 fine debris was separated from the surface of granules. For both samples, a large proportion of the impact energy was dissipated by the impact site densification and stable crack propagations. However, the irregular and porous structure of these granules provided sufficient stress concentration by which fragmentation and disintegration of the granule to be occurred at high impact velocities. Therefore, in spite of the macroscopic plastic behaviour of the impact site and microscopic ductile failure within the crack openings, the breakage pattern of the granules seems to be more comparable with semi-brittle failure modes.

Variation of the environmental conditions such as temperature and humidity affected the breakage pattern. For Sample 3, the meridian and brittle breakage together with local disintegration of the impact site was seen as the result of the subzero temperature effect. In contrast, humidifying the sample increased the ductility of the granules through altering the binder characteristics presumably due to the viscosity change.

6 QUANTITATVE ANALYSIS OF THE IMPACT TESTS

6.1 Introduction

The impact observations of calcium carbonate (Sample 1) and detergent based granules (Samples 2 and 3) exhibited different failure modes (Chapter 5). In general Samples 1, 2 and 3 granules failed in semi-brittle mode depending on the granule size and impact velocity.

Very limited experimental work has been reported on the impact breakage behaviour of these types of granules. Most of the studies have concentrated on the much stronger solid particles. Nevertheless, there is a great interest to characterise the failure characteristics of such agglomerates under different modes of loading in order to control their comminution or the unwanted attrition.

The objective of this chapter is to quantify the dependence of the extent of breakage on the impact velocity, granule size, number of impact and impact angle. The breakage is analysed by the gravimetric method. The results are compared with the findings reported in the literature.

6.2 Experimental

In these experiments, a model agglomerate of calcium carbonate powders (Durcal) granulated by PEG binder (Sample 1) and two detergent based granule types (Samples 2 and 3) have been tested. These samples have different evolved structures arisen from their different manufacturing methods (Chapter 3). Samples 1 and 2 have been produced by fluidised bed granulation but Sample 3 has been made, using high shear mixing granulation. Samples 2 and 3 have the same formulation. SEM images of Sample 1 granules reveal an irregular shape and highly porous structure with large primary particles, completely different from Samples 2 and 3. Compared to Sample 3, a cauliflower structure with higher porosity is observed for Sample 2.

In contrast, Sample 3 is more spherical and denser with smoother surface. In fact, the original granule in Sample 2 has been made of a large number of small clusters of very fine primary particles (about 1μm size), aggregated by a paste type binder, whilst the primary particles have been embedded in the cluster as filler of the same binder (Chapters 3 and 5). However, in Sample 3, no clusters are seen as the primary particles have been directly granulated by the binder.

The impact experiments have been performed, using a modified design of the single particle impact apparatus, developed by Yüregir *et al.* (1986). Details of the impact rig and its accessories have been presented in Chapter 5. In these experiments, the impact velocity of particles inside the apparatus is set by manipulating the vacuum pressure. The vacuum gauge pressure in the rig is initially calibrated for a range of impact velocities using the test material. Figure 6.1 shows a typical calibration curves obtained for three sieve sizes of Sample 3 granules. Each data point and error bar shows average and standard deviation of the impact velocity, respectively. The average impact velocities have been obtained for approximately 500 granules.

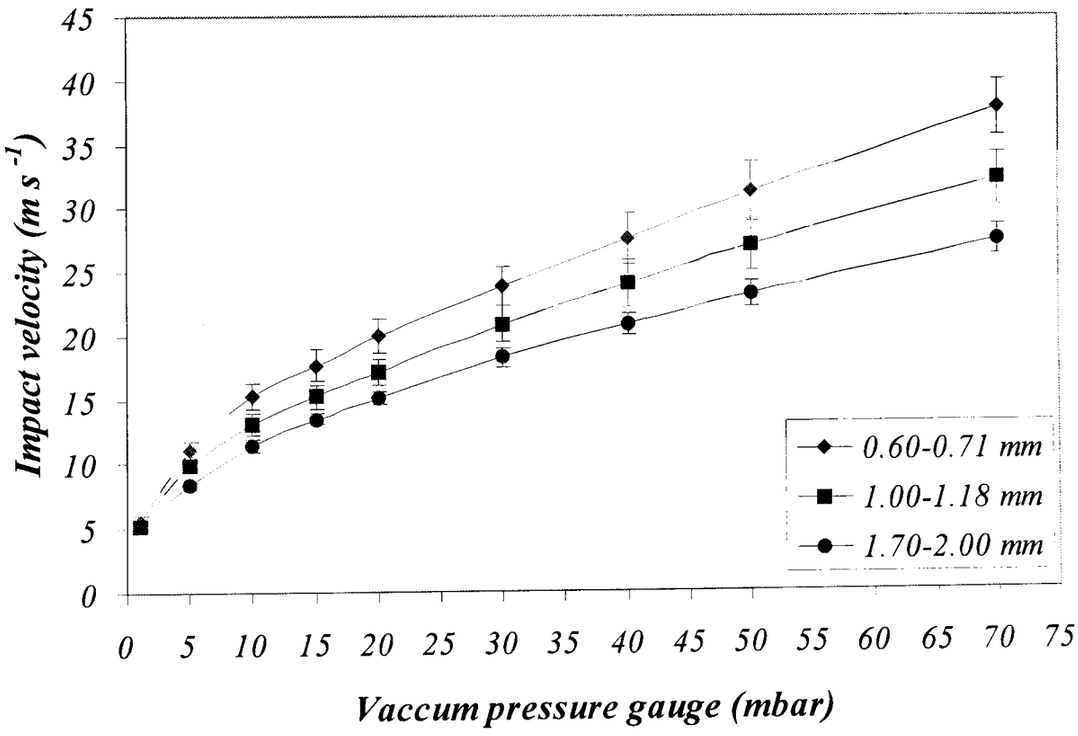

Figure 6.1: *Impact velocity calibration curve for three granule sizes of the Sample 3.*

For the main tests, the vacuum is initially adjusted to achieve the required velocity according to the calibration curve. However, the actual impact velocity is obtained based on the average velocity of about 5000 granules measured in the main test, and not the calibration curve. A large number of granules are tested to ensure a good reliability of the results. The granules are fed in an array one by one to the impact rig, into which they are sucked through the acceleration tube and are impacted on the target. Once all the granules are impacted, the airflow is stopped, the collection chamber is dismantled, the particles are taken out and the internal surfaces of collection chamber are cleaned to ensure the minimum possible loss of the material. The product is weighed to obtain the collection mass, M_C.

For quantifying the breakage, the impact product is sieved using an appropriate BS 410 sieve or a set of them. Following the procedure of Papadopoulos and Ghadiri, 1996, in the chipping regime the impact product is sieved by using a single sieve to separate the debris from the mother particles. This sieve has a mesh opening size which is two standard sizes below the original feed size. In this case, most of the separated chips are much smaller than the selected sieve aperture and are completely distinguishable from the original granules. After sieving, the mass of particles retained on the sieve (M_m) and the debris passing through the sieve (M_{de}) are quantified. The classified impact product is then stored in the sample vials for further microscopy analysis. For the fragmentation mechanism, a complete sieve analysis of material after impact is done as the broken granules may be distributed over all sieve sizes. The criterion for selecting the single sieve in the classification of mother particles and debris or employing the full sieve analysis method is addressed in more detail in the section 6.5.5.

In this study, a round sapphire plate, 25 mm in diameter and 6 mm thick is used as the target material in the normal impacts. However, in some experiments the wedge shaped stainless steel targets, machined at different angles with horizontal plane (φ_1), are substituted in order to investigate the effect of impact angle on extent of breakage of the granules (Figure 6.2). The complementary angle (θ) is defined as the impact angle.

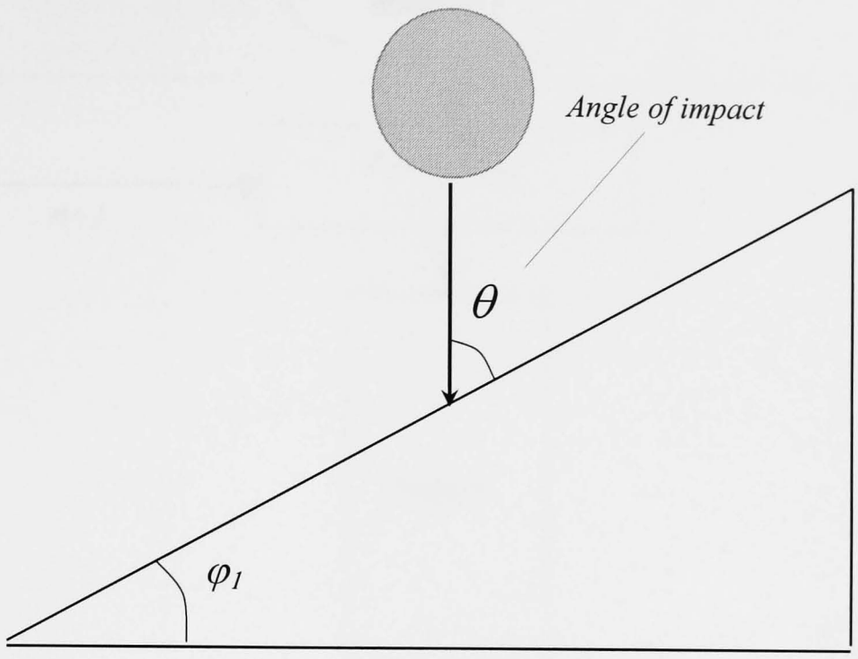

Figure 6.2: *Definition of the impact angle (θ) for impact along the gravity direction at an oblique target.*

In this study, the susceptibility of the granules to the repeated impacts is also investigated for a number of granule sizes of Samples 2 and 3. In this case, after each impact and related gravimetric analysis the mother particles are introduced back to the rig for the next stage of impact, while the debris is stored in the vials.

Figure 6.3 shows the experimental procedure of the single and repeated impacts as the block diagrams for the chipping regime. In the fragmentation regime a full sieve analysis of the collected mass is carried out. In the repeated impact the mother particles are recycled to the rig for the next impact. In this case, the quantified extent of breakage in the single stage of impact is termed as the incremental breakage while the total amount of breakage from first impact until the latest one is termed as the cumulative breakage. The mass balance correlations for the calculation of extent of breakage are explained in the following section.

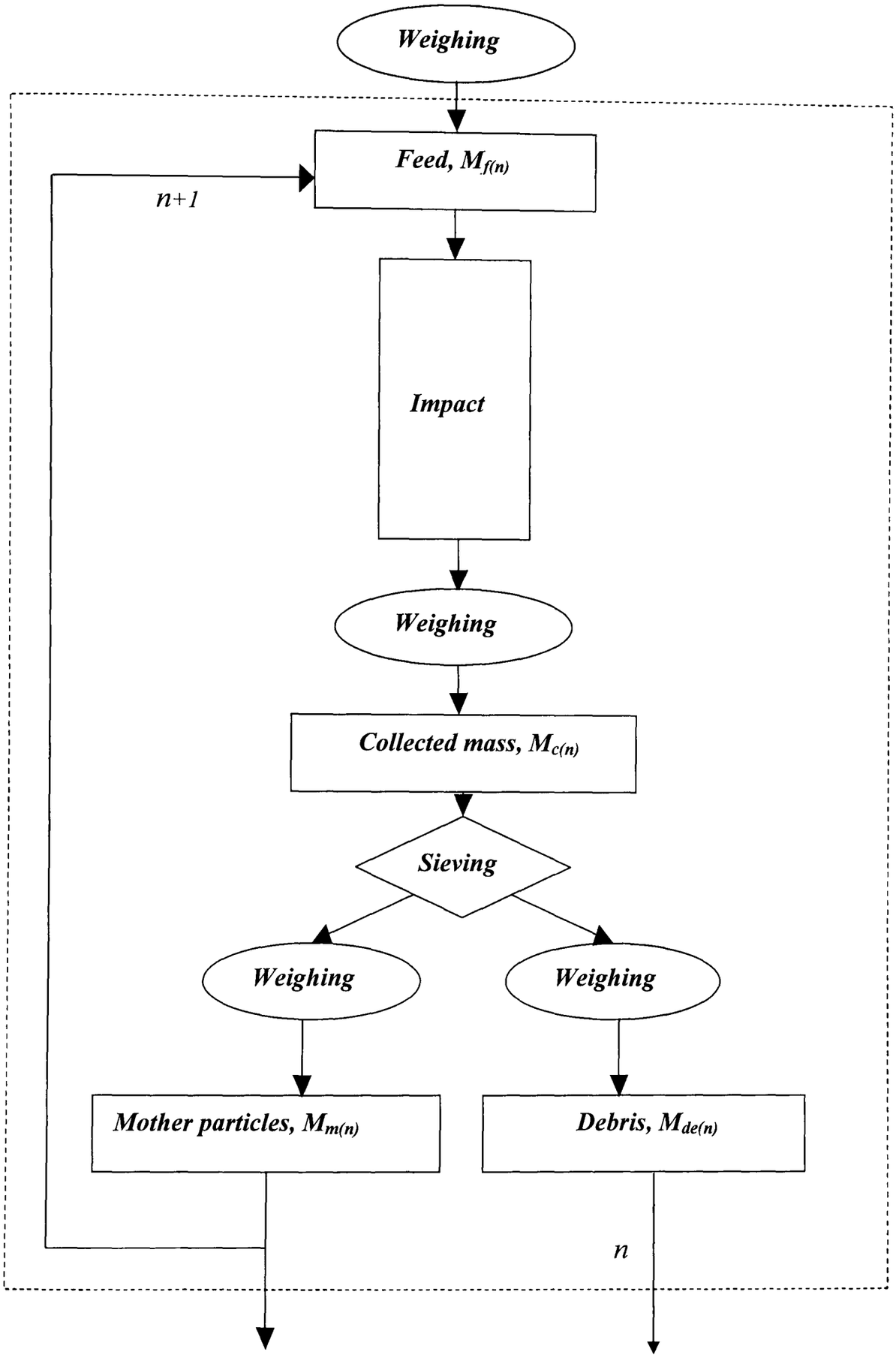

Figure 6.3: *Block diagram of the experimental procedure based on single sieving.*

6.3 Gravimetric analysis of breakage

In the single granule impact tests, the extent of breakage can be assessed as either the ratio of the number of broken particles to the total number of particles (Rumpf and Schönert, 1973; Salman *et al.* 1995) or the gravimetric method. In the latter, the mass distribution over the size range of interest is quantified (Vervoorn and Austin, 1990; Papadopoulos and Ghadiri, 1996). The gravimetric analysis is used in this study. For the repeated impact experiments, just the single sieve procedure is employed, because the damage for each individual impact is usually small.

6.3.1 Single sieve analysis method

The extent of breakage in the single sieve method is simply quantified by the mass fraction of the broken particles. In practice, there is always a small handling loss of material during collection and sieving in each test. This handling loss can consist of either debris, or mother particles, or both. To take account of the handling loss, Ghadiri and Zhang (1992) defined two extreme values for the extent of breakage per impact. The lower limit of breakage is based on the assumption that only mother particles are lost due to mishandling. In this case, the estimation of the breakage is based on the mass of debris, as shown in the following equation:

$$\xi_i^- = \frac{M_{de(i)}}{M_{f(i)}} \tag{6.1}$$

where ξ_i^- refers to the incremental lower limit of breakage at i^{th} impact, $M_{f(i)}$ is the mass of particles fed to the i^{th} impact and $M_{de(i)}$ is the mass of debris after the i^{th} impact.

In a similar manner, the estimation of the incremental upper breakage limit, ξ_i^+, is based on the assumption that the handling losses are only due to debris. The corresponding formula is given by:

$$\xi_i^{+} = \frac{M_{f(i)} - M_{m(i)}}{M_{f(i)}} \tag{6.2}$$

where $M_{m(i)}$ is the mass of the mother particles after the i^{th} impact.

In practice, the actual breakage usually lies somewhere between the lower and upper limits. Therefore, in order to have reliable data, it is necessary to reduce the handling losses so that the gap between the two limits becomes small. It is reasonable to assume that the handling loss of the large particles after impact is low, as compared to the debris. Therefore, in this case, the upper limit of breakage must give the results that are more reliable. Nevertheless, for highly water adsorbent materials, due to adsorption of humidity by the material during test, in Equation 6.2, M_m might be higher than expected and then, (M_f - M_m) may becomes lower than real amount, sometimes about zero or even negative at the very low extent of breakages. In this case, the upper limit of breakage may show smaller amounts than the lower limit.

An alternative way to calculate the breakage per impact is based entirely on the impact product given by:

$$\xi_i^{*} = \frac{M_{de(i)}}{M_{m(i)} + M_{de(i)}} \tag{6.3}$$

where ξ_i^{*} refers to the incremental breakage of the $i^{th.}$ impact based on the mass of the impact products. ξ_i^{*} usually lies between lower and upper limits.

For the experiments with only one impact the above equations is simplified with elimination of i subscript in the Equations 6.1- 6.3.

When the effect of repeated impacts on the breakage is investigated, Equations 6.1-6.3 provide the incremental values of the breakage. These equations can be modified to give a cumulative value of breakage for n number of impacts, according to the mass balance equations given by:

$$\xi^{-}_{c(n)} = \frac{\sum_{1}^{n} M_{de(i)}}{M_{f(1)}} \tag{6.4}$$

$$\xi^{+}_{c(n)} = \frac{M_{f(1)} - M_{m(n)}}{M_{f(1)}} \tag{6.5}$$

$$\xi^{*}_{c(n)} = \frac{\sum_{1}^{n} M_{de(i)}}{M_{m(n)} + \sum_{1}^{n} M_{de(i)}} \tag{6.6}$$

where $M_{f(1)}$ and $M_{m(n)}$ are the masses of the particles fed to the first impact and mother particles after n^{th} impact, respectively. In the above equations, $\sum_{1}^{n} M_{de(i)}$ is the sum of the debris separated from the first impact to the n^{th} impact, and $\xi^{-}_{c(n)}$, $\xi^{+}_{c(n)}$ and $\xi^{*}_{c(n)}$ of ξ^{-}, ξ^{+} and ξ^{*} are cumulative values.

In this study, the results of the repeated impact tests are also presented as average incremental breakage per impact. In fact, this parameter can be considered as an average extent of breakage per impact over n impacts with units of mass fraction. The average incremental breakage per impact, k_n is defined based on the following relationship.

$$k_n = \frac{\xi_{c(n)}}{n} \tag{6.7}$$

where $\xi_{c(n)}$ can be any of cumulative extent of breakage $\xi^{-}_{c(n)}$, $\xi^{+}_{c(n)}$ and $\xi^{*}_{c(n)}$. As it will be shown later, for the test material in this work, k_n varies with the number of impacts and depends on the granule size and impact velocity.

Vervoorn and Austin (1990), proposed the specific breakage constant, s_l, for particle size of l, based on a first order differential equation as follows:

$$-\frac{dM_{m(n)}}{dn} = s_1 M_{m(n)} \tag{6.8}$$

Integrating the above equation yields:

$$s_1 = -\frac{1}{n} ln\left(\frac{M_{m(n)}}{M_f}\right) \tag{6.9}$$

Rearranging Equation 6.9 and combining it with Equation 6.5 is outlined as follows:

$$\xi^{+}_{c(n)} = 1 - exp(-s_1 n) \tag{6.10}$$

The parameters s_1 and k_n depend on the process conditions, such as impact velocity and material property. Comparing Equations 6.7 and 6.10 reveals that two parameters of s_1 and k_n can not be equal except in a limited range close to zero, where they are constant and independent of the number of impact. In fact, this condition is only achieved for the case of low extent of breakage per impact. Zhang (1994) and Papadopoulos (1998) showed that for the processes with low breakage propensity, the average breakage per impact is approximately equal to the specific breakage rate.

6.3.2 Full sieve analysis method

Two methods are used for presenting the gravimetric size distribution of the impact products. The first one is based on plotting the cumulative mass fraction undersize as a function of size (L) on log-log scale according to Gates-Gaudin-Schaumann (1940) plot. In this plot, the size is normalised with respect to the feed particle size or to the size of the largest fragment produced on breakage, L_o (Arbiter et al., 1969; Thornton et al., 1995; Potapov and Campbell, 1997; Papadopoulos, 1998). The size distribution in this work is presented as normalised size with respect to the largest feed size (e.g. for feed sieve size of 1.00-1.18 mm, normalisation is made with respect to 1.18 mm).

In the second method, the size distribution is plotted as a histogram of mass percentage of materials on each sieve ($d\phi$), normalised by the size difference between the two consecutive standard sieves (dx), as a function of the arithmetic mean size (x) of each sieve unit ($d\phi/dx$ *vs.* x). The choice of the size intervals (dx) is important and is based on the requirement that the resolution defined as size interval divided by the mean sieve size (dx/x) should be kept fairly constant (Allen, 1981).

6.4 Results

The effect of various parameters on the extent of breakage of the test materials is presented here. These parameters are impact velocity, granule size, impact angle and number of impact. As a large number of experiments have been performed, only a selection of the most important figures is shown in this section. Further graphs are given in the appendix B.

The presentation of the results is followed by discussion in the next section. The reliability of the results, as an important section, including the systematic errors, reproducibility and extension of handling losses, are also assessed in the discussion.

6.4.1 Impact test results

In this section, the effects of impact velocity, feed size, impact angle and some other factors such as temperature and material's moisture content on the breakage are investigated for the single stage impact. The dependency of the breakage on impact velocity and granule size under normal impact condition is investigated for Samples 1, 2 and 3. The effect of impact angle on breakage is presented for Samples 2 and 3 and the effects of temperature and moisture content are investigated for Sample 3. The effects of impact angle and impact number on the breakage of Sample 1 are not addressed here due to the concentration of the large number of planned tests on Samples 2 and 3 as well as less interest on investigation of these effects for Sample 1.

6.4.1.1 Effect of impact velocity and feed size

Normal impact tests were performed on different feed sizes and impact velocities. The samples were kept under ambient laboratory temperature and relative humidity.

Single sieve analysis method

Figure 6.4 shows the lower and upper percentage of breakages of Sample 1 granules, presented according to the single sieve analysis method using a sieve where is two sizes less than feed size.

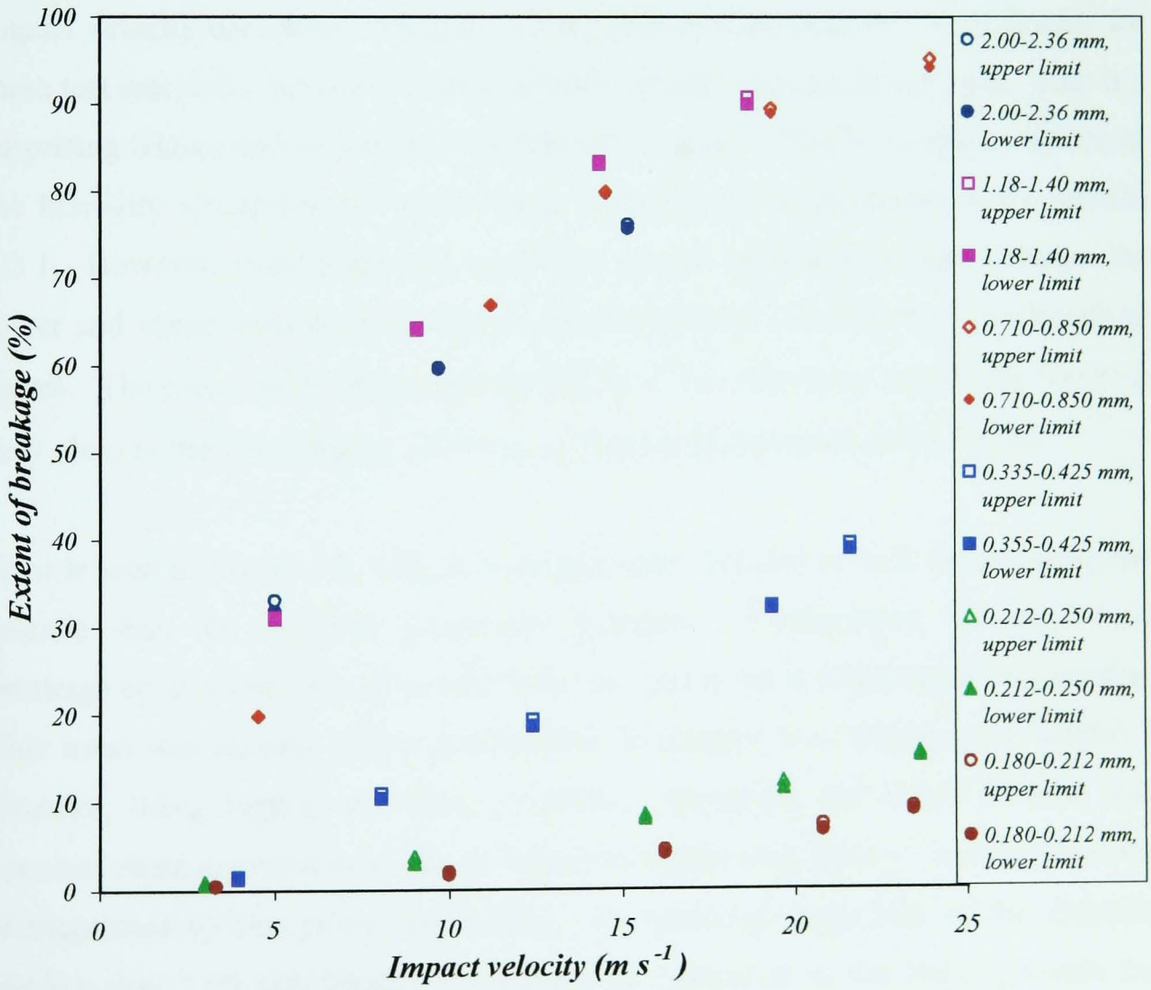

Figure 6.4: *Extent of breakage as a function of impact velocity, obtained for different feed granule sizes of Sample 1.*

As it is seen, there is a close agreement between the lower and upper limits of breakage (maximum 1%, but mainly about 0.5% difference), showing low handling losses. The figure also indicates that the extent of breakage increases with impact velocity for a constant feed size and with the granule size for impact velocity. However, the large feed size granules (0.710-2.360 mm) show a similar logarithmic trend (Figure B1), which is different from the fine granules (less than 0.212 mm). The latter is best fitted by power law trend (Figure B2). Therefore, for the large granules, single sieve analysis is inappropriate, as it doesn't show the size distribution of debris, and a complete particle size analysis should be performed. Single sieve analysis should be applied for a size range, where chipping is the predominant regime of breakage (Figure B2).

The lower and upper extents of breakage of Sample 2 granules as a function of impact velocity are shown in Figure 6.5 for four feed sieve sizes. As it is seen for these test materials, the upper limit is actually smaller than the lower limit. This is a surprising feature and in contrast with Sample 1 results. This is thought to be due to the humidity adsorption of water vapour in Sample 2, as explained in the section 6.3.1. However, even under this condition, a close agreement is seen between the lower and upper extents of breakages, which it can be considered as low handling losses. The extent of breakage represented by ξ^* has also been calculated, which is very close to the lower limits. However, ξ^* has not been shown in the figures.

As it is seen in Figure 6.5, with increasing impact velocity as well as increasing the granule size, the breakage propensity increases. Furthermore, the extents of breakage up to about 20 m s^{-1} is relatively low, and is not strongly dependent on size. This trend was already shown qualitatively in Chapter 5 as chipping of Sample 2 granules, using high-speed video recording. However, the effect of feed size becomes more appreciable at impact velocities higher than 20 m s^{-1} and the plots are distinguished by two power law trends. The breakage propensity of the granules smaller than 1.00 mm increases smoothly as compared to the large granules for which a sharp increase is observed at around 20 m s^{-1}. There appears a change in the slope, which is thought to be due to a change of the breakage mechanism from

chipping to fragmentation. This mechanism change of large granules can be seen in Figures 5.4, 5.5 and 5.6 in Chapter 5.

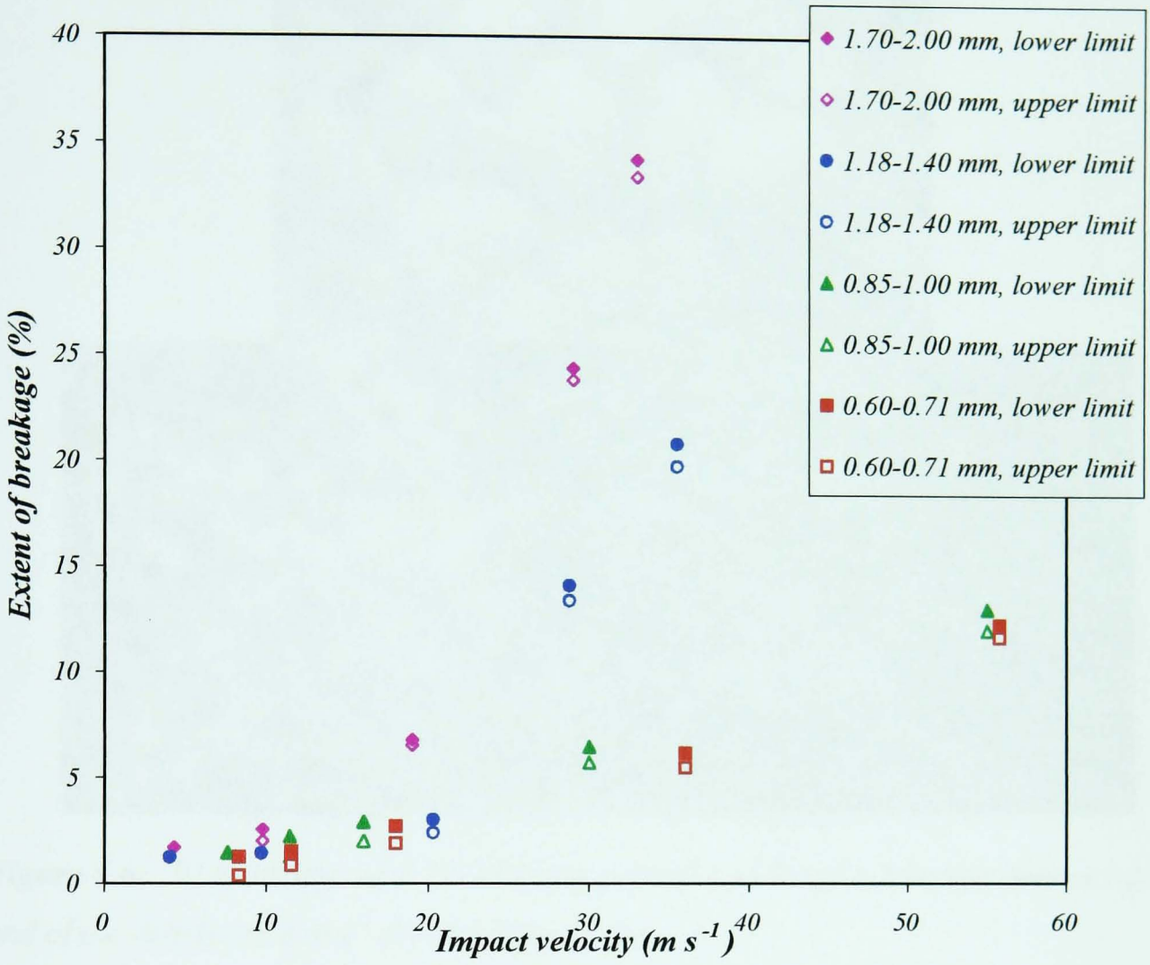

Figure 6.5: *Extent of breakage as a function of impact velocity, obtained for different feed granule sizes of Sample 2.*

Figure 6.6 illustrates the RLM images of 1.70-2.00 mm granules of Sample 2 before impact (Figure 6.6a) and of the debris produced as a result of impact at about 18 m s^{-1} (Figure 6.6b) and 25 m s^{-1} (Figure 6.6c). The debris has been separated from mother particles by sieving using a single 1.18 mm sieve. Comparing the images of debris with the feed granules shows the effect of impact velocity on the size of debris and the extent of breakage. As it is seen, increasing the impact velocity produces larger debris.

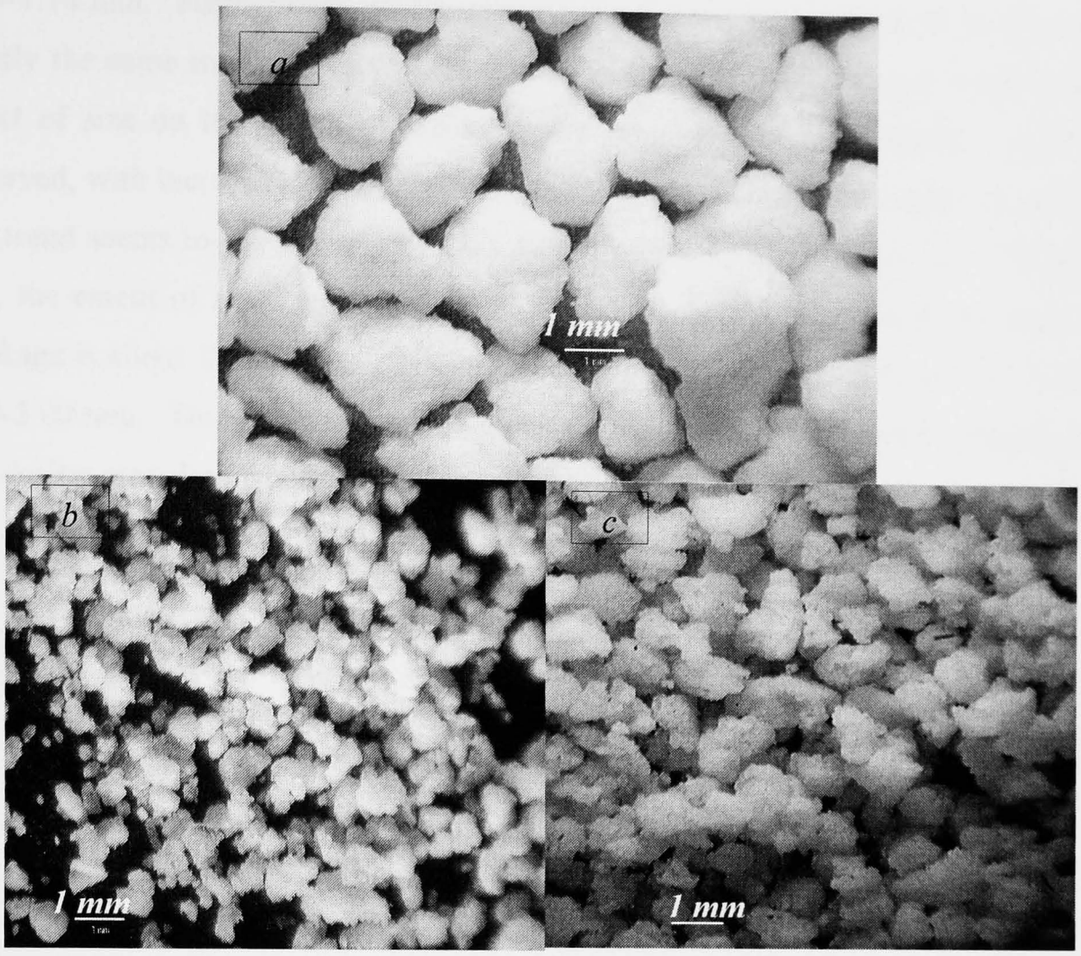

Figure 6.6: *RLM images of 1.70-2.00 mm granules of Sample 2 before impact (a), and of the debris at 18 m* s^{-1} *(b) and 29 m* s^{-1} *(c).*

Figure 6.7 shows the lower and upper extents of breakage as a function of impact velocity for different feed granule sizes of Sample 3. As it is seen, the upper limit results are again smaller than those of the lower limit for this sample. In this case, the upper limit of the breakage of some impact tests (less than 10 m s^{-1}) was about zero or even slightly negative. These data points have not in fact been shown in the figure and just their lower limits are presented here. Furthermore, ξ^* was calculated, which was in less than 0.5% difference with lower limit. ξ^* has not been shown in Figure 6.7.

In Figure 6.7, slope changes are observed for all feed granule sizes, suggesting a transition in the breakage mechanism from chipping to fragmentation. This mechanism change can be observed in the high-speed video images of Figure 5.7. The slope changes are seen at about 25 m s^{-1} for 500-600 μm and about 20 m s^{-1} for

1.00-1.18 mm. Furthermore, all the granule sizes tested up to about 15 m s^{-1} show mostly the same trend with less than 2% breakage. Over this impact velocity, the effect of size on the extent of breakage becomes more distinguishable. As it is observed, with increasing the granule size the breakage increases initially. However, this trend seems to prevail up to 1.18-1.40 mm. For larger granules, e.g. 1.70-2.00 mm, the extent of breakage is lower. For example, at 30 m s^{-1} the lower limit of breakage is about 18% for the 1.18-1.40 mm feed size, whilst it is about 14% for the 1.70-2.00 mm. This might be as the result of a structure change with increasing the size during granulation process.

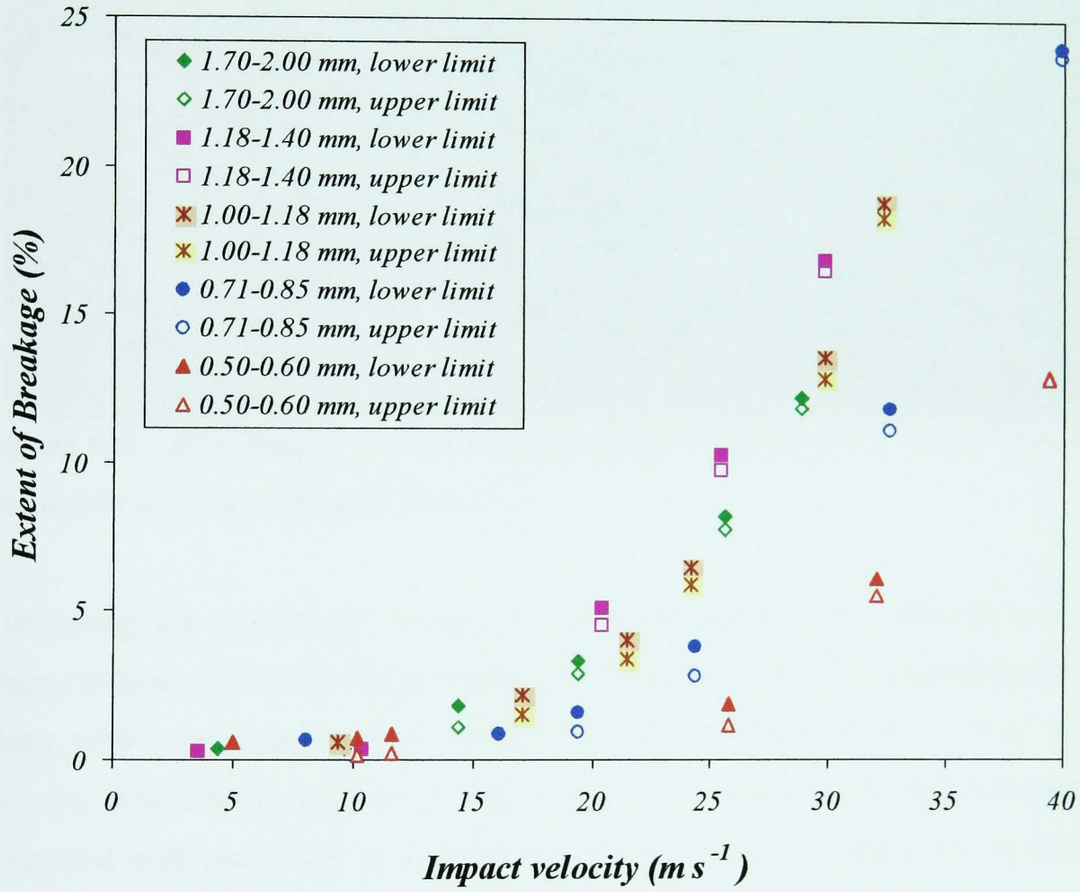

Figure 6.7: *Extent of breakage as a function of impact velocity, obtained for various feed granule sizes of Sample 3.*

Figure 6.8 illustrates the RLM images of 1.70-2.00 mm granules before impact (Figure 6.8a) and two images of the debris (Figures 6.8b and 6.8.c), all from Sample 3. The debris has been separated from the impact product of the 1.70-2.00 mm feed size granules, impacted at about 15 m s^{-1} (Figure 6.8b) and 26 m s^{-1} (Figure 6.8c).

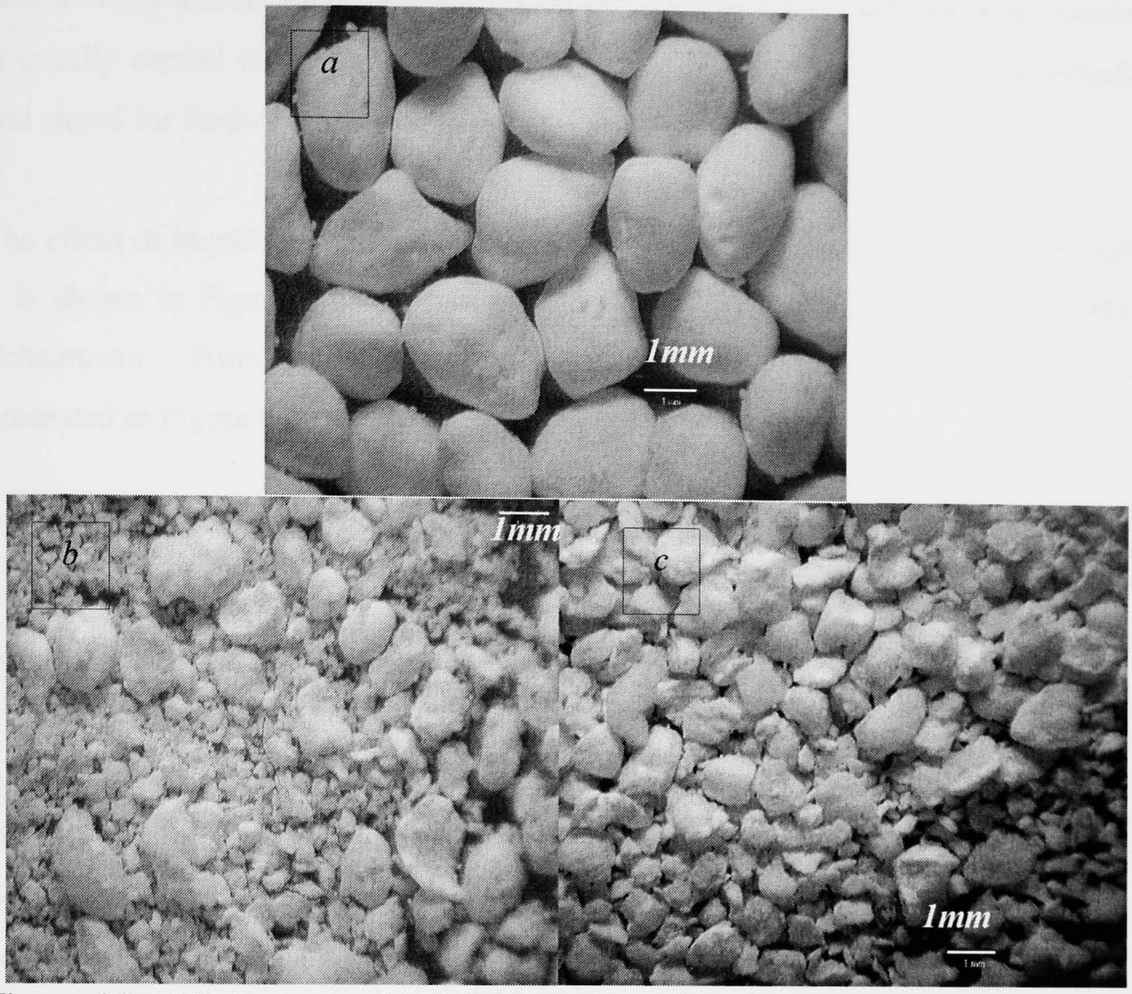

Figure 6.8: *RLM images of 1.70-2.00 mm granules of Sample 3 before impact (a), and debris at 15 m s^{-1} (b) and 26 m s^{-1} (c).*

Comparing the microscopic images of debris indicates clearly that the extent of fragmentation of the granules increases with the impact velocity. Extensive chipping along with some fragmentation of the granules are observed at 19 m s^{-1} impact velocity, whilst fragmentation dominates at 26 m s^{-1}. The size of debris can easily be compared with each other and with the feed size as all the images are on the same scale. Furthermore, comparing Figures 6.6 and 6.8 indicates qualitatively a wider size distribution of Sample 3 debris, as compared to Sample 2.

Full sieve analysis method

In this method, the impact product is collected and weighed and analysed for the full size distribution by sieving, as described in section 6.3.2. In this context, the

selection of the sieve range depends on the feed particle size of test material. Sieving is usually carried out down to 75 μm. Each sieve fraction is weighed individually and stored for further examination.

The effect of impact velocity on the size distribution of the impact product of Sample 1 is shown in Figure 6.9 for four feed sizes, based on the plot of Gates-Gaudin-Schaumann. Furthermore, the effect of granule size on the size distribution is presented in Figure 6.10 for two impact velocities.

The results are also presented in Figure 6.11 in the form of frequency histogram of $\mathrm{d}\phi/\mathrm{d}x$ vs. x. The preference of the second method is the clear comparability of size distributions due to constant integral area underneath the distribution curves.

As it is apparent from Figure 6.9, the trend of data is not a straight line on the log-log plots of the cumulative mass fraction under size versus the normalised size except for the feed size 180-212 μm (Figure 6.9d). This is in contrast to the breakage of other types of granules reported previously by Couroyer *et al.* (2000) and Papadopoulos (1998). There exist a natural cut in the size distribution plots particularly at low velocities for feed size 180-212 μm. This corresponds to a distinction between large fragments and debris. The natural cut separates each distribution plot roughly into two distinguishable and almost straight lines with different slopes. The distribution line with the larger slope is termed as the residue line and that with the lower slope complement line. In Figure 6.9d, as the velocity increases, the natural cut gradually disappears and the two distinct straight lines tend to make a single one. This could be a manifestation of the gradual transition from chipping to fragmentation. This implies that for the velocities higher than 20 m s^{-1}, fragmentation may be the dominant mechanism of breakage. Furthermore, the size distributions in Figure 6.9d show that the amount of debris increases substantially as the impact velocity increases. For instance, almost a 5 times increase in velocity from 4 to 21 m s^{-1} results in a change of approximately 20 fold in the mass fraction under the size ratio of 0.5. Figure 6.9c shows the effect of velocity on the size distribution of 350-425 μm feed size. In this case, the natural cut is only observed for 4 m s^{-1} impact velocity and for the higher velocities, there is no natural cut and the trends are non-linear. For

the feed sizes of 710-850 μm and 1.18-1.40 mm, however, all the plots are non-linear (Figures 6.9a and 6.9b).

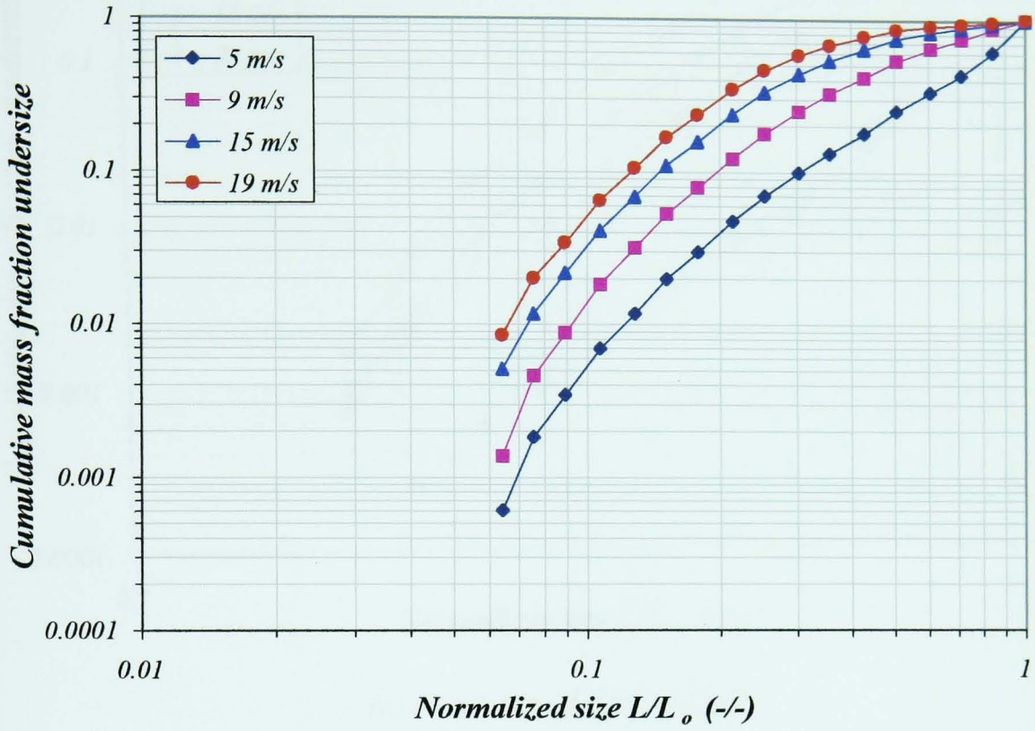

(a) Feed size of 1.18-1.40 mm

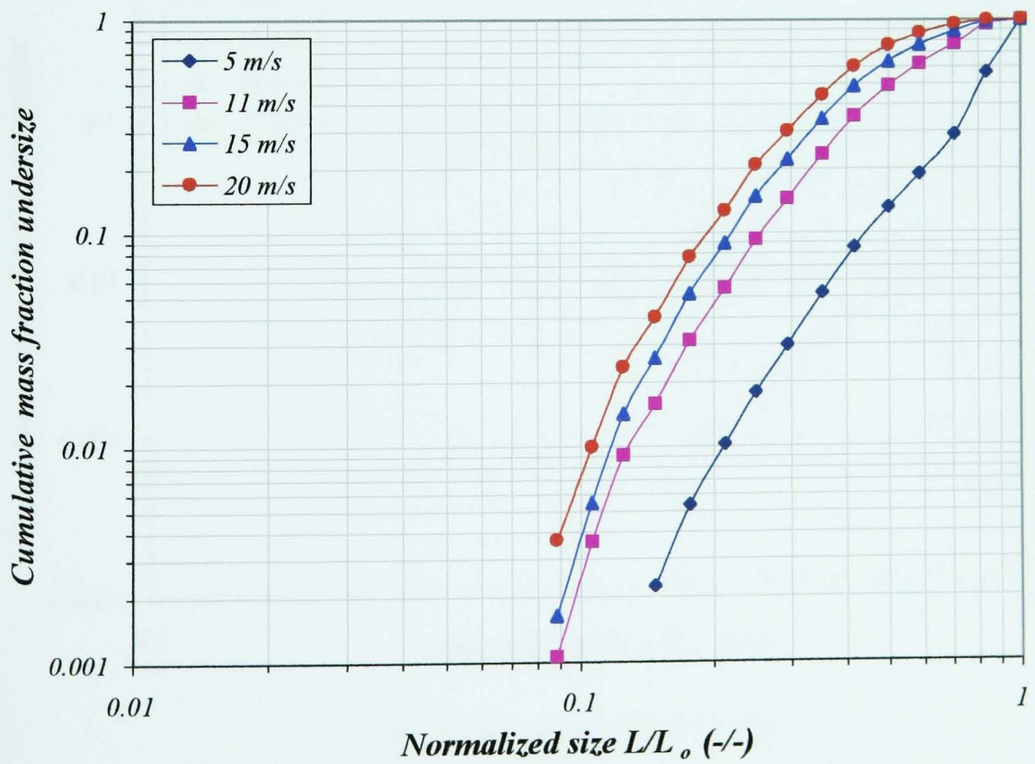

(b) Feed size of 710-850 μm

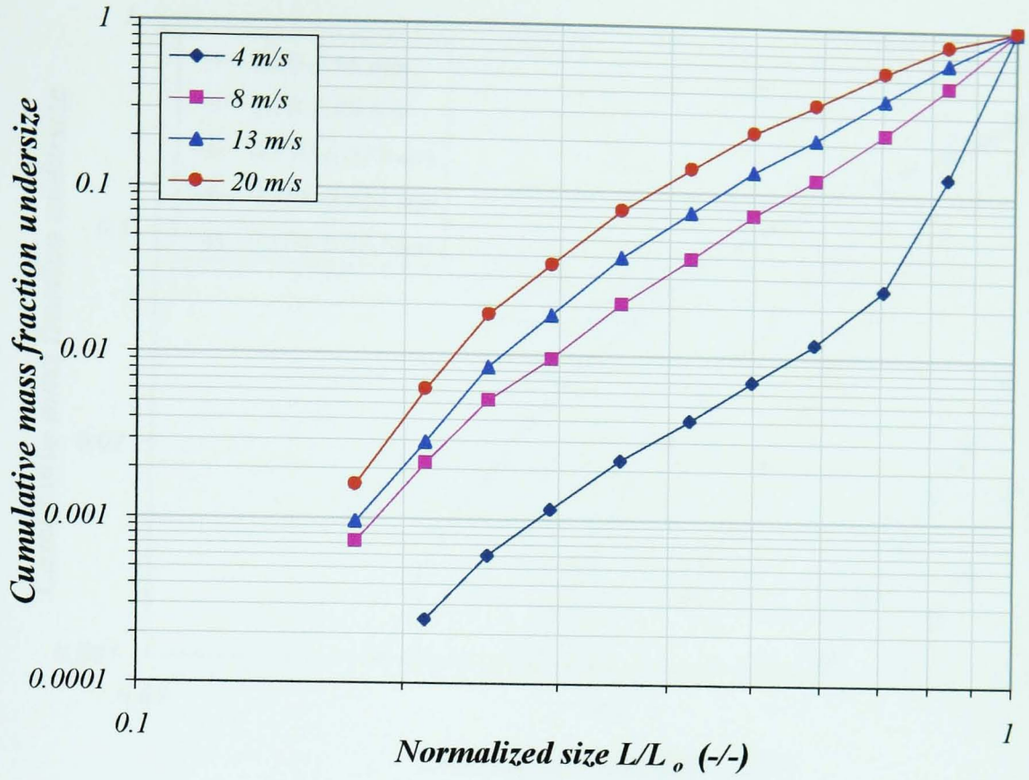

(c) Feed size of 355-425 μm

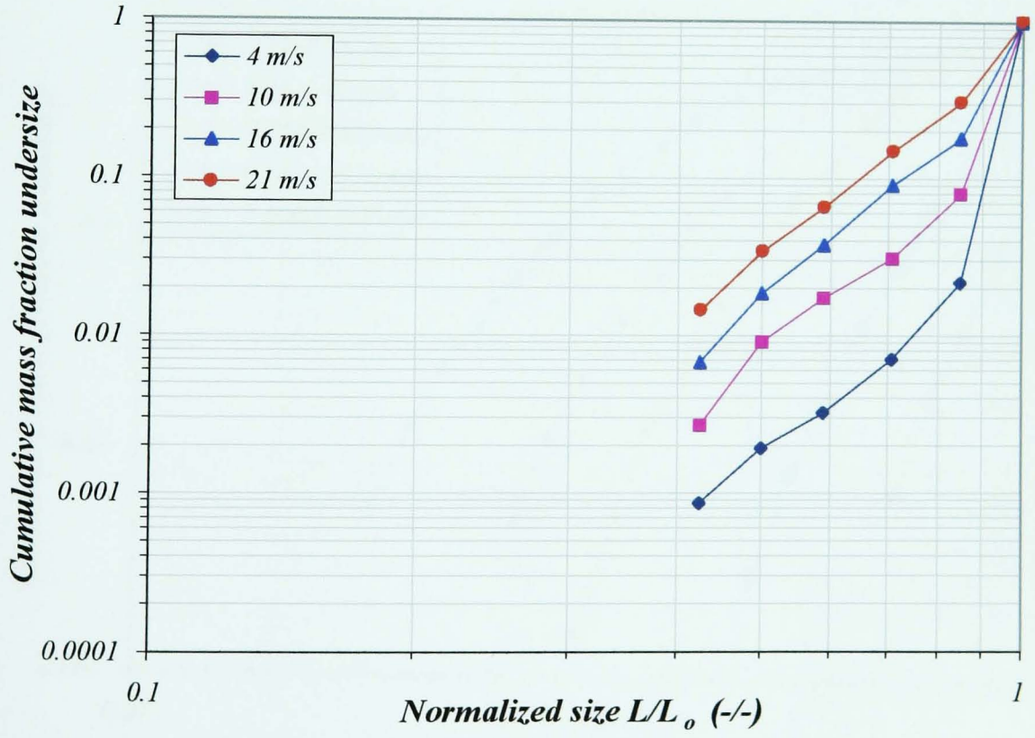

(d) Feed size of 180-212 μm

Figure 6.9: *Effect of impact velocity on the size distribution of impact product of Sample 1.*

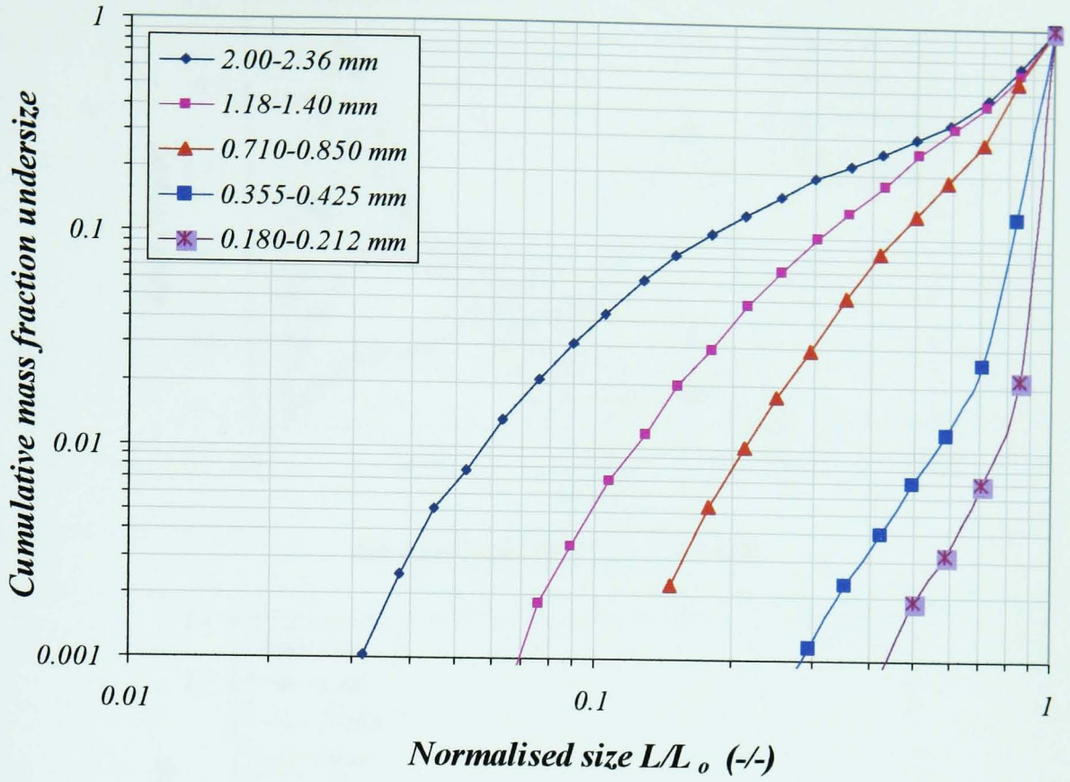

(a) Impact velocity about 4 m s^{-1}

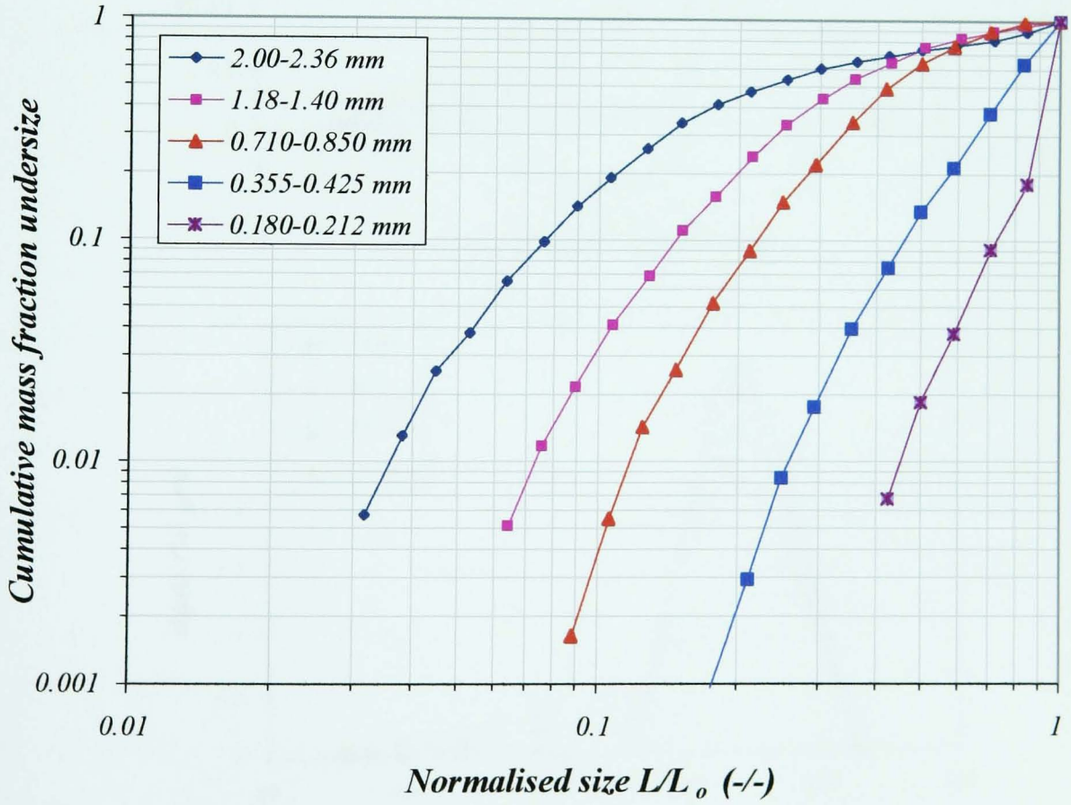

(b) Impact velocity about 15 m s^{-1}

Figure 6.10: *Effect of granule size on the size distribution of impact product of Sample 1.*

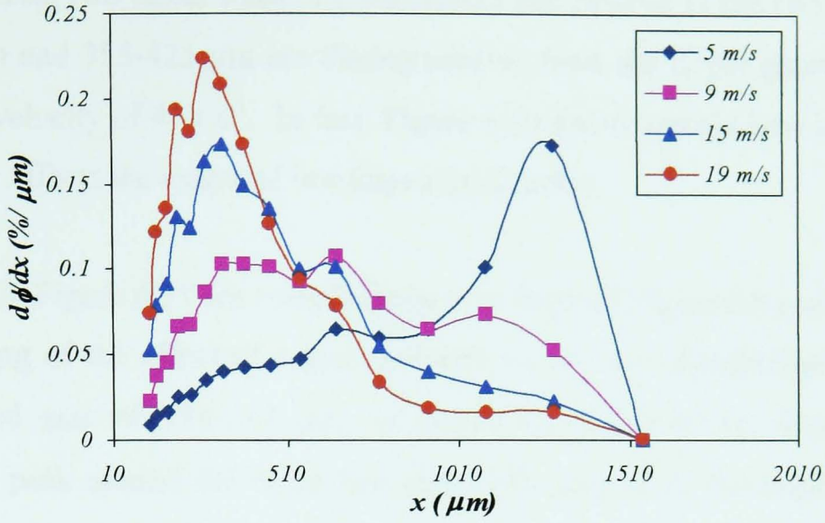

(a) Feed size of 1.18-1.40 mm

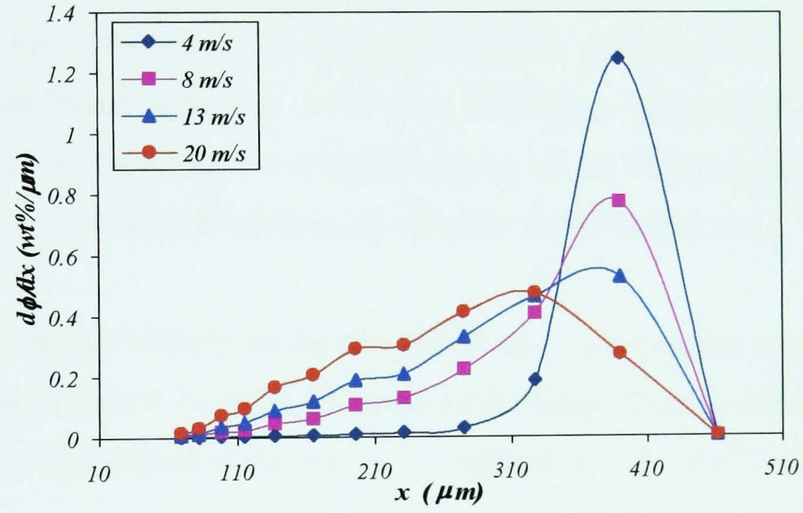

(b) Feed size of 355-425 μm

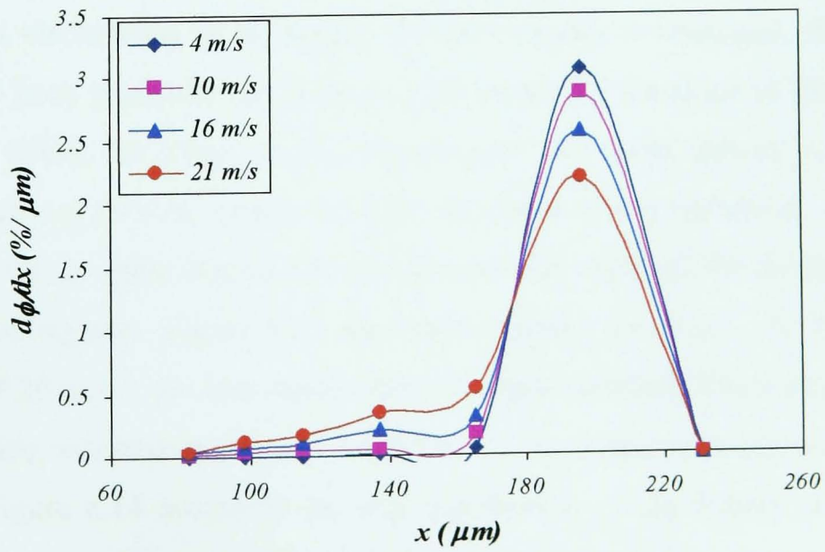

(c) Feed size of 180-212 μm

Figure 6.11: *Effect of velocity on the size distribution of impact product of Sample 1.*

In Figure 6.10a, two linear lines of complement and residue of the two feed sizes of 180-212 μm and 355-425 μm are distinguishable from the larger granules, at about the impact velocity of 4 m s^{-1}. In fact, Figure 6.10 shows clearly how increasing the granule size affects the extent of breakage significantly.

The graphs in Figure 6.11 are complementary to those of Figure 6.9 and give a better understanding of the effect of impact velocity on the size distribution of granules. For the feed size of 180-212 μm, as shown in Figure 6.11c, there is a clear distribution peak around the mean feed size (196 μm) of all the impact velocities. This peak for the feed size of the 355-425 μm is seen just at 4 m s^{-1}. At higher than this impact velocity the frequencies are widely distributed over all sizes (Figure 6.11b). For the 1.18-1.40 mm feed size, as it is clear from Figure 6.11a, the product is widely distributed within all sieve sizes, indicating extensive fragmentation of agglomerates. In this case, the size distribution of the impact product at 19 m s^{-1} velocity shows another peak completely different from the feed size.

The effect of impact velocity on the size distribution of the impact product of Sample 2 is shown in Figures 6.12 and 6.13 based on the plots of Gates-Gaudin-Schaumann and frequency histograms of $\mathrm{d}\phi/\mathrm{d}x$ vs. x, respectively, for two feed granule sizes. As it is apparent from Figure 6.12, a natural cut is seen for both feed sizes of 1.70-2.00 mm and 1.18-1.40 mm at about 5 and 10 m s^{-1}, indicating chipping as the predominant mechanism of breakage. As the velocity is increased, the distinction between the lines gradually disappears. This occurs by the slope of the residue line decreasing, whilst the slope of the complement line stays almost constant. The impact velocity of 20 m s^{-1} seems to be the threshold of this transition. At 29 and 33 m s^{-1}, however, a single line of the size distribution suggests the domination of the fragmentation regime. Figure 6.13 also shows clearly this trend. At about 5 m s^{-1}, 10 m s^{-1} and 20 m s^{-1}, the size distribution of impact products has a peak around the mean feed size, whereas at 29 m s^{-1} and 33 m s^{-1}, the frequencies are distributed over all sizes. Figure 6.14 compares the size distribution of the impact product of two feed granule sizes at three impact velocities. It shows that the extent of breakage of the 1.70-2.00 mm feed size at 20 m s^{-1} is higher as compared to the 1.18-1.40 mm granules at 35 m s^{-1}.

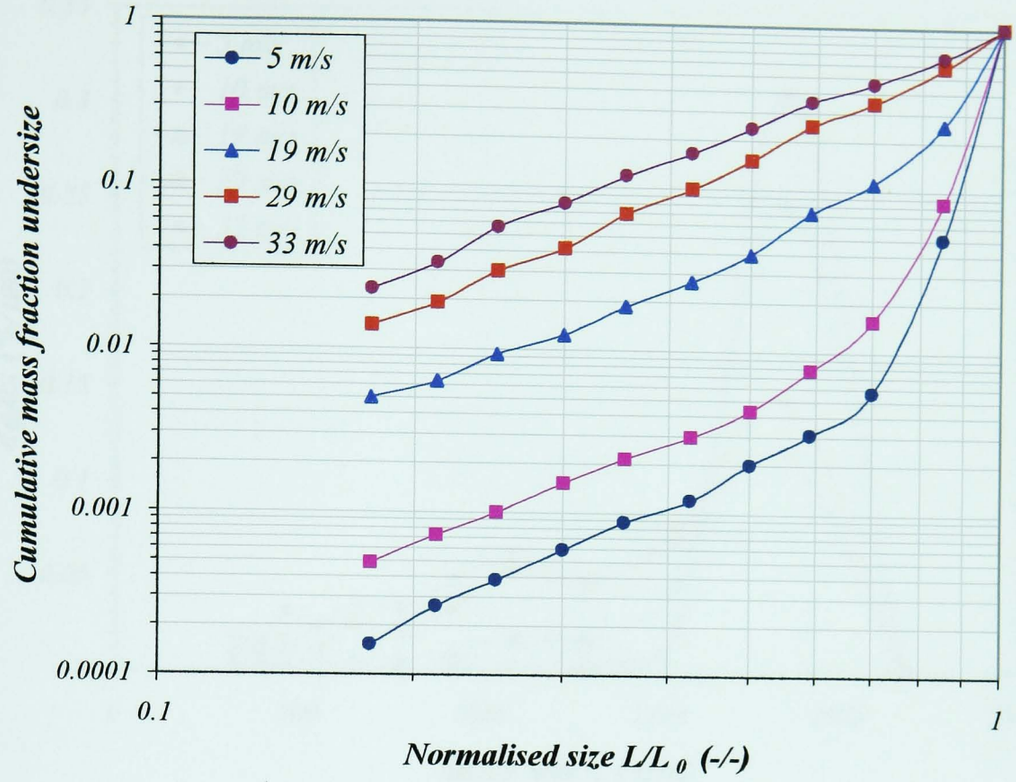

(a) Feed size of 1.70-2.00 mm

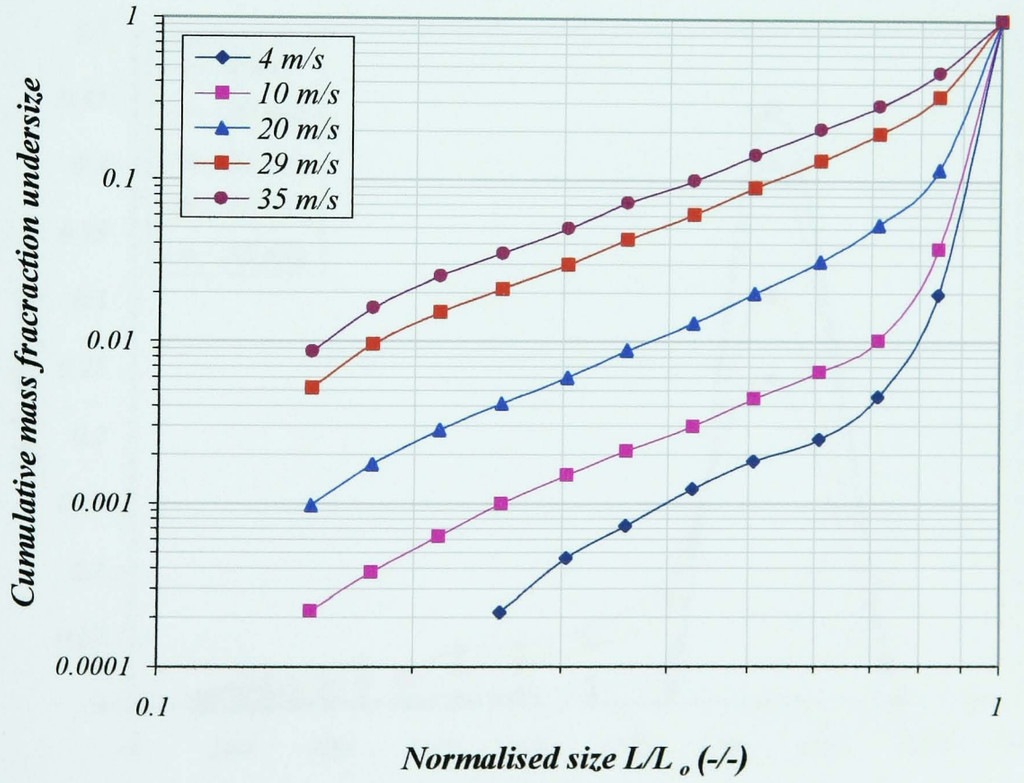

(b) Feed size of 1.18-1.40 mm

Figure 6.12: *Effect of velocity on size distribution of impact product of Sample 2.*

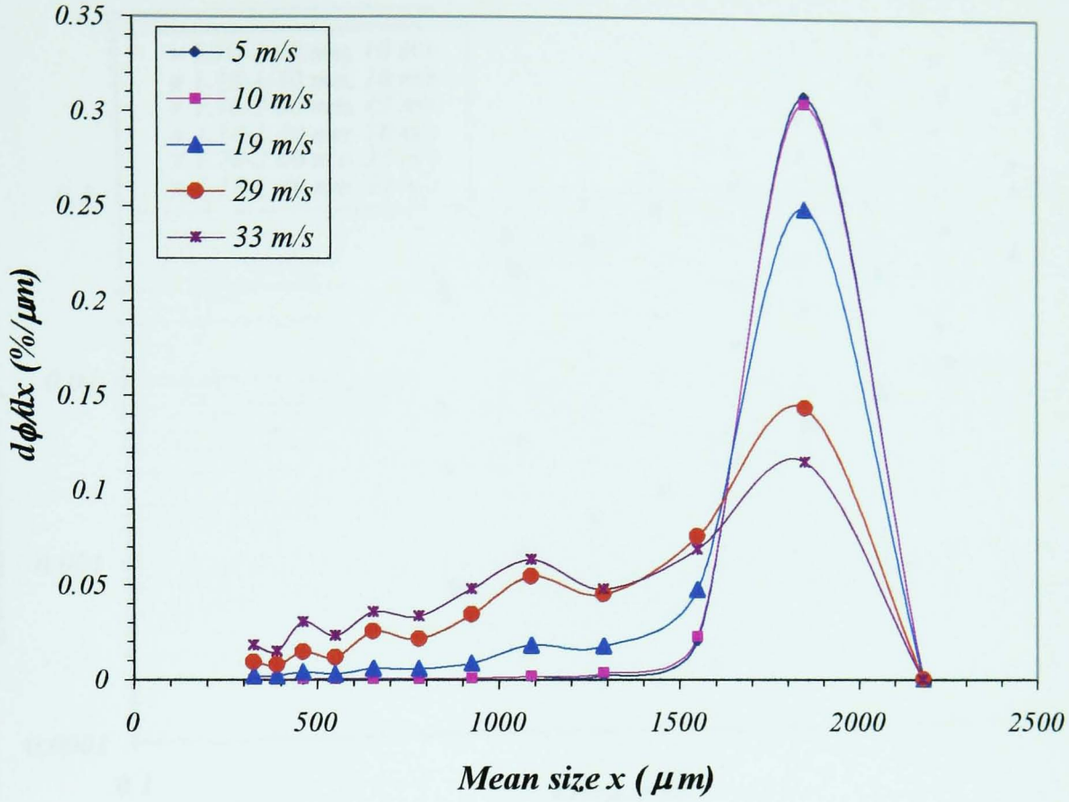

(a) Feed size of 1.70-2.00 mm

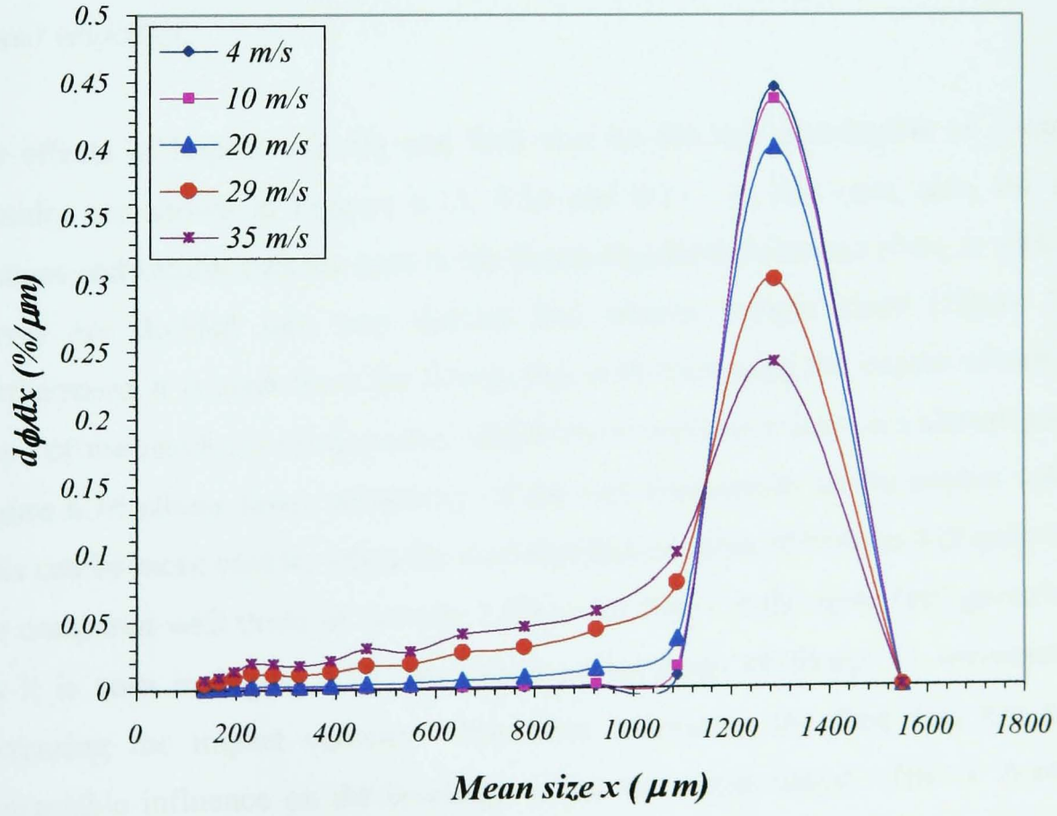

(b) Feed size of 1.18-1.40 mm

Figure 6.13: *Effect of velocity on size distribution of impact product of Sample 2.*

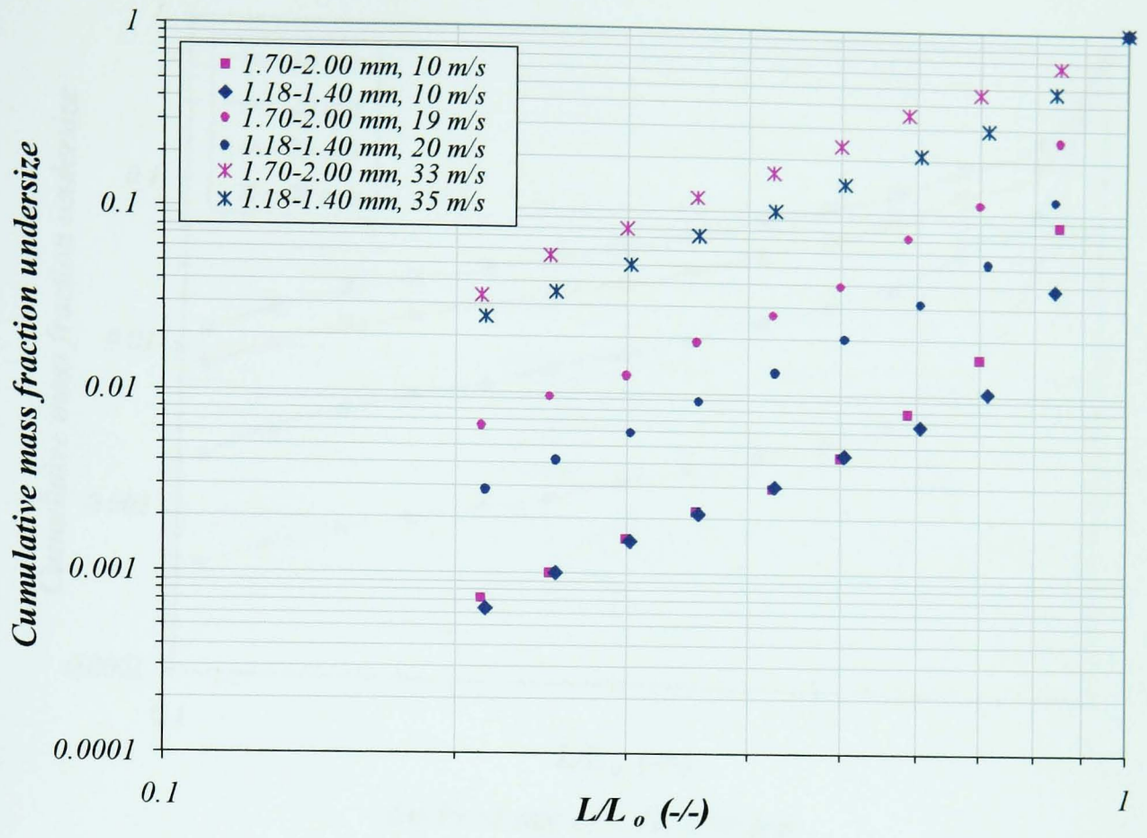

Figure 6.14: *Comparison of size distribution of impact product of Sample 2 at three impact velocities.*

The effects of impact velocity and feed size on the size distribution of Sample 3 granules are shown in Figures 6.15, 6.16 and 6.17. In this case, also, the slope changes and natural cuts are seen in the Gates-Gaudin-Schaumann plots, in which the curves are divided into two distinct and almost straight lines (Figure 6.15). Furthermore, it is clear from the figures that with increasing the impact velocity, the slope of the residue lines decrease, whilst the complement lines are almost parallel. Figure 6.16 shows lower sensitivity of the size frequencies to the impact velocity. This can be more visible, when the size distribution plots of Sample 3 (Figure 6.16a) are compared with those of Sample 2 (Figure 6.13a) for the same feed granule size. As it is seen in Figure 6.17, the extent of breakage of Sample 3 increases with increasing the impact velocity. However, increasing the feed size has not an appreciable influence on the breakage in the size range tested. This is in contrast with Sample 2 results (Figure 6.14), for which the extent of breakage has been significantly affected by both impact velocity and feed size.

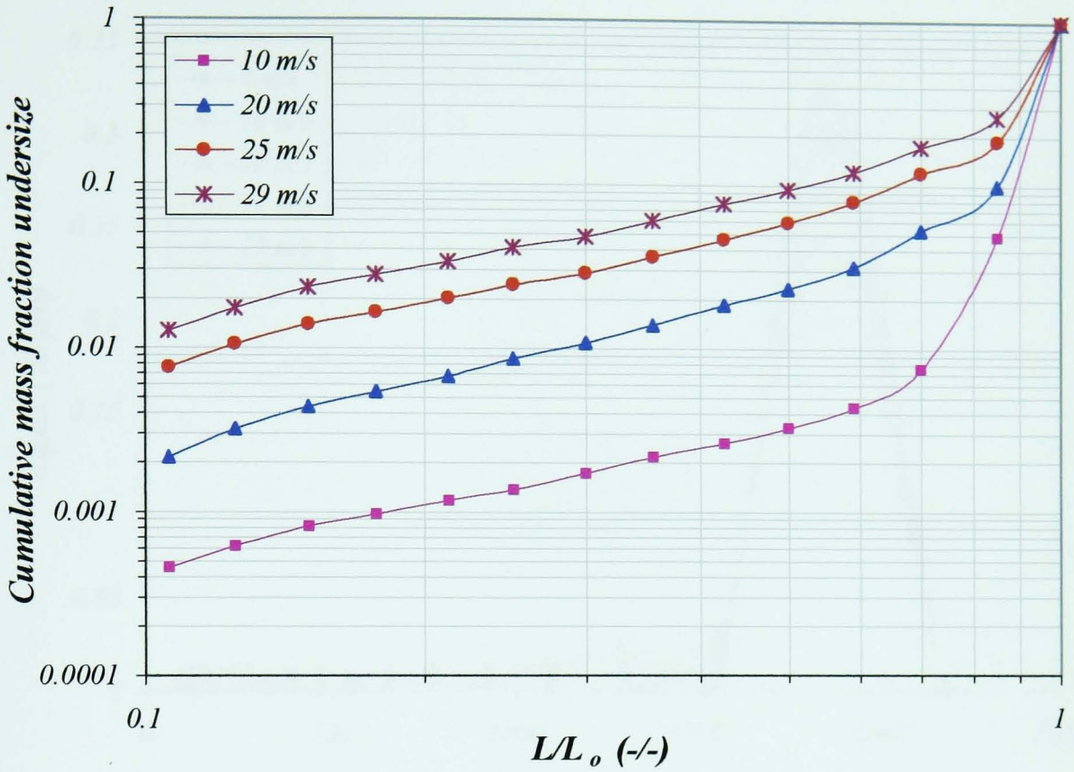

(a) Feed size of 1.70-2.00 mm

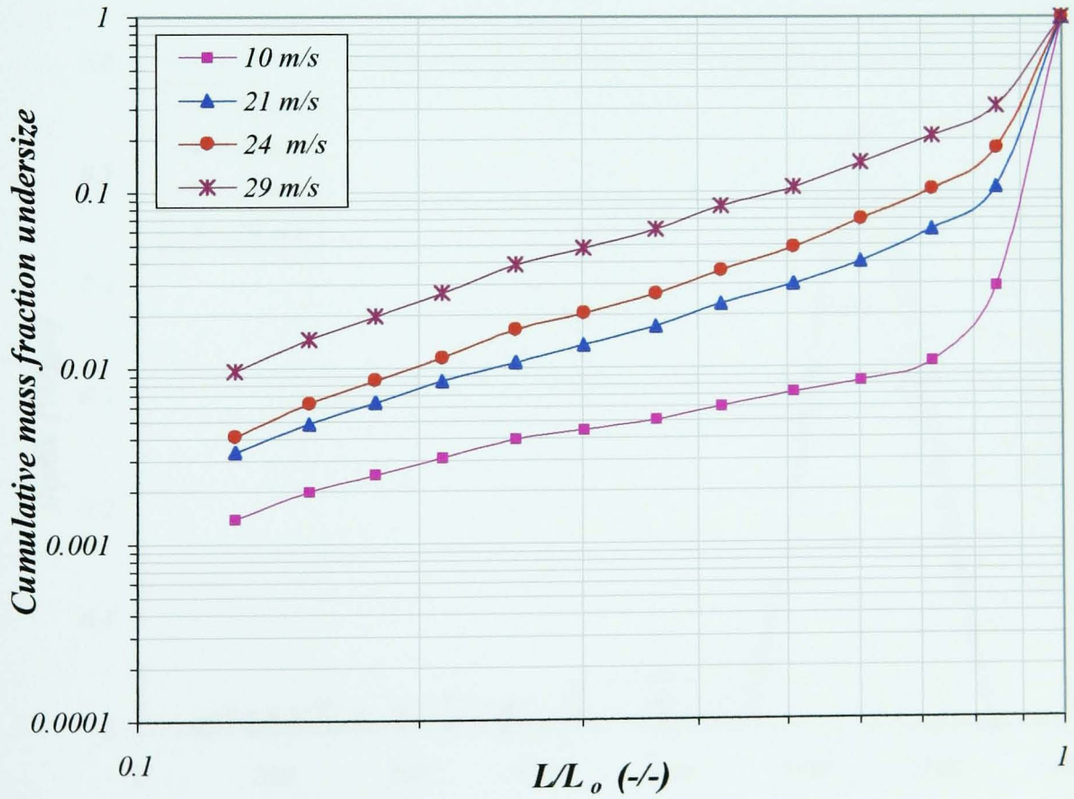

(b) Feed size of 1.00-1.18 mm

Figure 6.15: *Effect of velocity on size distribution of impact product of Sample 3.*

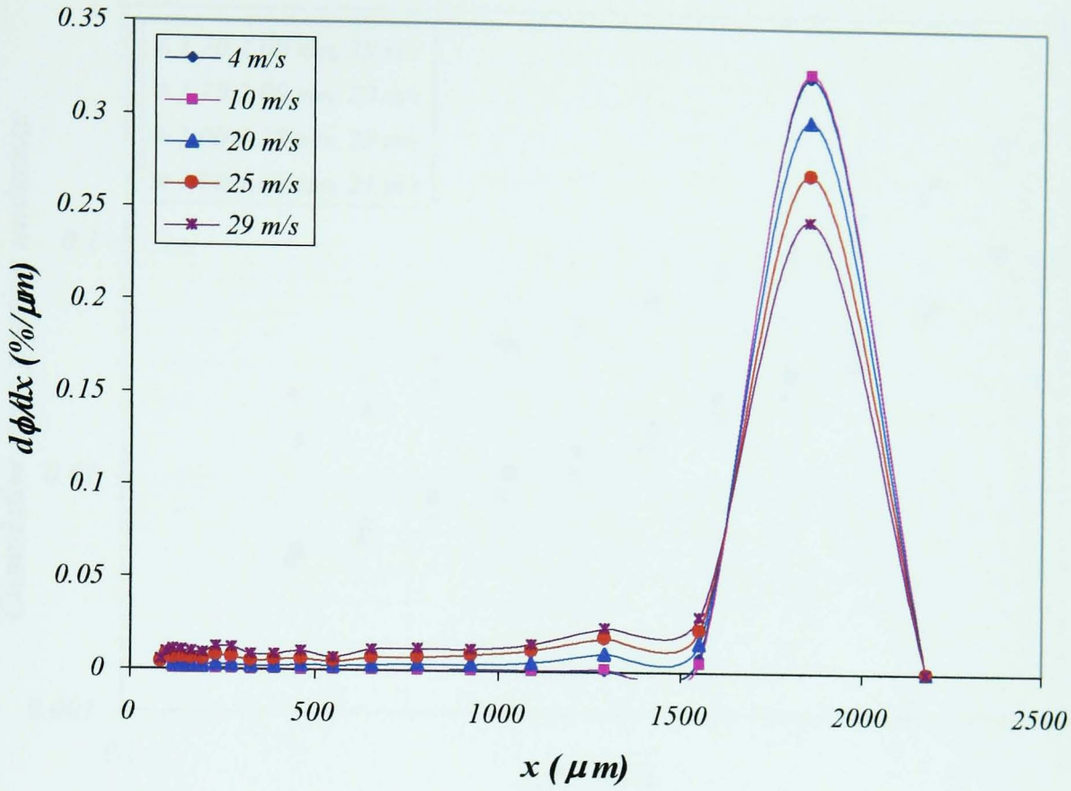

(a) Feed size of 1.70-2.00 mm

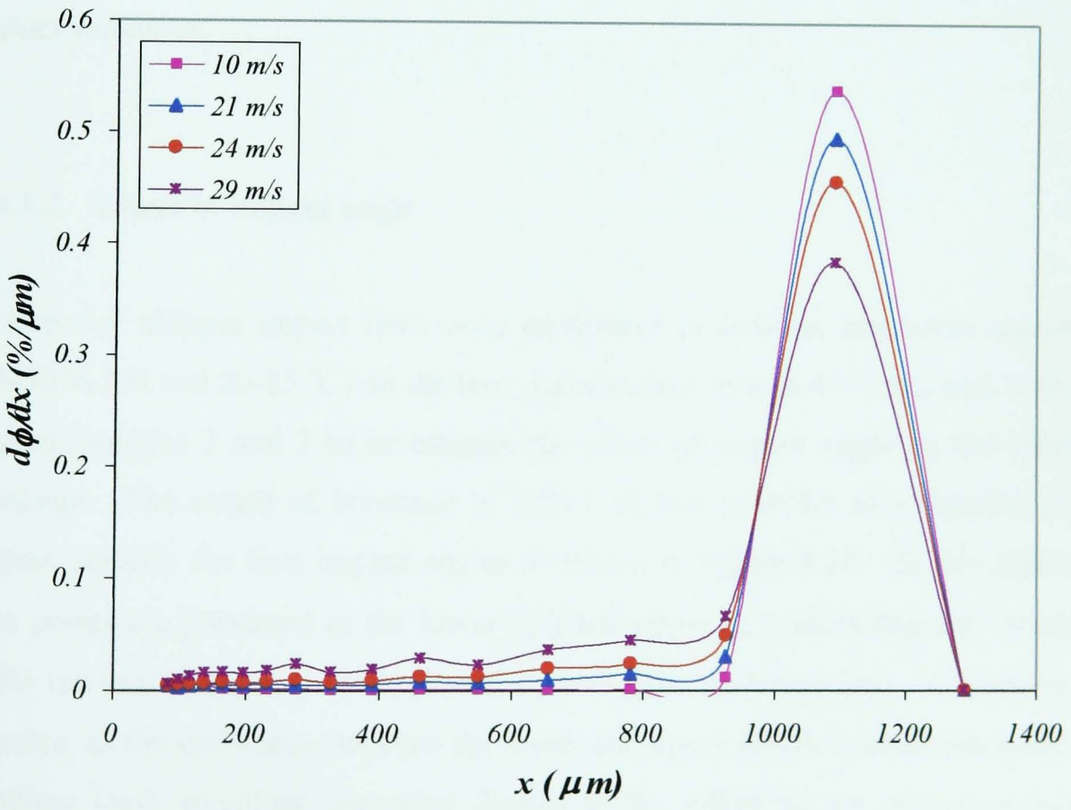

(b) Feed size of 1.00-1.18 mm

Figure 6.16: *Effect of velocity on size distribution of impact product of Sample 3.*

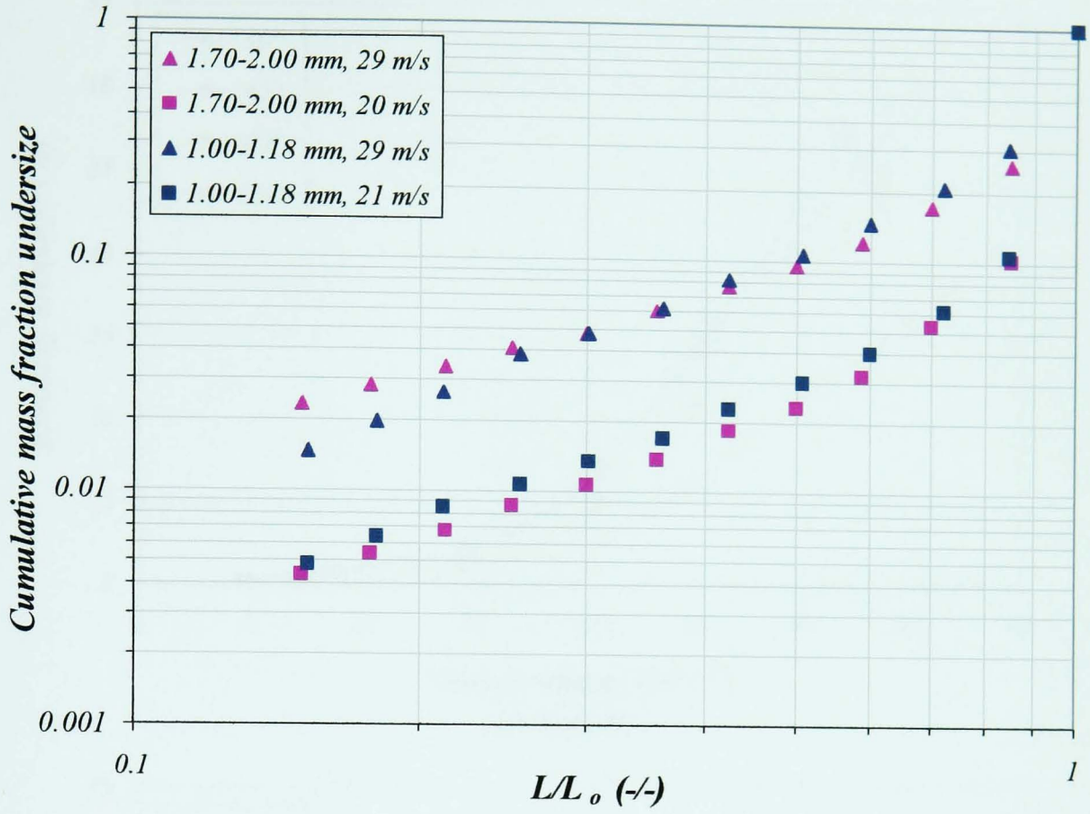

Figure 6.17: *Comparison of impact product size distribution of Sample 3 at two impact velocities.*

6.4.1.2 Effect of impact angle

A series of oblique impact tests were performed at ambient laboratory conditions (45-50 % RH and 20-25 °C) on the feed granule sizes of 0.60-0.71 mm and 1.00-1.18 mm of Samples 2 and 3 to investigate the effect of impact angle on the extent of breakage. The extent of breakage of 1.00-1.18 mm granules as a function of the impact velocity for four impact angles is shown in Figure 6.18. In this figure the data points are presented as the lower (ξ^-) and upper (ξ^+) percentages of breakage, while the trend lines have been plotted according to the lower limit of breakage. In practice, as the difference between the lower and upper limits is small (showing low handling loss), therefore, the other figures in the following are only presented in terms of the lower percentage of breakage (ξ^-).

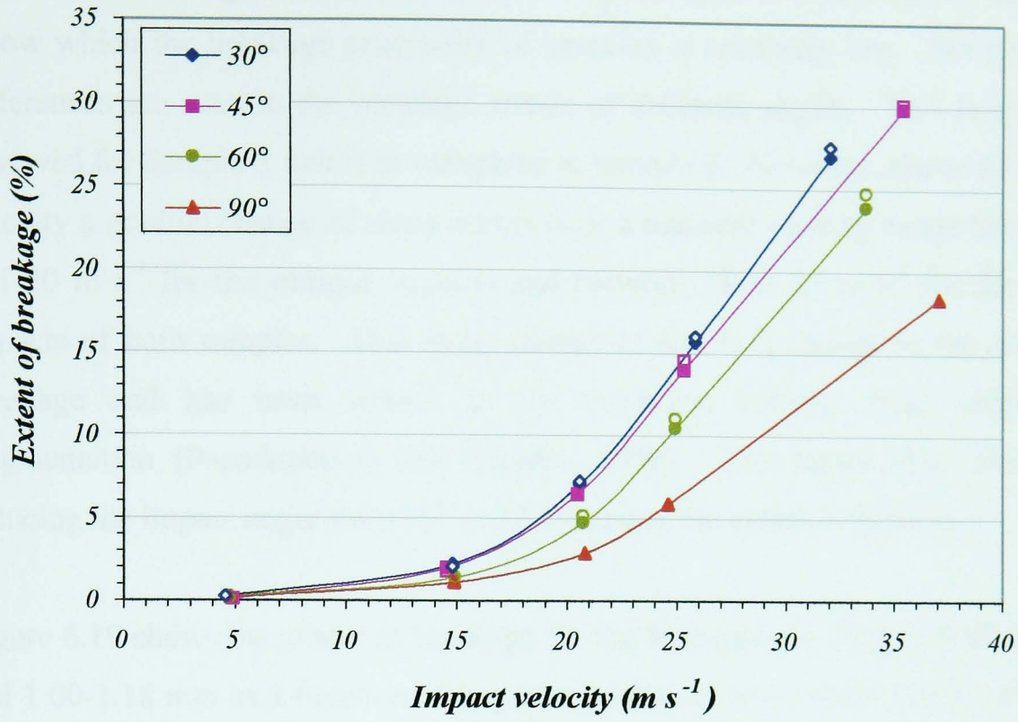

(a) Sample 2

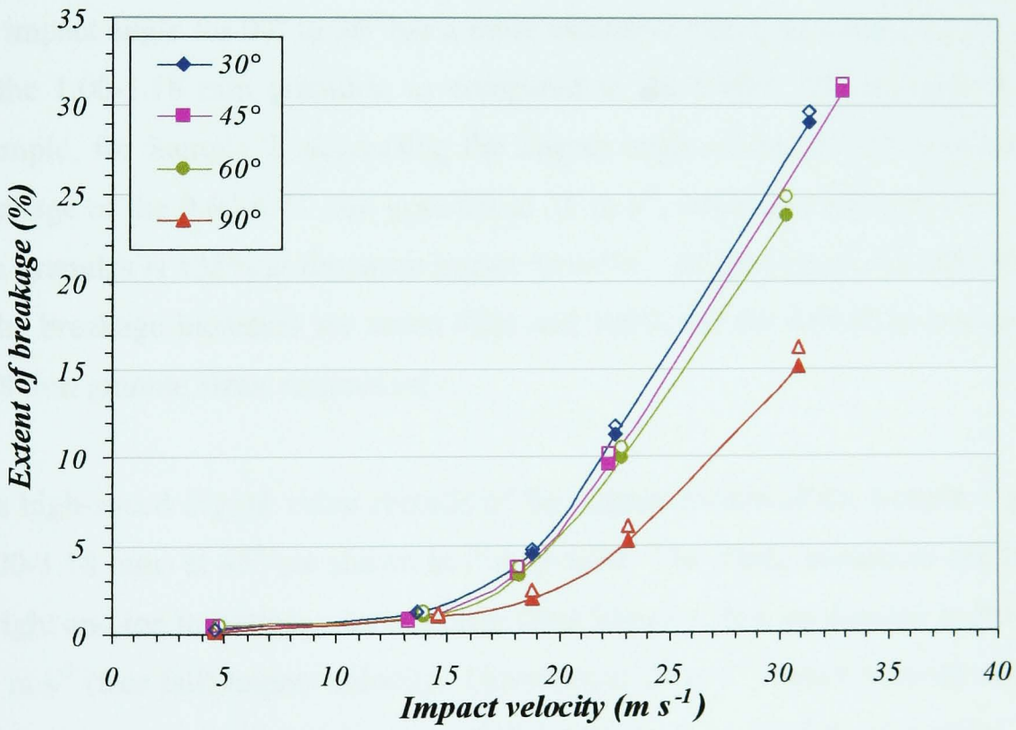

(b) Sample 3

Figure 6.18: *Lower and upper limits of the extent of breakage of 1.00-1.18 mm feed size versus impact velocity for four impact angles. a) Sample 2, b) Sample 3. Empty legends designate the upper limit and the full solid legends designate the lower limit.*

As it is seen in Figure 6.18, there is a threshold impact velocity (about 15 m s^{-1}), below which the breakage propensity of granules is relatively low. No significant differences are seen in the breakage trends of different angles. This is especially observed for Sample 3 trends as compared to Sample 2. However, above this impact velocity a gradual change of slope occurs over a transient velocity range between 15 and 20 m s^{-1} for the oblique impacts and between 18 to 23 m s^{-1} for the normal impacts of both samples. This slope change is due to a change in the regime of breakage and has been termed as the transition velocity from chipping to fragmentation (Papadopoulos and Ghadiri, 1996). The figure also reveals that reducing the impact angle from 90° to 30° increases the extent of breakage.

Figure 6.19 shows the extent of breakage for the feed granule sizes of 0.60-0.71 mm and 1.00-1.18 mm as a function of impact velocity for two impact angles of 30° and 90° of Samples 2 and 3. Comparing the results in Figure 6.19 indicates that reducing the impact angle for 90° to 30° has a more extensive effect on enhancing the damage of the 1.00-1.18 mm granules, as compared to the 0.60-0.710 mm granules. For example, for Sample 2, decreasing the impact angle causes a 70% increase in the breakage of the 0.60-0.71 mm granules at 25 m s^{-1}, while this increase for 1.00-1.18 mm granules is 138% at the same impact velocity. At the impact velocity of 30 m s^{-1}, the breakage increases are about 40% and 100% for the 0.60-0.71 mm and 1.00-1.18 mm granule sizes, respectively.

The high-speed digital video records of the impact events of the sample 3 granules (1.00-1.18 mm) at 45° are shown in Figure 6.20. The frame sequences are from left to right and top to bottom. As it is clear from Figure 6.20a, no damage is observed at 4.5 m s^{-1} (free fall) impact velocity. However, at 24 m s^{-1} impact velocity substantial breakage occurs by fragmentation of the granule to a number of smaller clusters (Fig.6.20b). Figure 6.21 shows a normal impact of a granule of Sample 3 (same size as oblique impact) at about 20 m s^{-1}. In this case, extensive chipping together with fragmentation is observed. Comparing Figures 6.20b and 6.21 shows that a more extensive damage occurs at the oblique impact inline with the data trends presented in Figure 6.18. °

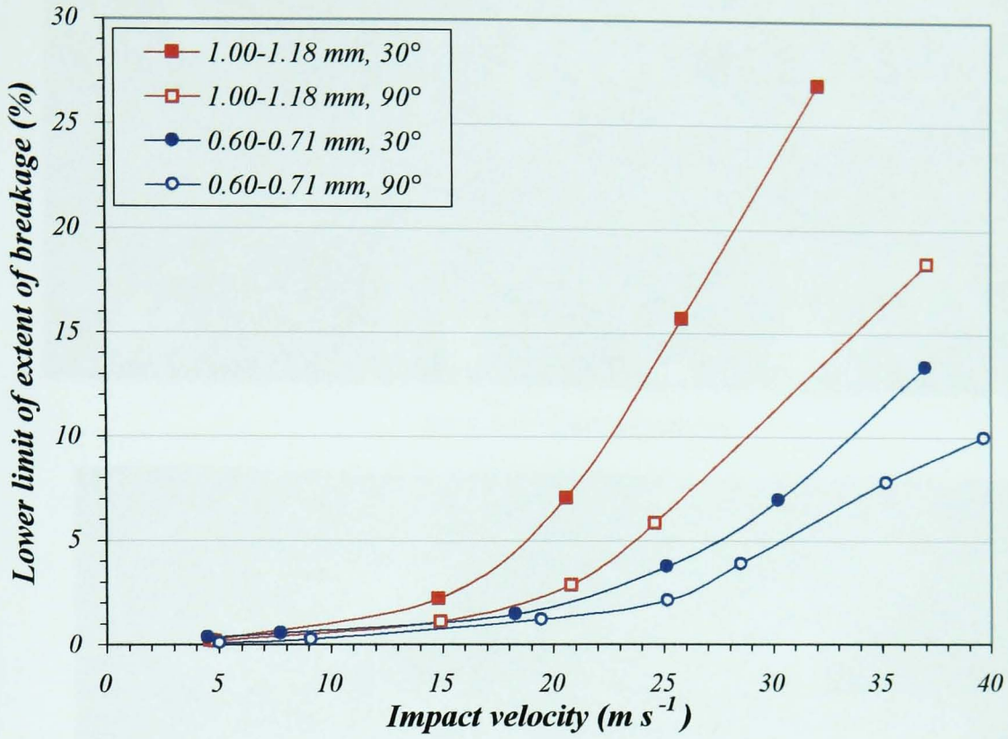

(a) Sample 2

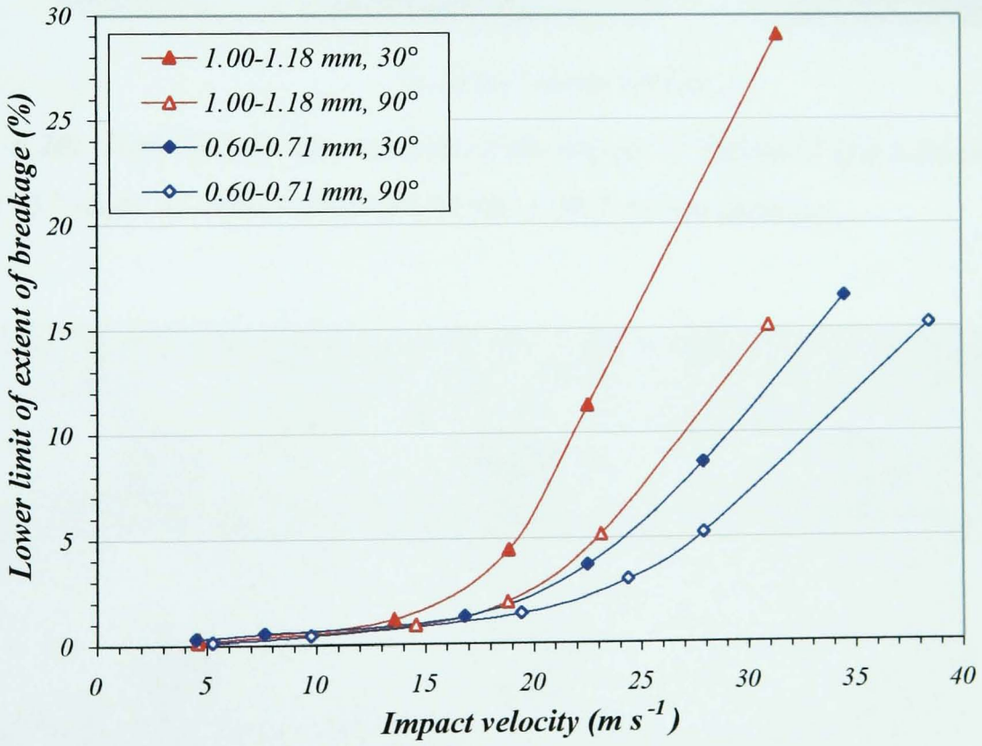

(b) Sample 3

Figure 6.19: *Lower limits of the extent of breakage versus impact velocity, presented for two impact angles of two feed sizes of 0.60-0.71 mm and 1.00-1.18 mm feed size, a) Sample 2, b) Sample 3*

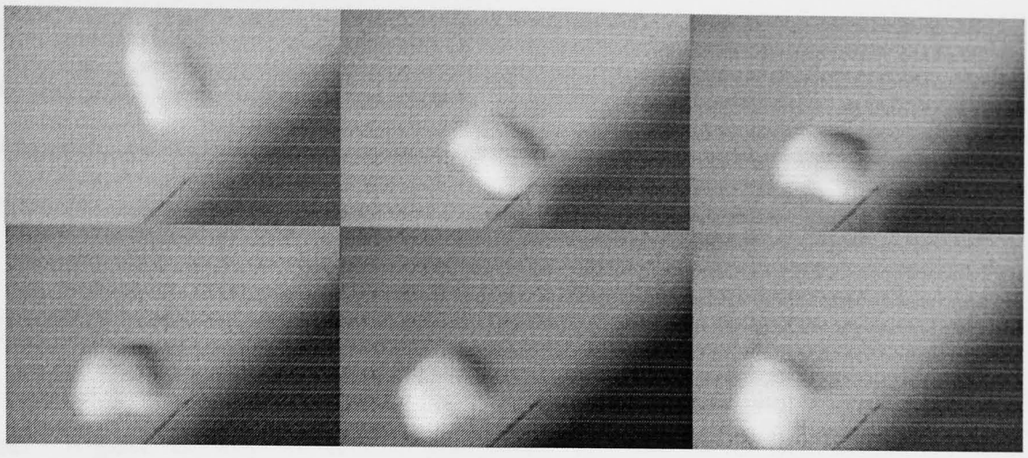

(a) 4.5 m s^{-1} impact velocity.

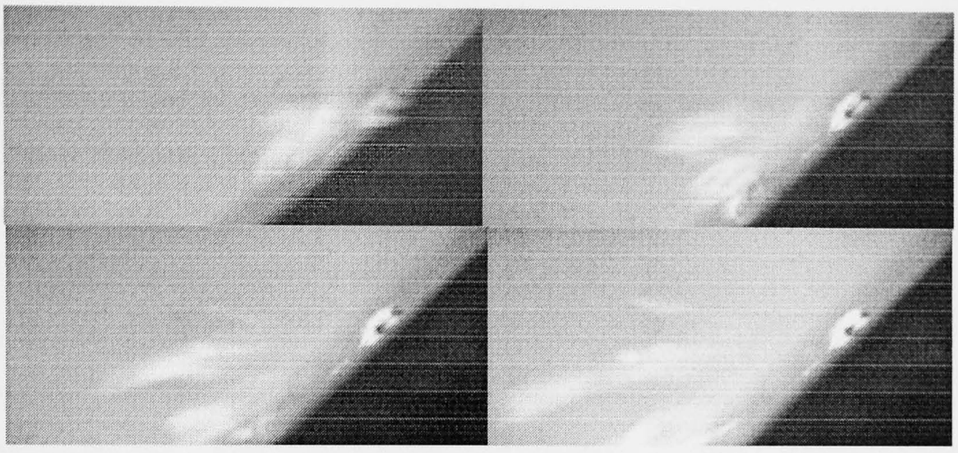

(b) 24 m s^{-1} impact velocity.

Fig. 6.20: *High-speed video records of the impact of Sample 3 granules on a target with 45 ^{o} angle of impact obtained for the 1.00-1.18 mm granules.*

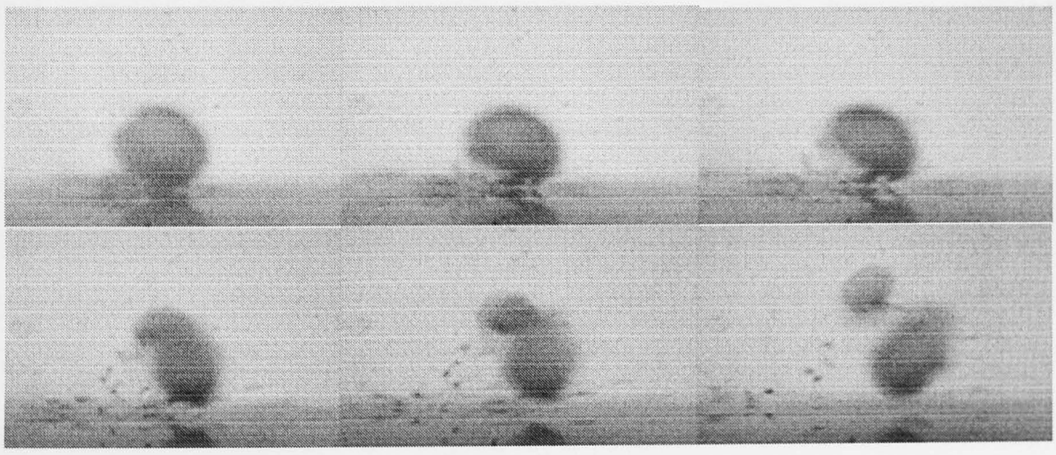

Fig. 6.21: *High-speed video records of the normal impact of a Sample 3 granule obtained for the 1.00-1.18 mm granule size at about 20 m s^{-1}.*

Full sieve analysis of the impact products are presented in Figure 6.22 in two ways, where the effects of the impact angle and velocity on the size distribution of the impact products are shown for Sample 3 granules (1.00-1.18 mm). Similar trends are observed for Sample 2 granules, which are presented in Appendix B (Figure B3).

In Figure 6.22a, the cumulative mass fraction undersize of the impact products have been drawn as a function of the normalised sized, for two impact velocities and angles. Figure 6.22b, illustrates the same results as Figure 6.22a but in mass frequency per particle size range. In Figure 6.22b, at 15 m s^{-1} impact velocity, the size distribution of the impact products is seen around the feed size, and they overlap for the impact angles of 90° and 30°. In Fig. 6.22a, chipping is recognised for 15 m s^{-1} as there is a sharp slope change. However, at 32 m s^{-1}, where the fragmentation consistently occurs, the slope change disappears and the two straight lines with distinct slopes become almost a single line. At this velocity the impact products are distributed over a wide sieve sizes (Fig. 6.22b). As it is seen in Fig. 6.22a, at 32 m s^{-1}, the extent of breakage is higher over all sieve sizes for the impact angle of 30° as compared to the 90°. This is particularly noticeable for impact velocity of 32 m s^{-1}, although marginal difference also prevails at 15 m s^{-1}. This is an interesting behaviour, which has so far only been observed for these granules.

Figure 6.23 shows images obtained by reflected light microscopy (RLM) of the mother particles and debris produced from 1.00-1.18 mm feed size granules of Sample 3. In these experiments, mother particles and debris were separated by a 710 μm BS standard sieve, which is two standard sizes smaller than the feed size of 1.00-1.18 mm. Therefore, the granules larger and smaller than this size are nominated as mother particles and debris, respectively. The microscopic images show clearly the occurrence of chipping and a low extent of breakage at 15 m s^{-1} and fragmentation at 32 m s^{-1} for both impact angles. Figure 6.23 also indicates qualitative differences of the shape of the breakage products between the two angles of 30° and 90° at 32 m s^{-1}.

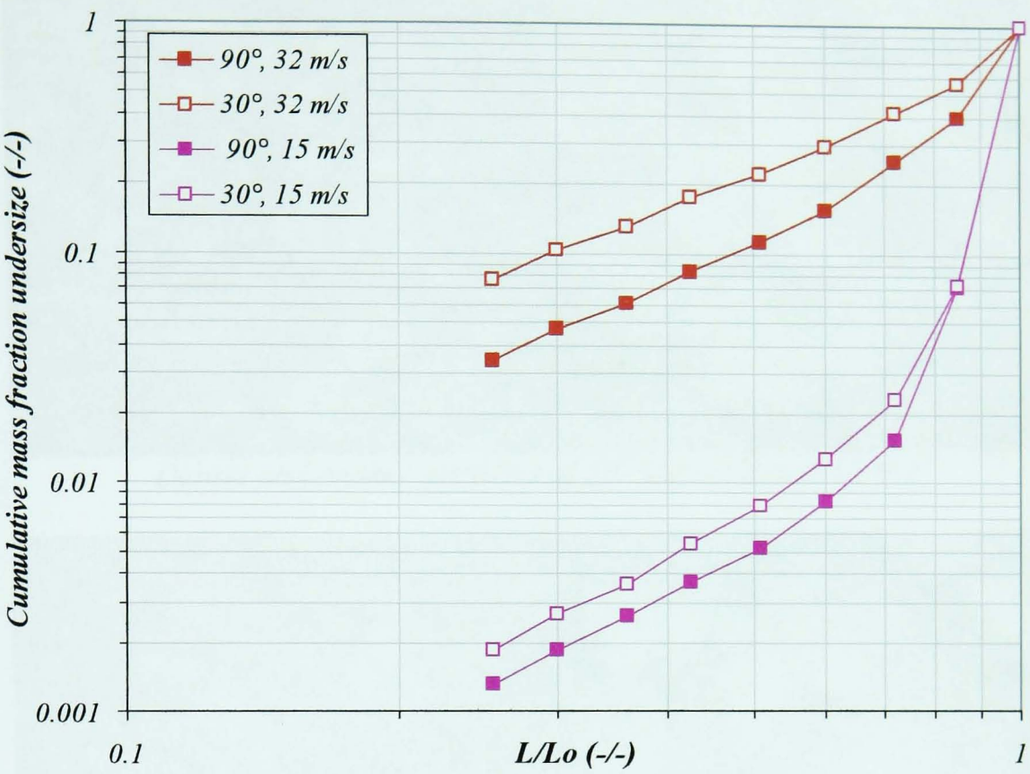

(a)

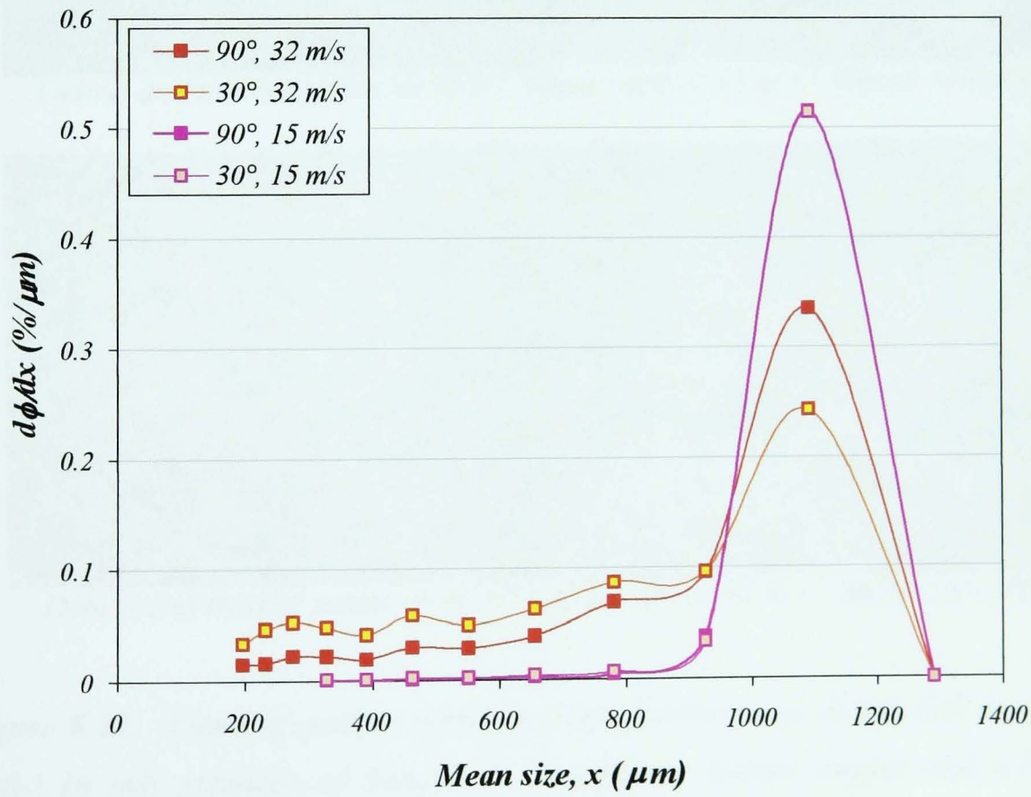

(b)

Figure 6.22: *Effect of the impact angle and velocity on the size distribution of impact products of 1.00-1.18 mm feed size of Sample 3 granules.*

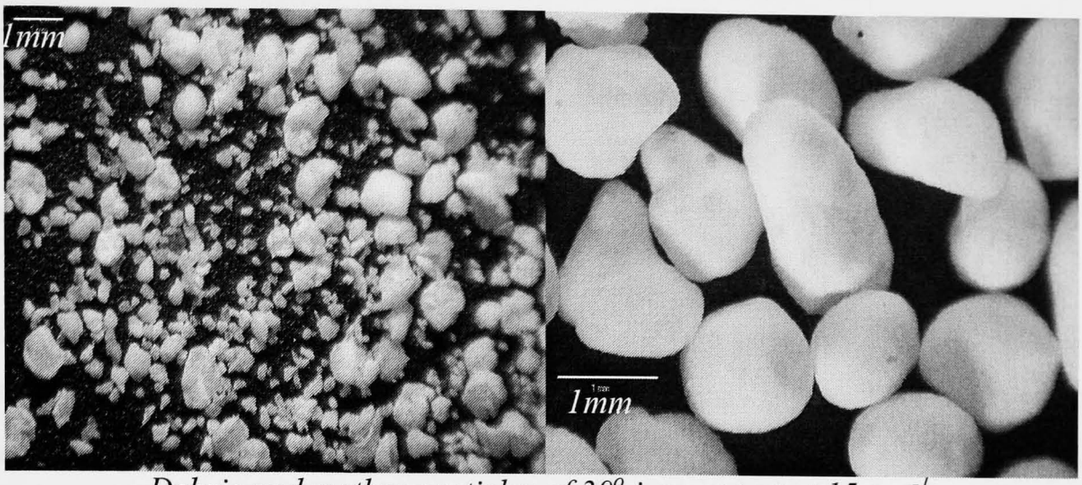

Debris and mother particles of 30° impact test at 15 m s^{-1}

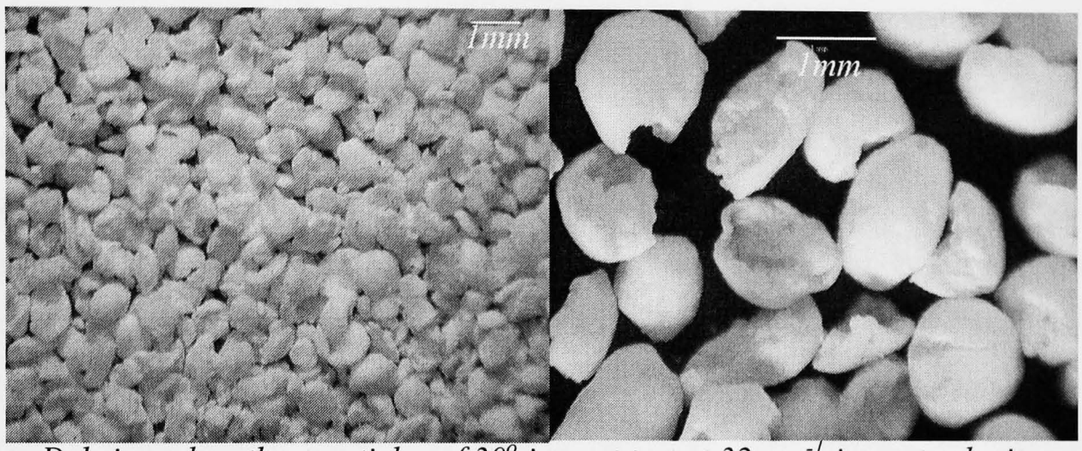

Debris and mother particles of 30° impact test at 32 m s^{-1} impact velocity

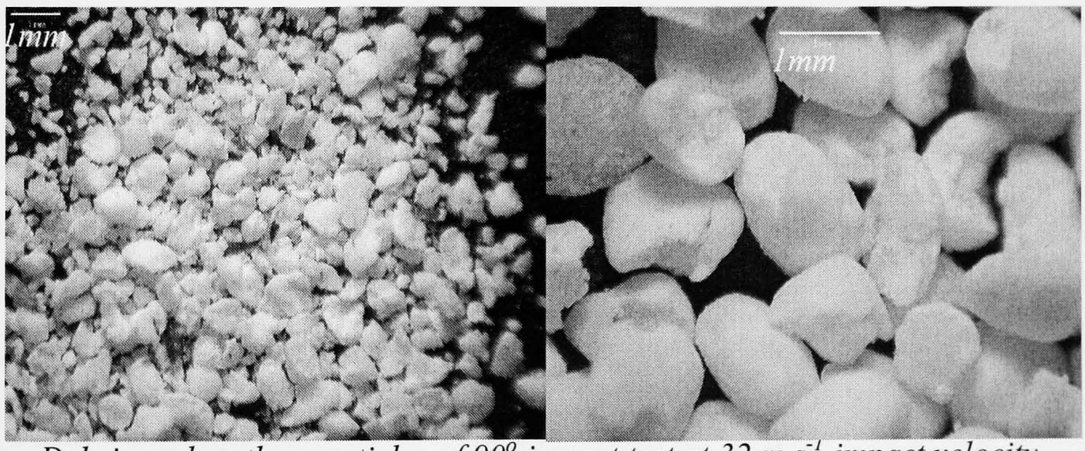

Debris and mother particles of 90° impact test at 32 m s^{-1} impact velocity

Figure 6.23: *Views of mother particles (right images) and debris (left images) of 1.00-1.18 mm granules of Sample 3, at different impact angles and velocities, obtained by reflected light microscopy.*

6.4.1.3 Effect of temperature and moisture content of granules

To investigate the effects of temperature and moisture content on the extent of breakage, a number of single impact tests were performed on the fresh granules of Sample 3 at different conditions.

The effect of temperature on the breakage of 0.60-0.71 mm and 1.00-1.18 mm feed sizes are shown in Figure 6.24. Normal impact tests were performed on the samples, which were kept for a few days at –20 °C (in the freezer), +4 °C (in the refrigerator) and 24 °C (in the laboratory ambient temperature). Great care was taken during handling of the samples from sub-ambient chambers to the rig to keep the temperature of samples constant by insulating each sample's container and by performing the tests rapidly. The time elapsed for carrying the sample to the rig was less than a minute and the residence time of each particle in the impact rig before impact was about 0.03-0.25 second depending on the impact velocity. There is some temperature rise in the agglomerate during the impact process. Kwan (2003) has conducted detail analysis of warming up effect during impact on her particles stored at –20 °C using similar impact rigs used in this work. By coupling the effects of conduction within a particle and forced convection at the surface of the particle, Kwan (2003) reported that the surface of 180-212 μm microcrystalline cellulose and 355-425 μm α-lactose monohydrate particles had warmed up from the initial temperature of –20 °C to –1 °C and 7 °C, respectively, at the time of impact. However, the cores of these two samples still remained close to the initial temperature of –20 °C due to low heat conductivity of these samples. The agglomerates that had been subjected to sub-ambient impact testing in this work are considerably larger than those used by Kwan (2003). Thus it is believed that the warming up of these samples at time of impact should be negligible. The results presented in the following also show clearly the effect of the cooling of samples to –20 °C on breakage approving negligible effect of warming up of the particles.

As it is observed in Figure 6.24 that there is no significant difference in the breakage of granules kept at the +4 °C and ambient temperature. However, decreasing the temperature to –20 °C causes a major increase in the extent of breakage of the feed

granule sizes. The SEM image of a broken granule kept at the –20 °C was previously shown in Chapter 5 (Figure 5.15a), showing a meridian breakage along with local disintergration of the impact site similar to brittle breakage pattern. It seems, cooling the granules to –20 °C reduces deformability behaviour of the granules during impact. Coupling this to the presence of the large pre-existing internal flaws leads to the observed brittle breakages. Therefore, it can be concluded that for these granules there exists a transition temperature in mode of breakage from semi-brittle to brittle, which is thought to be between –20 °C and +4 °C.

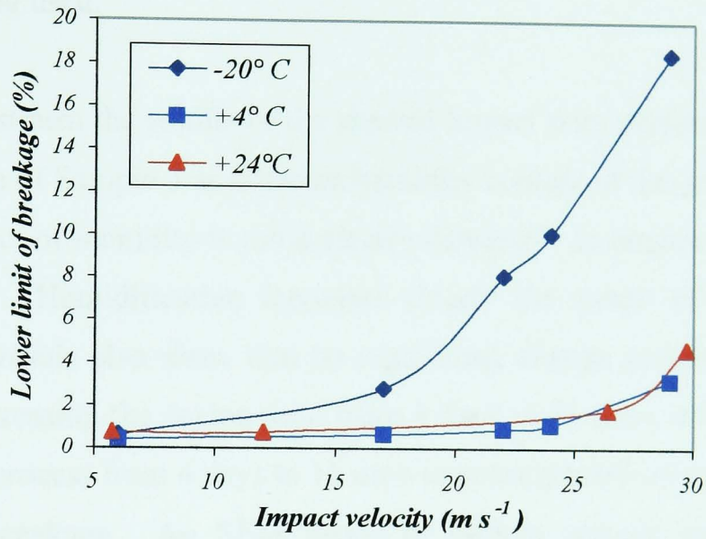

(a) feed granule size of 0.600-0.710 mm

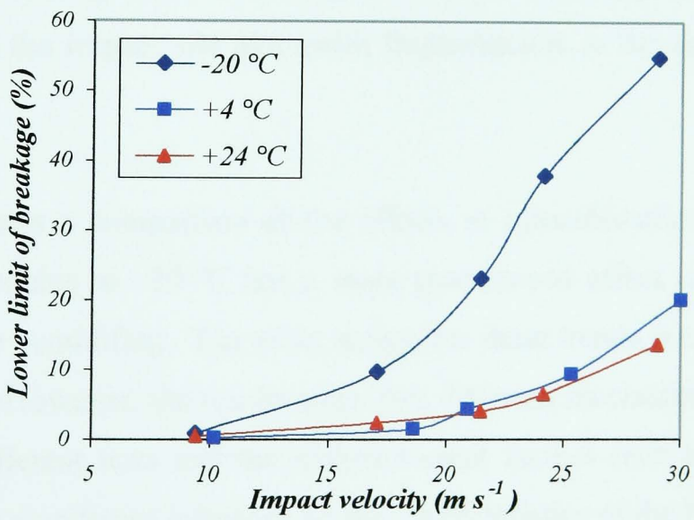

(b) Feed size granule of 1.00-1.18 mm

Figure 6.24: *Effect of temperature on extent of breakage of Sample 3 granules.*

To investigate the effect of exposure to different humidity conditions on the extent of breakage, granules with 1.00-1.18 mm sieve size were kept in three different humidity conditions. These samples are termed as dried (kept at dried atmosphere),

humidified (kept at about 80% RH) and ambient (kept at laboratory ambient humidity) all at room temperature. For obtaining a dried sample, granules were placed in an airtight container together with dry silica gel. For humidified sample, the granules were exposed to about 80% RH atmosphere (established by a saturated sodium carbonate solution in an airtight container) at room temperature. The ambient sample was obtained by keeping the granules in the ambient laboratory conditions (45-50% RH and 20-25 °C). The humidified and dried samples were exposed to the above-mentioned conditions in the airtight chambers for 4 and 11 days before being used.

Figure 6.25 illustrates the results of the normal impact tests performed on 1.00-1.18 mm granule size of Sample 3 at different humidity content of the granules. As it can be seen the effect of humidity is more clearly detectable at impact velocities greater than 17 $m\,s^{-1}$. Humidification increases clearly the extent of breakage of the granules. The resuls also show that no significant change occurs in the extent of breakage by increasing the drying time from 4 days to 11 days, while extending the humidification process from 4 days to 11 days is accompanied by further increases of the extent of breakage. An SEM image of broken granule kept at humidified condition was already shown in Figure 5.15b. The figure shows extensive deformation on the impact site alongwith fragmentaion as the dominant pattern of failure.

Fiugre 6.26 shows a comparison of the effects of humidification and temperature. Cooling the granules to –20 °C has a more pronounced effect on the breakage, as compared to the humidifing. The exact reason for these trends is not well understood at the moment. However, the results show that different mechanisms of breakage are operating in different tests and the environmental factors such as temperature and humidity have a significant influence on the characteristics of the bonds.

It was already shown that fresh granules of Samples 2 and 3 are highly water absorbent so that even during impact tests under ambient conditions the mass increase of materials was noticeable. This affected the breakage analysis as a shift in the priority of lower and upper limits of breakage (section 6.4.1.1). However, for the

samples kept under the same ambient conditions for a period of time (e.g. six months) the priority of upper limit over lower limit of breakage was as expected (section 6.4.1.2). The comparison of the impact tests results performed under the similar conditions (e.g. normal impact of 1.00-1.18 mm granules of Sample 3, Figures 6.7 and 6.18) but at two different times shows some differences in the extent of breakage. This means that aging has an effect on the extent of breakage change. However, the quantitative trends are not affected.

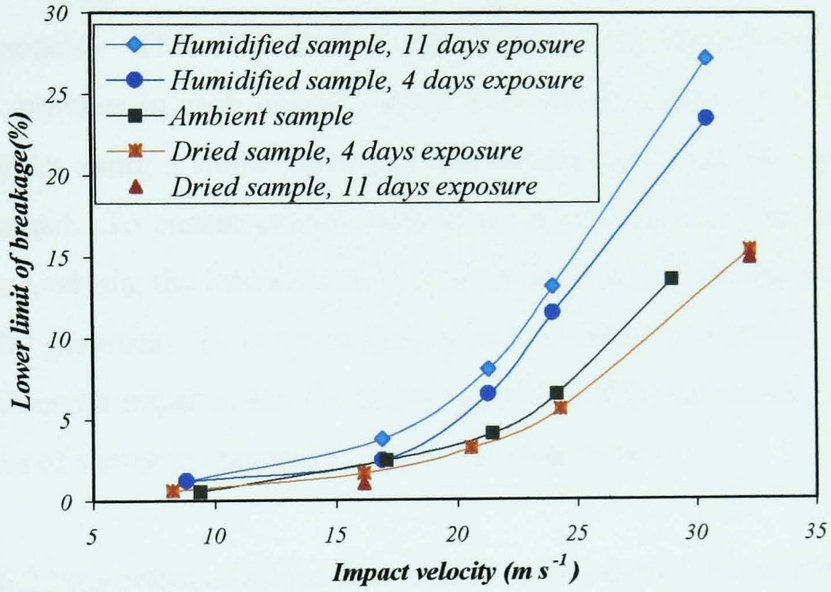

Figure 6.25: *Effect of moisture content of granules on extent of breakage of 1.00-1.18 mm feed granule size of Sample 3.*

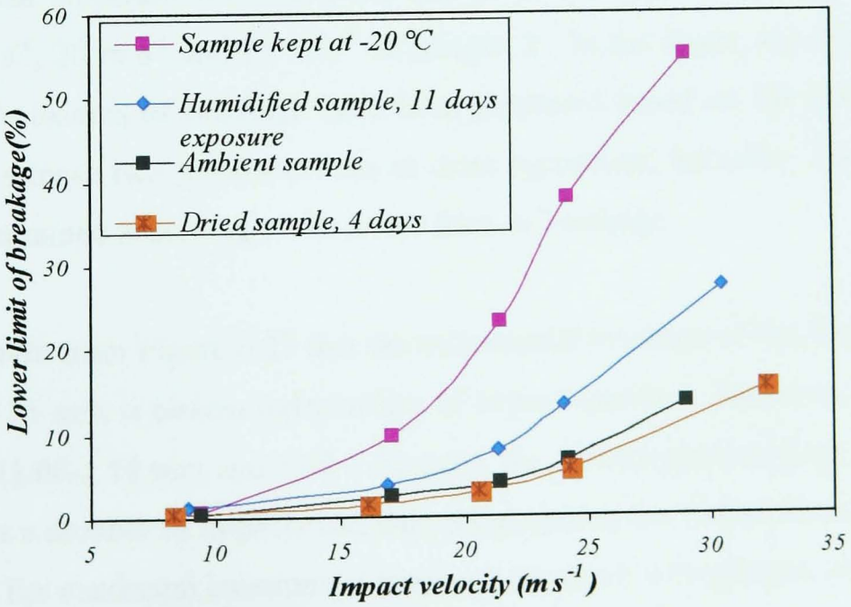

Figure 6.26: *Effect of temperature and moisture content of granules on extent of breakage of 1.00-1.18 mm feed granule size of Sample 3.*

6.4.2 Repeated impact test results

Repeated impact tests were conducted on Samples 2 and 3, employing the single sieve analysis procedure. For each type of sample, a matrix of parameter pairs consisting of initial feed size and impact velocity was set to test the sizes of 0.60-0.71 mm, 1.00-1.18 mm and 1.70-2.00 mm, and the velocities of 15 m s^{-1}, 20 m s^{-1} and 25 m s^{-1}. In practice, 18 repeated impact tests were carried out and in each test, granules were subjected to minimum 10 repeated impacts (in some tests up to 20 repeated impacts). Therefore, totally, 240 impacts were carried out, using a large number of granules in each impact. After each impact, debris was separated from impact product using a single sieve and mother particles were recycled as feed for the next impact. To ensure enough number of granules for all impacts and reliable gravimetric analysis, the initial mass of feed to the first impact was set equivalent to about 10000 granules. In some experiments, the debris product of the first, fifth, tenth and fifteenth impacts, and the mother particles of the last impact were analysed with a series of sieves to characterise their size distribution.

In Figure 6.27 the effect of initial feed size on incremental (ξ_n) and cumulative ($\xi_{c(n)}$) breakage and average incremental breakage per impact (k_n) of Sample 2 granules are shown for 20 repeated impacts at about 15 m s^{-1} impact velocity. Similar figures are shown in the Appendix B (Figures B4-B8) for 20 m s^{-1} and 25 m s^{-1} of Sample 2 and for 15 m s^{-1}, 20 m s^{-1} and 25 m s^{-1} of Sample 3. In the figure, the incremental and cumulative extents of breakage have been presented based on the lower and upper limits. As these two parameters are in close agreement, hereafter, the other results are just presented according to the lower limit of breakage.

It is apparent from Figure 6.27 that the incremental breakage of the feed granule size of 0.60-0.71 mm is almost independent of impact number. However, for the larger granules (1.00-1.18 mm and 1.70-2.00 mm), the incremental breakage increases to a peak after a number of impacts and then drops during the further impacts. For these granules, the maximum incremental breakage increases with granule size.

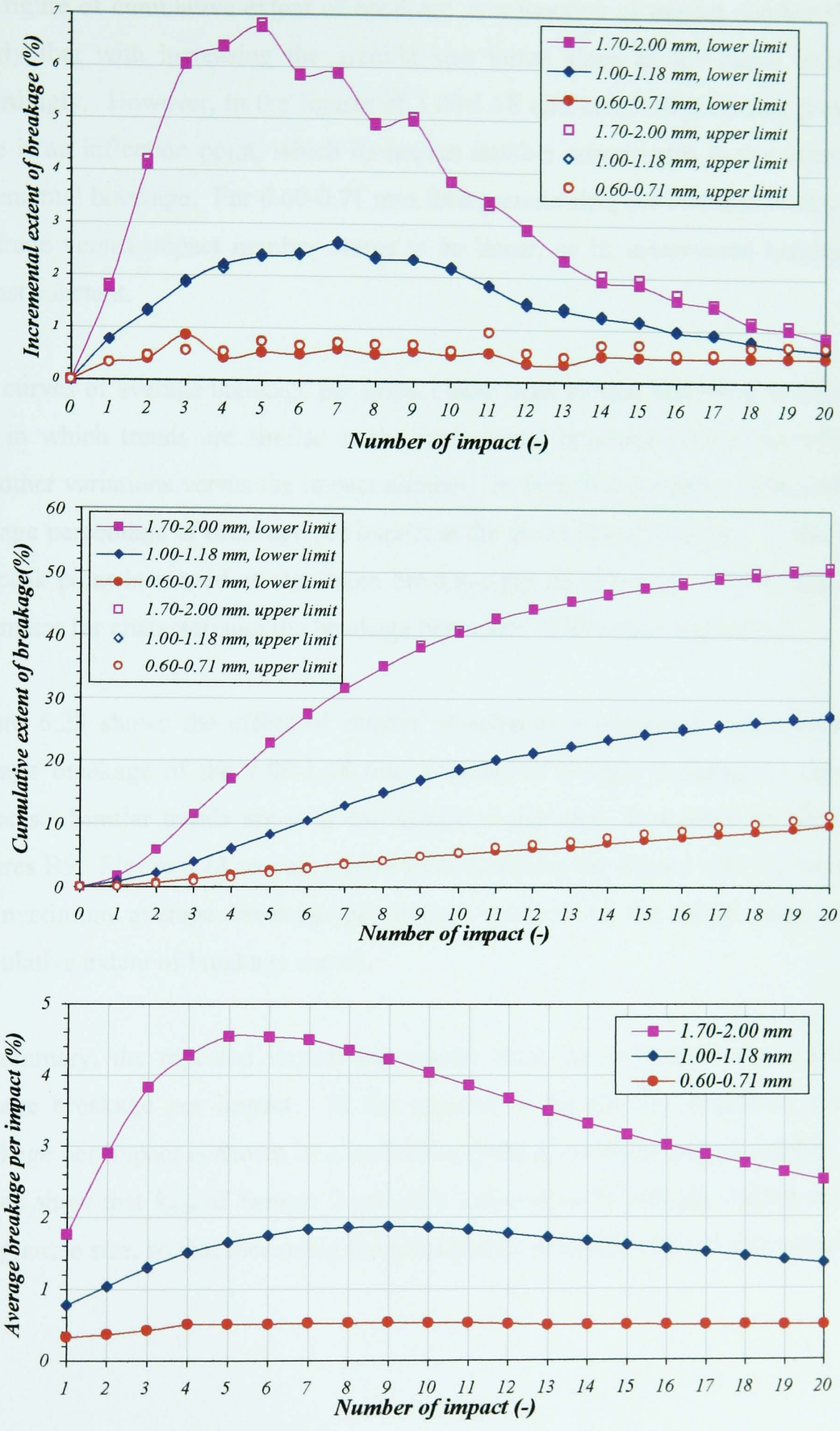

Figure 6.27: *Effect of feed size on incremental and cumulative breakage, and average breakage per impact of Sample 2 granules at impact velocity of 15 m* s^{-1}.

The figure of cumulative extent of breakage as a function of impact number shows clearly that with increasing the granule size initial slope of the curve increases accordingly. However, in the figures of 1.00-1.18 mm and 1.70-2.00 mm granules, there is an inflection point, which its impact number corresponds to the maximum incremental breakage. For 0.60-0.71 mm feed granule size, the cumulative extent of breakage versus impact number seems to be linear, as its incremental breakage is almost constant.

The curves of average breakage per impact have been plotted according to Equation 6.7, in which trends are similar as the incremental breakage curves but with the smoother variations versus the impact number. In fact, this parameter represents the average percentage of breakage per impact at the given impact number. In this case, the peak point is termed as maximum breakage per impact, k_{max}. This is important parameter for characterising the breakage behaviour of this type of granules.

Figure 6.28 shows the effect of impact velocity on incremental, cumulative and average breakage of the 1.00-1.18 mm granules of Sample 2 during 13 repeated impacts. Similar trends are seen for Sample 3 granules, as it has been shown in Figures B9. Figure 6.28 reveals clearly that increasing the impact velocity increases the maximum average breakage per impact, as well as the initial slope of the cumulative extent of breakage curves.

In summary, the repeated impact test results show the existence of a maximum average breakage per impact. In the cumulative curves, the maximum average breakage per impact is shown by a deflection point at the same impact number. The results show that k_{max} of Sample 2 granules varies directly with the impact velocity and granule size, so that increasing the granule size or impact velocity increases k_{max}.

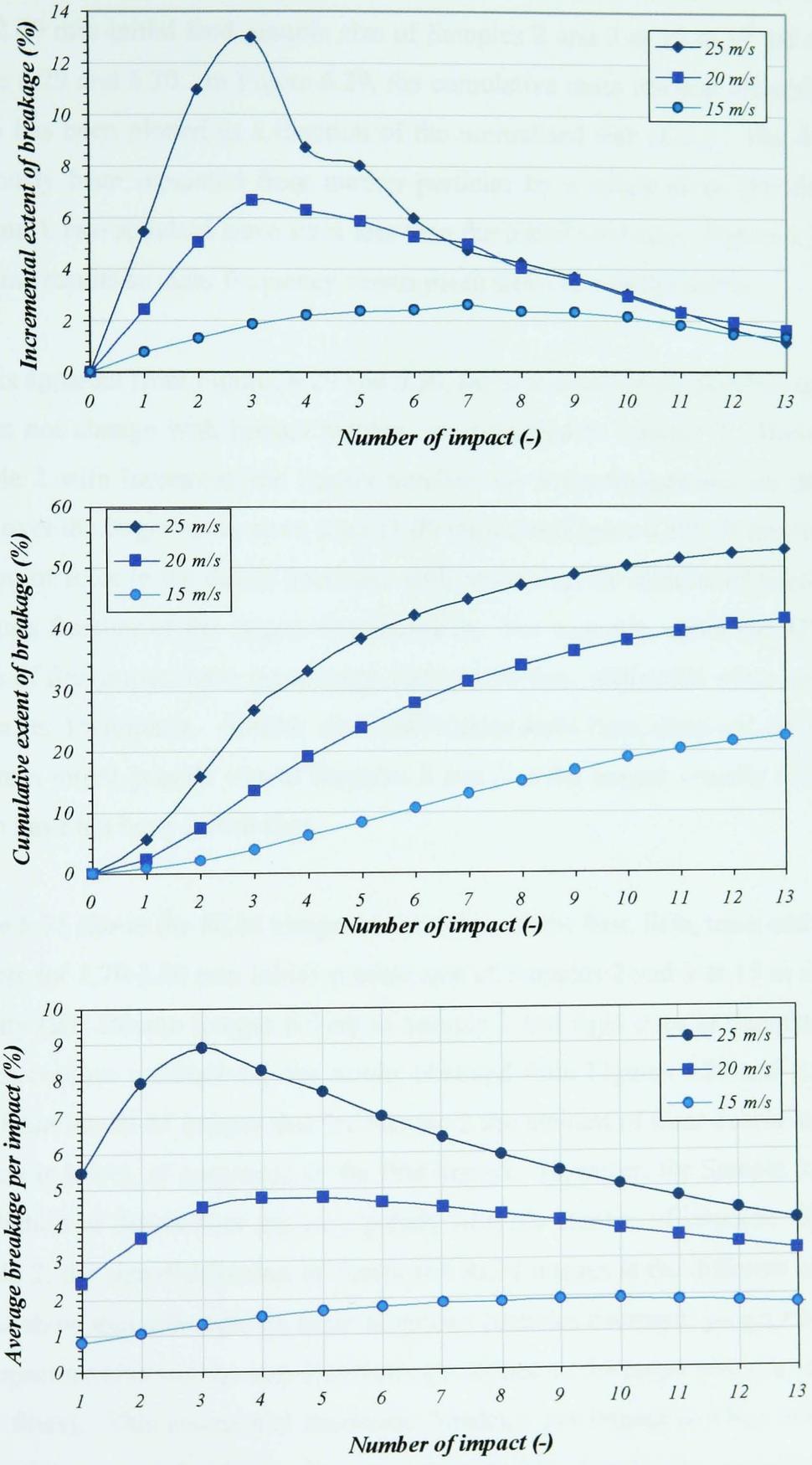

Figure 6.28: *Effect of impact velocity on incremental, cumulative breakage and average breakage per impact of 1.00-1.18 mm feed granule size of Sample 2.*

The size distribution of debris of the first, fifth, tenth and fifteenth impacts of the 1.70-2.00 mm initial feed granule size of Samples 2 and 3 at 15 m s^{-1} are shown in Figure 6.29 and 6.30. In Figure 6.29, the cumulative mass fraction undersize of the debris has been plotted as a function of the normalised size (L/L_o). The debris has previously been separated from mother particles by a single sieve (for these tests 1.18 mm), two standard sieve sizes less than the initial feed size. Figure 6.30 shows the same results as mass frequency versus mean sieve size of the debris.

As it is apparent from Figures 6.29 and 6.30, the size distribution of debris of Sample 3 does not change with impact number, as compared to Sample 2. However, for Sample 2 with increasing the impact number, the mass frequencies are distributed more over the larger mean sieve sizes (1.09 mm) (see Figure 6.30). It means that the amount of fines in the debris decreases with increasing the number of impact whilst the mass fraction of the largest size increases. For example, about the 42% of the debris of first impact have the average size of 1.09 mm, whilst this value increases to 67% after 15 impacts. Similar size distributions have been observed for the 1.70-2.00 mm initial granule size of Samples 2 and 3 at the impact velocity of 25 m s^{-1}, which have not been shown here.

Figure 6.31 shows the RLM images of the debris of the first, fifth, tenth and fifteenth impacts for 1.70-2.00 mm initial granule size of Samples 2 and 3 at 15 m s^{-1} impact velocity (left column images belong to Sample 2 and right ones to Sample 3). The images confirm qualitatively the results obtained from Figures 6.29 and 6.30. It is clear from the RLM images that for Sample 2 the amount of finer debris in the later impacts is lower, as compared to the first impact. However, for Sample 3, the size distribution of debris does not vary greatly with the number of impacts. In fact for Sample 2, the size distribution of debris and RLM images at the different number of impact show that although the mass of mother particles decreases progressively with the impact number but the size distribution is shifted to the larger size (i.e. producing fewer fines). This means that maximum breakage per impact is a key point above which the rate of breakage decreases presumably due to the consolidation of granules.

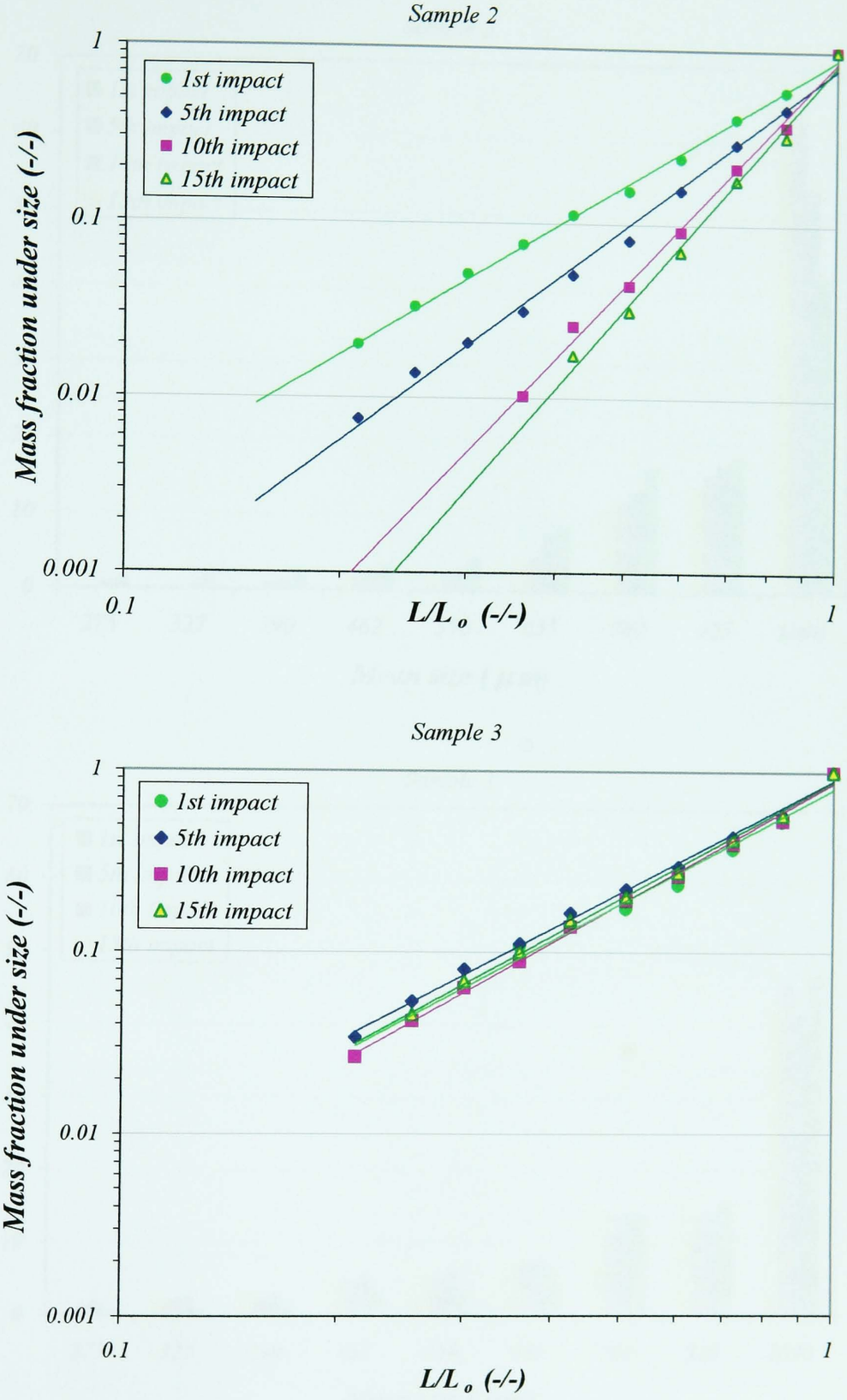

Figure 6.29: *Size distribution of debris (less than 1.18 mm) of samples with initial feed granule size of 1.70-2.00 mm impacted at 15 m* s^{-1}.

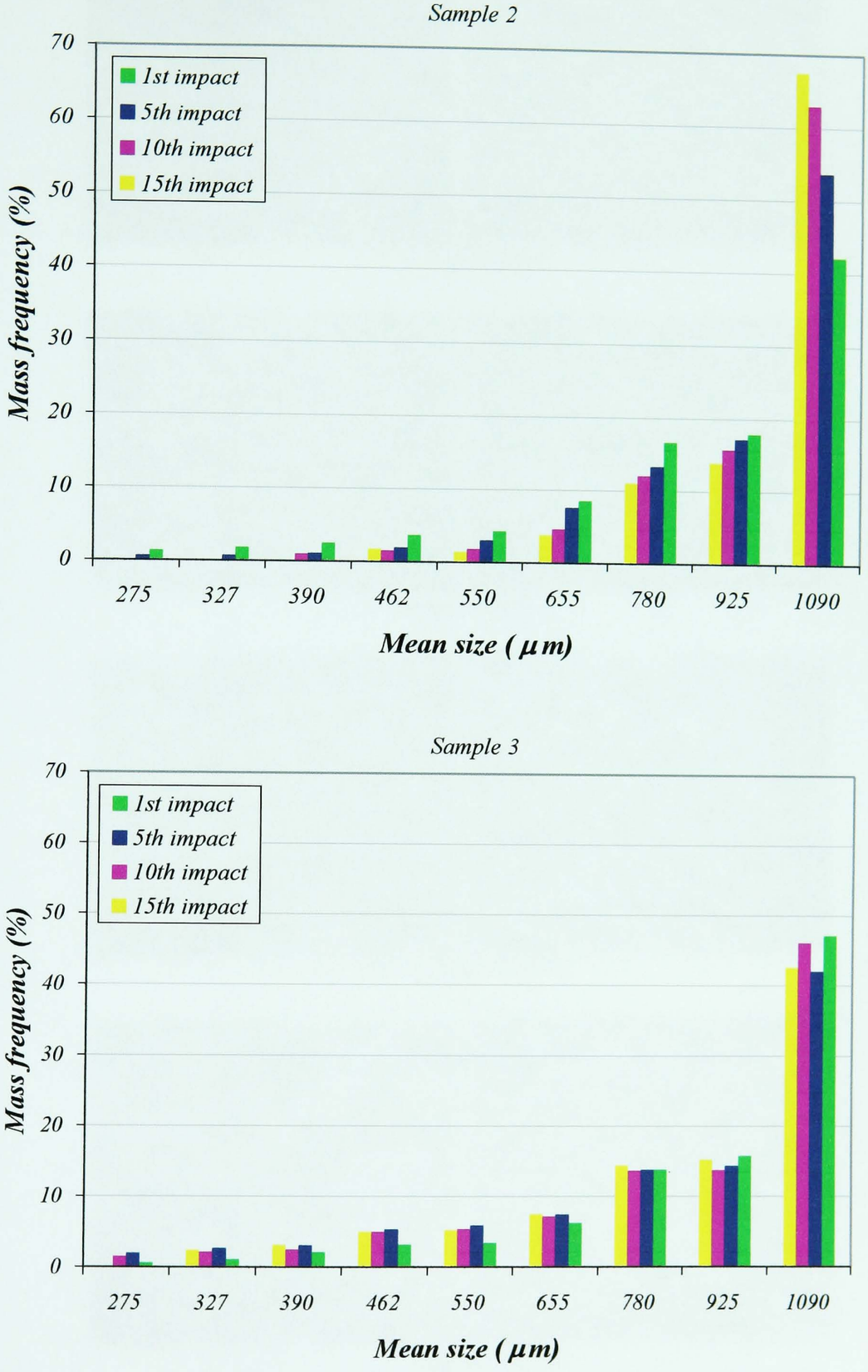

Figure 6.30: *Mass frequency of debris (less than 1.18 mm) of samples with initial feed granule size of 1.70-2.00 mm, impacted at average 15 m* s^{-1}.

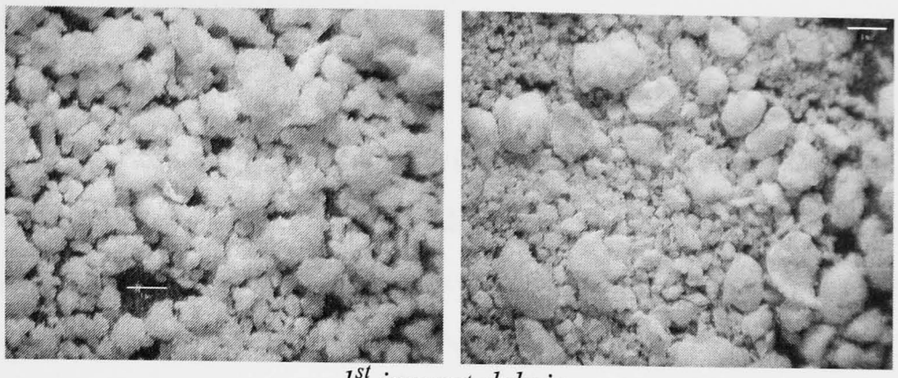

1st impact debris

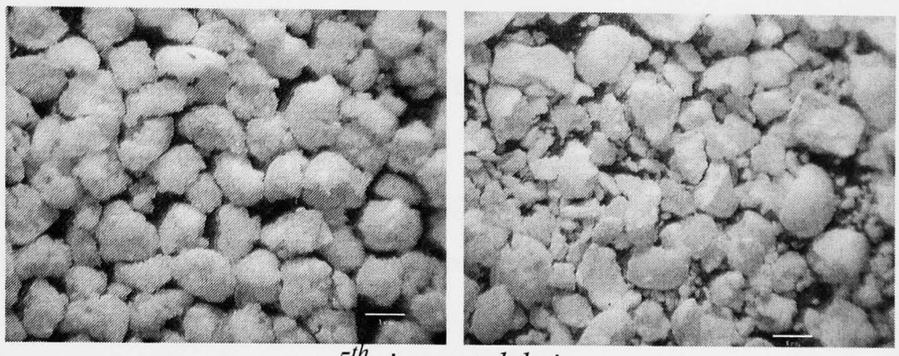

5th. impact debris

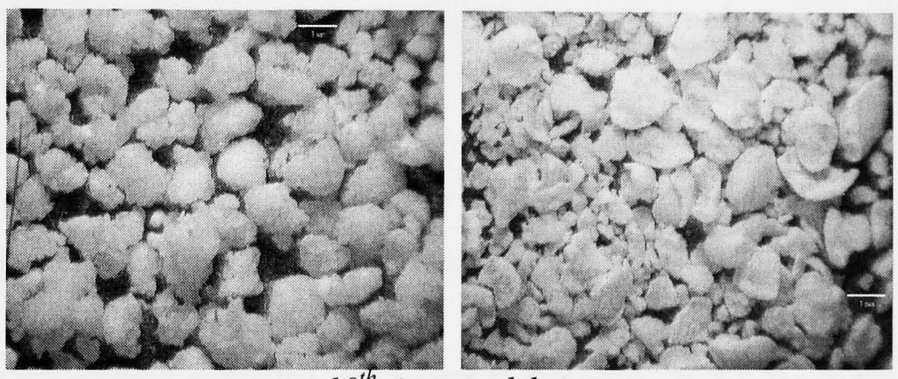

10th. impact debris

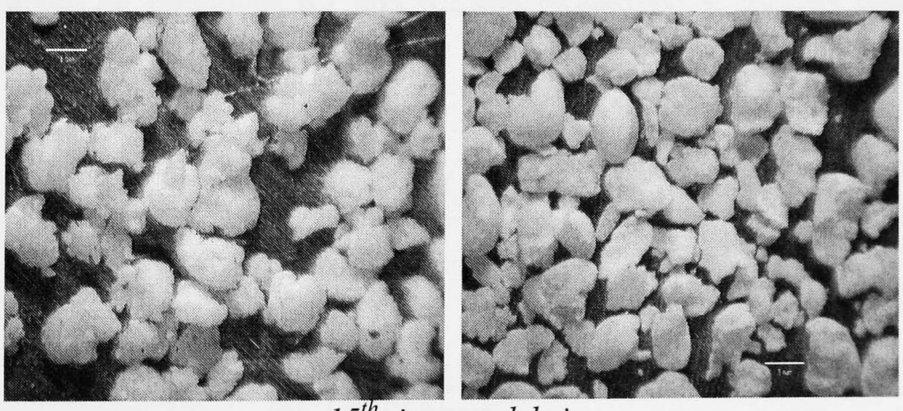

15th. impact debris

Figure 6.31: *RLM images of debris (all less than 1.18 mm) of Sample 2 (left column) and Sample 3 (right column), with initial feed granule size of 1.70-2.00 mm impacted at 15 m* s^{-1}.

6.5 Discussion

In this section, the reliability of the experimental results is first assessed. Then the impact tests results are discussed regarding the effects of impact velocity, size, impact angle and number of impact on extent of breakage. The criterion for selection of sieve size in single sieve analysis method is discussed at the end.

6.5.1 Assessment of the reliability of the experimental results

Three factors are addressed here regarding the reliability of the impact test results. First, the systematic error analysis of the primary parameters and their effects on the propagated errors in the correlations are assessed. Second, the reproducibility of the test is examined through repeating the experiments. Third, a discussion is made regarding the difference between lower and upper limits of breakage and its variation with sample type and age of samples.

6.5.1.1 Systematic error analysis of extent of breakage

Similar to the method presented in Chapter 4, the propagated error in the extent of breakage given by Equations 6.1 and 6.2 can be derived as follows based on the Equations 4.7 and 4.8.

$$\left|\delta\xi_i^-\right| \cong \frac{\left|\delta M_{de(i)}\right|}{M_{f(i)}} \tag{6.10}$$

$$\left|\delta\xi_i^+\right| \cong \sqrt{2}\,\frac{\left|\delta M_{de(i)}\right|}{M_{f(i)}} \tag{6.11}$$

where, $|\delta M_{f(i)}|$ and $|\delta M_{de(i)}|$ show the resolution of the balance, which in this case is about of 10^{-5} g. The parameters of $|\delta\xi^-_i|$ and $|\delta\xi^+_i|$ are the propagated errors of

the lower and upper limits. As it is apparent from the Equations 6.10 and 6.11, the systematic error of the extent of breakage can be reduced by increasing the amount of feed material or increasing the balance resolution. However, the highest systematic error observed in these experiments was essentially about 0.2%, which was for the small granules at free fall impacts with low extent of breakages. Therefore, the systematic error in the impact test is negligible and hence does not affect the accuracy of the results.

6.5.1.2 Reproducibility of the experimental results

A number of single impact tests were repeated to assess the reproducibility of the experiments. In general, two factors of the number of feed granules and impact velocity were found to influence the reproducibility of the results of a given size. In this context, in a series of experiments, Sample 3 granules with 1.00-1.18 mm size were subjected to impact at two different impact velocities of 5 and 35 m s^{-1}. For each impact velocity, four samples were prepared with about 2000 and 5000 granules. Therefore, each test at the predetermined conditions of impact velocity and granules number was repeated twice. Table 6.1 shows the lower limit of breakage as well as the percentage of variation of results in each case.

Table 6.1: *Reproducibility of the results of the impact tests of Sample 3 granules.*

Impact velocity (m s^{-1})	Number of granules (-)	$\bar{\xi}$ (%)		$\frac{\lvert\delta\bar{\xi}\rvert}{\xi_1}100$
		1st. impact test	2nd. impact test	
5	2000	0.34	0.57	67.64
5	5000	0.28	0.36	21.43
35	2000	18.34	20.01	9.11
35	5000	17.97	18.53	3.12

The results show clearly that increasing the number of granules from 2000 to 5000 has a significant effect on improving the reproducibility of results. As it is seen, at impact velocity of 35 m s^{-1}, for both granules numbers, the breakage variation is less than 10%. However, at 5 m s^{-1} the reproducibility is not high due to the very low

extent of breakage of granules. This level of reproducibility is essentially general for such an industrial material, especially at low impact velocities. This is because the strength of granules are non-uniform, hence, the damage of granules may be affected by the presence of even one weak granule. However, increasing the number of granules can improve the reproducibility of the results.

Another reproducibility examination is made by comparing the impact tests results of the same granule size using the big and small impact rigs because the big rig was used for granules larger than 0.710 mm. Figure 6.32 illustrates this comparison for the 0.71-0.85 mm granules of Samples 1 and 3. This size has been selected as the test size, as it is operationally compatible with both impact rigs.

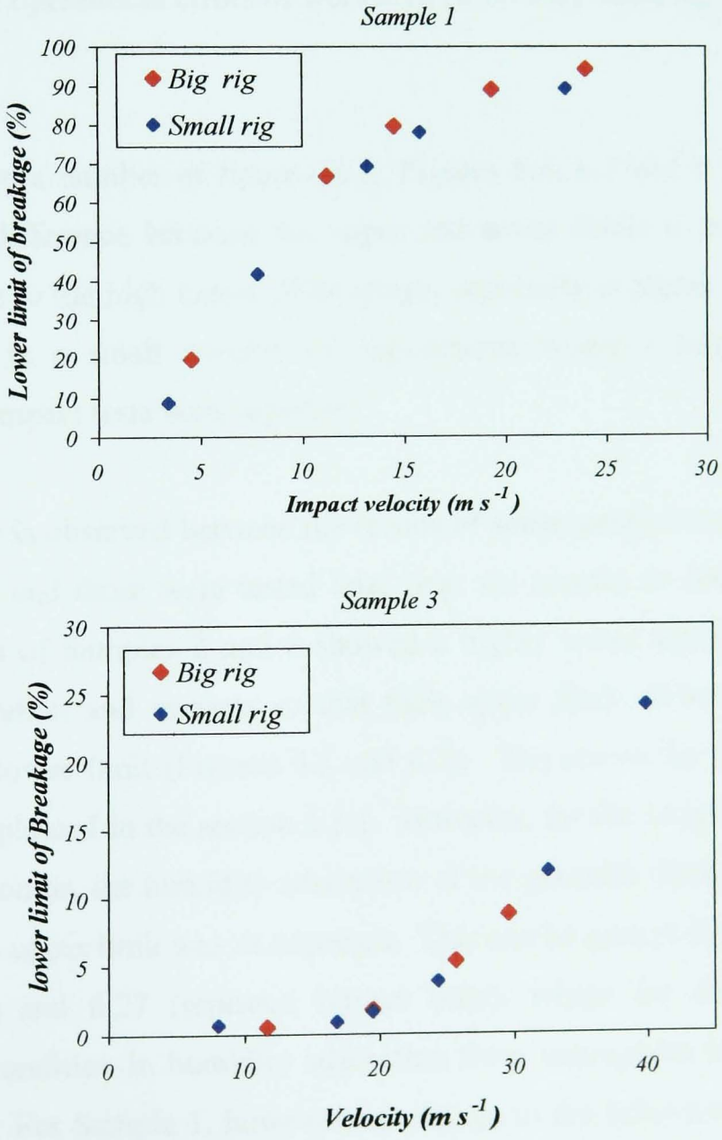

Figure 6.32: *Comparison of the test results of big and small impact rigs for 0.71-0.85 mm granule sizes of Samples 1 and 3.*

As it is clear form the figures, reasonable agreement is observed between the test results of both rigs.

6.5.1.3 Assessment of handling losses

For all of the impact tests results, the lower and upper limits of breakage were quantified using Equations 6.1 and 6.2 to assess the reliability of the impact tests. The actual extent of breakage lies somewhere between the lower and upper limits. Handling losses and/or gravimetric analysis errors are thought to be the main reasons of the gap between the lower and upper limits. Handling losses, however, depend strongly on the operational errors of worker in collecting, handling and sieving of the particles.

As it is seen in a number of figures (e.g. Figures 6.4, 6.5 and 6.7), in most of the experiments, difference between the upper and lower limits is negligible. This is essentially due to the high extent of breakage, especially at higher impact velocities. Nevertheless, in a small number of experiments where a large difference was obtained, the impact tests were repeated.

A discrepancy is observed between the results of some samples tested at early stages of the project and those were tested later (e.g. six months or one year later). The fresh granules of Samples 2 and 3 showed a highly water adsorbent characteristic during preparation and impacts so that their upper limit of breakage was in fact smaller than lower limit (Figures 6.5 and 6.7). The reason for this behaviour was previously explained in the section 6.3.1. However, for the samples that were tested after a few months, the humidity adsorption of the granules diminished significantly and hence the upper limit was as expected. This can be seen in Figures 6.18 (oblique impact tests) and 6.27 (repeated impact tests), where the establishment of an equilibrium condition in humidity adsorption from atmosphere is thought to be the main reason. For Sample 1, however, no change in the behaviour was observed, as these granules were not as water adsorbent as Samples 2 and 3.

6.5.2 Effect of impact velocity and granule size on breakage in single impacts

The breakage per impact of granules can be determined based on the sieving method, using either a single sieve or series of sieves. In chipping regime, the criterion is to distinguish between mother particles and debris. Therefore, employing a single sieve, whose size is two standard sizes below the original one, is satisfactory, as the size of debris is much smaller than that of the mother particles. For chipping, this criterion is selected to minimise the sieving effort. However, for fragmentation a full sieve analysis is necessary as the impact product may be distributed widely over a number of sieves. Nevertheless, in this case, also, the product of fragmentation may be partitioned into two categories; large fragments, which contain partially damaged mother particles, and small fragments and debris. This is essentially the distinction between the residue and complement, which was adopted in the literature (Arbiter *et al.* 1969; Thornton *et al.* 1995, Papadopoulos 1998) and was observed in this work with a natural cut in size distribution curves. As it is seen in Figures 6.12 and 6.15, the natural cut separates the residue and complement of Samples 2 and 3 on the normalised size (L/L_o) of about 0.72 of British standard sieves. This corresponds to the criterion of two sieve sizes less than the largest feed size. In the size distribution analyses of impact products performed by Arbiter *et al.* (1969), Kafui and Thornton (1993), Thornton *et al.* (1995), and Papadopoulos (1998), they considered the normalised size of 0.5 as the criterion for distinguishing between residue and complement. Then, they defined the slope of size distribution line of the complement as the distribution modulus, λ, when the mass fraction undersize is plotted as a function of normalised size, L/L_o, in logarithmic scale. For Samples 2 and 3, however, the regression analysis shows no significant change in the distribution modulus, using either criterion of 0.50 or 0.72. Therefore, in this work, the criterion of 0.72 is employed as set point for characterising the distribution modulus of the complement. Figure 6.33 shows the size distribution trends of the complements of Sample 2. The graphs have been presented for three feed granule sizes, each size at different impact velocities. As it is seen, the distribution trends of each feed size are generally parallel straight lines in the range tested impact velocity, i.e. following the Gates-Gaudin-Schaumann distribution law. However, the average distribution modulus seems to change in a certain size range.

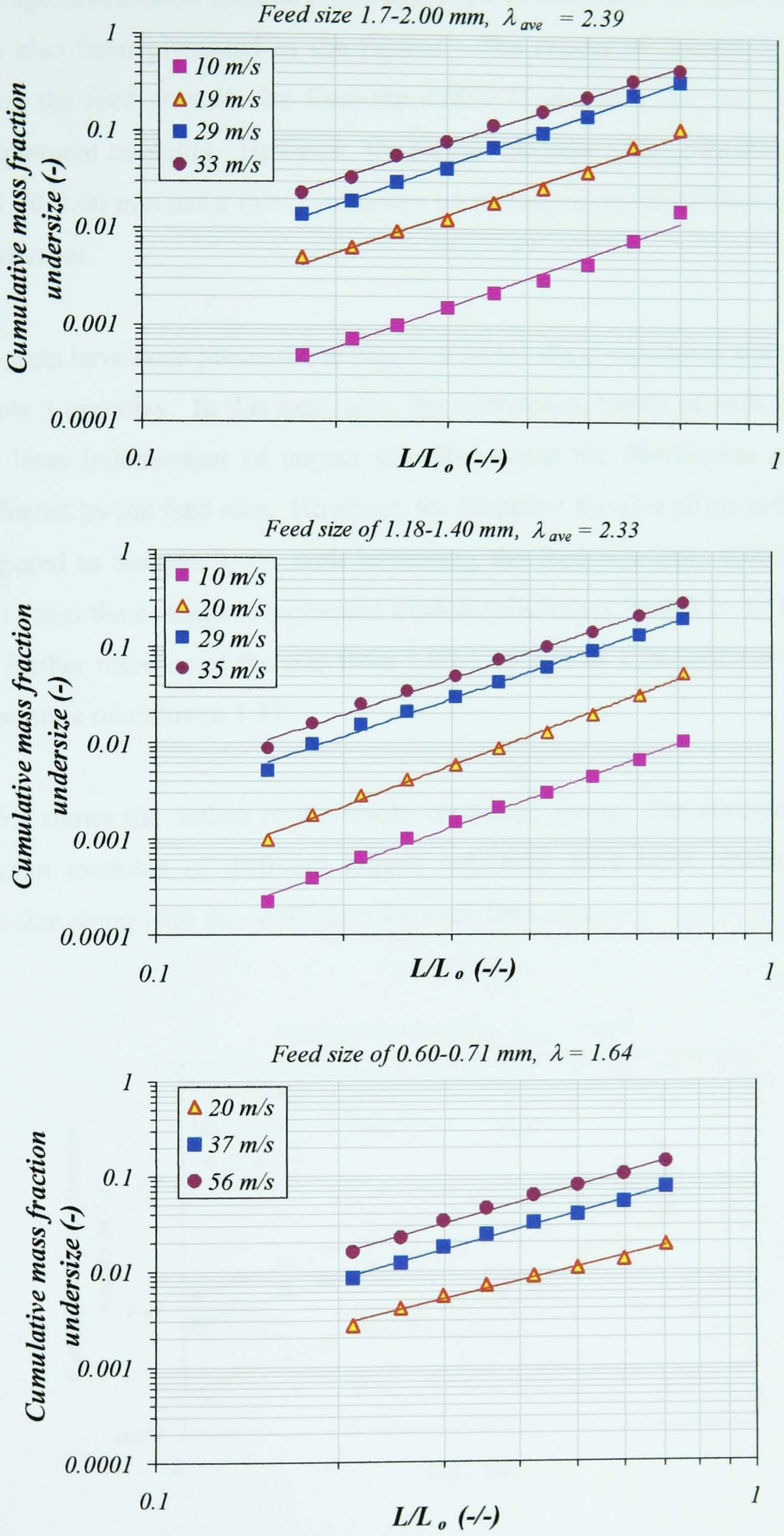

Figure 6.33: *The size distribution of complements of Sample 2, obtained for three feed sizes, each size at three different impact velocities.*

The average distribution modulus (average slope of the lines) for each feed granule size has also been presented in the figures. The results of Sample 2 reveal that increasing the feed granule size from the 0.60-0.71 mm to 1.18-1.40 mm increases the complement modulus. However, the further increase of the size from 1.18-1.40 mm to 1.70-2.00 mm has a minor influence on increasing the distribution of modulus of complement.

Similar plots have been presented in Figure 6.34 for the complement size distribution of Sample 3 granules. In this case, also, the distribution trends of each feed size are parallel lines independent of impact velocity, whilst the distribution modulus has been affected by the feed size. However, for Sample 3 the size effect is the opposite, as compared to Sample 2, i.e. with increasing the feed size from 0.60-0.71 mm to 1.00-1.18 mm the average complement modulus decreases from 2.36 to 1.56. In this case, a further increase of the size from 1.00-1.18 mm to 1.70-2.00 mm reduces the complement's modulus to 1.37.

Table 6.2 shows the outline of the results discussed above. The standard deviations of average modulus of different impact velocities have been obtained for each granule size along with the coefficient for each fitted line.

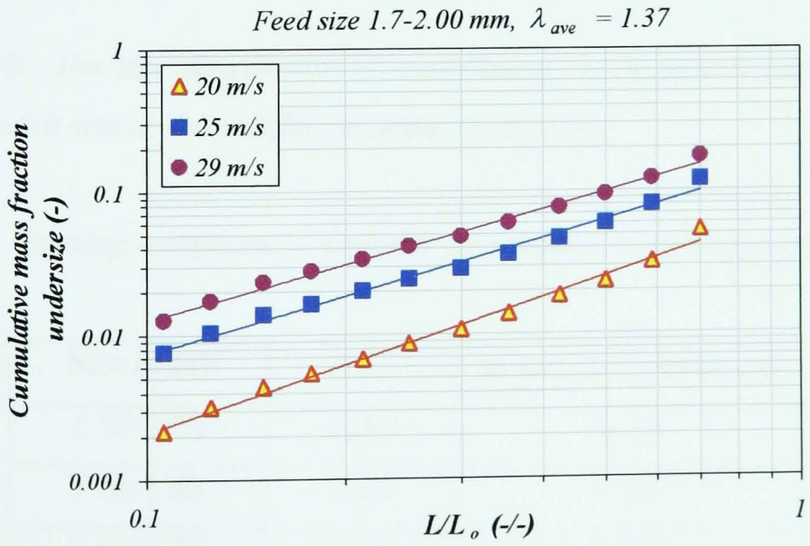

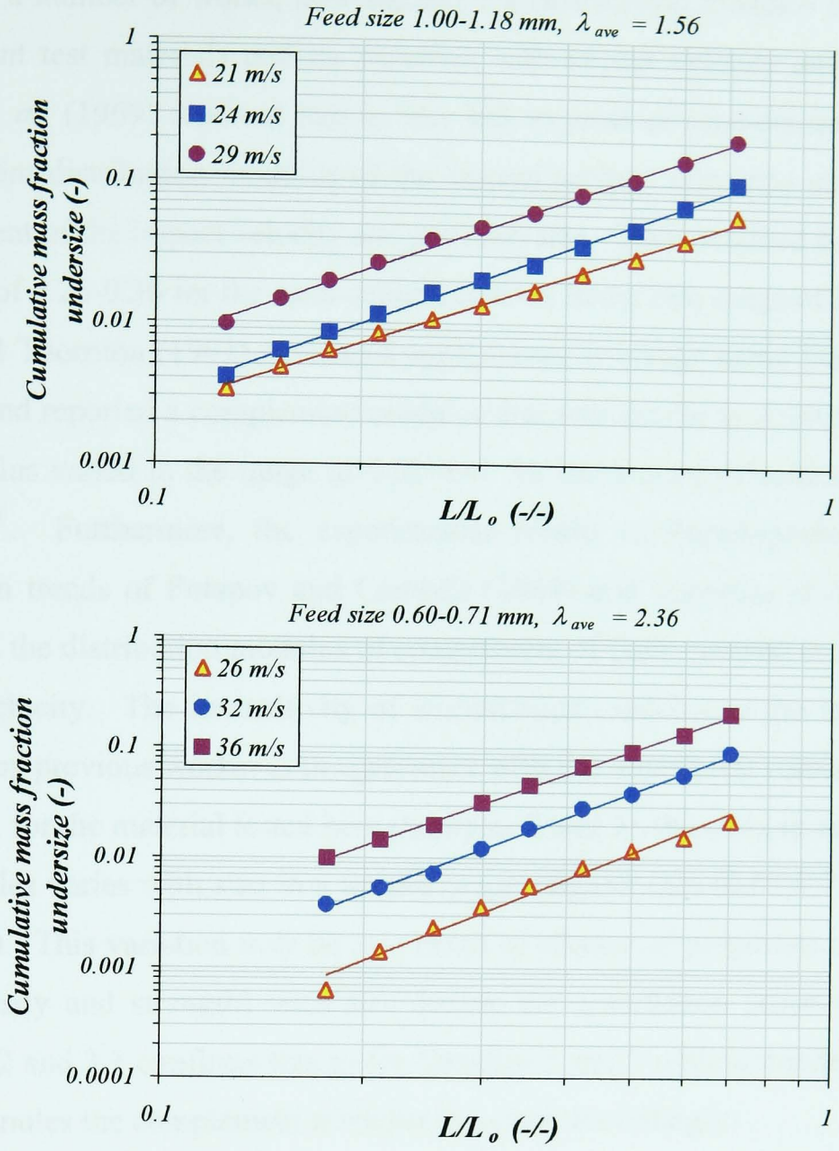

Figure 6.34: *The size distribution of complements of Sample 3, obtained for three feed sizes, each size at three different impact velocities.*

Table 6.2: *Average complement modulus of Samples 2 and 3 for different granule sizes.*

Sample	Size (mm)	λ_{ave}	Standard deviation (±)	R^2 (%)
2	1.70-2.00	2.39	0.125	99.20
	1.18-1.40	2.33	0.129	99.52
	0.60-0.71	1.64	0.149	99.17
3	1.70-2.00	1.37	0.120	98.90
	1.00-1.18	1.56	0.207	99.39
	0.60-0.71	2.36	0.126	98.61

There are a number of works, investigating the distribution modulus of complement of different test materials and its variation with impact velocity and particle size. Arbiter *et al.* (1969) reported that in free fall impacts of sand-cement spheres, the complement distribution modulus of the impact product remained almost constant, independent of the impact velocity and particles size. They obtained the complement modulus of 0.25-0.30 for the sand-cement spheres in the size range of 3.3-4.9 inches. Kafui and Thornton (1993) simulated agglomerate breakage using Distinct Element Method and reported a complement modulus that was similar to Arbiter's one, where the modulus varied in the range of 0.22-0.47 for the impact velocities range of 0.5-1.5 m s^{-1}. Furthermore, the experimental results of Papadopoulos (1998) and simulation trends of Potapov and Cambell (1994) and Thornton *et al.* (1995) also show that the distribution modulus of complement of their material is independent of impact velocity. The insensitivity of complement modulus to the impact velocity reported by previous worker is in agreement with the impact test results of this work. However, for the material tested here (Samples 2 and 3), the complement modulus of the granules varies with size in a certain range of sieve cuts (0.60-0.71 mm to 1.00-1.18 mm). This variation may be as a result of change of properties of the granules (i.e. porosity and strength) with size during the granulation process. Comparing Tables 6.2 and 3.1 confirms this as for Samples 2 and 3 with increasing the porosity of the granules the complement modulus increases accordingly.

Although, a large number of impact test results shows relatively constant value of the complement modulus independent of impact velocity, nevertheless, there are other results, which show the variation of modulus in relatively wider range of impact velocity. For example, for Paracetamol crystals, an appreciable variation of the distribution modulus with impact velocity was reported by Artega *et al.* (1995), for which the distribution modulus varied in the range of 0.75-3.00 at the impact velocity range of 7-20 m s^{-1}.

The experimental and simulation results performed on different materials shows wide extent of the distribution modulus. The minimum values have been obtained by Arbiter *et al.* (1969) for sand-cement spheres in the range of 0.25-0.30, impacted at 6 to 9 m s^{-1}. The simulation results obtained by Thornton et al. (1995) show the values

about 1.00 at the impact velocities less than 0.50 m s^{-1}. Potapov and Cambell (1994) simulated fracture of solid bodies and obtained moduli about 1 at the velocities less than 0.5 m s^{-1}. A wide variety of test materials have been investigated by Papadopoulos (1998). He obtained the modulus values of 1.58 for PMMA extrudates (2.36-2.80 mm, 20-72 m s^{-1}), 1.96 for one type of porous silica granules (1.00-1.18 mm, 12-20 m s^{-1}) and 2.25 for another type of porous silica (2.00-2.36 mm, 12-20 m s^{-1}). Excluding the modulus reported by Papadopoulos (1998) for PMMA, which is in a wide range of impact velocity (20-72 m s^{-1}), the other results have been obtained for a limited range of impact velocities and particles sizes. The complement modulus obtained in this work is close to the results of Papadopoulos (1998), although their material properties are very different.

In general, the complement distribution modulus characterises the breakage behaviour of the particulate solids. Physical significance of the distribution modulus of complement and factors affecting that are of practical interest. A large distribution modulus implies that the impact product is made of mainly narrow size distribution, which is desirable for comminution purposes.

The functional dependence of the size distribution on the impact velocity has been investigated by a number of workers as shown in Chapter 2 (see section 2.4.2). Equations 6.12, 6.13 and 6.14 are some of those that have been developed by Arbiter *et al.* (1969), Kafui and Thornton (1993) and Papadopoulos (1998), respectively. Except Equation 6.13, which is a theoretical model, the two other models are empirical. Equations 6.12 and 6.14 were developed based on impact test results of sand-cements and porous silica agglomerates, respectively.

$$Y(L) = C_1 L^{\lambda} (V^2 - V_c^2) \tag{6.12}$$

$$Y(L) = C_2 \left[kV^2 \left(\frac{L}{L_o} \right)^{\lambda} \right] \tag{6.13}$$

$$Y(L) = C_3 \left[(V^2 L_o) \left(\frac{L}{L_o} \right) \right]^{\lambda} \tag{6.14}$$

where, $Y(L)$ is the mass fraction of fragments under the size L in the complement region, L_o is initial particle size, C is a constant, λ is the distribution modulus of complement, and V and V_c are impact velocity and critical velocity, respectively. Critical velocity is defined as the velocity below which no fragmentation occurs. As it is clear from Equations 6.12 and 6.14, these empirical models seem to be independent of the original particle size (L_o). In Equation 6.14, however, Papadopoulos (1998) presented the correlation in the above form deliberately to keep the term $V^2 L_o$ similar to the chipping model of Ghadiri and Zhang (1992 and 2002). Although the above models show some similarities in shape (i.e. the same power indices of 2 and λ for the impact velocity and particle size, respectively), however, there are also some discrepancies between the models (i.e. independency of Equations 6.12 and 6.14 to initial particle size or existence of a critical impact velocity in Equation 6.12).

In view of the above discrepancies and similarities, an attempt was made to explore if a new empirical correlation could be found, which provides a better unification of the effect of particle size and impact velocity for the granules tested in this study. In this context, data analysis of complements of 1.70-2.00 mm granules of Samples 2 and 3 reveal that the best unification of the results is observed, when $Y(L)$ is drawn versus $(V L_o (L / L_o))$ as shown in Figure 6.35. As it is seen, the power index of equation and then velocity varies with the complement modulus of the granules (i.e. for 1.70-2.00 mm granules, the value of λ is obtained as 2.54 for Sample 2 and 1.37 for Sample 3). Similar trend is found for the other granule sizes of Samples 2 and 3, which are not shown here.

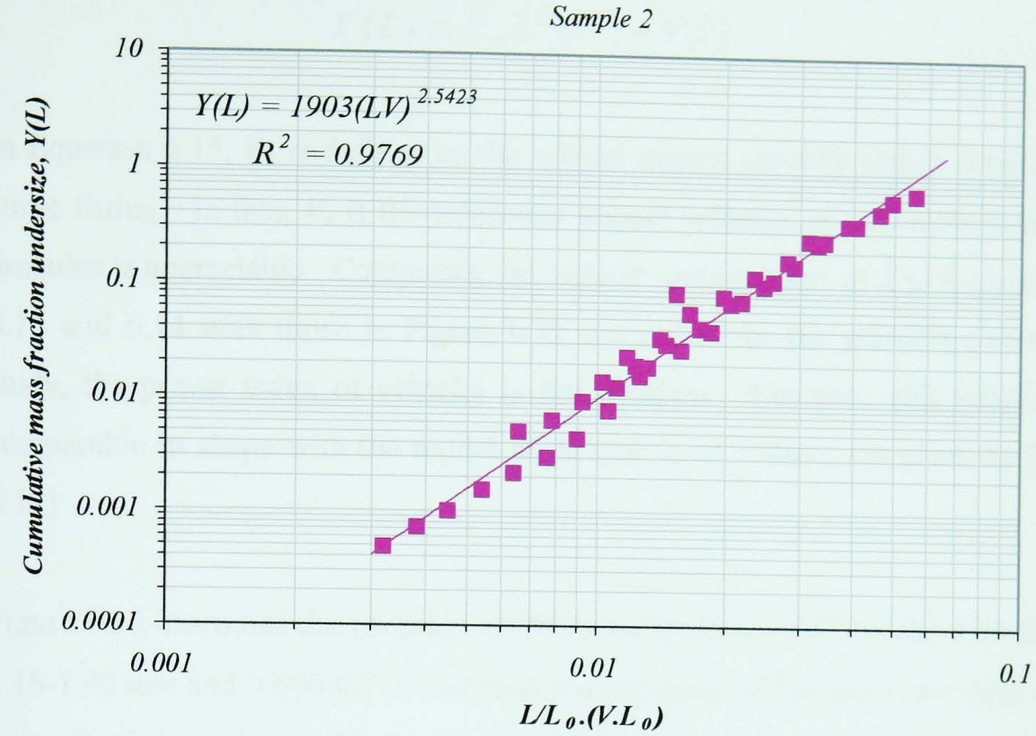

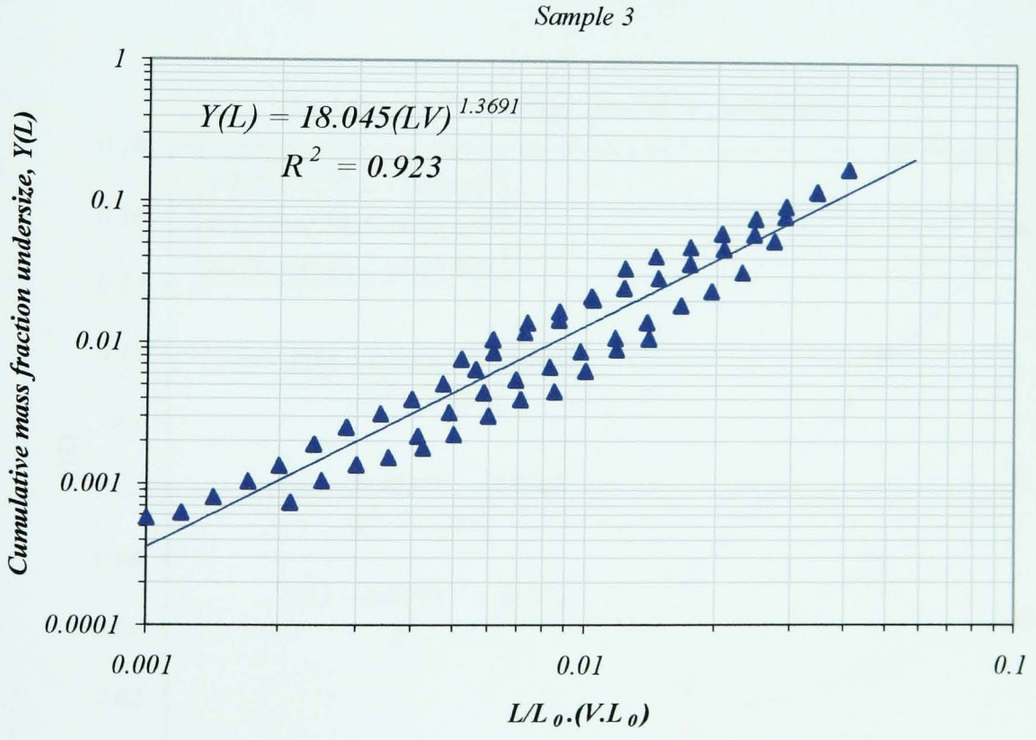

Figure 6.35: *Size distribution of complement of 1.70-2.00 mm of Samples 2 and 3 showing Y(L) as a function of combination of size and impact velocity.*

Further analysis of the results showed that Equation 6.15 provided the best fit to the experimental data.

$$Y(L) = C_4 L^{\lambda} (V^{\lambda} - V_c^{\lambda}) \tag{6.15}$$

In Equation 6.15, V_c is defined as the critical impact velocity and is determined by curve fitting. In fact, V_c is the minimum impact velocity, at which the breakage of granules is appreciable. Comparing the velocity power index of 2 in Equations 6.12, 6.13 and 6.14 with those in Figure 6.35 show that for the granules tested in this study, the power index of velocity is not constant. However, this relationship is comparable in shape with the model of Arbiter *et al.* (1969), (as given by Equation 6.12)

Figure 6.36 illustrates the variation of $Y(L)$ as a function of V^{λ} for the 1.70-2.00 mm, 1.18-1.40 mm and 0.600-0.710 mm feed granule sizes of Sample 3, for three constant normalised sizes (L/L_o). The results are deliberately presented in this way in order to determine the critical impact velocity from the intercept with abscissa.

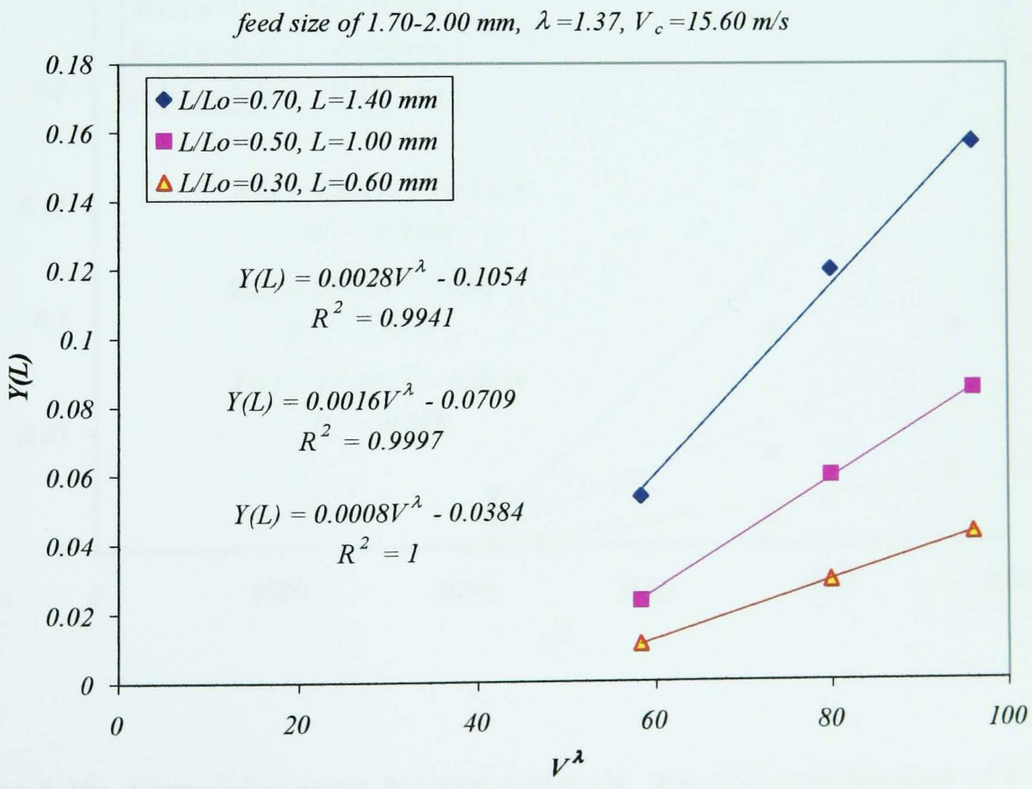

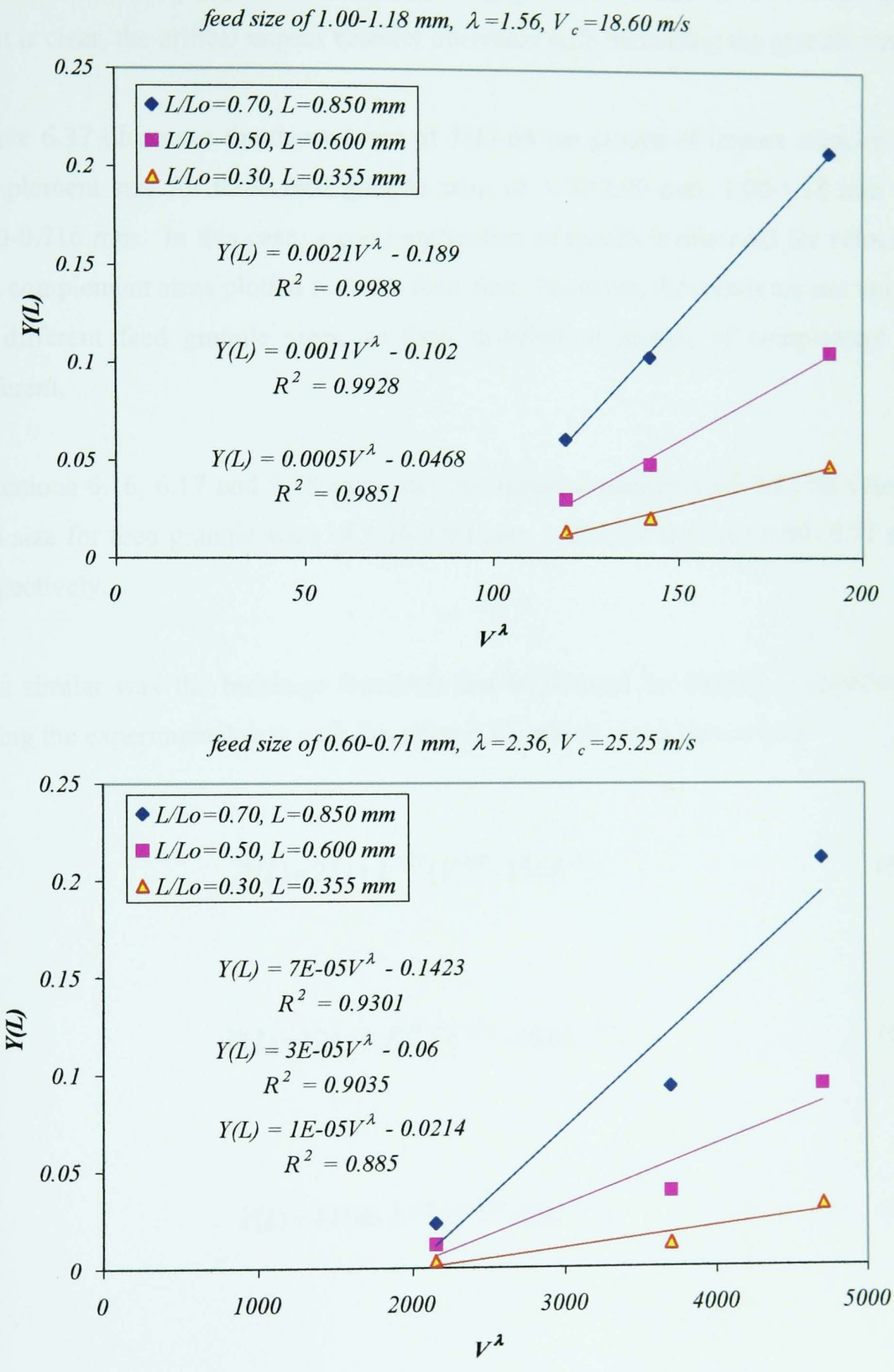

Figure 6.36: *Cumulative mass fraction under the size of L as a function of V^{λ} for three feed granule sizes of Sample 3, for three constant normalised sizes.*

The critical velocity obtained for each initial granule size is shown in its own figure. As it is clear, the critical impact velocity decreases with increasing the granule size.

Figure 6.37 illustrates the dependence of *Y(L)* on the groups of impact velocity and complement size for three feed granule sizes of 1.70-2.00 mm, 1.00-1.18 mm and 0.60-0.710 mm. In this case, a good unification of results is observed for velocities and complement sizes plotted for each feed size. However, the trends are not unified on different feed granule sizes, as their distribution moduli of complement are different.

Equations 6.16, 6.17 and 6.18 show the functional dependence of *Y(L)* on velocity and size for feed granule sizes of 1.70-2.00 mm, 1.00-1.18 mm and 0.60- 0.71 mm, respectively.

In a similar way the breakage functions can be derived for Sample 2 granules by fitting the experimental data with Equation 6.15, which is not shown here.

$$Y(L)=23.11\,L^{1.37}\,(V^{1.37}-15.64^{1.37}) \tag{6.16}$$

$$Y(L)=124.63\,L^{1.56}\,(V^{1.56}-18.60^{1.56}) \tag{6.17}$$

$$Y(L)=44146\,L^{2.36}\,(V^{2.36}-25.5^{2.36}) \tag{6.18}$$

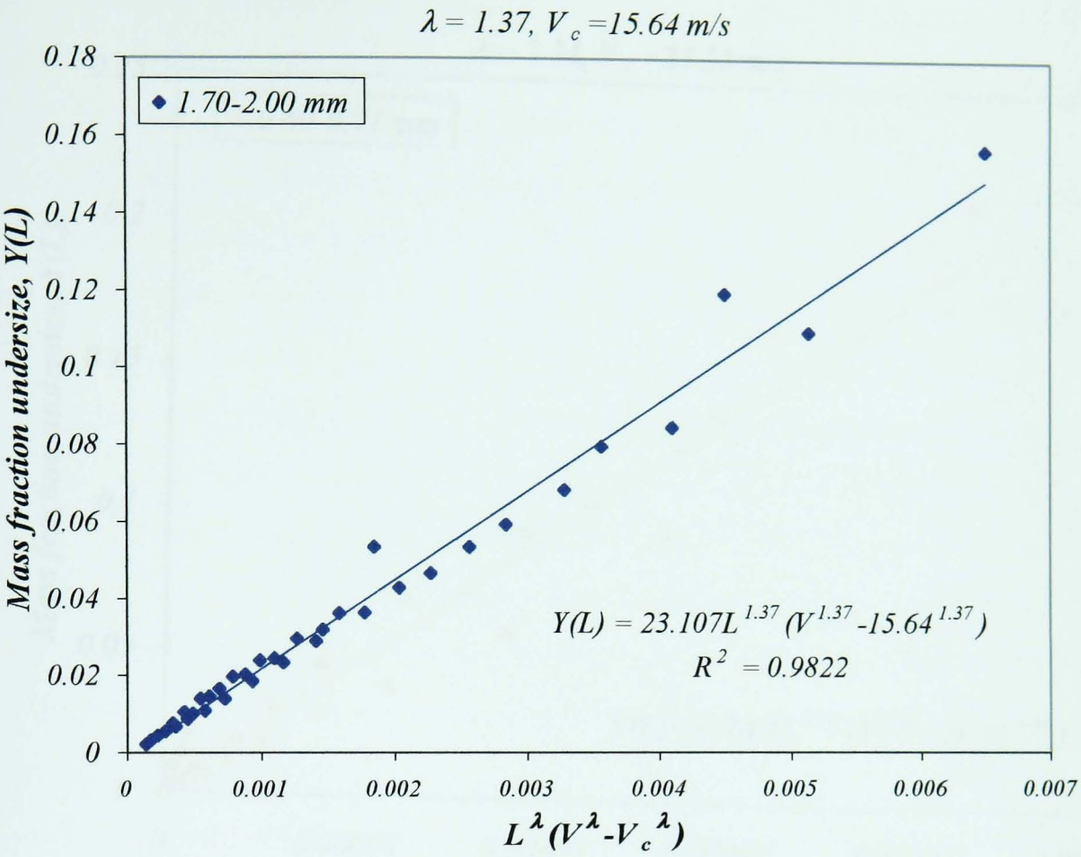
λ = 1.37, V_c =15.64 m/s
1.70-2.00 mm
Mass fraction undersize, Y(L)
0.18
0.16
0.14
0.12
0.1
0.08
0.06
0.04
0.02
0
0
0.001
0.002
0.003
0.004
0.005
0.006
0.007
L^λ(V^λ-V_c^λ)
Y(L) = 23.107L^1.37 (V^1.37 -15.64^1.37)
R^2 = 0.9822

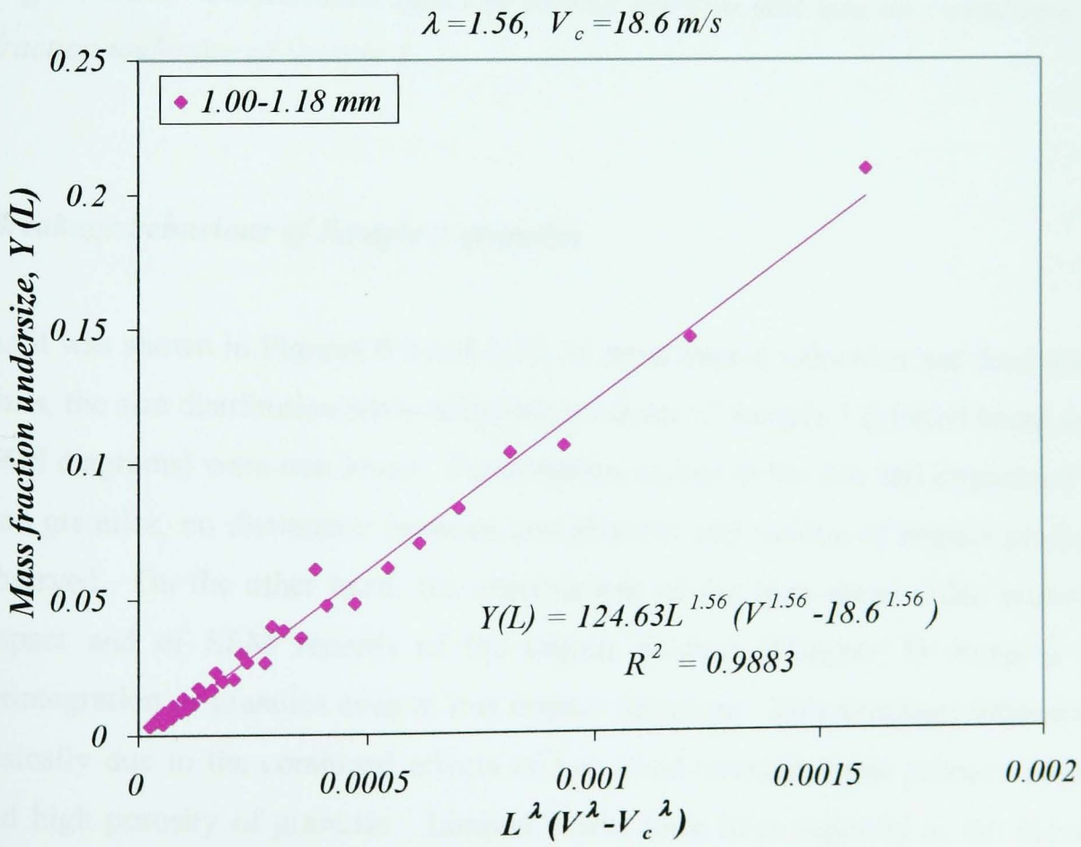
λ =1.56, V_c =18.6 m/s
1.00-1.18 mm
Mass fraction undersize, Y (L)
0.25
0.2
0.15
0.1
0.05
0
0
0.0005
0.001
0.0015
0.002
L^λ(V^λ-V_c^λ)
Y(L) = 124.63L^1.56 (V^1.56 -18.6^1.56)
R^2 = 0.9883

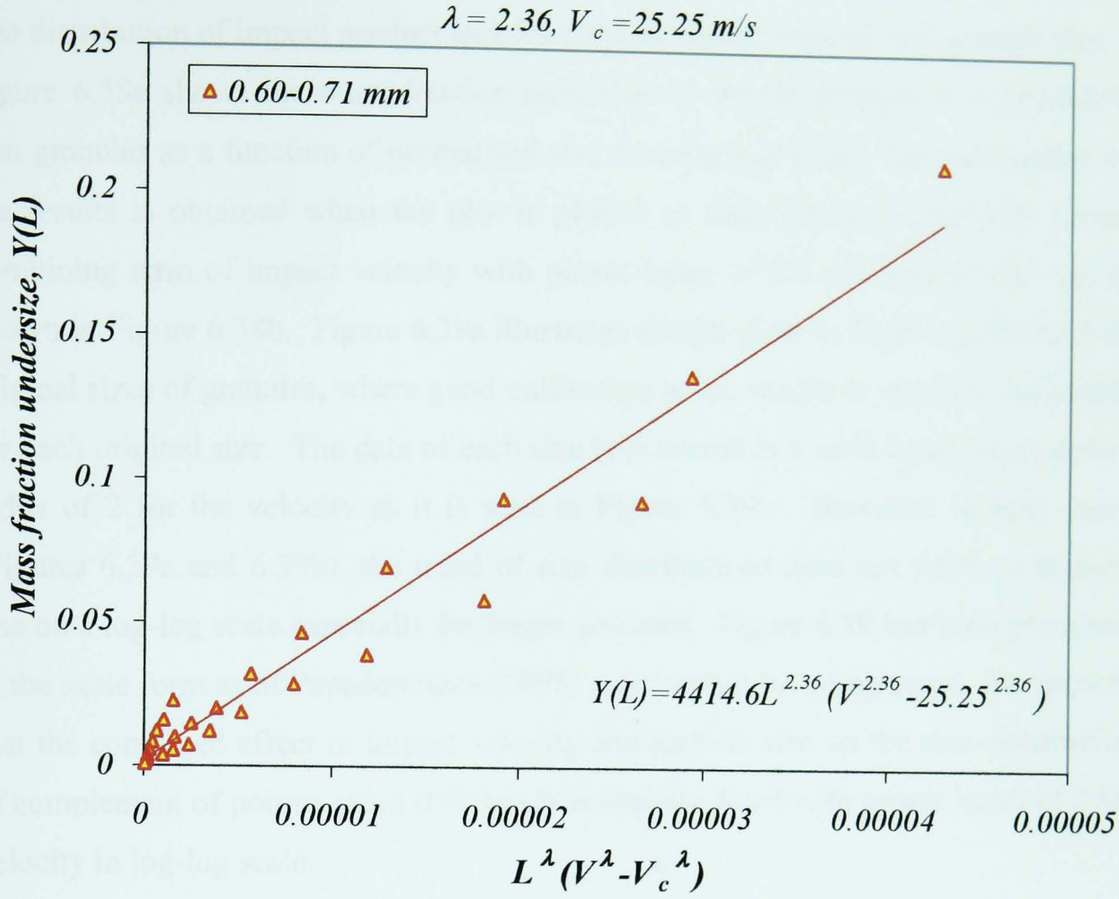

Figure 6.37: *Combination effect of impact velocity and size on cumulative mass fraction undersize of Sample 3.*

Breakage behaviour of Sample 1 granules

As it was shown in Figures 6.9 and 6.10, in most impact velocities and feed granule sizes, the size distribution plots of impact products of Sample 1 (plotted based on the GGS diagrams) were non-linear. Furthermore, except in the free fall impacts of very fine granules, no distinction between complement and residue of impact product is observed. On the other hand, the observations of the high-speed video records of impact and of SEM records of the impact product (Chapter 5) reveal a high disintegration of granules even at low impact velocities. This breakage behaviour is basically due to the combined effects of low bond strength, large primary particles and high porosity of granules. Limited works have been reported in the literature regarding the size distribution investigation of this type of materials. Nevertheless,

there is a great interest to develop a relationship for such weak granules showing the size distribution of impact product as a function of impact velocity and granule size. Figure 6.38a shows the mass fraction undersize of impact product of 0.710-0.850 mm granules as a function of normalised size on a log-log scale. Best unification of the results is obtained when the plot is plotted as mass fraction undersize versus combining term of impact velocity with power index of 0.5 and normalised size as shown in Figure 6.38b. Figure 6.39a illustrates similar plots to Figure 6.38b for four original sizes of granules, where good unification of the results is obtained separately for each original size. The data of each size is scattered in a wide band, using power index of 2 for the velocity as it is seen in Figure 6.39b. However, in both cases (Figures 6.39a and 6.39b), the trend of size distributions does not follow a straight line on a log-log scale especially for larger granules. Figure 6.39 has been presented in the same form as of Papadopoulos (1998) relationship for comparison. He showed that the combined effect of impact velocity and particle size on the size distribution of complement of porous silica (PS) beads is linearly fitted with power index of 2 for velocity in log-log scale.

The non-linear size distributions of the fragments in Figure 6.39 can be considered as a breakage characteristic of weak agglomerates such as Sample 1. The non-linearity is more distinct for the larger granules. However, for 0.180-0.212 mm granules, as it is clear from Figure 6.39a, a linear trend is pronounced. This is due to the large size of the primary particles (100 μm) so that the granules are confined to the singlets and doublets.

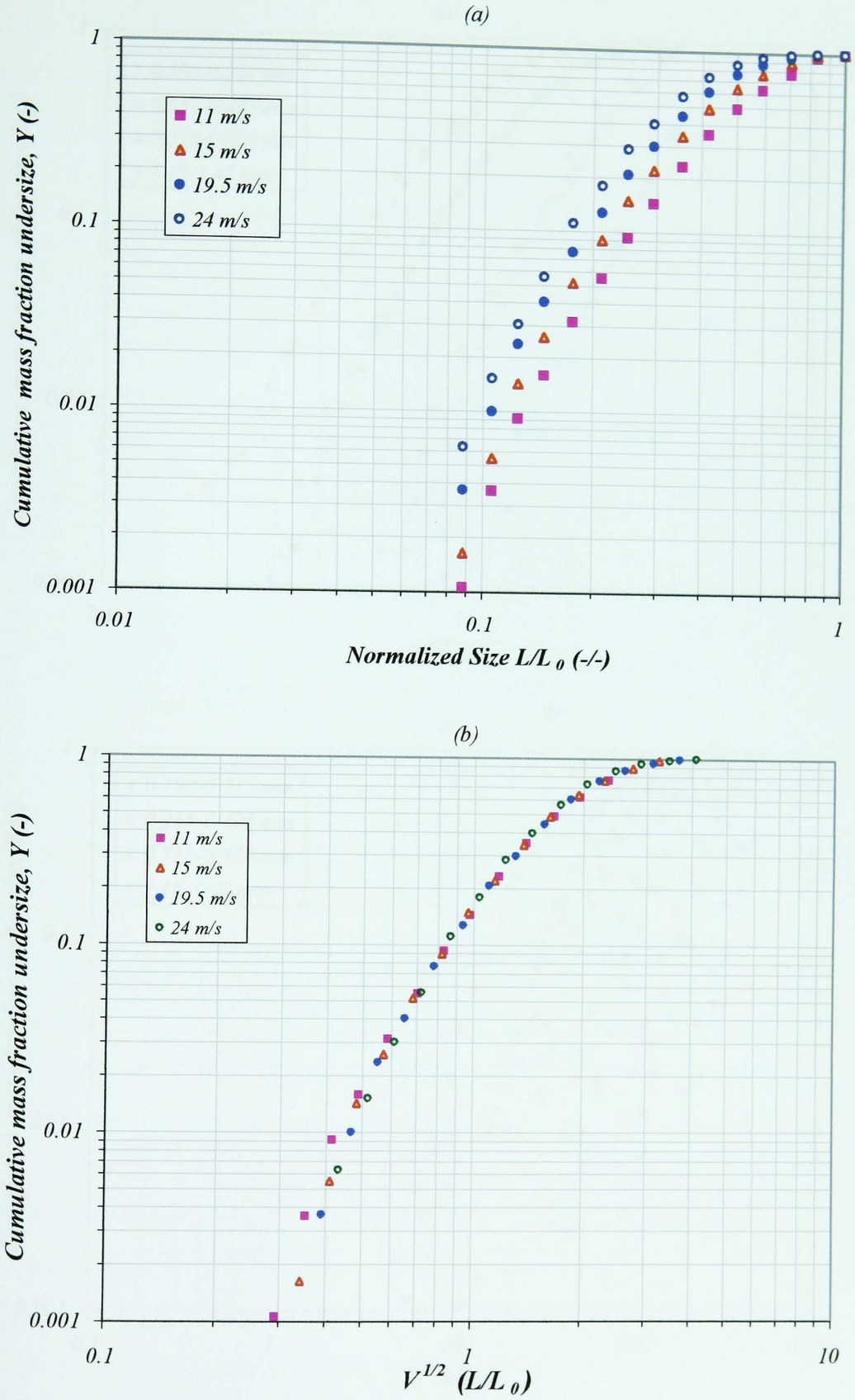

Figure 6.38: *Variation of the cumulative mass fraction undersize as a function of combined functional group of impact velocity and size for 0.710-0.850 mm feed granule size of Sample 1.*

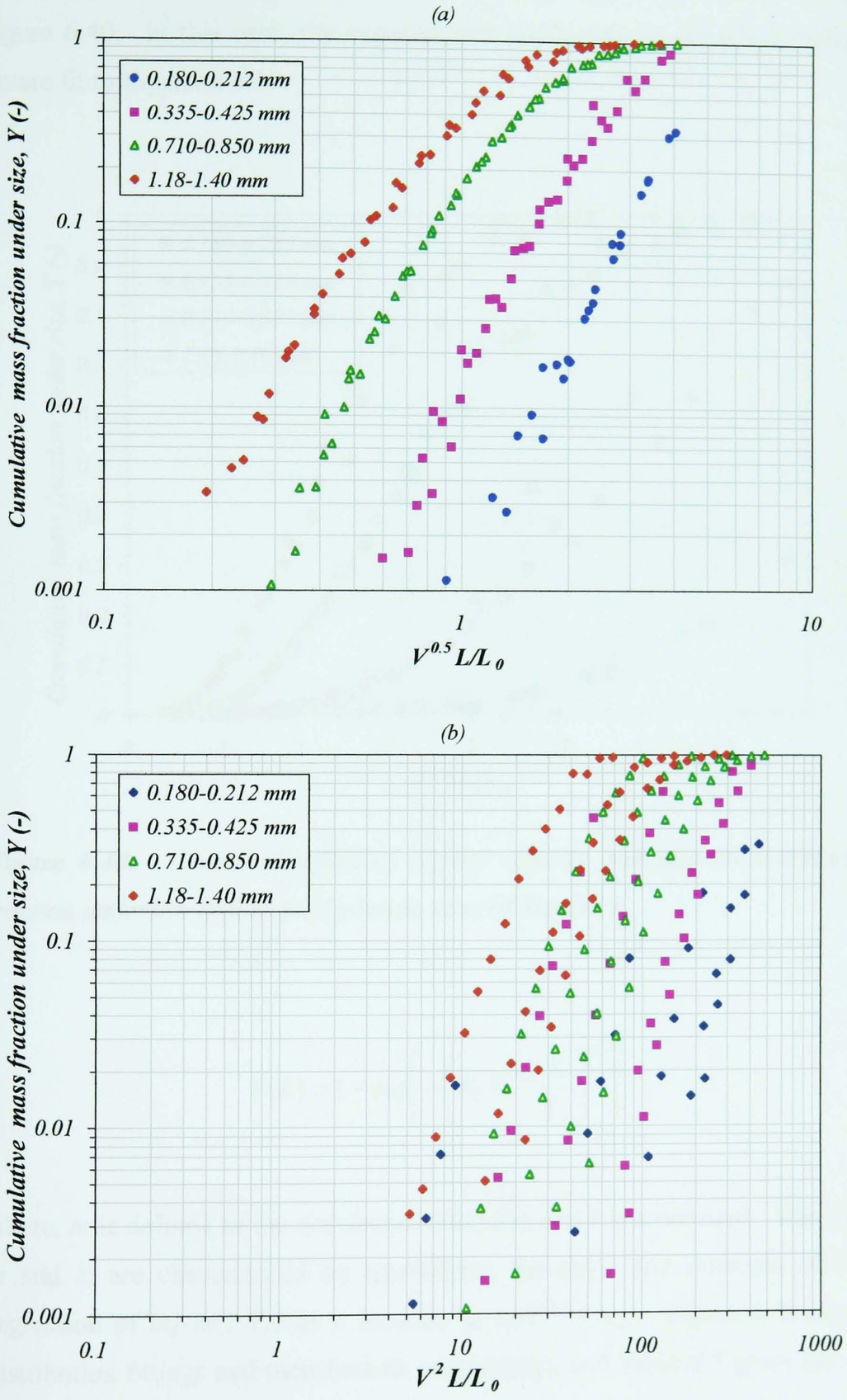

Figure 6.39: *Variation of the cumulative mass fraction undersize as a function of combined functional group of impact velocity and size for different feed granule size of Sample 1.*

The data presented in Figure 6.39a can also be plotted in a linear form as shown in Figure 6.40. In this case, the experimental results can be described using a least square fit to Equation 6.19:

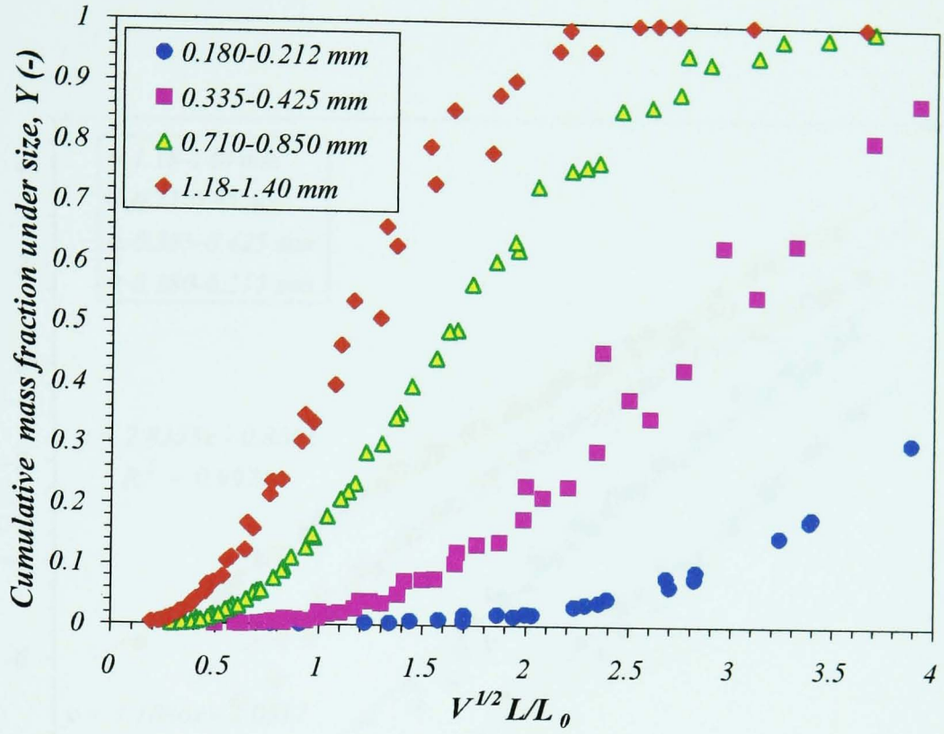

Figure 6.40: *Combined effect of impact velocity and size on cumulative mass fraction undersize of four feed granule sizes of Sample 1.*

$$Y(L) = 1 - \exp\left(-\left(k_1 V^{0.5} \frac{L}{L_o}\right)^m\right) \tag{6.19}$$

where, m is defined as the distribution modulus and k is a constant. The parameters m and k_1 are characterised by quantifying the slope and intercept of the linear regression of $ln[-ln(1-Y)]$ as a function of $ln(V^{0.5}\ L/L_o)$. Figure 6.41 shows these distribution fittings and their best-fit relationships and Table 6.3 gives the values of m and k_1 for four original granule sizes, tested here. The examination of Table 6.3 reveals that k_1 is a linear function of L_o, and this is shown in Figure 6.42. Therefore, further unification of the results can be assessed by normalizing the data in Figure 6.40 in the form of $V^{1/2}L_o(L/L_o)$. This is shown in Figure 6.43, where the individual

distribution curves partially overlapped, as compared to Figure 6.40. In fact this is the best fitting obtained for Sample 1, showing the parameter of cumulative mass fraction undersize as a function of combined impact velocity and size of broken granules (L). As it is seen for Sample 1 also the breakage function is independent of original size of granules.

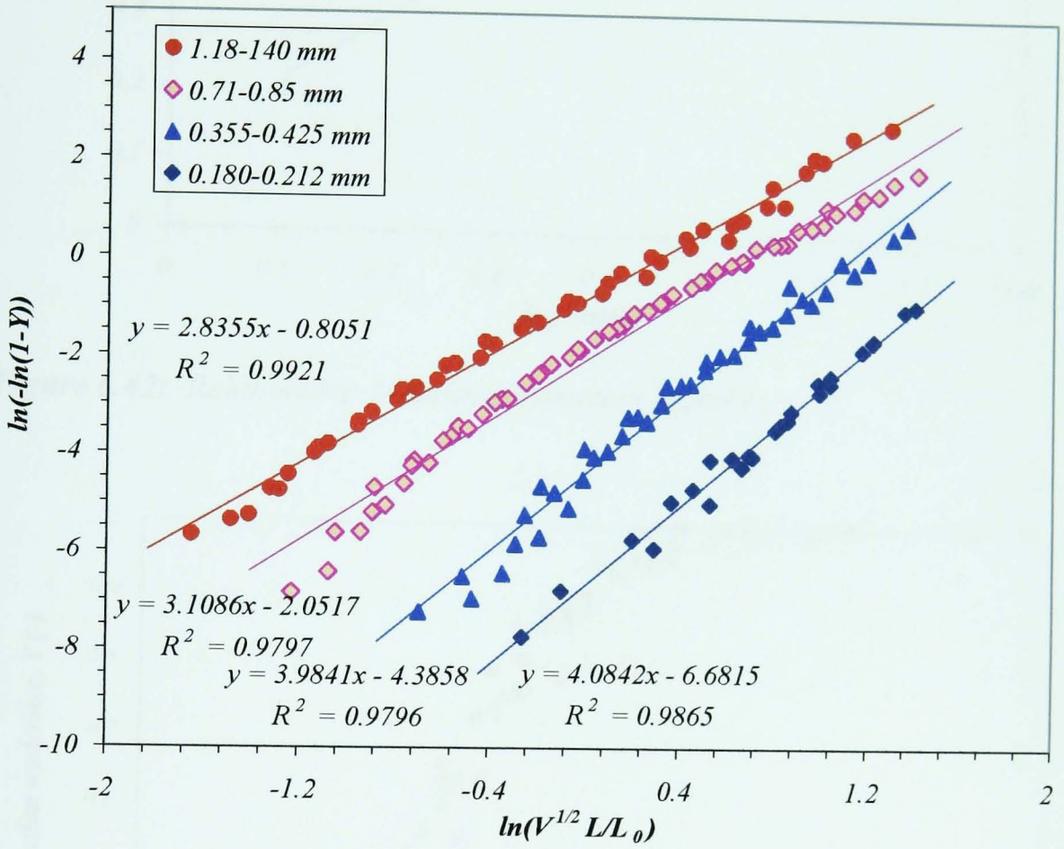

Figure 6.41: *Size distribution plots of the impact product of Sample 1 for different feed granule size.*

Table 6.3: *Curve fitting parameters of the size distribution relationship of impact product for sample 1 versus largest feed granule size (L_o).*

L_o (mm)	m	k_l
0.212	4.084	0.194
0.425	3.984	0.332
0.850	3.108	0.517
1.400	2.836	0.753

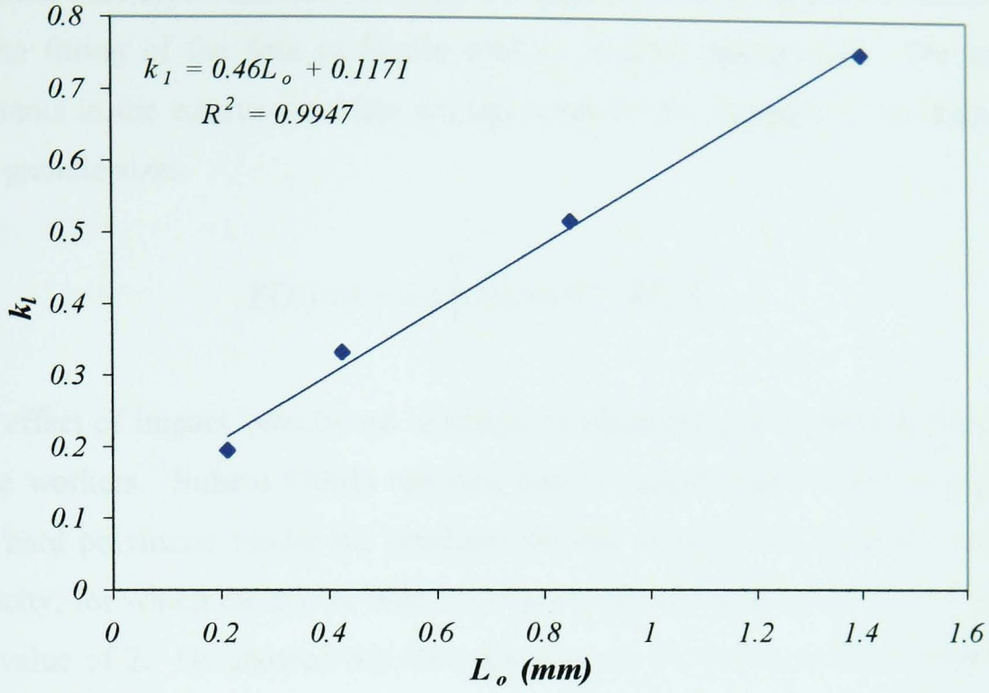

Figure 6.42: *Relationship between parameters k_1 and L_o.*

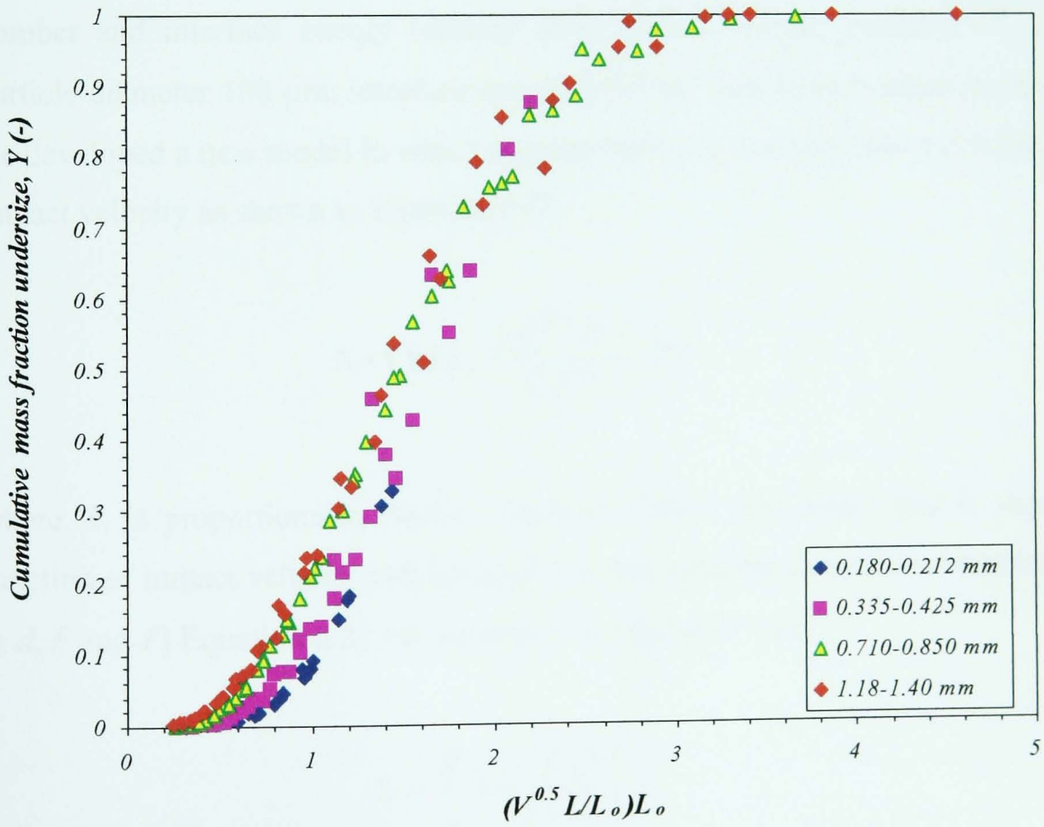

Figure 6.43: *Combined effect of impact velocity and size on cumulative mass fraction undersize of granules of Sample 1.*

Equation 6.20 represents the breakage function of Sample 1 granules obtained based on the fitting of the data in Figure 6.44 to Weibull relationship. The numerical constants in the equation are the average value of the constants of the equations of four granule sizes

$$Y(L) = 1 - \exp\left[-\left(0.58\, V^{0.5}\, L\right)^{3.5}\right] \tag{6.20}$$

The effect of impact velocity on breakage of agglomerates has been investigated by some workers. Subero (2001) reported that for agglomerates made of glass beads and hard polymeric binder the breakage showed a power-law increase with impact velocity, for which the power index was generally in the range 1.00-1.80, i.e. below the value of 2. He showed that the variations of the power index depended on the agglomerate structure, e.g. macro-void number. Moreno (2003) investigated the impact breakage of agglomerates using DEM simulation for different agglomerate sizes (1.03-2.65 mm) but with the same primary particle properties, co-ordination number and interface energy (density 2000 kg m^{-3}, elastic modulus 31, primary particle diameter 100 μm, interface energy 3.5 J m^{-2} and co-ordination number 5.6). He developed a new model in which damage ratio (Δ) was varied as a function of the impact velocity as shown in Equation 6.21.

$$\Delta = 1.03\, k_v \frac{\rho\, d^{5/3}\, E^{2/3}}{Z\, \Gamma^{5/3}} V^2 \tag{6.21}$$

where, k_v is proportionality factor. Moreno (2003) then found that k_v was also a function of impact velocity and for agglomerates with the same characteristics (same ρ, d, E and Γ) Equation 6.21 can be shown as Equation 6.22.

$$\Delta' = \frac{Z}{2}\Delta = \frac{C_5 V^2}{1 + C_6 V^2} \tag{6.22}$$

Where Z is the coordination number and Δ' is the number of broken contact per particle. Figure 6.44 shows DEM simulation results of impact of agglomerates in

which the number of broken contact per particle has been presented as a function of impact velocity. In the figure the each average data point and its standard deviation represent the impact result of 8 agglomerates with different sizes. Furthermore, Figure 6.44 shows the best fitting of the simulated data to Equation 6.22 (red curve). Moreno (2003) discusses that at the impact velocities lower than 1 m s^{-1}, where the velocity term in the denominator of Equation 6.22 ($0.26V^2$) is much less than 1, the number of broken contact per particle correlates with power index 2 (blue curve). As it is clear from Equation 6.22 and Figure 6.44, the number of broken contacts per particle, Δ', is independent of the initial size of agglomerate. As damage ratio (Δ) is in relation with Δ' (see Equation 6.22), therefore, damage ratio can also be independent of the agglomerate size if co-ordination number is constant.

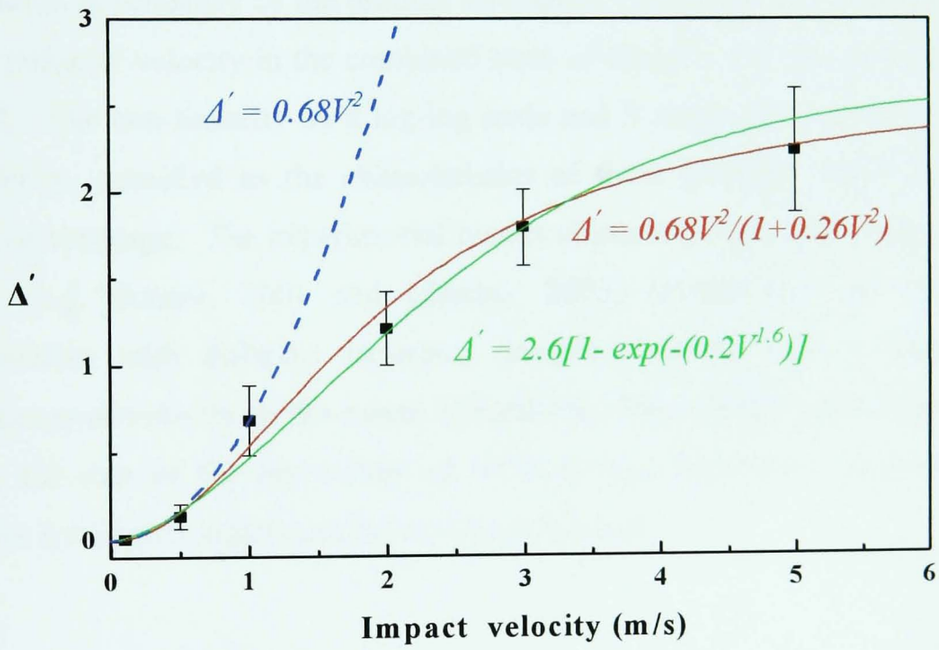

Figure 6.44: *Plot of number of broken contact per impact as a function of impact velocity plotted according DEM simulation data of Moreno (2003).*

Further investigation of the simulation data of Moreno (2003) reveals that the governing fitted relationship can also be presented based on the exponential distribution as shown in Figure 6.44 (green curve and its regression relationship). Comparing Equation 6.20 with the exponential relationship in Figure 6.44 reveals that the power indices of both relationships are close and less than 2 (i.e. 1.70 in

Equation 6.20 and 1.60 in Figure 6.44). Furthermore, both equations are independent of initial size. In fact, for a specific fragment size (L) of the experimental agglomerates, the mass fraction of complements less than this size is a function of impact velocity in a similar relationship as the damage ratio of the simulated agglomerates. This similarity of the trends might be due to the same primary particle size (100 μm) of the experimental and the simulation agglomerates.

In summary, some specific characteristics are observed for the size distribution relationship of impact product of Sample 1, which in some cases are different from the other particulate solids reported in the literature. Firstly, the size distribution is non-linear on the log-log scale with no distinction between complement and residue. Secondly, for Sample 1 granules an exponential correlation can describe the size distribution dependency of the product on impact velocity of granules. Thirdly, the power index of velocity in the combined form of velocity and size does not fit with value 2. The non-linearity on a log-log scale and S shape plots on linear scale can however be classified as the characteristics of these granules which have a high extent of breakage. The experimental results obtained in this study and some other results (e.g. Subero, 2001 and Moreno, 2003) reveals that the breakage of agglomerates with different structures doesn't likely fit with a square power dependency of velocity on the extent of breakage. More investigations are needed to clarify the role of the parameters of structure and mechanical properties of the granules for a better understanding of their behaviour.

6.5.3 Effect of impact angle on breakage of granules in single impact

To identify the effect of the impact angle on the extent of breakage, the latter is plotted in Figure 6.45 as a function of the normal component of impact velocity for Sample 3 granules. As it is seen, the curves of the four impact angles do not coincide except at very low values of the abscissa. If only the normal component of the impact velocity affects the granules breakage then the results should be unified as a single curve. This is obviously not the case.

Figure 6.46 shows the effect of the impact angle on the extent of breakage for four constant normal components of impact velocity. As it is seen, at constant normal component of 5 m s^{-1}, the extent of breakage is relatively low and independent of impact angle. In this case, the normal component of the impact velocity is responsible for chipping of the granules. A similar trend is observed for the 10 m s^{-1} normal component of velocity in the angle range of 45°-90°. However, below 45° the breakage appears to increases. Furthermore, Figure 6.46 reveals that for 15 and 25 m s^{-1} normal components, the breakage increases with decreasing the impact angle from 90° to 30°, presumably due to the influence of the tangential component of impact velocity.

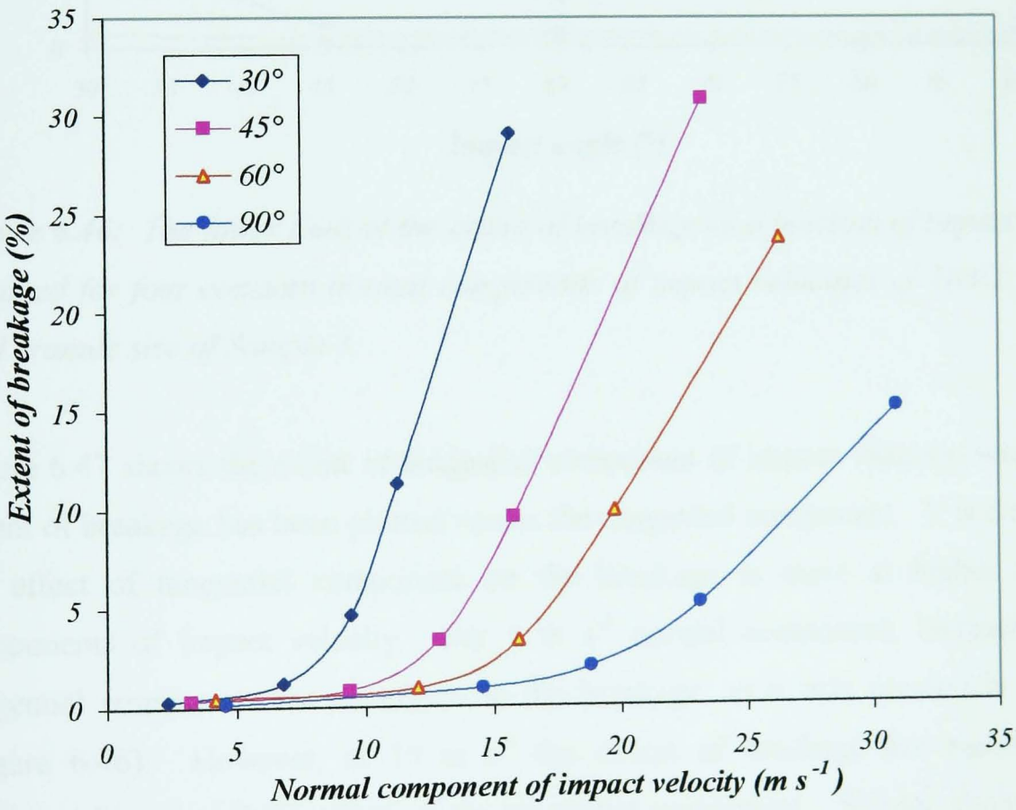

Figure 6.45: *The lower limit of extent of breakage as a function of normal component of impact velocity, obtained for four different impact angles of 1.00-1.18 mm feed granule size of Sample 3.*

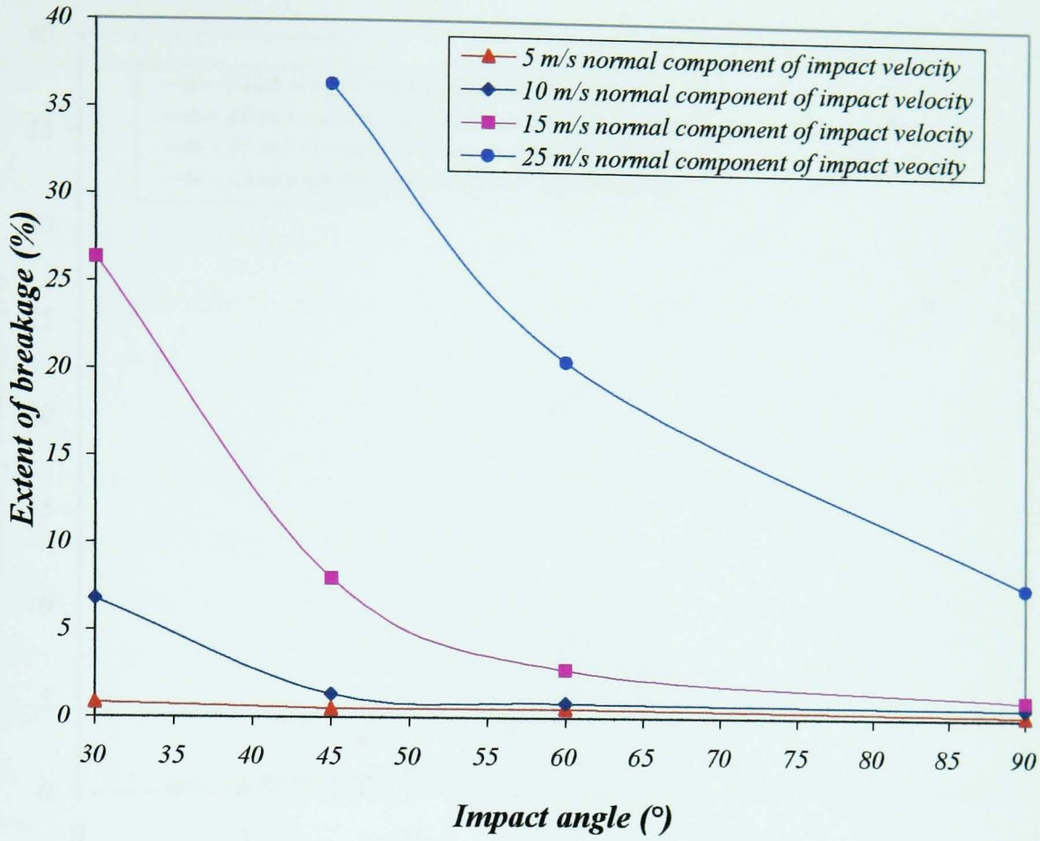

Figure 6.46: *The lower limit of the extent of breakage as a function of impact angle, obtained for four constant normal components of impact velocities of 100-1.18 mm feed granule size of Sample 3.*

Figure 6.47 shows the effect of tangential component of impact velocity, where the extent of breakage has been plotted versus the tangential component. It is clear that the effect of tangential component on the breakage is more at higher normal components of impact velocity. For 5 m s^{-1} normal component, increasing the tangential component has no effect on the breakage, as it was previously shown (Figure 6.46). However, at 15 m s^{-1} the extent of breakage has significantly increased because of the effect of the tangential component. Similar results have been obtained for Sample 2 granules that these have been presented in Appendix B (B10-B12).

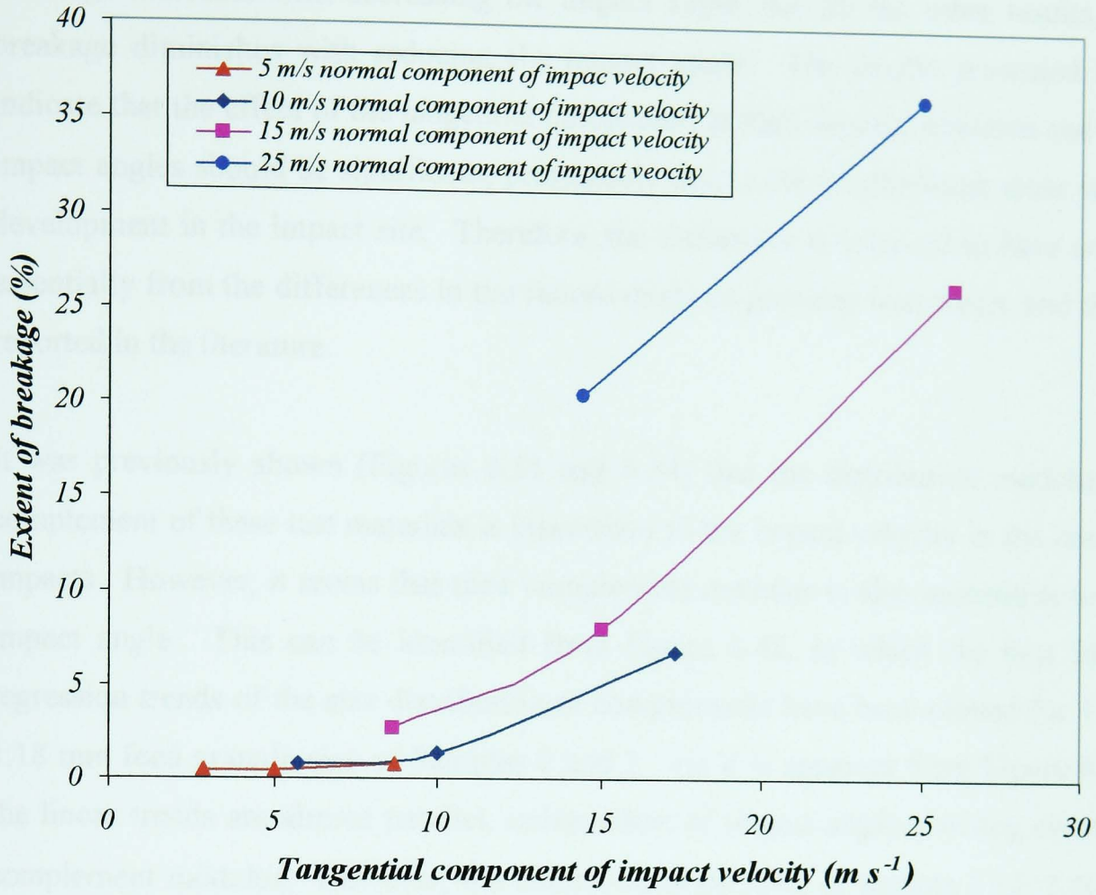

Figure 6.47: *The lower limit of extent of breakage as a function of tangential component of impact velocity for four constant normal components of impact velocities of 1.00-1.18 mm feed granule size of Sample 3.*

In summary, for the granules tested here, the normal component of the impact velocity determines the extent of breakage at low impact velocities when chipping dominates. However, at high velocities, where fragmentation occurs, the tangential component of impact velocity plays a major role in the breakage, the extent of which increases significantly with decreasing the impact angle. The above conclusions are in one sense compatible with the results of Vervoorn (1986) and Salman *et al.* (1995) obtained for alumina extrudates, Maxim *et al.* (2002) obtained for fertiliser granules and Papadopoulos (1998) obtained for porous silica particles. The contribution of the normal component of impact velocity is predominant in the chipping regime and the tangential contribution becomes equally important at higher impact velocities, where fragmentation occurs. However, there is a major difference between the results reported here and those reported in the literature. In this case, the extent of

breakage increases with decreasing the impact angle, but for the other results, the breakage diminishes with reducing the impact angle. The results presented here indicate that the effect of the tangential component at high impact velocities and low impact angles should be significant, presumably due to the predominant shear stress development in the impact site. Therefore, the difference is believed to have arisen essentially from the differences in the failure mode of granules tested here and those reported in the literature.

It was previously shown (Figures 6.33 and 6.34) that the distribution modulus of complement of these test materials is insensitive to the impact velocity in the normal impacts. However, it seems that their complement modulus is also insensitive to the impact angle. This can be identified from Figure 6.48, in which the best linear regression trends of the size distribution of complements have been plotted for 1.00-1.18 mm feed granule size of Samples 2 and 3. As it is apparent from Figure 6.48, the linear trends are almost parallel, independent of impact angle showing constant complement modulus. However, the complement modulus of Sample 2 (λ=2.46) is higher than that of the Sample 3 (λ=1.60).

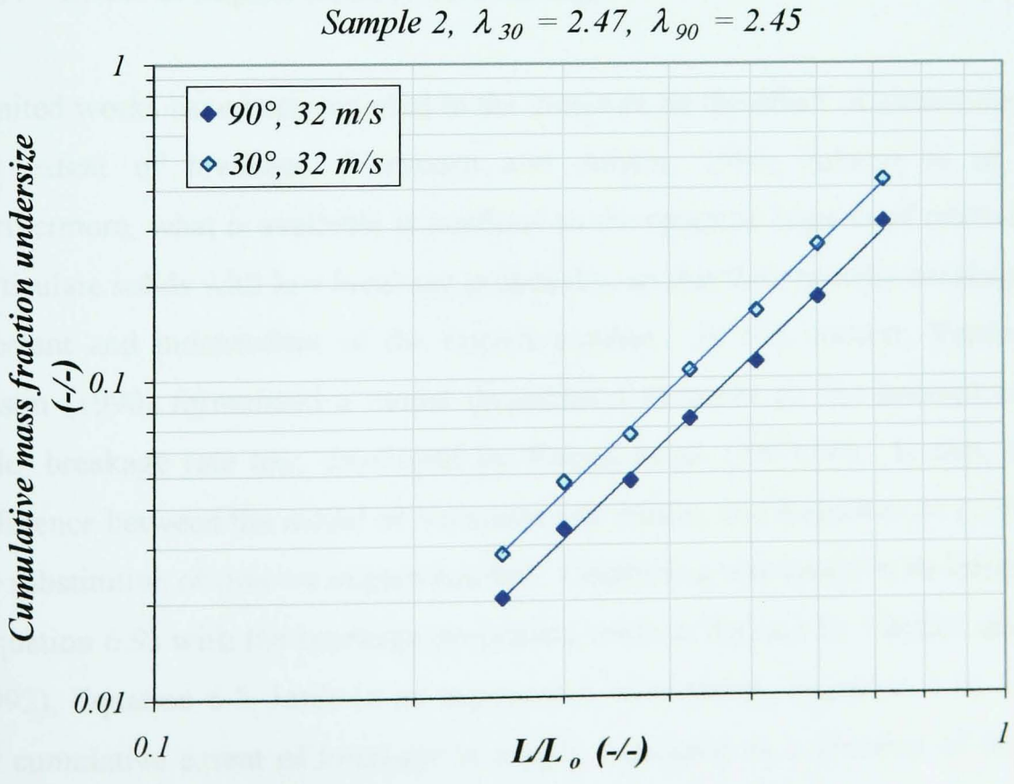

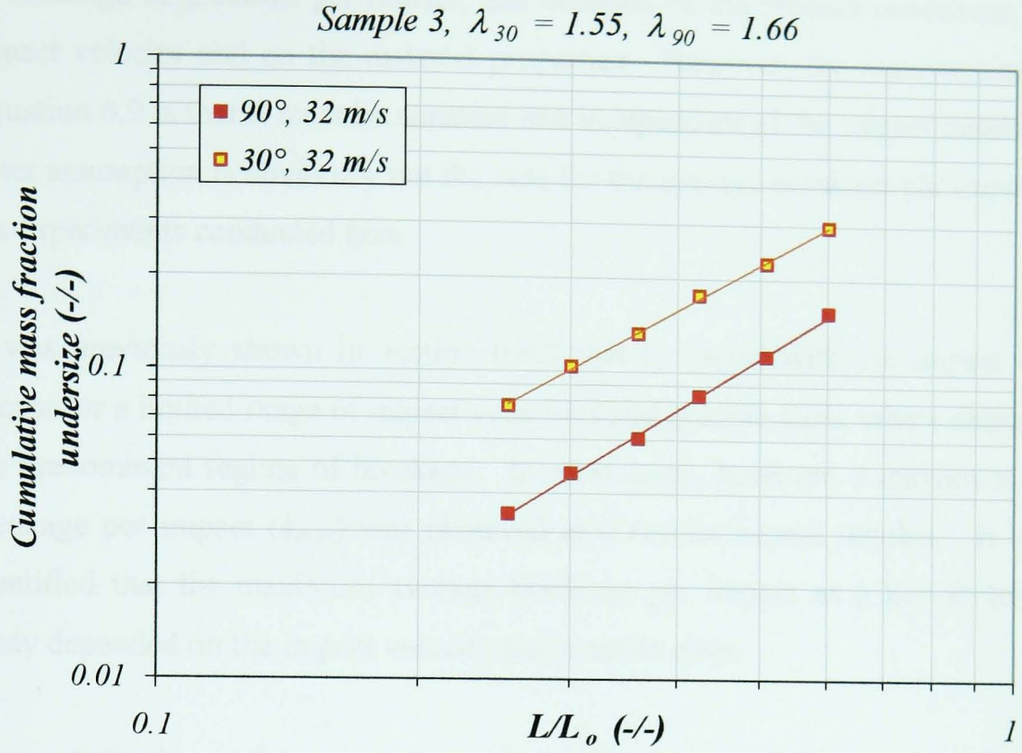

Figure 6.48: *Size distribution of complement of 1.00-1.18 mm granule size of Samples 2 and 3, impacted at 35 m s^{-1}.*

6.5.4 Effect of impact number on breakage

Limited works have been reported in the literature on the effect of impact number on the extent of breakage (Vervoorn and Austin, 1990; Salman *et al.* 2002). Furthermore, what is available is confined to the repeated impacts of relatively hard particulate solids with low breakage propensity, so that their specific breakage rate is constant and independent of the impact number. In this context, Vervoorn and Austin (1990) formulated a model (Equation 6.8) based on the concept of a first order breakage rate law, developed by Kelsall *et al.* (1967/68). In fact, the only difference between the model of Vervoorn and Austin, and Kelsall *et al.* (1967/68) is the substitution of time by impact number. Combining this model in its integral form (Equation 6.9) with the breakage propensity relation defined by Ghadiri and Zhang (1992), Equation 6.5, leads to an exponential relationship, Equation 6.10, in which the cumulative extent of breakage is simply explained as a function of the impact number. The specific breakage rate constant (s_I) in Equation 6.9 represents the rate

of breakage of granules per impact, and depends on the process conditions, such as impact velocity and on the material properties. However, the main assumption in Equation 6.9 is that s_l must be constant and independent of the impact number. This latter assumption is obviously not the case for the average breakage per impact, k_n, in the experiments conducted here.

It was previously shown in section 6.4.2 that k_n varied with the impact number, except for a limited range of impact velocities and granule sizes, where chipping was the predominant regime of breakage. In most cases, however, a maximum average breakage per impact (k_{max}) was observed at a certain impact number. It was also identified that the maximum average breakage per impact as a key factor in this study depended on the impact velocity and granule sizes.

Figure 6.49 shows the cumulative extent of breakage of Sample 2 versus impact number for 10 repeated impacts. The figure represents a combination of three feed granule sizes and three impact velocities, hence, includes nine plots.

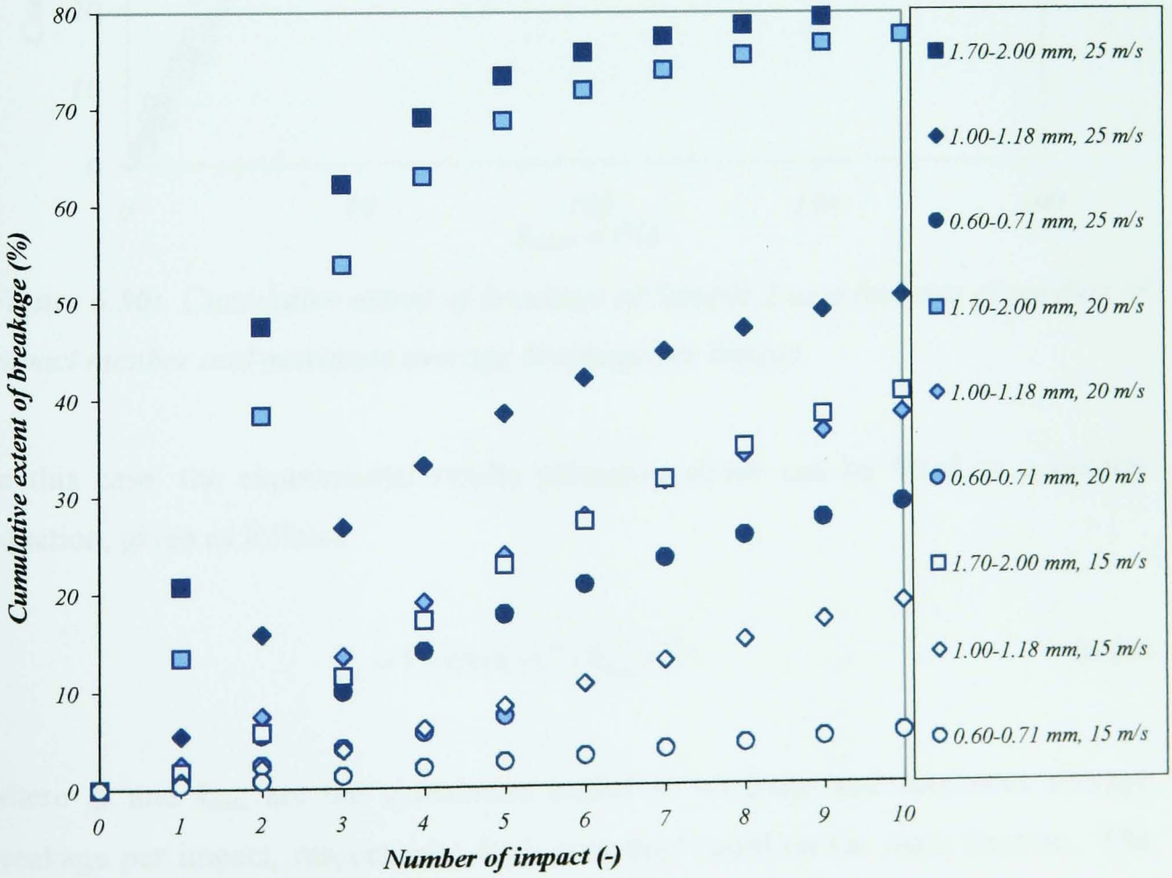

Figure 6.49: *Cumulative extent of breakage of Sample 2 as a function of impact number.*

The similar trends are observed for Sample 3 granules as shown in Appendix B (Figure B13). Surprisingly, a good unification of the results is attained when the cumulative extent of breakage is plotted as a function of the product of maximum average breakage per impact and impact number ($k_{max}\ n$). This is shown in Figure 6.50 for sample 2 and Figure B14 in Appendix B for Sample 3, in which nine plots in each figure are unified in one diagram.

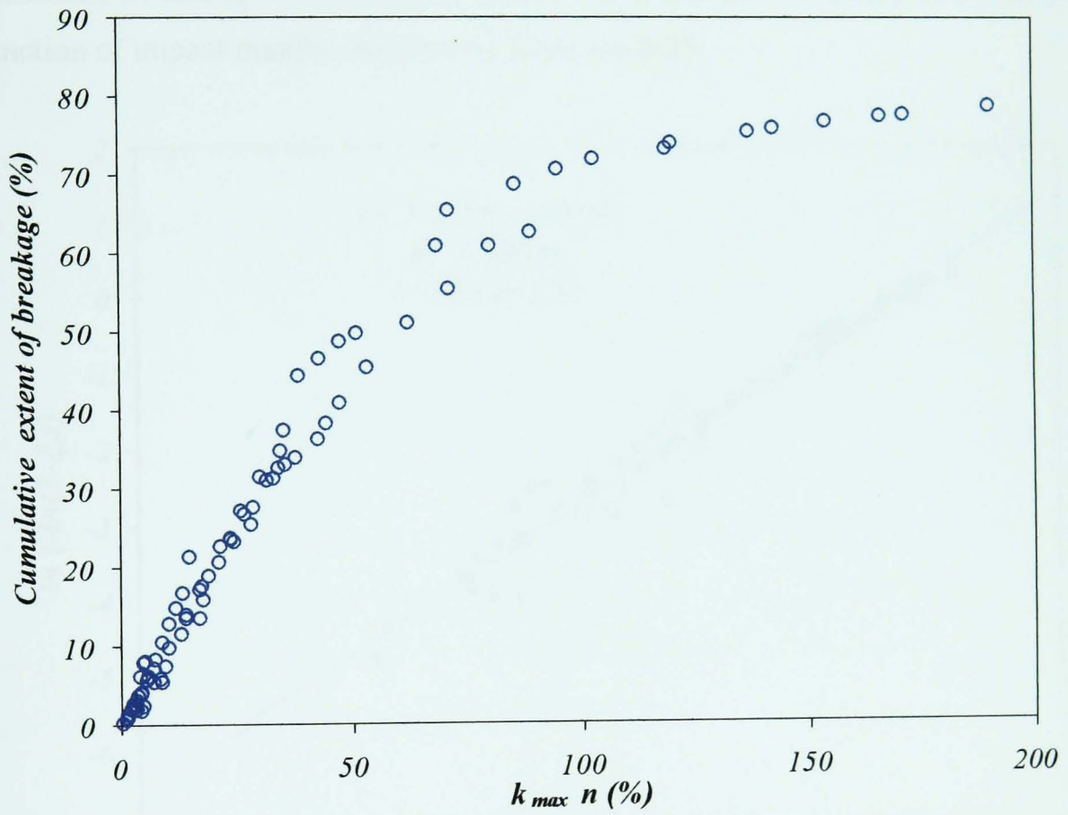

Figure 6.50: *Cumulative extent of breakage of Sample 2 as a function of product of impact number and maximum average breakage per impact.*

In this case, the experimental results presented above can be fitted to a general equation, given as follows:

$$\xi_c = 1 - \exp(-C_7\, k_{\max} n)^{a_c} \tag{6.23}$$

where ξ_c and k_{max} are the cumulative extent of breakage and maximum average breakage per impact, respectively, both presented based on the mass fraction. The factors C_7 and a_c are constants, which are quantified using the slope and intercept of

the linear regression of $ln[-ln(1-\xi_c)]$ as a function of $ln(k_{max}\, n)$, according to the following relationship.

$$\ln\left(-\ln(1-\xi_c)\right) = a_c \ln(k_{\max} n) + a_c \ln C_7 \tag{6.24}$$

Figure 6.51 shows this linear regression, the fitted relationship and the values of constants, C_7 and a_c. The resultant correlation of cumulative extent of breakage as a function of impact number is given by Equation 6.25.

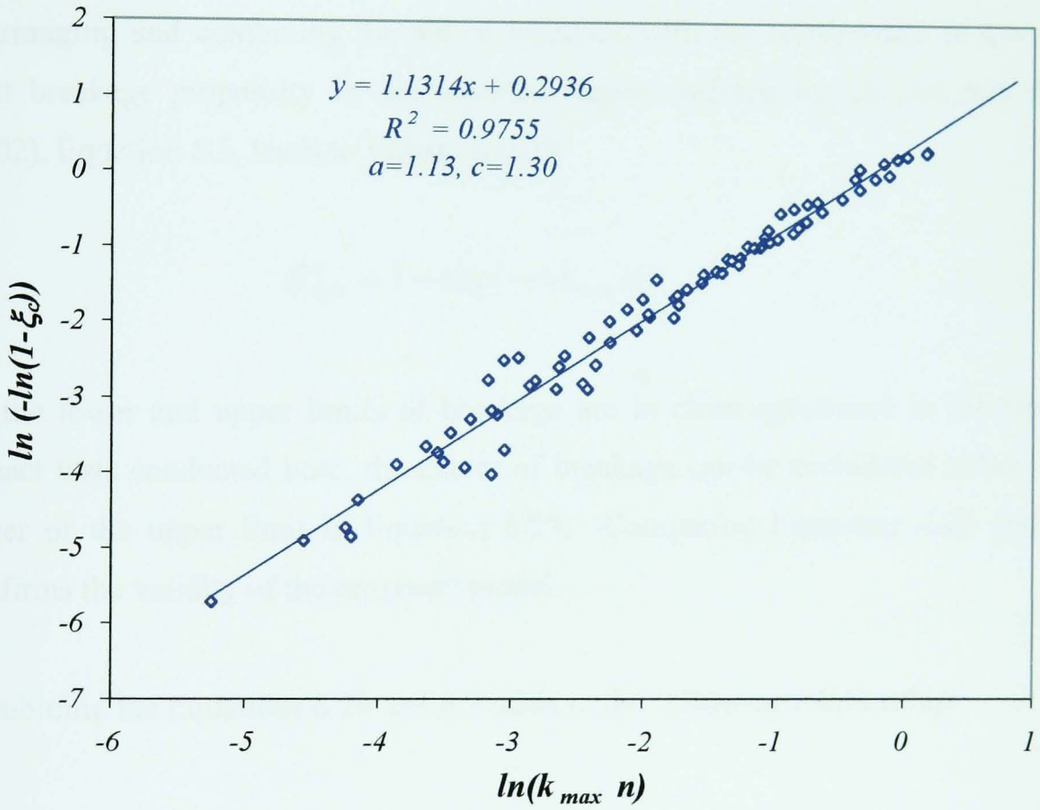

Figure 6.51: *The linear regression of $ln[-ln(1-\xi_c)]$ as a function of $ln(k_{max}\, n)$ obtained from repeated impact of Sample 2 granules.*

$$\xi_c = 1 - \exp(-1.30 k_{\max} n)^{1.13} \tag{6.25}$$

Adopting the kinetic approach concept and the first order breakage differential equation given as follow can theoretically prove equation 6.25:

$$-\frac{dM_{m(n)}}{dn} = c_1 k_{\max} M_{m(n)} \tag{6.26}$$

Equation 6.26 is obtained by substitution of s_1 in Equation 6.8 by $c_1 k_{max}$. Integrating the above equation yields Equation 6.27.

$$c_1 k_{\max} = -\frac{1}{n} ln\left(\frac{M_{m(n)}}{M_f}\right) \tag{6.27}$$

Rearranging and combining the above equation with the relationship of the upper limit breakage propensity in the repeated impact defined by Ghadiri and Zhang (2002), Equation 6.5, leads to Equation 6.28.

$$\xi^{+}_{c(n)} = 1 - \exp(-c_1 k_{\max} n) \tag{6.28}$$

As the lower and upper limits of breakage are in close agreement in the repeated impact tests conducted here; the extent of breakage can be considered either as the lower or the upper limit in Equation 6.27. Comparing Equations 6.25 and 6.28 confirms the validity of the proposed model.

Combining the Equations 6.28 and 6.7 leads to the following relationship:

$$k_n = \frac{1 - \exp(-c_1 k_{\max} n)}{n} \tag{6.29}$$

In fact, Equation 6.29 shows the functionality of average breakage per impact in the repeated impact as a function of impact number.

Figure 6.52 shows the dependency of k_{max} on the impact velocity and granule size. Furthermore, as it was shown in Chapter 4 that the crushing strength of granules might also be varied with size, therefore, maximum average breakage per impact may depend also on the strength. This dependency is seen in Figure 6.52b, where the maximum average breakage per impact is plotted as function of granule strength.

The apparent strength of the granules has been obtained based on the bulk compression of granules at strain rate of 1 mm min^{-1}.

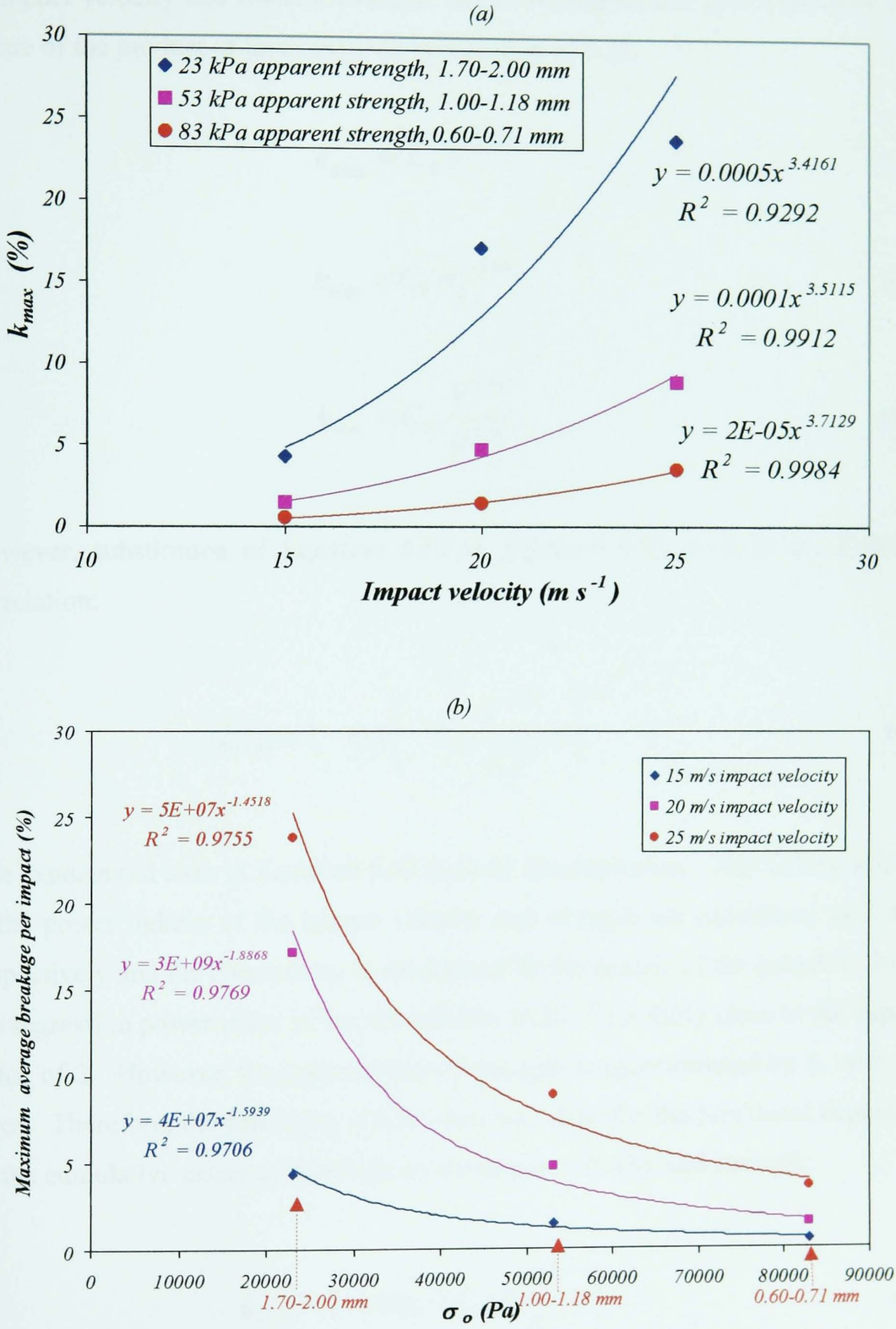

Figure 6.52: *Dependency of maximum specific breakage on the impact velocity and granules strength of Sample 2.*

Averaging the power indices of the impact velocity and strength in Figure 6.52 leads to Equations 6.30 and 6.31. As maximum average breakage per impact is a function of impact velocity and fracture strength, therefore, hence, it is also a function route square of the product of them as given in Equation of 6.32.

$$k_{\max} = C_8 V^{3.55} \tag{6.30}$$

$$k_{\max} = C_9 \sigma_o^{-1.64} \tag{6.31}$$

$$k_{\max} = C_{10} \frac{V^{1.88}}{\sigma_o^{1.28}} \tag{6.32}$$

However, substitution of Equation 6.32 in Equation 6.25 leads to the following correlation:

$$\xi_{c(n)} = 1 - \exp\left(- C_{11} \frac{V^{1.88}}{\sigma_o^{1.28}} n \right)^{1.13} \tag{6.33}$$

The exponential term in Equation 6.33 must be dimensionless. This will be achieved if the power indices of the impact velocity and strength are considered as 2 and 1 respectively and the constant c_{11} is substituted by the density of the granules. In fact, the regression power index of impact velocity ($1.88^{1.13}$) is fairly close to the expected value of 2. However, the power index of strength is approximated by 1, with more error. Therefore, the following relationship may describe the functional dependence of the cumulative extent of breakage on the impact velocity and strength:

$$\xi_{c(n)} = 1 - \exp\left(- C_{12} \rho \frac{V^2}{\sigma_o} n \right) \tag{6.34}$$

where ρ is the density of the granules and C_{12} is the a dimensionless constant. In this context, Figures 6.53 and B15 in Appendix B show the experimental unification

of the results for Sample 2 granules, plotted based on Equations 6.33 and 6.34, respectively.

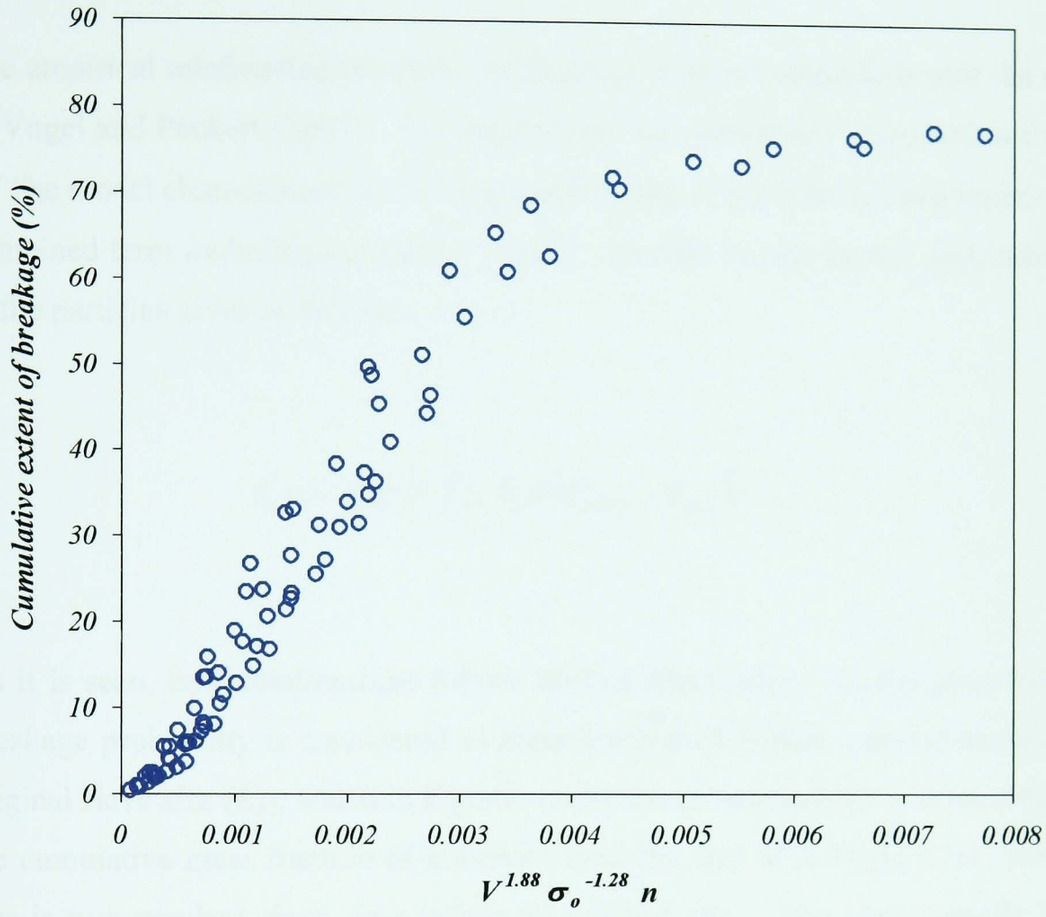

Figure 6.53: *Cumulative extent of breakage of Sample 2 as a function of group given in Equation 6.33.*

In a similar approach, the following correlations can be obtained for the repeated impact of Sample 3.

$$\xi_{c(n)} = 1 - \exp(-1.34\,k_{\max} n)^{1.26} \tag{6.35}$$

$$\xi_{c(n)} = 1 - \exp\left(-C_{13}\,\frac{V^{1.73}}{\sigma_o^{0.9}}\,n\right)^{1.26} \tag{6.36}$$

Figure B16 (Appendix B) shows the plot of ξ_c as a function of $V^2\sigma_o^{-1}n$ for Sample 3. In this case, a better fitting of data is observed for Sample 3, as compared to Sample 2.

The empirical relationship presented as Equation 6.34 is comparable with the model of Vogel and Peukert (2003). The latter model was previously discussed in Chapter 2. The model characterises the breakage probability of particles (ζ) as a function of a combined term including number of impacts, specific impact energy and initial size of the particles given as follows:

$$\zeta = 1 - \exp\left\{-f_{mat}\, L_o\, n\left(E_{m,kin} - E_{m,c}\right)\right\} \tag{6.37}$$

As it is seen, both relationships follow Weibul distribution. In Equation 6.37, the breakage probability is considered as mass fraction of broken material smaller than original sieve size (L_o), whilst in Equation 6.34 the corresponding function represents the cumulative mass fraction of material under the size of a single sieve, which its size is two standard sieve sizes below the original size. Two mass-specific kinetic energies of $E_{m,kin}$ and $E_{m,c}$ (J kg^{-1}) are impact energy and critical impact energy, respectively which are substituted by square of impact velocity in Equation 6.34. f_{mat} (kg J^{-1} m^{-1}) is a fitted parameter and is suggested to reflect material properties. Vogel and Peukert (2003) employed this model to different materials (PMMA polymers, limestone and glass) of various sizes (95 μm to 8 mm) and could describe the breakage probability of them by a single master-curve. However, the model developed in this work is independent of initial size of particles and depends on crushing strength of agglomerates instead of unknown material property f_{mat}.

It must be noted that the strength of the granules in this study has been obtained indirectly by the quasi-static bulk compression method and does not reflect the dynamic strength of granules. More investigation must be carried out in this regard to elucidate the exact dependency of the cumulative extent of breakage on the impact velocity, dynamic strength and impact number.

6.5.5 Criterion for selection of single sieve

In this study, the extent of breakage of granules during impacts was determined based on the sieving method, using either a single sieve or series of sieves. In the chipping regime of breakage, single sieving method was adopted using a sieve that was two standard sizes below the feed granule size to minimise the sieving effort. This method was quite satisfactory in the chipping, as the fine debris was completely distinguishable from the large mother particles. However, for fragmentation a full sieve analysis was conducted as the impact product was distributed over all sieves. Nevertheless, in the fragmentation, the impact product might be partitioned into two categories; the large fragments, which contain partially, damaged mother particles and small fragments, including the debris. This was shown as a distinct natural cut in the log-log scale size distribution curves between the residue and complement. The natural cut was approximately positioned at the normalised size (L/L_0) of 0.70.

In the literature, breakage indices have been used as alternatives to particle size distribution functions. The traditional indices in single particle tests are usually determined based on either the ratio of the number of broken particles to the total number of particles impacted (Rumpf and Schönert, 1973; Salman *et al.*, 1995) or the mass fraction of material under a certain size (Vervoorn and Austin, 1990, Ghadiri and Zhang, 2002; Papadopoulos and Ghadiri, 1996). As it was previously mentioned, in this work, the extent of breakage was characterised according to the gravimetric sieving method. However, in the single sieve analysis, the selection of a proper sieve size to characterise the breakage is a deterministic factor.

In Figure 6.54, mass fraction undersize of the impact product of Sample 3 has been plotted as a function of velocity for different size ratios. The results have been presented for two feed granule sizes in the single impacts. For feed granule size of 0.60-0.71 mm (Figure 6.54a), in a wide range of impact velocity up to 25 m s^{-1}, the mass fraction undersize of the size ratios 0.70 or less is almost constant independent of sieve size at that range. It means that any sieve with the size equivalent to the size ratio 0.7 or less is adequate to be used for determining the extent of breakage. However, at the higher impact velocities, the size of impact product is distributed

over wider sieve size range in which the extent of breakage varies with the size ratio. For feed granule size of 1.70-2.00 mm (Figure 6.54b), the insensitivity of the extent of breakage to the size ratio less than 0.7 is limited to the impact velocities lower than 10 m s^{-1}, i.e where chipping regime prevails.

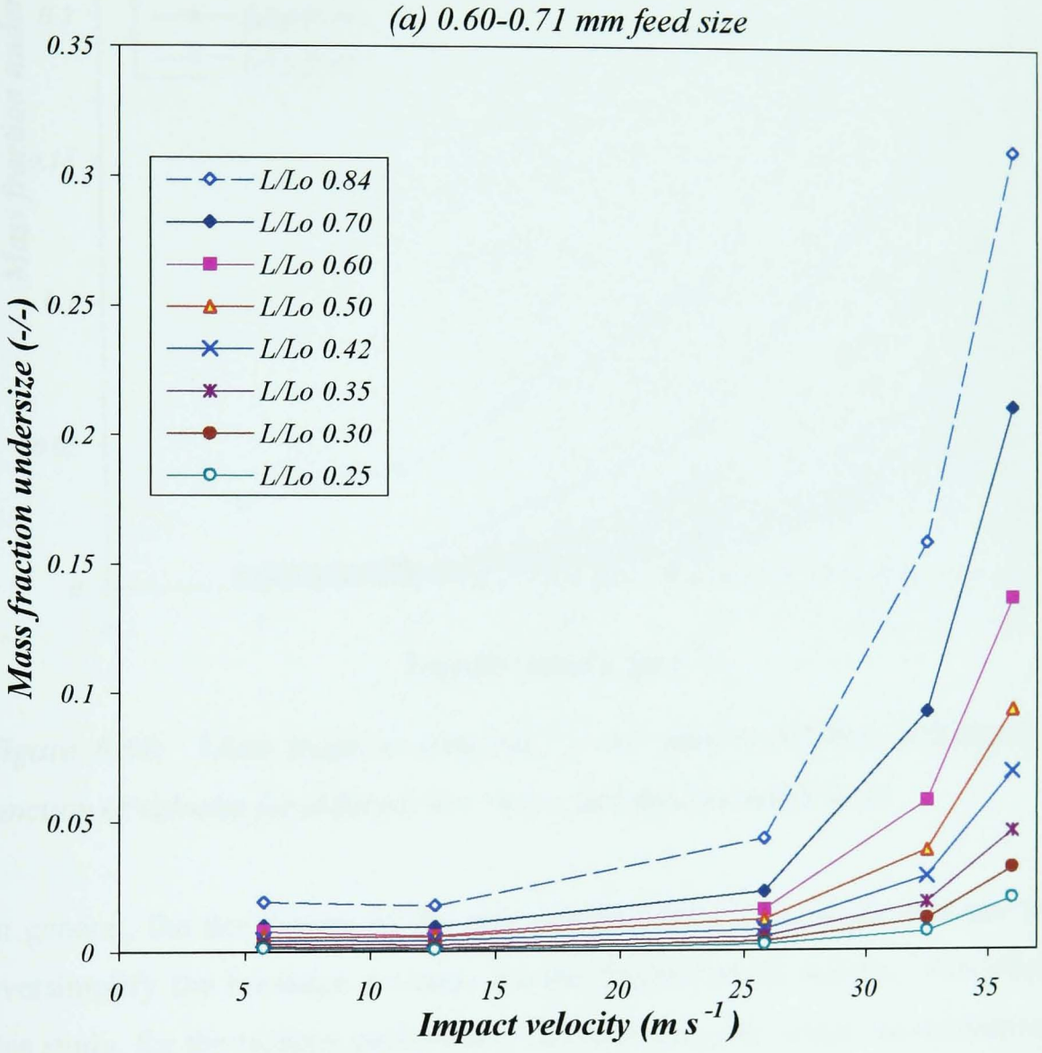

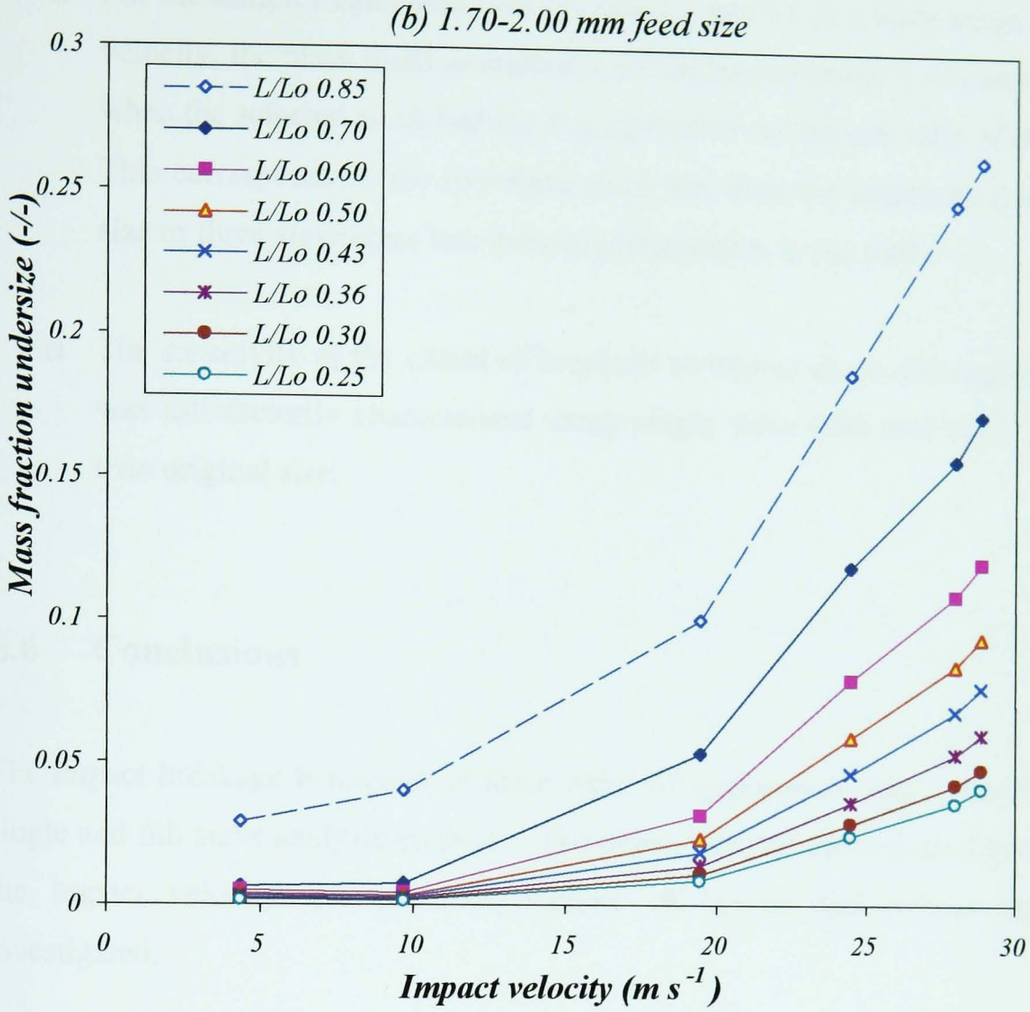

Figure 6.54: *Mass fraction undersize of the impact product of Sample 3 as a function of velocity for different size ratios and feed granules sizes.*

In general, the description of the size distribution with a single measure seems to oversimplify the breakage process, for the fragmentation regime. Nevertheless, in this study, for the reasons explained in the following, the single sieve analysis (using two sieve sizes less than feed size) has also been conducted in addition to the full sieve analysis for the following reasons.

- Single sieve analysis reduces the hard work of sieving. This method was especially effective in conducting a large number of repeated impact tests.

- The transition condition from chipping to fragmentation could simply be determined by a sudden slope change in the trends of extend of breakage as a function of impact velocity.

- For the samples examined here (Samples 2 and 3), in a wide range of impact velocity, the mass fraction undersize of the impact product was less than 5%, when the selected sieve had the size equivalent to the size ratio of 0.6 or less. This corresponds to the two sieve sizes less than the minimum feed granule size or three sieve sizes less than largest granules in the feed.

- The sensitivity of the extent of breakage to impact angle and impact number was satisfactorily characterised using single sieve with two sieve sizes less than original size.

6.6 Conclusions

The impact breakage behaviour of three types of agglomerate was quantified using single and full sieve analysis methods. The dependency of the extent of breakage on the impact velocity, granule size, number of impact and impact angle was investigated.

The reliability of the impact test results was assessed addressing the systematic errors, reproducibility of the results and handling losses in the impact tests. The systematic errors were found to be negligible. The reproducibility of the results was found to be sensitive to the number of impacted granules, as it improved by increasing the number of granules from 2000 to 5000. The accuracy of the extent of breakage depended on the handling losses and/or errors associated with gravimetric analysis. In this context, a breakage variation band was determined by defining the lower and upper limits of breakage. The real extent of breakage lied somewhere between the lower and upper limits. In most cases, however, the difference between lower and upper limits was found small, showing low handling losses.

The full sieve analyses of Samples 1, 2 and 3 were carried out and the size distributions of the impact product were plotted based on the mass fraction undersize versus normalised size (L/L_o) on the log-log scale. For Samples 2 and 3, a natural cut in the size distribution plots was observed between two linear trends of complement

and residue. The natural cut gradually disappeared by increasing the impact velocity and the two distinct straight lines became a single one. For Sample 1, however, the size distribution plots were non-linear, except in the case of very fine feed granule sizes and low impact velocities (free fall impacts). For Samples 2 and 3 the slope of complement trend line, defined as the distribution modulus of complement, was found to be independent of impact velocity as well as impact angle. However, it varied with the granule size. The concept of the complement modulus was not applicable to Sample 1 due to the non-linearity of the size distribution plots of Sample 1 on log-log scale.

Two empirical models were proposed for the breakage of Sample 1, and Samples 2 and 3 in single impacts. The models described the functional dependence of the mass fraction undersize on impact velocity and size of the impact product. For sample 1, good unification of the results was observed for a range of impact velocities, independent of original granule size. However, for Samples 2 and 3, breakage varied with original size depending on the complement modulus of breakage.

The effect of impact angle on the extent of breakage of Samples 2 and 3 were investigated in single impacts. The results showed that at low impact velocities where chipping regime dominated, the normal component of the impact velocity determined the extent of breakage, independent of impact angle. However, at higher velocities, where fragmentation occurred consistently the contribution of the tangential component of impact velocity was also important. A major difference was found between the results reported here and those in the literature. In these experiments, the extent of breakage increased with decreasing the impact angles. In contrast, the results reported in the literature for other materials showed that the breakage diminished with reducing the impact angle. The difference is believed to have arisen due to the difference in the failure mode of granules. The results presented in this work revealed that the effect of the tangential component of impact velocity was significant at high impact velocities and low impact angles. This is presumably due to the predominant shear stress in the impact site. The materials

tested here should be more sensitive to shear stresses than the other materials tested previously.

For Samples 2 and 3, the effect of impact number on the extent of breakage was studied using single sieve analysis method. It was shown that the incremental extent of breakage and average breakage per impact increased to a maximum at a certain impact number. The maximum average breakage per impact varied directly with impact velocity and granule feed size. An empirical correlation was proposed based on the concept of a first order breakage rate (Equations 6.28 or 6.34). The model relates the cumulative extent of breakage to a group combining the impact number and maximum average breakage per impact. A good fit of experimental data was obtained in the repeated impacts of Samples 2 and 3 using equations 6.28 and 6.34.

$$\xi_{c(n)} = 1 - \exp\left(-C_1 k_{\max} n\right) = 1 - \exp\left(-C_{12}\rho \frac{V^2}{\sigma_o} n\right) \qquad (6.28)\ (6.34)$$

Combining Equations 6.28 or 6.34 and 6.7 led to the following relationships showing the functional dependence of average breakage per impact on the number of impact, velocity and strength of granules as shown in Equations 6.29 and 6.38.

$$k_n = \frac{1 - \exp\left(-C_1 k_{\max} n\right)}{n} = \frac{1 - \exp\left(-C_{12}\rho \frac{V^2}{\sigma_o} n\right)}{n} \qquad (6.29)\ (6.38)$$

When average breakage per impact was small or constant (i.e. at low impact velocities and/or high strength of granule), cumulative breakage was increased linearly with number of impact. In this case, average breakage per impact equalled to the specific breakage rate (s_l). However, in other cases (i.e high impact velocities and/or large granules) specific breakage rate was found proportional to the maximum average breakage per impact, as shown in Equation 6.39.

$$s_l = C_1 k_{\max} \qquad (6.39)$$

7 OVERALL CONCLUSIONS AND FUTURE WORK

7.1 Overall conclusions

A comprehensive literature review showed that for agglomerates with highly discontinuous and heterogeneous characteristics, it was impossible to develop a universal model of strength and mechanical properties covering all conditions (i.e. the theoretical and semi-empirical models of agglomerate strength assume only brittle mode of breakage). For this reason, the mechanical properties of agglomerates are still characterised based on the empirical correlations and experimental methods. On the other hand, the application of the classic definitions of failure mode as brittle, semi-brittle and ductile to agglomerates has not been well developed. For agglomerates, the microscopic inter-particle bonds may fail in different mode as compared to the whole of the agglomerates on the macroscopic scale. Ning *et al.* (1997) and Boerefijn *et al.* (1998) reported macroscopic ductile and microscopic brittle inter-particle failures for weak lactose agglomerates. In contrast, Samimi *et al.* (2003) observed an extensive plastic deformation and consequently semi-brittle breakage in macroscopic scale and ductile failure within the binders of soft agglomerates.

Three samples were investigated in this work. Sample 1 was made of calcium carbonate powders as the primary particles and polyethylene glycol (PEG) as the binder. The primary particles are large and non-porous (100 μm). Fluidised bed granulation with molten PEG binder produced granules with thick solid bridges containing a large number of internal flaws and low co-ordination number. Close SEM observations of the granules after impact showed the location of the internal flaws mainly on the broken planes of the bridges.

Samples 2 and 3 had the same formulation, but were produced through two different processing methods of fluidised bed granulation and high shear mixing granulation. The SEM observations of Sample 2 granules revealed that these granules were made of a large number of small clusters, aggregated by a paste type binder, where the

primary particles (about 1 μm size) acted as filler of the same binder. In contrast, in Sample 3 no small clusters were seen and the primary particles were directly embedded in the binder. A denser structure with a more spherical shape and smoother surfaces prevailed in Sample 3, as compared to Sample 2.

The yield stress and elastic modulus of Sample 3 granules were estimated by fitting the theoretical model of elastic-perfectly plastic of Thornton and Ning (1998) to the early parts of force-displacement data (maximum load of 0.01 N) obtained from single granule compression tests. For 1.70-2.00 mm and 1.00-1.18 mm granules of Sample 3 the average value of yield stress was found about two times of the yield pressure (P_y) obtained based on the Heckel analysis. DEM simulations of Heckel parameter (P_y=1/K) also confirmed this conclusion, in which the properties of the single particle, used as the input data in DEM simulations, were similar to the granules used in this work.

The strength of the granules of Samples 2 and 3 were determined based on the single and bulk compression analysis. In the bulk compression tests, the strength of single granules was determined using models of Kawakita and Lüdde (1970), and Adams *et al.* (1994). It was found that the strength of granules obtained based on the single granule compression is in close agreement with the values obtained based on the bulk compression analysis at zero aspect ratio. Furthermore, the strength of granules showed size and strain rate sensitivities, in which strength was increased with decreasing the granule size and increasing the strain rate.

It was shown that the yield stress and strength of this detergent type granules correlated based on Equation 4.27, in which strength was described as a function of yield stress of the granules, and pressure and friction factors of the bed.

The high-speed video recordings of the impact events as well as SEM observations of the broken granules of Sample 1 indicated that the high extent of disintegration of granules was the result of synergistic effects of low bond strength, high porosity and low co-ordination number of the granules. The presence of pre-existing internal flaws within the PEG solid bridge as well as extensive macro-voids in the granules

suggested that the predominant mode of breakage was likely to be brittle. However, a precise examination of the impact sites revealed the occurrence of some plastic deformation of PEG surface layer especially on the sharp corners. The latter observations, therefore, indicated that for Sample 1 the semi-brittle mode of breakage should be the prevailing mode of breakage.

The chipping of Sample 2 granules occurred through the breakage of small clusters from the surface protuberances, whereas for Sample 3 fine debris was separated from the surface of granules. For both samples, a large proportion of the impact energy was dissipated by the impact site densification and by stable crack propagations. However, the irregular and porous structure of these granules provided sufficient stress concentration by which fragmentation and disintegration of the granule to be occurred at high impact velocities. Therefore, in spite of the macroscopic plastic behaviour of the impact site and microscopic ductile failure within the crack openings, the breakage pattern of the granules is comparable with semi-brittle failure mode.

The effects of impact velocity, granule size, impact number and impact angle were quantified using single and full sieve analysis methods. In general, different size distribution trends were obtained for the impact product of Samples 1, 2 and 3. The data were presented based on the mass fraction undersize as a function of normalised size on a log-log scale (Figure 7.1). For Samples 2 and 3 a natural cut in the size distribution plots was observed between two linear trends of complement and residue at low impact velocities. This form of size distribution was representative of a predominant chipping mode of breakage (plot *a*). The slope of complement line, defined as the distribution modulus of complement, was found to be independent of impact velocity (at the range of impact velocities employed in this work) and impact angle. However, it varied with feed granule size. Increasing the impact velocity eliminated the natural cut and then the two distinct straight lines became a single one (plot *b*). This type of plot was observed under fragmentation mode of breakage. In this case, the size distribution line usually was parallel to the complement parts at lower impact velocities with the same granule size before impact (Plot *a*). For Sample 1, however, due to the high extent of breakage the size distributions of

impact products were usually non-linear (plot *c*), except in the cases of very fine feed sizes and low impact velocities. For Sample 1, therefore, the concept of complement modulus was not applicable.

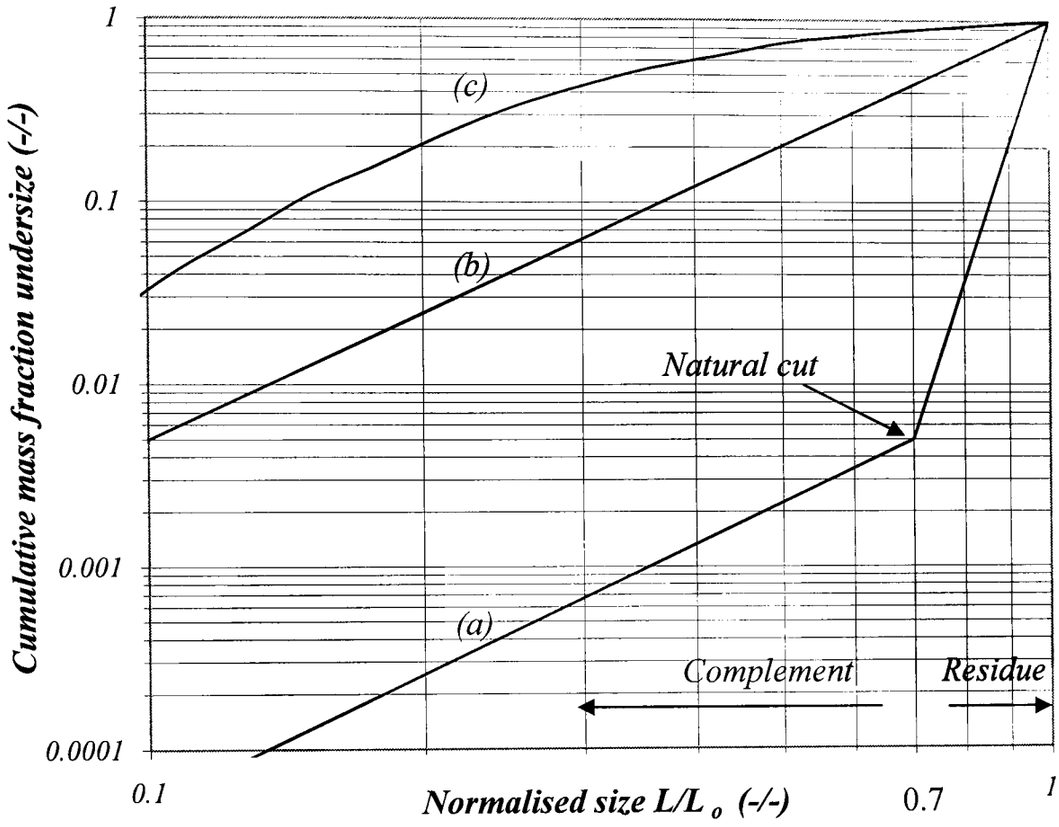

Figure 7.1: *Different shapes of size distribution curves obtained for Sample1, 2 and 3 under different conditions such as impact velocity.*

Two empirical models were proposed for the size distribution of impact product of Sample 1 (Equation 6.20) and Samples 2 and 3 (Equation 6.15) for single impacts. The models describe the functional dependence of the mass fraction undersize on impact velocity and size of the broken material. For Sample 1, good unification of the results was observed for a range of impact velocities, independent of original size of granules. However, for Samples 2 and 3, breakage varied as a function of impact velocity and complement modulus.

The effect of impact angle on the extent of breakage of Samples 2 and 3 were investigated in single impacts. A major difference was found between the results

reported here and those in the literature. In these experiments, the extent of breakage increased with decreasing the impact angles. In contrast, the results reported in the literature for other materials showed that the breakage diminished with reducing the impact angle. The difference is believed to have arisen due to the difference in the failure mode of these soft granules with the brittle material used in the other works. The results presented in this work revealed that the effect of the tangential component of impact velocity was significant at high impact velocities and low impact angles. This has significant implications for the choice of milling mechanisms.

For Samples 2 and 3, the effect of impact number on the extent of breakage was studied using single sieve analysis method. It was shown that the parameters of incremental extent of breakage and average breakage per impact increased to a maximum at a certain impact number. It was found that this maximum average breakage per impact varied directly with impact velocity and granule feed size. An empirical correlation was proposed based on the concept of a first order breakage rate (Equations 6.28 or 6.34). The model related the cumulative extent of breakage to a group combining the impact number and a parameter defined as maximum average breakage per impact. The results obtained in this study revealed that for Samples 2 and 3 with semi-brittle breakage behaviour first order breakage rate equations could satisfactorily describe the effect of impact number on the extent of breakage.

7.2 Future work

In this work, an attempt was made to investigate systematically the deformation and breakage behaviour of agglomerates. A variety of challenging research lines has been identified as described below.

1) Future work needs to concentrate on agglomerates with well-characterised mechanical and structural properties. For soft agglomerates used in this work no information was available for their mechanical and structural properties. To obtain a

fundamental understanding of deformation and breakage of these materials, the role of the structure of agglomerates on the deformation and breakage should be identified. In this context, the micro-structural properties such as porosity and interface energy and their relationship with macroscopic mechanical properties such as the elastic modulus, hardness and fracture toughness still need to be investigated. The limited understanding of the breakage behaviour of agglomerates stems essentially from the difficulty in obtaining the agglomerates with well-defined microstructure properties as well as from the complexity of their structure, which prevents a proper analysis of their macroscopic mechanical properties based on the classic methods. In this context, some attempts have recently been made to produce mono-disperse agglomerates with a controlled structure using glass beads and brittle polymeric glue (Subero, 2001). A novel technique has been developed by Subero, 2001 to fabricate these agglomerates with the well-defined characteristics. Similar methodology might be employed to make agglomerates but with smaller primary particle size and soft binders as compared to the previous work. For this type agglomerates, using sophisticated mechanical testing instruments such as nano-indentation and nano-crusher is useful to characterise their mechanical properties. However, a difficulty might arise in interpreting the nano-indentation results if a sharp indenter tip is used for highly porous structure agglomerates. In this case, a challenging task would be to explore using a blunt indenter (e.g. spherical indenter) to minimise the interaction of indenter with pores.

2) In this Thesis a collaborative work was carried out with Mr A. Hassanpour in order to compare the experimental results and DEM simulations of the bulk compression of soft granules. Good comparison of the results suggests that the computer simulation can be used as a powerful tool to enhance the knowledge of deformation and damage of the agglomerates in the bulk. However, due to limitations of computer power, in DEM analysis used in this work, bulk compression of the continuum particulate solids was simulated instead of the agglomerates but with the same mechanical properties as the granules used in the experimental tests. The limitation in the creation and deformation of agglomerates in the bed was due to the calculation time and computer memory restrictions. Therefore, for future work, it is recommended that a faster computer with a larger memory to be used to facilitate

the simulations and to get more realistic results. Furthermore, DEM analysis of bulk compression can be employed to examine the validation of the models used and the experimental results obtained in this work by investigating the effects of strain rate, agglomerate size and aspect ratio on strength and yield stress of single agglomerates.

3) Extending the classic definitions of the failure modes to the agglomerates has not been well developed and still needs to be verified in more detail especially for ductile failure mode. In this context, the failure mode of wider range of agglomerate types is suggested to study by observation of the crack morphology and breakage patterns during quasi-static compression and impact of the single agglomerates.

4) The complement modulus of the particle size distribution has been considered by a number of investigators as a key parameter in characterising the size distribution of impact product. For Samples 2 and 3 it was shown that the modulus was independent of impact velocity and impact angle in the range of velocity and angles used in this Thesis. In this context, the physical significance of the modulus and factors affecting it (e.g. structure of agglomerates) are of practical interest and need to be investigated for different types of agglomerate.

5) The functional dependency of the size distribution of the impact product on the impact velocity was investigated by some workers for different particulate solids, in which the governing relationships were commonly correlated with the velocity to the power index of 2. However, for agglomerates this functionality is not obvious and needs to be investigated in more detail. Subero (2001) in his attempt to quantify the impact breakage of agglomerates made of glass beads and brittle polymeric binder showed the velocity index in the range of 1.00-1.80, i.e. below the value of 2. In this Thesis two empirical models were proposed for the size distribution of the impact products of Samples 1, 2 and 3, in which different power indices were obtained for impact velocity.

6) For the first time it was shown in this Thesis that for a specific type of agglomerates made of soft binders and very fine primary particles (Samples 2 and 3) the extent of breakage of granules was increased with decreasing the impact angle.

This result reveals that in the size reduction processes of soft agglomerates oblique impacts would be more effective than normal impact. This result opens a new line of challenge to investigate in more detail the effect of impact angle on breakage of such materials. Although, the results were similar for Samples 2 and 3 with different degrees of sphericity, it is recommended that the experiments to be carried out with the more spherical agglomerates having same characteristics as those used in this work to reveal the effect of shape of agglomerates.

7) The validity of the model proposed in this Thesis to relate the extent of breakage to the impact number needs to be investigated experimentally using a wider range of agglomerates and/or through computer simulations. Furthermore, the dependency of the new parameter defined as the maximum average breakage per impact on the granule size, impact velocity and mechanical properties should be investigated.

PAGE
MISSING
IN
ORIGINAL

LIST OF REFERENCES

Abdel-Ghani, M., Petrie, J.G., Seville, J.P.K., Clift, R. and Adams, M.J. (1991). Mechanical properties of cohesive particulate solids. *Powder Technol.*, **65**, 113-123.

Adams, M.J. (1985). The strength of particulate solids. *J. of Powder & Bulk Solids Technol.*, **9** (4), 15-20.

Adams, M.J., Mullier, M.A. and Seville, J.P.K. (1994). Agglomerate strength measurement using a uniaxial confined compression test. *Powder Technol.* **78**, 5-13.

Adams, M.J. and McKeown, R. (1996). Micromechanical analyses of the pressure-volume relationships for powders under confined uniaxial compression. *Powder Technol.*, **88**, 155-163.

Adams, M.J., Williams, D. and Williams, J.G. (1989). The use of linear elastic fracture mechanics for particulate solids. *J. Mat. Sci.*, **24**, 1772-1776.

Allen, T. (1981). Particle size measurement. 3rd ed. Chapman and Hall.

Arbiter, N., Harris, C.C. and Stamboltzis, G.A. (1969). Single fracture of brittle spheres. *Trans. AIME,* **244**, 118-133.

Arteaga, P. and Tüzün, U. (1990). Flow of binary mixtures of equal-density granules in hoppers-size segregation, flowing density and discharge rates. *Chem. Eng. Sci.,* **45**(1), 205-223.

Arteaga, P.A., Ghadiri, M., Lawson, N.S. and Pollock, H.M. (1993). Use of nanoindentation to assess potential attrition of particulate solids. *Tribology International*, **26**:5, 305-310.

Atkins, A.G. and May, Y.W. (1985). Elastic and plastic fracture. Ellis Horwood Ltd., Chichester.

Barnard, W.J. and Bull, F.A. (1985). The characterising of particles by the manner in which they break. *Part. Charact.* **2**, 25-30.

Bemrose, C.R. and Bridgwater, J. (1987). A review on attrition and attrition test methods. *Powder Technol.*, **49**, 97-126.

Boerefijn, R., Duo, W. and Ghadiri, M. (1997). Impact attrition of fluid cracking catalyst. In *Proc. 1997 IChemE Research Event*, Nottingham/Lounghborough, 7-9 April, 385-388.

Boerefijn, R., Ning, Z. and Ghadiri, M. (1998). Disintegration of weak lactose agglomerates for inhalation applications. *Int. J. Pharmaceutics*, Vol. 172, **1-2**, 199-209.

Boerefijn, R., Gudde, N.J. and Ghadiri, M. (2000). A review of attrition of fluid catalyst particles. *Adv. Powder Technol.*, **11**(2), 145-174.

Briscoe, B.j. and Evans, P.D. (1991). Wall friction in the compaction of agglomerated ceramic powers. *Powder Technol.*, **65**, 7-20.

Briscoe, B.J., Luckham, P.F., Maung, R., and Aydin, I. (1998). Nano and micro-mechanics of agglomerates. *Proc. World Cong. On Part. Technol. 3* (Brighton, UK).

Broek, D. (1989). The practical use of fracture mechanics. Kluwer Academic Publishers, The Netherlands, p. 48-87.

Capes, C.E. (1980). Handbook of powder technology. Vol.1. Particle size enlargement. Elsevier, Amsterdam.

Chaudri, M.M., Wells, J.K. and Stephans, A. (1981). Dynamic hardness, deformation and fracture of simple ionic crystals at very high rates of strain. *Phil. Mag. A* **43**(3) 643-664.

Cleaver, J.A.S., Ghadiri, M. and Rolfe, N. (1993). Impact attrition of sodium carbonate monohydrate crystals. *Powder Technol.*, **76**, 15-22.

Capeci, S. and Welch, R.G. (1998). Powdered detergents. In: Powdered Detergents, ed. M.S. Showell, Marcel Dekker, New York, 21-42.

Carneim, R.D. and Messing, G.L. (2001). Response of granular powders to uniaxial loading and unloading. *Powder Technol.*, **115**, 131-138.

Couroyer, C., Ning, Z., Ghadiri, M., Brunard, N., Kolenda, F., Borzmeyer, D. and Lavel, P. (1999). Breakage of macroporous alumina beads under compressive loading: simulation and experimantal validation. *Powder Technol.*, **105**, 57-65.

Couroyer, C., Ghadiri, M., Lavel, P., Brunard, N. and Kolenda, F. (2000). Methodology for investigating the mechanical strength of reforming catalyst beads. *Oil & Gas Sci. and Technol. – Rev. IFP,* **55**(1), 67-85.

Dean, W.R., Snedonand, I.M. and Parsons, H.W. (1952). Strength and testing materials, Part II, testing methods and test results. In *Selected Government Research Reports.* HMSO, London, Vol. **6**, 212.

Denessuk, M., Smith, Smith, G.L., Zelinski, B.J.J., Kreidl, N.J. and Uhlmann, D.R., (1993). Capillary penetration of liquid droplets into porous materials, *J. Colloid Interface Sci.* **158,** 114-120.

Denny, P.J. (2002). Compaction equations: a comparison of the Heckel and Kawakita equations. *Powder Technol.*, 127, 162-172.

Davies, R. (1995). The future of particle science and technology in the USA. *IFPRI Newsletter* **8,** 9-10.

Ennis, B.J., Tardos, G. and Pfeffer, R. (1991). A microlevel-based characterization of granulation phenomena. *Powder Technol.*, **65**, 257-272.

Ennis, B.J., Sunshine, G. (1993). On wear as a mechanism of granule attrition. *Trib. Int.*, **26**(5), 319-327.

Ennis, B.J. and Litster, J.D. (1997). Principles of size enlargement. In *Perry's Chemical Engineers Handbook – 7th Edition* (Eds. R.H. Perry and D.W. Green).

Evans, A.G. and Wilshaw, T.R. (1976). Quasi-static solid particle damage in brittle solids –1. Observations, analysis and implications. *Acta Met.* **24**, 939-955.

Evans, A.G. (1979). Impact damage mechanics: solid projectiles. In *Treaties on Materials Science and Technology* (ed. C.M. Preece). Vol. **16,** New York, Academic press.

Es-Saheb, M.H.H. (1992). Uniaxial strain rate effects in pharmaceutical powders during cold compaction. *J. Mat. Sci.* **27**, 4151-4159.

Es-Saheb M.H.H. (1993). Powder compaction interpretation using the power law. *J. of Mat. Sci.* **28**, pp 1269-1275.

Forsythe, W.L., Jr. and Hertwig, W.R. (1949). Attrition characteristics of fluid cracking catalysts. *Ind. Eng. Chem.* **41**, 1200-1206.

Fu, J., Salman, A.D. and Hounslow, M.J. (2002). Experimental study on impact deformation and rebound of wet granules. In *4th. World Cong. On Powder Technol.* 21-25 July, Sydney Australia.

Gahn, C. and Mersmann, A. (1995). The brittleness of substances crystalized in industial processes. *Powder Technol.* **85,** 71-81.

Ghadiri, M. (1997). Hardness of particles. In *Powder Technology Handbook (Eds. K. Gotoh, H. Masuda and K. Hogashitani)*, Marcel Dekker, Inc., New York.

Ghadiri, M. and Zhang, Z. (1992). Impact attrition of particulate solids. IFPRI Final Report, FRR 16-03, University of Surrey, UK.

Ghadiri, M., Cleaver, J.A.S., Tuponogov, V.G. and Werther, J. (1994). Attrition of FCC powder in the jetting region of fluidised bed. *Powder Technol.* **80**, 175-178.

Ghadiri, M., Ning, Z., Kenter, S.J. and Puik, E. (2000). Attrition of granular solids in a shear cell. *Chem. Eng. Sci.*, **55**, 5445-5456.

Ghadiri, M. and Zhang, Z. (2002). Impact attrition of particulate solids. Part 1: a theoretical model of chipping. *Chem. Eng. Sci.*, **57**, 3659-3669.

Ghadiri, M., Yüregir, K.R., Pollock, H.M., Ross, J.D.J. and Rolfe, N.J. (1991). Influence of processing conditions on attrition of NaCl crystals, *Powder Technol.*, **65**, 311-320.

Gorham, D.A. and Salman, A.D. (1998). The fracture of glass spheres. In *Proceedings of the 9th European Symposium on Comminution*, Albi (France), 71-80.

Green J.L., Petty C.A. and Grulke E.A. (1997), Impact grinding of thermoplastics: a size distribution function model, *J. Polymer Eng. and Sci.*, **37** (5), . 888-895.

Griffith, A.A. (1920). The phenomena of rupture and flow in solids. *Philosophical Transactions of the Royal Society A (Mathematics and Physics)*, **221**, 163-198.

Gwyn, J.E., (1969). On the particle size distribution function and the attrition of cracking catalysts. *AIChE J.* **15**(1), 35-41.

Hagan, J.T. (1981). Impossibility of fragmenting small particles: brittle-ductile transition. *J. Mater. Sci.* **16**, 2909-2911.

Hagan, J.T. and Swain, M.V. (1978). The origin of median and lateral cracks around plastic indents in brittle materials. *J. Phys. D: Appl. Phys.*, **11**, 2091-2102.

Hamilton, G.M. and Goodman, L.E. (1966). The stress field created by a circular sliding contact. *J. Appl. Mech.* **33**, 371-376.

Hassanpour, A. and Ghadiri M., (2003). Simulation of uniaxial bulk compression using Distinct Element Method (DEM): Evaluation of Heckel Analysis, In *proc 4th Int. Conf. for Conv. and Handl. of Particulate Solids,* 12.45 (27-30 May), Budapest, Hungary.

Heckel, R.W. (1961). Density-pressure relationship in powder compaction. *Trans. Metall. Soc. AIME* **221,** 671-675.

Hiramatsu, Y. and Oka, Y. (1966). Determination of the tensile strength of rock by a compression test of an irregular test piece. *Int. J. Rock Mech. Min. Sci.* **3**, 89-99.

Hodgkinson, J.M. and Williams, J.G. (1982). Development in impact testing of polymers. *Polymer Eng.* **13**, 152-158.

Holm, P., Jungersen, O., Schaefer, T. and Kristensen, H.G. (1983). Granulation in high shear mixers: Part 1. Effects of process variables during kneading. *Pharm. Ind.* **45**, 806-811.

Hutching, I.M. (1992). *Tribology: Friction and Wear of Engineering Materials.* London, Edward Arnold.

Hutching, I.M. (1993). Mechanism of wear in powder technology, *Powder Technol.*, **76**(3), 13.

Irwin, G.R. (1958). In *Handbuch der Physik,* Vol. 5, Springer- Verlag, Heidelberg.

Iveson, S.M., Litster, J.D. and Ennis, B.J. (1996). Fundamental studies of granule consolidation part 1: Effects of binder content and binder viscosity. *Powder Technol.* **88**, 15-20.

Iveson, S.M. and Litster, J.D. (1998). Fundamental studies of granule consolidation part 2: quantifying the effects of particle and binder properties. *Powder Technol.* **99**, 243-250.

Iveson, S.M. and Litster, J.D. (1998a). Growth regime map for liquid-bound granules. *Powder Technol. and Fluid., AIChE J.,* **44**(7), 1510-1518.

Iveson, S.M. and Litster, J.D. (1998b). Liquid-bound granule impact deformation and coeficient of restitution. *Powder Technol.*, **99**, 234-242.

Iveson, S.M., Litster, J.D., Hapgood, K. and Ennis, B.J. (2001). Nucleation, growth and breakage phenomena in agitated wet granulation processes: a review. *Powder Technol.*, **117**, 3-39.

Jenike, A.W., Johnson, J.T. (1969), *Trans. ASME B91.*

Johnson, K.L. (1985). Contact Mechanics. Cambridge University Press.

Johnson, K.L., Kendall, K. and Roberts, A.D. (1971). Surface energy and the contact of elastic solids. *Proc. R. Soc. London*, **A324**, 301-313.

Kafui, D. and Thornton, C. (1993). Computer simulated impact of agglomerates. In *Proceedings of Powders & Grains 93 (Ed. C. Thornton)*, Balkema, Rotterdam.

Kawakita, K. and Lüdde, K.H. (1970). Some considerations on powder compression equations. *Powder Technol.* **4,** 61-68.

Kelsall. D.F., Reid, K.J. and Restarick, C.J. (1967/68). Continuous grinding in a small wt ball mill. Part I.: A study of the influence of the ball diameter. *Powder Technol.* **1,** 291-300.

Kendall, K. (1978). The impossibility of comminuting small particles by compression. *Nature* **272,** 710-711.

Kendall, K. (1978a). Complexities of compression failure. *Proc. R. Soc. Lond.* **A361,** 245-263.

Kendall, K. (1988). Agglomerate strength. *Powder Metallurgy*, **31** (1), 28-31.

Kendall, K., Alford, N.McN. and Birchal, J.D. (1986). The strength of green bodies. *Inst. Ceram. Proc. Special Ceramics*, **8**, 255-265.

Kendall, K., Alford, N.McN. and Birchal, J.D. (1987). Elasticity of particles assemblies as a measure of the surface energy of solids. *Proc. R. Soc. London*, **A412**, 269-283.

Kendall, K., Alford, N.McN. and Birchal, J.D. (1987a). A new method for measuring the surface energy of solids. *Nature*, **325** (26), 794-796.

Keningley, S.T., Knight, P.C. and Marson, A.D. (1997). An investigation into the effects of binder viscosity on agglomeration behaviour. *Powder Technol.*, **91**, 95-103.

Klimpel, R.R. and Austin, L.G. (1965). The statistical theory of primary breakage distribution for brittle materials. *Trans. Soc. Min. Eng. AIME,* **232,** 88-94.

Knight, P.C. and Seville, J.P.K. (1998). Effects of binder viscosity on agglomeration processes, In *World Congr. Part. Technol., IChemE,* 3, Paper 118.

Knight, P.C., Instone, T., Pearson, J.M.K. and Hounslow, M.J. (1998). An investigation into the kinetics of liquid distribution and growth in high shear mixer agglomeration. *Powder Technol.*, **97**, 246-257.

Knight, P.C, Johansen, A., Kristensen, H.G., Schaefer, T. and Seville. J.P.K., (2000). An investigation of the effects on agglomeration of changing the speed of a mechanical mixer. *Powder Technol.*, **110**, 204-209.

Knight, P.C. (2001). Structuring agglomerated products for improved performance, *Powder Technol.*, **119**, 14-25.

Knudsen, F.P. (1959). Dependence of Mechanical strength of brittle polycrystalline specimens on porosity and grain size, *J. of the Am. Ceram. Soc.*, **42**(8), 376-387.

Kohlus, R. (2002). Quantitative descriptors for granule structure characterisation, In *4th World Cong. on Powder Technol.*, 21-25 July, Australia.

Kwan, C.C., (2003). Analysis of milling behaviour of pharmaceutical powders, PhD Thesis, University of Leeds, UK.

Lawn, B.R. (1991). In *Fundamental of friction: Macroscopic and microscopic processes* (eds. I.L. singer and H.M. Pollok), London, Kluwer Academic Publishers, p. 137.

Lawn, B.R. (1993). Fracture of brittle solids (2nd Edition). (Cambridge Solid State Science Series) *Cambridge University Press*, Cambridge.

Lawn, B.R. and Marshall, D.B. (1979). Hardness, toughness and brittleness: an indentation analysis. *J. Am. Cerm. Soc.*, **62**(7-8), 347-350.

Lawn, B.R., Swain, M.V. and Phillips, K. (1975). Mode of chipping fracture in brittle solids. *J. Mater. Sci.* **10**(7), 1236-1239.

Litster, J.D., Iveson, S.M. and Hapgood, K.P. (1998). Predicting and controlling granule properties in granulation processes. In *Proc. of World Cong. of Part. Technol. 3*, paper 92, Brighton, UK.

Marshal, D.B., Lawn, B.R. and Evans, A.G. (1982). Elastic/Plastic indentation damage in ceramics: the lateral crack system. *J. Am. Cerm. Soc.*, **65**(11), 561-566.

Maxim, R.E., Salman, A.D. and Hounslow, M.J. (2002). Impact of granules: Failure distribution, In *Proc. World Cong. on Part. Technol. 4,* Sydney.

Mills, P.J.T., Seville, J.P.K., Knight, P.C. and Adams, M.J. (2000). The effect of binder viscosity on particle agglomeration in low shear mixer / agglomerator. *Powder Technol.*, **113**, 140-147.

Mishra, B.K. and Thornton, C. (2001). Impact breakage of particle agglomerates, *Int. J. Miner. Process.*, **61**, 225-239.

Moore, E. (1975). Detergents. A Unilever Educational booklet revised ordinary series No 1.

Moreno, R. (2003). Computer simulation of impact behaviour of spherical agglomerates using Distinct Element Method, PhD Thesis, University of Surrey.

Mort, P. (2000). Automated generation and analysis of powder compaction diagrams. In *Proc. 3rd Israel conf. for Conveying and Handling of particulate solids* (Israel).

Mullier, M.A. (1991). The strength of agglomerates and their breakage during fluidisation. PhD Thesis, University of Surrey, UK.

Mullier, M.A., Seville, J.P.K. and Adams, M.J. (1987). A fracture mechanics approach to the breakage of particle agglomerates. *Chem. Eng. Sci.*, **42** (4), 667-677.

Neil, A.U., and Bridgwater, J. (1994). Attrition of particulate solids under shear. *Powder Technol.* **80,** 207-219.

Nicklasson, F. and Alderborn, G. (2000). Analysis of the compression mechanics of pharmaceutical agglomerates of different porosity and composition using the Adams and Kawakita equations. *Pharm. Research,* **17**(8), 949-954.

Ning, Z. (1995). Elasto-plastic impact of fine particles and fragmentation of small agglomerates with a surface. PhD. Dissertation, University of Aston, UK.

Ning, Z., Boerefijn, R., Ghadiri, M. and Thornton, C. (1997). Distinct element simulation of impact breakage of lactose agglomerate. *Adv. Powder Technol.,* **8** (1), 15-37.

Ning, Z. and Ghadiri, M., (1996). Computer simulation of granular solids under shearing. In *Proc. 5th World cong. Chem. Eng. / 2nd Int. Particle Technol. Forum*, AIChE, San Diego, CA, 14-18 July, Vol. V, 343-354.

Okuda, S. and Choi, W.S. (1979). Fracture characteristics of single particles of polymeric material under impact loading. *J. Chem. Eng. Japan* **12(5),** 383-388.

Oliver, W.C., and Pharr, G. M. (1992). *J. Mater. Res.,* 7(56), 1564.

Ouwerkerk, C.E.D. (1991). A micro-mechanical connection between the single-particle strength and the bulk strength of random packings of spherical particles. *Powder Technol.* **65**, 125-138.

Papadopoulos, D.G. (1998). Impact breakage of particulate solids. PhD Thesis, University of Surrey, UK.

Papadopoulos, D.G. and Ghadiri, M. (1996). Impact breakage of poly-methylmethacrylate (PMMA) extrudates. I. Chipping. *Adv. Powder Technol.*, 7:3, 183-197.

Paramanathan, B.K. and Bridgwater, J. (1983). Attrition of solid-I. Cell development. *Chem. Eng. Sci.* **38**(2), 197-206.

Paramanathan, B.K. and Bridgwater, J. (1983a). Attrition of solid-I. Material behaviour and kinetics of attrition. *Chem. Eng. Sci.* **38**(2), 207-224.

Pepin, X, Simons, S.J.R., Blanchon, S., Rossetti, D. and Couarraze, G. (2001). Hardness of moist agglomerates in relation to interparticle friction, granule liquid content and nature. *Powder Technol.* **117**, 123-138.

Pietsch, W. (1991). Size enlargement by agglomeration. Wiley; Aarau; Salle & Sauerländer, Chichester.

Pitchmani, R., Meesters, G.M.H. and Scarlett, B. (2001). Breakage behaviour of enzyme granules in a repeated impact test, In *Proc. 7th International Symposium on Agglomeration,* Albi, France.

Pitchmani, R., Gupta, N., Meesters, G.M.H. and Scarlett, B. (2002). Analysis of single particle attrition during impact experiments. In *4th World Cong. on Powder Technol.,* 21-25 July, Australia.

Plati, E. and Williams, J.G. (1975). The determination of the fracture parameters for polymers in impact. *Polymer Eng. Sci.*, **15** (6), 470-477.

Pollock, H.M. (1992). Nano-indentation. In *friction, Lub. And Wear Technol.* (Metals hand book Vol. 18, P.J. Blau ed.), 419-429.

Pollock, H.M., Maugis, D., and Barquins, M. (1986). In *Micro-indentation Techniq. in Mat. Sci. and Eng.* (P. J. Blau and B. R. Lawn, eds), ASTM, Philadelphia, p. 47.

Potapov, A.V. and Campbell, C.S. (1994). Computer simulation of impact-induced particle breakage. *Powder Technol.* **81**, 207-216.

Potapov, A.V. and Campbell, C.S. (1997). The two mechanisms of particle impact breakage and velocity effect. *Powder Technol.* **93**, 13-21.

Puttick, K.E. (1980). The correlation of fracture transitions. *J. Phys. D: Appl. Phys.* **13,** 2249-2262.

Puttick, K.E. (1993). Energy scaling in elastic and plastic-elastic fracture. In *The Griffith centenary meeting,* Liverpol, 23-25 March.

Puttick, K.E. and Badrick, A.S.T. (1987). The mechanical breakdown of sodium chloride crystals. *Chem. Eng. Sci.* **42**(4), 855-868.

Roberts, R.J. and Rowe, C. (1985). The effect of punch velocity on the compaction of the variety of material. *J. Pharm. Parmacol.,* **37**, 377-384.

Roberts, R.J. and Rowe, C. (1987). The compaction of Pharmaceutical and other model matrials – a pragmatic approach. *Chem. Eng. Sci.,* **42**(4), 903-911.

Rosin, P. and Rammler, E. (1933). The laws governing the fineness of powdered coal. *J. Inst. Fuel,* **7,** 29-36.

Rumpf, H. (1962). The strength of granules and agglomerates. In *Agglomeration* (ed. W.A. Knepper), *Proceedings of the First International Symposium on Agglomeration*, Philadelphia. John Wiley and Sons, New York/London.

Rumpf, H. (1973). Physical aspects of comminution and a new formulation of a law of comminution, *Powder Technol.* **7**, 145-159.

Rumpf, H. (1990). Particle technology. Chapman and Hall; translated by Bull F.A. from origin German language 1975 Carl Hanser Verlag, Minich/FRG.

Rumpf, H. and Schönert, K. (1973). Single particle crushing. In *Proc. of Harold Heywood Memorial Symp.,* Loughborough, 17-18 September.

Salman, A.D., Gorham, D.A. and Verba, A. (1995). A study of solid particle failure under normal and oblique impact. *Wear*, **186-187**, 92-98.

Salman, A.D. and Gorham, D.A. (1997). The fracture of glass spheres under impact loading. In *Proceedings of Powders & Grains 97 (Eds. R. P. Behringer and J.T. Jenkins)*, Balkema, Rotterdam.

Salman, A.D., Hounslow, M.J. and Verba A. (2002). Particle fragmentation in dilute phase pneumatic conveying. *Powder Technol.* **126,** 109-115.

Salman, A.D., Biggs, C.A., Fu, J., Angyal, I., Szabo, M. and Hounslow, M.J. (2002). An experimatal investigation of Particle fragmentation using single particle impact studies. *Powder Technol.* **128,** 36-46.

Samimi, A., Ghadiri, M., Boerifijn, R. and Groot, A. (2001). Effect of humidity and fatigue on impact breakage of agglomerats. In *Inter. Cong. For Particle Technol.,* 27-29 March, Nuremberg, Germany,. Paper No 207.

Samimi, A., Boerifijn, R., Ghadiri, M., and Kohlus, R. (2002). Breakage of soft granules under uniaxial bulk compression and impact conditions. In *4th World Cong. on Powder Technol.,* 21-25 July, Australia.

Samimi, A., Ghadiri, M., Boerifijn, R., Groot, A. and Kohlus, R. (2003). Effect of structural characteristics on impact breakage of agglomerates. *Powder Technol.*, **130**, 428-435.

Sarumi, M.A. and Al-Hassani S.T.S. (1991) High and low strain rate properties of powders for continuum analysis. *Powder Technol.* **65**, 51-59.

Seville, J.P.K. (1994) Disruption of agglomerates. In *Proc. of the First Royal Society Forum in Mat. Sci. and Eng. (Solid-Solid Interactions Ed.: Imp. Col. Press)* pp. 225-237.

Schaafsma, H. Vonk, P., Segers, P., and Kossen, N.W.F. (1998). Description of agglomerate growth, *Powder Technol.* **97**, 183-190.

Schaefer, T. and Mathiesen, C. (1996). Melt pelletization in a high shear mixer: VIII. Effects of binder viscosity, *Int. J. Pharm.* **139**, 125-138.

Schaefer, T. and Mathiesen, C. (1996). Melt pelletization in a high shear mixer: IX. Effects of binder particle size, *Int. J. Pharm.* **139**, 139-148.

Schumann, R. (1940). Principles of comminution. *Trans. AIME,* Tech. Publ., 1189.

Shapiro, I., (1944). PhD Thesis, University of Minnesota.

Shipway, P.H. and Hutchings, I.M. (1993). Fracture of brittle spheres under compression and impact loading. I. Elastic stress distributions. *Phil. Mag. A* **67**, 1389-1404.

Shipway, P.H. and Hutchings, I.M. (1993a). Fracture of brittle spheres under compression and impact loading. II. Results for lead-glass and sapphire spheres. *Phil. Mag. A* **67**, 1405-1421.

Shipway, P.H. and Hutchings, I.M. (1993b). Attrition of brittle spheres by fracture under compression and impact loading. *Powder Technol.*, **76**, 23-30.

Showell, M.S. (1998). Powdered detergents. In: Powdered Detergents, ed. M.S. Showell, Marcel Dekker, New York, 1-19.

Simons, S.J.R., Seville, J.P.K. and Adams, M.J. (1994). Analysis of rupture energy of pendular liquid bridges. *Chem. Eng. Sci.*, **49**(14), 2331-2339.

Simons, S.J.R. (1996). Modelling of agglomerating systems: From spheres to fractals. *Powder Technol.*, **87**, 29-41.

Simons, S.J.R., Fairbrother, R.J. (2000). Direct observation of liquid binder-particle interactions: the role of wetting behaviour in agglomerate growth. *Powder Technol.*, **110**, 44-58.

Smith, W.O., Foote, P.D. and Busang, P.F. (1930). Capillary retention of liquids in assemblages of homogeneous spheres. *Physical Review*, **36**, 524-530.

Soliman, M.S. (1987). *J. Mater. Sci.*, **22**, 3529.

Subero, J. (2001). Impact breakage of agglomerates. PhD Thesis, University of Surrey, UK.

Subero, J. and Ghadiri, M. (2001). Breakage patterns of agglomerates, *Powder Technol.*, **120**, 232-243.

Subero, J., Ning, Z., Ghadiri, M. and Thornton, C. (1999). Effect of interface energy on the impact strength of agglomerates. *Powder Technol.*, **105**, 66-73.

Swallowe, G.M., Field, J. E. and Walley, S.M. (1984). Heat generation during impact of polymers. In *Proc. 3rd Conference in Mechanical Properties at High rates of Strain,* Oxford, Inst. Phys. Conf. Ser. No. 70, 443-444.

Tardos, G.I., Irfan Khan, M. and Mort, P.R. (1997). Critical parameters and limiting conditions in binder granulation of fine powders, *Powder Technol.*, **94**, 245-258.

Tavares, L.M. and King, R.P. (2002). Modeling of particle fracture by repeated impacts using continuum damage mechanics, *Powder Technol.*, **123**, 138-146.

Taylor, J.R. (1980). An introduction to error analysis. University Science Books.

Thornton, C. (2000). How do agglomerates break?. Talk presented at the *Meeting on Agglomeration, Particle Technology Subject Group, IChemE*, Sheffield, 16th of May.

Thornton, C. and Ning, Z. (1998). A theoretical model for the stick/bounce behaviour of adhesive, elastic-plastic spheres. *Powder Technol.*, **99**, 154-162.

Thornton, C., Kafui, D. and Ciomocos, T. (1995). Numerical Simulations of agglomerate attrition, fracture and fragmentation. In *Proc. of IFPRI Annual Conference,* Urbana, July 11-16.

Thornton, C., Yin, K.K. and Adams, M.J. (1996). Numerical simulation of the impact fracture and fragmentation of agglomerates. *J. Phys. D: Appl. Phys.*, **29**, 424-435.

Thornton, C., Ciomocos, M.T. and Adams, M.J. (1999). Numerical simulations of agglomerate impact breakage. *Powder Technol.*, **105**, 74-82.

Veesler, S., Boistelle, R., Lamerant, J.M. and Philiponneau, G. (1993). Attrition of Hydragillite ($Al(OH)_3$): mechanism and quantification of particle fragility by a new attrition index. *Powder Technol.* **75**, 49-57.

Vervoorn, P.M.M. (1986). Particle attrition. IFPRI Final report FRR 13-01, Delft University of Technology, the Netherlands.

Vervoorn, P.M.M., Austin, G.L. (1990). The analysis of repeated breakage events as an equivalent rate process. *Powder Technol.* **63**, 141-147.

Vogel, L., Peukert, W. (2003). Breakage behaviour of different materials-construction of a mastercurve for the breakage probability, *Powder Technol.* **129**, 101-110.

Vu-Khahn, T. (1988). Determination of impact fracture parameters in ductile polymers. *Polymer,* **29**, 1979- 1984.

Yüregir, K.R., Ghadiri, M. and Clift, R. (1987). Impact attrition of sodium chloride crystals. *Chem. Eng. Sci.*, **42:**4, 843-853.

Zajic, L., and Buckton, G., (1990). The use of surface energy values to predict optimum binder selection for granulation. *Int. J. of Pharm.*, **59,** 155-164.

Zhang, Z. (1994). Impact attrition of particulate solids. PhD Thesis, University of Surrey, UK.

APPENDIX A

SUPPLEMENTRY PHOTOGRAPHS AND FIGURES RELATED TO CHAPTER 4

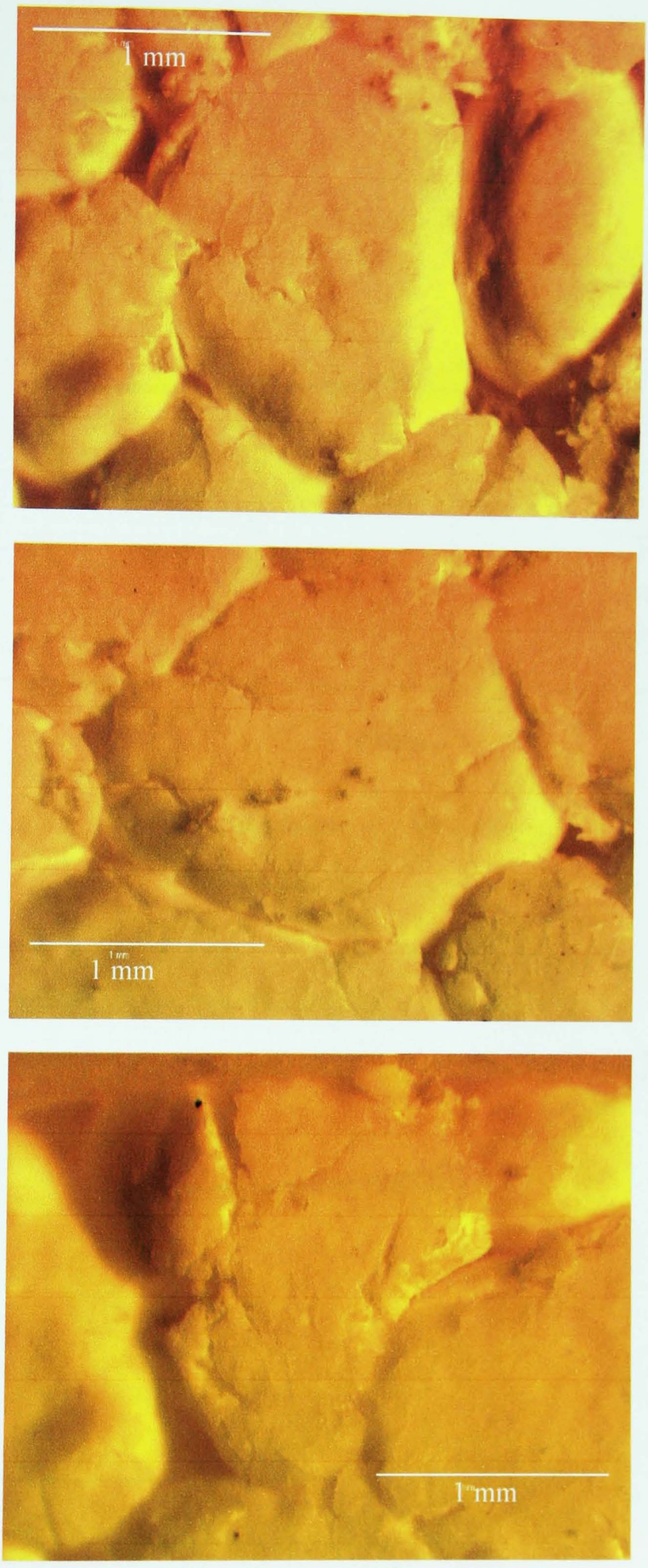

Figure A1: *Bulk compression of 1.70-2.00 mm granules of Sample 3.*

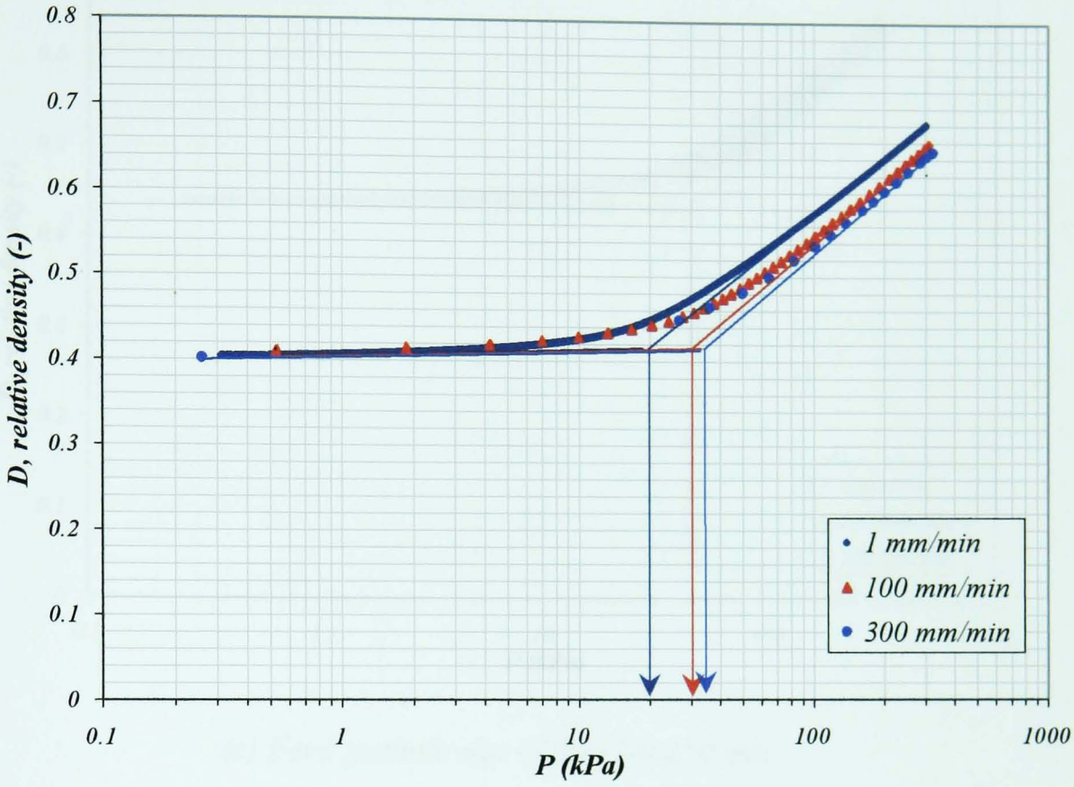

(a) Feed granule size of 1.00-1.18 mm

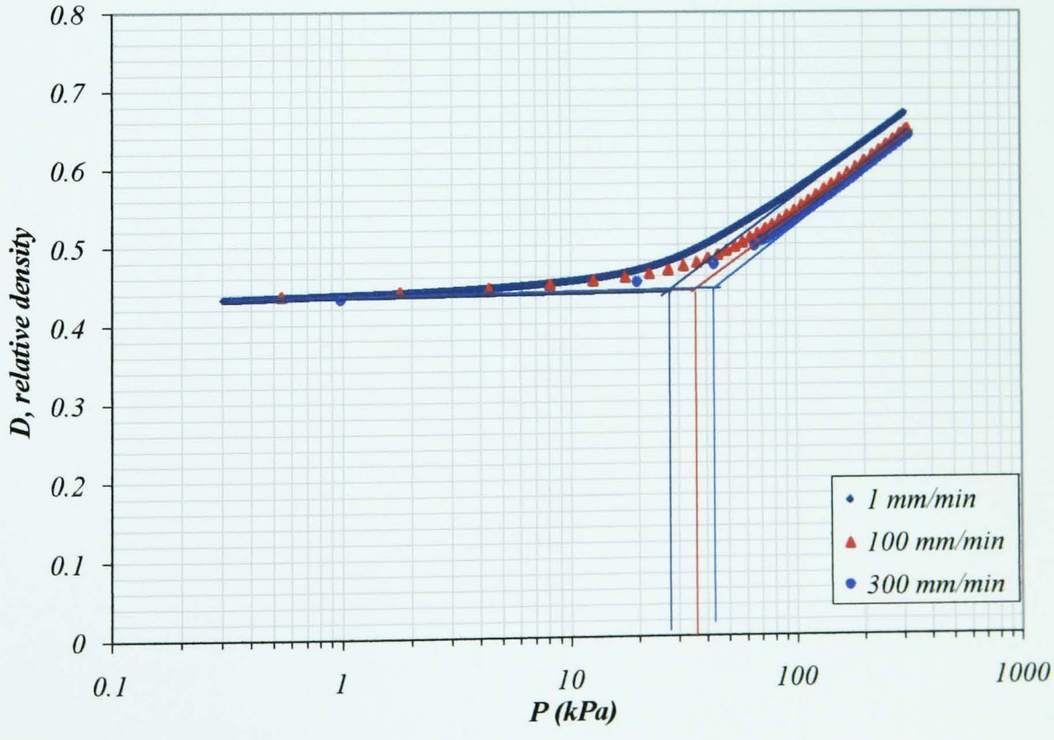

(b) Feed granule size of 0.600-0.710 mm

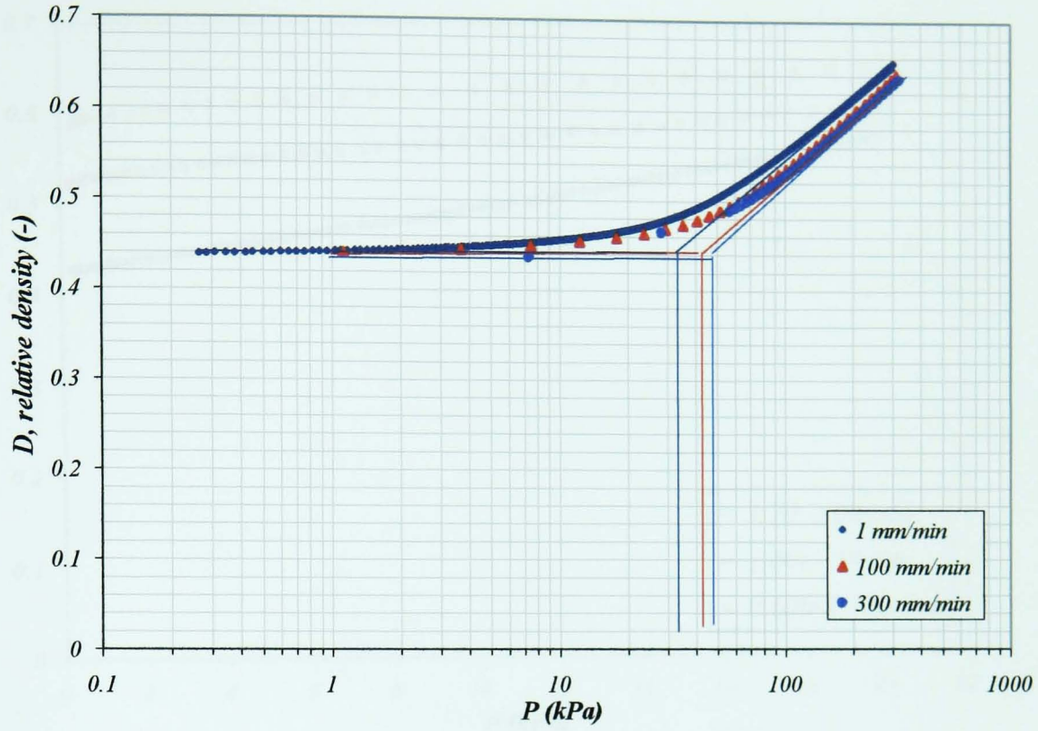

(c) Feed granule size of 0.212-0.250 mm

Figure A2: *Effect of compression rate on the apparent yield stress of Sample 3 granules, at 1 mm min^{-1} compression speed and initial aspect ratio of 0.9.*

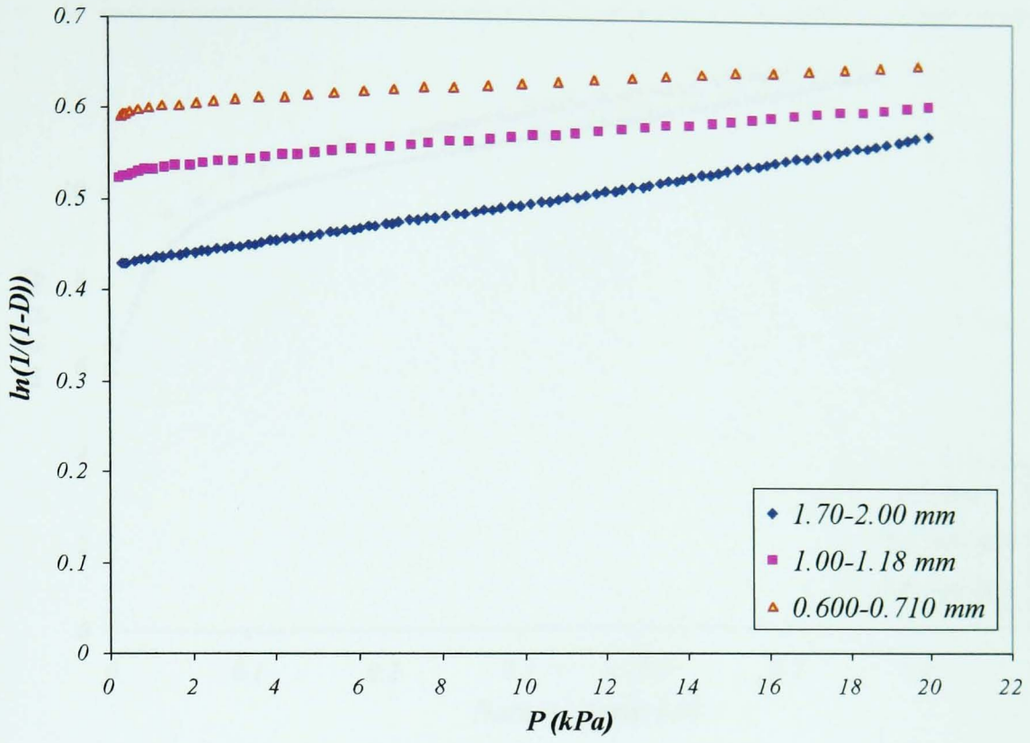

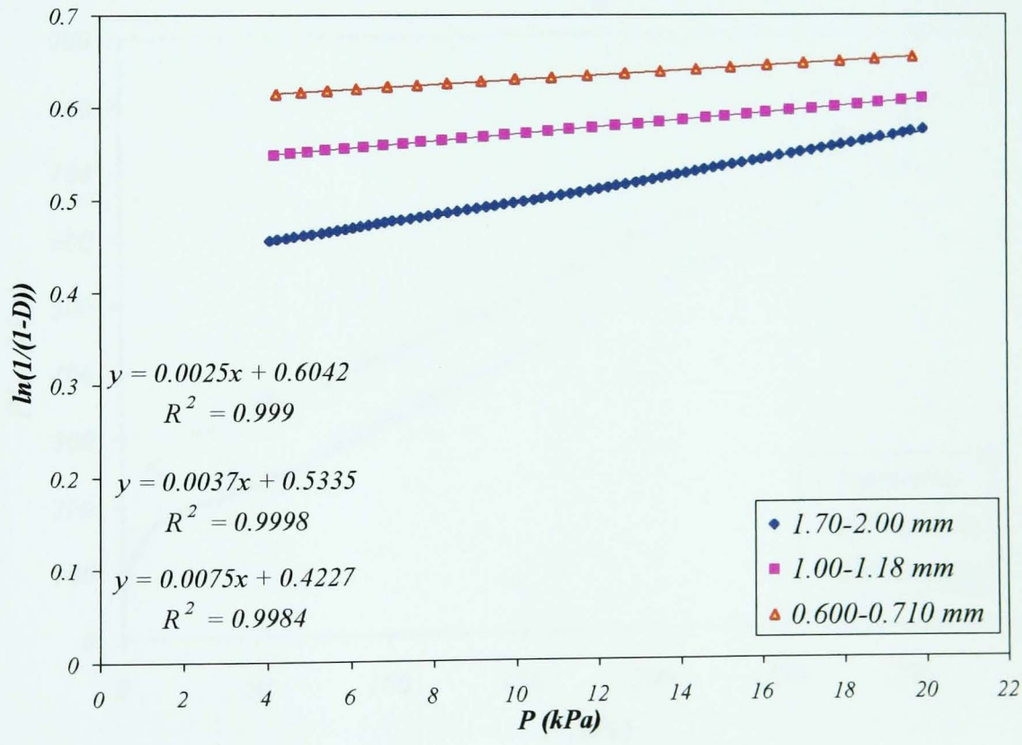

Figure A3: *Initial part of the compression curve of Heckel of Sample 3 granules at 0.9 aspect ratio for four granules sizes a) whole curves b) best linear regression.*

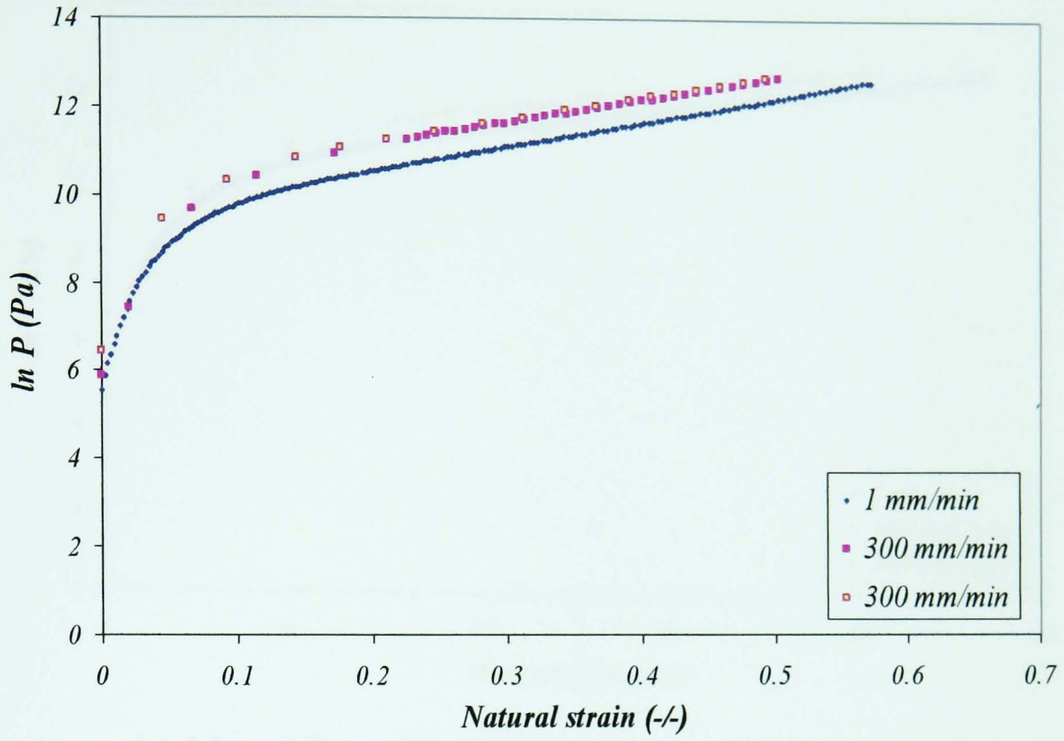

(a) Adams relationship, 1.00-1.18 mm granules of Sample 2.

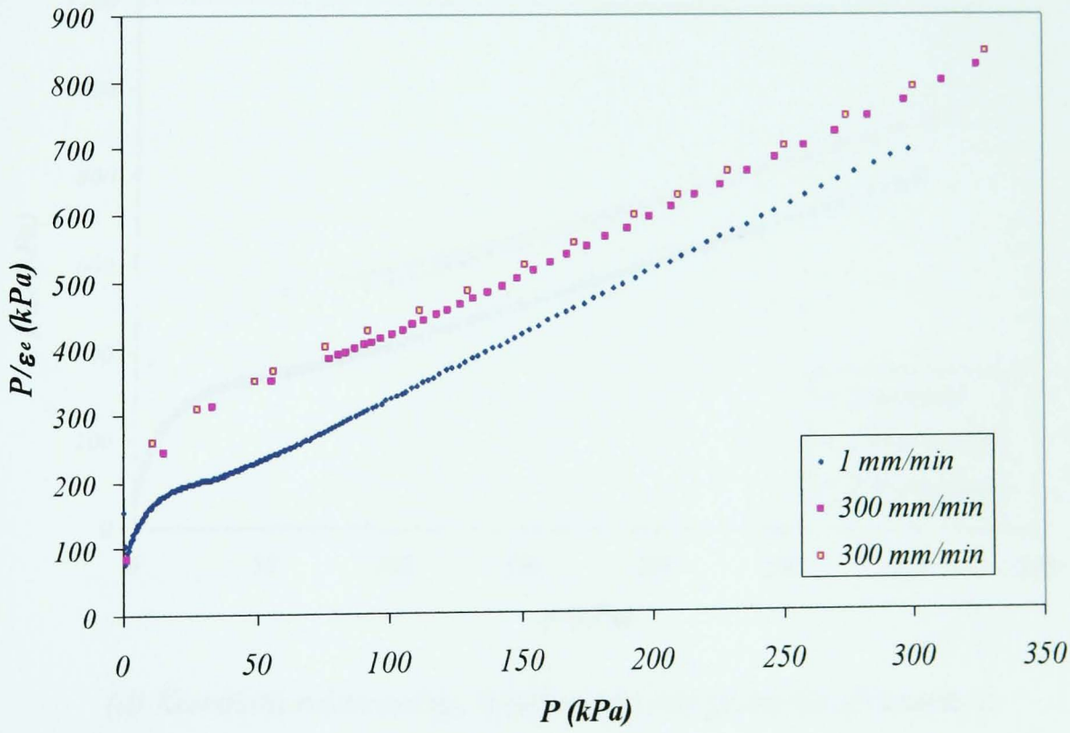

(b) Kawakita relationship, 1.00-1.18 mm granules of Sample 2.

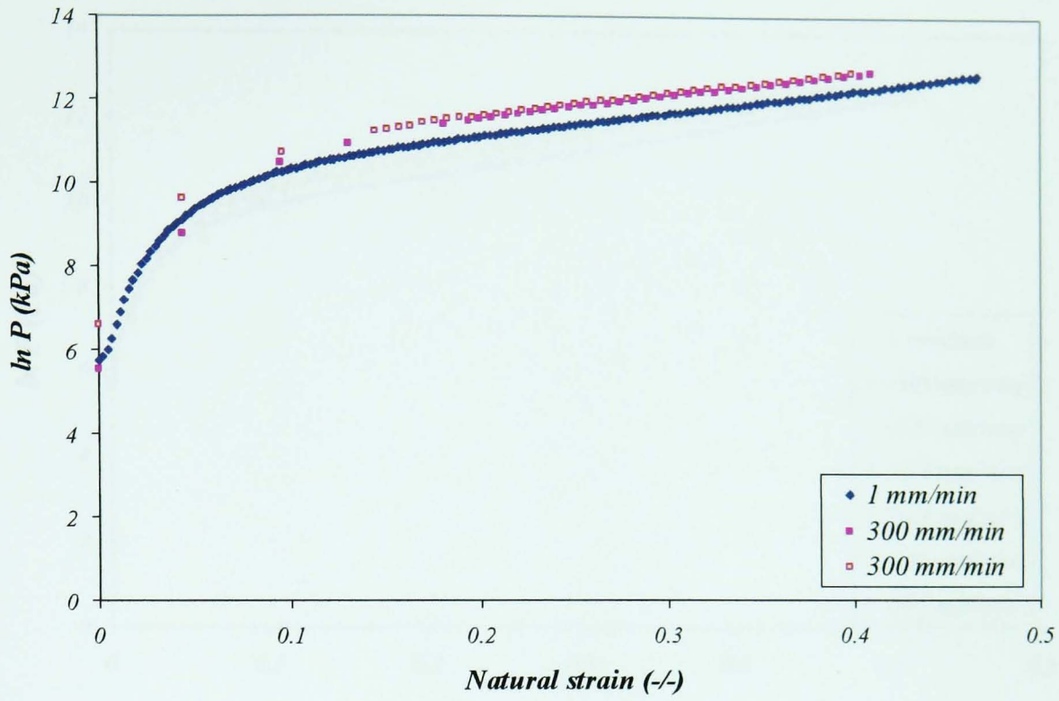

(c) Adams relationship, 0.600-0.710 mm granules of Sample 2.

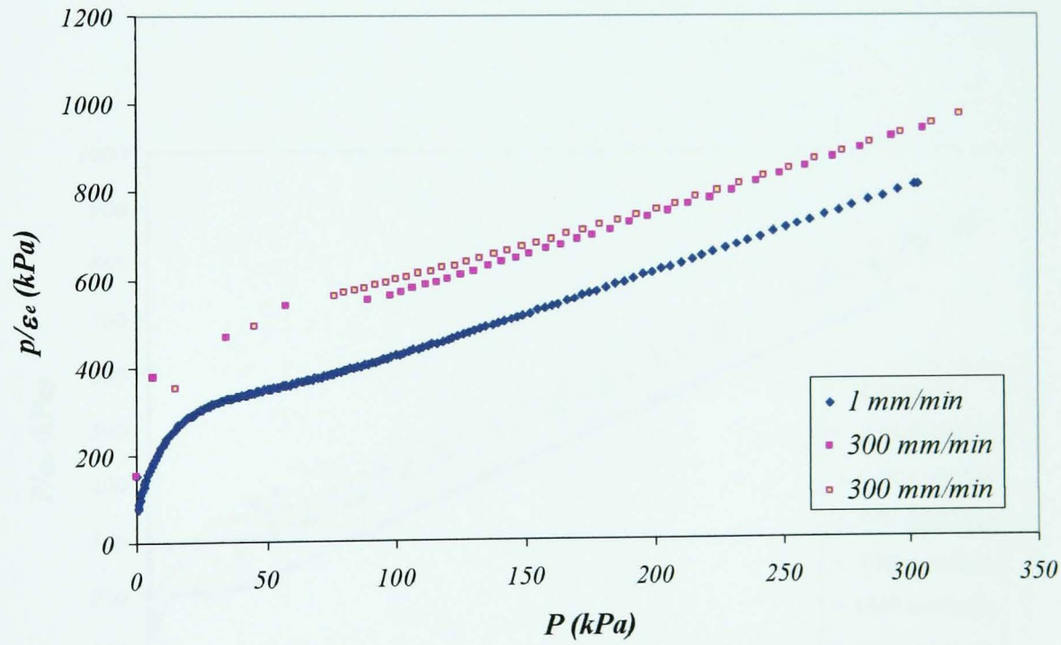

(d) Kawakita relationship, 0.600-0.710 mm granules of Sample 2.

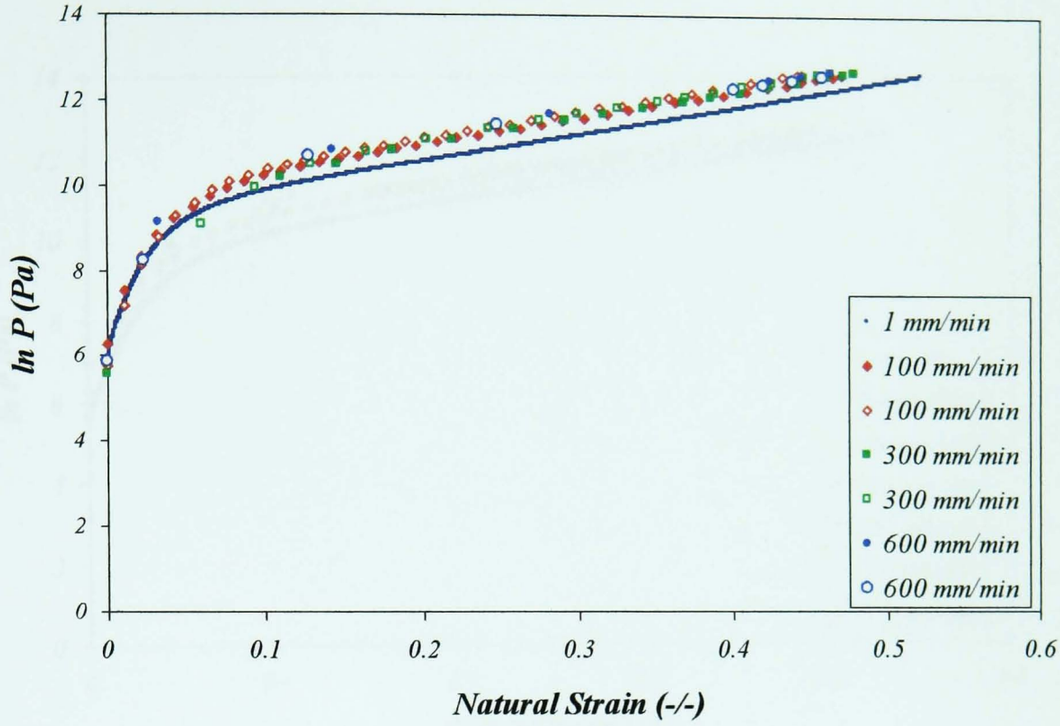

(e) Adams relationship, 1.00-1.18 mm granules of Sample 3.

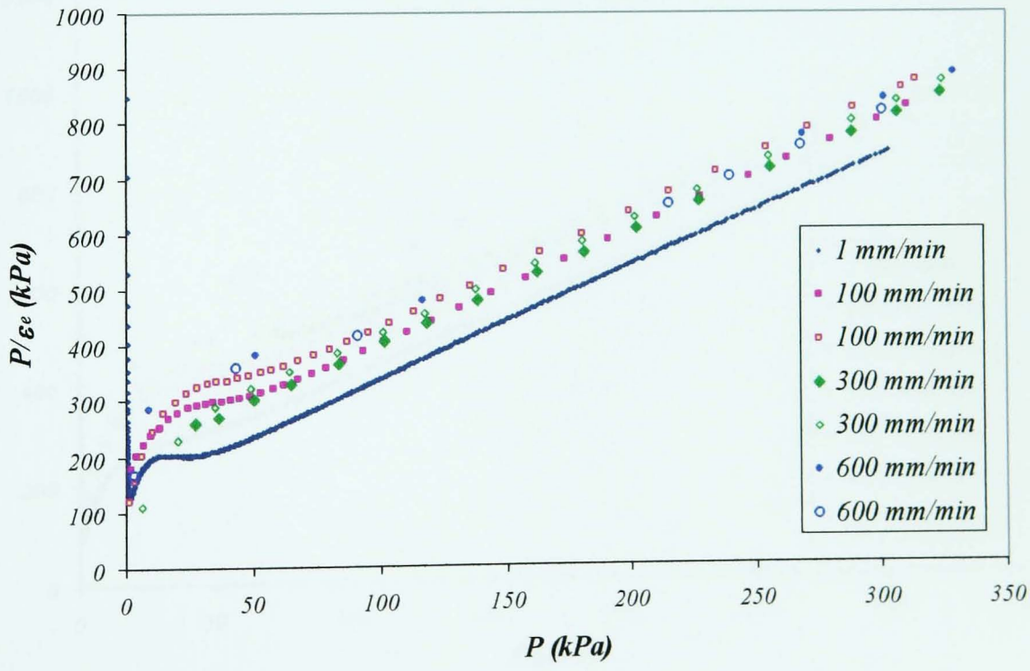

(f) Kawakita relationship, 1.00-1.18 mm granules of Sample 3.

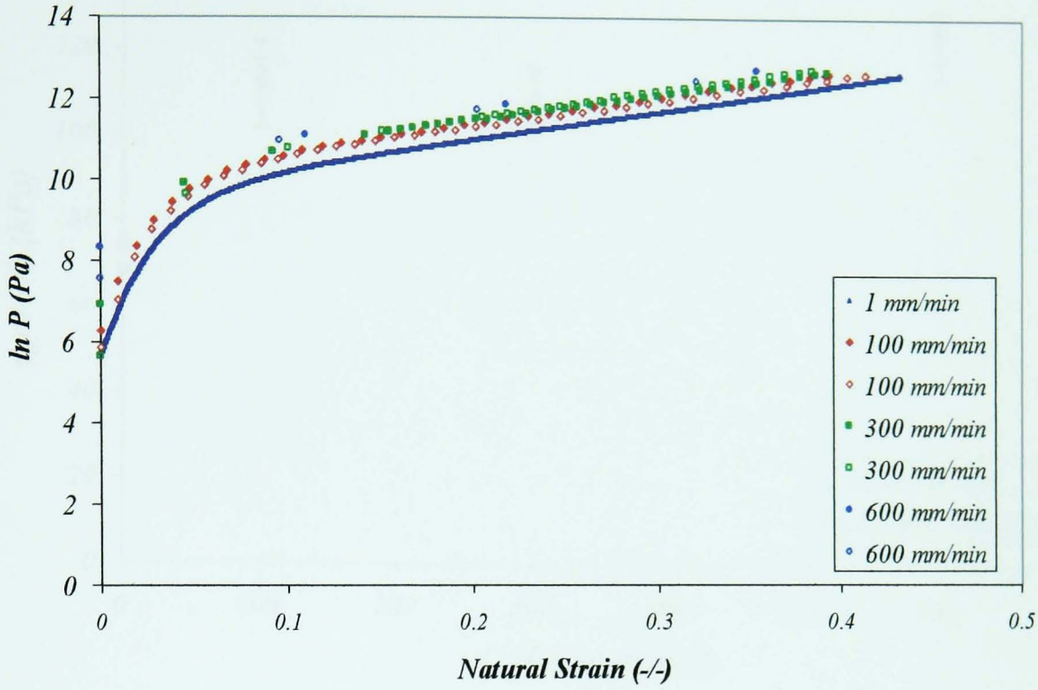

(g) Adams relationship, 0.600-0.710 mm granules of Sample 3.

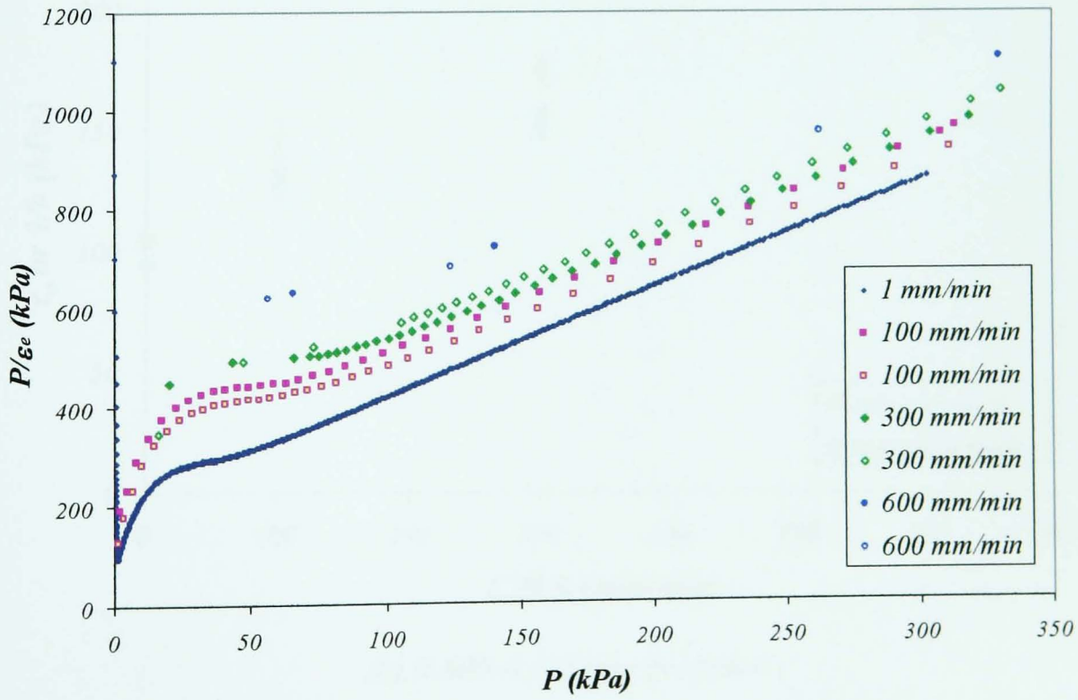

(h) Kawakita relationship, 0.600-0.710 mm granules of Sample 3.

Figure A4: *Pressure- strain curves of Samples 2 and 3, effect of strain rate.*

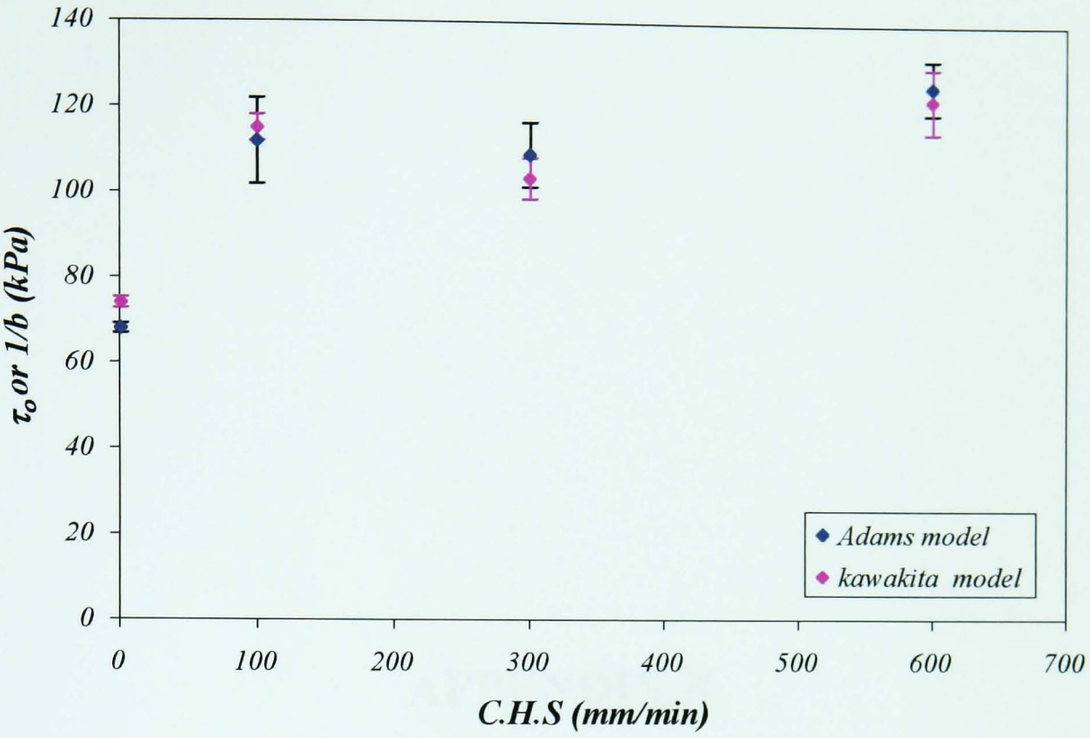

(a) 1.00-1.18 mm granules.

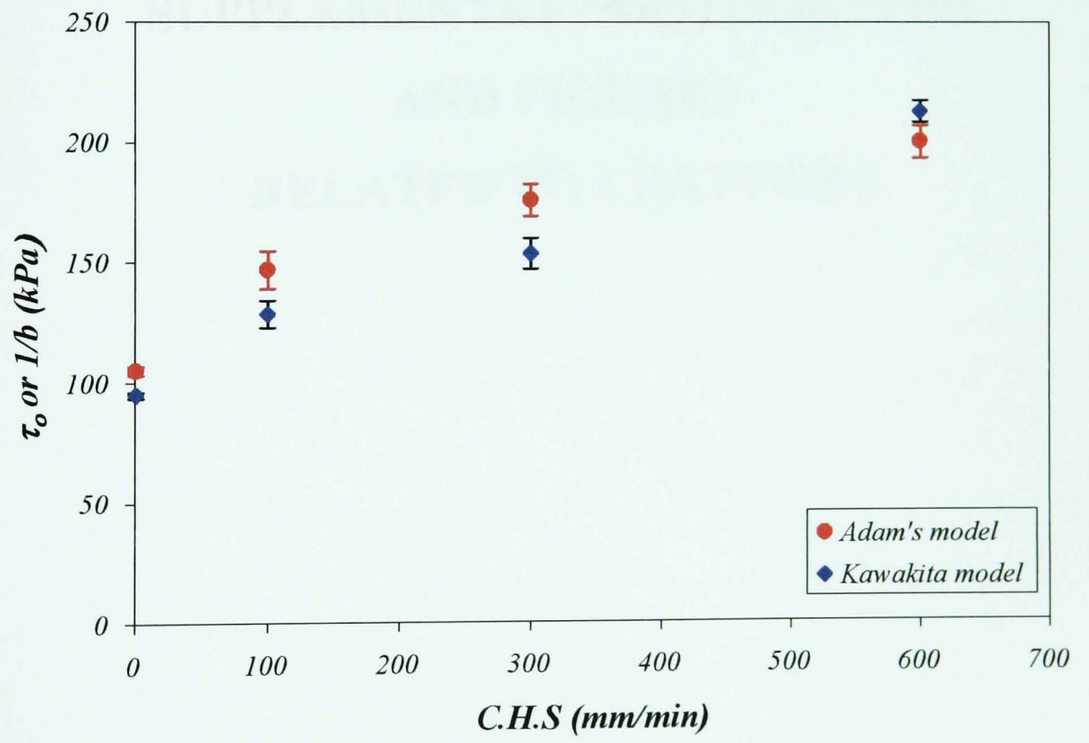

(b) 0.600-0.710 mm granules.

Figure A5: *Apparent strength of sample 3 granules, characterised on the basis of Kawakita and Adams models as a function of the crosshead speed of punch.*

APPENDIX B

SUPPLEMENTRY PHOTOGRAPHS AND FIGURES RELATED TO CHAPTER 6

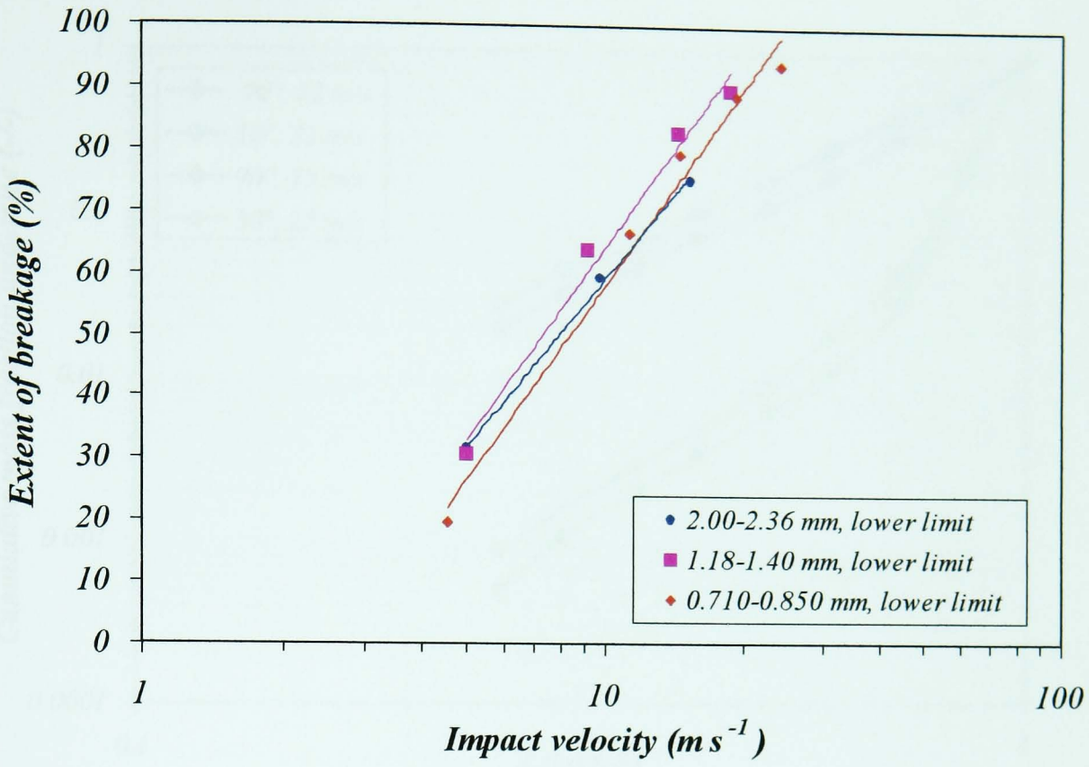

Figure B1: *Extent of breakage as a function of logarithm of impact velocity for larger feed sizes of the Sample 1 granules.*

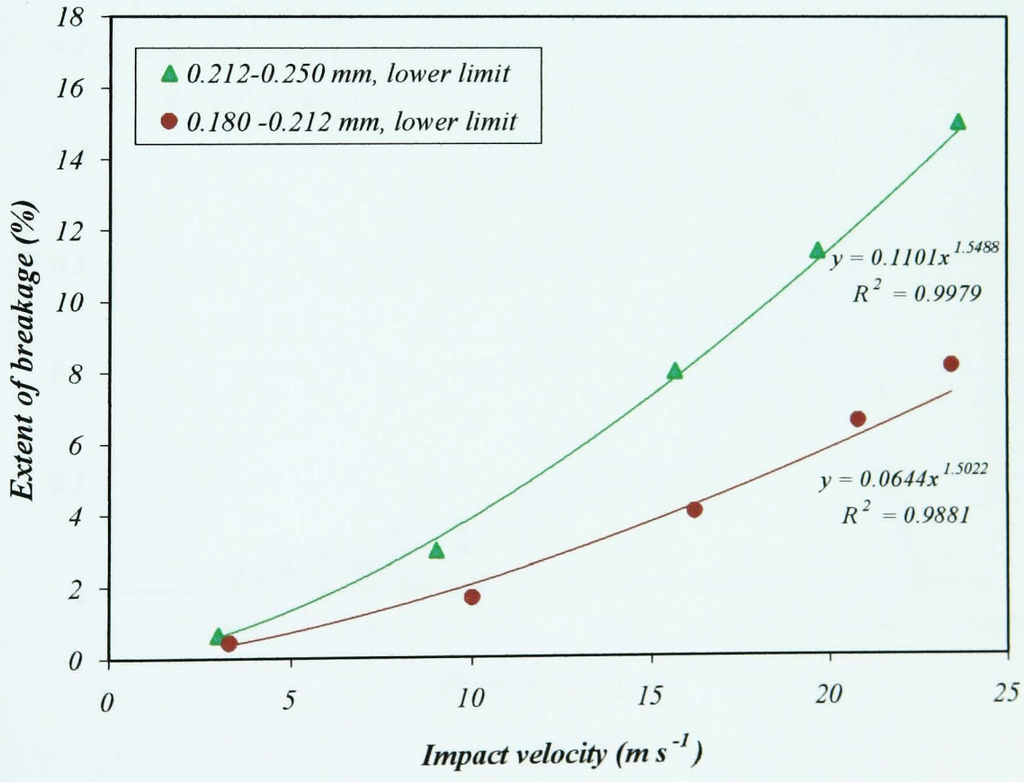

Figure B2: *Extent of breakage as a function impact velocity for finer feed sizes of the Sample 1 granules.*

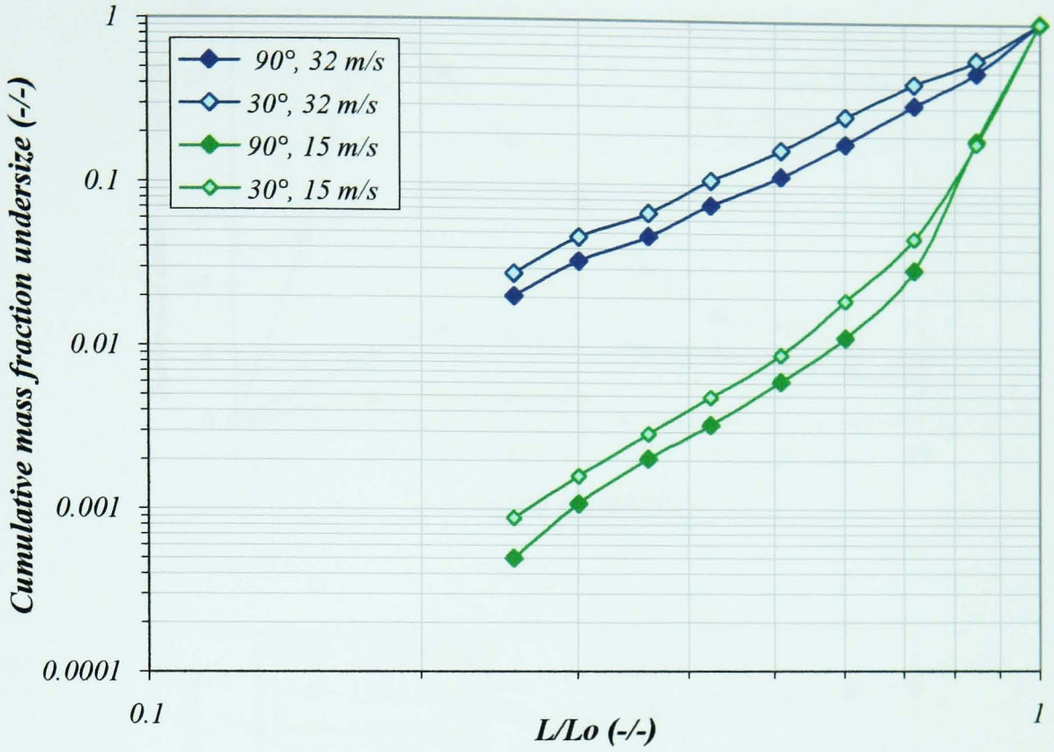

(a)

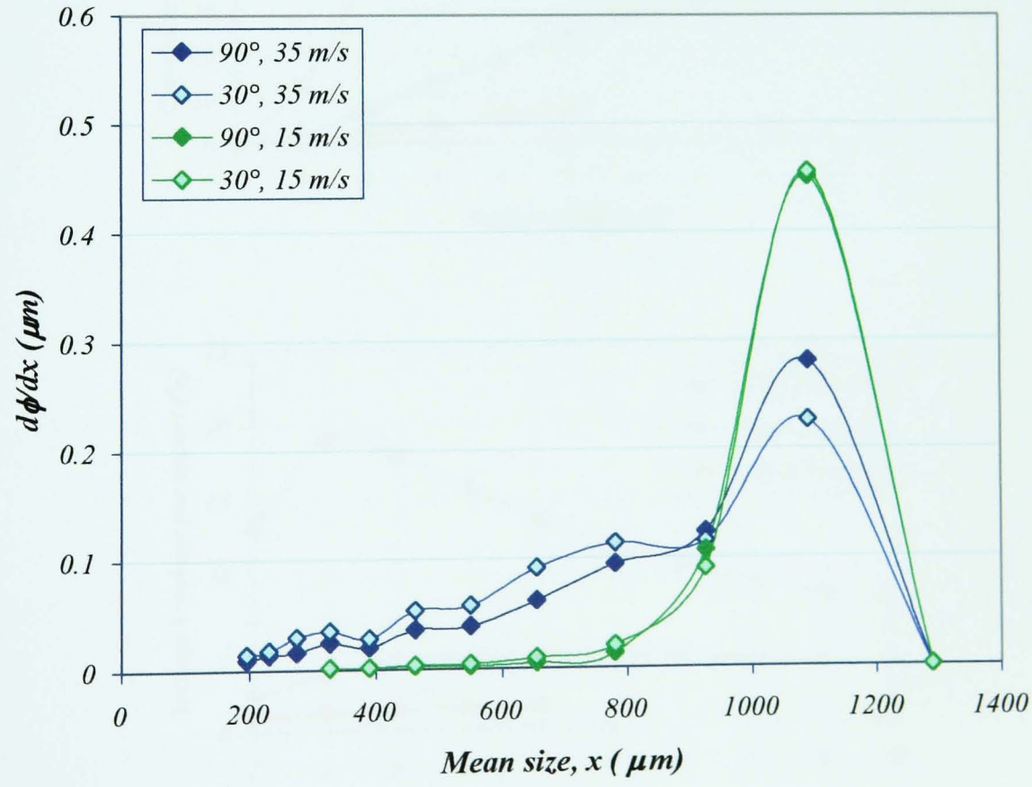

(b)

Figure B3: *Effect of impact angle and velocity on size distribution of impact products of 1.00-1.18 mm feed size of Sample 2.*

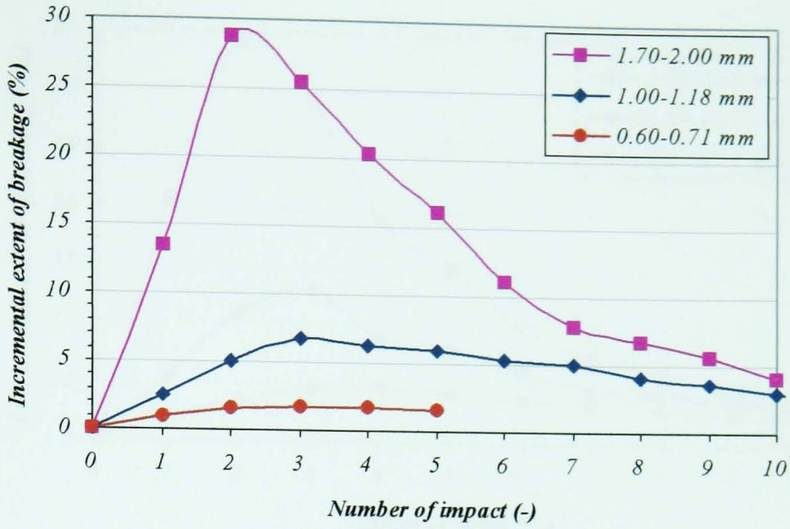

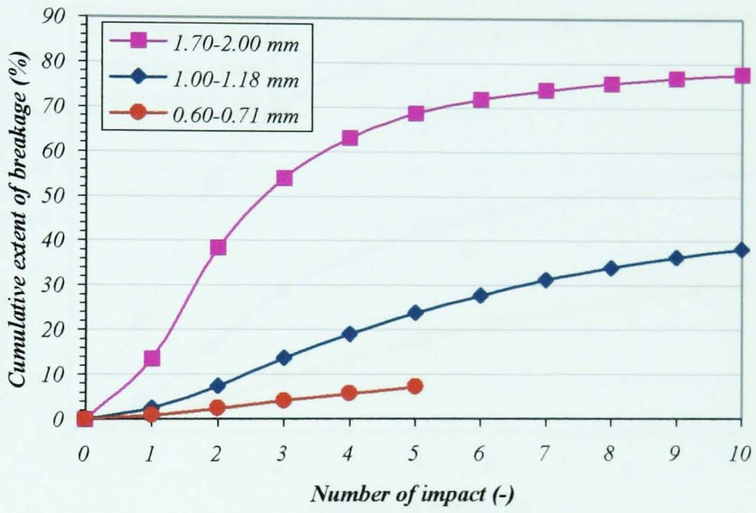

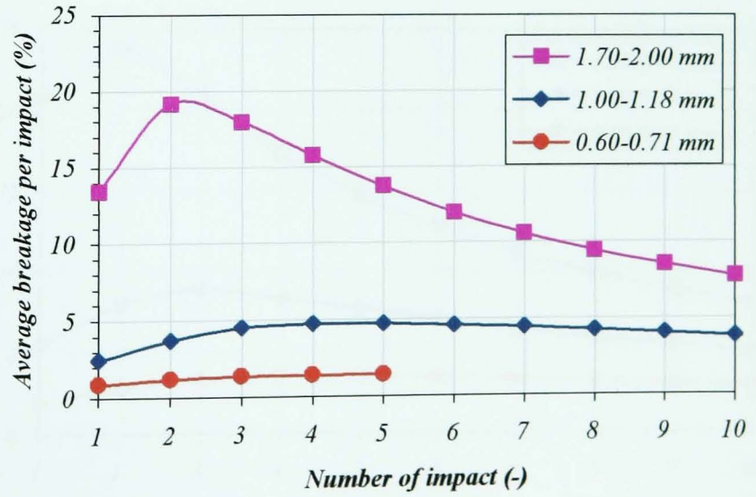

Figure B4: *Effect of feed size on incremental and cumulative breakage, and average breakage per impact of Sample 2 granules at impact velocity of 20 m* s^{-1}.

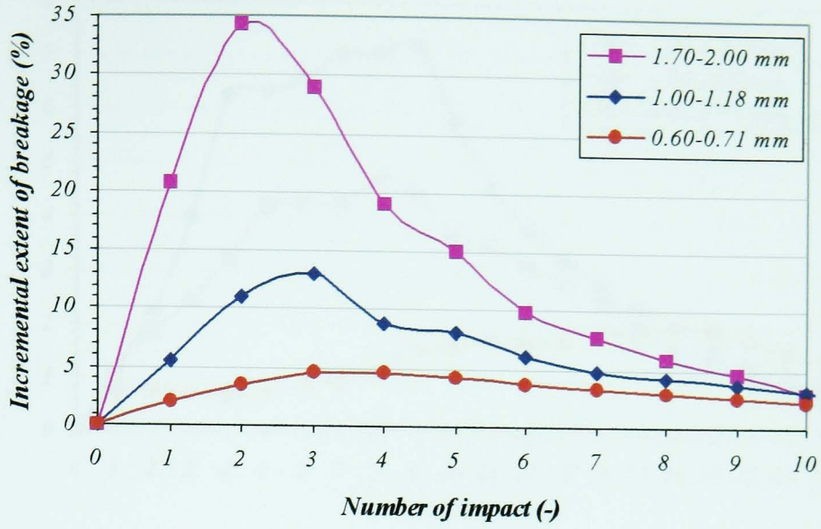

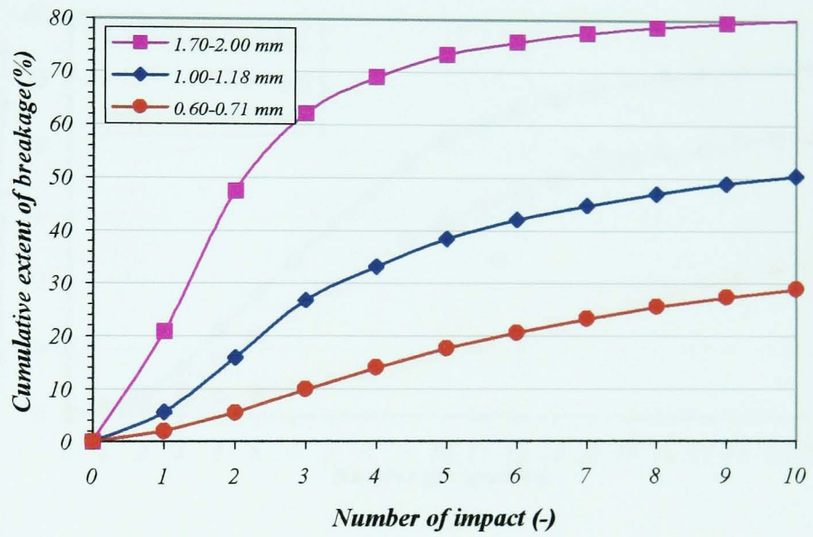

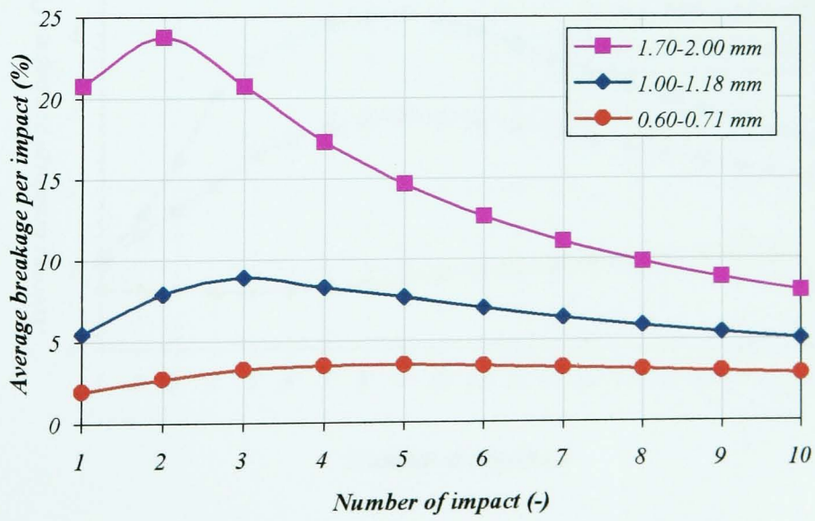

Figure B5: *Effect of feed size on incremental and cumulative breakage, and average breakage per impact of Sample 2 granules at impact velocity of 25 m* s^{-1}.

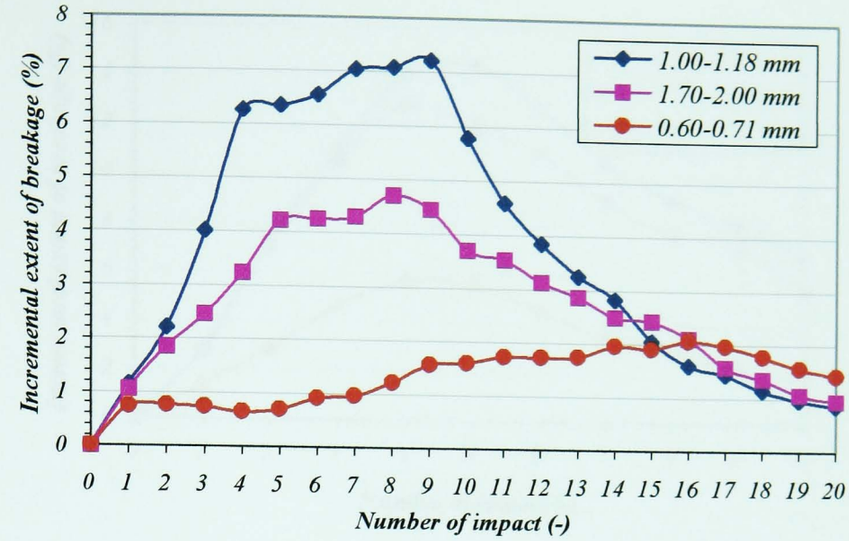

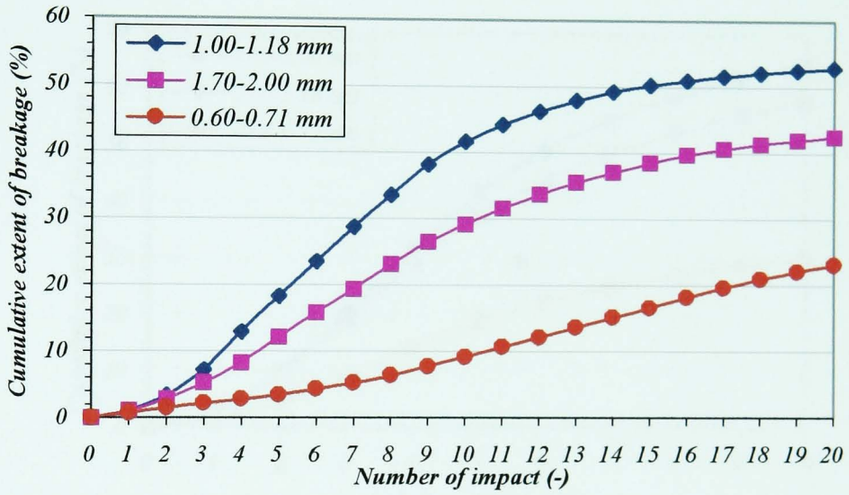

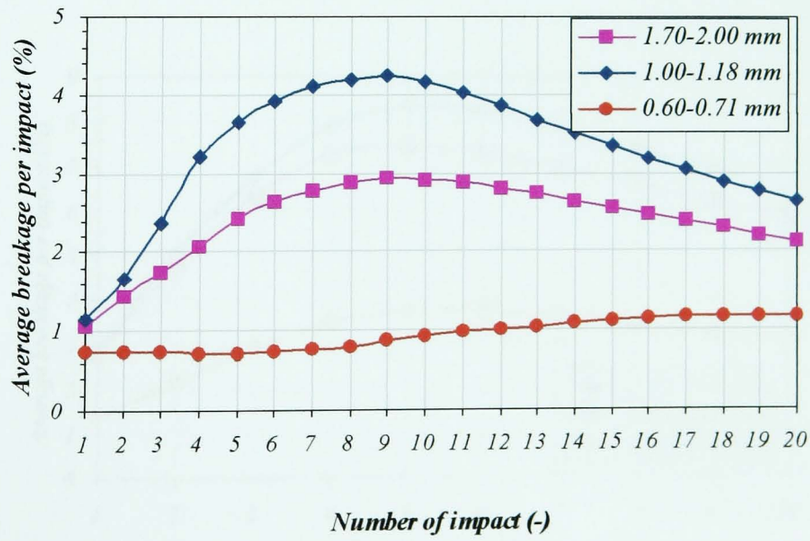

Figure B6: *Effect of feed size on incremental and cumulative breakage, and average breakage per impact of Sample 3 granules at impact velocity of 15 m* s^{-1}.

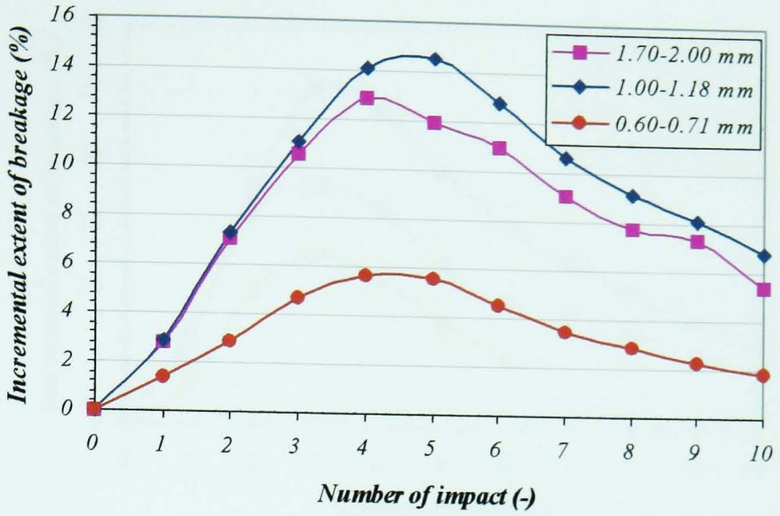

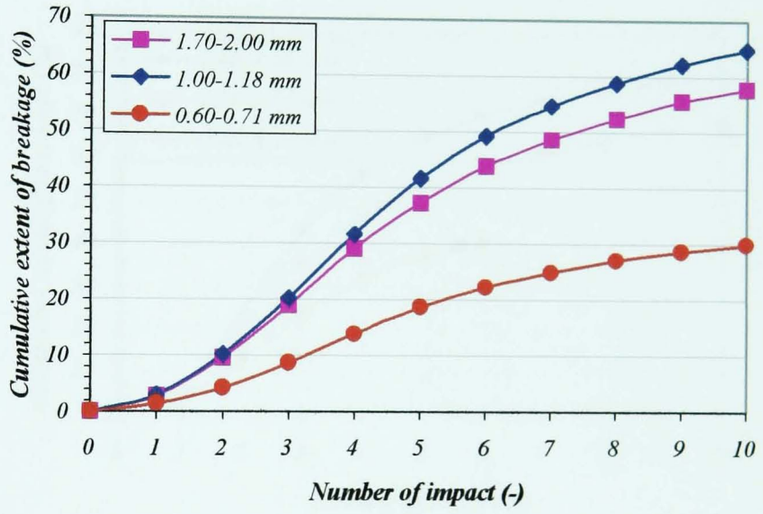

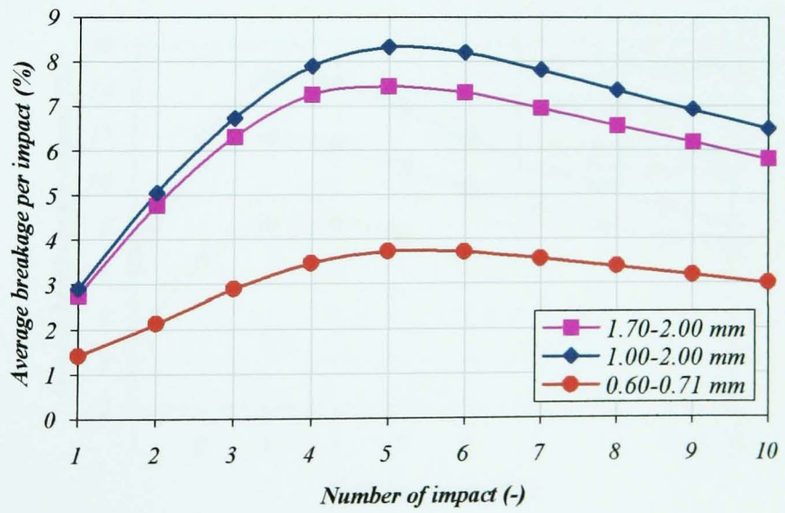

Figure B7: *Effect of feed size on incremental and cumulative breakage, and average breakage per impact of Sample 3 granules at impact velocity of 20 m* s^{-1}.

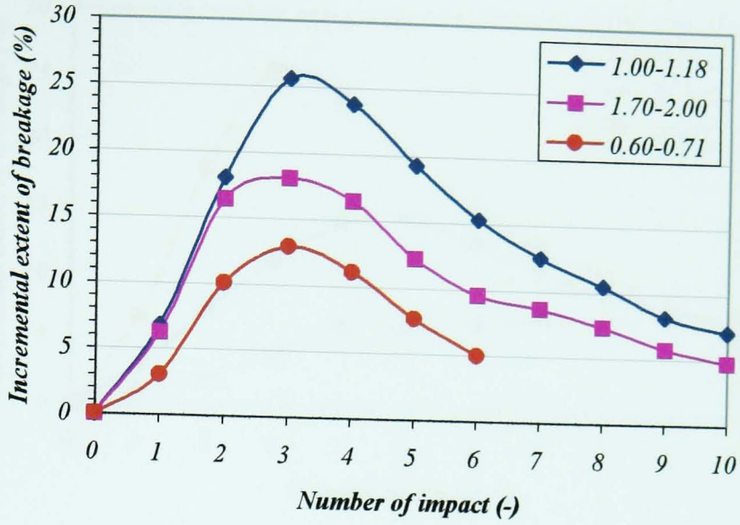

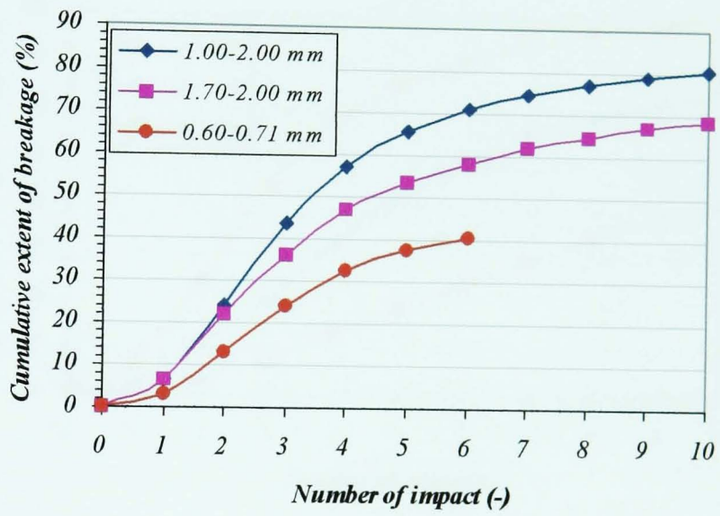

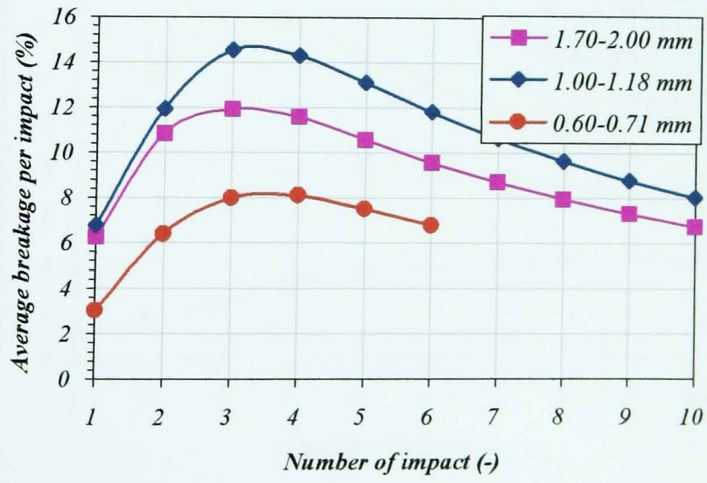

Figure B8: *Effect of feed size on incremental and cumulative breakage, and average breakage per impact of Sample 3 granules at impact velocity of 25 m* s^{-1}.

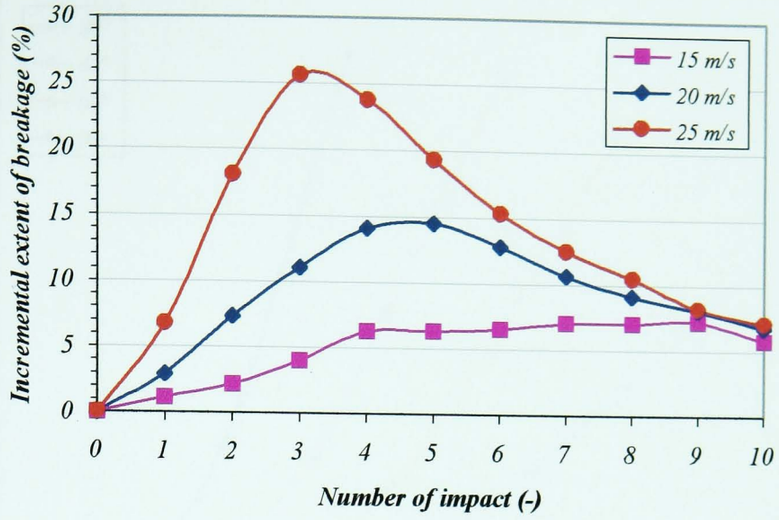

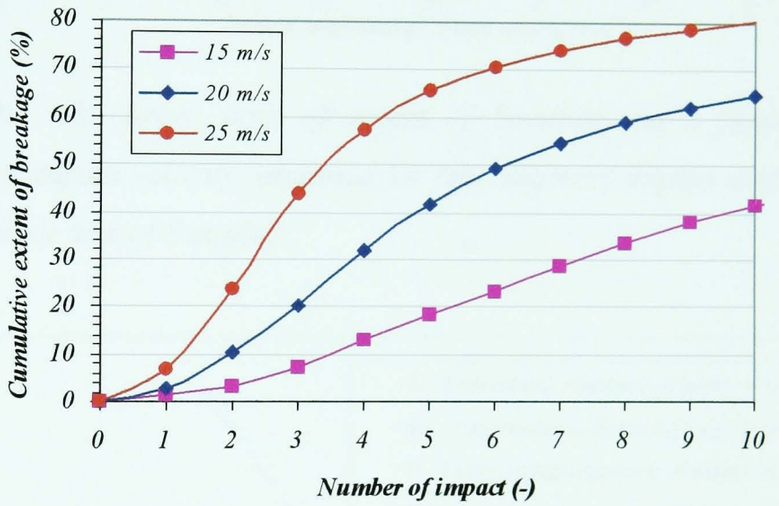

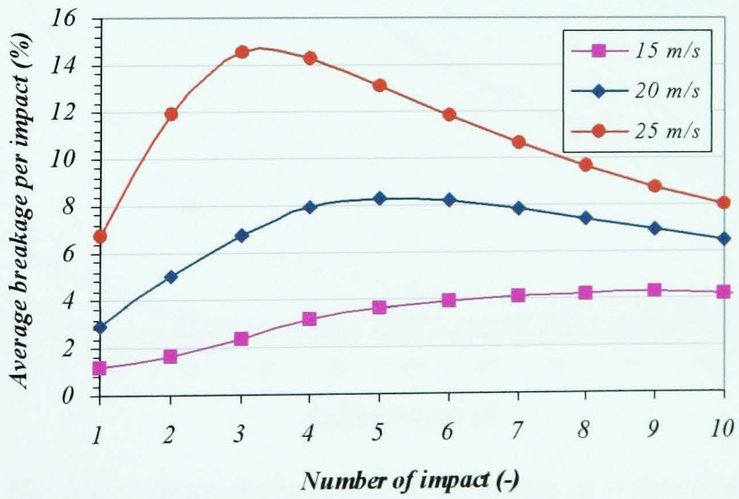

Figure B9: *Effect of impact velocity on incremental, cumulative breakage and average breakage per impact of 1.00-1.18 mm feed granule size of Sample 3.*

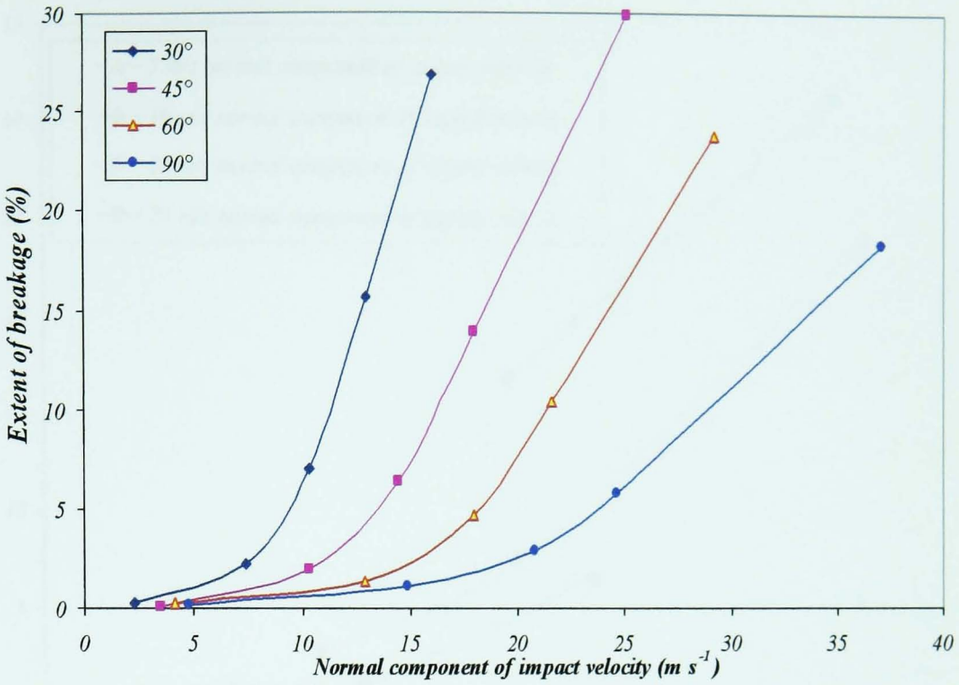

Figure B10: *The lower limit of extent of breakage as a function of normal component of impact velocity, obtained for four different impact angles of 1.00-1.18 mm feed granule size of Sample2.*

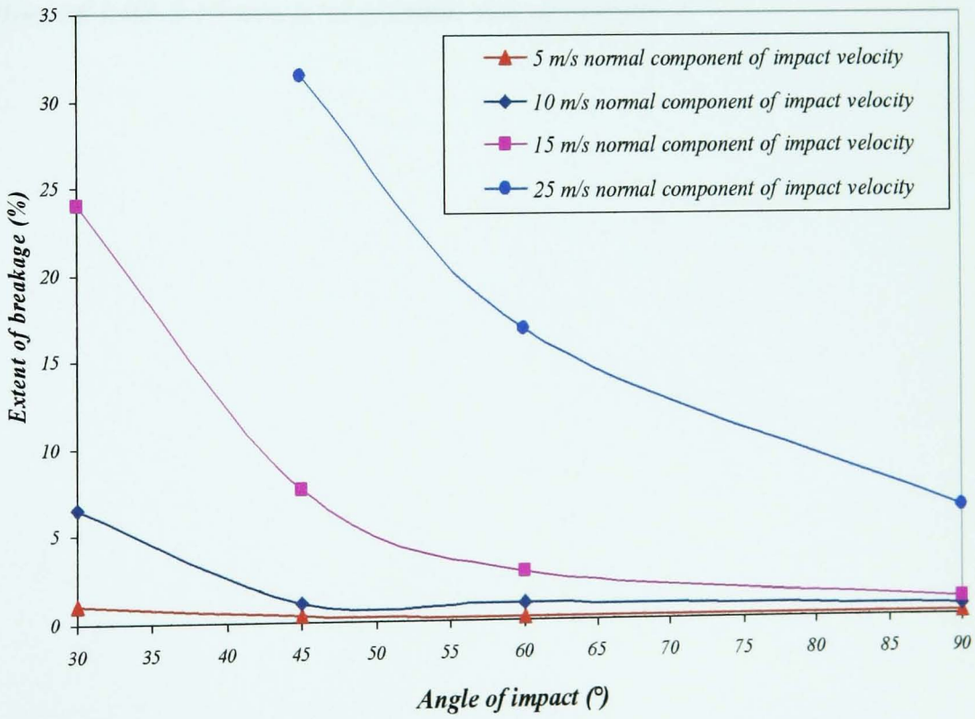

Figure B11: *The lower limit of the extent of breakage as a function of impact angle, obtained for four constant normal components of impact velocities of 100-1.18 mm feed granule size of Sample 2.*

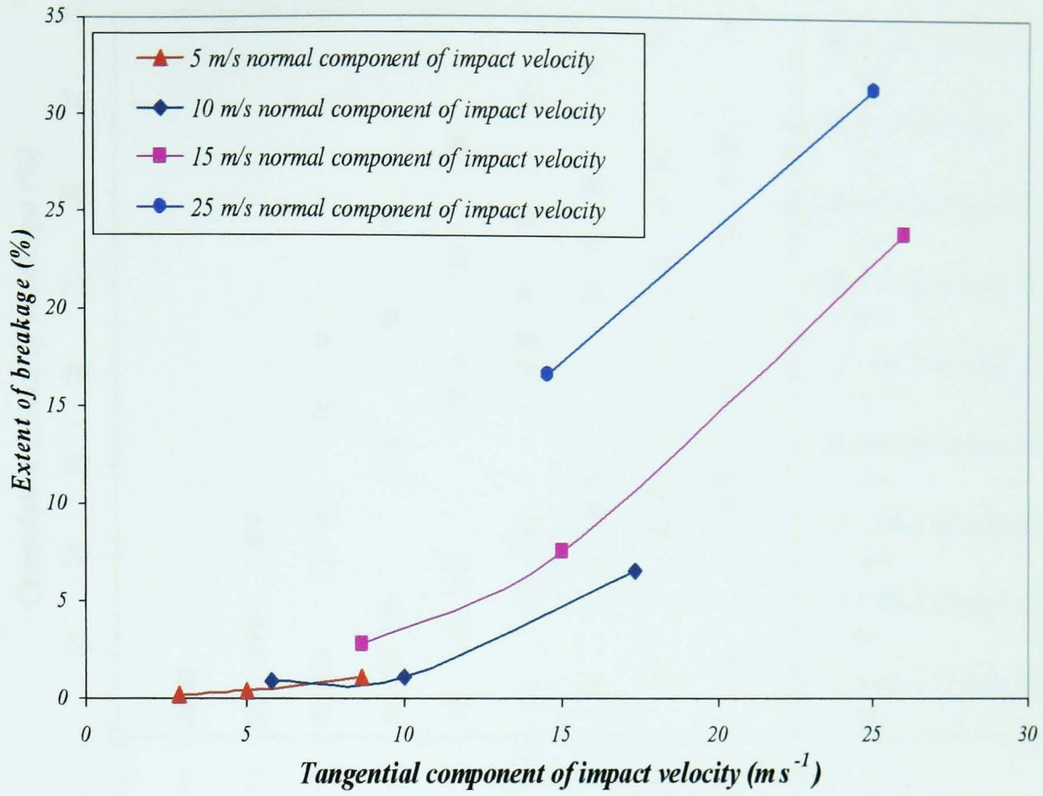

Figure B12: *The lower limit of extent of breakage as a function of tangential component of impact velocity for four constant normal components of impact velocities of 1.00-1.18 mm feed granule size of Sample 2.*

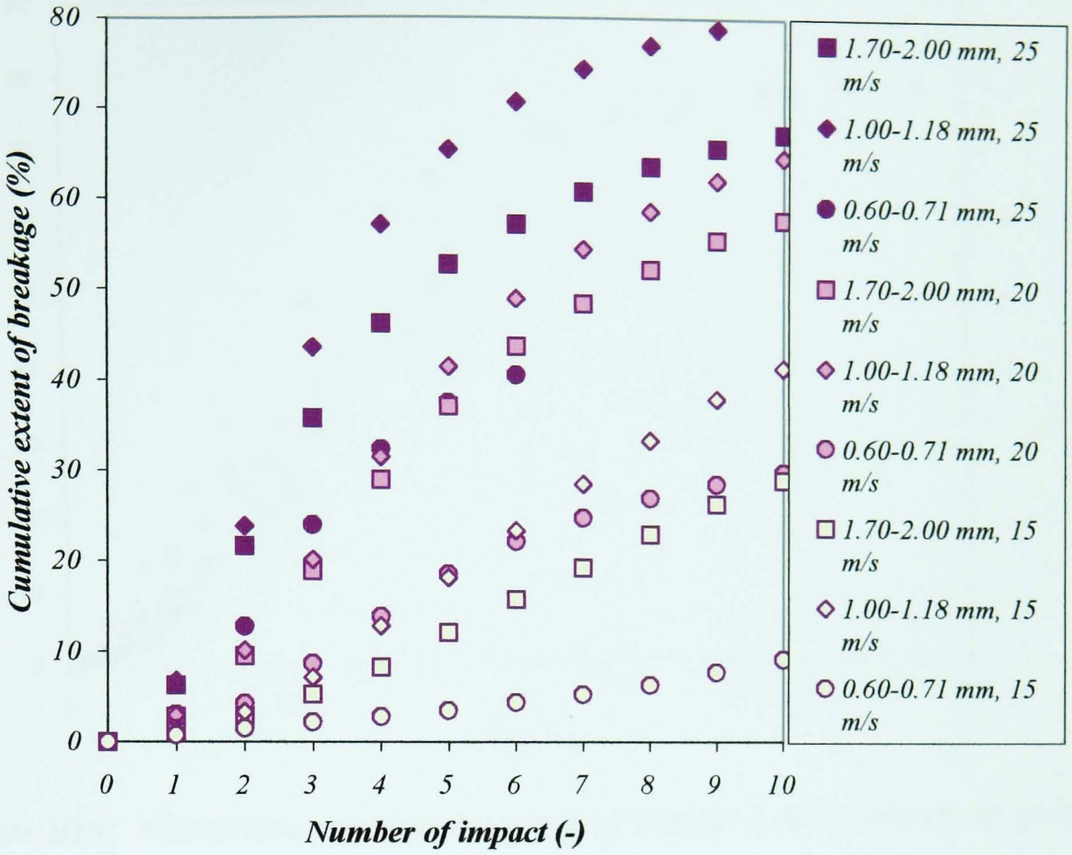

Figure B13: *Cumulative extent of breakage of Sample 3 as a function of impact number.*

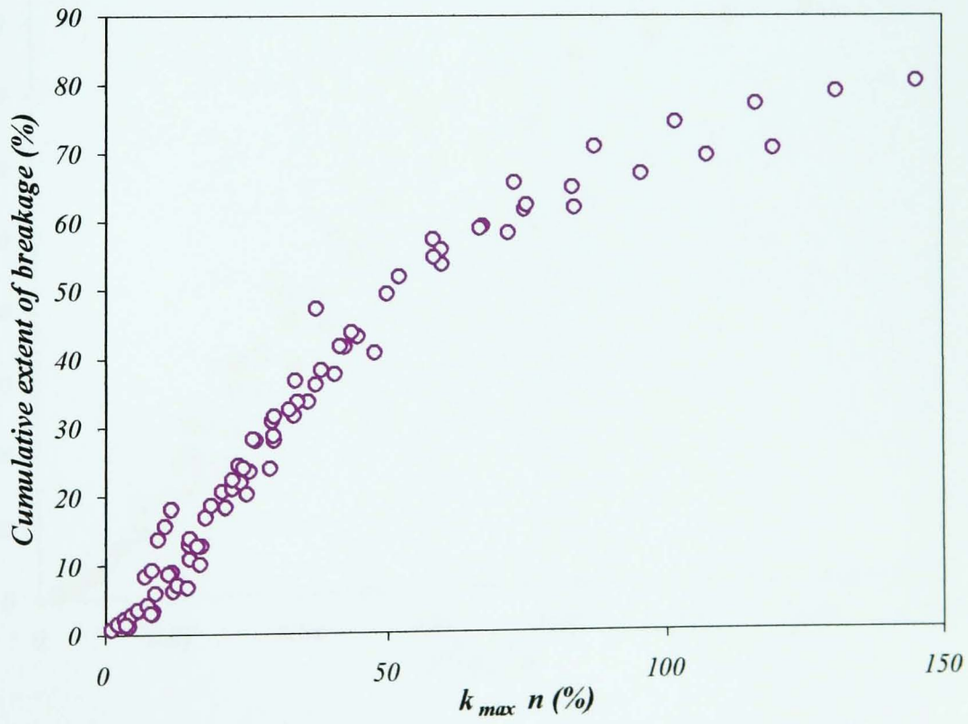

Figure B14: *Cumulative extent of breakage of Sample 3 as a function of product of impact number and maximum average breakage per impact.*

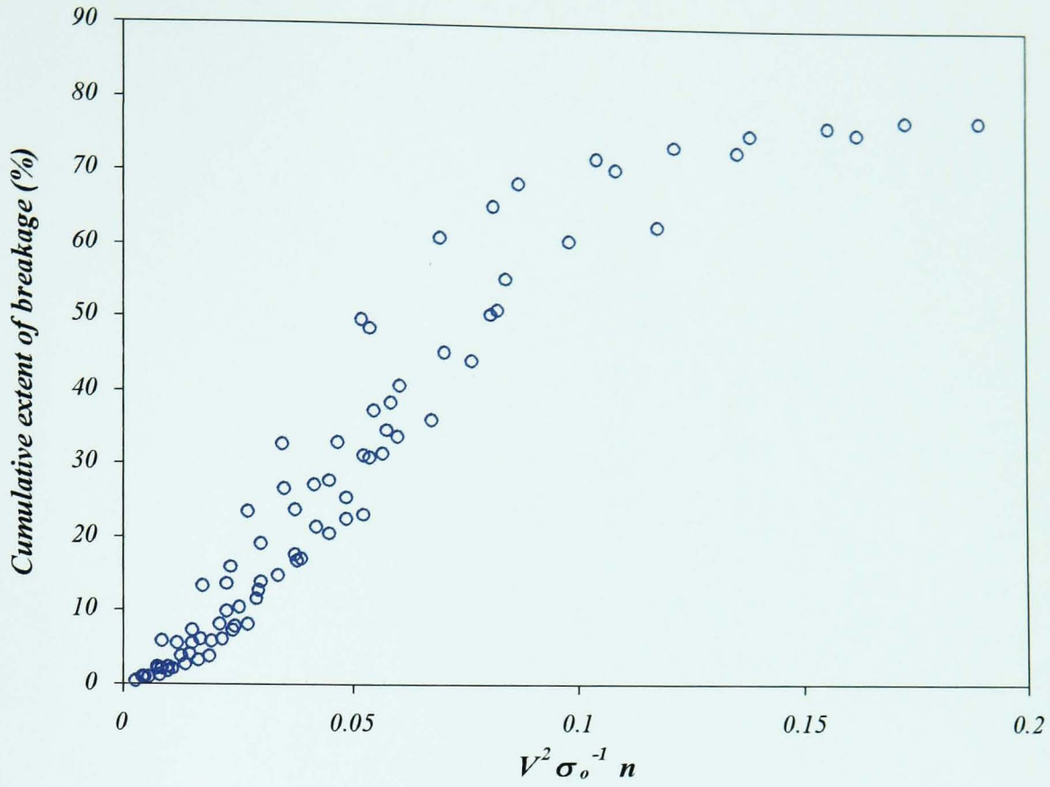

Figure B15: *Cumulative extent of breakage of Sample 2 as a function of group given in Equation 6.34.*

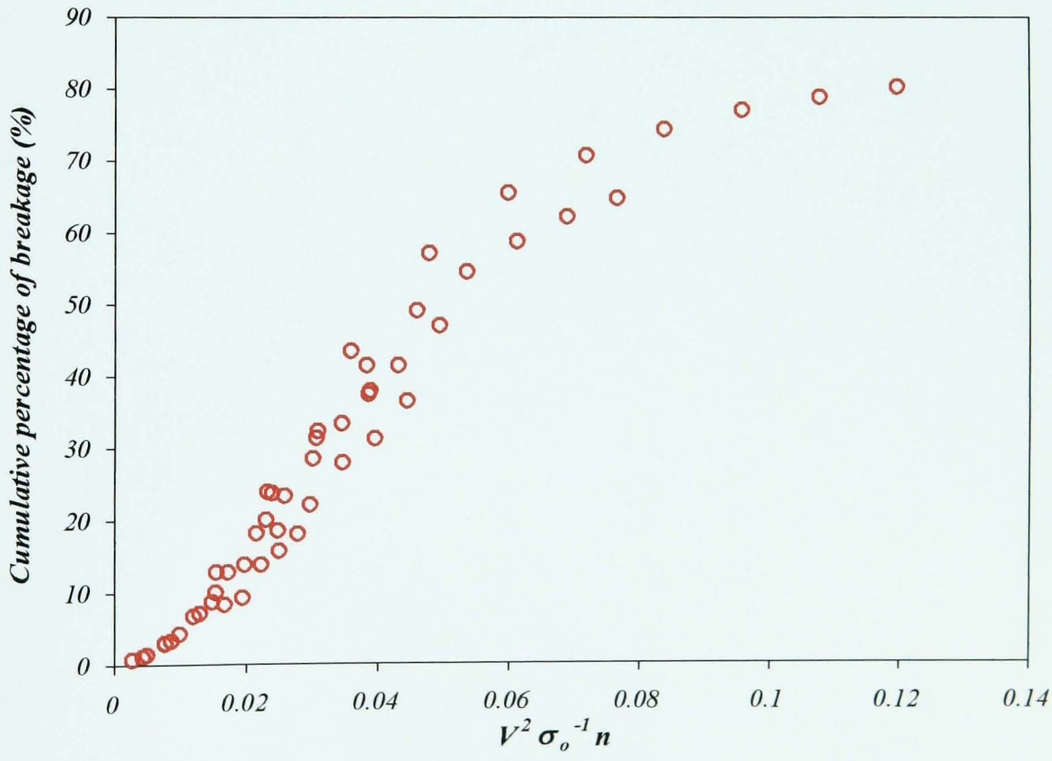

Figure B16: *Cumulative extent of breakage of Sample 3 as a function of group given in Equation 6.34.*